IntechOpen

Earthquake Research and Analysis

Statistical Studies, Observations and Planning

Edited by Sebastiano D'Amico

EARTHQUAKE RESEARCH AND ANALYSIS – STATISTICAL STUDIES, OBSERVATIONS AND PLANNING

Edited by **Sebastiano D'Amico**

Earthquake Research and Analysis - Statistical Studies, Observations and Planning
http://dx.doi.org/10.5772/2461
Edited by Sebastiano D'Amico

Contributors

Elvis Pontes, Sergio Kofuji, Adilson Guelfi, Anderson Silva, Samvel Gerasim Gevorgyan, Ming-Ching T. Kuo, Tomohiro Hasumi, Yoji Aizawa, Takuma Akimoto, Chien-Chih Chen, Yasuichi Kitamura, Youngseok Lee, Koji Okamura, Xuebin Du, Nuray Balkis, Huadong Guo, Liangyun Liu, Xiangtao Fan, Xinwu Li, Lu Zhang, Konstantinos Athanassios Eftaxias, Leszek R. Jaroszewicz, Zbigniew Krajewski, Krzysztof Teisseyre, Dumitru Stanica, Armand Dragos Stanica, Guangqi Chen, Yange Li, Yingbin Zhang, Jian Wu, Ivan Tikhonov, Michael Rodkin, Sule Tudes, Asta Gregoric, Drago Torkar, Sašo Džeroski, Janja Vaupotič, Boris Zmazek, Takeshi Sakaki, Yutaka Matsuo, Daniela Morelli, Giuseppina Immè, Robson Dos Santos França, Maria Das Graças B. Marietto, Nizam Omar, Margarethe Born Steinberger-Elias, Robin Crockett, Ayten Yigiter

Notice

First published in Croatia, 2012 by INTECH d.o.o.
eBook (PDF) Published by IN TECH d.o.o.
Place and year of publication of eBook (PDF): Rijeka, 2019.
IntechOpen is the global imprint of IN TECH d.o.o.
Printed in Croatia

Legal deposit, Croatia: National and University Library in Zagreb

Additional hard and PDF copies can be obtained from orders@intechopen.com

Earthquake Research and Analysis - Statistical Studies, Observations and Planning
Edited by Sebastiano D'Amico

p. cm.

ISBN 978-953-51-0134-5

eBook (PDF) ISBN 978-953-51-4338-3

Meet the editor

Dr Sebastiano D'Amico (Ph.D.) has been working as Research Officer III at the University of Malta, within the Physics Department, since 2010. He was enrolled in the Physics program of the University of Messina where he was awarded the title of "Dottore in Fisica". In 2005 he moved to Rome where he joined the Istituto Nazionale di Geofisica e Vulcanologia (INGV). In 2007 he married Rosarianna and together with his wife he moved to U.S.A. to join the Saint Louis University (Earth and Atmospheric Sciences Department). His research interests are in the applied aspects of earthquake seismology. He is the author of several publications in this field. In particular, he is interested in seismicity and tectonics of the Central Mediterranean, earthquake ground motion and seismic hazard, earthquake moment tensor solutions, and ambient noise measurements on soil and buildings

Contents

Preface XIII

Part 1 Statistical Seismology 1

Chapter 1 **The Weibull – Log-Weibull Transition of Interoccurrence Time of Earthquakes 3**
Tomohiro Hasumi, Chien-chih Chen, Takuma Akimoto and Yoji Aizawa

Chapter 2 **Change Point Analysis in Earthquake Data 25**
Ayten Yiğiter

Part 2 Studies on Earthquake Precursors and Forecasting 41

Chapter 3 **Current State of Art in Earthquake Prediction, Typical Precursors and Experience in Earthquake Forecasting at Sakhalin Island and Surrounding Areas 43**
I.N. Tikhonov and M.V. Rodkin

Chapter 4 **Earthquakes Precursors 79**
Dumitru Stanica and Dragos Armand Stanica

Chapter 5 **Earthquake Prediction: Analogy with Forecasting Models for Cyber Attacks in Internet and Computer Systems 101**
Elvis Pontes, Anderson A. A. Silva, Adilson E. Guelfi and Sérgio T. Kofuji

Chapter 6 **Identification of Simultaneous Similar Anomalies in Paired Time-Series 125**
R. G. M. Crockett

Chapter 7 **Radon as Earthquake Precursor 143**
Giuseppina Immè and Daniela Morelli

Chapter 8 **Application of Recurrent Radon Precursors for Forecasting Local Large and Moderate Earthquakes 161**
Ming-Ching T. Kuo

Chapter 9 **Radon as an Earthquake Precursor – Methods for Detecting Anomalies 179**
Asta Gregorič, Boris Zmazek, Sašo Džeroski, Drago Torkar and Janja Vaupotič

Chapter 10 **Changes in Apparent Resistivity in the Late Preparation Stages of Strong Earthquakes 197**
Du Xuebin, An Zhanghui, Yan Rui, Ye Qing, Fan Yingying, Liu Jun, Chen Junying and Tan Dacheng

Chapter 11 **Are There Pre-Seismic Electromagnetic Precursors? A Multidisciplinary Approach 217**
Konstantinos Eftaxias

Chapter 12 **The Effect of Marmara (Izmit) Earthquake on the Chemical Oceanography and Mangan Enrichment in the Lower Layer Water of Izmit Bay, Turkey 247**
Nuray Balkis

Part 3 Earthquake Observatories 273

Chapter 13 **Newly-Proposed Methods for Early Detection of Incoming Earthquakes, Tsunamis & Tidal Motion 275**
Samvel G. Gevorgyan

Chapter 14 **Earth Observation for Earthquake Disaster Monitoring and Assessment 293**
Huadong Guo, Liangyun Liu, Xiangtao Fan, Xinwu Li and Lu Zhang

Chapter 15 **Earthquake Observation by Social Sensors 313**
Takeshi Sakaki and Yutaka Matsuo

Chapter 16 **Fibre-Optic Sagnac Interferometer as Seismograph for Direct Monitoring of Rotational Events 335**
Leszek R. Jaroszewicz, Zbigniew Krajewski and Krzysztof P. Teisseyre

Part 4 Earthquakes and Planning 359

Chapter 17 **Experience with Restoration of Asia Pacific Network Failures from Taiwan Earthquake 361**
Yasuichi Kitamura, Youngseok Lee, Ryo Sakiyama and Koji Okamura

Chapter 18 **Earthquake Induced a Chain Disasters 383**
Guangqi Chen, Yange Li, Yingbin Zhang and Jian Wu

Chapter 19 **Correlation Between Geology, Earthquake and Urban Planning 417**
Sule Tudes

Chapter 20 **Simulating Collective Behavior in Natural Disaster Situations: A Multi-Agent Approach 435**
Robson dos Santos França, Maria das Graças B. Marietto, Margarethe Born Steinberger and Nizam Omar

Preface

Theoretical studies on earthquakes as well as practical applications are really important in order to define the assessment of seismic hazard and risk in a particular area. This is probably the most important contribution of seismology to society. Recent earthquakes have shown the inadequacy of a massive portion of the buildings erected in and around the epicentral areas, therefore research on earthquakes became more and more important. Up to date the scientific community agrees that the earthquake prediction is not possible. In fact, scientists cannot predict the exact location, magnitude and time of an earthquake striking a particular area. Scientists still do not know many of the details of the physical processes involved in earthquakes and they remain unpredictable. However, several scientists are working on earthquake precursors and forecasting studies and this represent a big challenge.

Chapters in this book will be devoted to various aspects of earthquake research and analysis, from theoretical advances to practical applications. The first two chapters are dedicated to statistical studies. About ten chapters in section II focus on studies about earthquake precursors and forecasting. Some chapters propose new methods for early detection, as well as the earthquake observation through the use of social sensors. The last section presents nice contributions that aim to link earthquakes and disaster triggered in the area struck by a large. The last chapter presents a study on simulating collective behavior during natural disasters.

I would like to express my special thanks to Mr. Igor Babic, Ms Ivana Lorkovic, and Ms Ivana Zec. Last but not least, I would like to thank the whole staff of InTech - Open Access Publisher, especially Mr Igor Babic, for their professional assistance and technical support during all the process steps that have led to the realization of this book.

Sebastiano D'Amico
Research Officer III
Physics Department
University of Malta
Malta

Part 1

Statistical Seismology

1

The Weibull – Log-Weibull Transition of Interoccurrence Time of Earthquakes

Tomohiro Hasumi[1], Chien-chih Chen[2], Takuma Akimoto[3] and Yoji Aizawa[4]
[1]*Division of Environment, Natural Resources and Energy, Mizuho Information and Research Institute, Inc., Tokyo*
[2]*Department of Earth Sciences and Graduate Institute of Geophysics, National Central University, Jhongli, Taoyuan*
[3]*Department of Mechanical Engineering, Keio University, Yokohama*
[4]*Department of Applied Physics, Advanced School of Science and Engineering, Waseda University, Tokyo*
[1,3,4]*Japan*
[2]*Taiwan*

1. Introduction

Earthquakes are great complex phenomenon characterized by several empirical statistical laws (1). One of the most important statistical law is the Gutenberg - Richter law (2), where the cumulative number of $n(> m)$ of magnitude m satisfy the following relation:

$$\log n(> m) = a - bm, \tag{1}$$

where a and b are constants. b is so-called b-value and is similar to unity. Another important statistical law is a power law decay of the occurrence of aftershocks, called Omori law (3).

The time intervals between successive earthquakes can be classified into two types: interoccurrence times and recurrence times (4). Interoccurrence times are the interval times between earthquakes on all faults in a region, and recurrence times are the time intervals between earthquakes in a single fault or fault segment. For seismology, recurrence times mean the interval times of characteristic earthquakes that occur quasi-periodically in a single fault. Recently, a unified scaling law of interoccurrence times was found using the Southern California earthquake catalogue (5) and worldwide earthquake catalogues (6). In Corral's paper (6), the probability distribution of interoccurrence time, $P(\tau)$, can be written as

$$P(\tau) = Rf(R\tau), \tag{2}$$

$$f(R\tau) = C\frac{1}{(R\tau)^{1-\gamma}}\exp(-(R\tau)^{\delta}/B), \tag{3}$$

where R is the seismicity rate. He has found that $f(R\tau)$ follows the generalized gamma distribution. In equation (3), C is a normalized constant and is $C = 0.50 \pm 0.05$. γ, δ, and B are parameters estimated to be $\gamma = 0.67 \pm 0.05, \delta = 0.98 \pm 0.05$, and $B = 1.58 \pm 0.15$. It should

Catalog Name	Coverage	Term	Number of Earthquakes	m_{min}	m_c^0
JMA	25° –50° N and 125° –150° E	01/01/2001–31/1/2010	170,801	2.0	2.0
SCEDC	32° –37° N and 114° –122° W	01/01/2001–28/2/2010	116,089	0.0	1.4
TCWB	21° N–26° N and 119° –123° E	01/01/2001–28/2/2010	189,980	0.0	1.9

Table 1. Information on earthquake catalogues.

be noted that the interoccurrence times were analyzed for the events with the magnitude m above a certain threshold m_c under the following two assumptions: (a) earthquakes can be considered as a point process in space and time; (b) there is no distinction between foreshocks, mainshocks, and aftershocks. It has been shown that the distribution of the interoccurrence time is also obtained by analyzing aftershock data (7) and is derived approximately from a theoretical framework proposed by Saichev and Sornette (8; 9). Abe and Suzuki showed that the distribution of the interoccurrence time, $P(> \tau)$, can be described by q-exponential distribution with $q > 1$, corresponding to a power law distribution (10), namely,

$$P(> \tau') = \frac{1}{(1+\epsilon\tau')^{\gamma}} = e_q(-\tau'/\tau_0) = [\big(1+(1-q)(-\tau'/\tau_0)\big)^{\frac{1}{1-q}}]_+, \tag{4}$$

where q_t, τ_0, γ, and ϵ are positive constants and $([a]_+ \equiv \max[0, a])$.

It has been reported that the sequence of aftershocks and successive independent earthquakes is a Poisson process (11; 12). However, recent works show that interoccurrence times are not independent random variables, but have “long-term memory" (13–16). Since an interoccurrence time depends on the past, it is difficult to determine the distribution of interoccurrence times theoretically. Therefore, the determination of the distribution of interoccurrence times is still an open problem. Moreover, an effect of a threshold of magnitude on the interoccurrence time statistics is unknown. We study the distribution of interoccurrence times by changing the threshold of magnitude. In this chapter, we review our previous studies (17; 18) and clarify the Weibull - log-Weibull transition and its implication by reanalyzing the latest earthquake catalogues, JMA catalogue (19), SCEDC catalogue (20), and TCWB catalogue (21). This study focuses on the interoccurrence time statistics for middle or big mainshocks.

2. Data and methodology

2.1 Earthquake catalogue

To study the interoccurrence time statistics, we analyzed three natural earthquake catalogues of the Japan Metrological Agency (JMA) (19), the Southern California Earthquake Data Center (SCEDC) (20) and the Taiwan Central Weather Bureau (TCWB) (21). Information on each catalogue is listed in Table 1, where m_{min} corresponds to the minimum magnitude in the catalogue and m_c^0 is the magnitude of completeness, that is the lowest magnitude at which the Gutenberg - Richter law holds. We basically consider events with magnitude greater than and equal to m_c^0 because events whose magnitudes are smaller than m_c^0 are supposedly incomplete for recording.

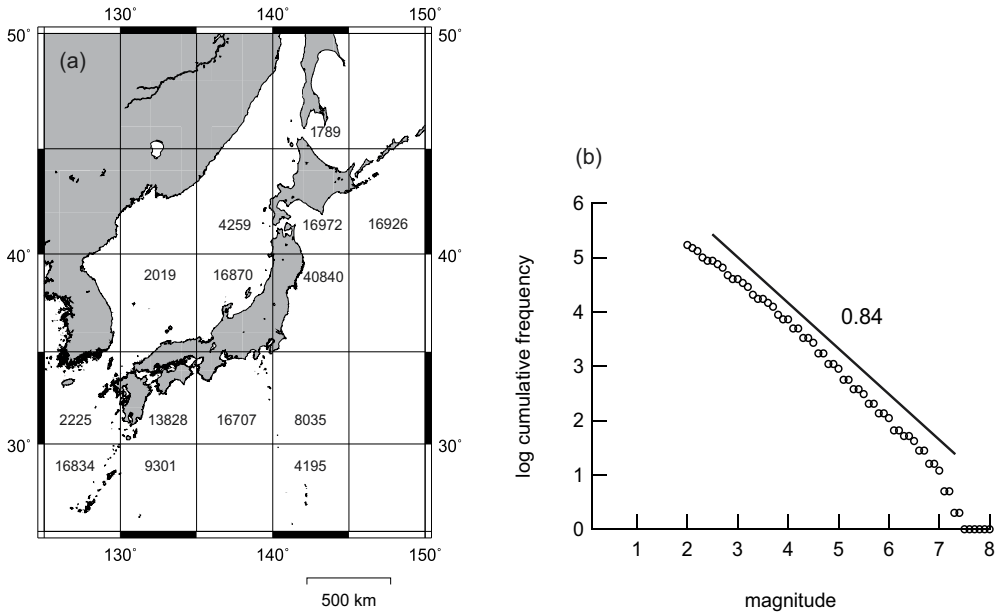

Fig. 1. Information on the Japan Metrological Agency (JMA) earthquake catalogues. (a) covering region. The number of each cell means the number of earthquakes. (b) the magnitude distribution. $b = 0.84$ is calculated from the slope of the distribution.

2.1.1 Japan Metrological Agency (JMA) earthquake catalogue

JMA catalogue is maintained by the Japan Metrological Agency, covering from 25° to 50° N for latitude, and from 25° to 150° E for longitude [see Figure 1 (a)] during from 1923 to latest. This catalogue consists of an occurrence of times, a hypocenter, a depth, and a magnitude. In this chapter, we use the data from 1st January 2001 to 31st January 2010. As can be seen from Figure 1 (b), the distribution of magnitude obeys the Gutenberg - Richter law and m_c^0 is estimated to be 2.0.

2.1.2 Southern California Earthquake Data Center (SCEDC) earthquake catalogue

SCEDC catalogue is maintained by the Southern California Earthquake Data Center, covering from 32° to 37° N for latitude, and from 114° to 122° W for longitude [see Figure 2 (a)] during from 1932 to latest. The information of an earthquake, such as an occurrence of times, a hypocenter, a depth, and a magnitude, is listed. Here, we analyze the earthquake data from 1st January 2001 to 28th February 2010. In Figure 2 (b), we demonstrate the magnitude distribution, and we obtain $b = 0.97$.

2.1.3 Taiwan Central Weather Bureau (TCWB) earthquake catalogue

TCWB catalogue is maintained by the Central Weather Bureau, covering from 21° to 26° N for latitude, and from 119° to 123° E for longitude [see Figure 3 (a)]. This catalogue consists of an occurrence of times, a hypocenter, a depth, and a magnitude. We use the data from 1st January 2001 to 28th February 2010. As shown in Figure 3 (b), the Gutenberg - Richter law is valid in a

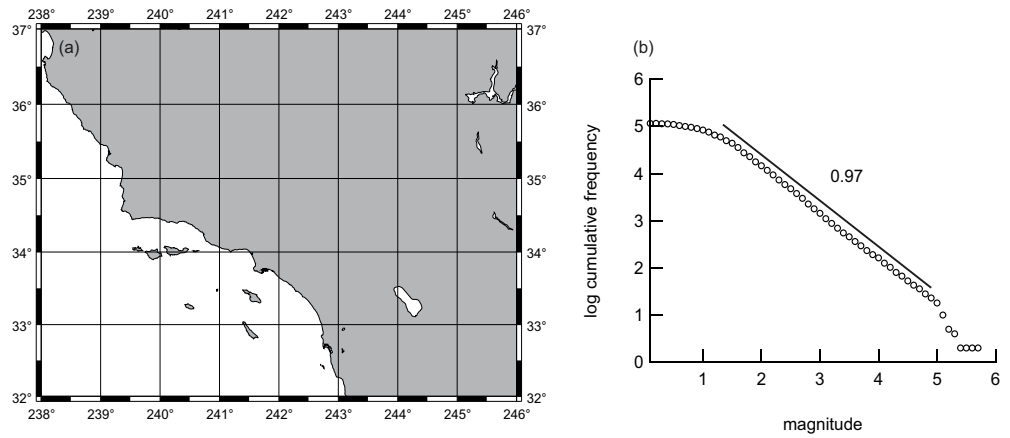

Fig. 2. Southern California Earthquake Data Center (SCEDC) earthquake catalogue information. (a) covering region. (b) the magnitude distribution. $b = 0.97$ is calculated from the slope of the distribution.

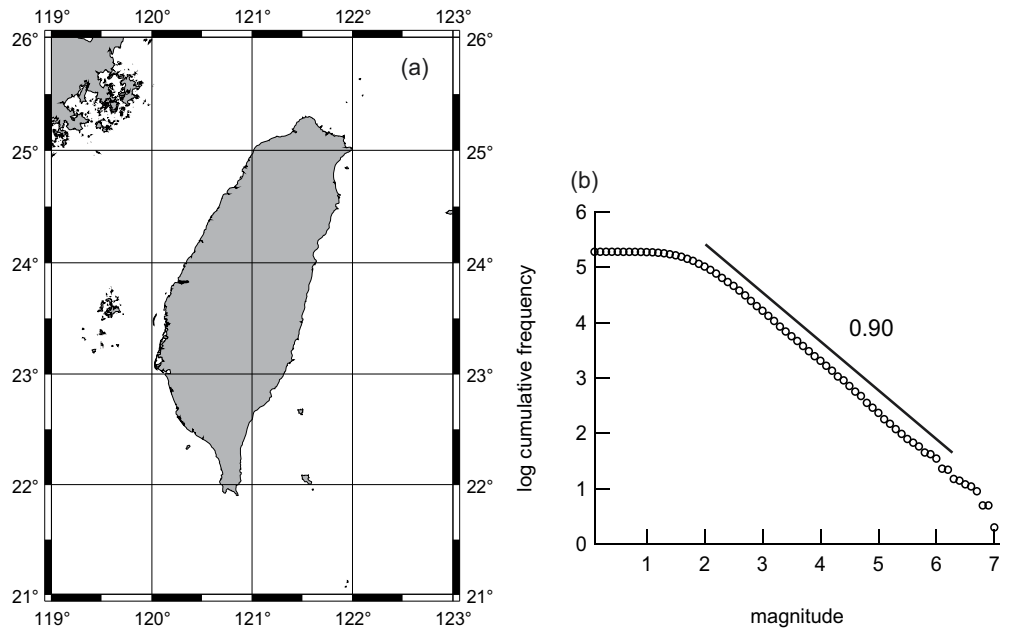

Fig. 3. Information on the Taiwan Central Weather Bureau (TCWB) earthquake catalogue. (a) covering region. (b) the magnitude distribution. $b = 0.90$ is calculated from the slope of the distribution.

magnitude range, $1.9 \leq m \leq 6.7$. b-value is calculated from the slope of the distribution, and is estimated to be 0.90.

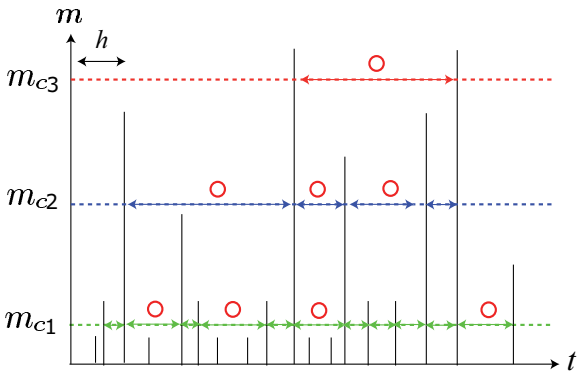

Fig. 4. Schematic diagram of the interoccurrence time of our analysis for different threshold of magnitude m_c. Circles (○) satisfy the condition. We analyze interoccurrence times greater than or equals to h.

2.2 Methodology (How to detect the appropriate distributions)

Our method is similar to the that of previous works (17; 18) (see Figure 4).

1. We divided the spatial areas into a window of L degrees in longitude and L degrees in latitude.
2. For each bin, earthquakes with magnitude m above a certain cutoff magnitude m_c were considered.
3. We analyzed interoccurrence times greater than and equals to h day.

For each bin, we analyzed interoccurrence times using at least 100 events to avoid statistical errors. h and L are taken to be 0.5 and 5, respectively. It is noted that for SCEDC and TCWB, we analyze earthquake covering the whole region. As shown in Figure 4, we investigated the interoccurrence time statistics for different 16 regions (14 regions in Japan, Southern California, and Taiwan). Aftershocks might be excluded from the study based on the information from previous studies (6; 12).

One of our main goals in this chapter is to determine the distribution function of the interoccurrence time. Here, we will focus our attention on the applicability of the Weibull distribution P_w, the log-Weibull distribution P_{lw} (22), the power law distribution P_{pow} (10), the gamma distribution P_{gam} (in the case of $\delta = 1$ in the paper (6)), and the log normal distribution P_{ln} (23), which are defined as

$$P_w(\tau) = \left(\frac{\tau}{\beta_1}\right)^{\alpha_1 - 1} \frac{\alpha_1}{\beta_1} \exp\left[-\left(\frac{\tau}{\beta_1}\right)^{\alpha_1}\right], \tag{5}$$

$$P_{lw}(\tau) = \frac{(\log(\tau/h))^{\alpha_2 - 1}}{(\log \beta_2)^{\alpha_2}} \frac{\alpha_2}{\tau} \exp\left[-\left(\frac{\log(\tau/h)}{\log \beta_2}\right)^{\alpha_2}\right], \tag{6}$$

$$P_{pow}(\tau) = \frac{1}{(1 + \beta_3 \tau)^{\alpha_3}}, \tag{7}$$

$$P_{gam}(\tau) = \tau^{\alpha_4 - 1} \frac{\exp(-\tau/\beta_4)}{\Gamma(\alpha_4) {\beta_4}^{\alpha_4}}, \tag{8}$$

$$P_{ln}(\tau) = \frac{1}{\tau \beta_5 \sqrt{2\pi}} \exp\left[-\frac{(\ln(\tau) - \alpha_5)^2}{2\beta_5^2} \right], \tag{9}$$

where α_i, β_i, and h are constants and characterize the distribution. $\Gamma(x)$ is the gamma function. i stands for an index number; $i = 1, 2, 3, 4$, and 5 correspond to the Weibull distribution, the log-Weibull distribution, the power law distribution, the gamma distribution, and the log normal distribution, respectively.

The Weibull distribution is well known as a description of the distribution of failure-occurrence times (24). In seismology, the distribution of ultimate strain (25), the recurrence time distribution (26; 27), and the damage mechanics of rocks (28) show the Weibull distribution. In numerical studies, the recurrence time distribution in the 1D (4) and 2D (29) spring-block model, and in the "Virtual California model" (30) also exhibit the Weibull distribution. For $\alpha_1 = 1$ and $\alpha_1 < 1$, the tail of the Weibull distribution is equivalent to the exponential distribution and the stretched exponential distribution, respectively. The log-Weibull distribution is constructed by a logarithmic modification of the cumulative distribution of the Weibull distribution. In general, the tail of the log-Weibull distribution is much longer than that of the Weibull distribution. As for $\alpha_2 = 1$, the log-Weibull distribution is equal to a power law distribution. It has been shown that the log-Weibull distribution can be derived from the chain-reaction model proposed by Huillet and Raynaud (22).

To determine the best fitting for the distribution of the interoccurrence time data, we used the root mean square (rms) and Kolomogorov-Smirnov (KS) tests as the measure of goodness-of-fit. The definition of the rms value is

$$\mathrm{rms} = \sqrt{\frac{\sum_{i=1}^{n} (x_i - x_i')^2}{n - k}}, \tag{10}$$

where x_i is actual data and x_i' is estimated data obtained from $P(\tau)$. n and k indicate the numbers of the data points and of the fitting parameters, respectively. In this study, the rms value is calculated using the cumulative distribution for decreasing the fluctuation of the data. The most appropriate distribution is, by definition, the smallest rms value. Also, in order to use the KS test, we define the maximum deviation of static DKS, which is so-called Kolomogorov-Smirnov statistic, as

$$\mathrm{DKS} = \max_i |y_i - y_i'|, \tag{11}$$

where y_i and y_i' mean the actual data of the cumulative distribution and the data estimated from the fitting distribution, respectively. Then, the significance level of probability of the goodness-of-fit, Q, is defined as

$$Q = 2 \sum_{i=1}^{\infty} (-1)^{i-1} e^{2i^2\lambda^2}, \tag{12}$$

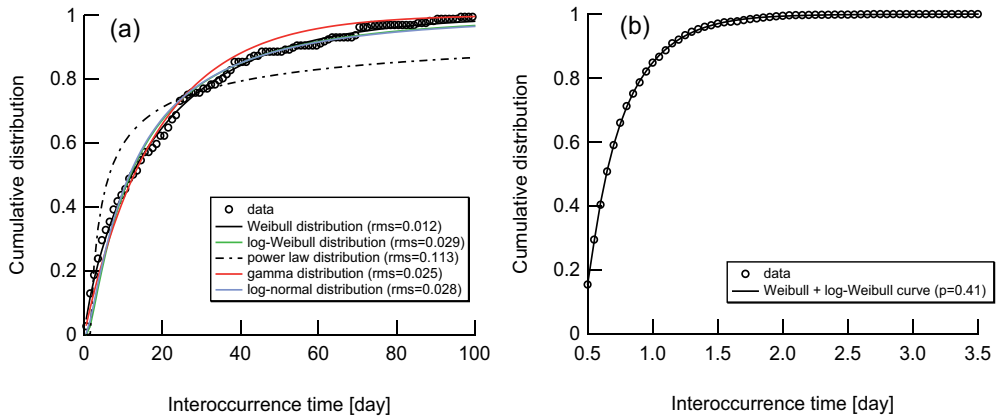

Fig. 5. Cumulative distribution of interoccurrence time at Okinawa region different m_c. The cumulative distribution is plotted by circles. (a) Several fitting curves are represented by lines ($m_c = 4.5$). (b) The superposition of the Weibull and the log-Weibull distribution is represented by line ($m_c = 2.0$).

where

$$\lambda = DKS\left(\sqrt{n'} + 0.12 + \frac{0.11}{\sqrt{n'}}\right), \tag{13}$$

where n' stands for the number of data points.

It is known that the preferred distribution shows the smallest value of DKS and the largest value of Q (31).

3. Results

3.1 Interoccurrence time statistics in Japan

First, we analyze the JMA data. Here, we consider the two region; Okinawa region (125°–130°E and 25°–30°N), and Chuetsu region (135°–140°E and 35°–40°N). The total number of earthquakes in Okinawa and Chuetsu are 16,834 and 16,870, respectively.

The cumulative distributions of the interoccurrence times for different m_c in Okinawa region and in Chuetsu region are displayed in Figures 5 and 6, respectively. We carried out two statistical tests, the rms and the KS test so as to determine the distribution function. The results for large magnitude ($m_c = 4.5$) in Okinawa and Chuetsu are shown in Table 2 and 3, respectively. For Okinawa, we found that the most suitable distribution is the Weibull distribution in all tests. In general, there is a possibility that the preferred distribution is not unique but depends on the test we use. However, the results obtained in Table 2 provide evidence that the Weibull distribution is the most appropriate distribution. As for Chuetsu, by two tests, the preferred distribution is suited to be the Weibull distribution as shown in Table 3, where the Weibull distribution is the most prominent distribution in the two tests. It follows that the Weibull distribution is preferred.

m_c		Distribution X		RMS test	KS test	
Region	distribution X	α_i	β_i [day]	rms [$\times 10^{-3}$]	DKS	Q
	P_w $(i=1)$	0.82 ± 0.007	19.0 ± 0.13	12	0.03	1
	P_{lw} $(i=2)$	3.08 ± 0.06	35.3 ± 0.57	29	0.1	0.15
4.5	P_{pow} $(i=3)$	1.48 ± 0.02	1.04 ± 0.12	113	0.23	3.8×10^{-3}
Okinawa	P_{gam} $(i=4)$	0.96 ± 0.005	19.5 ± 0.24	24	0.07	0.55
	P_{ln} $(i=5)$	2.45 ± 0.02	1.20 ± 0.02	28	0.09	0.33

Table 2. Results of rms value, DKS, and Q for different distribution functions for Okinawa area ($m_c = 4.5$). The error bars mean the 95% confidence level of fit.

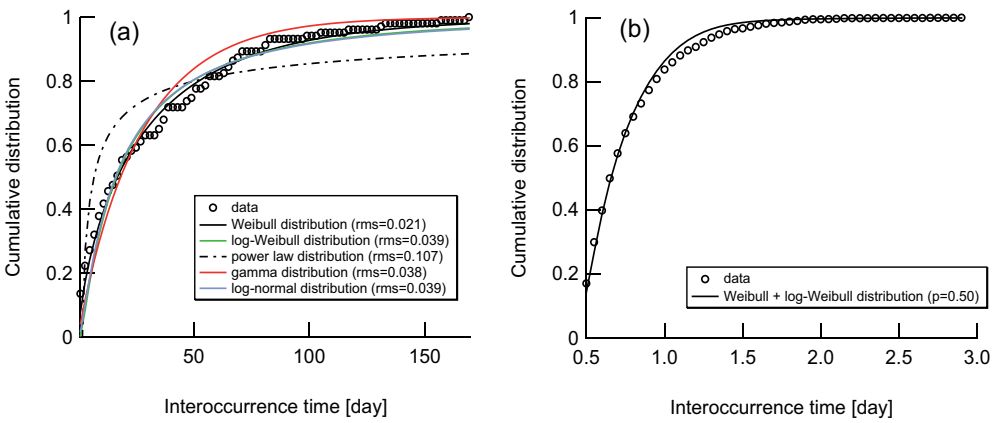

Fig. 6. Cumulative distribution of interoccurrence time for Chuetsu area different m_c. The cumulative distribution is plotted by circles. (a) Several fitting curves are represented by lines ($m_c = 4.5$). (b) The superposition of the Weibull and the log-Weibull distribution is represented by line ($m_c = 2.0$).

m_c		Distribution X		RMS test	KS test	
Region	distribution X	α_i	β_i [day]	rms [$\times 10^{-3}$]	DKS	Q
	P_l $(i=1)$	0.75 ± 0.01	27.6 ± 0.40	21	0.06	0.94
	P_{lw} $(i=2)$	3.12 ± 0.10	51.4 ± 1.39	39	0.14	0.06
4.5	P_{pow} $(i=3)$	1.47 ± 0.03	1.51 ± 0.21	107	0.19	4.8×10^{-3}
Chuetsu	P_{gam} $(i=4)$	0.94 ± 0.009	28.9 ± 0.67	38	0.11	0.27
	P_{ln} $(i=5)$	2.78 ± 0.03	1.33 ± 0.04	39	0.12	0.15

Table 3. Results of rms value, DKS, and Q for different distribution functions for Chuetsu area ($m_c = 4.5$). The error bars mean the 95% confidence level of fit.

m_c		Weibull distribution		Distribution X			RMS test	KS test	
Region	distribution X	α_1	β_1 [day]	α_i	β_i [day]	p	rms [$\times 10^{-3}$]	DKS	Q
	P_{lw} $(i=2)$	0.82 ± 0.007	19.0 ± 0.13	–	–	1	12	0.03	1
4.5	P_{pow} $(i=3)$	0.82 ± 0.007	19.0 ± 0.13	–	–	1	12	0.03	1
Okinawa	P_{gam} $(i=4)$	0.82 ± 0.007	19.0 ± 0.13	–	–	1	12	0.03	1
	P_{ln} $(i=5)$	0.82 ± 0.007	19.0 ± 0.13	–	–	1	12	0.03	1
	P_{lw} $(i=2)$	0.93 ± 0.009	8.47 ± 0.06	–	–	1	13	0.03	1
4.0	P_{pow} $(i=3)$	0.93 ± 0.009	8.47 ± 0.06	–	–	1	13	0.03	1
Okinawa	P_{gam} $(i=4)$	0.93 ± 0.009	8.47 ± 0.06	–	–	1	13	0.03	1
	P_{ln} $(i=5)$	0.93 ± 0.009	8.47 ± 0.06	–	–	1	13	0.03	1
	P_{lw} $(i=2)$	1.07 ± 0.008	3.45 ± 0.02	2.07 ± 0.04	6.25 ± 0.09	0.77 ± 0.02	5.3	0.02	1
3.5	P_{pow} $(i=3)$	1.07 ± 0.008	3.45 ± 0.02	1.81 ± 0.04	0.64 ± 0.04	0.94 ± 0.009	7.3	0.03	1
Okinawa	P_{gam} $(i=4)$	1.07 ± 0.008	3.45 ± 0.02	–	–	1	8.8	0.04	1
	P_{ln} $(i=5)$	1.07 ± 0.008	3.45 ± 0.02	0.85 ± 0.009	0.94 ± 0.01	0.65 ± 0.03	5.6	0.02	1
	P_{lw} $(i=2)$	1.44 ± 0.02	1.77 ± 0.02	1.40 ± 0.03	2.57 ± 0.04	0.58 ± 0.01	3.8	0.01	1
3.0	P_{pow} $(i=3)$	1.41 ± 0.02	1.63 ± 0.01	2.22 ± 0.04	0.55 ± 0.01	0.79 ± 0.01	8.8	0.07	0.73
Okinawa	P_{gam} $(i=4)$	1.41 ± 0.02	1.63 ± 0.01	–	–	1	17	0.1	0.34
	P_{ln} $(i=5)$	1.41 ± 0.02	1.63 ± 0.01	0.20 ± 0.003	0.72 ± 0.003	0.04 ± 0.03	5.4	0.04	1
	P_{lw} $(i=2)$	1.72 ± 0.02	1.14 ± 0.008	1.25 ± 0.01	1.68 ± 0.01	0.47 ± 0.006	2.1	0.007	1
2.5	P_{pow} $(i=3)$	1.90 ± 0.05	1.01 ± 0.008	2.84 ± 0.04	0.51 ± 0.005	0.58 ± 0.02	9.2	0.04	1
Okinawa	P_{gam} $(i=4)$	1.90 ± 0.05	1.01 ± 0.008	1.07 ± 0.02	0.94 ± 0.02	0.99 ± 0.04	22	0.14	0.04
	P_{ln} $(i=5)$	–	–	-0.20 ± 0.004	0.52 ± 0.005	0	12	0.07	0.61
	P_{lw} $(i=2)$	1.78 ± 0.03	0.76 ± 0.009	1.16 ± 0.01	1.44 ± 0.008	0.41 ± 0.008	2.0	0.007	1
2.0	P_{pow} $(i=3)$	2.57 ± 0.10	0.77 ± 0.007	3.61 ± 0.05	0.48 ± 0.003	0.40 ± 0.02	7.0	0.03	1
Okinawa	P_{gam} $(i=4)$	2.57 ± 0.10	0.77 ± 0.007	1.09 ± 0.03	0.68 ± 0.03	0.96 ± 0.05	25	0.14	0.18
	P_{ln} $(i=5)$	–	–	-0.41 ± 0.005	0.39 ± 0.008	0	15	0.08	0.78

Table 4. Interoccurrence time statistics of earthquakes in Okinawa region. The error bars mean the 95% confidence level of fit.

However, the fitting accuracy of the Weibull distribution becomes worse with a gradual decrease in m_c. We now propose a possible explanation which states that "the interoccurrence time distribution can be described by the superposition of the Weibull distribution and another distribution, hereafter referred to as the distribution $P_X(\tau)$,

$$\begin{aligned} P(\tau) &= p \times \text{Weibull distribution} + (1-p) \times \text{distribution X} \\ &= p \times P_w(\tau) + (1-p) \times P_X(\tau) \end{aligned} \tag{14}$$

where p is a parameter in the range, $0 \leq p \leq 1$ and stands for the ratio of P_w divided by $P(\tau)$. The interoccurrence time distribution obeys the Weibull distribution for $p = 1$. On the other hand, it follows the distribution $P_X(\tau)$ for $p = 0$. Here, the log-Weibull distribution, the power law distribution, the gamma distribution, and the log normal distribution are candidates for the distribution $P_X(\tau)$.

Next we shall explain the parameter estimation procedures;

(A); the optimal parameters are estimated so as to minimize the differences between the data and the test function by varying five parameters, $\alpha_1, \beta_1, \alpha_i, \beta_i$ and p.

m_c		Weibull distribution		Distribution X			RMS test	KS test	
Region	distribution X	α_1	β_1 [day]	α_i	β_i [day]	p	rms [$\times 10^{-3}$]	DKS	Q
	P_{lw} $(i=2)$	0.75 ± 0.01	27.6 ± 0.40	–	–	1	21	0.06	0.94
4.5	P_{pow} $(i=3)$	0.75 ± 0.01	27.6 ± 0.40	–	–	1	21	0.06	0.94
Chuetsu	P_{gam} $(i=4)$	0.75 ± 0.01	27.6 ± 0.40	–	–	1	21	0.06	0.94
	P_{ln} $(i=5)$	0.75 ± 0.01	27.6 ± 0.40	–	–	1	21	0.06	0.94
	P_{lw} $(i=2)$	0.81 ± 0.01	10.6 ± 0.13	–	–	1	17	0.03	1
4.0	P_{pow} $(i=3)$	0.81 ± 0.01	10.6 ± 0.13	–	–	1	17	0.03	1
Chuetsu	P_{gam} $(i=4)$	0.81 ± 0.01	10.6 ± 0.13	–	–	1	17	0.03	1
	P_{ln} $(i=5)$	0.81 ± 0.01	10.6 ± 0.13	–	–	1	17	0.03	1
	P_{lw} $(i=2)$	0.89 ± 0.006	4.84 ± 0.02	2.08 ± 0.06	8.70 ± 0.19	0.93 ± 0.02	6.1	0.03	1
3.5	P_{pow} $(i=3)$	0.89 ± 0.006	4.84 ± 0.02	1.66 ± 0.04	0.62 ± 0.05	0.98 ± 0.009	6.3	0.03	1
Chuetsu	P_{gam} $(i=4)$	0.89 ± 0.006	4.84 ± 0.02	–	–	1	6.9	0.04	1
	P_{ln} $(i=5)$	0.89 ± 0.006	4.84 ± 0.02	1.12 ± 0.02	1.11 ± 0.02	0.90 ± 0.04	6.2	0.03	1
	P_{lw} $(i=2)$	1.06 ± 0.02	2.00 ± 0.06	1.90 ± 0.16	5.13 ± 0.39	0.82 ± 0.03	3.9	0.012	1
3.0	P_{pow} $(i=3)$	1.09 ± 0.008	2.14 ± 0.01	1.98 ± 0.04	0.52 ± 0.02	0.92 ± 0.009	5.0	0.02	1
Chuetsu	P_{gam} $(i=4)$	1.09 ± 0.008	2.14 ± 0.01	–	–	1	6.5	0.03	1
	P_{ln} $(i=5)$	1.09 ± 0.008	2.14 ± 0.01	0.39 ± 0.008	0.91 ± 0.02	0.63 ± 0.03	3.7	0.014	1
	P_{lw} $(i=2)$	1.48 ± 0.02	1.21 ± 0.009	1.19 ± 0.02	1.91 ± 0.02	0.62 ± 0.008	2.5	0.01	1
2.5	P_{pow} $(i=3)$	1.56 ± 0.03	1.16 ± 0.009	2.53 ± 0.04	0.49 ± 0.008	0.71 ± 0.01	6.4	0.03	1
Chuetsu	P_{gam} $(i=4)$	1.56 ± 0.03	1.16 ± 0.009	1.03 ± 0.009	1.09 ± 0.03	0.99 ± 0.04	15	0.01	0.38
	P_{ln} $(i=5)$	–	–	-0.11 ± 0.003	0.64 ± 0.004	0	5.1	0.04	1
	P_{lw} $(i=2)$	1.85 ± 0.03	0.80 ± 0.009	1.18 ± 0.02	1.43 ± 0.01	0.50 ± 0.01	2.2	0.007	1
2.0	P_{pow} $(i=3)$	2.46 ± 0.09	0.78 ± 0.007	3.51 ± 0.06	0.48 ± 0.004	0.47 ± 0.03	8.2	0.02	1
Chuetsu	P_{gam} $(i=4)$	2.46 ± 0.09	0.78 ± 0.007	1.19 ± 0.05	0.69 ± 0.02	0.97 ± 0.05	2.6	0.12	0.46
	P_{ln} $(i=5)$	–	–	-0.40 ± 0.005	0.40 ± 0.008	0	14	0.06	0.99

Table 5. Interoccurrence time statistics of earthquakes in Chuetsu area. The error bars mean the 95% confidence level of fit.

If there is a parameter, where C_v, the ratio of the standard deviation divided by the mean for a parameter exceeds 0.1, another estimation procedure, (B), is performed.

(B); the Weibull parameters, α_1 and β_1, and the parameters of $P_X(\tau)$, α_i and β_i, are optimized dependently and then p is estimated.

According to those procedures (A) and (B), we obtain the fitting of results of $P(\tau)$. The results for Okinawa and Chuetsu region are listed in Table 4 and 5. We assume that the Weibull distribution is a fundamental distribution, because p becomes unity for large m_c, which means that the effect of the distribution $P_X(\tau)$ is negligible. As observed in Table 4 and 5, the log-Weibull distribution is the most suitable distribution for the distribution $P_X(\tau)$ according to the two goodness-of-fit tests. Thus, we find that the interoccurrence times distribution can be described by the superposition of the Weibull distribution and the log-Weibull distribution, namely,

$$\begin{aligned} P(\tau) &= p \times \text{Weibull distribution} + (1-p) \times \text{log-Weibull distribution}, \\ &= p \times P_w + (1-p) \times P_{lw}, \end{aligned} \tag{15}$$

$P(\tau)$ is controlled by five parameters, $\alpha_1, \alpha_2, \beta_1, \beta_2$, and p.

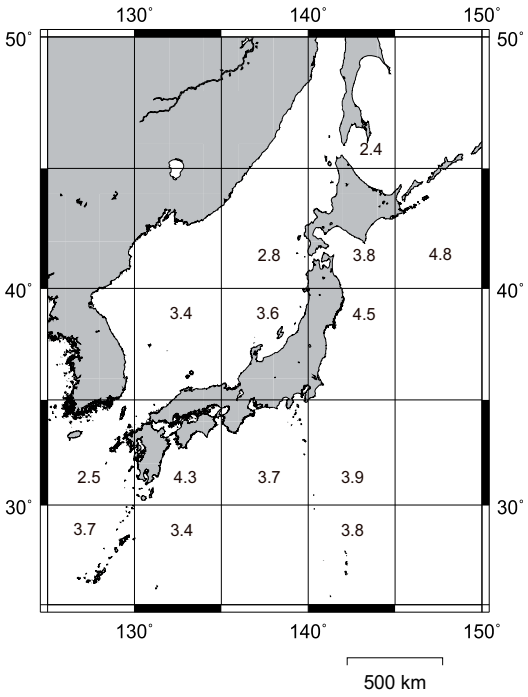

Fig. 7. The crossover magnitude from the superposition regime to the (pure) Weibull regime, denoted m_c^{**}, map around Japan.

It has been shown that the interoccurrence time distribution of earthquakes with large mc obeys the Weibulldistribution with the exponent $\alpha_1 < 1$. As shown in Tables 4 and 5, we stress the point that the distribution function of the interoccurrence time changes by varying m_c. This indicates that the interoccurrence time statistics basically contains both Weibull and log-Weibull statistics, and a dominant distribution function is changed according to the ratio p. In this case, the dominant distribution of the interoccurrence time changes from the log-Weibull distribution to the Weibull distribution when m_c is increased. Thus, the interoccurrence time statistics exhibit transition from the Weibull regime to the log-Weibull regime. The crossover magnitude from the superposition regime to the Weibull regime, denoted by m_c^{**}, depends on the spatial area. We demonstrate the values of m_c^{**} for each regime in Figure 7. As can be seen from the figure, m_c^{**} depends on the region and ranges from 2.4 (140°–145°E and 45°–50°N) to 4.8 (145°–150°E and 40°–45°N). Comparing Figure 1 (a) and Figure 7, we have found that the Weibull - log-Weibull transition occurs in all region, where we analyzed.

3.2 Interoccurrence time statistics in Southern California

Second, we analyze the interoccurrence time statistics using the SCEDC data. The cumulative distributions of interoccurrence time for $m_c = 4.0$ and $m_c = 2.0$ are shown in Figure 8 (a) and (b), respectively. By the rms test and KS test, we confirmed that the Weibull distribution is preferred for large m_c ($m_c = 4.0$) [see Table 6], which is the same result as that from JMA

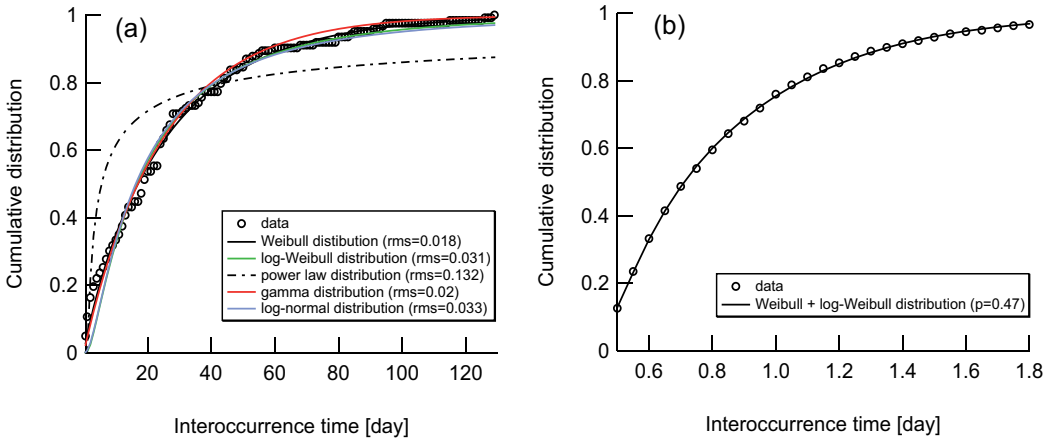

Fig. 8. Cumulative distribution of interoccurrence time in Southern California region different m_c and distribution functions. (a) $m_c = 4.0$ and (b) $m_c = 2.0$.

m_c		Distribution X		RMS test	KS test	
Region	distribution X	α_i	β_i [day]	rms [$\times 10^{-3}$]	DKS	Q
	P_l $(i=1)$	0.91 ± 0.01	25.4 ± 0.21	18	0.07	0.56
	P_{lw} $(i=2)$	3.66 ± 0.07	48.2 ± 0.68	31	0.14	0.11
4.0	P_{pow} $(i=3)$	1.44 ± 0.02	1.15 ± 0.15	133	0.49	1.6×10^{-9}
SCEDC	P_{gam} $(i=4)$	0.97 ± 0.004	25.6 ± 0.22	20	0.08	0.36
	P_{ln} $(i=5)$	2.79 ± 0.02	1.10 ± 0.02	33	0.13	0.02

Table 6. Results of rms value, DKS, and Q for different distribution functions in the case of $m_c = 4.0$ for Southern California earthquakes. The error bars mean the 95% confidence level of fit.

data. Unfortunately, the fitting accuracy of the Weibull distribution gets worse by decreasing a threshold m_c. We propose the following hypothesis, "the interoccurrence time distribution can be described by the superposition of the Weibull distribution and the distribution $P_X(\tau)$" which is the same in 3.1. As shown in Table 7, the log-Weibull distribution is the most suitable for the distribution $P_X(\tau)$, because the smallest rms-value, the smallest DKS value and the largest Q value can be obtained. Therefore, we find that the Weibull - log-Weibull transition shows in Southern California earthquakes. The crossover magnitude m_c^{**} is estimated to be 3.3.

3.3 Interoccurrence time statistics in Taiwan

Finally, the TCWB data was analyzed to investigate the interoccurrence time statistics in Taiwan. Figure 9 shows the cumulative distribution of interoccurrence time for $m_c = 4.5$ and $m_c = 3.0$, respectively. For large m_c, the Weibull distribution is preferred on the basis of the rms and KS test [see Table 8]. As the threshold of magnitude m_c decreases, the fitting accuracy of the Weibull distribution is getting worse, as is common in JMA and SCEDC. According to a hypothesis that the interoccurrence time distribution can be described by the superposition of

m_c		Weibull distribution		Distribution X			RMS test	KS test	
Region	distribution X	α_1	β_1 [day]	α_i	β_i [day]	p	rms [$\times 10^{-3}$]	DKS	Q
	P_{lw} $(i=2)$	0.91 ± 0.01	25.4 ± 0.21	–	–	1	18	0.07	0.56
4.0	P_{pow} $(i=3)$	0.91 ± 0.01	25.4 ± 0.21	–	–	1	18	0.07	0.56
SCEDC	P_{gam} $(i=4)$	0.91 ± 0.01	25.4 ± 0.21	–	–	1	18	0.07	0.56
	P_{ln} $(i=5)$	0.91 ± 0.01	25.4 ± 0.21	–	–	1	18	0.07	0.56
	P_{lw} $(i=2)$	0.83 ± 0.006	9.29 ± 0.05	–	–	1	11	0.03	1
3.5	P_{pow} $(i=3)$	0.83 ± 0.006	9.29 ± 0.05	–	–	1	11	0.03	1
SCEDC	P_{gam} $(i=4)$	0.83 ± 0.006	9.29 ± 0.05	–	–	1	11	0.03	1
	P_{ln} $(i=5)$	0.83 ± 0.006	9.29 ± 0.05	–	–	1	11	0.03	1
	P_{lw} $(i=2)$	1.01 ± 0.01	3.08 ± 0.04	1.37 ± 0.07	3.49 ± 0.19	0.80 ± 0.01	4.1	0.01	1
3.0	P_{pow} $(i=3)$	0.98 ± 0.008	2.85 ± 0.02	1.85 ± 0.03	0.58 ± 0.03	0.91 ± 0.009	6.1	0.03	1
SCEDC	P_{gam} $(i=4)$	–	–	0.99 ± 0.002	2.84 ± 0.01	1	8.2	0.05	1
	P_{ln} $(i=5)$	0.98 ± 0.008	2.85 ± 0.02	0.63 ± 0.009	1.00 ± 0.01	0.60 ± 0.03	5.0	0.03	1
	P_{lw} $(i=2)$	1.32 ± 0.01	1.72 ± 0.01	1.35 ± 0.01	2.40 ± 0.02	0.57 ± 0.005	2.0	0.01	1
2.5	P_{pow} $(i=3)$	1.33 ± 0.02	1.55 ± 0.009	2.27 ± 0.03	0.54 ± 0.008	0.76 ± 0.01	6.4	0.04	0.96
SCEDC	P_{gam} $(i=4)$	1.33 ± 0.02	1.17 ± 0.009	–	–	1	12	0.10	0.04
	P_{ln} $(i=5)$	–	–	0.13 ± 0.002	0.75 ± 0.003	0	4.4	0.04	0.92
	P_{lw} $(i=2)$	1.88 ± 0.03	0.92 ± 0.008	1.15 ± 0.02	1.56 ± 0.01	0.47 ± 0.008	2.7	0.007	1.1
2.0	P_{pow} $(i=3)$	2.18 ± 0.07	0.88 ± 0.008	3.14 ± 0.05	0.49 ± 0.005	0.52 ± 0.02	8.3	0.11	0.88
SCEDC	P_{gam} $(i=4)$	2.18 ± 0.07	0.88 ± 0.008	1.15 ± 0.04	0.80 ± 0.02	0.98 ± 0.05	26	0.13	0.72
	P_{ln} $(i=5)$	–	–	-0.31 ± 0.005	0.46 ± 0.007	0	7.5	0.007	1

Table 7. Interoccurrence time statistics of earthquakes in Southern California area. The error bars mean the 95% confidence level of fit.

the Weibull distribution and another distribution, we investigate the distribution $P_X(\tau)$. As shown in Table 9, the log-Weibull distribution is preferred as the distribution on the basis of the two goodness-of-fit tests. We estimated the crossover magnitude m_c^{**} to be 4.9.

3.4 Brief summary of the interoccurrence time statistics for earthquakes

Taken all together, we clarified that distribution of interoccurrence time is well fitted by the superposition of the Weibull distribution and log-Weibull distribution. For large m_c, $P(\tau)$ obeys the Weibull distribution with $\alpha_1 < 1$, indicating that the occurrence of earthquakes is not a Possion process. When the threshold of magnitude m_c decreases, the ratio of the Weibull distribution of $P(\tau)$ gradually increases. We suggest that the Weibull statistics and log-Weibull statistics coexist in interoccurrence time statistics, where the change of the distribution means the change of a dominant distribution. In this case, the dominant distribution changes from the log-Weibull distribution to the Weibull distribution by increasing the m_c. It follows that the Weibull - log-Weibull transition exists in Japan, Southern California, and Taiwan.

4. Discussion

4.1 Size dependency

To investigate the region-size, L dependency of the Weibull - log-Weibull transition, we change the window size L is varied from 3° to 25° (17). In (17), we use JMA data we used is from

m_c		Distribution X		RMS test	KS test	
Region	distribution X	α_i	β_i [day]	rms [$\times 10^{-3}$]	DKS	Q
	P_l $(i=1)$	0.86 ± 0.006	15.1 ± 0.08	8.4	0.02	1
	P_{lw} $(i=2)$	3.01 ± 0.06	27.9 ± 0.42	24	0.10	0.24
5.0	P_{pow} $(i=3)$	1.51 ± 0.03	0.93 ± 0.11	111	0.25	3.6×10^{-6}
TCWB	P_{gam} $(i=4)$	0.97 ± 0.003	15.3 ± 0.14	16	0.05	0.95
	P_{ln} $(i=5)$	2.23 ± 0.02	1.15 ± 0.02	24	0.08	0.53

Table 8. Results of rms value, DKS, and Q for different distribution functions in the case of $m_c = 5.0$ for Taiwan earthquakes. The error bars mean the 95% confidence level of fit.

m_c		Weibull distribution		Distribution X			RMS test	KS test	
Region	distribution X	α_1	β_1 [day]	α_i	β_i [day]	p	rms [$\times 10^{-3}$]	DKS	Q
	P_{lw} $(i=2)$	0.86 ± 0.006	15.0 ± 0.08	–	–	1	8.4	0.02	1
5.0	P_{pow} $(i=3)$	0.86 ± 0.006	15.0 ± 0.08	–	–	1	8.4	0.02	1
TCWB	P_{gam} $(i=4)$	0.86 ± 0.006	15.0 ± 0.08	–	–	1	8.4	0.02	1
	P_{ln} $(i=5)$	0.86 ± 0.006	15.0 ± 0.08	–	–	1	8.4	0.02	1
	P_{lw} $(i=2)$	0.88 ± 0.004	5.34 ± 0.02	–	–	1	4.3	0.01	1
4.5	P_{pow} $(i=3)$	0.88 ± 0.004	5.34 ± 0.02	–	–	1	4.3	0.01	1
TCWB	P_{gam} $(i=4)$	0.88 ± 0.004	5.34 ± 0.02	–	–	1	4.3	0.01	1
	P_{ln} $(i=5)$	0.88 ± 0.004	5.34 ± 0.02	–	–	1	4.3	0.01	1
	P_{lw} $(i=2)$	1.00 ± 0.01	2.30 ± 0.04	1.82 ± 0.05	4.06 ± 0.13	0.68 ± 0.01	2.8	0.009	1
4.0	P_{pow} $(i=3)$	1.08 ± 0.01	2.30 ± 0.02	1.95 ± 0.04	0.55 ± 0.02	0.89 ± 0.01	6.9	0.03	1
TCWB	P_{gam} $(i=4)$	1.08 ± 0.01	2.30 ± 0.02	–	–	1	10	0.05	0.99
	P_{ln} $(i=5)$	1.08 ± 0.01	2.30 ± 0.02	0.46 ± 0.005	0.92 ± 0.006	0.39 ± 0.02	2.8	0.007	1
	P_{lw} $(i=2)$	1.44 ± 0.03	1.29 ± 0.02	1.32 ± 0.05	2.15 ± 0.05	0.61 ± 0.02	4.5	0.01	1
3.5	P_{pow} $(i=3)$	1.52 ± 0.03	1.25 ± 0.01	2.41 ± 0.05	0.50 ± 0.01	0.74 ± 0.02	8.6	0.07	0.94
TCWB	P_{gam} $(i=4)$	1.52 ± 0.03	1.25 ± 0.01	–	–	1	18	0.09	0.73
	P_{ln} $(i=5)$	–	–	-0.04 ± 0.003	0.66 ± 0.004	0	5.4	0.03	1
	P_{lw} $(i=2)$	2.07 ± 0.06	0.75 ± 0.009	1.18 ± 0.03	1.47 ± 0.01	0.51 ± 0.01	3.2	0.01	1
3.0	P_{pow} $(i=3)$	2.62 ± 0.09	0.78 ± 0.006	3.58 ± 0.08	0.48 ± 0.005	0.53 ± 0.02	7.5	0.02	1
TCWB	P_{gam} $(i=4)$	2.62 ± 0.09	0.78 ± 0.006	1.26 ± 0.08	0.66 ± 0.03	0.97 ± 0.05	23	0.10	0.76
	P_{ln} $(i=5)$	–	–	-0.41 ± 0.004	0.38 ± 0.006	0	12	0.05	1
	P_{lw} $(i=2)$	5.35 ± 0.41	0.60 ± 0.005	0.86 ± 0.05	1.16 ± 0.007	0.43 ± 0.04	16	0.037	1
2.5	P_{pow} $(i=3)$	5.35 ± 0.41	0.60 ± 0.005	6.54 ± 0.09	0.49 ± 0.001	0.10 ± 0.04	10	0.041	1
TCWB	P_{gam} $(i=4)$	5.35 ± 0.41	0.60 ± 0.005	1.69 ± 2.04	0.33 ± 0.61	0.94 ± 0.07	46	0.17	0.41
	P_{ln} $(i=5)$	–	–	-0.58 ± 0.006	0.19 ± 0.01	0	35	0.11	0.87

Table 9. Interoccurrence time statistics of earthquakes in Taiwan area. The error bars mean the 95% confidence level of fit.

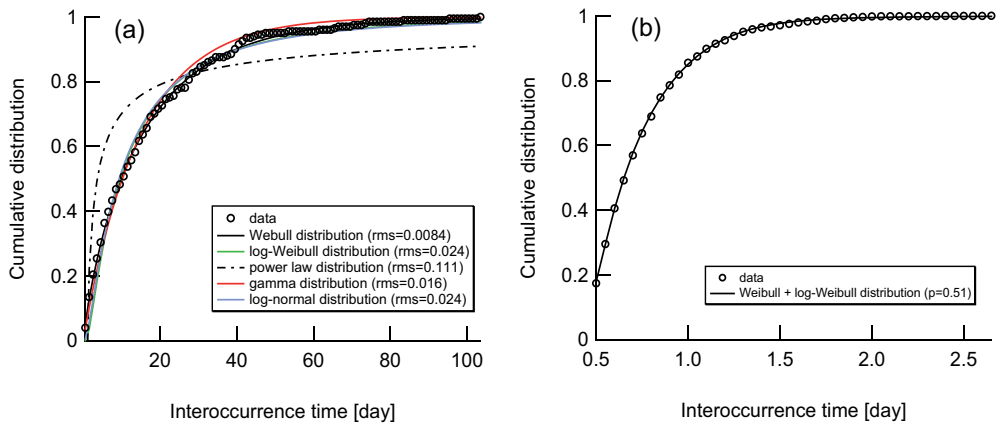

Fig. 9. Cumulative distribution of interoccurrence time for Taiwan for different m_c and distribution function. (a) and (b) represent interoccurrence time when $m_c = 4.5$ and $m_c = 3.0$, respectively.

L	Region	m_c	α_1	β_1 [day]	rms	m_c^{**}
$L = 3$	140°-143° E and 35°-38° N	3.9	0.88 ± 0.01	19.4 ± 0.18	0.011	4.6
$L = 5$	140°-145° E and 35°-40° N	4.0	0.75 ± 0.02	10 ± 0.19	0.014	4.7
$L = 10$	140°-150° E and 35°-45° N	4.2	0.94 ± 0.005	8.36 ± 0.04	0.0077	4.9
$L = 25$	125°-150° E and 25°-50° N	5.0	0.93 ± 0.01	17.8 ± 0.10	0.041	5.7

Table 10. Interoccurrence time statistics for different system size L by analyzing the JMA data from 1st January 2001 to 31st October 2007 (17).

1st January 2001 to 31st October 2007. We use the data covering the region 140°-143° E and 35°-38° N for $L = 3$, 140°-145° E and 35°-40° N for $L = 5$, 140°-150° E and 35°-45° N for $L = 10$, and 125°-150° E and 25°-50° N for $L = 25$. As for $L = 25$, the data covers the whole region of the JMA catalogue. The result of fitting parameters of $P(\tau)$, the crossover magnitude m_c^{**}, and the rms value are listed in Table 10. It is demonstrated that in all the cases, the Weibull exponent α_1 is less than unity and the Weibull - log-Weibull transition appears. m_c^{**} depends on L, namely $m_c^{**} = 3.9$ for $L = 3$, $m_c^{**} = 4.0$ for $L = 5$, $m_c^{**} = 4.2$ for $L = 10$, and $m_c^{**} = 5.0$ for $L = 25$. Therefore we can conclude that the interoccurrence time statistics, namely the Weibull - log-Weibull transition, presented here hold from $L = 3$ to $L = 25$.

4.2 Relation between the m_c^{**} and m_{max}

To study the feature of the Weibull - log-Weibull transition, we summarize our results obtained from 16 different regions (14 regions in Japan, Southern California, and Taiwan.) Interestingly, m_c^{**} is proportional to the maximum magnitude of an earthquake in a region, where we analyzed, denoted here m_{max} [see Figure 10]. We then obtain a region-independent relation between m_c^{**} and m_{max},

$$m_c^{**}/m_{max} = 0.56 \pm 0.08 \tag{16}$$

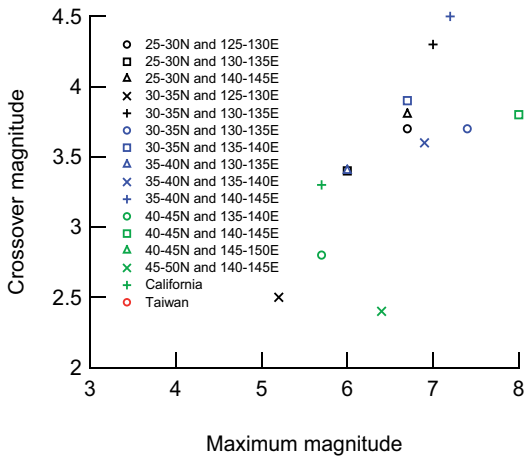

Fig. 10. The crossover magnitude m_c^{**} v.s the maximum magnitude m_{max} in 16 regions (14 region in Japan, Southern California, and Taiwan).

Region	relative plate motion	velocity [mm/yr]	m_c^{**}
Taiwan	PH-EU	71	4.90
East Japan	PA-PH	49	4.07 [1]
West Japan	PH-EU	47	3.74 [2]
California	PA-NA	47	3.30

Table 11. List of the crossover magnitude, m_c^{**} and the plate velocity (32; 33). The notation of PH, EU, PA, and NA represent PHilippine Sea plate, EUrasian plate, PAcific plate, and North American plate, respectively.

1 We take an average using three regions; 25°–30°N, 140°–145°E ($m_c^{**} = 3.8$), 30°–35°N, 140°–145°E ($m_c^{**} = 3.9$), 35°–40°N, 140°–145°E ($m_c^{**} = 4.5$).

2 We take an average using five regions; 25°–30°N, 125°–130°E ($m_c^{**} = 3.7$), 25°–30°N, 130°–135°E ($m_c^{**} = 3.4$), 30°–35°N, 130°–135°E ($m_c^{**} = 4.3$), 30°–35°N, 135°–140°E ($m_c^{**} = 3.7$), 35°–40°N, 135°–140°E ($m_c^{**} = 3.6$).

This relation can be useful to interpret the Weibull - log-Weibull transition of geophysical meaning.

4.3 Interpretation of the Weibull - log-Weibull transition

Although the scaled crossover magnitudes $m_c{*}{*}/m_{max}$ is region-independent, the crossover magnitude m_c^{**} from the superposition regime to the pure Weibull regime probably depends on the tectonic region (Figure 7). To investigate the Weibull - log-Weibull transition further, we consider the plate velocity with m_c^{**}, which can shed light on the geophysical implication of the region-dependent m_c^{**}. As shown in Table 11, m_c^{**} is on the average proportional to the plate velocity. That means that the maximum magnitude m_{max} for a tectonic region is more or less proportional to the plate velocity since $m_c^{**}/0.56 = m_{max}$. Such an interesting

consequence is reminiscent of the early study by Ruff and Kanamori (1980) (34). They showed a relation that the magnitude of characteristic earthquake occurred in the subduction-zone, M_w is directly proportional to the plate-velocity, V, and is directly inversely proportional to plate-age T, namely,

$$M_w = -0.000953T + 1.43V + 8.01. \tag{17}$$

The relation $m_c{*}{*}/0.56 = m_{max}$ can thus be explained on the basis of their early observation about the velocity-dependence of the characteristic earthquake magnitude. The physical interpretation of the Weibull - log-Weibull transition remains open. However, it might suggest that the occurrence mechanism of earthquake could probably depend on its magnitude then, inevitably, the distribution of the interoccurrence time statistics changes as the threshold of magnitude m_c is varied. It is well known that the Weibull distribution for life-time of materials can be derived in the framework of damage mechanics (4; 24; 35–37). Our present results thus suggest that larger earthquakes might be caused by the damage mechanism driven by the plate motion, whereas the effect of the plate-driven damaging process might become minor for smaller earthquakes. Hence, the transition from the Weibull regime to the log-Weibull regime could be interpreted from the geophysical sense as the decrement of the plate-driven damaging mechanics.

4.4 A universal relation and intrinsic meanings of the Gutenberg-Richter parameter

Here we consider the interrelation between the Gutenberg-Richter law, denoted in this subsection $P(m) \propto e^{-bm}$ and the Weibull distribution for the interoccurrence time ($P(\tau) \propto t^{-\alpha-1} \cdot e^{(\tau/\beta)^\alpha}$). We assume that these two statistics are correct over wide ranges, and the parameters (α, β) are depending on the magnitude, i.e., $\alpha(m)$ and $\beta(m)$, then the following relation is easily obtained from the calculation of the mean interoccurrence time between two earthquakes whose magnitude is larger than m ,

$$\beta(m_1)e^{-bm_1}\Gamma\left(1+\frac{1}{\alpha_1}\right) = \beta(m_2)e^{-bm_2}\Gamma\left(1+\frac{1}{\alpha_2}\right), \tag{18}$$

where m_1 and m_2 are arbitrary values of m. This implies that the quantity defined by $\beta(m_1)e^{-bm_1}\Gamma\left(1+\frac{1}{\alpha_1}\right)$ is a universal constant when we consider the local earthquakes in a relatively small area.

One of the most important results derived from equation (18) is that the GR parameter b is determined by two parameters, in other words, the parameters (α, β) depend on the magnitude m as well as on the GR parameter b,

$$\begin{aligned} \alpha &= f_\alpha(m, b) \\ \beta &= f_\beta(m, b), \end{aligned} \tag{19}$$

where the functional forms of f_α and f_β characterize the time series of earthquakes under consideration.

It is difficult to determine those forms completely from any seismological relations known so far, but it is possible for us to obtain the universal aspects of f_α and f_β by a perturbational

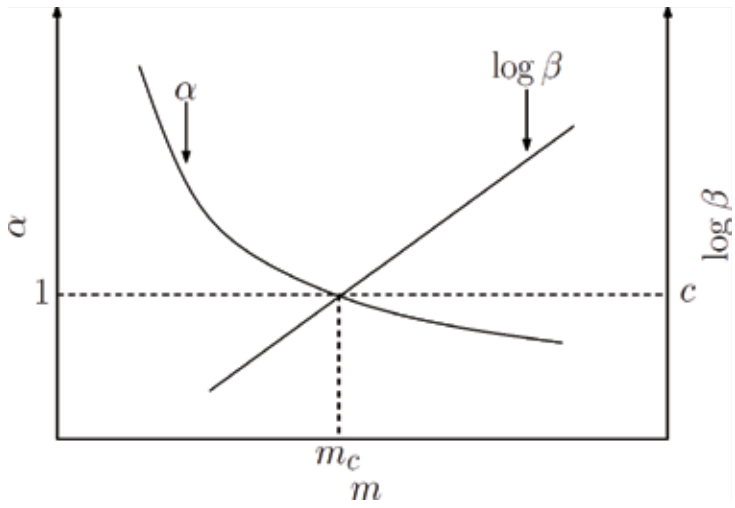

Fig. 11. Schematic picture of universal behavior of $f_\alpha(m,b)$ and $f_\beta(m,b)$ near $m \simeq m_c$.

approach. Here we consider a particular solution of equation (19) which satisfies the following conditions; $f_\beta(m,b) = \exp[b(m-m_c)+c]$ and $f_\alpha(m_c,b)$, namely, the characteristic time β is a exponentilally increasing function of m, and the interoccurrence time distribution is an exponential one ($\alpha = 1$) at $m = m_c$, where b' and c are constant parameters. By use of this simplification, equation (18) is rewritten by putting $m_1 = m$ and $m_2 = m$,

$$(b'-b)(m-m_c) = -\log\Gamma\left(1+\frac{1}{\alpha(m)}\right) \cong \frac{1}{2}\Delta - \frac{3}{4}(\Delta)^2 + \cdots, \quad (\Delta = \alpha(m-1). \tag{20}$$

Here we used the Taylor expansion near $m \cong m_c$ (i.e., $\alpha(m) \cong \alpha(m_c)$). Figure 11 shows the schematic result of equation (20). One can see that the universal relation is recognized in many cases treated in this chapter (section 4.3.3.), though the exponential growth of β, $\log\beta(m) \simeq b'(m-m_c)+c$ is a little bit accelerated.

We have to remind that the solution mentioned above is not unique, but many other solutions for equation (19) are possible under the universal relation of equation (18). Further details will be studied in our forthcoming paper (38).

4.5 Comparison with previous works

Finally, we compared our results with those of previous studies. The unified scaling law shows a generalized gamma distribution [see in equations (2), and (3)] which is approximately the gamma distribution, because δ in Corral's paper (6) is close to unity ($\delta = 0.98 \pm 0.05$). For a long time domain, this distribution decays exponentially, supporting the view that an earthquake is a Poisson process. However, we have demonstrated that the Weibull distribution is more appropriate than the gamma distribution on the basis of two goodness-fit-tests. In addition, for large m_c, the distribution in a long time domain is similar

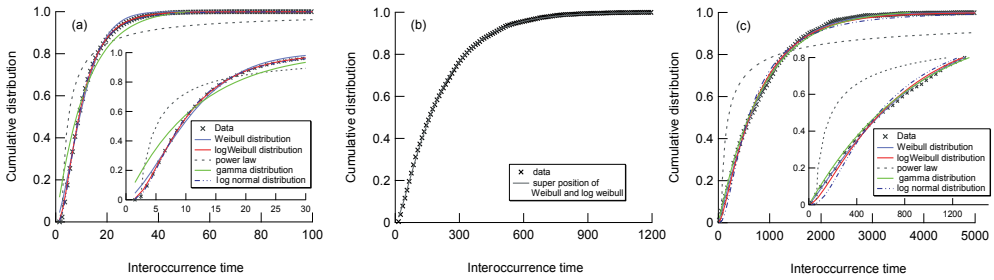

Fig. 12. Interoccurrence time statistics for different magnitude m_c by analyzing catalogue produced by the two-dimensional spring-block model (29).

to the stretched exponential distribution because α_1 is less than unity, suggesting that an occurrence of earthquake is not a Poisson process but has a memory. We provide the first evidence that the distribution changes from the Weibull to log-Weibull distribution by varying m_c, i.e., the Weibull - log-Weibull transition. Recently, Abaimov *et al.* showed that the recurrence time distribution is also well-fitted by the Weibull distribution (4) rather than the Brownian passage time (BPT) distribution (23) and the log normal distribution. Taken together, we infer that both the recurrence time statistics and the interoccurrence time statistics show the Weibull distribution.

In this chapter, we propose a new insight into the interoccurrence time statistics, stating that the interoccurrence statistics exhibit the Weibull - log-Weibull transition by analyzing the different tectonic settings, JMA, SCEDC, and TCWB. This stresses that the distribution function can be described by the superposition of the Weibull distribution and the log-Weibull distribution, and that the predominant distribution function changes from the log-Weibull distribution to the Weibull distribution as m_c is increased. Note that there is a possibility that a more suitable distribution might be found instead of the log-Weibull distribution. Furthermore, the Weibull - log-Weibull transition can be extracted more clearly by analyzing synthetic catalogs produced by the spring-block model [see Figure 12] (29).

5. Conclusion

In conclusion, we have proposed a new feature of interoccurrence time statistics by analyzing the Japan (JMA), Southern California, (SCEDC), and Taiwan (TCWB) for different tectonic conditions. We found that the distribution of the interoccurrence time can be described clearly by the superposition of the Weibull distribution and the log-Weibull distribution. Especially for large earthquakes, the interoccurrence time distribution obeys the Weibull distribution with the exponent $\alpha_1 < 1$, indicating that a large earthquake is not a Poisson process but a phenomenon exhibiting a long-tail distribution. As the threshold of magnitude m_c increases, the ratio of the Weibull distribution in the interoccurrence time distribution p gradually increases. Our findings support the view that the Weibull statistics and log-Weibull statistics coexist in the interoccurrence time statistics. We interpret the change of distribution function as the change of the predominant distribution function; the predominant distribution changes from the log-Weibull distribution to the Weibull distribution when m_c is increased. Therefore, we concluded that the interoccurrence time statistics exhibit a Weibull - log-Weibull

transition. We also find the region-independent relation, namely, $m_c^{**}/m_{max} = 0.56 \pm 0.08$. In addition, the crossover magnitude m_c^{**} is proportional to the plate velocity, which is consistent with an earlier observation about the velocity-dependence of the characteristic earthquake magnitude (34). Although the origins of both the log-Weibull distribution and the Weibull - log-Weibull transition remain open questions, we suggest the change in the distribution from the log-Weibull distribution to the Weibull distribution can be considered as the enhancement in the plate-driven damaging mechanics. We believe that this work is a first step toward a theoretical and geophysical understanding of this transition.

6. Acknowledgments

The authors thank the editor of this book and Intech publisher for giving us the opportunity to take part in this book project. We would like to thank the JMA, SCEDC and TCWB for allowing us to use the earthquake data. The effort of the Taiwan Central Weather Bureau for maintaining the CWB Seismic Network is highly appreciated. TH is supported by the Japan Society for the Promotion of Science (JSPS) and the Earthquake Research Institute cooperative research program at the University of Tokyo. This work is partly supported by the Sasagawa Scientific Research Grant from The Japan Science Society by the Waseda University.. CCC is also grateful for research supports from the National Science Council (ROC) and the Department of Earth Sciences at National Central University (ROC).

7. References

[1] I. G. Main, "Statistical physics, seismogenesis, and seismic hazard", *Review of Geophysics*, vol. 34, pp. 433-462, 1996.

[2] B. Gutenberg and C. F. Richter, "Magnitude and energy of earthquakes", *Annals of Geophysics*, vol. 9, pp.1-15, 1956.

[3] F. Omori, "On the after-shocks of earthquakes", *Journal of the College of Science, Imperial University of Tokyo*, vol. 7, pp. 111-200, 1894.

[4] S. G. Abaimov, D. L. Turcotte, R. Shcherbakov, and J. B. Rundle, "Recurrence and interoccurrence behavior of self-organized complex phenomena", *Nonlinear Processes in Geophysics*, vol. 14, pp. 455-464, 2007.

[5] P. Bak, K. Christensen, L. Danon, and T. Scanlon, "Unified Scaling Law for Earthquakes", *Physical Review Letters*, vol. 88, 178501, 2002.

[6] A. Corral, "Long-Term Clustering, Scaling, and Universality in the Temporal Occurrence of Earthquakes", *Physical Review Letters*, vol. 92, 108501, 2004.

[7] R. Shcherbakov, G. Yakovlev, D. L. Turcotte, and J. B. Rundle, "Model for the Distribution of Aftershock Interoccurrence Times", *Physical Review Letters*, vol. 95, 218501, 2005.

[8] A. Saichev and D. Sornette, ""Universal" Distribution of Inter-Earthquake Times Explained", *Physical Review Letters*, vol. 97, 078501, 2006.

[9] A. Saichev and D. Sornette, "Theory of earthquake recurrence times", *Journal of Geophysics Research*, vol. 112, B04313, 2007.

[10] S. Abe and N. Suzuki, "Scale-free statistics of time interval between successive earthquakes", *Physica A*, vol. 350, pp. 588-596, 2005.

[11] J. K. Gardner, L. Knopoff, Is the sequence of earthquakes in southern California with aftershocks removed, Poissonian?, *Bulletin of the Seismological Society of America*, vol. 64, pp.1363-1367, 1974.
[12] B. Enescu, Z. Struzik, and K. Kiyono, On the recurrence time of earthquakes: insight from Vrancea (Romania) intermediate-depth events, *Geophysical Journal International*, vol. 172, pp. 395-404, 2008.
[13] A. Bunde, J. F. Eichner, J. W. Kantelhardt, and S. Havlin, Long-Term Memory: A Natural Mechanism for the Clustering of Extreme Events and Anomalous Residual Times in Climate Records, *Physical Review Letters*, vol. 94, 048701, 2005.
[14] V. N. Livina, S. Havlin, and A. Bunde, Memory in the Occurrence of Earthquakes, *Physical Review Letters*, vol. 95, 208501, 2005.
[15] S. Lennartz, V. N. Livina, A. Bunde, and S. Havlin, Long-term memory in earthquakes and the distribution of interoccurrence times, *Europhysics Lettters*, vol. 81, 69001, 2008.
[16] T. Akimoto, T. Hasumi, and Y. Aizawa, "Characterization of intermittency in renewal processes: Application to earthquakes", *Physical Review E* vol. 81, 031133, 2010.
[17] T. Hasumi, T. Akimoto, and Y. Aizawa, "The Weibull - log-Weibull distribution for interoccurrence times of earthquakes", *Physica A*, vol. 388, pp. 491-498, 2009.
[18] T. Hasumi, C. Chen, T. Akimoto, and Y. Aizawa, "The Weibull - log-Weibull transition of interoccurrence times for synthetic and natural earthquakes", *Techtonophysics*, vol. 485, pp. 9-16, 2010.
[19] Japan Meteorological Agency Earthquake Catalog
: http://wwweic.eri.u-tokyo.ac.jp/db/jma1.
[20] Southern California Earthquake Data Center: http://www.data.scec.org
[21] Taiwan Central Weather Bureau: http://www.cwb.gov.tw/
[22] T. Huillet and H. F. Raynaud, "Rare events in a log-Weibull scenario-Application to earthquake magnitude data", *The European Physical Journal B*, vol. 12, pp. 457-469, 1999.
[23] M. V. Matthews, W. L. Ellsworth, and P. A. Reasenberg, "A brownian model for recurrent earthquakes", *Bulletin of the Seismological Society of America*, vol. 92, pp. 2233-2250, 2002.
[24] W. Weibull, A statistical distribution function of wide applicability, *Journal of Applied Mathematics*, vol. 18, pp. 293-297, 1951.
[25] Y. Hagiwara, "Probability of earthquake occurrence as obtained from a Weibull distribution analysis of crustal strain", *Tectonophys*, vol. 23, pp. 313-318, 1974.
[26] W. H. Bakun, B. Aagard, B. Dost, *et al.*, "Implications for prediction and hazard assessment from the 2004 Parkfield earthquake", *Nature*, vol. 437, pp. 969-974, 2005.
[27] S. G. Abaimov, D. L. Turcotte, and J. B. Rundle, "Recurrence-time and frequency-slip statistics of slip events on the creeping section of the San Andreas fault in central California", *Geophysical Journal International*, vol.170, pp. 1289-1299, 2007.
[28] K. Z. Nanjo, D. L. Turcotte, and R. Shcherbakov, "A model of damage mechanics for the deformation of the continental crust", *Journal of Geophysics Research*, vol. 110, B07403, 2005.
[29] T. Hasumi, T. Akimoto, and Y. Aizawa, "The Weibull - log-Weibull transition of the interoccurrence statistics in the two-dimensional Burridge-Knopoff earthquake model", *Physica A*, vol. 388, pp. 483-490, 2009.

[30] G. Yakovlev, D. L. Turcotte, J. B. Rundle, and P. B. Rundle, "Simulation-Based Distributions of Earthquake Recurrence Times on the San Andreas Fault System", *Bulletin of the Seismological Society of America*, vol. 96, pp. 1995-2007, 2006.

[31] W. H. Press, S. A. Teukolsky, W. T. Vetterling, and B. P. Flannery, *Numerical Recipes in C 2nd edition*, Cambridge University Press, Cambridge, 1995.

[32] T. Seno, S. Seth, and E. G. Alice, "A model for the motion of the Philippine Sea plate consistent with NUVEL-1 and geological data", *Journal of Geophysics Research*, vol 98, pp. 17941-17948, 1993.

[33] C. M. R. Fowler, *The Solid Earth: An Introduction to Global Geophysics*, Cambridge University Press, New York, 1990.

[34] L. Ruff and H. Kanamori, "Seismicity and the subduction process", *Physics of the Earth and Planetary Interiors*, vol. 23, pp. 240-252, 1980.

[35] T. Wong, R. H. C. Wong, K. T. Chau, and, C. A. Tang, "Microcrack statistics. Weibull distribution and micromechanical modeling of compressive failure in rock", *Mechanics of Materials*. vol. 38, pp. 664-681, 2006.

[36] A. Ghosh, "A FORTRAN program for fitting Weibull distribution and generating samples", *Computational Geosciences*, vol. 25, pp. 729-738, 1999.

[37] D. L. Turcotte, W. I. Newman, R. Shcherbakov, "Micro and macroscopic models of rock fracture", *Geophysical Journal International*, vol. 152, pp. 718-728, 2003.

[38] Y. Aizawa and T. Hasumi, in preparation (2011).

2

Change Point Analysis in Earthquake Data

Ayten Yiğiter
Hacettepe University, Faculty of Science, Department of Statistics Beytepe-Ankara Turkey

1. Introduction

Earthquake forecasts are very important in human life in terms of estimating hazard and managing emergency systems. Defining of earthquake characteristics plays an important role in these forecasts. Of these characteristics, one is the frequency distribution of earthquakes and and the other is the magnitude distribution of the earthquakes. Each statistical distribution has many parameters describing the actual distribution.

There are various statistical distributions used to model the earthquake numbers. As is well known, these are binomial, Poisson, geometric and negative binomial distributions. It is generally assumed that earthquake occurrences are well described by the Poisson distribution because of its certain characteristics (for some details, see Kagan, 2010; Leonard & Papasouliotis, 2001). In their study, Rydelek & Sacks (1989) used the Poisson distribution of earthquakes at any magnitude level. The Poisson distribution is generally used for earthquakes of a large magnitude, and the earthquake occurrences with time/space can be modeled with the Poisson process in which, as is known, the Poisson distribution is one that counts the events that have occurred over a certain period of time.

There is a significant amount of research on the change point as applied to earthquake data. Amorese (2007) used a nonparametric method for the detection of change points in frequency magnitude distributions. Yigiter & İnal (2010) used earthquake data for their method developed for the estimator of the change point in Poisson process. Aktaş et al. (2009) investigated a change point in Turkish earthquake data. Rotondi & Garavaglia (2002) applied the hierarchical Bayesian method for the change point in data, taken from the Italian NT4.1.1 catalogue.

Recently, much research in the literature has focused on whether there is an increase in the frequency of earthquake occurrences. It is further suggested that any increase in the frequency of earthquakes, in some aspects, is due to climate change in the world. There is considerable debate on whether climate change really does increase the frequency of natural disasters such as earthquakes and volcano eruptions. In many studies, it is emphasized that there is serious concern about impact of climate change on the frequencies of hazardous events (Peduzzi, 2005; Lindsey, 2007; Mandewille, 2007 etc.). In Peduzzi's study (2005), there are some indicators about increasing number of the earthquakes especially affecting human settlements, and it is also reported that there is an increase in the percentage of earthquakes affecting human settlements from 1980 onwards. The change point analysis can be used to study the increase or decrease in the frequency of the earthquake occurrences.

The change point analysis is a very useful statistical tool to detect an abrupt or a structural change in the characteristic of the data observed sequentially or chronologically. Many different statistical methods are available to detect the change point in the distribution of a sequence of random variables (Smith, 1975; Hinkley, 1970; Boudjellaba et al., 2001 in many others). Multiple change points have also been investigated for many years (Hendersen & Matthews, 1993; Yao, 1993; Chen & Gupta, 1997, among others.).
In this study, we aimed to find an evidence of increased or decreased in world seismic activities after 1901. Earthquake frequencies are modeled by the Poisson distribution as the most commonly used discrete distribution. We modeled the earthquakes in the world with the Poisson process since the number of earthquakes is counted with Poisson distribution. We investigated any abrupt change point(s) in parameters of the model using the frequentist (maximum likelihood) and Bayesian method. When the magnitude of the earthquakes is taken into account in the process, it is then called the compound Poisson process. We also investigated a change in the magnitudes of the world earthquakes. For this purpose, Poisson process and compound Poisson process are introduces in Section 2. The frequentist and Bayesian methods used for change point estimates are explained in Section 3. Worldwide earthquake data and change point analysis of this data are given Section 4.

2. Poisson process

The Poisson process has an important place in stochastic processes. It is a Markov chain with a continuous parameter.
A stochastic process $\{N_t, t \geq 0\}$ is said to be a homogeneous Poisson process if

i. $\{N_t, t \geq 0\}$ has stationary independent increments
ii. for any times s and t such that s<t the number of events occurred in time interval (s, t) has Poisson distribution with parameter λ(t-s).

In the homogeneous Poisson Process, events occur independently throughout time. The number of events occurred time interval (0, t] has Poisson distribution with parameter λt,

$$\begin{aligned} P(N_t = i) &= e^{-\lambda t}\frac{(\lambda t)^i}{i!}, \qquad i = 0,1,\ldots \\ &= 0, \qquad\qquad\quad \text{otherwise} \end{aligned} \tag{1}$$

where λ is called the occurrence rate of the event in unit time. The occurrence rate is assumed to be a constant throughout the process.
Let $S_0, S_1, S_2, \ldots$ be occurrence times of the events where $S_0 = 0$ and $T_1 = S_1 - S_0$, $T_2 = S_2 - S_1, \ldots$ be time intervals between the events. $T_1, T_2, \ldots$ are independent identically exponential random variables with parameter λ. The distribution of the random variables $T_1, T_2, \ldots$ is:

$$\begin{aligned} f(t) &= \lambda e^{-\lambda t}, \quad t \geq 0 \\ &= 0, \qquad\quad t < 0 \end{aligned} \tag{2}$$

2.1 Compound poisson process

A stochastic process $\{X_t, t \geq 0\}$ is said to be a compound Poisson process if it can be presented, for $t \geq 0$, by

$$X_t = \sum_{i=1}^{N_t} Y_i \tag{3}$$

in which $\{N_t, t \geq 0\}$ is a Poisson process, and $\{Y_i, i = 1,2,\ldots\}$ are independent identically distributed (i.i.d.) random variables. The compound Poisson distribution has stationary independent increments, and the mean and variance of the X_t,

$$\begin{aligned} E(X_t) &= E(N_t)E(Y) \\ V(X_t) &= E(N_t)E(Y^2). \end{aligned} \tag{4}$$

See Parzen (1962) for some details about Poisson processes.

3. Methods for Estimating Change Point

The Maximum likelihood method and the Bayesian method are basic methods in statistical change point analyses for point estimation and hypothesis testing.

3.1 Change point estimation with the maximum likelihood method (frequentist method)

Let $X_1, X_2, \ldots, X_n$ be a sequence of the random variables such that X_i $(i = 1,\ldots,\nu)$ has probability density function $f(x,\theta_1)$ and X_i $(i = \nu+1,\ldots,n)$ has probability density function $f(x,\theta_2)$ where the change point ν is unknown discrete parameter and the parameters θ_1, θ_2 can be assumed to be either known or unknown. The single change point model in the sequence of the random variables is written:

$$\begin{aligned} X_1, X_2, \ldots, X_\nu &\sim f(x,\theta_1) \\ X_{\nu+1}, X_{\nu+2}, \ldots, X_n &\sim f(x,\theta_2). \end{aligned} \tag{5}$$

Under model Eq.(5), for the observed values of the sequence of the random variables, the likelihood function is

$$L(\theta_1, \theta_2, \nu \mid x_1, \ldots, x_n) = L(\theta_1, \theta_2, \nu) = \prod_{i=1}^{\nu} f(x_i, \theta_1) \prod_{i=\nu+1}^{n} f(x_i, \theta_2) \tag{6}$$

and the logarithm of the likelihood function is:

$$\ell nL(\theta_1, \theta_2, \nu) = \sum_{i=1}^{\nu} \ell nf(x_i, \theta_1) + \sum_{i=\nu+1}^{n} \ell nf(x_i, \theta_2) \tag{7}$$

After adding the expression $\pm\sum_{i=1}^{\nu} \ell nf(x_i, \theta_2)$ in Eq.(7) then Eq.(7) can be re-written as follows:

$$\ell nL(\theta_1, \theta_2, \nu) \propto \sum_{i=1}^{\nu} \left[\ell nf(x_i, \theta_1) - \ell nf(x_i, \theta_2)\right] \tag{8}$$

When the parameters, θ_1, θ_2 are unknown, for any fixed values of change point ν, the maximum likelihood estimator of the parameters θ_1, θ_2 are found to be the derivative of Eq.(8) θ_1 and θ_2 respectively:

$$\frac{\partial \ell nL(\theta_1,\theta_2;\nu)}{\partial \theta_1}=0\,, \tag{9}$$

$$\frac{\partial \ell nL(\theta_1,\theta_2;\nu)}{\partial \theta_2}=0\,. \tag{10}$$

After solving the equations system given in Eq.(9) and (10), the maximum likelihood estimator of the parameters θ_1, θ_2, $\hat{\theta}_1$, $\hat{\theta}_2$ are obtained. The maximum likelihood estimate of the change point ν is:

$$\hat{\nu}=\arg\max_{k=1,\ldots n-1}\sum_{i=1}^{k}\left[\ell nf(x_i,\hat{\theta}_1)-\ell nf(x_i,\hat{\theta}_2)\right] \tag{11}$$

3.2 Change point estimation with the Bayesian method

The Bayesian method differs from the frequentist method in that each parameter is assumed to be a random variable and each one has a probability function called prior distribution. The estimate of the unknown parameter is obtained by deriving a posterior distribution on the basis of the prior distributions and the likelihood function. The posterior distribution is obtained:

$$\text{Posterior} \propto \text{likelihood} \times \text{prior}.$$

Under change point model given in Eq.(5), let $p_0(\theta_1,\theta_2|\ \nu)$ be the joint prior distribution of parameters θ_1, θ_2 and let $p_0(\nu)$ be the prior distribution of change point ν. The likelihood function is given by Eq.(6) and so the joint posterior distribution is written as follows:

$$p_1(\theta_1,\theta_2,\nu)\propto L(\theta_1,\theta_2,\nu)p_0(\theta_1,\theta_2|\ \nu)p_0(\nu)\,. \tag{12}$$

Integrate Eq.(12) with respect to the parameters, the marginal posterior distribution of change point is proportional to

$$p_1(\nu)\propto\int_{\theta_2}\int_{\theta_1}L(\theta_1,\theta_2,\nu)p_0(\theta_1,\theta_2|\ \nu)p_0(\nu)d\theta_1 d\theta_2 \tag{13}$$

and the Bayesian estimate $\hat{\nu}$ of the change point ν is found by maximizing the marginal posterior distribution given by Eq.(13). Assuming uniform priors, the joint posterior mode, which gives the maximum likelihood estimates, is at $\hat{\nu}$, $\hat{\theta}_1$, $\hat{\theta}_2$ (Smith, 1975).

4. Detecting change point in worldwide earthquake data and findings

This study investigates whether there is a change point in worldwide earthquake activities such as the number of earthquake occurrences and their magnitude. At first, assuming that the occurrences of the earthquakes follow the homogeneous Poisson process, a change point is investigated in the occurrence rate of the earthquake in unit time; secondly, the magnitudes of the earthquake are assumed to be normally distributed random variables; a change point is investigated in the mean of the normally distributed random variables describing the earthquake magnitudes.

To detect a change point in earthquakes, the relevant data is taken from the website of the U.S. Geological Survey (2011), consisting of 819 earthquakes worldwide of magnitude 4.0 or above covering the period from 3-March-1901 until 11-March-2011. It is assumed that the earthquake occurrences follow the homogeneous Poisson process. The earthquakes are observed at times $S_1, S_2, \ldots, S_{818}$ in the continuous time interval $(0, T]$. For the earthquakes data, the starting point S_0 is in 3-March-1901 and the end point S_{818}=T is in 11-March-2011. $T_1, T_2, \ldots, T_{818}$ are exponentially distributed random variables as given in Eq.(2). Under the assumption that τ is equal to the occurrence time of an event, the likelihood function can be written under the change point model in the sequence of exponentially distributed random variables:

$$L(\lambda_1, \lambda_2, \tau) = \lambda_1^{N_\tau} e^{-\lambda_1 \tau} \lambda_2^{n-N_\tau} e^{-\lambda_2 (T-\tau)} . \quad (14)$$

Where τ shows change point and is a continuous parameter defined time interval $(0, T]$, λ_2 is the occurrence rate in the time interval $(\tau, T]$ and N_τ is the number of events that occurred in the time interval $(0, \tau]$ and T is the sum of the time interval between the earthquake occurrences, that is $T = \sum_{i=1}^{818} t_i$ (Raftery & Akman, 1986; Akman & Raftery, 1986). The logarithm of the likelihood function is

$$\ell n L(\lambda_1, \lambda_2, \tau) = N_\tau \ell n(\lambda_1/\lambda_2) - \tau(\lambda_1 - \lambda_2) + n \ell n \lambda_2 - \lambda_2 T \quad (15)$$

After the derivation of the log likelihood function given by Eq.(15) for λ_1 and λ_2, the maximum likelihood estimations of λ_1 and λ_2 are obtained respectively:

$$\hat{\lambda}_1 = \frac{N_\tau}{\tau}, \quad \hat{\lambda}_2 = \frac{n - N_\tau}{T - \tau} \quad (16)$$

For the possible values of τ, $s_1, s_2, \ldots, s_n$, and the variable N_τ takes the values $1, 2, \ldots, n$, and so the estimations $(\hat{\lambda}_{11}, \hat{\lambda}_{21}), (\hat{\lambda}_{12}, \hat{\lambda}_{22}), \ldots, (\hat{\lambda}_{1n}, \hat{\lambda}_{2n})$ are calculated from Eq.(16) and then these estimations are substituted into Eq.(15). One of $(\hat{\lambda}_{1i}, \hat{\lambda}_{2i}, s_i)$, $i = 1, 2, \ldots, n$, gives the maximum of this function, say $\hat{\lambda}_1$, $\hat{\lambda}_2, \hat{\tau}$. Hence $\hat{\lambda}_1$, $\hat{\lambda}_2$ and $\hat{\tau}$ are the maximum likelihood estimation for λ_1, λ_2 and τ.

The scatter plot of the time intervals between the earthquakes is shown in Figure 1. From Figure 1, it is clearly seen that there is a change (or at least one change) in the occurrence rate of the earthquakes.

When we assume a single change point in the data and the method explained above is applied this data and the results are given in Table 1.

As is shown in Table 1, the occurrence rate of the earthquake in unit time (in day or in year) increased considerably after February 3, 2002, approximately ten times of the occurrence rate of the earthquakes in unit time before February 3, 2002.

From the log likelihood function of the change point in Figure 2, it can be seen that there are at least two change points in the data. There many methods are used to detect multiple change points in the data. One of the basic methods used for this purpose is binary

segmentation procedure (Chen & Gupta, 1997; Yang & Kuo, 2001). In the binary segmentation procedure, the data is divided into two homogeneous groups according to the estimated change point, and a change point is searched in each subdivided data until there is no change in the subdivided data. The results are given in Figure 3.

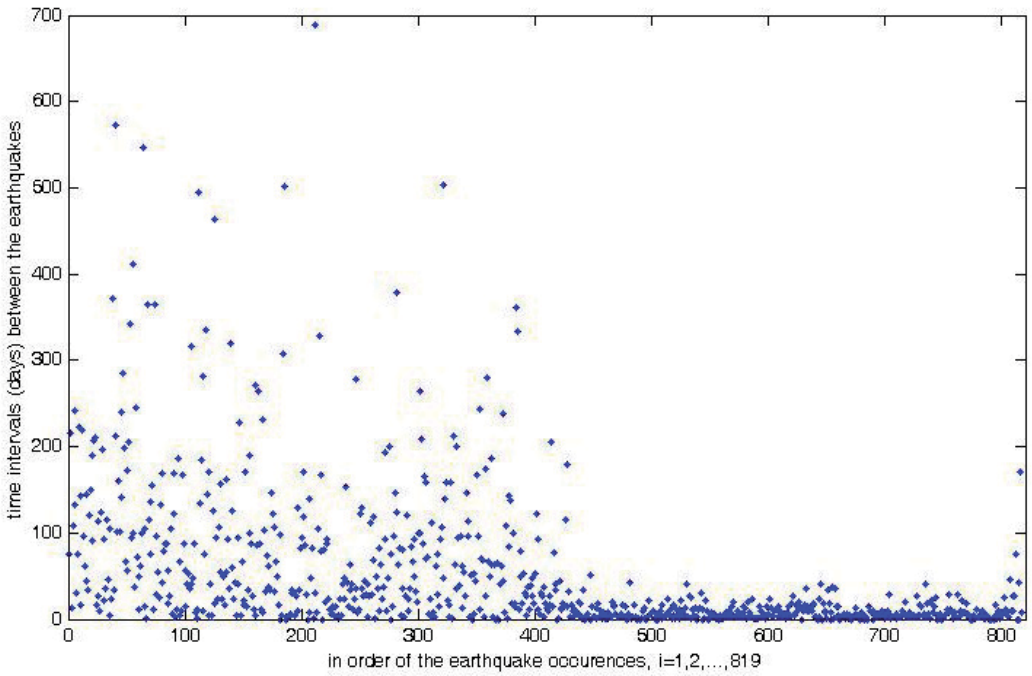

Fig. 1. The time intervals (days) between the earthquakes according to the earthquake occurrences.

n = 818, T= 40185 days		
Before the change point $\hat{\lambda}_1$	Estimated change point $\hat{\tau}$ $N_{\hat{\tau}}$ =429	After the change point $\hat{\lambda}_2$
0.0116380 (in days) 4.1896804 (in years)	03-Feb-2002	0.1170628 (in days) 42.1426080 (in years)

Table 1. Estimated parameters for the earthquake data.

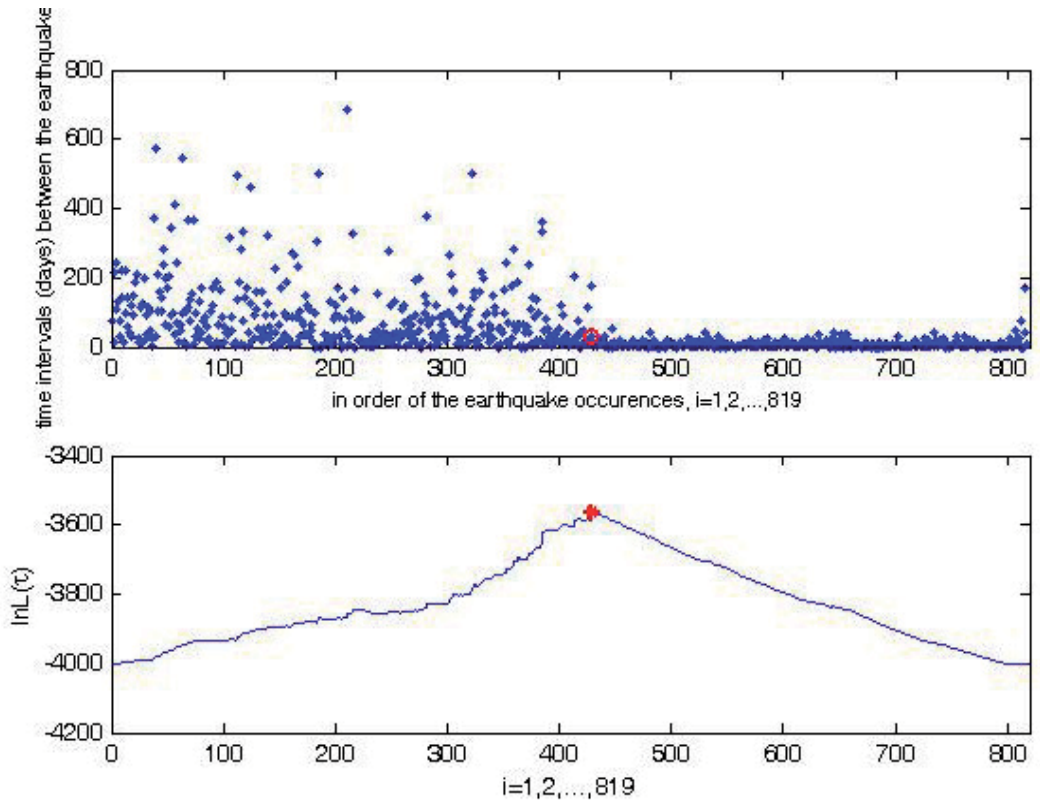

Fig. 2. The maximum point of log likelihood function given in Eq.(16) is shown as a red star and the corresponding change point estimate is shown with a red circle.

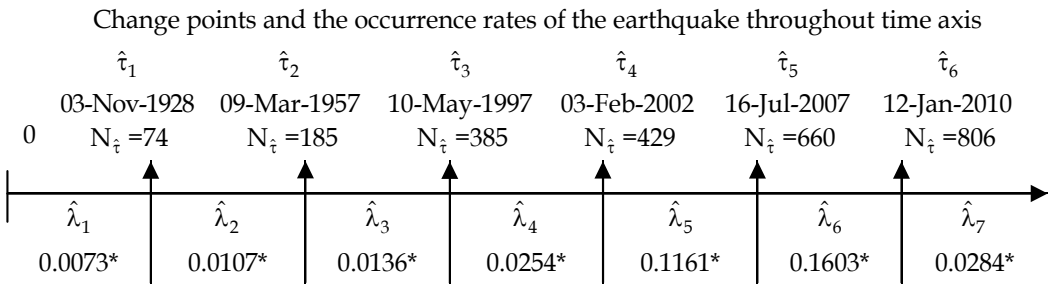

Fig. 3. The maximum likelihood estimations of parameters for multiple change points in the earthquake data (*in days).

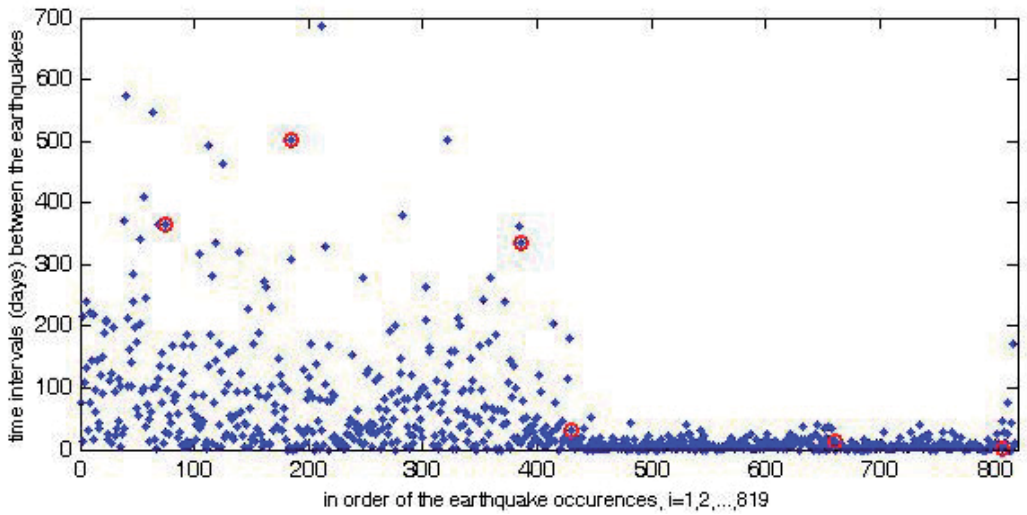

Fig. 4. Multiple change points in the earthquake data.

Estimated change points are shown on the scatter plot of the time intervals between the earthquakes.

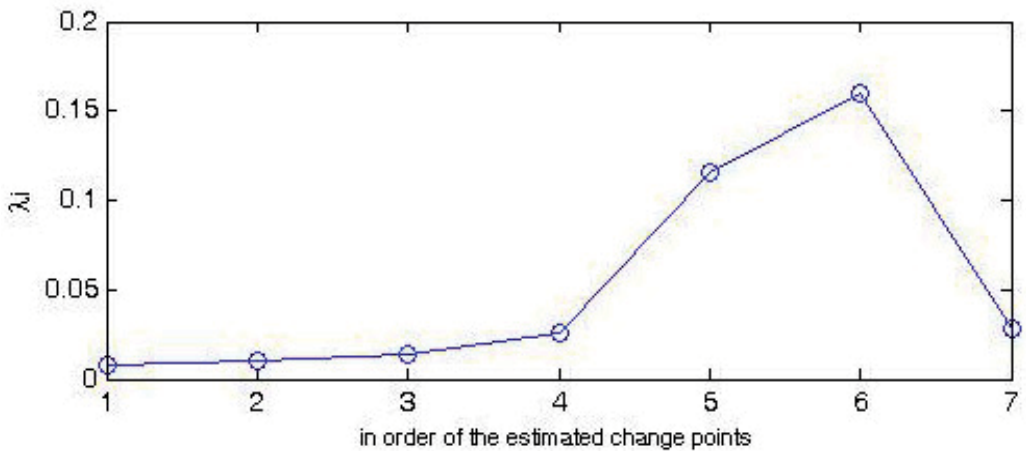

Fig. 5. The estimated occurrence rate of earthquakes in order of change points.

As can be seen in Figure 4 and Figure 5, the occurrence rate of the earthquakes increases slowly up until 03-February-2002, goes up sharply between 03- February-2002 and 12-January-2010, and tends to fall thereafter.

When using Bayesian method, the prior distributions of the parameters λ_1, λ_2 and τ, are taken to be respectively,

$$p_0(\lambda_1,\lambda_2|\ \tau)=\frac{1}{\lambda_1\lambda_2},\qquad \lambda_1,\lambda_2>0$$
$$p_0(\tau)=\frac{1}{T},\qquad 0<\tau<T \tag{17}$$

where the prior distributions are called uninformative priors. The joint posterior distribution of the parameters is can be written as:

$$\begin{aligned} p_1(\lambda_1,\lambda_2,\tau) &\propto L(\lambda_1,\lambda_2,\tau)p_0(\lambda_1,\lambda_2|\ \tau)p_0(\tau) \\ &\propto \lambda_1^{N_\tau}e^{-\lambda_1\tau}\lambda_2^{n-N_\tau}e^{-\lambda_2(T-\tau)}\frac{1}{\lambda_1\lambda_2 T} \end{aligned} \tag{18}$$

With integrate Eq. (18) with respect to the parameters λ_1,λ_2, the marginal posterior distribution of change point is proportional to

$$p_1(\tau) \propto \frac{\Gamma(N_\tau)\Gamma(n-N_\tau)}{\tau^{N_\tau}(T-\tau)^{n-N_\tau}}\left(\frac{1}{T}\right) \tag{19}$$

where $\Gamma(.)$ is gamma function. The marginal posterior distributions of λ_1 and λ_2 are not obtained analytically because of discontinuity in τ and the close form of the marginal posterior distributions of λ_1 and λ_2 are respectively proportional to

$$p_1(\lambda_1) \propto \frac{1}{T}\int_0^T \lambda_1^{N_\tau}e^{-\lambda_1\tau}\frac{\Gamma(n-N_\tau)}{(T-\tau)^{n-N_\tau}}d\tau,$$

$$p_1(\lambda_2) \propto \frac{1}{T}\int_0^T \lambda_2^{n-N_\tau}e^{-\lambda_2(T-\tau)}\frac{\Gamma(N_\tau)}{\tau^{N_\tau}}d\tau$$

where, for the possible values of τ, $s_1,s_2,\ldots,s_n$, and the variable N_τ takes the values $1,2,\ldots,n$.

Form Eq.(19), the Bayesian estimate $\hat{\tau}$ of the change point in the earthquake data is found to be the date 03-February-2002 2002 which corresponds to the posterior mode. The posterior distribution of the change point is given in Figure 6.

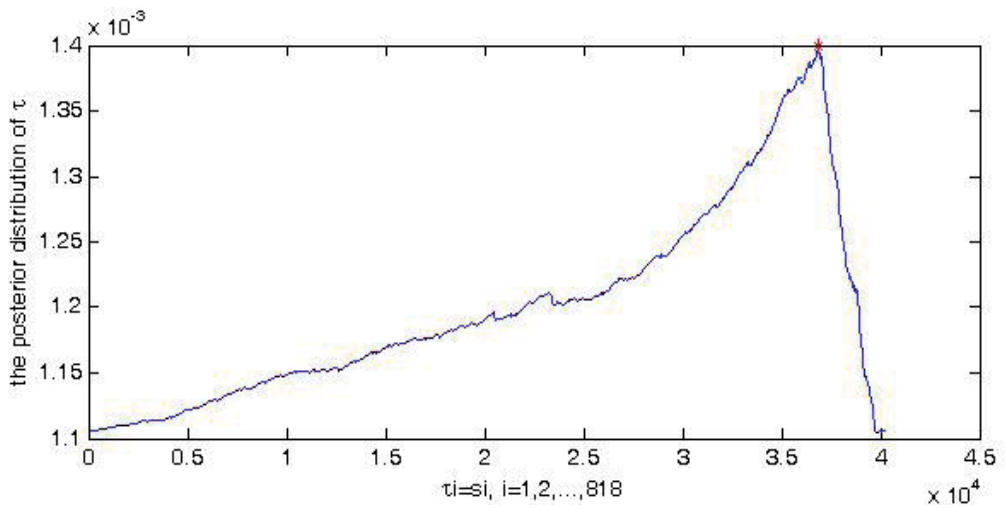

Fig. 6. The posterior distribution of change point and the posterior mode.

The Bayesian estimates of the parameters λ_1 and λ_2 would be the same as the maximum likelihood estimates because of uninformative prior distributions.
For multiple change points, the binary Bayesian segmentation procedure can be easily used. The procedure is employed as the mode of the posterior distribution of change point decreases considerably until the one before the posterior mode is found. The results are given in Figure 7.

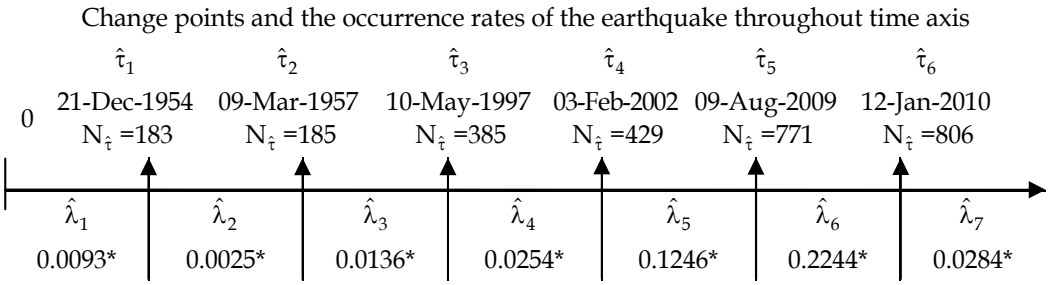

Fig. 7. The Bayesian estimations of parameters for multiple change points in the earthquake data (*in days).

When comparing the maximum likelihood estimates and the Bayesian estimates of the change points, we can see that the change points corresponding to dates such as 9-March-1957, 10-May-1997, 03-February-2002 and 12-January-2010 overlap. These dates are investigated in depth from many aspects, including overall world temperature, other disasters, and astronomical events.
When we look at the magnitudes of the earthquakes in the data, those of magnitude 6 to 6.9 number 291 (35.57%) and those of magnitude 7 to 7.9 number 258 (31.54%) (Table 2). The histogram of the magnitudes is given in Figure 6. Furthermore, using the Kolmogorov-Smirnov test, the distribution of the magnitudes is found to be almost normal (p=0.000).

Magnitude	4-4.9	5-5.9	6-6.9	7-7.9	8-8.9	≥9
The number of earthquakes	54	93	291	258	40	82
%	0.0660	0.1137	0.3557	0.3154	0.0489	0.1002

Table 2. The number of earthquakes with respect to magnitudes.

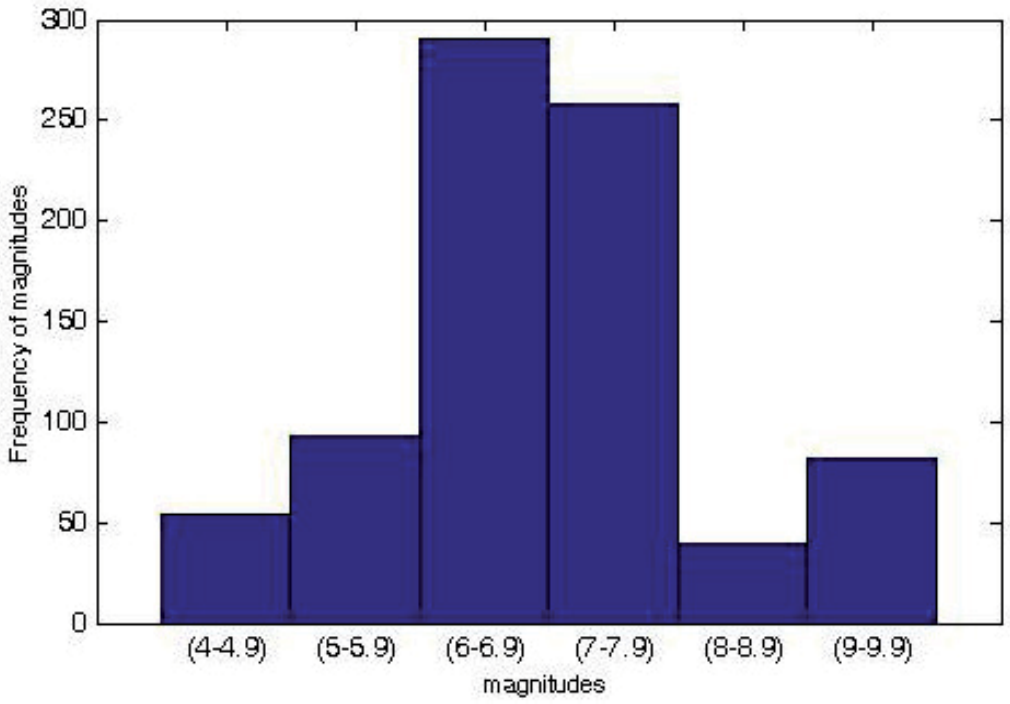

Fig. 8. Histogram of the earthquake magnitudes.

The sequence of the earthquake magnitudes $Y_1, Y_2, \ldots, Y_n$ can be assumed to be normally distributed random variables. The change point model in the mean of the normally distributed random sequences is written,

$$\begin{aligned} &Y_1, Y_2, \ldots, Y_\nu \sim N(\mu_1, \sigma^2) \\ &Y_{\nu+1}, Y_{\nu+2}, \ldots, Y_n \sim N(\mu_2, \sigma^2) \end{aligned} \tag{20}$$

where ν is an unknown change point in the mean of the sequence of the normally distributed random variables. To investigate whether there is a change point in the earthquake magnitudes, under the change point model, the likelihood function of the observed values, $y_1, y_2, \ldots, y_n$,

$$\begin{aligned} L(\theta_1, \theta_2, \nu) &= \prod_{i=1}^{\nu} f(y_i, \mu_1, \sigma^2) \prod_{i=\nu+1}^{n} f(y_i, \mu_2, \sigma^2) \\ &\propto \frac{1}{(\sqrt{2\pi\sigma^2})^n} \exp\left\{ -\frac{1}{2\sigma^2} \left(\sum_{i=1}^{\nu} (y_i - \mu_1)^2 - \sum_{i=\nu+1}^{n} (y_i - \mu_2)^2 \right) \right\}. \end{aligned} \tag{21}$$

and the logarithm of the likelihood function in Eq. (21) is:

$$\ell n L(\theta_1, \theta_2, \nu) \propto -\frac{1}{2\sigma^2} \left(\sum_{i=1}^{\nu} (y_i - \mu_1)^2 - \sum_{i=1}^{\nu} (y_i - \mu_2)^2 \right) \tag{22}$$

For any given value of ν, the maximum estimates of unknown parameters μ_1, μ_2, are $\bar{y}_1 = \frac{\sum_{i=1}^{\nu} y_i}{\nu}$ and $\bar{y}_2 = \frac{\sum_{i=\nu+1}^{n} y_i}{n-\nu}$ respectively. The estimates are substituted into Eq.(22), and with the maximized the log likelihood function given by Eq.(22), we can obtain the maximum likelihood estimate of the change point,

$$\hat{\nu} = \arg \max_{k=1,\ldots n-1} \left[\frac{1}{2\sigma^2} \left(\nu \bar{y}_1^{-2} - (n-\nu) \bar{y}_2^{-2} \right) \right] \tag{23}$$

From Eq. (23), the change point is estimated to be the date 28-February-2011 corresponding to ν=817. The estimated change point is close to end of the sequence such that it refers to no change point in the sequence. We can model both the number of the earthquake occurrences and the magnitudes of the earthquakes with compound Poisson process. Let $\{X_t, t \geq 0\}$ be a compound Poisson process as defined in Subsection 2.1

$$X_t = \sum_{i=1}^{N_i} Y_i$$

where N_t is the number of earthquakes in time interval $(0,t]$, which is a Poisson distributed random variable with parameter λt, and $\{Y_i, i = 1,2,\ldots\}$ are the magnitudes of the earthquakes, which are normally distributed random variables with parameters μ_i and σ^2. The mean and variance of the magnitudes of the earthquakes according to the estimated change points dates, (9-March-1957, 10-May-1997, 03-February-2002 and 12-January-2010) are given in Table 3.

Estimated Change points	Up to 9-Mar-1957	Between 9-Mar-1957 and 10-May-1997	Between 10-May-1997 and 03-Feb-2002	Between 03-Feb-2002 and 12-Jan-2010	After 12-Jan-2010
Occurrence rate of the earthquakes	0.0090*	0.0136*	0.0254*	0.1300*	0.0284*
Mean of the magnitudes	6.9622	6.7250	7.0795	6.4562	7.1167
Variance of the magnitudes	0.9305	0.8821	0.5579	0.9845	1.2706

Table 3. Means and variances of the magnitudes with respect to estimated change point (*in days).

Using Table 3, we compute the recurrence periods for certain earthquakes of magnitude y, corresponding to the change point, 12-January-2010. The recurrence period of an earthquake with magnitude y is computed by

Reccurence period=1/(Expected number of earthquakes).

The expected number of earthquakes of magnitude y is computed by the multiplying the probability of occurrence class of magnitude with the expected number of earthquakes over a certain period of time.

Class Magnitude (y)	$F_Y(L)$ Expected	$F_Y(U)$ Expected	$P(L \le y \le U)$ Expected	Expected number of earthquakes (year)	Average recurrence period (year)
4-4.9	0.0028	0.0246	0.0218	0.2257	4.4306
5-5.9	0.0302	0.1402	0.1100	1.1404	0.8769
6-6.9	0.1609	0.4238	0.2629	2.7248	0.3670
7-7.9	0.4588	0.7565	0.2977	3.0856	0.3241
8-8.9	0.7834	0.9432	0.1598	1.6566	0.6037
≥9	0.9526	1.0000	0.0474	0.4912	2.0360

Table 4. The estimation of recurrence periods for certain earthquakes after the change point 12-January-2010.

Time	Expected number of earthquakes	Expected total magnitudes of earthquakes
30 days	0.8520	6.0634
3 months	2.5560	18.1902
6 months	5.1120	36.3805
1 years	10.3660	73.7717
2 years	20.7320	147.5434
3 years	31.0980	221.3151
4 years	41.4640	295.0868
5 years	51.8300	368.8585
10 years	103.6600	737.7171
20 years	207.3200	1475.4342

Table 5. Expected number of earthquakes and the expected total magnitudes of earthquakes with respect to the change point 12-January-2010.

Number of earth.	30 days 11-Feb-10	3 months 12-Apr-10	6 months 11-Jul-10	1 year 12-Jan-11	2 years 11-Jan-12	3 years 11-Jan-13	4 years 11-Jan-14	5 years 11-Jan-15	10 years 11-Jan-20	20 years 11-Jan-30
0	0.426560956	0.077614579	0.006024023	3.1485E-05	9.91304E-10	3.12112E-14	0	0	0	0
1	0.363429935	0.198382863	0.030794805	0.000326373	2.05517E-08	9.70605E-13	0	0	0	0
2	0.154821152	0.253533299	0.078711521	0.001691593	2.13039E-07	1.50919E-11	0	0	0	0
3	0.043969207	0.216010371	0.134124431	0.005845017	1.47224E-06	1.56443E-10	1.16755E-14	0	0	0
4	0.009365441	0.138030627	0.171411023	0.015147361	7.63063E-06	1.21627E-09	1.21028E-13	0	0	0
5	0.001595871	0.070561256	0.17525063	0.031403509	3.16396E-05	7.56469E-09	1.00366E-12	0	0	0
6	0.000226614	0.030059095	0.149313537	0.054254796	0.000109326	3.92078E-08	6.93599E-12	0	0	0
7	2.75821E-05	0.010975864	0.109041543	0.080343602	0.000323791	1.74183E-07	4.10848E-11	0	0	0
8	2.9375E-06	0.003506789	0.069677546	0.104105222	0.000839104	6.77095E-07	2.12943E-10	3.99619E-14	0	0
9	2.78083E-07	0.000995928	0.039576846	0.119906081	0.001932923	2.33959E-06	9.8105E-10	2.30136E-13	0	0
10	2.36927E-08	0.000254559	0.020231684	0.124294643	0.004007336	7.27565E-06	4.06783E-09	1.1928E-12	0	0
11	1.83511E-09	5.91503E-05	0.009402215	0.117130752	0.007552736	2.05689E-05	1.53335E-08	5.62024E-12	0	0
12	1.30292E-10	1.2599E-05	0.004005344	0.101181448	0.01304861	5.33044E-05	5.29823E-08	2.42747E-11	0	0
13	8.53917E-12	2.47716E-06	0.001575024	0.08068053	0.020809521	0.000127512	1.68989E-07	9.67815E-11	3.26026E-14	0
14	5.19669E-13	4.52259E-07	0.000575109	0.05973817	0.030815928	0.000283241	5.00498E-07	3.58299E-10	1.44839E-13	0
15	2.95172E-14	7.70649E-08	0.000195997	0.041283058	0.042591721	0.000587215	1.38351E-06	1.23804E-09	6.00562E-13	0
16	0	1.23111E-08	6.26211E-05	0.026746261	0.055188223	0.001141327	3.58536E-06	4.01048E-09	2.33453E-12	0
17	0	1.85101E-09	1.88305E-05	0.016308926	0.067303661	0.002087822	8.74491E-06	1.22273E-08	8.5411E-12	0
18	0	2.62844E-10	5.34787E-06	0.009392129	0.077518861	0.003607061	2.01444E-05	3.52077E-08	2.95123E-11	0
19	0	3.53594E-11	1.43886E-06	0.005124148	0.084585317	0.005903809	4.39614E-05	9.60429E-08	9.66079E-11	0
20	0	4.51893E-12	3.67772E-07	0.002655846	0.08768114	0.009179833	9.11408E-05	2.48895E-07	3.00431E-10	0
25	0	0	2.01378E-10	4.98583E-05	0.052673373	0.041877043	0.001752055	1.46016E-05	4.38567E-08	0
30	0	0	4.11104E-14	3.48963E-07	0.011797303	0.071223597	0.012557101	0.000319369	2.3869E-06	0
35	0	0	0	1.07217E-09	0.001159888	0.05317575	0.039506887	0.003066385	5.70261E-05	0
40	0	0	0	1.6252E-12	5.62613E-05	0.019586801	0.061322008	0.014525139	0.000672161	4.94125E-13
150	0	0	0	0	0	0	0	0	0	3.67978E-06

Table 6. Probability of earthquake occurrences after the change point 12-January-2010.

5. Conclusion

Predicting earthquakes is of crucial importance these days. Many researchers have studied earlier attempts at earthquake detection. The change point analysis is used in both backward (off-line) and forward (on-line) statistical research. In this study, it is used with the backward approach in the worldwide earthquake data. The change points found in the worldwide earthquake data are useful in making reliable inferences and interpreting the results for further research. Each date found as the change point in the earthquake data should be carefully investigated with respect to other geographical, ecological, and geological events or structures in the world.

6. References

Akman V. E. & Raftery A. E. (1986). Asymptotic inference for a change-point Poisson process, *The Annals of Statistics*, Vol.14, No.4, pp. 1583–1590.

Aktaş, S.; Konşuk, H. & Yiğiter, A. (2009). Estimation of change point and compound Poisson process parameters for the earthquake data in Turkey, *Environmetrics*, Vol. 20, No.4, pp. 416-427

Amorese, D. (2007). Applying a Change-Point Detection Method on Frequency-magnitude Distributions, *Bulletin of the Seismological of America*, Vol.97, No.5, pp.1742-1749

Boudjellaba, H.; MacGibbon, B. & Sawyer, P. (2001). On exact inference for change in a Poisson Sequence. *Communications in Statistics A: Theory and Methods,* Vol.30, No.3, pp. 407–434

Chen J. & Gupta A. K. (1997). Testing and locating variance change points with application to stock prices, Journal of the American Statistical Association: JASA, Vol.92, No. 438, pp. 739-747

Fotopoulos S. B. & Jandhyala V. K. (2001). Maximum likelihood estimation of a change-point for exponentially distributed random variables, *Statistics & Probability Letters*, 51: 423–429

Kagan, Y. Y. (2010). Statistical Distributions of Earthquake Numbers: Consequence of Branching Process, *Geophysical Journal International*, Vol.180, No.3, pp.1313-1328

Leonard T. & Papasouliotis, O. (2001). A Poisson Model for Identifying Characteristic Size Effects in Frequency Data: Application to Frequency-size Distributions for Global Earthquakes, "Starquakes", and Fault Lengths, *Journal of Geophysical Research*, Vol.106, No.B7, pp.13,413-13,484

Lindsey H. (June 2007). 'Natural' catastrophes increasing worldwide, 14.06.2007, Available from: http://www.wnd.com/news/article.asp?ARTICLE_ID=40584/

Mandeville M. W. (June 2007). "Eight Charts Which Prove That Chandler's Wobble Causes Earthquakes, Volcanism, El Nino and Global Warming", 14.06.2007, Available from: http://www.michaelmandeville.com/polarmotion/spinaxis/vortex_correlations2.htm

Parzen, E. (1962). *Stochastic Processes*, Holden-Day, ISBN 0-8162-6664-6, San Francisco, USA

Raftery A. E. & Akman V. E. (1986). Bayesian analysis of a Poisson process with a change point, *Biometrika*, Vol.73, pp.85–89

Rotondi R. & Garavaglia, E. (2002). Statistical Analysis of the Completeness of a Seismic Catalogue, *Natural Hazards*, Vol.25, No. 3, pp. 245-258

Rydelek, P. A. & Sacks I. S. (1989). Testing the completeness of earthquake catalogues and the hypothesis of self-similarity, *Nature*, Vol. 337, pp.251–253

Schorlemmer, D. & Woessner, J. (2008). Probability of Detecting an Earthquake, *Bulletin of the Seismological of America*, Vol.98, No.5, pp. 2103-2117

Smith, A. F. M. (1975).A Bayesian approach to inference about a change point in a sequence of random variables, *Biometrika*,Vol.62, pp. 407-416

U.S. Geological Survey web page 16. 03. 2011, Available from: http://earthquake.usgs.gov/regional/world/historical.php

Yang, T. Y. & Kuo, L. (2001). Bayesian binary segmentation procedure for a Poisson process with multiple change points, *Journal of Computational and Graphical Statistics,* Vol. 10, pp. 772–785

Yao, Q. (1993). Tests for change-points with epidemic alternatives. *Biometrika,* Vol.80, pp. 179-191

Yigiter, A. & İnal, C. (2010). Estimation of change points in a homogeneous Poisson process with an application to earthquake data, *Pakistan Journal of Statistics*, Vol. 26, No. 3, pp. 525-538

Part 2

Studies on Earthquake Precursors and Forecasting

3

Current State of Art in Earthquake Prediction, Typical Precursors and Experience in Earthquake Forecasting at Sakhalin Island and Surrounding Areas

I.N. Tikhonov[1] and M.V. Rodkin[1,2]
[1]*Institute of Marine Geology and Geophysics FEB RAS, Yuzhno-Sakhalinsk*
[2]*International Institute of Earthquake Prediction Theory and Mathematical Geophysics RAS, Moscow*
Russia

1. Introduction

Despite of over a century of scientific effort, the understanding in earthquake forecasting remains immature. Moreover, even the theoretical possibility of earthquake forecasting is debatable. Especially problematic is a possibility of an effective short- and intermediate-term earthquake forecasting. The aim of this paper is to present the new evidence in support of possibility of the short- and intermediate-term earthquake forecasting. This possibility is shown through the discussion of seismic regime in the generalized vicinity of strong earthquake and through the description of an experience in an earthquake forecasting in the case of the Sakhalin Island and the surrounding areas.

USGS/NEIC catalog and Harvard seismic moments catalog are used to construct the generalized space–time vicinity of strong (M7+) earthquake to reveal the robust typical long-, intermediate, and short-term precursor anomalies. The very essential increase in available information resulted from this procedure gives possibility to detail the character of precursors of strong earthquake. The typical parameters of the fore- and aftershock cascades were detailed. A few other revealed precursory anomalies indicate the development of softening in the source area of a strong earthquake. The set of the precursory anomalies indicates the approaching of a strong event quite definitely. Thus one can conclude that the effective short- and intermediate-term earthquake forecasting appears to be possible in the case of essential increase of volume of statistical information available for the forecasting.

The current state of art in the earthquake forecasting is illustrated by the case of experience in the earthquake forecasting for the Sakhalin Island and the surrounding areas performed in the Institute of Marine Geology and Geophysics of the Far East Branch of the Russian Academy of Science, Yuzhno-Sakhalinsk, Russia. Four examples of successful prognosis (three of them performed in a real time), and one false alarm took place. Thus, despite the evident deficient in available information the results of forecasting appear to be encouraging

enough. In any case they are much better than they could be in the case if the seismic roulette model would be valid.

In the early 1980s a few examples of successful earthquake prognosis were known, and the final successes in decision of the problem of earthquake prognosis seemed to be close. But the substantial increase in a number of different sensors used in earthquake monitoring, and the corresponding increase in available information didn't improve the quality of prognosis. The situation was discussed widely in the 90s, and the dominant opinion elaborated by the world scientific community was quite pessimistic. An earthquake generating system was found to be very unstable. A minor change in parameters of such systems can significantly change their evolution; as a result an effective prognosis of behavior of such systems is impossible. Thus an earthquake prognosis was declared to be impossible (Geller, 1997; Geller et al., 1997; Kagan, 1997; and references herein). Despite of this dominating opinion a few groups of researchers have continued their investigations in earthquake forecasting. First of all the effectiveness of the suggested earlier algorithms of strong earthquake prediction was tested in real time. The results of the use of the M8 and Mendocino Scenario algorithms suggested earlier in (Keilis-Borok & Kossobokov, 1986, 1990; Kossobokov, 1986) were examined during more than twenty years. It was shown that the results of prognosis were significantly better than it could be in case of a seismic roulette procedure (Shebalin, 2006; Kossobokov, 2005). However neither these algorithms nor the other ones tested at shorter time intervals (Sobolev et al., 1999; Papazachos, 2005; Zavyalov, 2006; and others) showed results quite suitable for practical use. There were substantial probabilities to miss an earthquake or declare false alarm.

Low efficiency of earthquake prediction is connected to extremely irregular character of seismic regime. Due to the high level of irregularity of seismic regime parameters of earthquake precursors are vague, and even the very existence of precursor phenomena remains debatable. As a result in the absence of well known precursors any algorithm of forecasting based on the use of these precursors could hardly be very effective.

Thus verification of used precursor phenomena is an urgent problem. A precursory process and occurrence of large earthquake is commonly treated as an example of critical phenomenon (Akimoto & Aizawa, 2006; Bowman et al., 1998; Keilis-Borok & Soloviev, 2003; Malamud et al., 2005; Nonlinear …, 2002; Sornette, 2000; etc.). Many of the precursors used currently, such as development of foreshock cascade, an increase in correlation length, and an abnormal clustering of earthquakes, are expected to occur in critical processes. Moreover, some of these precursors came in the use because the process of strong earthquake occurrence is treated in terms of the critical phenomenon model. In this situation a natural question may arise: to what extent are such model processes really typical of scenarios of occurrence of large earthquake? Romashkova and Kossobokov (2001) have considered the evolution of foreshock and aftershock activity in the vicinities of eleven strong earthquakes occurring from 1985 to 2000. This examination has not supported the universality of power-law growth in foreshock activity toward the moment of a large earthquake. It also turned out that the aftershock sequences in a number of cases differ significantly from the Omori law. As a result it was hypothesized (Romashkova & Kossobokov, 2001; Kossobokov, 2005) that scenarios of aftershock sequences deviating from the Omori law can exist.

It seems natural to ask whether the observed deviations of the seismic process from the theoretically expected universal scenario have a stochastic nature or different scenarios can

be put into effect in different foreshock and aftershock sequences. The answer to that question can be obtained by investigation of mean features inherent to vicinities of a large number of strong earthquakes. A strong earthquake vicinity is understood here as a space-time domain where evolution of seismicity is influenced by occurrence of a given strong earthquake. Using the approach presented in (Rodkin, 2008) we have constructed the mean generalized space–time vicinity of a large number of strong earthquakes and examined the mean anomalies inherent to this vicinity.

2. Construction of generalized vicinity of strong earthquake

We have used the Harvard worldwide seismic moment catalog for 1976–2005, and the USGS/NEIC catalog for 1968–2007. In both cases only shallow earthquakes with depth H < 70 km were examined. Two subsets of data can be used, first one includes all earthquakes from the catalog and the second includes stronger earthquakes that are only completely reported. Below we present the results from processing of the Harvard catalog using the first subset of data (all reported events) and the results for the USGS/NEIC catalog using only completely reported events. In the latter case the events with magnitude M ≥ 4.7 were used, a total number of events was 97615. A similar cutoff for the Harvard catalog would reduce the available data too much to get statistically robust results.

Both used data sets were searched for events falling into the space–time domains surrounding the source zones of large (M7+) earthquakes, with due account for the seismic moment in the Harvard catalog and the maximum magnitude for the USGS/NEIC catalog. A generalized vicinity of large earthquake is understood as a set of events falling into the zone of influence of any of these strong earthquakes. The zones of influence were defined as following, see also (Rodkin, 2008) for the details. Spatial dimensions of the zones of influence for earthquakes of different magnitudes were calculated from the approximate relationship (Sobolev & Ponomarev, 2003) between typical source size L and earthquake magnitude M:

$$L\ (\text{km}) = 10^{0.5M\ -\ 1.9}. \tag{1}$$

In the examination below the earthquakes located at distances within $7\times L$ from the epicenter of the given strong earthquake were taken into account.

For constructing a time vicinity of strong earthquake we used the conclusion that duration of a failure cycle weakly depends on earthquake magnitude (Smirnov, 2003). Hence the simple epoch superposition method can be used for comparing the time vicinities of earthquakes with close magnitudes. At the figures below all earthquakes located in the area $7\times L$ of the corresponding strong event were taken into account. This choice allows the most complete use of available data. Negative consequences of this choice are a lower statistical significance at the edges of the time interval because of shortage of data there, and a false effect of a systematic growth of a number of earthquakes towards the centre of the used time interval. However these errors can be taken into account, so they do not distort the results.

The generalized vicinity of large earthquake which was constructed contained more than 60000 earthquakes for the Harvard catalog and more than 300000 earthquakes for the USGS/NEIC catalog. Such a big number of events resulted from the fact that one and the same earthquake can belong to the space–time vicinities of different strong earthquakes.

Such an increase in a number of events has considerably enhanced the possibility of statistical examination.
Time and space position of each earthquake falling into the generalized vicinity of large earthquake is characterized by the time shift from the origin time of the corresponding strong earthquake and by the distance from the epicenter of this main event (norm to the source size of this main event). Both catalogs (USGS/NEIC and Harvard) were used for examination of the relative space-time density of earthquakes. The Harvard catalog was used in this paper mostly for the verification of results, which were obtained from examination of the USGS/NEIC catalog.

3. Regularities in rate of fore- and aftershock cascades

The most well known feature of seismic behavior occurring in the vicinities of large earthquakes is the existence of aftershock and foreshock power-law cascades. Figures 1*a* and 1*b* show the foreshock and aftershock sequences in the generalized vicinity of strong earthquake, which were obtained from USGS/NEIC data (similar results were obtained from examination of the Harvard catalog). The earthquakes rate is presented by time density of group of earthquakes consisting of subsequent 50 events taken with step 25 events (rate of events is given in n/day for convenience).
As can be seen in Fig. 1, the evolution of foreshocks and aftershock sequences well correlates with a power law. The Omori law (Utsu et al., 1995; Sobolev, 2003) is known to be a good fit to the aftershock rate:

$$n \sim 1/\ (c + t)^{-p}, \tag{2}$$

where n is the rate of aftershock occurrences, t is the time interval after the main shock occurrence, c – parameter fitting the rate of earthquakes in the closest vicinity of the main shock, and p is the parameter of the Omori law. The Omori law (2) is a good fit for the interval until one hundred days or somewhat later after the main shock occurrence.
The foreshock cascade occurring before the main shock time can be described in a similar manner; in this case t is the time before the main shock origin, and c = 0. The foreshock cascade was found to be quite noticeable in the generalized vicinity 10-20 days before the main shock occurrence (Fig. 1).
Of special interest is the deviation of the aftershock rate from the power law during the first hours after the main shock occurrence. The deficit of earlier aftershocks described by parameter c in (2) is explained sometimes by difficulty in recording all of too numerous aftershocks occurring immediately after a large earthquake. However, this factor is hardly capable of providing a full explanation of the phenomenon (Lennartz et al., 2008; Shebalin, 2006). The deviation from the power law toward lower rates of events during a few first hours of the aftershock sequence can be seen clearly in Fig. 1b; the rate of aftershocks reaches the values obeying the power law only 2–3 hours after the strong earthquake. At that time the mean rate of earthquakes with $M \geq 4.7$ occurring in the vicinity of a mean large earthquake (but not in the generalized vicinity of large earthquake) is a little above one event per hour. Such rate can not cause any problem in events recording. Thus, the effect of a lower rate of earlier aftershocks probably has a physical nature. This conclusion is similar with those presented in (Lennartz et al., 2008; Lindman et al., 2010; Shebalin, 2006).

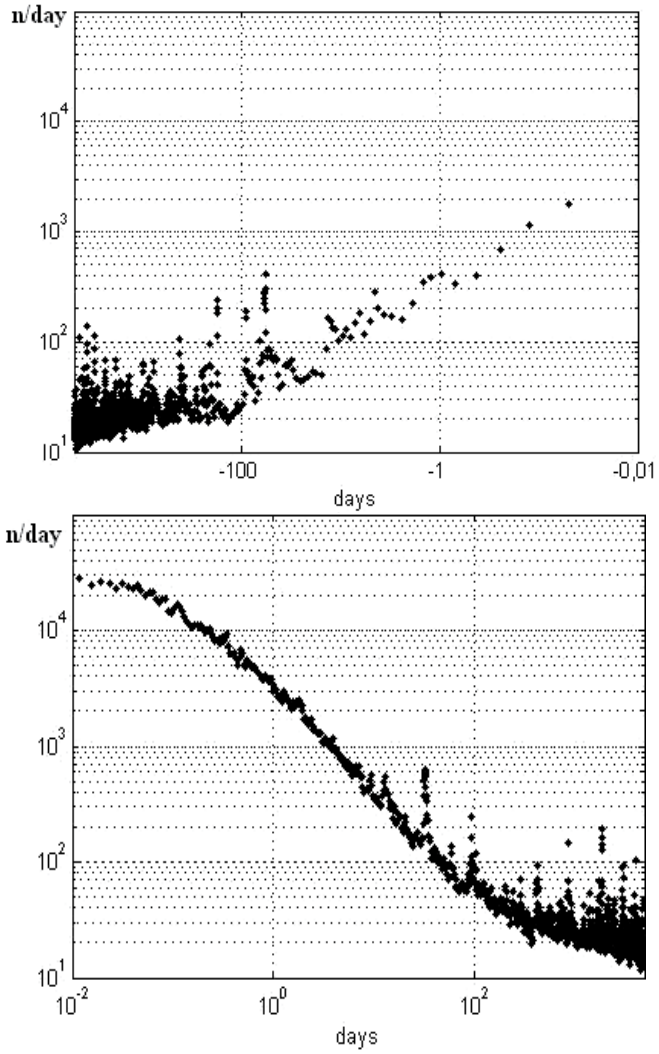

Fig. 1. The fore- (upper panel) and aftershock (lower panel) sequences in the generalized vicinity of strong earthquake, events flow is given in a number of events per day, zero time corresponds to the moment of occurrence of the generalized main shock.

Note that as it can be seen in Fig. 1, the mean duration of the foreshock process is significantly shorter than that of the aftershocks, and the rate of increase for foreshocks toward the moment of main shock occurrence is noticeably slower than the decay of the aftershock rate. From this it follows that the typical maximum rate of foreshock sequence is an order smaller than the maximum rate of aftershock process. This result is intimately related to the problem of predictability of large earthquakes; the prediction problem would have been solved already, if the rate of foreshocks would be equal to the rate of aftershocks. It seems important to note that upon closer examination the seismicity increase in the generalized vicinity of large earthquakes is not confined to the foreshock and aftershock cascades. Essentially weaker but quite noticeable increase above the mean rate level occurs

in the time interval about ±100-300 days around the main shock date. The analysis of the Harvard seismic moment catalog gives similar results; however, these data testify for a broader area of seismicity increase, roughly within ±500 days around the main shock date. This type of long-term pre- and post-shock seismic activity agrees with the suggestion that the final time interval of strong earthquake preparation prolongs a few years.

We now characterize the changes in the seismicity increase as functions of the distance to the main shock epicenter. The distances are compared in units of the magnitude-dependent main shock source dimension L from equation (1). Fig. 2 shows the distance–time diagram of rate of a number of events in the vicinity of the main shock. The horizontal axis indicates the time (in days) from the main shock occurrence time; an analogue of longtime scale is used near the main shock occurrence moment. The vertical axis indicates the distance from the main shock epicenter in units of earthquake source size L. Events' rate is given in logarithmic scale, $\ln(n)$, where n is the number of events in a cell of the distance–time diagram.

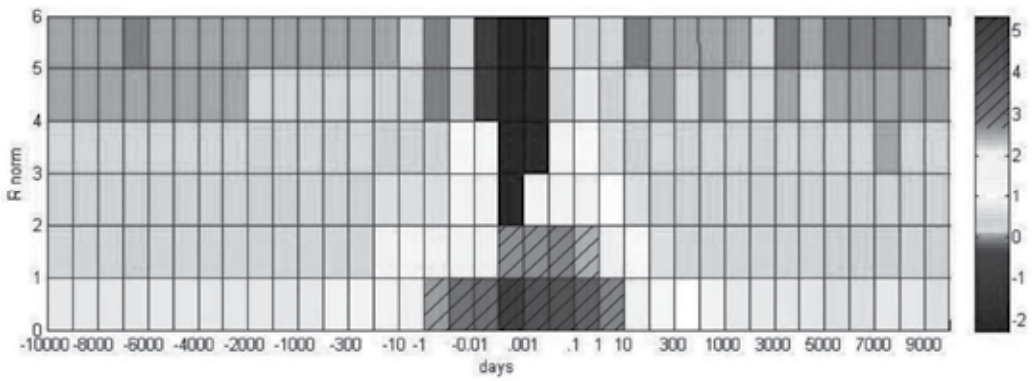

Fig. 2. Spatial-temporal change of number of earthquakes lg (density of events per day) in the generalized vicinity of strong earthquake, distance R_{norm} from the main shock epicenter is given in norm source size units.

As can be seen in Fig. 2, the rate of earthquakes in the vicinity of the main shock begins to increase one-three hundred days before the main shock, and this activity increase accelerates toward the moment of the main shock. The increase in seismic activity occurs at a distance of about three source sizes L from the main shock. This estimate of the radius of influence is in agreement with the size of the areas where predictive functions are usually estimated in earthquake prediction algorithms (Kossobokov, 2005; Shebalin, 2006). Seismic activity outside the zone of 3–4 earthquake source sizes decreases in the close time vicinity of strong earthquake. This feature can result from softening in the source of ongoing strong earthquake. Some other indications of strength decrease in the strong earthquake vicinity are presented in (Rodkin, 2008). In this case one can expect the strain rearrangement from the outer "rigid" region into the inner "soft" zone where the strong earthquake is about to occur. As a result of this rearrangement, the probability of earthquake occurrence in the outer "rigid" zone of the future rupture would become somewhat lower.

The decrease in b-value is known to be used as an indicator of an increase in probability of a strong earthquake occurrence (Shebalin, 2006; Zavyalov, 2006). Catalog USGC/NEIS was

used to examine the change in b-value in the generalized vicinity of strong earthquake (the similar results were obtained from examination of the Harvard catalog). The maximum likelihood method was used for the *b*-values estimation (Utsu, 1965). By this method the *b*-value is calculated from

$$b = lg(e) / (M_{av} - M_c) \tag{3}$$

where M_{av} is the average magnitude for each subset of data and M_c is the lower magnitude limit used in the analysis, here M_c=4.7. Discreteness of magnitude values because of

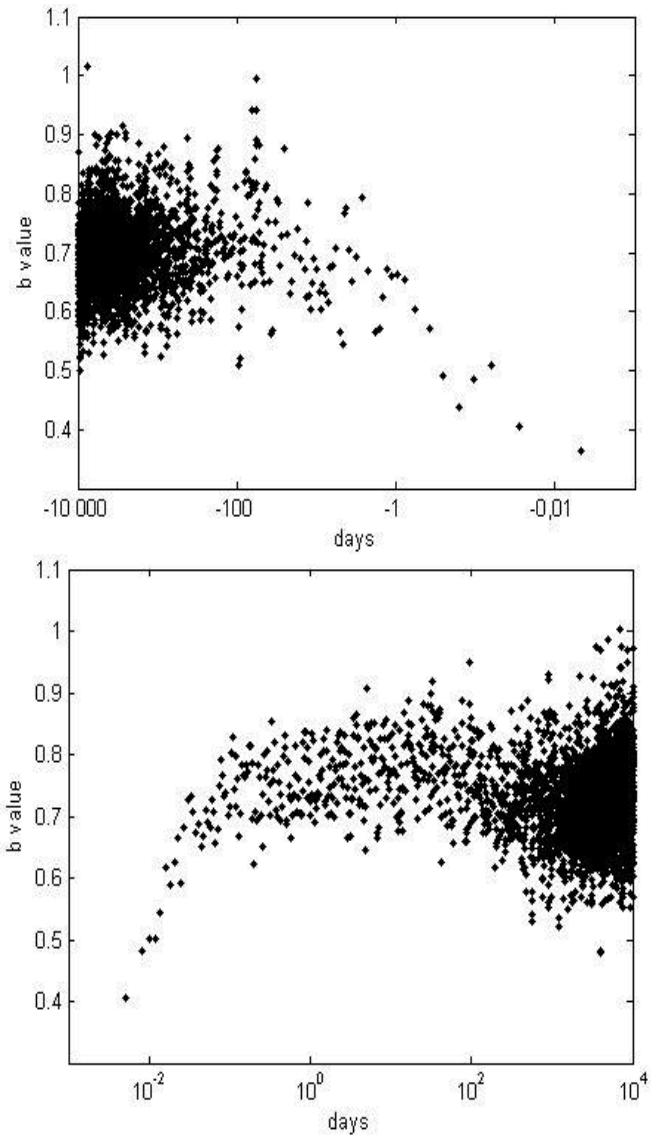

Fig. 3. The change of mean b-values in the generalized vicinity of strong earthquake. The values obtained for 50 events groups are given by dots. Panels as in Fig. 1.

aggregation in 0.1-bins is small, it influences the *b*-values weakly and uniformly; therefore it was not taken into account. The maximum likelihood method (3) gives a suitable *b*-value estimation for a number of events exceeding 50. Having this in mind the groups consisting of 50 subsequent events were used in *b*-value determination. The data points in Fig. 3 reflect the *b*-values obtained for such groups with step 25 events; thus the data points are independent of those next to the adjacent ones.

As it can be seen in Fig. 3, there is an evident tendency of decrease in *b*-values in the time vicinity of the generalized main shock; and this decrease increases strongly with approaching the moment of the main shock. In the foreshock sequence the noticeable decrease begins about one hundred days before the main shock. In the aftershock sequence the sharp increase in *b*-values takes place during the first several days after the main shock. A slow increase in *b*-values takes place in the following 100 days. It is necessary to notice that the *b*-values appear to be increased in comparison with the background value in the time interval 10-100 days after the main shock occurrence. These features agree with a tendency of lowermost *b*-values in the very beginning of the aftershock sequences and with an increase of *b*-value in the further evolution of the aftershock sequences (Rodkin, 2008; Smirnov & Ponomarev, 2004). The similar tendency was found in the examination of acoustic emission data (Smirnov & Ponomarev, 2004). New findings consist in the stronger decrease than it was found before and in rather symmetrical character of this decrease for fore- and aftershock sequences. Note that the amplitude of the *b*-value decrease appears to be proportional to the logarithm of time remaining from the moment of the main shock. Such type of behavior is typical of critical processes.

Note however that the well known and widely used below effect of "seismic quiescence" was not found in the generalized vicinity of strong earthquake. It can be connected with anisotropic character of this type of precursor anomaly in relation to a strong earthquake epicenter that is mentioned in (Zavyalov, 2006). In this case this effect can be eliminated by summarizing data from vicinities of a large number of differently oriented strong earthquakes.

4. Experience in earthquake prediction at the Sakhalin Island and surrounding areas

Region under study includes the Sakhalin Island and the Kuril Islands arc. In a few cases the area of the Japan Islands was also taken into account. This territory belongs to the transitive zone between the Pacific and the Eurasian continent and includes the active island arc characterized by one of the highest levels of seismicity on the Earth. Because of variability in quality of available catalogs the methodology of prognosis is more or less different in every particular case of strong earthquake prognosis, which is described below.

To avoid misunderstanding and controversial interpretations, we follow below the definition of the term "earthquake prediction," which was formulated by the Panel on Earthquake Prediction with the US National Academy of Sciences (Allen et al., 1976):

"An earthquake prediction must specify the expected magnitude range, the geographical area within which it will occur, and the time interval within which it will happen with sufficient precision so that the ultimate success or failure of the prediction can readily be judged. Only by careful recording and analysis of failures as well as successes can the eventual success of the total effort be evaluated and future directions charted. Moreover,

scientists should also assign a confidence level to each prediction." (Predicting earthquakes …, 1976).
In the case when the demands of this definition are not fulfilled the term "earthquake forecasting" is used.
We use such definition instead of another one when the term "prediction" means a deterministic prognosis as it was formulated in (Operational Earthquake Forecasting: State of Knowledge and Guidelines for Utilization. International Commission on Earthquake Forecasting for Civil Protection, http://www.protezionecivile.gov.it/cms/attach/ex_sum_finale_eng1.pdf). We suggest that deterministic prognosis is impossible now and hardly will be possible even in future, thus such use of the term "prediction" seems to be inefficient.

4.1 Case 1 - Diagnostics of a dangerous period before the 1994 Mw 8.3 Shikotan earthquake (the South Kuril region)

4.1.1 Seismic region and data

The region under study in case 1 includes the Kuril Islands zone and the area to the east of Hokkaido Island. In 1992 we have prepared in computing form the earthquake M ≥ 4.0 catalog of the Kuril-Okhotsk region for the period 1962-1990. It was formed on the basis of yearly publications (The earthquakes in USSR…, 1964-1991). During the next years the catalog was updated by the Operative catalog data of the Sakhalin Branch of Geophysical Survey of the RAS. We used this regional catalog for testing the M8 algorithm (Keilis-Borok & Kossobokov, 1986, 1990) which provided a suitable procedure for prediction of large earthquakes.

4.1.2 Methodology

The intermediate-term earthquake prediction technique, named M8 algorithm, is based on an assumption that a number of functions, defined for a particular earthquake sequence, become extremely large in values, within several months prior to a major shock. The functions used are following (Keilis-Borok & Kossobokov, 1986, 1990):
N – cumulative number of main shocks (aftershocks are excluded according to (Keilis-Borok et al., 1980)) describes an increase in seismic activity;
L – describes deviation of N from the long-term trend value;
Z – describes a linear concentration of earthquake sources;
B – describes the bursts of aftershocks.
All functions, except the last one, were calculated twice: for a standard variant of small statistics (10 events or less per year) and for a standard variant of large statistics (20 events or more per year); where the numbers of events change by choice of threshold of magnitude taken into account. Two statistics are used for increasing robustness of results of prognosis. Values of these seven functions were used for adjusting the M8 algorithm, and then for diagnostics of Time of Increased Probability (TIP) for large earthquake (M ≥ 7.5) occurrence within the circular areas with a fixed radius.
Besides the method described above, we used a visualization technique to display space-time distribution of seismicity to detect seismic gaps of the second kind. A gap of the second kind (seismic quiescence) refers here to a portion of a seismic area of low seismic activity with no observed earthquakes with M≥6.0 for a period of several years. This approach follows the concept of K. Mogi (1985).

4.1.3 Results of analysis and precursors phenomena

Seismicity of circular areas with a radius of 427 km with the centers located in the points: 44^0 N, 149^0 E; and 48^0 N, 155^0 E has been examined. These two circles overlap all the territory of

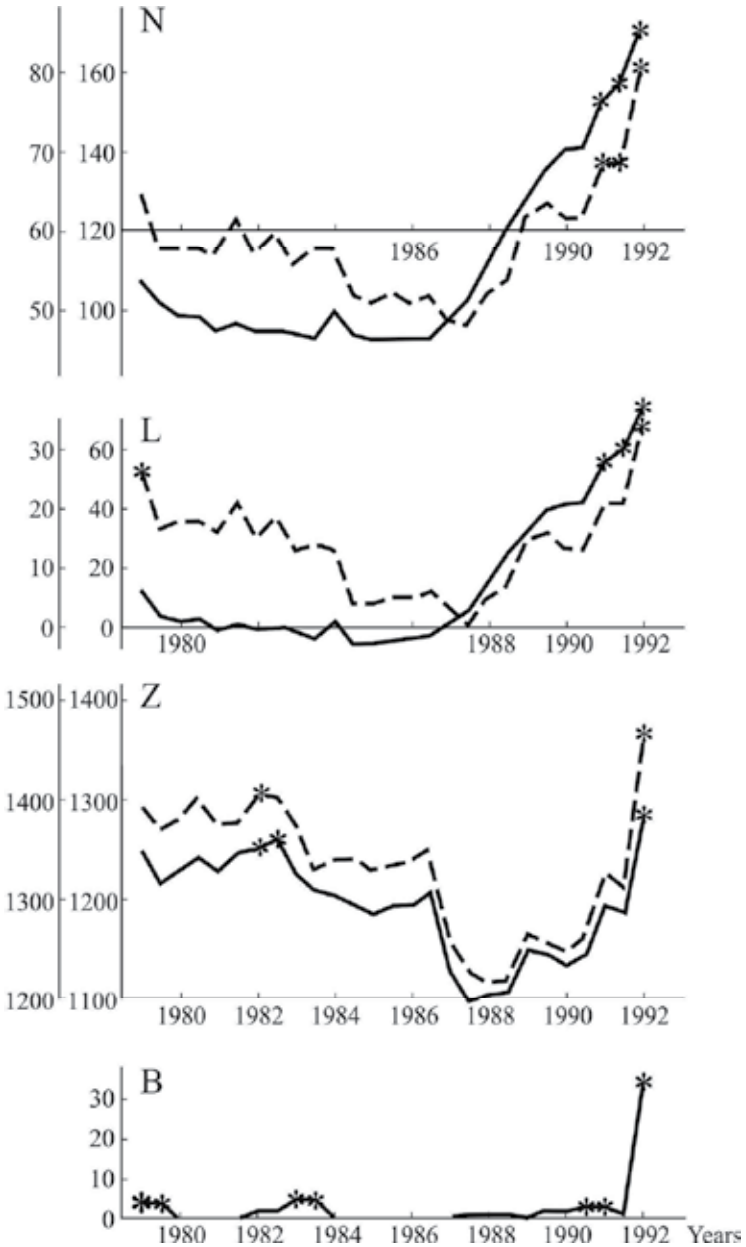

Fig. 4. The behavior in time of seven functions of the M8 algorithm for the Southern Kuril region during the diagnostics period, 1979-1992. The solid lines show the values, calculated for large statistics (20 events or more per year), and the dash lines show the values for small statistics (10 events or less per year). Star symbols mark anomalous values.

the Southern and Northern Kuril Islands. The catalog data have been processed by the M8 algorithm for the time period from 1962 to July 1992, with the functions being calculated for every six months.

Some results of the processing are presented in Fig. 4, which demonstrates the behavior of all seven functions in the first circular area (Southern Kuril Islands) during the diagnostics period (1979-1992). All the functions have become extremely anomalous, large in values to the July of 1992, which means, that the M8 algorithm diagnoses the TIP for a large earthquake occurrence during next 5 years (1993-1997). The alarm should be kept if anomalous values of almost all the functions are kept in the next six months.

The similar results have been derived by the authors of the M8 algorithm on the base of processing of the NEIC/USGS catalog data (Kossobokov et al., 1994, 1996). All needed parameters of the prognosis of the future strong earthquake were indicated, and thus we suggest that in case 1 the term "prediction" is suitable.

For the second circular area (Northern Kuril Islands) anomalous value has been obtained for the B function (bursts of aftershocks) only, and it means, that M8 algorithm diagnoses no TIP for a large earthquake occurrence in this area within the next 5 years.

The above mentioned suggested a high probability of occurrence of large earthquake within the Southern Kuril zone in the nearest years. This suggestion was found to be in an agreement with the space-time distribution of earthquakes with M ≥ 6.0 within the Kuril seismic zone since 1987 (Fig. 5). A large seismic gap of the second kind can be seen within a big area from the southern part of Urup Island to the northern end of Hokkaido Island.

4.1.4 Realization of prediction

The prediction described above was submitted in July of 1992 to the Russian Academy of Sciences and the Ministry of Emergency Situations (REC RAS/EmerCom). It was written in the conclusion that "the Southern Kuril region and the area to the east of Hokkaido Island will remain in a state of high probability of a large (M=7.5-8.5) earthquake occurrence during 5 years, which started since the middle of 1992" (Kossobokov et al., 1994, 1996).

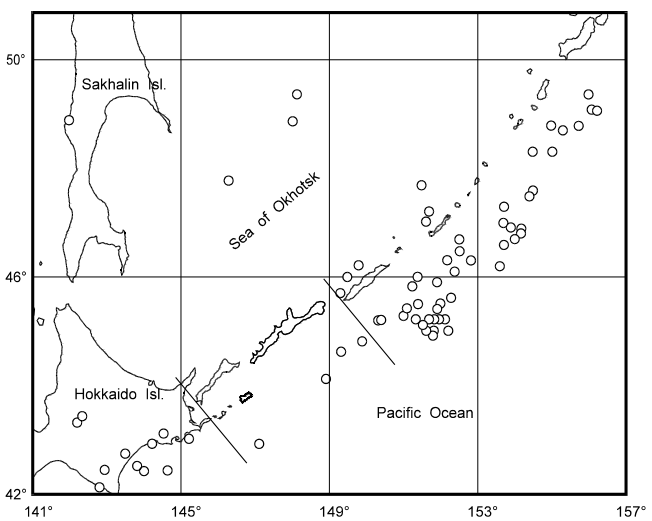

Fig. 5. The distribution of epicenters of earthquakes with M ≥ 6.0 in the Kuril-Hokkaido area for the period from March 1987 to July 1992. The area limited by solid lines is the area seismic gap of the second kind.

A large Mw 8.3 shallow-focus (h ~ 40 km) earthquake has occurred on 04 October 1994 at 13:22 GMT to the east of Shikotan Island (Russia) (Fig. 6). Thus, the intermediate-term prediction of July 1992 was confirmed.

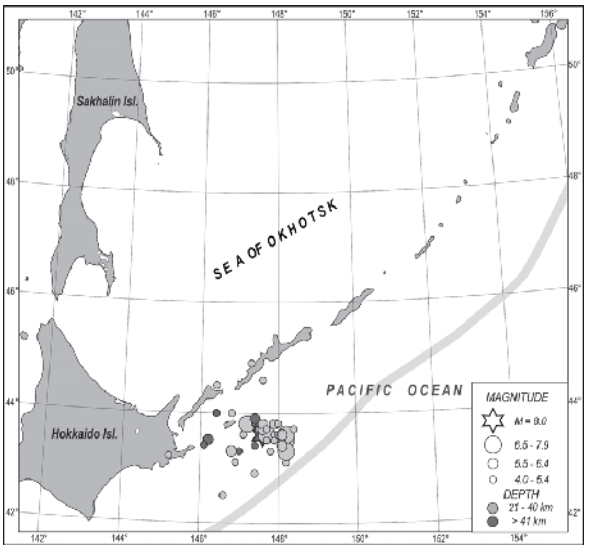

Fig. 6. Epicenters of the 1994, Mw 8.3 Shikotan earthquake and first-day aftershocks of magnitude M ≥ 5.0.

Just before the Mw 8.3 Shikotan earthquake the seismic stations in Kurilsk and at Shikotan Island were closed because of the economic crisis. In this situation we have no data to attempt to perform a short-term prognosis. But using a posteriori data from USGS/NEIC a short-term prognosis of this event was done. We used the method of self-developing processes, which was suggested by Malyshev (Malyshev, 1991; Malyshev et al., 1992). It is described below (case 4) where it was applied in a real time. By the use of this method the one and a half year foreshock sequence of events was analyzed and the date of the strong earthquake occurrence was a posteriori estimated with a few days delay (Fig. 7).

4.1.5 Case 1 summary

Some characteristics of the earthquake flux for the period from 1962 to July 1992 in the Kuril seismic zone have been investigated on the basis of two methods: (1) the intermediate-term earthquake prediction algorithm M8; (2) a visualization of space-time distribution of seismicity. The M8 algorithm diagnosed the Time of Increased Probability for a large earthquake occurrence in the circular area with the radius of 427 km at the point (44^0 N, 149^0 E) during the period 1993-1997. By means of the second method the seismic gap of the second kind was detected within a big area from the southern part of Urup Island to the northern end of Hokkaido Island. The quiescence began in March 1987. A catastrophic shallow-focus (h ~ 40 km) Mw 8.3 earthquake has occurred on 04 October 1994 at 13:22 GMT to the east of Shikotan Island (Russia).

A posteriori short-term prognosis by the method of self-developing processes data was performed using USGS/NEIC data. The date of the strong earthquake occurrence was a posteriori estimated with a few days delay (Fig. 7).

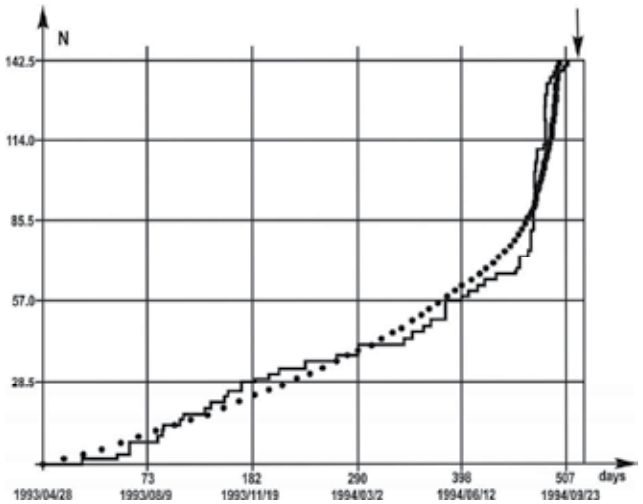

Fig. 7. The cumulative number of earthquakes observed by USGS/NEIC in the Southern Kuril Islands area as a function of time through April 1993–November 1994.

The stair-case curve is empirical data, and the smooth curve simulates the data according to the method of self-developing processes. The vertical line is the asymptote corresponding to the prognostic event date three days after the earthquake occurrence (the arrow).

4.2 Case 2 - Partly retrospective forecasting of the May 27, 1995 Mw 7.1 Neftegorsk earthquake, North-Eastern part of Sakhalin Island, Russia

4.2.1 Seismic region and data

Seismicity of the northern part of the Sakhalin region (north of latitude 50^0 N) was the object of this investigation. It had a moderate level of seismicity in comparison with seismic activity of the Kuril Islands. Destructive earthquakes like the 1995 Mw 7.1 Neftegorsk earthquake are rare events here. Paleoseismological reconstruction within the Upper Piltun fault, which was reactivated during the Neftegorsk earthquake, showed that recurrence of such earthquake is about one event per several hundred years (Shimamoto et al., 1996). Seismicity patterns were analyzed on the basis of the regional catalog of shallow-focus $M \geq 3.0$ earthquakes, issued by ESSN (The earthquakes in USSR…, 1964-1991).

4.2.2 Methodology

In this case same methods as in the case of the Shikotan earthquake were used. A magnitude for identification of a seismic quiescence area for the Sakhalin region was taken M = 3.0.

4.2.3 Results of analysis and precursors phenomena

The second kind seismic gap area taking place along the eastern coast of the Northern Sakhalin has indicated the approximate location of a possible future large earthquake (Fig. 8) (Kim, 1989). The gap of the second kind was recognized in 1989, i.e. 6 years before the Neftegorsk earthquake, it was outlined in the area of 200 by 60 km including the shelf and coastal areas from the southern part of the Shmidt Peninsula to the Gulf of Chaivo. There were no earthquakes with $M \geq 3$ in this area since 1984.

We have confirmed the existence of the quiescence zone in (Saprygin et al., 1993). In this paper we advised to reinforce the Northern Sakhalin network of seismic monitoring. However, in this very time because of the economic problems in this country four seismic stations from six, which controlled this region, were closed down. A large number of objects of industrial and civilian purposes were built with the reference seismicity of 6-7 of the *MSK*-64 intensity scale. Thus, there was a deficit of seismic-resistant buildings and structures. That became evident when the May 27, 1995 Neftegorsk earthquake has occurred. The observed ground shaking intensity was 8-9 (MSK-64 scale) in Neftegorsk, and 1841 inhabitants were killed (A memory …, 2000; Streltsov, 2005).

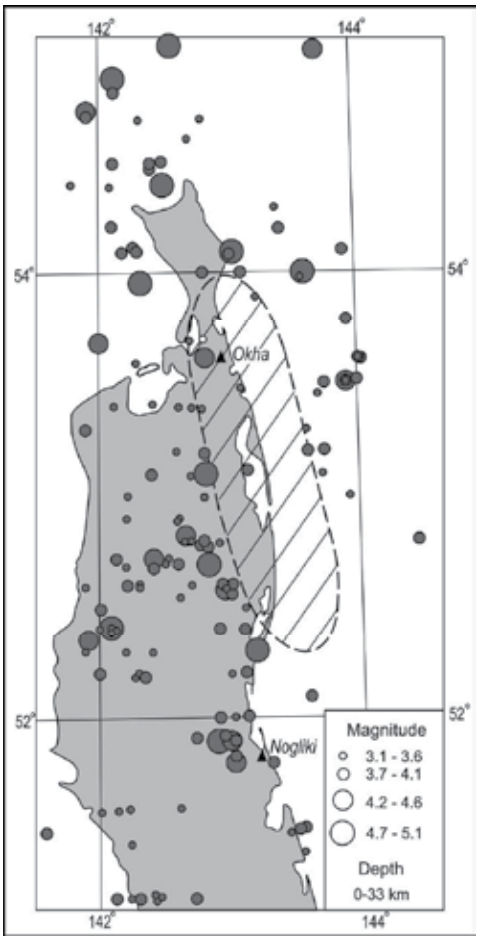

Fig. 8. A seismic quiescence zone (hatched area) in the northern region of Sakhalin Island recognized on the basis of absence the magnitude $M \geq 3.0$ events since July 1984 (Kim, 1989). The map shows a state of seismicity in April 1988.

We have investigated the intermediate-term precursors of the Neftegorsk earthquake by means of the M8 algorithm (Keilis-Borok & Kossobokov, 1986, 1990; Tikhonov, 2000). It was applied for the retrospective diagnostics of TIP for this earthquake. We used the declustered

regional catalog (Keilis-Borok et al., 1980). The M8 algorithm was adjusted to the earthquake catalog for the period 1964 – 1978. A dangerous period was found after 1979 (Fig. 9).
In this case data processing was performed under a strong shortage of data (only 4-5 events per year). Dr. Kossobokov analyzed two cases in the similar poor data conditions for the use of the M8 algorithm - deep earthquakes of the Vrancha region (Kossobokov, 1986) and seismicity in Greece (Latoussakis & Kossobokov, 1990). In the first case small and "large" statistics was equal to 2 and 4 events per year but in the second case it was equal to 5 and 10 events per year. However, even under such unfavorable conditions the M8 algorithm has demonstrated an ability to recognize the danger.
In our case only one dangerous period was revealed a posteriori since 1991 when six functions became anomalous (B function was undefined because of poor statistics of small earthquakes). The alarm period was interrupted by the May 27, 1995 Mw 7.1 Neftegorsk earthquake (Fig. 10).

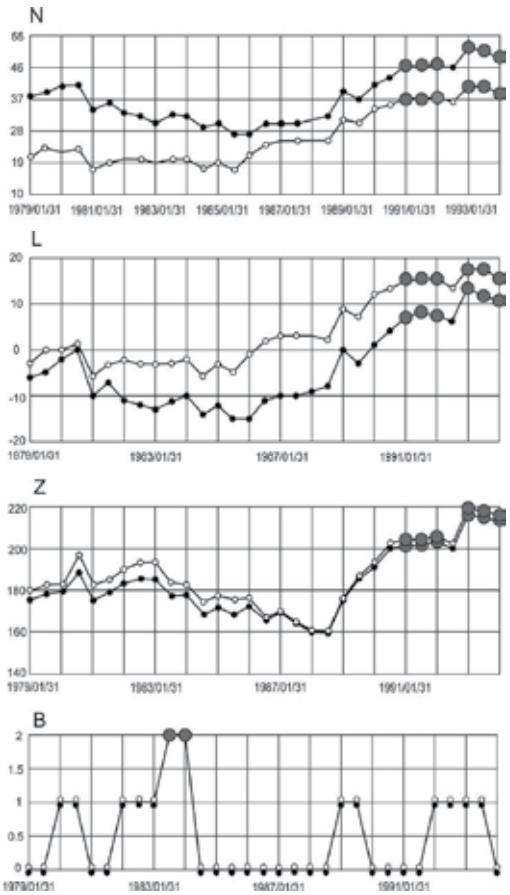

Fig. 9. The behavior in time of seven functions of the algorithm M8 for the northern region of Sakhalin Island during the diagnostics period (1979-1993) before the May 27, 1995 Mw 7.1 Neftegorsk earthquake (Tikhonov, 2000). The white circles show the values, calculated for "large" statistics (5 events or more per year), and the black circles show the values for small statistics (4 events or less per year). Large black circles mark anomalous values.

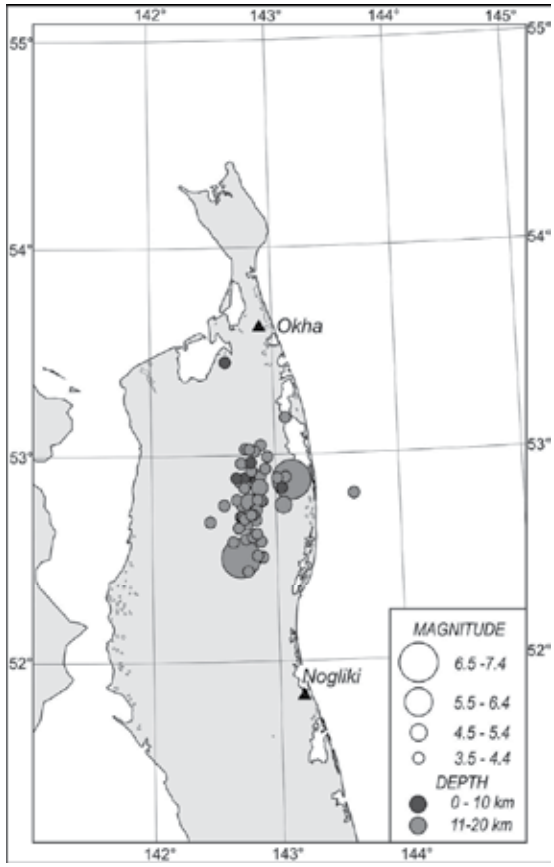

Fig. 10. Epicenters of the May 27, 1995 Mw 7.1 Neftegorsk earthquake and first-day aftershocks of magnitude M ≥ 3.5.

4.3 Case 3 - Incomplete forecasting of the Tokachi-oki Mw 8.3 earthquake (Hokkaido Island, Japan)

The M8 algorithm has failed in prognosis of the Tokachi-oki Mw 8.3 earthquake (http://mitp.ru/predictions/html, this site is of access for experts only since 2000 year). Despite of the failure of the M8 algorithm, the described below ZMAP-technique performed by one of the authors was successful (Tikhonov, 2003; 2005).

4.3.1 Seismic region and data

In this case the territory of the Japanese Islands including the adjacent shelf areas (Fig. 11) was examined. The Japan Meteorological Agency earthquake catalog from January 1974 until July 2002 was used. Earthquakes with $M \geq 3.8$, $H \leq 100$ km were found to be completely recorded, and these events were taken into account (Fig. 11). This data set is quite homogeneous throughout the whole region of Japan. It permits to apply the ZMAP-technique (Wiemer & Wyss, 1994) for examination. This method could not be applied in the cases 1 and 2 because of a shortage of data and difference in data availability for the Northern and Southern areas of the Sakhalin Island.

4.3.2 Methodology

The ZMAP method (Wiemer & Wyss, 1994) was developed to reveal a change in rate of seismicity as a function of space and time. The authors have used a rectangular grid with a spacing of 2 km for the total studied area about 100 by 100 km. For each grid point N_i nearest epicenters are selected and the maximum distance of an earthquake from the i-th grid point $r(N_i)$ was calculated. Thus the defined $r(N_i)$ is a function of space proportional to the local density of earthquakes. The significance of change in seismicity rate for each grid point is evaluated using the standard z test (Habermann, 1981, 1982)

$$z(t) = (R_{\text{all}} - R_{wl}) / (\sigma^2_{\text{all}} / n_{\text{all}} + \sigma^2_{wl} / n_{wl})^{1/2}, \quad (4)$$

where R_{all} и R_{wl} are the mean rates of seismic process in all observation period (from t_o to t_e) and in sliding window wl, respectively. n indicates the number of samples, σ is the standard deviation.

To visualize the changes in the rate of seismicity the authors plotted z(t) values on a map. Moment t moves through the whole period of the catalog from t_o to t_e. To identify the strongest rate changes between two intervals (from t_o to t and from t to t_e) they have used the $AS(t)$ function (*Habermann, 1983, 1987, 1991*). This function gives the most probable moment of seismic quiescence occurrence:

$$AS(t) = (R_1 - R_2) / (\sigma^2_1 / n_1 + \sigma^2_2 / n_2)^{1/2}, \quad (5)$$

where R_1 , R_2 are the mean rates of seismic process in two periods (from t_o to t and from t to t_e), n_1 and n_2 are the numbers of samples in these periods, σ_1, σ_2 are the standard deviations in these periods.

In the process of application of the ZMAP-technique the following tasks were executed for detection of seismic quiescence periods in the Japan region (Tikhonov, 2003, 2005):

- A modification of the ZMAP-method for application to a large territory in a real time scale has been executed. After the modification the task was implemented using the standard deviate z test (Habermann, 1981, 1982) in two steps: (1) Detection of seismic quiescence in a studied region using a coarse rectangular grid with a moderate number of nodes (with a spacing of 0.25^0); (2) Covering the cells where seismic quiescence was detected by a detailed grid (with a spacing of 0.1^0) and calculation of a configuration of anomalous area with a given value of seismicity rate decrease.
- An adjusting of the modified ZMAP-technique to the JMA earthquake catalog for the detection of possible seismic quiescence periods before the strong shallow earthquakes with $M \geq 6.8$, $H \leq 100$ km.
- An investigation of the precursor seismic quiescence since July 2001 within the studied area.

4.3.3 Results of analysis and precursors phenomena

In order to effectuate the first step of methodology we divided the studied territory into grids spacing 0.25^0 in latitude and longitude (Fig. 11). An adjustment of a modified method was performed to the declustered earthquake catalog for the period 1975 – 1988. The values of $z(t)$ function were identified as anomalous if they exceeded a proper threshold calculated for the adjusting time span. Thresholds U_i for detection of quiescence in separate nodes was defined in the following way:

$$U_i\,(coef) = \mu_i + coef\ \sigma_i\,, \quad (6)$$

where μ_i , σ_i are the average and the root mean square values of function $z(t)$ in node i for the learning time, respectively; *coef* is empirical constant. The value of $z(t)$ were identified as anomalous if $z(t) \geq U_i$ *(coef).* The constant *coef* was taken equal to 4. Thresholds for nodes were selected to minimize a probability of omission of a real seismic quiescence prior the strong earthquakes with M ≥ 6.8.

Detection of the areas with anomalous values of $z(t)$ function has been fulfilled for the declustered catalog data since 1989. Thus, there were facilities for detection of seismic quiescence periods occurring prior a series of large seismic events, which occurred in 1992 – 2002. As a result, we obtained a set of maps of the Japan region showing the location of such areas at different moments of time. Dynamics of the appearance and evolution of the anomalous areas was compared visually with dynamics of the occurrence of the strong earthquakes (M ≥ 6.8, H ≤ 100 km). It was established that correlation between the most outstanding anomalies and the strong earthquakes was suitable in space and time. In general the maximum size of anomaly is observed about 0.5 – 1.5 yr before the corresponding strong shock. The results of processing of the catalog since 1989 were the following: in 7 cases the occurrence of the strong seismic events was forestalled by seismic quiescence near its epicenters. In general the epicenter is located near the border of the corresponding anomalous zone. In two cases there was no quiescence before the strong earthquakes, and in two cases anomalous areas were observed before swarms of moderate size earthquakes (M = 6.2 – 6.6).

Obviously, the recent seismic quiescence zone revealed in the northern part of Japan had attracted an interest (Fig. 12). The term "recent" dates here back to the time of investigation (the middle of 2002). As a result of the second step of the procedure (with a detailed spacing of 0.1^0 grid size) the most outstanding recent anomaly of 75 km size was located near the Cape Erimo (Hokkaido Isl.) (Fig. 13). It was characterized by a seismicity rate decrease of 75% starting from January 1998. Inside this anomalous area there was a circle with R=25 km with no earthquake occurrence with M≥ 3.8, H ≤ 100.

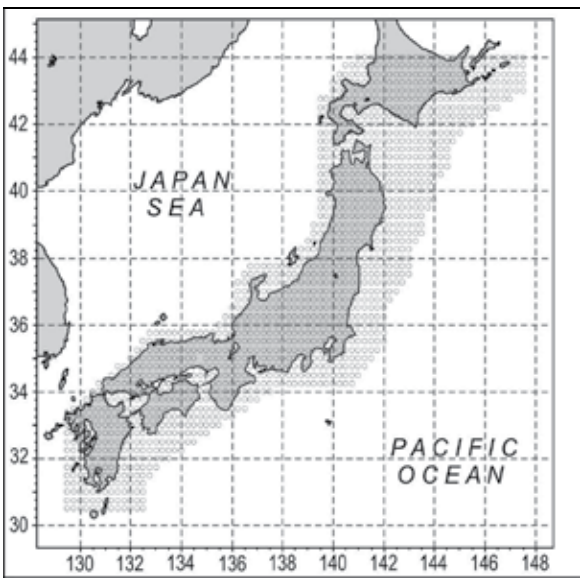

Fig. 11. Map displaying the grid with spacing of 0.25^0 used for detection of seismic quiescence. This grid contains 1354 nodes.

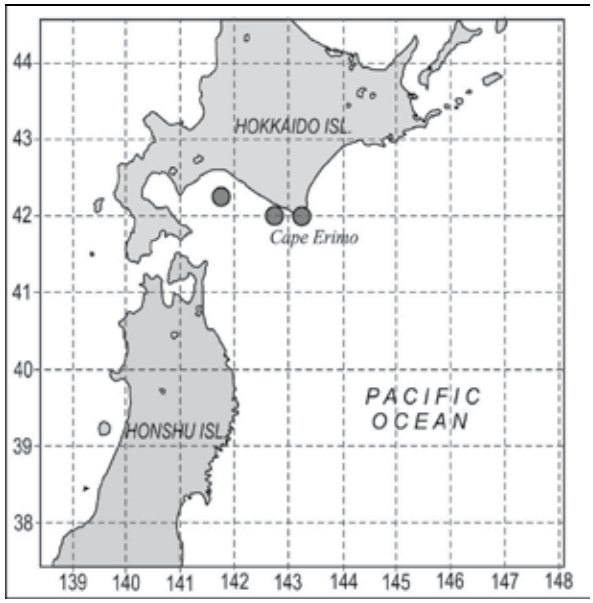

Fig. 12. The location of the seismic quiescence in the northern part of Japan as on June 1, 2002. Gray circles denote the anomalous nodes. The anomaly of seismic quiescence started in January 1998.

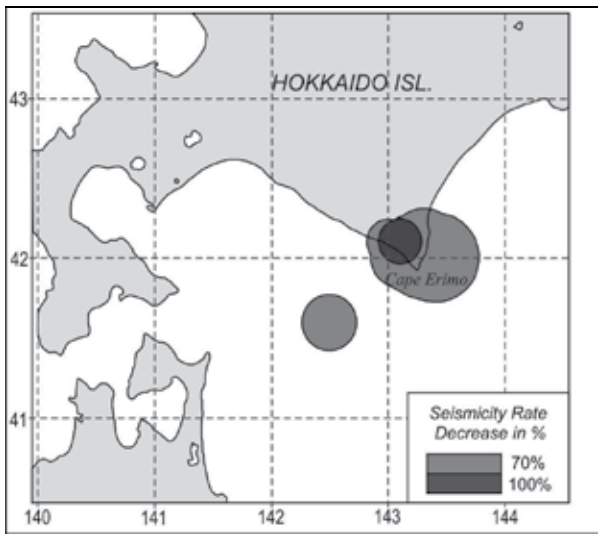

Fig. 13. Map of the seismicity rate decrease calculated for the grid with spacing of 0.1^0 at the middle of 2002. The seismic quiescence anomaly within the Cape Erimo started in January 1998.

4.3.4 The realization of forecasting

The Tokach-oki earthquake forecasting was presented during the XXIII General Assembly of IUGG, which was held in Sapporo (June 30 – July 11, 2003) (Tikhonov, 2003). Besides, these

results were published in (Tikhonov, 2005). The manuscript of the paper was received by the Journal of Volcanology and Seismology on 6 August 2003, i.e. before the occurrence of the Tokachi-oki earthquake. The Tokachi-oki earthquake Mw 8.3 occurred on September 26, at 4 h 50 min JST time near the southern coast of Hokkaido close to the seismic quiescence zone (Fig. 14).

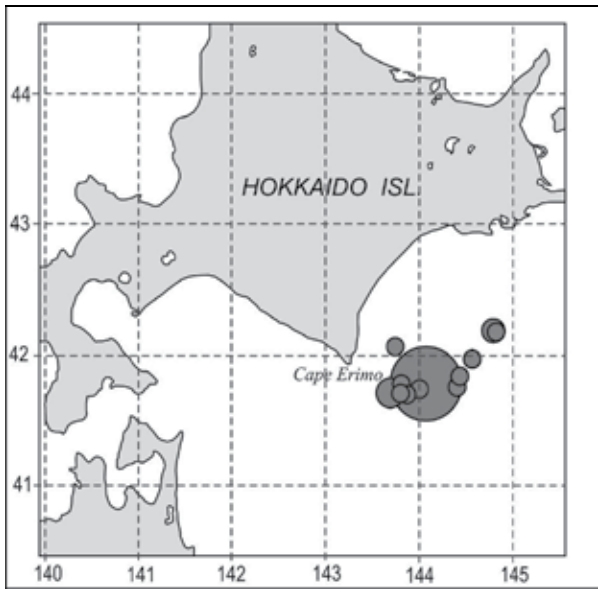

Fig. 14. Map of the 26 September, Mw 8.3 Tokachi-oki earthquake epicenter (large circle) and its first-day aftershocks of magnitude M≥5.0 (small circles).

4.3.5 Case 3 summary

The modified ZMAP-method has been applied to detect precursory seismic quiescence zones in the Japan region. The anomalies revealed for the period 1989 – 2000 correlate in space and time with the strong event occurrences. The greatest size of anomalous area took place typically about 0.5 – 1.5 yr before the corresponding strong shock.

The anomalous decrease of shallow seismicity ($M \geq 3.8$) was detected in the southern part of Hokkaido islands at the middle of 2002. In result of the second stage of the procedure the anomaly of 75 km size was determined. It was characterized by a seismicity rate decrease of 75% from January 1998. Moreover, inside this zone there was a circle of 25 km radius with 100% decrease of the rate. The Tokachi-oki earthquake Mw 8.3 has occurred on September 26, at 4 h 50 min JST time close to the seismic quiescence zone (Fig. 14).

4.4 Case 4 - A successful prediction of the 2 August, 2007 Nevelsk earthquake (Mw 6.2) in Southern Sakhalin Island

4.4.1 Seismic region and data

The object of this investigation was the southern part of the Sakhalin Island (south of latitude 48°N). The basic feature of the Earth's crust in this region is characterized by close

arrangement of three major fault systems marked by recent seismic activity. These are the Rebun–Moneron, the Western, and the Central Sakhalin fault zones (Fig. 15).

We used two data sets in this study: (1) the catalog of shallow earthquakes for 1992–2002 from the IRIS-2 system, installed at the "Yuzhno-Sakhalinsk" seismic station in 1992 (Kraeva, 2003); (2) the catalog of network of digital "Datamark" and "DAT" autonomous seismic stations, operating since 2001. The first catalog provides a record of all M > 2.6 seismic events within epicenter distances up to 70 km from the station. The second catalog is more detailed and provides analysis of seismicity patterns in the whole southern part of Sakhalin Island.

4.4.2 Methodology

This prediction was based on the detection of seismic gaps of the first and second kind. Let us describe these terms for the examined situation of the moderate seismic activity of the Sakhalin Island in detail. A gap of the first kind refers to a portion of a seismic area that has been in a state of relative rest for a long time (100 years and more), i.e., there have been no earthquakes with magnitude M ≥ 6.0 during this period. A gap of the second kind (seismic quiescence) refers to a portion of a seismic area of low seismic activity with no earthquakes with M ≥ 3.0 observed for a period of several years. Note that in the case 1 the second kind gap was examined for the magnitude threshold M = 6.0 because of the higher seismic level of the Kuril Islands.

We have used also the method of self-developing processes suggested by Malyshev (Malyshev, 1991; Malyshev et al., 1992). It was found that behavior of empirical earthquake sequences before and after large seismic events is satisfactory described by solutions of a nonlinear differential equation of the second order:

$$\frac{d^2x}{dt^2} = k\left|\left(\frac{dx}{dt}\right)^2 - V_0^2\right|^{\gamma}, \qquad (7)$$

where x is a parameter of process (for example, a cumulative sum of a number of shocks – N parameter), $V_0 = \left(dx/dt\right)_0$ is a rate of seismic process in stationary state, k and γ are empirical constants. Particular solution of the equation in case of $2\gamma > 1$ has a vertical asymptote. The time position of this asymptote is shown to be close to the origin time of the ongoing strong earthquake.

4.4.3 Precursors phenomena and characteristics of prediction

Apparently, each of three above mentioned fault zones has the potential to originate major earthquakes Ms 7.0–7.5. However, evidence is currently limited to the Rebun–Moneron (the 1971 Moneron earthquake, Ms 7.5) and the Central Sakhalin (paleoseismological data) fault zones. The Western Sakhalin fault zone showed no magnitude M > 5.0 events in its southern part during the whole history of instrumental observations up to 2006 (Fig. 15). However in its northern part (latitude>48°N) it has originated large earthquakes in 1907 (Alexandrovsk–Sakhalinsk, Ms 6.5), 1924 (Lesogorsk–Uglegorsk, Ms 6.9), and 2000 (Uglegorsk, Ms 7.2) (Fig. 16). Besides these three major fault zones in the studied area there are a number of small fault zones of lower seismic potential.

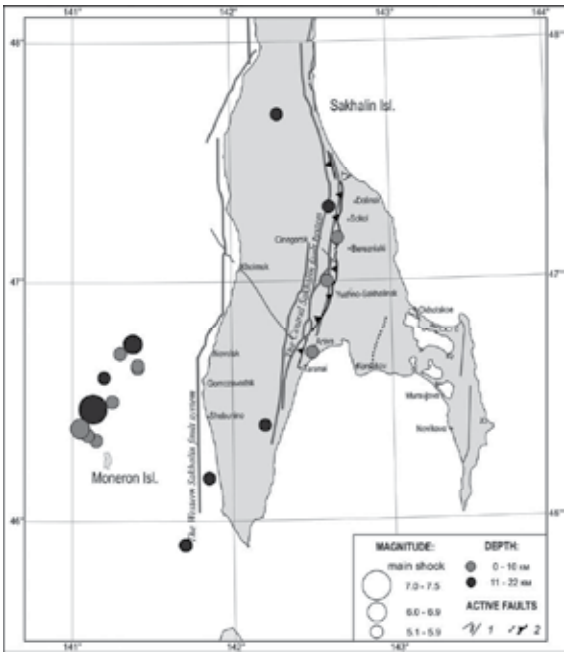

Fig. 15. Map of crust earthquake M > 5.0 epicenters of southern Sakhalin, 1906–2005, and the main fault zones.
Notes: The active faults are plotted according to M.I. Streltsov of IMG&G FEB RAS, Yuzhno-Sakhalinsk (1) and A.I. Kozhurin, of GIN AS, Moscow (2).

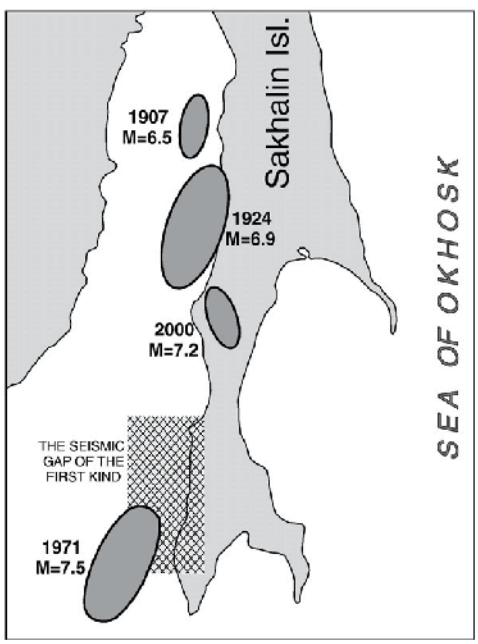

Fig. 16. Sources of large earthquakes at the western coast of Sakhalin Island (grey ovals) and the approximate location of the seismic gap of the first kind (hatched rectangle).

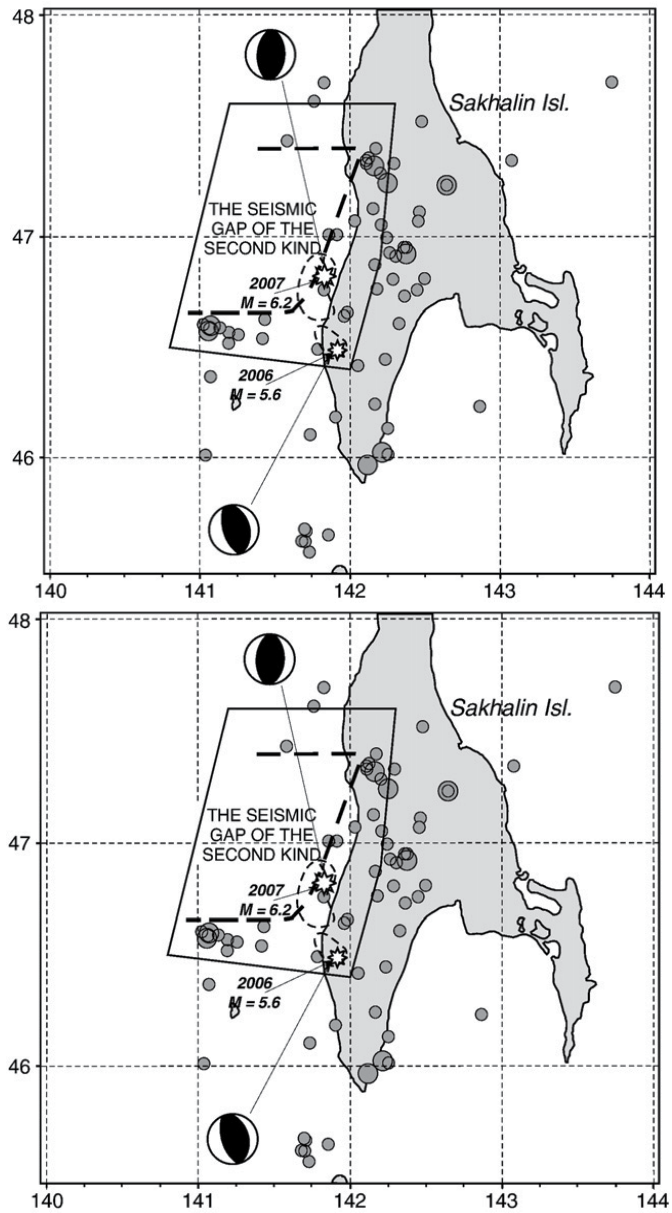

Fig. 17. Map of crust earthquake M≥3.0 epicenters, 1993–2005, recorded by the "Datamark" network of stations and the "IRIS-2" system, installed at the "Yuzhno–Sakhalinsk" seismic station.
Note: the area of the seismic gap of the second kind is outlined with the bold dash line, while the source zones of the 17 August 2006, Mw 5.6 Gornozavodsk and the 2 August 2007, Mw 6.2 Nevelsk earthquakes, with a thin dash line; asterisks indicate the epicenters of main shocks; focal mechanisms are given based on data from [http://www.globalcmt.org]. The area limited by the polygon is the geographical area within which a large earthquake M=6.6±0.6 may occur.

An earlier publication (Tikhonov, 1997) recognized an incipient of the second kind gap (seismic quiescence) within one of the gaps of the first kind, situated on the western coast of southern Sakhalin. In December 2005 our analysis of the southern Sakhalin network data permitted to made it possible to: (1) outline rather precisely the area of a seismic gap of the second kind, where shallow earthquakes with magnitudeM ≥ 3.0 did not occur from at least the middle of 2003 (Fig. 17); and (2) observe the appreciable revival of seismic activity that eventually encircled this area by 2003 (Fig. 18).
Furthermore, the rise of activity around the seismic quiescence zone, and the area south of it, has accelerated (Fig. 18) with culminations linked to the 30 May 2004 Kostroma, Ms=4.8 earthquake in the Western Sakhalin fault zone and the 18 December 2004 Moneron, Ms=4.7 earthquake in the epicenter area of the major 1971 Moneron earthquake. This happened while the seismic sequence of the abovementioned 2001 Takoye earthquake swarm in the Central Sakhalin fault zone was still ongoing.

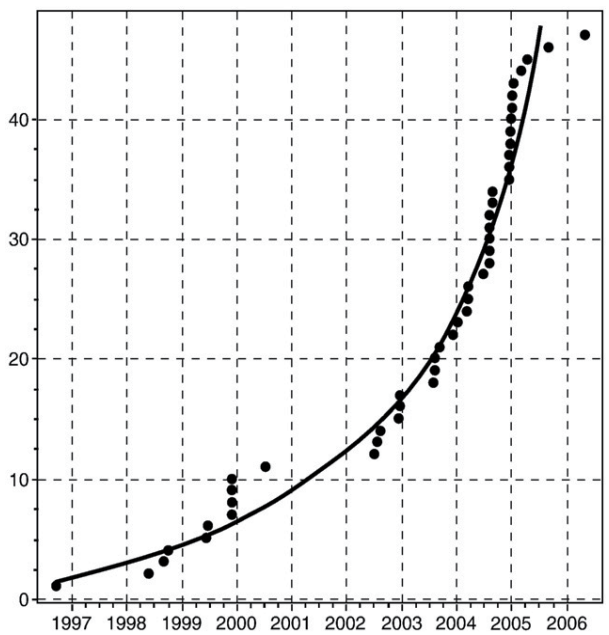

Fig. 18. The cumulative number of shallow earthquakes (depth above 30 km) of magnitude 3 or more inside 45.5–46.75°N and 140.8–142.2°E (i.e., next to the southern area of the identified seismic gap of the second kind) as a function of time in September 1996–May 2006.
Note: the smooth line models the inverse power law acceleration of the empirical data according to the method suggested by Malyshev et al. (1992). The line has the asymptote at 26 August 2007.

At the time, Dr. Tikhonov, in collaboration with Ch.U. Kim, A.I. Ivashchenko and L.N. Poplavskaya (Institute of Marine Geology and Geophysics, Yuzhno–Sakhalinsk) issued the long-term prediction of major earthquake near the western coast of southern Sakhalin (Tikhonov, 2006). This strong earthquake prediction summarized in Table 1 was made by taking into account 1) the seismic gap of the first kind in the Western Sakhalin system of faults, where large earthquakes were absent for at least 100 years (Fig. 16); 2) the seismic gap

of the second kind in the area of 90 by 60 km where seismic quiescence was confirmed by accurate data from "Datamark" digital network (Fig. 17); and 3) the accelerated sequence of earthquakes in the area adjacent to it (Fig. 18). The prediction was the following:

- The location of the incipient hypocenter is most likely to occur at shallow depths within 0–30 km inside the polygon (Fig. 17): (47.6° N; 141.2° E); (46.5° N; 140.8° E); (46.4° N; 142.0° E); (46.9° N; 142.2° E); (47.6° N; 142.3° E).
- The magnitude Ms of the incipient event was estimated in two different ways. The first is the formula by K. Tanaka (1980) lg R=0.33 M−0.07, which relates the linear size of the gap of the second kind, R, to the magnitude of expected earthquake, M. It was used first to determine the expected magnitude M=6.1.
- The second estimate was obtained from the two empirical relations: (1) lg L=(0.5±0.01) M−(1.77±0.07) (Tarakanov, 1995); and (2) L ≈ 1/3 R, where L is the linear size of the aftershock zone (Shebalin, 1961). Substituting an expression (2) in the formula (1), we obtain:

$$\lg R=(0.5\pm0.01)\,M-(1.77\pm0.07)+\lg 3. \quad (8)$$

  This gives M=6.6.
- Of the two estimates, the second appears to be preferable because it takes into account the worst earthquake scenario as well as some uncertainty in estimates. Therefore, Ms=6.6±0.6 was selected as a final magnitude estimate of the expected large earthquake.
- The duration of alarm was determined to be about 7.5 years. This was based on an average time-span of approximately 10 years, observed for seismic quiescence zones that occurred before large earthquakes off the western coast of Japan and Sakhalin, while accounting for no less than 2.5 years of a given quiescence zone's initiation.
- The likelihood of an earthquake occurrence was estimated at 75%, based on the recurrence rate of the large (M ≥ 6.5) earthquakes in the south of Sakhalin (Oskorbin & Bobkov, 1997) and the lifespan of a given quiescence zone.
- The expected intensity of ground shaking (in the MSK-64 scale) was calculated for the three epicenter locations inside the seismic gap of the second kind and the magnitude close to the maximal expected. Fig. 19 displays the results obtained with the epicenter in the middle of the quiescence zone.

The beginning and end of alarm	Magnitude and depth of earthquake	Position of earthquake epicenter	Probability of earthquake occurrence	Maximal macroseismic effect (MSK-64 scale)
January, 2006– July, 2013	M_S = 6.0 – 7.2 h = 0 – 30 km	See the text and Fig. 17	≥75%	9.0 (in epicenter) 8.0 (at the coast)

Table 1. Characteristics of anticipated earthquake (Tikhonov, 2006, page 179).

The prediction described was submitted in January 2006 to the Russian Expert Council for Earthquake Prediction, Seismic Hazard and Risk of the Russian Academy of Sciences and the Ministry of Emergency Situations (REC RAS/EmerCom). As a result of the discussion at the REC Meeting, the prediction was approved as being scientifically motivated. It was then reported to EmerCom headquarters, which had run urgent command-staff exercises in August 2006, referred to as "Mitigating the consequences of destructive earthquake and

tsunami in Sakhalin–Kuril region." The scientific motivations of the prediction have been published (Tikhonov, 2006).

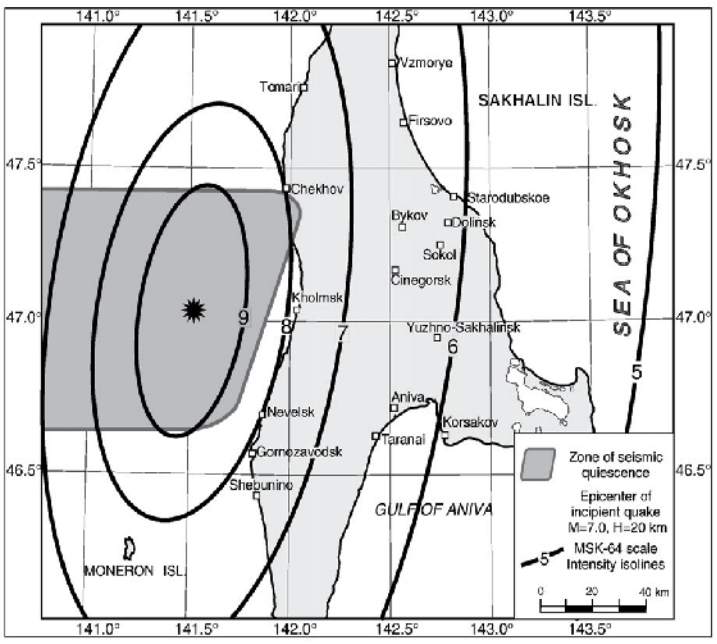

Fig. 19. An expected ground shaking intensity (MSK-64 scale) for the model occurrence of an earthquake of Ms 7.0 at a depth of 20 km in the central part of the seismic quiescence zone (computations by L.N. Poplavskaya of IMG&G FEB RAS made in December 2005).

4.4.4 The realization of the prediction

On 17 August 2006, a magnitude Mw 5.6 earthquake hit the Gornozavodsk settlement in the area of prediction (Levin et al., 2007). Upon analyzing the main shock and its aftershocks, a conclusion of the precursory character of this sequence was drawn. Specifically, it was concluded that the preparation of a large earthquake in the seismic quiescence zone had switched from a long-term to a short-term phase.

This was briefly formulated in the cover letter of an interim report to REC RAS/EmerCom, as follows: "In December 2005, the seismology team of IMG&G FEB RAS issued a long-term prediction of strong earthquake on southwest shelf of Sakhalin Island. Recent M 5.6 earthquake, which happened in this region on 17 (18) August 2006, has partially proved the prediction to be well-founded. Detailed analysis of post-earthquake seismicity allows to conclude that the development of predicted earthquake is in the short-term stage now…".

On August 2, at 13 h 37 min Sakhalin time (2 h 37 min GMT), in the Tatar Strait close to the city of Nevelsk (Sakhalin, Russia), an earthquake of magnitude Mw 6.2 occurred (Fig. 20). Two lives were lost and more than ten persons were wounded. The earthquake caused severe destruction. About six thousand of Nevelsk's fifteen thousand inhabitants became homeless. The earthquake was felt everywhere in the southern portion of Sakhalin Island. The observed groundshaking intensity (MSK-64 scale) was VII–VIII in Nevelsk, VI–VII in Gornozavodsk, V–VI in Holmsk and III–IV in Yuzhno-Sakhalinsk.

Inspections into the consequences of this disaster have shown that the city needs to be rebuilt practically anew. The losses totaled more than six billion rubles (i.e., $240 million).
The focal mechanism of the main shock, based on data from (http://www.globalcmt.org), suggests that the source region was under the sub-latitudinal and near-horizontal compression that resulted in the reverse-slip (Fig. 17). IMG&G and employees of the Sakhalin Branch of Geophysical Survey of the RAS carried out a general inspection of the region affected by the earthquake. Other organizations provided the aerial mapping and echo sounding of the sea-bottom. The seismic event appeared to be related to the West-Sakhalin system of deep crustal faults located along the western coast of the island. As a result of the general inspection, a number of unique observations for earthquakes of such size have been established. One of the most remarkable geodynamic phenomena associated with the 2007 Nevelsk earthquake is the uplift of the coastal terrace, formed by the Middle Miocene sedimentary rocks (Nevelsk suite), with an amplitude of 1.0–1.5 m (Fig. 21).
The 2 August 2007, Mw 6.2 Nevelsk earthquake occurred in the southern part of the seismic gap of the second kind (Fig. 17). Its parameters fall within the limits of the long-term prediction of a large earthquake expected in the southwest of Sakhalin Island, as it was listed in the Table 1.
Thus, the long-term prediction of December 2005 was confirmed. Note also that the decision that the 17 August 2006 Gornozavodsk earthquake was a foreshock of a future large event was declared just after this event (23 August 2006). More details concerning case histories of prediction of the 2006 Gornozavodsk and the 2007 Nevelsk earthquakes can be found in (Levin et al., 2007; Tikhonov & Kim, 2010).

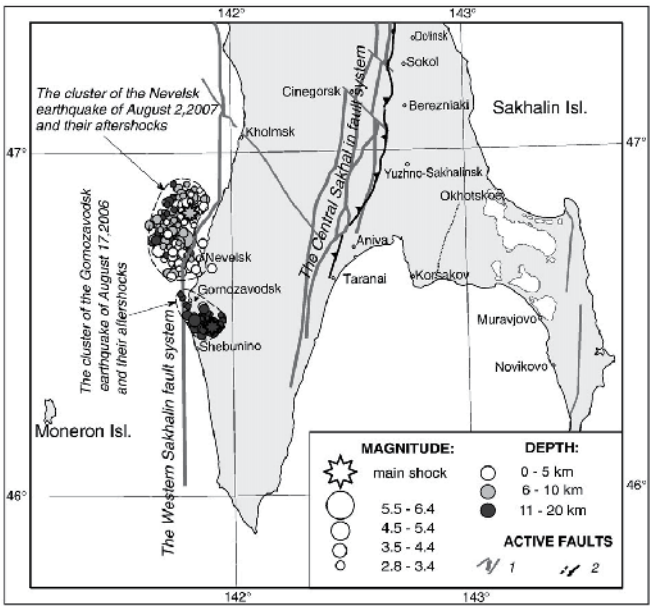

Fig. 20. Map of the 17 August 2006, Mw 5.6 Gornozavodsk and 2 August 2007, Mw 6.2 Nevelsk earthquake epicenters (asterisks) and their first-day aftershocks of magnitude M ≥ 2.8. Notes: the clusters of epicenters are outlined with a dash line. The active faults are plotted according to M.I. Streltsov of IMG&G FEB RAS, Yuzhno-Sakhalinsk (1) and A.I. Kozhurin, of GIN AS, Moscow (2).

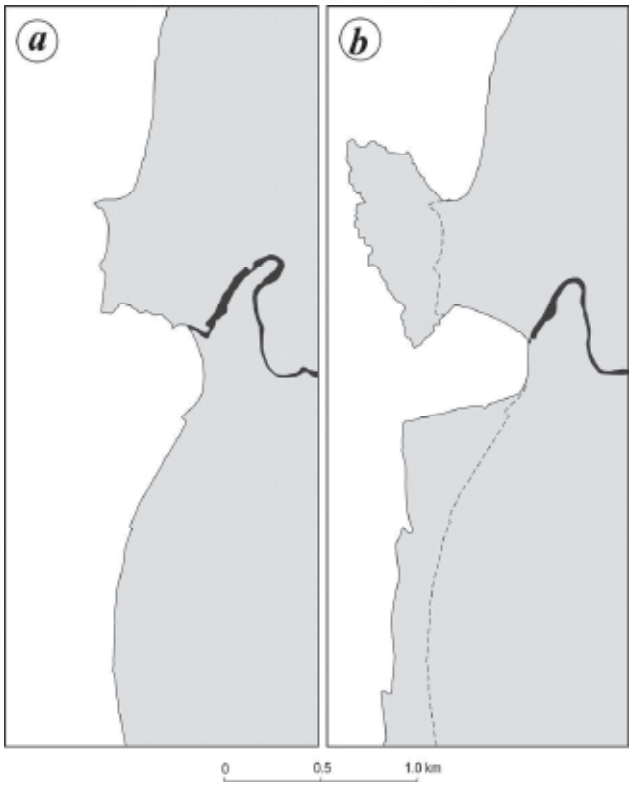

Fig. 21. Sketch showing a change of the coast-line occurred near Nevelsk as a result of the 2 August 2007 earthquake. a – position of the coast-line before the earthquake, b – uplifting portion of the sea-bottom after the earthquake; river Kazachka is shown as a black line.

4.4.5 Case 4 summary

In the case of the 2006 Gornozavodsk and the 2007 Nevelsk earthquakes the whole spectrum of prognoses from the long-term prediction to the short-term prediction of the 2007 Nevelsk earthquake was put into effect. The situation after the 2006 Gornozavodsk earthquake was interpreted correctly; the 2006 Gornozavodsk earthquake was treated as a foreshock of the stronger event. The short-term prediction was done for 7.5 months, but the 2007 Nevelsk earthquake had occurred three months later.

In case 4 the method of self-developing processes had resulted in an unexpectedly exact (Fig. 18) but maybe non-robust prognosis. The M8 algorithm was not applied in this case because of deficiency of data length for adjusting of the algorithm (the background level).

More details concerning the case 4 histories can be found in (Levin et al., 2007; Tikhonov, 2006; Tikhonov & Kim, 2010).

4.5 Case 5 - Unsuccessful intermediate-term prediction of a great earthquake at Southern Kuril Islands

4.5.1 Seismic region and data

This region includes the Urup, Iturup and Kunashir Islands (Fig. 22). The data used in earthquake forecasting were taken from the NEIC/USGS catalogues and contain earthquake

data from December 1995 until December 2007; events with M ≥ 4.0 were taken into account as presumably registered without admissions.

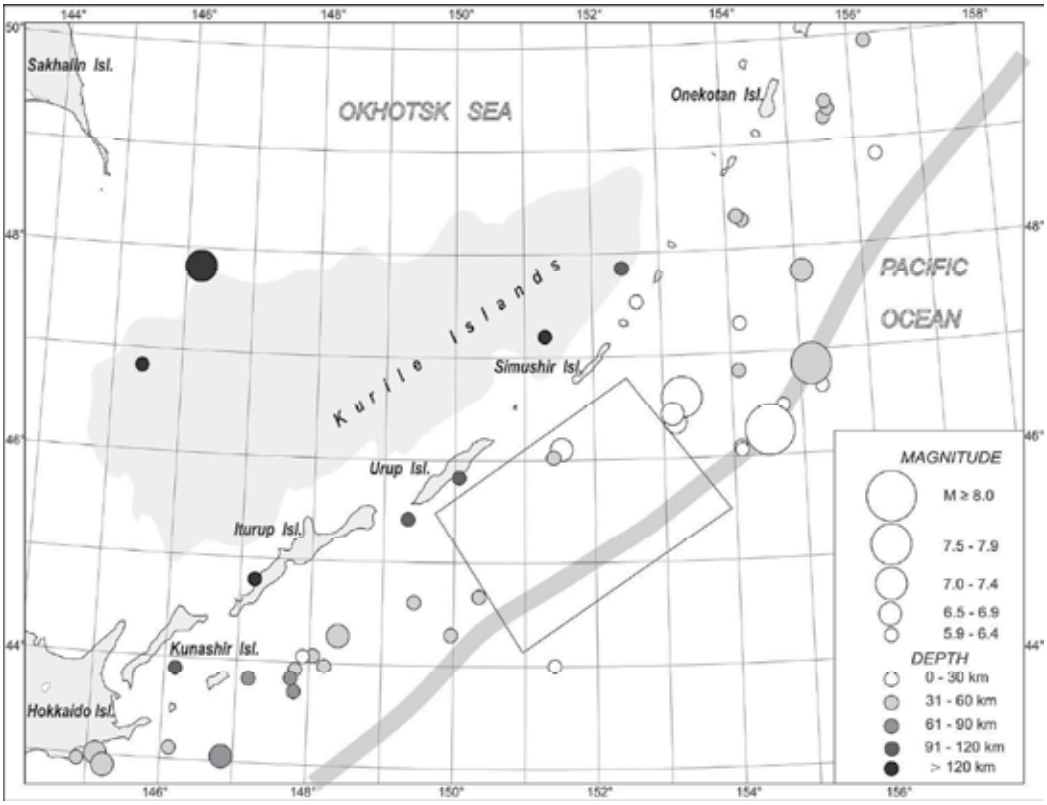

Fig. 22. Map of earthquake M ≥ 5.9 epicenters near Kuril Islands, May 1999 – January 2010. The area limited by the polygon is the area of the seismic gap of the second kind.

4.5.2 Methodology

It was shown by the examples above that the M8 algorithm and the detection of seismic gaps of the first and the second type provide a reasonable first approach to a long- and intermediate-term earthquake prognosis. The decrease in *b*-values is known also as a precursor of strong earthquake occurrence. In (Tikhonov, 1999, 2000) it was attempted to present and apply a new formal algorithm for detection of both areas of intermediate- and short-term seismic quiescence and change in b-value using a few functions that characterize these features of seismic regime. This algorithm was named Q1. It was elaborated in analogy with the structure of the M8 algorithm. The detailed description of the Q1 algorithm is presented in (Tikhonov, 2000). We do not describe the Q1 algorithm here in detail because the affectivity of application of this method was not supported by practice yet. For the similar reasons we do not describe here the details of the case 5 history that can be found in (Tikhonov, 2009).

4.5.3 Case 5 summary

The algorithm Q1 aimed at detection of joint occurrence of seismic gap and *b*-value change was presented in (Tikhonov, 1999; 2000). This algorithm has been applied to recognize the time of increased probability for large (M ≥ 7.5) earthquake in the Southern Kuril Islands since the last large earthquake occurring here in December 03, 1995. Algorithm was examined at the time period since 1962 until 1995. Than the use of the algorithm in the real time regime has begun. The anomalies in four predictive functions of the Q1 algorithm were revealed on December 2007. In Fig. 22 the area of seismic quiescence statistically proved by the use of the Q1 algorithm is shown. The hazardous period for an earthquake M ≥ 7.4 was declared for the next two years (2008-2009). Note that the use of the M8 algorithm (http://mitp.ru/predictions/html) had resulted in the alarm period for the similar space-time domain.

But the alarm has proved to be false. Till now there is no strong earthquake in the Southern Kuril Islands.

4.6 Case 1-5 summary

The summary of algorithms application is presented in Table 2. Note that the number of examples is insufficient for statistical estimation of relative validity of different applied algorithms.

Example No	Algorithms				
	M8	Seismic quiescence		Self-developing processes	Q1 algorithm
		ZMAP-technique	visual		
1	(+)	not used*	first type (not used) second type (+)	(+)	(no existed)
2	(+)	not used*	first type (not used) second type (+)	(not used)*	(no existed)
3	(-)	(+)	first type (not used) second type (not used)	(not used)	(no existed)
4	not used*	not used*	first type (+) second type (+)	(+)	(no existed)
5	(-)	not used*	first type (not used) second type (+)	(not used)	(-)

Table 2. The summary of algorithms application

(+) - means the algorithm was applied successfully;
(-) - means the algorithm failure;
(not used)* - means that the algorithm cannot be used due to different reasons;
(not used) - means the algorithm could be used but was not applied;
(not existed) – this new algorithm was developed later.

5. Discussion and conclusion

The analysis of behavior of seismicity within the generalized vicinity of large earthquake gives possibility to verify and to detail the characteristic parameters of the fore- and aftershock sequences and a number of other anomalies inherent to a vicinity of strong events (Rodkin, 2008). It was confirmed that the averaged fore- and aftershock cascades do obey the power law evolution. Power-law exponent of the foreshock cascade was found to be less than that of the aftershock cascade, and thus, the rate of increase of foreshocks number toward the moment of occurrence of the main event is slower than the rate of aftershocks decays. The typical duration of the aftershock process for M7+ events is about 100 days, while the average duration of the foreshock cascade in the constructed generalized vicinity was found to be quite noticeable during 10-20 days. The confirmation of a power law evolution for both fore- and aftershock cascades testifies that large earthquakes can be examined in terms of the critical phenomena. In this case it can be expected that the process of strong earthquake occurrence will be accompanied by other anomalies with a critical-like character of behavior. And factually, in parallel with the power-law fore- and aftershock cascades a stress-strain instability was shown to take place in the generalized vicinity of strong earthquake (see (Rodkin, 2008) for a more detailed description of these anomalies). It is worth mentioning also that much weaker increase in a number of events and the process of softening were revealed in a broader (few hundred days) time vicinity of a large earthquake beyond the domain of the fore- and aftershock cascades occurrence.

The set of precursory anomalies indicates the approaching of a strong event quite definitely. Thus one can conclude that the effective short- and intermediate-term earthquake forecasting appears to be possible in the case of an essential increase of volume of statistical information available for forecasting. Now in every particular case of earthquake forecasting the volume of available information is much less than it is available in the generalized vicinity of strong earthquake, and correspondingly the results of forecasting are expected to be substantially less certain. It does take place actually.

The state of art in a practice of earthquake forecasting is presented by an example of earthquake forecasting performed for the Sakhalin Island and the surrounding areas in the Institute of Marine Geology and Geophysics of the Far East Branch of the Russian Academy of Science, Yuzhno-Sakhalinsk, Russia. In two cases (1 and 4) from the five described above the whole set of earthquake parameters were successfully forecasted and thus these cases satisfy the term of "earthquake prediction". This practice suggests that at least in some cases earthquakes can be forecasted despite the shortage of available data.

All the used algorithms of earthquake forecasting are based upon the general properties of seismic regime in vicinity of strong earthquake. These properties (besides the seismic quiescence) are similar with those revealed in the generalized vicinity of strong earthquake. The "seismic quiescence" was not found in the generalized vicinity of strong earthquake because of anisotropic character of this type of precursor anomaly in relation to epicenter of the corresponding main shock.

We expect that the precursor features of the seismic regime behavior revealed in the generalized vicinity of strong earthquake can be useful in an earthquake prediction. These typical anomalies can be used as ideal images of precursory anomalies developing in process of preparation of individual strong earthquakes. Having in mind the volume of data

used in the construction of the generalized vicinity of strong earthquake it can be suggested that a robust prognosis of strong earthquakes will be possible when the volume of data available in prognostic practice increases by one-two orders.

6. Acknowledgements

This work was supported by the Russian Foundation for Basic Research, grant No. 11-05-00663, and the European grant FP7 No. 262005 SEMEP.

7. References

Akimoto, T. & Aizawa, Y. (2006). Scaling Exponents of the Slow Relaxation in Non-hyperbolic Chaotic Dynamics. *Nonlinear phenomena in complex systems.* Vol.9, No.2, pp. 178-182, ISSN 1561-4085.

Bowman, D.D., Ouillon, G., Sammis, C.G., et al. (1998). An Observational Test of the Critical Earthquake Concept. *J. Geophys. Res.* Vol. 103, pp. 24359–24372, ISSN 0148-0227.

Geller, R.J. (1997). Earthquake prediction: a critical review. *Geophys. J. Inter.* Vol. 131, pp. 425–450, ISSN 1365-246X.

Geller, R.J., Jackson, D.D., Kagan, Y.Y. & Mulargia, F. (1997). Earthquakes cannot be predicted. *Science.* Vol. 275, pp. 1616–1619, ISSN 0036-8075.

Global Hypocenter Data Base CD-ROM. NEIC/USGS. - Denver, 1989.

Habermann, R. E. (1981). Precursory seismicity patterns: stalking the mature seismic gap. *Earthquake Prediction*, Maurice Ewing Series 4, D. W. Simpson & P. G. Richards, (Editors) American Geophysical Union, Washington, D.C., 2942.

Habermann, R. E. (1982). Consistency of teleseismic reporting since 1963. *Bull. of Seismol. Soc. Am.* Vol. 72. pp. 93-112, ISSN 0037-1106.

Habermann, R. E. (1983). Teleseismic detection in the Aleutian Islands arc. *J. Geophys. Res.* Vol. 88. pp. 5056-5064, ISSN 0148-0227.

Haken, H. (1978). *Synergetics.* Springer-Verlag, Berlin Heidelberg.

JMA Earthquake Catalog (Japan Meteorological Agency; 1926.1.1 – 2002.1.01).

Kagan, Y.Y. (1997). Are earthquakes predictable? *Geophys. J. Inter.* Vol. 131, pp. 505–525, ISSN 1365-246X.

Keilis-Borok, V.I. & Kossobokov, V.G. (1986). Time of Increased Probability for the Largest Earthquakes of the World. *Mathematical Methods in Seismology and Geodynamics, Comp. Seismol.* Vol. 19, pp. 48-57, ISSN 0203-9478, Nauka, Moscow (in Russian).

Keilis-Borok, V.I. & Kossobokov, V.G. (1990). Premonitory activation of earthquake flow: algorithm M8. *Physics of the Earth and Planetary Interiors.* Vol. 61, Nos. 1-2, pp. 73-83, ISSN 0031-9201.

Keilis-Borok, V.I. & Soloviev, A.A. (2003). *Nonlinear Dynamics of the Lithosphere.* Springer-Verlag, ISBN 354043528X, Berlin.

Keilis-Borok, V.I. & Soloviev, A.A., (Eds). (2002). *Nonlinear Dynamics of the Lithosphere and Earthquake Prediction*. Springer-Verlag, ISBN 978-3-540-43528-0, Berlin.

Keilis-Borok, V.I., Knopoff, L. & Rotwain, I.M. (1980). Bursts of aftershocks long term precursons of strong earthquakes. *Nature.* Vol. 283, pp. 259-263, ISSN 0028-0836.

Kim, Ch. U. (1989). Peculiarities of seismic energy release in space and time within the northern Sakhalin region. In: *The 1988 bulletin of Kuril-Sakhalin seismo-forecasting testing area (quarterly).* No. 4. pp. 46-51, IMGG FEB RAS, Yuzhno-Sakhalinsk (in Russian).

Kossobokov, V.G. (2005). Earthquake Prediction: Principles, Implementation, Perspectives, In: *Earthquake Prediction and Geodinamic Processes, Comp. Seismol.* Vol. 36, pp. 1-179, ISSN 0203-9478, Nauka, Moscow (in Russian).

Kossobokov, V.G. (1986). Testing the algorithm M8: the Vrancha region. In: *Long-term earthquake prediction: methodical recommendations*. Sadovsky M.A. IPE AS USSR, Moscow, p. 102 (in Russian).

Kossobokov, V.G., Healy, J.H., Dewey, J.W., Shebalin, P.N. & Tikhonov, I.N. (1996). A real-time intermediate-term prediction of the October 4, 1994 and December 3, 1995 Southern-Kuril Islands earthquakes. *Comp. Seismol.* Vol. 28, pp. 46–55, ISSN 0203-9478, Nauka, Moscow (in Russian).

Kossobokov, V.G., Shebalin, P.N., Tikhonov, I.N., Healy, J.H. & Dewey, J.W., (1994). A real-time intermediate-term prediction of the October 4, 1994 Shikotan earthquake. In: *The Federal system of seismological observation and earthquake prediction. The informative-analytical bulletin. The 1994/10/4(5) Shikotan earthquake: Extraordinary issue*. Moscow, pp. 71-73 (in Russian).

Kraeva, N.V. (2003). Techniques and results of continued observations (1992-2002) of the South Sakhalin seismicity by the digital system IRIS. *Proceedings of problems of seismicity of the Far East and Eastern Siberia: Reports of the International Scientific Symposium*, Vol. 2, pp. 89-112, ISBN 5-7442-1358-9, Yuzhno-Sakhalinsk, September, 2002 (in Russian).

Latoussakis, J. & Kossobokov, V.G. (1990). Intermediate Term Earthquake Prediction in the Area of Greece: Application of the Algorithm M8. *Pure Appl. Geophys.* Vol. 134, No. 2, pp. 261-282, ISSN 0033-4553.

Lennartz, S., Bunde, A. & Turcotte, D.L. (2008). Missing data in aftershock sequences: Explaning the deviations from scaling laws. *Rev. E. Stat. Nonlin Soft Matter Phys,* Vol. 78, pp. 41115-41123, ISSN 1550-2376.

Levin, B.V., Kim, Ch.U., Tikhonov, I.N. (2007). The Gornozavodsk earthquake of 17(18) August, 2006, in the south of Sakhalin Island. *J. Pacific Geol.* Vol. 1, No. 2, pp. 102–108, ISSN 0207-4028 (in Russian).

Lindman M., Lund, B. & Roberts, R. (2010). Spatiotemporal characteristics of aftershock sequences in the South Iceland Seismic Zone: interpretation in terms of pore pressure diffusion and poroelasticity. *Geophys. J. Int.* Vol. 183, No. 3, pp. 1104–1118, ISSN 1365-246X.

Malamud, B.D., Morein, G. & Turcotte, D.L. (2005). Log-periodic behavior in a forest-fire model. *Nonlinear Processes in Geophysics.* Vol. 12, pp. 575-585, ISSN 1023-5809.

Malyshev, A.I. (1991). Dynamics of self-developing processes. *J. Volcanology and Seismology*. No. 4, pp. 61–72, , ISSN 0203-0306 (in Russian).

Malyshev, A.I., Tikhonov, I.N. & Dugartsyrenov, K.Ts. (1992). The technique of mathematical modeling the Kurile foreshock-aftershock strong earthquake sequences. Preprint IMGG, Yuzhno-Sakhalinsk (in Russian).

Mogi, K. (1985). *Earthquake prediction.* Academic Press (Harcourt Brace Jovanovich, Publishers), New York.

Oskorbin, L.S. & Bobkov, A.O. (1997). Seismic behavior of the Far East seismogenic zones. In: *Problems of seismic hazard of Far East region: Geodynamic of tectonosphere of the Pacific–Eurasia conjunction zone*, Tarakanov R.Z. & Ivaschenko A.I., Vol. VI, pp. 179–197, IMG&G, ISBN 5-7442-1028-8 (T. 6),Yuzhno–Sakhalinsk (in Russian).

Papazachos, C.B., Karakaisis, G.F., Scordilis, E.M. & Papazachos, B.C. (2005). Global Observational Properties of the Critical Earthquake Model. *Bull. Seismol. Soc. Am.* Vol. 95, No. 5, pp. 1841-1855, ISSN 0037-1106.

Quick Epicenter Determination (QED). The NEIC/USGS Branch of Global Seismology and Geomagnetism On-line Information System, 1992.

Rodkin, M.V. (2008). Seismicity in the Generalized Vicinity of Large Earthquakes. *J. Volcanology and Seismology*. Vol. 2, No. 6, pp. 435–445, ISSN 0203-0306 (in Russian).

Romashkova, L.L. & Kosobokov, V.G. (2001). The Dynamics of Seismic Activity before and after Great Earthquakes of the World, 1985–2000. *Comp. Seismol.* Vol. 32, pp. 162–189, ISSN 0203-9478, Nauka, Moscow (in Russian).

Shebalin, N.V. (1961). Intensity, magnitude and depth of an earthquake source. *Earthquakes in USSR.* AS USSR, Moscow, pp. 126–138 (in Russian).

Shebalin, P.N., (2006). A Methodology for Prediction of Large Earthquakes with Waiting Times Less than One Year. *Comp. Seismol.* Vol. 37, pp. 7–182, ISSN 0203-9478, Nauka, Moscow (in Russian).

Shimamoto, T., Watanabe, M., Suzuki, Y., Kozhurin, A.I., Streltsov, M.I. & Rogozhin, E.A. (1996). Surface faults and damage associated with the 1995 Neftegorsk earthquake. *J. Geol. Soc. Jpn.* Vol. 102 (10), pp. 894–907, ISSN 1684-9876.

Smirnov, V.B. & Ponomarev, A.V. (2004). Patterns in the Relaxation of Seismicity from Field and Laboratory Observations. *Izv. RAN, Fizika Zemli*. No. 10, pp. 26–36, ISSN 0002-3513 (in Russian).

Smirnov, V.B., (2003). Estimating the Duration of the Fracture Cycle in the Earth's Lithosphere from Earthquake Catalogs. *Izv. RAN, Fizika Zemli.* No. 10, pp. 13–32, ISSN 0002-3513 (in Russian).

Sobolev G.A., Tyupkin Yu.S. & Zavyalov A.D. (1999). Map of expected algorithm and RTL prognostic parameter: joint application. *Russ. J. Earthquake Sciences.* Vol. 1. No 4. pp. 301-309, ISSN 1681-1206.

Sobolev, G.A. & Ponomarev, A.V. (2003). *Physics of earthquakes and precursors.* Nauka, ISBN 5-02-002832-0, Moscow (in Russian).

Sobolev, G.A. (1993). *Principles of Earthquake Prediction.* Nauka, ISBN 5-02-002287-X, Moscow (in Russian).

Sornette, D. (2000). *Critical Phenomena in Natural Sciences*. Springer-Verlag, ISBN 354067424 , Berlin–Heidelberg.

Streltsov, M.I. (2005). *The May 27(28), 1995 Neftegorsk earthquake on Sakhalin Island*. Ivaschenko A.I., Kozhurin A.I. & Levin B.W. Yanus-K, ISBN 5-8037-0256-0, Moscow (in Russian).

Tanaka, K. (1980). Formation pattern of seismic gaps before and after large earthquakes. *Zisin. J. Seismol. Soc. Jpn*. Vol. 33, No. 3, pp. 369–377.

Tarakanov, R.Z. (1995). Source dimensions of large Kuril–Kamchatka and Japan earthquakes and maximum possible magnitude problem. *J. Volcanology and Seismology*. No. 1, pp. 76–89, ISSN 0203-0306 (in Russian).

Tikhonov, I. N. (1999). A method of intermediate-term prediction of time occurrence of strong (M ≥ 7.5) earthquakes (on the example of the territory around the Southern Kurile Islands), Preprint IMGG, Yuzhno-Sakhalinsk (in Russian).

Tikhonov, I. N. (2001). A method of intermediate-term prediction of probably periods of occurrence of strong earthquakes in application to the Kuril Islands region. *Proceedings of problems of geodynamics and earthquakes forecasting. The I Russian-Japanese Workshop*, pp. 158-169, ISBN 5-7442-1275-2, Khabarovsk, September, 2000 (in Russian).

Tikhonov, I.N. (1997). Some patterns in seismic regime dynamics of the Southern Sakhalin region. *Bull. Seismol. Assoc. Far East*, Vol. 3 No. 2, pp. 192–211.

Tikhonov, I.N. (2000). Precursors of the 1995 Neftegorsk earthquake and a recent precursory situation in the southern Sakhalin, *Proceedings of a memory and lessons of the 1995 Neftegorsk earthquake. The scientific-technical seminar-meeting. Collected reports*, pp.72-74, ISBN 5-94137-015-7, Yuzhno-Sakhalinsk, May 2000. POLTEX, Moscow (in Russian).

Tikhonov, I.N. (2003). Seismic quiescence before the strong earthquakes of Japan, *Proceedings of XXIII General Assembly of the International Union of Geodesy and Geophysics*, Sapporo, Japan, June – July, 2003. Abstracts Week A, P A.479-A.480.

Tikhonov, I.N. (2005). Detection and mapping of seismicity quiescence prior to large Japanese earthquakes. *J. Volcanology and Seismology*. No. 5, pp. 1–17 (in Russian).

Tikhonov, I.N. (2006). *Methods of earthquake catalog analysis for purposes of intermediate- and short-term prediction of large seismic events.* Vladivostok, Yuzhno–Sakhalinsk: IMGG FEB RAS, ISBN 5-7442-1415-1, Yuzhno–Sakhalinsk (in Russian).

Tikhonov, I.N. (2009). A technique of the strong earthquake prediction from the flux of seismicity in the North-Western part of the Pacific belt. Ph. Dr. Thesis. IMGG FEB RAS, Yuzhno-Sakhalinsk (in Russian)

Tikhonov, I.N., Kim, Ch.U. (2010). Confirmed prediction of the 2 August 2007 MW 6.2 Nevelsk earthquake (Sakhalin Island, Russia). *Tectonophysics.* Vol. 485, issues 1-4, pp. 85-93, ISSN 0040-1951.

Utsu, T., Ogata, Y., & Matsu'ura, R.S. (1995). The Century of the Omori Formula for Decay Law of Aftershock Activity. *J. Phys. Earth*, Vol. 43, pp. 1–33.

Vvedenskaya N.A., Kondorskaya N.V. et al. (Eds.). 1964 – 1991. *Earthquakes in USSR, 1962 – 1990*, Nauka, Moscow (in Russian).

Wiemer, S., Wyss, M. (1994). Seismic quiescence before the Landers (M=7.5) and Big Bear (M=6.5) 1992 earthquakes. *Bull. of Seismol. Soc. Am.* Vol. 84. No. 3, pp. 900-916, ISSN 0037-1106.

Zavyalov, A.D. (2006). *Intermediate-Term Earthquake Prediction: Principles, Techniques, Implementation*. Nauka, ISBN 5-02-033946-6, Moscow (in Russian).

4

Earthquakes Precursors

Dumitru Stanica and Dragos Armand Stanica
Institute of Geodynamics of the Romanian Academy
Romania

1. Introduction

Strong earthquake of magnitude 7 or more (on the Richter scale) strikes about once a year somewhere in the world and, several times triggers a cascade of follow-on events, such as tsunamis, floods, landslides, nuclear power plant crisis and public health catastrophes in the affected regions. Thus, during the 2004 Sumatra–Andaman earthquake and Indian Ocean tsunami nearly 230,000 people were killed and more than one million people were left homeless in 13 countries surrounding the Indian Ocean. The May 12th, 2008 earthquake in Western Sichuan, China and January 8th, 2010 earthquake in Haiti caused a death toll well over 75,000 and 320,000 people, respectively. The latest M9 Tohoku earthquake of March 11th 2011 in Japan was the biggest recorded earthquake ever to hit Japan. The earthquake triggered extremely destructive tsunami waves of up to 10 meters that struck Japan minutes after the quakes and caused about 26,000 deaths and 3000 injured. Recent catastrophic earthquakes (2004–2011) occurred in Asia, Europe and America have provided and renewed interest in question of the existence of precursory signals related to earthquakes. In these circumstances, the science community is struggling on how to provide early information related to the occurrence time of such events in order to reduce the loss of human life and property. Previous studies (Gotoh et al., 2002; Fraser-Smith et al., 1990; Freund et al., 1999; Hattori et al., 2006; Hayakawa & Fujinawa, 1994; Hayakawa & Molchanov, 2002; Kopytenko et al., 1994; Liu et al., 2004; Ouzounov et al., 2006; Parrot et al., 2007; Pulinets et al., 2004; Stanica & M. Stanica, 2007; Stanica & D.A. Stanica, 2010; Tramutoli et al., 2005; Tronin et al., 2004; Varotsos, 2005) have shown that there were precursory signals observed on the ground and in space associated with several earthquakes. In the last 10 years, the interdisciplinary group for Electromagnetic Study of Earthquakes and Volcanoes (EMSEV) have demonstrated that the existence of the electromagnetic earthquake precursors by terrestrial and satellite observations is not trivial, and it is necessary a wide international cooperation and several more years of research with primary focus in the following directions: (i) what is the possible generation mechanisms of the electromagnetic phenomena; and (ii) whether electromagnetic precursors systematically precede earthquakes. In this respect, taking into account that the seismic-active Vrancea zone, Romania is one of the "hot" subjects in the Eastern Europe, this paper is focused on the specific methodology able to emphasize the short–term electromagnetic (EM) precursory parameters, associated to intermediate depth earthquakes (70-180Km). We consider that one of the realistic mechanisms for triggering such events in the seismogenic volume can be the dehydration of rocks which make fluid-assisted faulting possible. The changes of electrical conductivity occurred before an earthquake, as a sequence of geodynamic processes

associated with fluid migration through faulting system developed into and in the close vicinity of the seismogenic volume, could be detected by means of the anomalous behavior of the Bzn parameter taken throughout the frequency range less than 1.66E-2 Hz (Stanica & M. Stanica, 2007; Stanica & D.A. Stanica, 2010). According to the electromagnetic information acquired in 2009-2010 years correlated with seismic events, it is relieved that some days before an EQ occurred, the daily mean variation of the Bzn parameter have an anomalous behavior marked by a significant increase versus its normal distribution identified in non seismic conditions.

2. Geodynamic models and possible mechanisms of intermediate depth earthquakes

The seismic active Vrancea zone is situated at the curvature of the Carpathians and it is bounded on the north-east by the East European Platform, to southward by the Moesian Platform, and on the north-west by Transylvanian Basin (Fig.1).
The hypocenters of the intermediate depth earthquakes are concentrated within a very small seismogenic volume and they are much denser than any other mantle events of intra-continental origin known in the world. In the past century, 4 large seismic events have

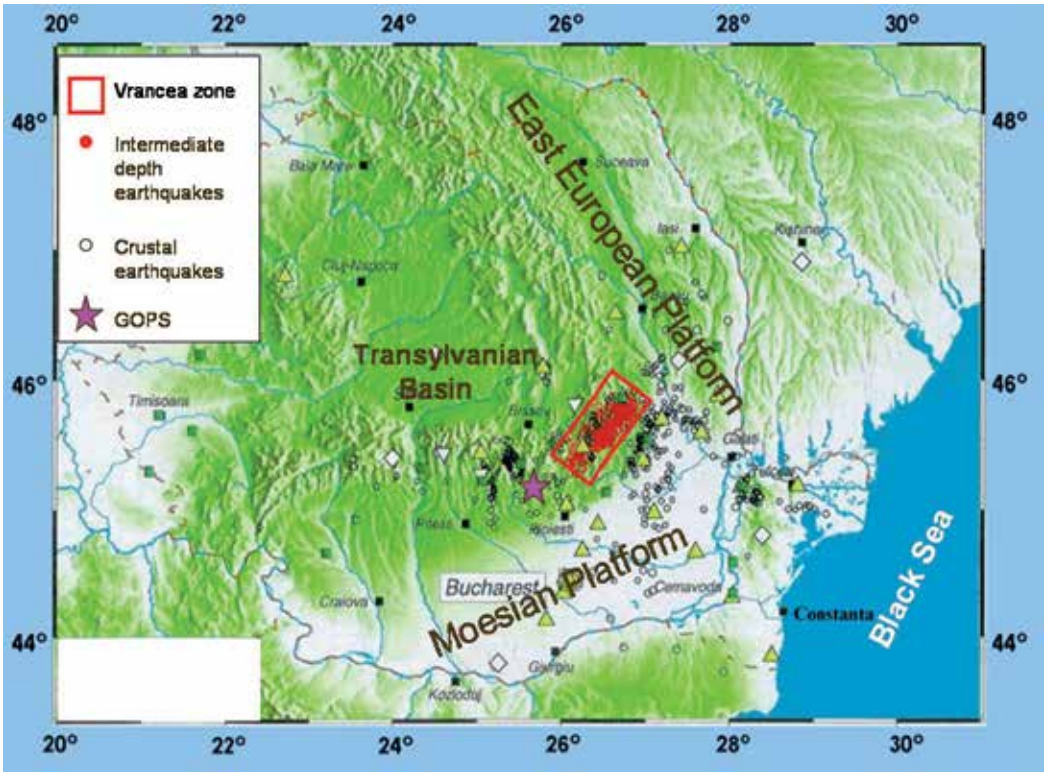

Fig. 1. Map of the seismic active Vrancea zone: crustal (white circles) and intermediate depth (red circles) epicenters of the earthquakes taken from ROMPLUS catalogue; pink star represents the Geodynamic Observatory Provita de Sus (GOPS) used as monitoring site of the earthquake precursors

occurred in the intermediate depth range of 70 to 180 km (in 1940 with moment magnitude Mw7.7, in 1977 with Mw7.4, in 1986 with Mw7.1, and in 1990 with Mw 6.9) and all of them cause destruction in Bucharest, the capital city of Romania, and shake central and eastern European cities several hundred kilometers away from their epicenters.

Several geodynamic models related to the triggering mechanism of the intermediate depth earthquakes have been elaborated in this area. Oncescu (1984) and Oncescu at al., (1984) proposed a double subduction model on the basis of 3-D seismic tomographic images: in their interpretation, the intermediate-depth earthquakes are generated within a vertical surface separating the sinking slab from stable lithosphere.

Trifu & Radulian (1989), analyzing the seismic behavior of the Vrancea zone, proposed a model based on the existence of two active zones located at depths of 80-110 km and 120-170 km. Both zones are characterized by local stress inhomogeneities capable of generating large earthquakes.

Khain & Lobkosky (1994) suggest that the Vrancea zone results from delamination processes occurred during continental collision and lithosphere sinking into the mantle.

Linzer (1996) explains the nearly vertical position of the Vrancea slab as the final rollback stage of a small fragment of oceanic crust.

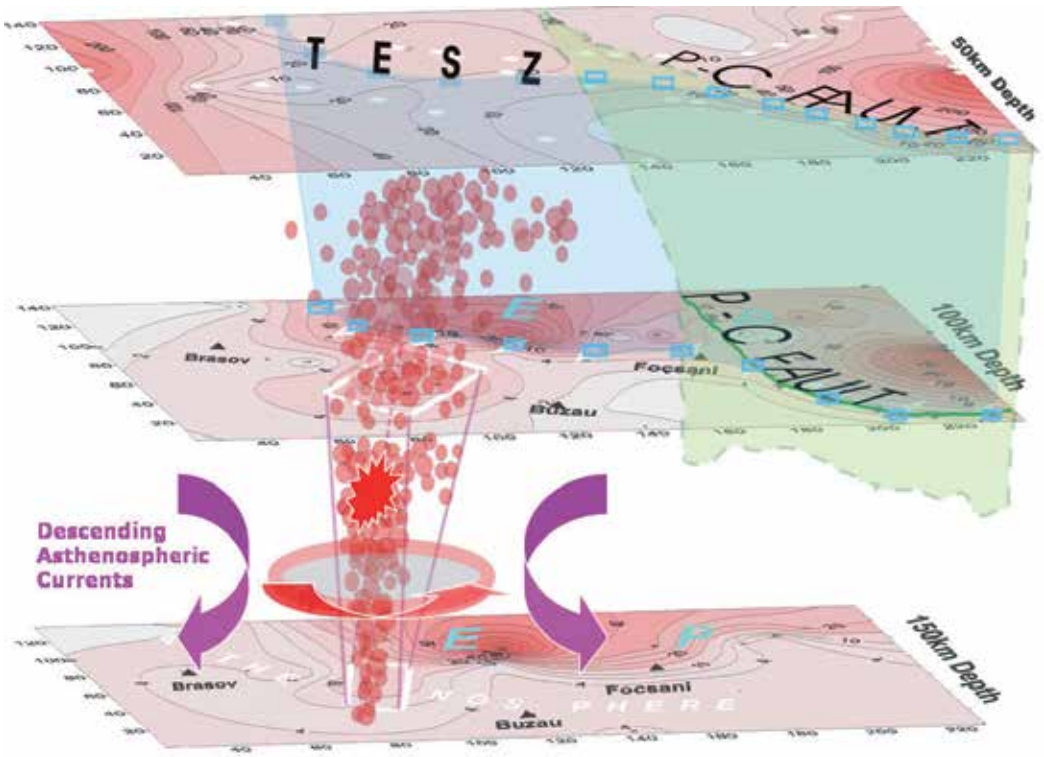

Fig. 2. 3D resistivity tomographic image at sub-crustal level in the seismic active Vrancea zone: red circles are intermediate depth earthquakes; blue square delineate the Trans-European Suture Zone (M. Stanica et al., 1999); green line is Peceneaga-Camena fault (P-C fault); pink arrows show the direction of the asthenospheric currents; red arrow shows the direction of the torsion process of the relic slab

Sperner, B., the Collaborative Research Center [CRC] 461 Team, (2005), taking into consideration that the geometry of the subduction zone was not unequivocally defined, proposed four possible configurations for the Vrancea zone: (i) subduction beneath the suture zone; (ii) subduction beneath the fore deep area; (iii) two interacting subduction zones, and (iv) subduction beneath the suture, followed by delamination.
Various types of slab detachment or delamination have been proposed to explain the present-day seismic images of the descending slab (Girbacea & Frisch, 1998; Gvirtzman, 2002; Sperner et al., 2001; Wortel & Spakman, 2000).
Viscous flows due to the sinking seismogenic slab together with dehydration-induced faulting can be considered as possible triggering mechanism explaining the intermediate-depth seismicity in Vrancea (Ismail-Zadeh et al., 2000)
Stanica et al., (2004) show, on the base of the three-dimensional (3D) resistivity tomographic image carried out using magnetotelluric data, that the possible triggering mechanism of the intermediate-depth earthquakes in the Vrancea zone may be the rock response to the active torsion processes sustained by the descending asthenospheric currents and the irregular shape of the relic slab. In their opinion, this torque effect may generate the increase shear stress and drive faulting process within the rigid slab (Fig.2).

3. Generation mechanisms and theoretical base of the electromagnetic precursors to earthquakes

3.1 Possible generation mechanisms of electromagnetic precursors

This paper is not intended to present an exhaustive analysis of all of literature published in this field. Instead, we have tried to provide only some representative hypothetic mechanisms related to the electromagnetic precursors to earthquakes.
The theory of semiconductors launched by Freund (2000) is considered the most comprehensive one. According to this theory, the solid rocks (e.g. granites) begin to crack under the action of a stress exceeding their elasticity limit, what leads to a release of electric charges. These charges, carried by water moving through the rocks fissures, generate currents of high amperage that, in their turn, create disturbances of the magnetic field and, also, infrared signature in the bands of 8μm and 11μm, when the charges are neutralized at the surface of the Earth.
In accordance with this theory, to have seismo-electric signals it is necessary that a few compulsory conditions to be fulfilled:

- Presence of major tectonic accidents able to produce an important stress;
- Existence of quartz or rocks with a rich content of quartz;
- Fluid carrying electric charges through porous rock what generates electric currents that lead to disturbances of the magnetic field.

The resistivity of porous rocks is changed as a function of compression and shearing (Brace et al., 1965) and may be measured by using passive experiments (magnetotelluric method), or experiments with active methods (Park et al., 1993).
Revol et al., (1977) have shown that the magnetic properties of rocks are changed depending on the applied stress and are associated to the changes of stress emphasized on fault rupture, what produces oscillations of the magnetic field of a few nT (Johnston, 1978, 1997); this mechanism is due to the piezomagnetic effect.
When a conductive fluid is forced to flow close to a surface with stationary electric charges, an electrokinetic effect appears generating currents that start to flow either through fluid, or

through the surrounding rock, what, in conditions imposed by real crustal parameters, may create surface magnetic fields of a few nT (Fenoglio et al., 1995).
Another theory supposes the generation of the magnetic signal either by conductive fluid flowing in presence of the magnetic field of the Earth, or by magnetohydrodynamic conversion of the seismic signal into an electric signal during the propagation through a conductive medium (Molchanov et al., 2001). While these mechanisms were proved in laboratory conditions, it is unclear, yet, how this process takes place in conditions rather similar to those specific to the Earth, owing to the lack of measurements in active fault zones.

3.2 Theoretical base of the electromagnetic precursors

At the Earth surface the vertical geomagnetic component (Bz) is entirely secondary field and its existence is an immediate indicator of lateral inhomogeneity. For a two-dimensional (2D) structure, the vertical geomagnetic component (Bz) is produced essentially by the horizontal geomagnetic component perpendicular ($B_{\perp}$) to geoelectric structure orientation and, consequently, the normalized Bzn function defined as:

$$Bzn\,(f) = \frac{Bz(f)}{B_{\perp}(f)} \tag{1}$$

should be time invariant in non geodynamic conditions (Ward et al., 1970), but it becomes unstable due to the geodynamic processes and, therefore, it could be used as a precursory parameter of the intermediate depth seismic activity (Stanica and D.A. Stanica, 2010).
In order to explain cause (earthquake) - effect (anomalous Bzn) relationship, we introduce the following equations:

$$\rho z\,(f) = \frac{0.2}{f}\left|\frac{E_{||}(f)}{Bz(f)}\right|^2 \tag{2}$$

where: ρz is vertical resistivity [Ωm = VmA^{-1}], f is the frequency [Hz] and the $E_{\parallel}$ is the electric field parallel to strike [Vm^{-1}], Bz is the vertical component of the magnetic induction [Tesla (T) = V s m^{-2}].
Also, it is possible to write the relation:

$$\rho_{||}(f) = \frac{0.2}{f}\left|\frac{E_{||}(f)}{B_{\perp}(f)}\right|^2 , \tag{3}$$

where: $\rho_{\parallel}$ is the resistivity parallel to strike[Ωm], $B_{\perp}$ is the component of the magnetic induction perpendicular to strike
[Tesla (T) = V s m^{-2}].
From the relations (2) and (3) we may estimate the normalized function Bzn (f), in terms of resistivities as follows:

$$\left|Bzn\,(f)\right| = \sqrt{\frac{\rho_{||}(f)}{\rho z\,(f)}} \tag{4}$$

This estimation of Bzn is in error for non two-dimensional geoelectrical structure.

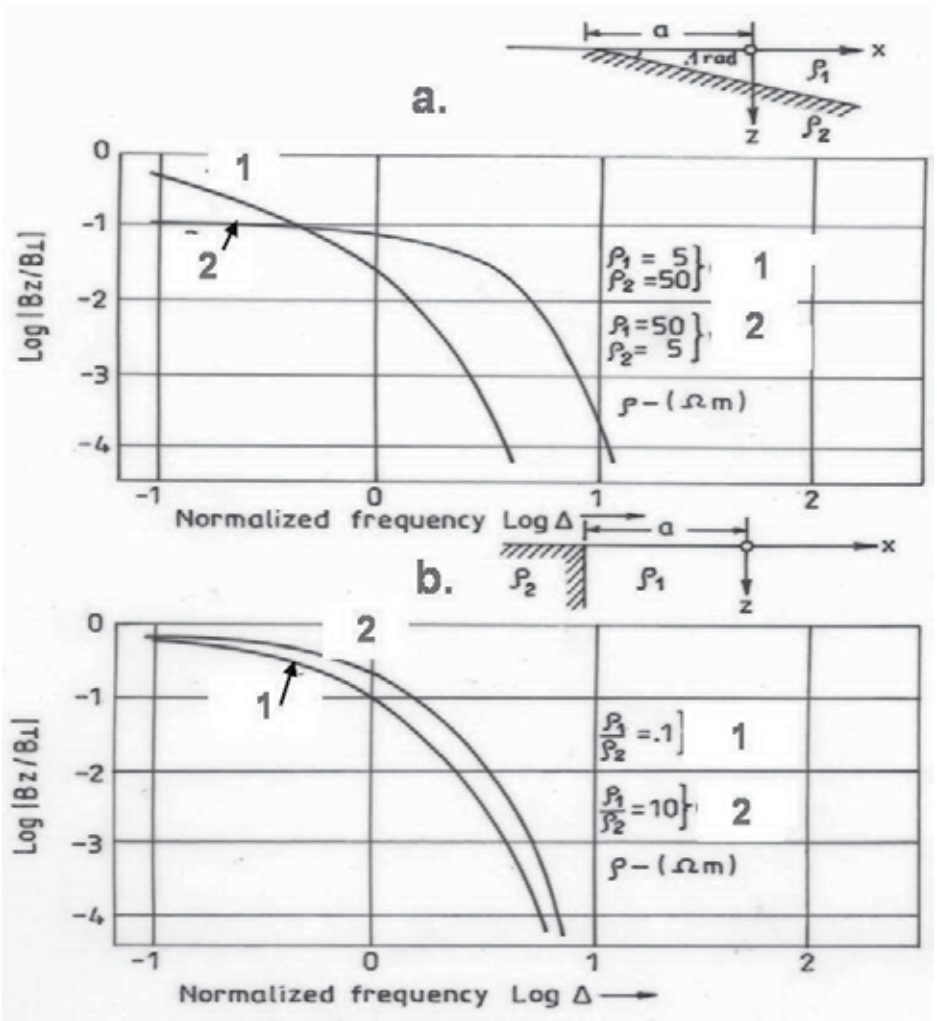

Fig. 3. Bzn distribution versus normalized frequency for sloping interface (a.) and vertical contact (b.): $\Delta=a/\delta_1$

The relation (4) demonstrates that normalized function Bzn could be linked to the resistivity/conductivity variation along the faulting systems acting as high sensitive path (represented by the Carpathian electrical conductivity anomaly) through the lithosphere and its right part lead to the normalized resistivity defined as:

$$\rho n(f) = \frac{\rho_{\parallel}(f)}{\rho z(f)} \tag{5}$$

Approximate field solutions were computed for two simple 2D geoelectric structures to illustrate the robustness of the relation (1). Solutions for the sloping interface and vertical contact models were obtained using finite element code (Wannamaker et al., 1986) and the results are presented in Fig. 3. These models represent two extremes in dipping angle of the interface and similarity in the properties of the normalized function Bzn obtained for the

model (Fig.3, b.) is of interest in selecting the site (GOPS) for continuous monitoring of the geomagnetic field. The normalized frequency scale (Δ) is proportional to distance along the x-axis and inverse-proportional to penetration depth (δ_1) in medium of resistivity ρ_1. The electromagnetic skin depth or penetration depth is given by:

$$\delta_1[\text{km}] = \frac{1}{2\pi}\sqrt{\frac{10\rho_1[\Omega\text{m}]}{f[\text{Hz}]}} \tag{6}$$

4. Electromagnetic (EM) methodology and results

4.1 Electromagnetic data collection

As we have seen in relation (1), Bzn could be used as precursory parameter of seismic event by measuring the vertical geomagnetic component (Bz) and horizontal component perpendicular to the strike ($B_\perp$) which have been collected at the Geodynamic Observatory Provita de Sus (GOPS), placed on the Carpathian electrical conductivity anomaly (CECA). This anomaly is delineated by the Wiese induction arrows, and it can represent a zone of partial melting or of hot highly-mineralized fluids in sedimentary layers, formed at the collisional limit between the both platforms (East European and Moesian) with Carpathian Alpine structures (Fig.4). It is also quit possible that these two varieties of fluid anomalies to co-exist and gradually flow one into another, as indicated by the fact that geoelectric parameters remain fairly constant throughout its entire length (Pinna et al., 1993, Rokityansky & Ingerov, 1999).

Induction arrows are vector representations of the ratio of vertical to horizontal magnetic field components. Since vertical magnetic fields are generated by lateral conductivity gradients, induction arrows map can be used to infer the presence, or absence of lateral variation of conductivity/resistivity. In the Wiese convection (Wiese, 1962) the vectors point away from the conductivity anomaly generated by anomalous internal concentrations of current, while in the Parkinson convection (Parkinson, 1959), the vectors point towards anomalous internal concentrations of current. Thus, insulator-conductor boundaries extended through a 2D geoelectrical structure (like CECA) give rise to induction arrows that orientate perpendicular to their geoelectrical strike, and have magnitude proportional to the intensity of anomalous current concentration (Jones & Price, 1970), which are in turn determined by the magnitude of conductivity gradient.

In our methodology, it was also supposed that pre-seismic conductivity changes, due to the fluid migration through faulting system, may generate changes of the normalized function Bzn, having magnitude proportional to the intensity of anomalous current concentrations through CECA.

The Geodynamic Observatory Provita de Sus (Fig.1) is located at about 100 km towards south-west of seismic active Vrancea zone and the criteria of selection as monitoring site are:

- Existence of logistic base able to supply optimal EM data;
- Placement on the Carpathian electrical conductivity anomaly where, ideally, the condition for a 2D type geoelectric structure is fulfilled (Fig. 4);
- Real time wireless data transfer to the central office (Institute of Geodynamics, Bucharest).

In order to select the frequency range where the relation (1) is valid (i.e., existence of a 2D geoelectrical structure and its strike orientation), as a first step in our EM methodology, at the GOPS we made a magnetotelluric sounding using the magnetotelluric (MT) equipment

GMS-06 (METRONIX - Germany). This geophysical system has 5 channels (two electric Ex, Ey and three magnetic Bx, By, Bz components), 24 bit resolution, GPS, two frequency ranges (LF: 4096sec.-1kH; HF=0.5kH-10kH) and for data processing "MAPROS" software packages.

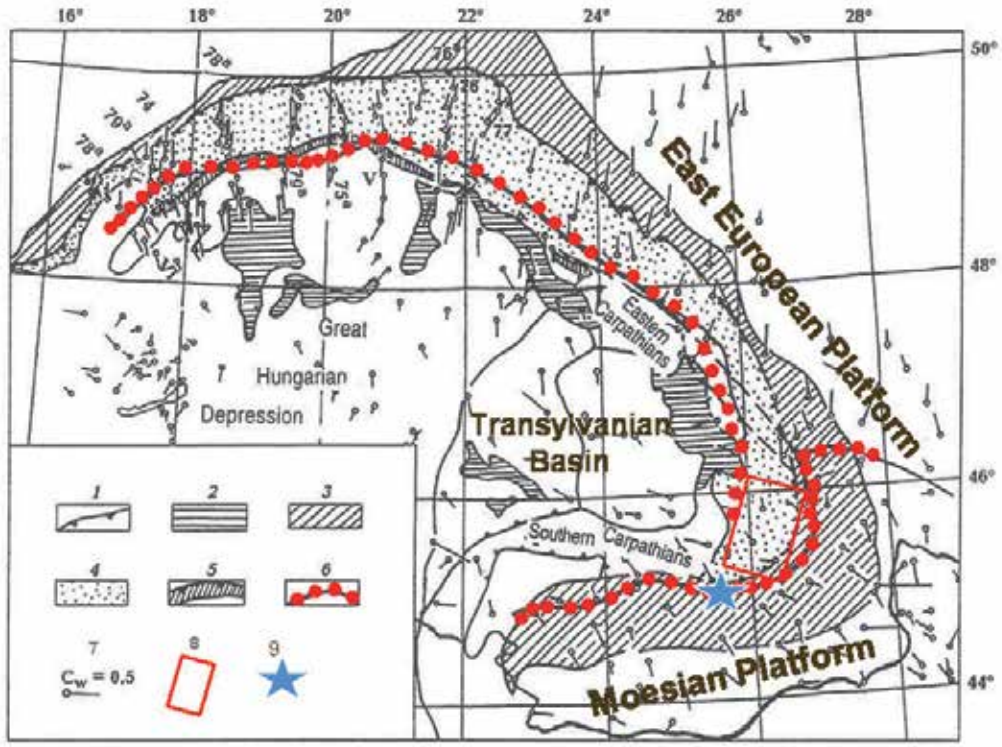

Fig. 4. Carpathian electrical conductivity anomaly and Wiese induction arrows on a tectonic sketch map: 1) main boundaries and fractures (over thrusts) of regional structures; 2) Neogene volcanic rocks; 3) Carpathian fore-deep; 4) Carpathian flysch nape system; 5) Piena and Marmarosh cliff belt; 6) Carpathian electrical conductivity anomaly (CECA); 7) Wiese induction vectors magnitude; 8) seismic active Vrancea zone (intermediate-depth earthquakes); 9) Geodynamic Observatory Provita de Sus (GOPS) used for the electromagnetic data collection (Modified after Rokityansky & Ingerov, 1999)

It is well known that the magnetotelluric (MT) method is a passive technique that involves measuring fluctuations of natural electric (E) and magnetic (B) fields in orthogonal directions at the surface of the Earth (Kaufman, & Keller, 1981). The orthogonal components of the horizontal electric (Ex, Ey) and magnetic (Bx, By) fields are related by the complex impedance tensor, Z:

$$\begin{pmatrix} Ex \\ Ey \end{pmatrix} = \begin{pmatrix} Zxx & Zxy \\ Zyx & Zyy \end{pmatrix} \begin{pmatrix} Bx \\ By \end{pmatrix}, \text{ or } E = ZB \tag{7}$$

Where: Zxx, Zxy, Zyx, Zyy are elements of the impedance tensor [VA^{-1}]
For a 2D structure, in which the conductivity varies along one horizontal direction as well as with depth, the following relations are fulfilled:

$$\begin{aligned} Zxx &= -Zyy \\ Zxy &\neq -Zyx \end{aligned} \tag{8}$$

Using single site magnetotelluric impedance tensor decomposition technique (Bahr, 1988), it was possible to identify the following two parameters: skewness and strike orientation.
The skewness is a dimensionality parameter of the impedance tensor, defined as:

$$\text{Skew} = \frac{\left\| Zxx + Zyy \right\|}{\left\| Zxy + Zyx \right\|} \tag{9}$$

This parameter should be less than 0.3 to interpret the structure as 2D.
The tensor impedance from relation (7) can be rotated to obtain the strike orientation of the 2D geoelectrical structure using the relation:

$$\alpha = \frac{1}{4}\arctan\frac{2\text{Re}(Zxy + Zyx)(\overline{Zxx - Zyy})}{(|Zxx - Zyy|^2 - |Zxx + Zyx|^2)} \tag{10}$$

Where: α (strike) is rotation angle [^{0}].

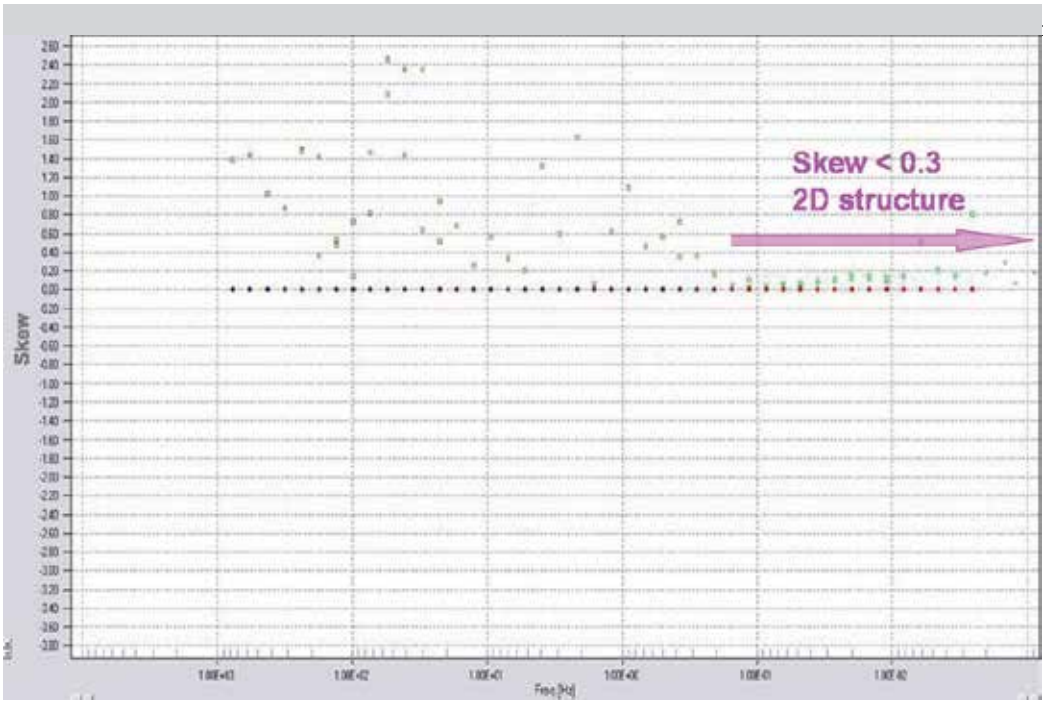

Fig. 5. Skewness parameter versus frequency (Hz): pink arrow delineates the frequency range for 2D structure

The MAPROS software packages include all these mathematical relations presented above and have been applied to MT sounding carried out at GOPS. This program performs the following basic tasks:

- Real time data acquisition and processing;
- Robust estimation of the magnetotelluric transfer functions;
- Real time display of time series and all important electromagnetic parameters ($\rho_{\perp}$, $\rho_{\parallel}$, skewness and strike, etc).

Thus, on the base of MT results, a 2D geoelectrical structure has been identified on the frequency range less than 1.66 E-2 Hz where skewness < 0.3 (Fig.5) and average strike orientation is N96^{0}E (Fig.6). This frequency range is also associated with the intermediate-depth earthquakes interval (70-180km) where EM precursors are generated.

These results confirm, once more, that the CECA's geoelectrical structure is of 2D type with strike orientation approximately east-west, and forms not only a tectonic boundary between Moesian Platform and Carpathian Alpine structures, but also represents a peculiar conducting channel extended to the seismic active Vrancea zone (Fig.4).

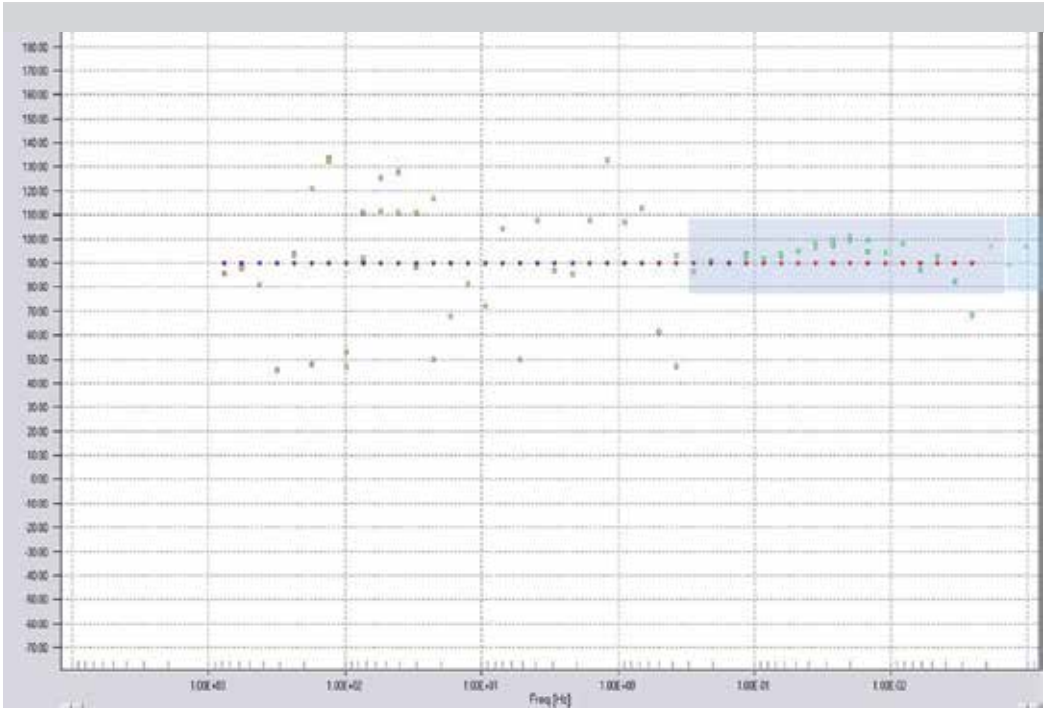

Fig. 6. Strike orientation (degrees) versus frequency (Hz): blue rectangle delineates the frequency range for 2D structure with average strike orientation of N96^{0}E

The next step in our study was to realize a continuous monitoring of the geomagnetic components ($B_{\perp}$, $B_{\parallel}$, Bz) using the acquisition module MAG-03 DAM (Bartington-England), with 6 channels, 24 bit resolution and three axis magnetic field sensor MAG-03 MSL (frequency range: DC - 1kHz). In order to obtain $B_{\perp}$ component of the geomagnetic field, one of the horizontal components of the three axis magnetic sensor must be orientated perpendicular to strike. The parameters of the data acquisition card are under software control and additional program collects information at each five seconds and stored them, every 60 seconds (Table.1), on the PC HD. Using the wireless connection, all the data are transferred from GOPS to the central unit, placed at the Institute of Geodynamics in Bucharest, for real-time data processing and analysis (Fig.7).

Fig. 7. Monitoring system of the geomagnetic components (Bx, By and Bz) and real time data transfer : acquisition module MAG-03DAM (a); computer (b) for data storage; monitor (c) for real time geomagnetic data display (d); data transfer program (e) ; wireless connection (f)

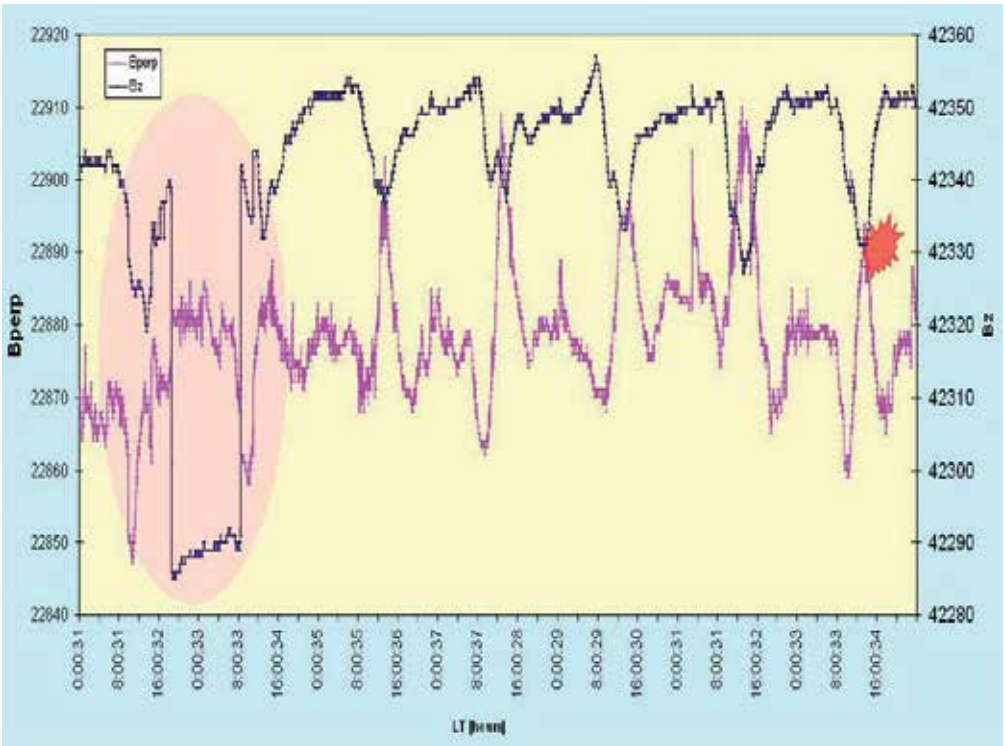

Fig. 8. Geomagnetic time series (Bperp and Bz) recorded at the GOPS for 7 days interval (April19- April 25, 2009); Bperp is $B_{\perp}$; red star is earthquake of M5.0; pink ellipse marks a pre-seismic disturbance of the vertical component (Bz) of geomagnetic field (lead time is about 6 days before the earthquake).

Date	Time [s]	$B_{\perp}$[μT]	$B_{\parallel}$[μT]	Bz[μT]	Bzn	Bzn average (1day data)	STDEV
7/17/2009	0:00:37	22.869	0.22	42.367	1.852595	1.852561	0.000281
7/17/2009	0:01:37	22.869	0.22	42.367	1.852595		
7/17/2009	0:02:37	22.869	0.22	42.367	1.852595		
7/17/2009	0:03:37	22.868	0.22	42.367	1.852676		
7/17/2009	0:04:37	22.868	0.22	42.367	1.852676		
7/17/2009	0:05:37	22.868	0.221	42.367	1.852676		
7/17/2009	0:06:37	22.869	0.22	42.367	1.852595		
7/17/2009	0:07:37	22.868	0.22	42.367	1.852676		
7/17/2009	0:08:37	22.868	0.221	42.367	1.852676		
7/17/2009	0:09:37	22.868	0.22	42.367	1.852676		
7/17/2009	0:10:37	22.868	0.22	42.367	1.852676		
7/17/2009	0:11:37	22.869	0.221	42.368	1.852639		
7/17/2009	0:12:37	22.868	0.22	42.368	1.85272		
7/17/2009	0:13:37	22.868	0.221	42.368	1.85272		
7/17/2009	0:14:37	22.869	0.221	42.368	1.852639		
7/17/2009	0:15:37	22.868	0.22	42.367	1.852676		
7/17/2009	0:16:37	22.868	0.221	42.367	1.852676		
7/17/2009	0:17:37	22.869	0.221	42.367	1.852595		
7/17/2009	0:18:37	22.868	0.221	42.367	1.852676		
7/17/2009	0:19:37	22.869	0.221	42.367	1.852595		
7/17/2009	0:20:37	22.869	0.221	42.368	1.852639		
7/17/2009	0:21:37	22.869	0.221	42.368	1.852639		
7/17/2009	0:22:37	22.869	0.221	42.368	1.852639		
7/17/2009	0:23:37	22.869	0.221	42.368	1.852639		
7/17/2009	0:24:37	22.87	0.221	42.368	1.852558		
7/17/2009	0:25:37	22.869	0.221	42.368	1.852639		
7/17/2009	0:26:37	22.869	0.221	42.367	1.852595		
7/17/2009	0:27:37	22.869	0.221	42.367	1.852595		
7/17/2009	0:28:37	22.869	0.221	42.367	1.852595		
7/17/2009	0:29:37	22.869	0.221	42.367	1.852595		
7/17/2009	0:30:37	22.869	0.221	42.368	1.852639		
7/17/2009	0:31:37	22.869	0.221	42.367	1.852595		
7/17/2009	0:32:37	22.869	0.222	42.367	1.852595		
7/17/2009	0:33:37	22.869	0.222	42.367	1.852595		
7/17/2009	0:34:37	22.868	0.222	42.367	1.852676		
7/17/2009	0:35:37	22.869	0.222	42.367	1.852595		
7/17/2009	0:36:37	22.868	0.221	42.367	1.852676		
7/17/2009	0:37:37	22.869	0.221	42.367	1.852595		
7/17/2009	0:38:37	22.869	0.221	42.367	1.852595		
7/17/2009	0:39:37	22.869	0.221	42.367	1.852595		
7/17/2009	0:40:37	22.868	0.221	42.367	1.852676		
7/17/2009	0:41:37	22.869	0.221	42.367	1.852595		
7/17/2009	0:42:37	22.868	0.222	42.367	1.852676		

Table 1. Geomagnetic time series $B_{\perp}$, $B_{\parallel}$ and Bz recorded on July 17th 2009 (42 minutes record): Bzn average is computed for 1day data; STDEV of the Bzn average.

The geomagnetic time series recorded at the GOPS for 7 days interval (April19- April 25, 2009), including the occurrence time of the earthquake of M5.0 (April 25), are presented in Fig. 8. The pre-seismic disturbance of the vertical component (Bz) occurred about 6 days before earthquake. But, as we have seen later on, this disturbance is masked by the superposition effect started on March 9, 2009.

4.2 Results

In this paper, daily mean distribution of the normalized function Bzn and its standard deviation are performed in the frequency range less than 1.666E-2 Hz, where 2D structural condition is fulfilled. The concept of this analysis is based on the idea that signal associated with solar-terrestrial origin is constant, according to relation (1), while lithospheric origin signal from the underground current flowing along the CECA is considered to have a vertical component (see fig.8). With the other words, the normalized function Bzn shows a small and certain value for its normal trend (in non seismic condition) and increased values in pre-seismic conditions.

To assess the robustness of the presented methodology, some examples of Bzn distribution acquired in a span of about two years (2009 -2010) are shown in correlation with the intermediate depth earthquakes, with magnitude (Mw) higher than 4.0 (Richter scale), selected from the catalogue issued by National Institute of the Earth Physics-Bucharest.

The first particular case of the Bzn distribution correlated with the both standard deviation (STDEV) and intermediate depth earthquakes, within the interval January 16 – May 11, 2009 is shown in Fig. 9.

The Bzn distribution emphasizes two domains, the first one, with normal values of about 1.842 on the interval January16 - March 8 and second one, on March 9- May 11 interval, having values between 1.850-1.856, and all earthquakes are marked by vertical arrows.

Average value of 1.842, associated with earthquakes of M< 3.3 occurred on the interval January 16 – March 8 represents the threshold limit between the so called "normal trend" of Bzn and its second anomalous domain, which started on March 9, which may represent a superposition effect of the four earthquake of M4.0 (March 21), M4.1 (April 12), M5.0 (April 25) and M5.0 (May 11).

The earthquake of magnitude 5.0 was triggered in the Vrancea zone, at 109 km depth, on April 25 at 20:18:48 (local time), being felt in Bucharest and over a large area extended from the epicentral zone towards NE and SW directions, corresponding with the fault plane orientation of the focal mechanism.

Similar results have been obtained in the Bzn distribution (Fig.10) on the interval February 1–March 31, 2010, where the threshold limit of about 1.842 separates also two domains, one with normal trend (earthquakes of M<3.4) extended on the interval February 01- February 18, and anomalous one, on the interval February 21- March 31, having Bzn values between 1.850- 1.855. The last interval could be correlated with the superposition effect produced by the two earthquakes of M4.2, and the pre-seismic lead time is about 10 days before the first earthquake of M4.2 occurred.

Figures 11 and 12 depict results of Bzn distribution observed at GOPS on the two intervals May 28 - August 26, 2009 and the whole September month, 2009.

Figure 11 reveals three anomalous domains of Bzn which may be related to 5 earthquakes with magnitude larger than 4. First domain, extended on the interval June 4 – July 10, is

characterized by enhanced values of Bzn comprised between 1.852 and 1.854, and may be related to the superposition effect generated by the two earthquakes of M3.9 (June 20) and M4.0 (June 27). Pre-seismic increased values of Bzn are extended on 16 days interval for this group of earthquakes.

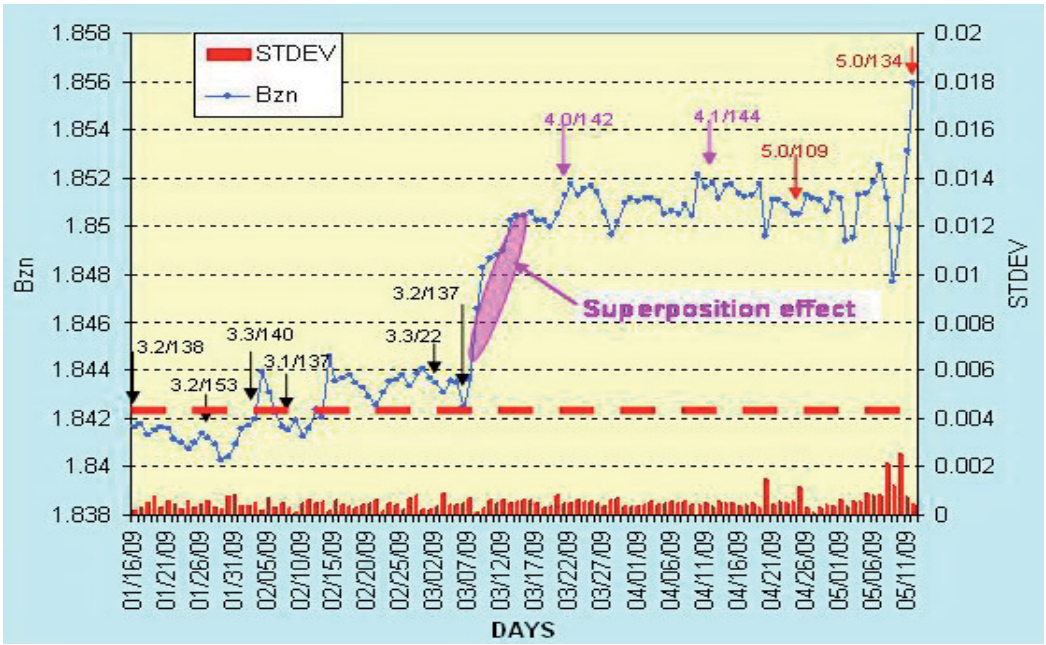

Fig. 9. Bzn and STDEV distributions at the GOPS, within the interval January 16 – April 30, 2009; vertical arrows are earthquakes and ratio 5.0/109 is the magnitude/hypocenter depth of earthquake in [km]; dashed red line is threshold limit between normal trend and anomalous behaviour of the normalized function Bzn

The second anomalous domain, with an average value of Bzn of about 1.855, is extended on the interval July 14 – August 7 and reflects also superposition effect of the two earthquakes of magnitude 5.1 and 5.2, occurred on July 24 and August 5, respectively. The pre-seismic superposition effect of the Bzn started on July 15 and is developed in 9 days interval up to

the occurrence of M5.1 earthquake (July 24). In the last anomalous domain (August 11-August 26), the normalized function Bzn has values between 1.853 -1.454 and could be associated with the two earthquakes of M4.1 occurred on August 17 and 26. Here, the pre-seismic occurrence interval is of about 7 days.
Figure 12 illustrates the Bzn distribution for September 2009, where similar pre-seismic characteristics are observed. Thus, enhanced values of Bzn are correlated with the increased values of earthquake magnitudes and decreased foci depth.

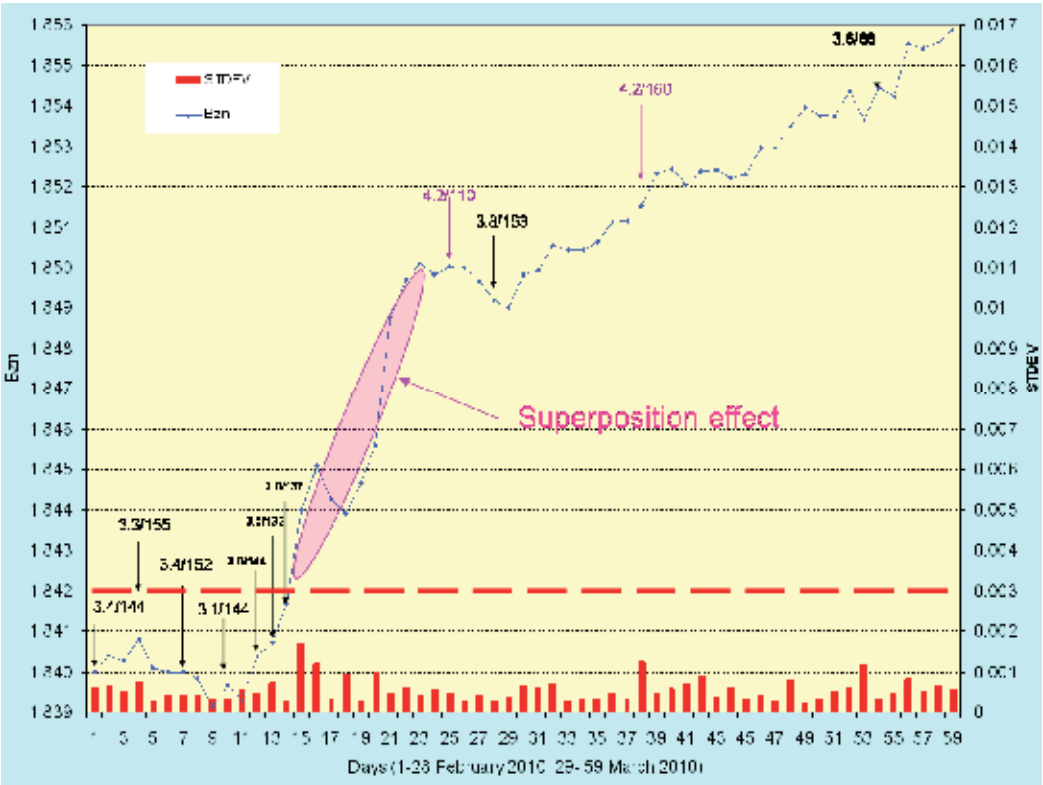

Fig. 10. Bzn and STDEV distributions at the GOPS, within the interval February01– March 31, 2010; vertical arrows are earthquakes and ratio 4.2/110 is the magnitude/hypocenter depth of earthquake in [km]; dashed red line is threshold limit between normal trend and anomalous behaviour of the normalized function Bzn

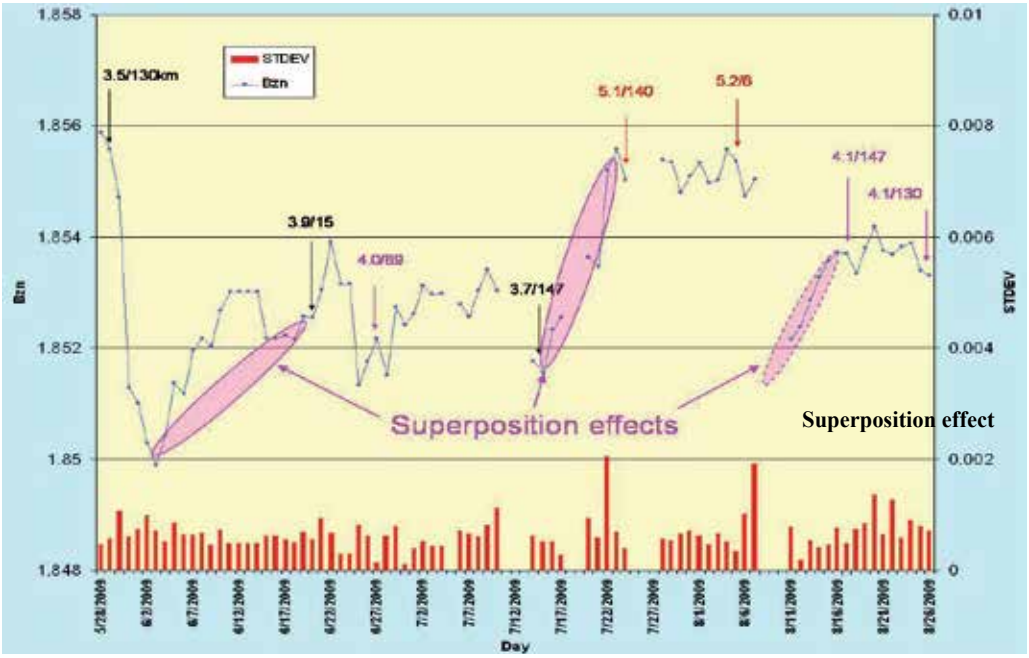

Fig. 11. Bzn and STDEV distributions at the GOPS, within the interval May 28– August 26, 2010; vertical arrows are earthquakes and ratio 5.1/140 is the magnitude/hypocenter depth of earthquake in [km]

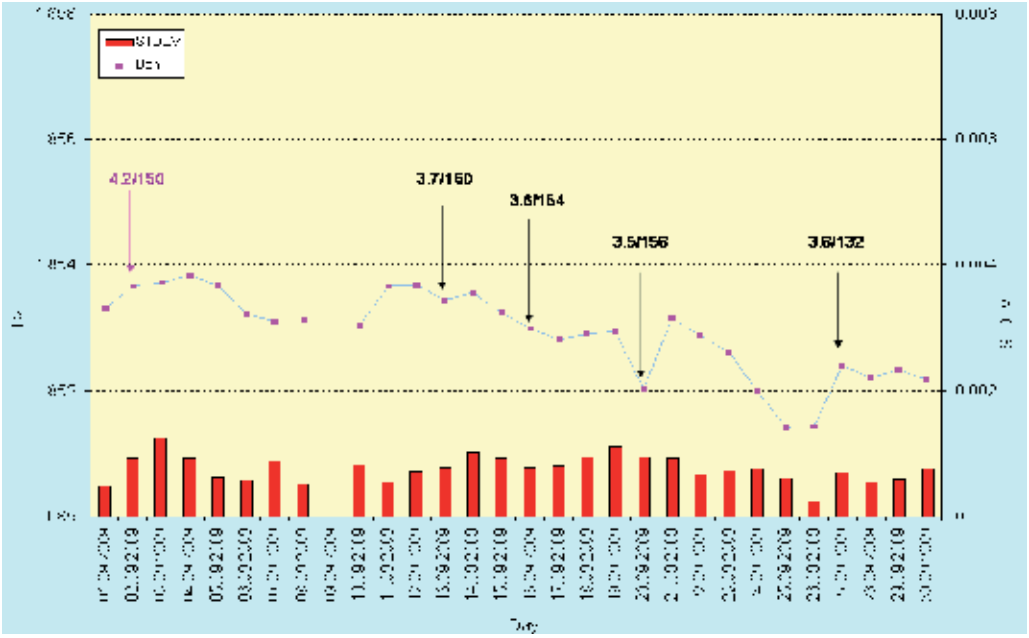

Fig. 12. Bzn and STDEV distributions at the GOPS, within the interval 01February – March 31, 2010; vertical arrows are earthquakes and ratio 4.2/150 is the magnitude/hypocenter depth of earthquake in [km]

The local variation of earthquakes energy (Es) carried out for the analyzed interval in 2009 year is shown on Fig. 12. The relationship between earthquake magnitude and energy in foci is:

$$\log Es = 11.8 + 1.5\,M \tag{11}$$

Where: E_S is energy [Erg], M is earthquake magnitude.

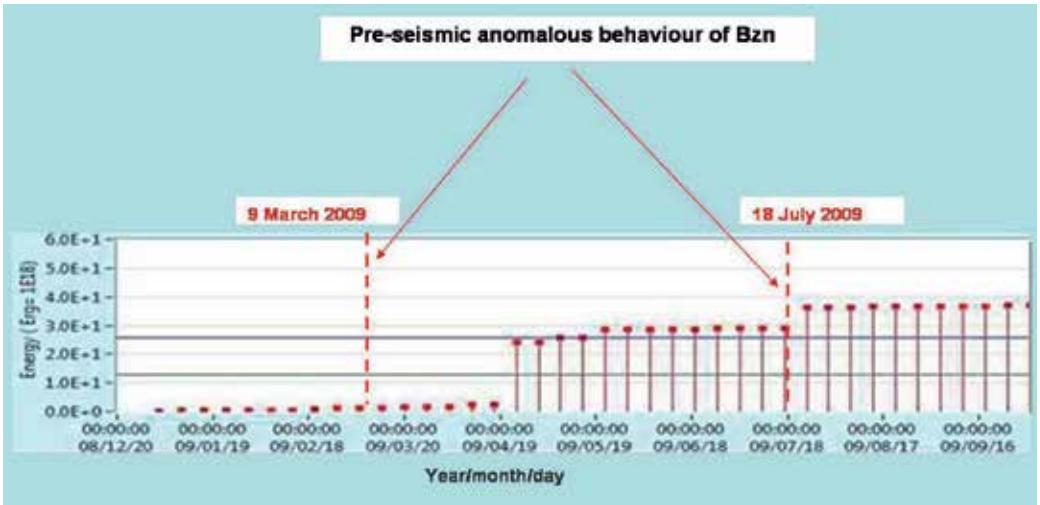

Fig. 13. Variation of earthquakes energy (in foci) on the interval January 01– September 30, 2009: vertical red dashed lines represent lead time of the pre-seismic anomalous behaviour of the normalized function Bzn

It is quite obvious that the pre-seismic anomalous behaviour of Bzn observed on March 9 (Fig.9) and July 18 (Fig.10) respectively, may be correlated with the increased seismic energy reflected by Fig. 13, as follows: more than 15 days interval for the earthquake of M4.0 (March 21) and, about 7 days for earthquakes of M5.1 (July 24). This seismic activity support a possible generation mechanism of the electromagnetic precursors based on the stress generation followed by dehydration of rocks and fluid migration through the faulting system, which may produce concentration of induced currents in highly conductive elongated structure such as Carpathian electrical conductivity anomaly. These induced currents may cause distortion of the vertical geomagnetic component (Fig. 8) which is reflected by increased values of Bzn (Fig.9). The pre-seismic lead time of the normalized function Bzn is between 7days and 15 days for all the data presented in this paper.

5. Conclusions

The results carried out in this paper are based on the hypothesis according to the pre-seismic conductivity changes, due to the fluid migration through faulting system, may generate increased values of the normalized function Bzn proportionally with the intensity of anomalous current concentrations through CECA.

The normalized function Bzn carried out at GOPS has been analyzed in order to detect its pre-seismic anomalous behaviour related to the intermediate depth earthquakes with M≥ 4. Before all the earthquakes of M ≥ 4 the Bzn distribution exhibit significant enhancements from the normal trend and the pre-seismic lead time is about 7-15 days. The Bzn average value of 1.842 (Fig.9), associated with earthquakes of M≤3.3 occurred on the period January 16 – March 7, represents the threshold limit between the normal trend and its pre-seismic anomalous behaviour, taken as possible earthquake precursor.

When anomalous behavior and normal trend domains are much closed, as a multitude of earthquakes of different magnitude occurred at short time intervals, then a superposition effect has been observed.

For the Vrancea zones, two correlations between the magnitude of seismic events and Bzn are highlighted (Fig.14):

i. earthquake of M ≥ 4 is expected to occur when Bzn ≥ 1.847;
ii. anomalous behaviour of Bzn ≥ 1.854 may be use as pre-seismic value for an earthquake of M ≥ 5.

Sometimes, superposition effects may generate exceptions to the above rules.

As this methodology allows us to know always the structure changes after any seismic event (on the base of dimensionality parameters), what permit to use further on the most adequate electromagnetic techniques, it becomes an interesting subject of studying the earthquake mechanism and the associated electromagnetic precursors.

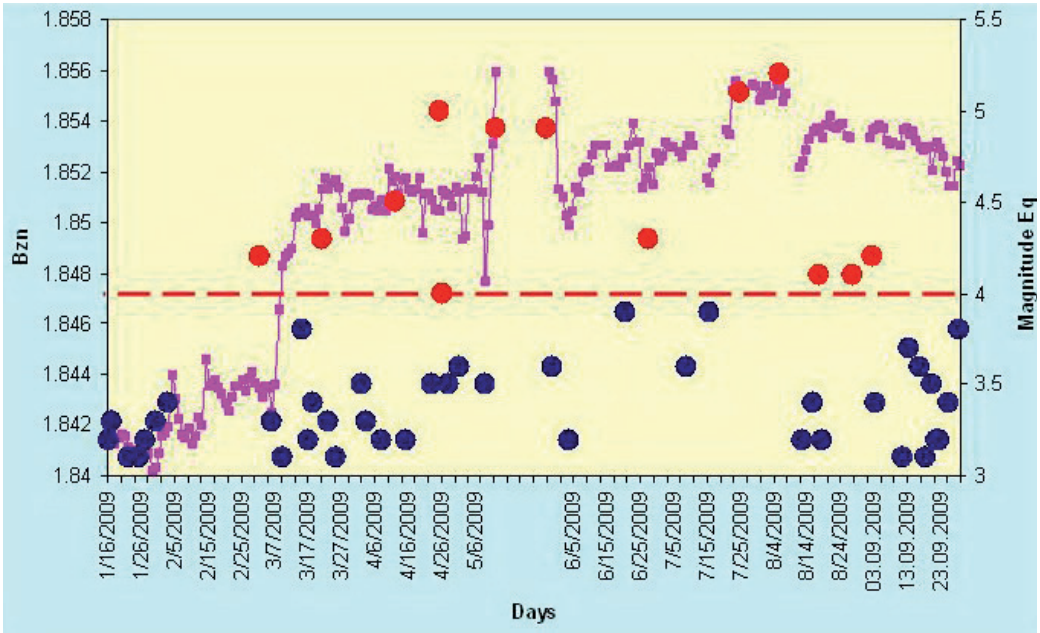

Fig. 14. Distributions of the normalized function Bzn and earthquake magnitude on the 2009 analyzed interval; blue circles are earthquakes with M< 4; red circles are earthquakes with M ≥4; red dashed line represents the limit above to which one earthquake of M ≥4 is possible to occur.

6. Acknowledgment

This work was supported by the CNCSIS - UEFISCDI, project number 1028/2009, PN II – IDEI code 14/2008. We would also like to thank to the Institute of Geodynamics of the Romanian Academy for providing electromagnetic data and facilities for the present research project.

7. References

Bahr, K. (1988). Interpretation of the magnetotelluric impedance tensor: regional induction and local telluric distortion, *J. Geophys.,* 62, pp.119-127

Brace, W.F.; Orange, A. S. & Madden, T.N. (1965). The effect of pressure on the electrical resistivity of water-saturated crystalline rocks. *Journal of Geophysical Res.*, 70 (22), pp. 5669-5678

Fenoglio, M.A.; Johnston M.J. & Bierlee, J.D. (1995). Magnetic and electric fields associated with changes in high pore pressure in fault zones: application to the Loma Prieta ULF emissions. *J.Geophys.Res.* 100, pp. 12951-12958

Fraser-Smith, A.C.; Bernardi, A.; Mc Gill, P.R.; Ladd, M. E.; Halliwell, R.A. & Villard, Jr. O.G. (1990). Low frequency magnetic field measurements near the epicenter of the M 7.1 Lomma Prieta earthquake. *Geophys. Res. Lett.,* 17, pp.1465-1468.

Freund, F.; Gupta, A.; Butow, S.J. & Tenn, S. (1999). Molecular hydrogen and dormant charge carriers in minerals and rocs, In: *Atmospheric and ionospheric electromagnetic phenomena associated with earthquakes,* Hayakawa, & Molchanov, pp. 839-871, Terra Sci. Publ. Comp., Tokyo

Freund, F. (2000). Time-resolved study of charge generation and propagation in igneous rocks. *Journal of Geophysical Res.,* B, 105, pp.11001-11019

Girbacea, R. & Frisch, W. (1998). Slab in the wrong place: Lower lithospheric mantle delamination in the last stage of the Eastern Carpathian subduction retreat. *Geology* 26, pp.611-614

Gotoh, K.; Akinaga, Y.; Hayakawa, M. & Hattori, K .(2002). Principal component analysis of ULF geomagnetic data for Izu island earthquake in July 2000. *J.Atms. Electr.* 22, pp.1-12

Gvirtzman, Z. (2002). Partial detachment of a lithospheric root under the southeast Carpathians: toward a better definition of the detachment concept. *Geology* 30, pp. 51-54

Hattori, K..; Serita, A.; Yoshino, C. Hayakawa, M. & Isezaki, N. (2006). Singular spectral analysis and principal component analysis for signal discrimination of ULF geomagnetic data associated with 2000 Izu Island earthquake swarm. *Phys. Chem. Earth,* 31, pp. 281-291

Hayakawa, M. & Fujinawa, A.Y. (1994). *Electromagnetic Phenomena related to Earthquake Prediction*, Terra Scientific Pub. Comp, Tokyo

Hayakawa, M. & Molchanov, O.A. (2002). *Seismo-Electromagnetics: Lithosphere-Atmosphere-Ionosphere Coupling,* Terra Scientific Pub. Comp., ISBN 9784887041301, Tokyo

Ismail-Zadeh, A.T.; Panza, G.F. & Naimark, B.M. (2000). Stress in the descending relic slab beneath the Vrancea region, Romania, *Pure Appl. Geophys.,* 157, pp.111-130

Johnston M.J.S. (1978). Local magnetic field variations and stress changes near a slip discontinuity on the San Andreas fault. *Journal of Geomagnet. And Geoelec.,* 30, pp. 511-548.

Johnston, M.J.S. (1997). Review of electric and magnetic fields accompanying seismic and volcanic activity. *Surv. Geophys.,* 18, pp. 441-475

Jones, F. W. & Price, A.T. (1970). The perturbations of alternating geomagnetic fields by conductivity anomaly. *Geophys.J.R. Astr. Soc.,* 20, pp. 317-334

Kaufman, A. A. & Keller, G.V. (1981). *The magnetotelluric sounding method,* Elsevier Scientific Publishing Comp., Amsterdam-Oxford-New York.

Khain, V.E. & Lobkosky, L.I. (1994). Conditions of Existence of the Residual Mantle Seismicity of the Alpine Belt in Eurasia, *Geotectonics,* 2, pp. 54-60.

Kopytenko, Y.A.; Matiashvili, T.G.; Voronov, P.M. & Kopytenko, E.A. (1994). Observation of electromagnetic ultralow-frequency lithospheric emission in the Caucasian seismically active zone and their connection with earthquakes, In: *Electromagnetic Phenomena related to Earthquake Prediction,* Hayakawa & Fujinawa, 175-180, Terra Scientific Pub. Comp, Tokyo

Linzer, H.-G. (1996), Kinematics of retreating subduction along the Carpathian arc, Romania, *Geology* 24 (2), pp. 167-170

Liu, J.Y.; Chuo, Y.J.; Shan, S.J.; Tsai, Y.B.; Chen Y.I.; Pulinets, S.A. & Yu, S.B. (2004). Pre-earthquake ionospheric anomalies registered by continuous GPS TEC measurements. *Annals Geophysicae,* 22, pp.1585-1593

Molchanov, O.; Kulchitschy, A. & Hayakawa, M. (2001). Inductive seismo-electromagnetic effect in relation to seismogenic ULF emission. *Natural Hazards and Earth System Sciences*, 1, pp. 61-68

Oncescu, M.C. (1984). Deep structure of the Vrancea region, Romania, inferred from simultaneous inversion for hypocenters and 3-D velocity structure. *Ann. Geophys.,* 2, pp. 23-28

Oncescu, M.C.; Burlacu, V.; Anghel, M. & Smalbergher, V. (1984). Three-dimensional P-wave velocity image under Carpathian Arc. *Tectonophysics,* 106, pp. 305-319.

Ouzounov, D.; Bryant, N.; Logan, T.; Pulinets, S. & Taylor, P. (2006). Satellite thermal IR phenomena associated with some of the major earthquakes in 1999-2003. *Physics and Chemistry of the Earth,* 31, pp.154-163

Parck, S.K.; Johnston, M.J.S.; Madden, T.R.; Morgan, F.D. & Morrison, H.F. (1993). Electromagnetic precursors to earthquakes in the ULF band: a review of observations and mechanisms. *Rev.Geophys.,* 31, 117-132.

Parkinson, W. (1959). Directions of rapid geomagnetic variations. *Geophys. J. R. Astr. Soc.* 2, pp.1-14

Parrot, M.; Manninen, J.; Santolik, O.; Nemec, F.; Turner, T.; Rait, T. & Macusova, E. (2007). Simultaneous observations on board of satellite and on the ground of large-scale magnetospheric line radiation. *Geophys. Res. Lett.* 34. L19102

Pinna, E.; Soare, A.; Stanica, D. & Stanica, M. (1993). Carpathian conductivity anomaly and its relation to deep substratum structure. *Acta Geodaet. Geophys. et Montanistica,* Vol. 27(1), pp.35-45

Pulinets, S.A.; Gaivaronska, T.A.; Leyva-Contreras, A. & Ciraolo, L. (2004). Correlation analysis technique reveling ionospheric precursors opf earthquakes. *Nat. Hazards Syst. Sci.,* 4, pp. 697-702

Revol, J.; Day, R. & Fuller, M. (1977). Magnetic behavior of magnetite and rocks stressed to failure-relation to earthquake prediction. *Earth Planet.Sci.Lett.,* 37, pp.296-306.

Rokityansky, I.I. & Ingerov, A.I. (1999). Conductive structure of Ukrainian Carpathians from EM observations. *Phys. Chem. Earth (A),* 24 (9), pp. 849-852

Sperner, B.; Lorenz, F.; Bonjer, K.; Hettel, S.; Muller, B. & Wenzel, F. (2001). Slab break-off-abrupt cut or gradual detachment? New insights from the Vrancea region (SE Carpathians, Romania). *Terra Nova,* 13, pp.172-179

Sperner, B., the Collaborative Research Centre [CRC], 461 Team (2005). Monitoring of slab detachment in the Carpathians, In:*Challenges for Earth Sciences in the 21st Century,* Wenzel, pp.187-202, Springer-Verlag, Heidelberg

Stanica, D.; Stanica, M.; Piccardi, L.; Tondi, E., & Cello, G. (2004). Evidence of geodynamic torsion in the Vrancea zone (Eastern Carpahians). *Rev. Roum. GEPHYSIQUE,* Vol. 48, pp.15-19

Stanica, D., & Stanica, M. (2007). Electromagnetic monitoring in geodynamic active areas. *Acta Geodinamica et Geomaterialia,* Vol.4, No.1(145), pp. 99-107

Stanica, D., & Stanica, D.A. (2010). Constraints on Correlation Between the Anomalous Behaviour of Electromagnetic Normalized Functions (ENF) and the Intermediate Depth Seismic Events Occurred in Vrancea Zone (Romania). *Terr. Atmos.Ocean.Sci.,*Vol.21, pp.675-683

Stanica, M.; Stanica, D., & Marin-Furnica, C. (1999). The placement of the Trans-European Suture Zone on the Romanian Territory. *Earth Planets Space,* 51, 1073-1078

Tramutoli, V.; Cuomo, V; Fillizzola, C., & Pietrapertosa, C. (2005). Assessing the potential of thermal infrared satellite surveys for monitoring seismically active areas. The case of Kocaely (Izmit) earthquake, August 17-th, 1999. *Remote Sensing of Environment,* 96, pp.409-426

Trifu, C. I., & Radulian, M. (1989). Asperity distribution and percolation as fundamentals of earthquakes cycles. *Phys. Earth Planet. Inter.,* 58, pp.277-288

Tronin, A.A.; Biaggi, P.F., & Molchanov, O.A. (2004). Temperature variations related to earthquakes from simultaneous observations at the ground stations and by satellites in Kamchatka area. *Physics and Chemistry of the Earth,* Vol. 209, pp. 501-506

Wannamaker, P.E.; Stodt, J.A., & Rijo, L. (1986). A stable finite element solution for two-dimensional magnetotelluric modeling. *Geophys. J. R. Astr. Soc.,* 88, pp. 277-296

Varotsos, P. (2005). *The Physics of Seismic Electric Signals* (2005), TERRAPUB, ISBN 4-88704-136-5,Tokyo

Wiese, H. (1962). Geomagnetische tiefensondierung. Teil II: Die Streichrichtung der Undergrundstrukturen des elektrischen Widerstandes, erschlossen aus geomagnetischen variationen. *Geofis. Pura et Appl.,* 52, pp.83-103

Word, R. D.; Smith, H. W., & Bostick Jr., F. X. (1970). *An investigation of the magnetotelluric tensor impedance method,* Electronics Research Center, The University of Texas at Austin, Austin, Texas 78712

Wortel, M.J.R., & Spakman, W. (2000). Subduction and slab detachment in Mediterranean-Carpathian region. *Science,* 290, pp. 1910-1917

5

Earthquake Prediction: Analogy with Forecasting Models for Cyber Attacks in Internet and Computer Systems

Elvis Pontes, Anderson A. A. Silva, Adilson E. Guelfi and Sérgio T. Kofuji
Laboratory of Integrated Systems, Polytechnic School of the University of São Paulo
Brazil

1. Introduction

Currently, security of the cyber space (computer networks and the Internet) is mostly based on detection and/or blocking of attacks by the use of Intrusion Detection and Prevention System (IDPS), according to (National Institute of Standards and Technology [NIST SP800-94], 2010). However IDPS lacks in security as it is based on *postmortem* approaches - threats and attacks are identified and/or blocked only after they can inflict serious damage to the computer systems either while attacks are happening, or when attacks have already imposed losses to the systems (Haslum et al, 2008).
On the subject of earthquakes, one can notice the same kind of limitation: once an earthquake has already begun, devices can provide warnings with just few seconds before major shaking arrives at a given location (Bleier & Freund, 2005), (Su & Zhu, 2009). In the cyber space context, intending to cover the deficiency of late warnings, predicting techniques have already been approached in a small number of studies for cyber attacks in the last few years (Pontes & Zucchi, 2010), (Haslum et al, 2008), (Lai-Chenq, 2007), (Yin et al 2004).

1.1 Motivation

Although studies based on 1) historical earthquake records and 2) monitoring the earth's surface had contributed to map affected regions, short-term earthquake predictions are not efficient yet (Bleier & Freund, 2005).
Some researchers are studying and correlating signals gathered in the ionosphere that can precede earthquakes, like odd radio noise and lights in the sky.
According to (Bleier & Freund, 2005) "both the lights and the radio waves appear to be electromagnetic disturbances that happen when crystalline rocks are deformed--or even broken--by the slow grinding of the earth that occurs just before the dramatic slip that is an earthquake".
Some occurrences of earthquakes show signals and disturbances like following reported ones:

- Loma Prieta, San Francisco,1989: two weeks before a 7.1-magnitude earthquake, strong signals (20 times that of normal background noise at the 0.01 Hz frequency) of magnetic

disturbance were detected. Three times before the quake the signals jumped to 60 times normal size at the 0.01 Hz frequency;
- Spitak, Armenia, 1988: signals occurred shortly before a 6.9-magnitude quake;
- Guam, Pacific Ocean, 1993: signals were observed before a 8.0-magnitude quake;
- Parkfield, California, 2003: nine hours before a 6.0-magnitude quake, spikes of activity, four to five times normal size (0.2 to 0.9 Hz frequency) were detected;
- Taiwan, 1999: sensors registered unusually large disturbance in a normally quiet signal before the 7.7-magnitude earthquake. Researchers calculated the current required to generate those magnetic-field disturbance: between 1 million and 100 million amperes.

Those examples show that the occurrence of electromagnetic signals does not justify a public warning, but it is an important source of data for forecasters and are also useful for directing the course of research on earthquake prediction such as changes in the conductivity of the air over the quake zone caused by current welling up from the ground, that contribute to the formation of the so-called earthquake lights in the Mojave Desert (Fig. 1).

Fig. 1. Earthquake lights (Bleier & Freund, 2005)

There are some theories about these signals generation, but details are not conclusive yet. Notwithstanding, electromagnetic effects of the signals can be detected in a number of ways (see Fig. 2 next page).

Ground-based sensors, monitor changes in the low-frequency magnetic field and measure changes in the conductivity level of the air. Satellites monitor noise level at extremely low frequency and monitor the infrared light which is probably emitted when rocks are deformed or even broken. Some example:
- after the 1989 Armenia earthquake, electromagnetic Extremely Lower Frequency (ELF) disturbances were observed by a Soviet Cosmos satellite by a month;
- an U.S. satellite detected ELF bursts before and after a 6.5-magnitude earthquake in 2003 at California;
- In 2004 France has launched a satellite for Detection of Electro-Magnetic Emissions Transmitted from Earthquake Regions (DEMETER) that unfortunately presented malfunctioning.

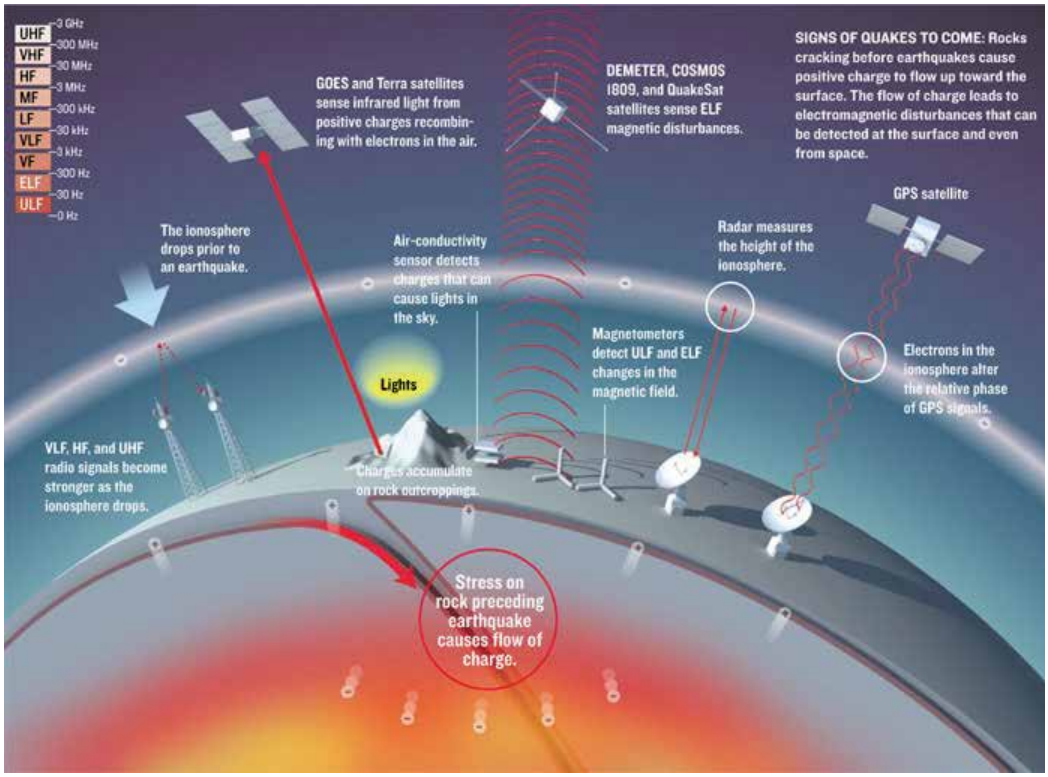

Fig. 2. Electromagnetic signals detection (Bleier & Freund, 2005)

According to (Bleier & Freund, 2005), "infrared radiation detected by satellites may also prove to be a warning sign of earthquakes to come". In China satellite-based instruments had registered the occurrence of several infrared signature instances with a jump of 4 to 5 oC before some earthquakes during the past two decades Sensors in NASA's Terra Earth Observing System satellite registered what NASA called a thermal anomaly on 21 January 2001 in Gujarat, India, just five days before a 7.7-magnitude quake there; the anomaly was gone a few days after the quake (Fig. 3). Accordingly with (Bleier & Freund, 2005), in both cases researches believe these sensosrs have detected an infrared luminescence generated by the recombination of electrons and holes, not a real temperature increase.

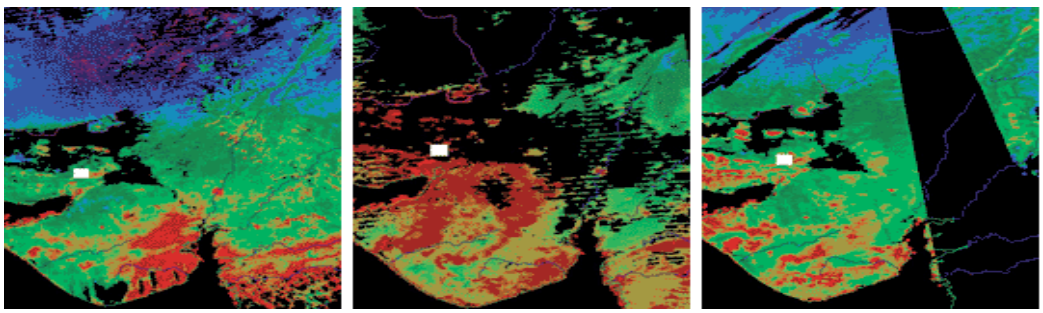

Fig. 3. Infrared radiation detected by satellites n (Bleier & Freund, 2005)

The connection between large earthquakes and electromagnetic phenomena in the ground and in the ionosphere is becoming increasingly solid. Researchers in many countries, including China, France, Greece, Italy, Japan, Taiwan, and the United States, are now contributing to the data by monitoring known earthquake zones.
Some correlations between historical data can be traced as well: monitoring 144 earthquakes (1997-1999), Taiwanese researches noticed significant changes in the electron content of the ionosphere some days before the quakes higher than 6-magnitude.
Therefore, the integration of: (1) several types of sensors (ground and space-based), (2) a network to bring together those signals, (3) a good distribution of the sensors (several sensors in a large area), (4) several types of detection (Ultral Low Frequency (ULF), ELF and magnetic-field changes, ionospheric changes, infrared luminescence, and air-conductivity changes--along with traditional mechanical and GPS monitoring of movements of the earth's crust and (5) the correlation of all data gathered, could make forecast more reliable.

1.2 Analogy with forecasting in cyber security

Cyber attacks can be classified as a set of actions with the purpose of compromising the integrity, confidentiality or availability of computer systems. Cyber attacks can be caused by users or malicious software, which try either to obtain access, to use systems in an unauthorized way, or to enumerate privileges (NIST SP800-94, 2010).
(Internet Crime Complaint Center [IC3], 2010) published a study in the United States about losses in 2009 concerning cyber-attacks: frauds in cyber space caused about $559.7 million of losses in 336,655 organizations. This was a 111,5% increase for the losses and a 22.3% increase for the complaints, as compared to 2008 when 275,284 complaints were received, reporting $264.6 million in total losses. According to (McPherson & Labovitz, 2010), in 2009 the largest reported volumetric Distributed Denial of Service (DDoS) attack exceeded 49 Gbps sustained towards a single target in Europe.
Beyond sheer attack size, (McPherson & Labovitz, 2010) indicated that cyber-attacks become more sophisticated, with attackers expressly aiming to exhaust resources other than bandwidth, such as firewalls, load-balancers, back-end database infrastructure and associated transaction capacity, cached data serving algorithms, etc. This increasing sophistication is a trend that has been captured in previous editions of the survey of (McPherson & Labovitz, 2010) as well. Regarding DDoS attacks, it is expected these attacks to become more common against independent media and human rights sites in 2011, as the recent highly publicized DDoS attacks on Wikileaks, and "Operation Payback" attacks by "Anonymous" on sites perceived to oppose Wikileaks (Zuckerman et al, 2010).
According to (Pontes et al, 2008), (Pontes & Guelfi, 2009a), (Pontes & Guelfi, 2009b), (Pontes & Zucchi, 2010), an early warning system showing a future trend outlook with an increasing number of cyber-attacks, exposed by forecasting analysis, may influence decisions on the security devices adoption (e.g. rules in IDPS combined with rules in firewalls) before incidents happen, according to the needs. Although, three major gaps lie in the studies about forecasting of cyber attacks: a) the use of few sensors and/or sensors employed locally; b) the use of just one forecasting technique; and c) lack of information sharing among sensors to be used for correlation (Pontes & Guelfi, 2009a). Correlation of information between IDPS and forecasters means looking for similar characteristics that may be related (Pontes & Guelfi, 2009a) (Abad et al, 2003). Throughout correlation it is possible to eliminate redundant and false data, to discover attack patterns and understand attack strategies (Zhay et al, 2006).

Nevertheless, forecasts and alert correlation may be challenging as they depend on the reliability of the source of the security alerts (Silva & Guelfi, 2010). Therefore, the precision level of the detection tools is an important issue for validating correlations. Multi-correlation or integration of alerts with information from different sources, e.g. tools for monitoring or operating system logs, can allow a new classification for alerts, improving accuracy of the results (Abad et al, 2003), (Zhay et al, 2006). References (Abad et al, 2003), (Zhay et al, 2006), (Zhay et al, 2004) employed multi-correlation; however neither a detailed analysis concerning influence of isolated alerts in the FP rates, nor forecasting techniques were not applied for predicting future attacks (forecasting).

Forecasting analysis in the information security area can be similar to forecasting methodologies used in any other fields: meteorology, for instance, use sensors to capture data about temperature, humidity, etc (Lajara et al, 2007), (Lorenz, 2005); seismology employs sensors to capture electromagnetic emissions from the rocks (Bleier & Freund, 2005); for economics, specifically stock market, data is collected from diverse companies (annual profit, potential customers, assets, etc) to draw trends about shares of companies (Prechter & Frost, 2002), (Mandelbrot & Hudson, 2006). For any field formal models can be applied to predict events over the collected data. But, before applying formal models, data regarding different kind of variables should be correlated (Armstrong, 2002). According to (Armstrong, 2002), to obtain a more accurate and realistic result about predictions it is suggested: (1) to use diverse forecasting techniques; (2) to analyze information regarding diverse variables and acquired data, from sensors for instance; (3) to employ diverse kind of employed forecasting models.

Concerning cyber attacks, (Lai-Chenq, 2007), (Yin et al 2004) employed forecasting models, however they used just one formal method for predicting events and they did not make use of any kind of correlation process. In this chapter, security events for cyber security are actions, processes that have an effect on the system, disregarding the kind of the effect – in other words, actions that could result in positive or negative effects on the system. In other hand, security alerts are types of security events, indicating anomalous activities or cyber attacks (Silva & Guelfi, 2010). In our earlier works we proposed the Distributed Intrusion Forecasting System (DIFS) (Pontes & Guelfi, 2009), (Pontes & Zucchi, 2010), which covered the following gaps of today's forecasting techniques in IDPS: a) the use of few sensors and/or sensors employed locally for capturing data; b) the use of just one forecasting technique; and c) lack of information sharing among sensors to be used for correlation. Notwithstanding, we faced huge amount of alerts which could have negative influence over forecasting results.

1.3 Proposal

The goal of this chapter is to propose a Distributed Intrusion Forecasting System (DIFS) with a two stage system which allows: (1) in the first stage it is possible to make a correlation of security alerts using an Event Analysis System (EAS); and (2) to apply forecasting techniques on the data (historical series) generated by the previous stage (EAS). The DIFS works with prediction models and sensors acting in different network levels (host, border and backbone), which enables the use of different forecasting techniques (e.g. Fibonacci sequence and moving averages), the cooperation among points of analysis and the correlation of predictions. Additionally to the main goal, the aim of this chapter is proposing an analogous approach for earthquake prediction. As results it is intended to increase reliability of incidents predictions (e.g. earthquake incidents, cyber attacks), to prevent

incidents in a proactive manner and to improve risk management employed for security of the homeland cyber space. A proof of concept of such architecture (DIFS) is presented, which allows concluding about the improvement of forecasts in the cyber space; furthermore, tests applied over two datasets - (Defense Advanced Research Projects Agency [DARPA], 1998) and (Knowledge Discovery and Data Mining Tools Competition [KDD], 1999) - with an IDPS have shown that the employed techniques define incidents trends.
This chapter is organized as follows: state of art concerning forecasting and event correlation in IDPS are in section 2. Section 3 introduces the proposal of this chapter: the DIFS and the two stage system for correlation regarding cyber attacks. Section 4 presents details about the tests and environment to validate the proposal. Results are analyzed in section 5 and section 6 summarizes conclusions and suggestions for new studies.

2. State of art – Cyber attacks, event correlation and forecasting

In this section we approach event correlation for detecting cyber-attacks, the forecasting methods used to predict cyber-attacks and Distributed Architecture for Intrusion Forecasting System (DIFS (Pontes & Guelfi, 2009), (Pontes & Zucchi, 2010).

2.1 Unwanted internet traffic and cyber attacks

The expression "unwanted traffic" was first introduced in the eighties and it has always been related to malicious activity as worms, virus, intrusions etc (Feitosa et al, 2008). Reference (Feitosa et al, 2008) defines unwanted Internet traffic (UIT) as unproductive and useless traffic, with malicious (worms, scans, spam) and benign (wrong setting in the routers) events. Reference (Soto, 2005) completes this definition: UIT may result from the noise in the telecommunication network. (Andersson et al, 2007) classified UIT as the malicious or useless one, with the objective to compromise vulnerable hosts, to spread malicious code, spam, DoS and DDoS. UIT may also be junk traffic, background traffic and anomalous traffic.
Symposiums and workshops have been done about the issue of UIT, like the one promoted by Internet Architecture Board (IAB), on March 2006 (Andersson et al, 2007) and April 2008: the intention was to share information among people from different fields and organizations, fostering an interchange of experiences, views, and ideas between the various research communities. As a result, the Request for Comments (RFC) 4948 details the UIT types, the main causes, existent solutions and the actions to be taken in short and long term. It was decided, in this workshop, that some other research topics about UIT would be managed by the IAB, Internet Engineering Task Force (IETF) and Internet Research Task Force (IRTF).
According to (Feitosa et al, 2008), several of the losses caused by UIT are due to the inefficiency of today's techniques and security devices (anti-spam, antivirus, Intrusion Detection and Prevention Systems (IDPS) (NIST, 2010), firewalls), whether for detecting and preventing the intrusion, or to treat the UIT. Furthermore, the high rates of false positives, false negatives and the lack of a forecasting approach for the Internet traffic are some of the reasons of the UIT increasing. Internet attacks continue apace, with UIT, such as phishing, spam, and distributed denial of service attacks increasing steadily. However, it is important to classify whether it is unwanted or not: Voip (Skype), peer-to-peer (P2P), instant messengers (MSN, Google talk, ICQ), online social networks. Different classification may be employed from one company to another, from user to user, from country to country. China,

for instance, does not allow calls from Skype to telephones. Another example: routers for backbone providers and for small companies - the UIT is differently classified in both cases (Feitosa et al, 2008).

2.2 Approaches for correlation of security events

Correlation techniques for security events can be classified into three categories: (1) rule-based, (2) based on anomaly and (3) based on causes and consequences (Prerequisites and Consequences (PC)) (Abad et al, 2003). The rule-based method requires some prior knowledge about the attack, so the target machine has to pass through a preparation phase called training. The goal of this phase is to make the target machine able to precisely detect the vulnerabilities in which the target machine was trained for (Abad et al, 2003), (Mizoguchi, 2000). Gaps of rule-based method are: (1) it is computer intensive; (2) it results in lots of data; (3) the method works only for known vulnerabilities.

The method based on anomaly analyzes network data flow, using correlation with statistical methods, using accumulation of gathered information and using observations of the occurred deviations throughout processes of network data flow; in a manner to allow detecting new attacks. For instance, (Manikopoulos & Papavassiliou, 2002) demonstrates a system for detecting anomalies which is characterized by monitoring several parameters simultaneously. Reference (Valdes & Skinner, 2001) presents a probabilistic correlation proposed for IDPS, based on data fusion and multi-sensors. However, the method which uses anomaly cannot detect anomalous activity hidden in a normal process, if it is performed at very low levels. Besides, as this method analyzes normal processes reporting only wrong deviations, hence the method is not suitable for finding causes of attacks (Ning et al, 2001).

The PC method lies on connections between causes (conditions for an attack to be true) and consequences (results of the exploitation of a cause), in order to correlate alerts based on the gathered information. This method is suitable for discovering strategies of attacks. Both causes and consequences are composed of information concerning attributes of alerts (specific features belonging to each alert) and are correlated. Arrangement of attributes is called tuple. According to Fig. 4, for the connections to be valid, a preparatory alert must have in its consequences at least one tuple, which repeats in the causes of the resulting alert. In other words, the preparatory alert contributes to the construction of the resulting alert, and therefore it can be correlated. For this connection, illustrated by Fig. 4, the timestamp of the preparatory alert has to come before the resulting alert (Silva & Guelfi, 2010), (Pontes & Guelfi, 2010), (Ning et al, 2001).

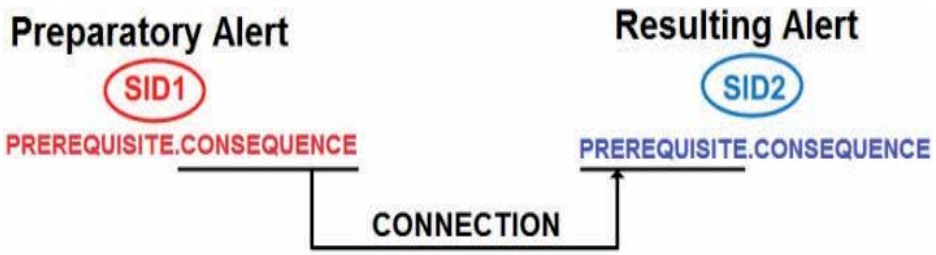

Fig. 4. Connections Between Alerts - Consequence of Preparatory Alert (SID1) is Connected to Prerequisites of Resulting Alert (SID2).

In order to reduce complexity, correlation can be shown in graphs where alerts are represented by nodes and connections are depicted by arrows (representing correlations between alerts).

Yet, some gaps in the PC method may be mentioned, such as the difficulty in obtaining causes and consequences of alerts (Pietraszek & Tanner, 2005), the impossibility to analyze isolated alerts (alerts that are not correlated) and the fact that missed attacks are hard to correlate. An alternative to minimize the problem is to apply complementary correlation techniques (Morin & Debar, 2003), using sensors to work in cooperation, in order to supervise the environment for minimizing missed detections. There are two techniques to map IDPS' alerts and logs obtained from other sources: descending analysis and ascending analysis (Abad et al, 2003), (Silva, 2010).

Descending analysis is based on the investigation of occurred attacks, verifying (correlating) whether other logs (e.g. logs from O.S.) have or do not have vestiges of the attacks' incident. For occurred attack, other traced logs (e.g. Operational System's logs) can be analyzed based on timestamp. This type of analysis is useful to trace evidences about strategies of events, in order to map attacks to its source.

The ascending technique is used to discover attacks by the analysis of several logs. Once an anomaly is detected in one of these logs, other logs are checked based on timestamp. Although ascending technique is computer intensive, this technique allows detecting new attacks.

In an earlier work we proposed the EAS (Silva & Guelfi, 2010), (Silva, 2010), intending to improve results of security events correlation and intrusion detection. EAS is able to make multi-correlation for events from Operational Systems (OSs) and from IDPS (log analysis), consequently, EAS is also capable for verifying the influence of isolated alerts in the cyber-security context.

The EAS architecture has 4 modules, as shown by Fig.5: (a) converter: the aim of this module is to handle the input data into the system (IDPS signatures, alerts and logs from the OS); (b) updating: it controls data which is going to be used by the system; (c) correlating: it does mappings for the correlation processes, FP identification, and the identification of isolated alerts; (d) calculator: it analyzes and compares FP, based on the results from the correlating module.

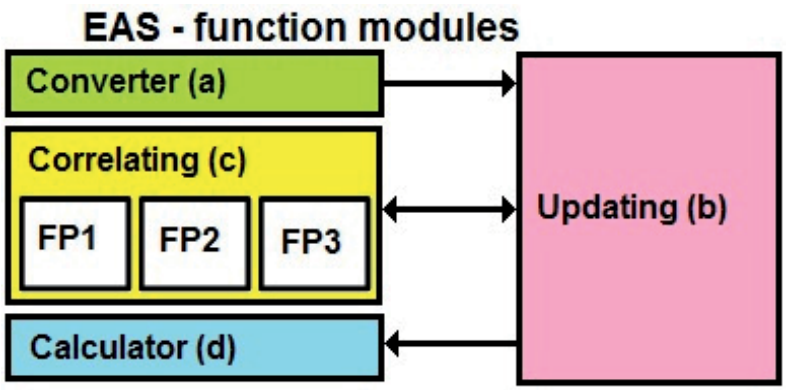

Fig. 5. EAS's Architecture (Silva, 2010), (Silva & Guelfi, 2010)

According to (Silva, 2010), (Silva & Guelfi, 2010), with the employment of the EAS it was possible to improve the today's results of correlation regarding security events, considering the following issues: (1) traceability for causes and consequences within the PC-correlation method (with multi-correlation criteria, correlation analysis (ascending/descending) and identification of FP alerts through tables and graphs); and (2) the process of results validation regarding the correlation. In (Silva, 2010), (Silva & Guelfi, 2010), results of correlating phase were evaluated in three steps (FP1, FP2 and FP3) using tables and graphs. The stepwise analysis allowed comparison of the results. EAS achieved an increase of 112.09% in the identification of FP alerts after the multi-correlation. Another important result of EAS was the evidence of preparatory connections between individual alerts that are in fact part of larger and more elaborated attacks. In other words, EAS can show that individual alerts can be grouped in a single attack, since they are part of the same attack strategy (Silva, 2010), (Silva & Guelfi, 2010).

2.3 Related forecasting methodologies for earthquakes

Statistical based forecast methodologies are used to understand and predict earthquake signals (Kagan, & Jackson, 2000). It is important to discuss these other researches to notice the variety of forecasting applications. Two forecast researches are summarized below.

2.3.1 Earthquake forecasting and its verification

Holliday et. al (2005) has based their forecast research on the association of occurrence of small earthquakes with probably future large ones. In fact, the method does not predict earthquakes, but spots regions (Hotspots regions) where they are most likely to occur in the future (about ten years).

Basically the research objective is to reduce risk areas analyzing the historical seismicity for anomalous behaviour.

The approach is based on a pattern informatics (PI) method which quantifies temporal variations in seismicity and is as follows Holliday et al, (2005):

1. The region of interest is divided into N_B square boxes with linear dimension Δx. Boxes are identified by a subscript i and are centered at x_i. For each box, there is a time series $N_i(t)$, which is the number of earthquakes per unit time at time t larger than the lower cut-off magnitude Mc. The time series in box i is defined between a base time t_b and the present time t.
2. All earthquakes in the region of interest with magnitudes greater than a lower cutoff magnitude M_c are included. The lower cutoff magnitude M_c is specified in order to ensure completeness of the data through time, from an initial time t_0 to a final time t_2.
3. Three time intervals are considered:

a. A reference time interval from t_b to t_1.
b. A second time interval from t_b to t_2, $t_2 > t_1$. The change interval over which seismic activity changes are determined is then $t_2 - t_1$. The time t_b is chosen to lie between t0 and t1. Typically we take t_0 = 1932, t_1 = 1990, and t_2 = 2000. The objective is to quantify anomalous seismic activity in the change interval t_2 to t_1 relative to the reference interval t_b to t_1.
c. The forecast time interval t_2 to t_3, for which the forecast is valid. The change and forecast intervals are taken and forecast intervals to have the same length. For the above example, t_3 = 2010.

4. The seismic intensity in box i, $I_i(t_b, t)$, between two times $t_b < t$, can then be defined as the average number of earthquakes with magnitudes greater than M_c that occur in the box per unit time during the specified time interval t_b *to* t. Therefore, using discrete notation, we can write:

$$I_i(t_b, t) = \frac{1}{t - t_b} \sum_{t'=t_b}^{t} N_i(t'), \tag{1}$$

Where the sum is performed over increments of the time series, say days.

5. In order to compare the intensities from different time intervals, it is required that they have the same statistical properties. Therfore, the seismic intensities are normalized by subtracting the mean seismic activity of all boxes and dividing by the standard deviation of the seismic activity in all boxes. The statistically normalized seismic intensity of box i during the time interval t_b to t is then defined by

$$\hat{I}_i(t_b, t) = \frac{I_i(t_b, t) - < I_i(t_b, t) >}{\sigma(t_b, t)}, \tag{2}$$

Where $< I_i(t_b, t) >$ is the mean intensity averaged over all the boxes and $\sigma(t_b, t)$ is the standard deviation of intensity over all the boxes.

6. The measure of anomalous seismicity in box i is the difference between the two normalized seismic intensities:

$$\Delta I_i(t_b, t_1, t_2) = \hat{I}_i(t_b, t_2) - \hat{I}_i(t_b, t_1). \tag{3}$$

7. To reduce the relative importance of random fluctuations (noise) in seismic activity, the average change in intensity is computed, $\underline{\Delta I_i(t_0, t_1, t_2)}$ over all possible pairs of normalized intensity maps having the same change interval:

$$\underline{\Delta I_i(t_0, t_1, t_2)} = \frac{1}{t_1 - t_0} \sum_{t_b=t_0}^{t_1} \Delta I_i(t_b, t_1, t_2), \tag{4}$$

Where the sum is performed over increments of the time series, which here are days.

8. The probability is defined as a future earthquake in box i, $P_i(t_0, t_1, t_2,)$, as the square of the average intensity change:

$$P_i(t_0, t_1, t_2,) = \underline{\Delta I_i(t_b, t_1, t_2)}^2. \tag{5}$$

9. To identify anomalous regions, it is desirable to compute the change in the probability $P_i(t_0, t_1, t_2,)$ relative to the background so that we subtract the mean probability over all boxes. This change in the probability is denoted by

$$\Delta P_i(t_0, t_1, t_2) = P_i(t_0, t_1, t_2) - < P_i(t_0, t_1, t_2) >, \tag{6}$$

Where $< P\ (t\ ,\ t\ ,\ t\ ) >$ is the background probability hotspots are defined to be the regions where $\Delta P_i(t_0, t_1, t_2)$ is positive. In these regions, $P_i(t_0, t_1, t_2)$ is larger than the average value for all boxes (the background level). Note that since the intensities are squared in defining probabilities the hotspots may be due to either increases of seismic activity during the

change time interval (activation) or due to decreases (quiescence). The following hypothesis is taken into account: earthquakes with magnitudes larger than $M_c + 2$ will occur preferentially in hotspots during the forecast time interval t_2 *to* t_3.
To evaluate the model a Relative Operating Characteristic (ROC) diagram, which can be viewed as binary forecast either to occur or not to occur, was used and presented significant results with a relative high proportion of hotspots representing locations of probably future large earthquakes.
Although good results, the model Holliday, J.R., et. al, (2005) could be used as an input in a larger forecast system like DIFSA which would provide the communication and correlation of data with others different models.

2.3.2 Probabilistic forecasting of earthquakes

(Kagan, & Jackson, 2000) has developed a research with both short and long-term forecast approach and testing both with a likelihood function to 5.8-magnitude (or larger) quakes. Although the long-term approach (see Table 1), is not completely developed and is suitable to estimation of occurrence of earthquakes, it is derived from statistical, physical and intuitive arguments while the short-term forecast seismicity model is based on a specific stochastic model and updated daily (see Table 1).
The research assumes that the rate density (probability per unit area and time) is proportional to a smoothed version of past seismicity and depends approximately on a negative power of the epicentral distance and linearly on magnitude of the past earthquakes.
The model (Kagan, & Jackson, 2000) does not use retrospective evaluation of seismic data. The parameters of long-term are evaluated on the basis of success in the forecasting of seismic activity also indicating possible earthquakes perturbations. A maximum likelihood procedure to infer optimal values are applied on short-term approach which can be incorporated into real-time seismic networks to provide seismic hazard estimate.
About the scientific results (Kagan, & Jackson, 2000) concluded that the research depicted a statistical relationship between successive earthquakes in a quantitative way that facilitate hypothesis testing. About the practical results the quantitative predictive assessment can be adopted into mitigation strategies.

Latitude	Longitude	Long-term forecast						Short-term forecast	
		Probability $m \geq 5.8$ eq/day*km^2	Focal mechanism *T*-axis Pl	*T*-axis Az	*P*-axis Pl	*P*-axis Az	Rotation angle degree	Probability $m \geq 5.8$ eq/day*km^2 time-dependent	Probability ratio time-dependent/ independent
119.5	19.5	3.18E-09	31	208	10	304	64.8	1.79E-14	5.62E-06
120.0	19.5	5.23E-09	17	213	32	314	68.8	1.41E-10	2.71E-02
120.5	19.5	4.28E-08	7	93	75	335	21.4	2.12E-07	5.0
121.0	19.5	3.02E-08	69	135	21	302	28.2	2.84E-07	9.4
121.5	19.5	1.82E-08	77	106	13	296	40.9	6.14E-08	3.4
122.0	19.5	7.81E-09	60	32	3	297	48.4	1.13E-10	1.45E-02
122.5	19.5	4.15E-09	81	228	4	113	51.8	1.00E-12	2.41E-04
123.0	19.5	3.01E-09	78	251	9	110	50.3	7.70E-16	2.56E-07
123.5	19.5	2.43E-09	76	273	13	107	49.5	1.08E-20	4.43E-12

Table 1. Example of long- and short-term forecast, 1999 February 11, north of Philippines.(Kagan, & Jackson, 2000)

The versatility of the methodology based on forecasts is evident in this work, presenting significant results. This scenario shows that quite different methods (e.g, that use and do not use historical data) can be used in conjunction with an approach that uses DIFSA.

2.4 Forecasting for cyber attacks

The forecasting approaches in IDPS lie mainly on stochastic methods (Ramasubramanian & Kannan, 2004), (Alampalayam & Kumar, 2004), (Chung et al, 2006). With no attention about predictions, references (Ye et al, 2001), (Ye et al, 2003), (Wong et al, 2006) applied diverse probabilistic techniques (decision tree, Hotelling's T^2 test, chi-square multivariate, Markov chain and Exponential Weighted Moving Average (EWMA)) on audit data as a way to analyze three properties of the UIT: frequency, duration, and ordering. Reference (Ye et al, 2001), (Ye et al, 2003) has come to the following findings: 1) The sequence of events is necessary for IDPS, as a single audit event at a given time is not sufficient; 2) Ordering (transaction (Wong et al, 2006)) provides additional advantage to the frequency property, but it is computationally intensive. According to (Ye et al, 2001), (Ye et al, 2003), (Wong et al, 2006), the frequency property by itself provides good intrusion detection. References (Ye et al, 2001), (Ye et al, 2003), (Wong et al, 2006) did not approach correlation for IDPS.

Moving averages (simple, weighted, EWMA, or central) with time series data are regularly used to smooth out fluctuations and highlight trends (NIST, 2009). EWMA may be applied for auto correlated and uncorrelated data for detecting cyber-attacks which manifest themselves through significant changes in the intensity of events occurring (Ye et al, 2001). Both (EWMA for auto correlated and uncorrelated) has presented good efficiency for detecting attacks. EWMA applies weighting factors which decrease, giving much more importance to recent observations while still not discarding older observations entirely. The statistic that is calculated is (NIST, 2009):

$$EWMA_t = \alpha Y_t + (1 - \alpha) EWMA_{t-1} \quad \text{for t=1, 2, …, n.} \tag{7}$$

Where: EWMA is the mean of historical data; Yt is the observation at time t; n is the number of observations to be monitored including EWMA; $0 < \alpha < 1$ is a constant that determines the depth of memory of the EWMA.

The parameter α determines the rate of weight of older data into the calculation of the EWMA statistic. So, a large value of α gives more weight to recent data and less weight to older data; a small value of α gives more weight to older data.

Reference (Cisar and Cisar, 2007) gives an overview of adopting EWMA with adaptive thresholds, based on normal profile of network traffic. The analysis of thresholds with EWMA may summarize huge amount of data in network traffic (Zhay et al, 2006), (Pontes & Zucchi, 2010). Diverse moving averages, combined with Fibonacci sequence forecasting approach, were also used by (Zuckerman et al, 2010) to spot trends of cyber attacks in the (DARPA, 1998) datasets.

A simple moving average (SMA) is the non weighted mean of the previous n data. For example, a 10-hours SMA of intrusive event X (DoS, e.g.) is the mean of the previous 10 hours' event X. If those events are: $e_M, e_{M-1}, \ldots, e_{M-9}$. Then the formula is (NIST, 2009), (Roberts, 1959):

$$SMA = \frac{e_M + e_{M-1} + \cdots + e_{M-9}}{10} \tag{8}$$

When calculating successive values, a new value comes into the sum and an old value drops out, meaning a full summation each time is unnecessary,

$$SMA_{current\ hour} = SMA_{last\ hour} - \frac{e_M - n}{n} + \frac{e_M}{n} \quad (9)$$

Nevertheless, the forecasting approaches which use moving averages to cope with cyber attacks in IDPS are limited to analyze cyber attacks individually, e.g. in just one IDPS. Therefore, there is no collaboration among the forecasters. Besides: the concept of sensors is not adopted in (Pontes et al, 2008), (Pontes & Guelfi, 2009a), (Pontes & Guelfi, 2009b), (Pontes & Zucchi, 2010), (Ishida et al, 2005), (Viinikka et al, 2006), (Ye et al, 2003).

3. The distributed intrusion forecasting system with the two stage system (Pontes et al, 2011)

Intrusion Forecasting Systems (IFS) can work proactively in cyber security contexts, as early warning systems, in order to indicate or identify UIT (incidents, threats, attacks) in advance. IFS can also represent an improvement of IDPS, which is based on postmortem approaches (UIT is identified and/or blocked only after they can inflict serious damage to the computer systems). IFS predicts UIT by the use of different forecasting techniques (for instance, moving average, Fibonacci sequence etc) applied either for local or distributed environment. Additionally, for distributed environments, e.g. DIFS, the use of cooperative sensors can improve accuracy about predictions of incidents.

Fig. 6 depicts the proposal of this chapter, i.e. the DIFS and the forecasting levels. Similarly to forecasting methodologies used in other fields (e.g. Meteorology), DIFS also spreads agents and/or sensors widely to make predictions about the different kinds of UIT (spam, virus, intrusion, abnormal network traffic). There are four levels of the IFS: level 1 - independent security devices of hosts; level 2 - integrated security devices of hosts; level 3 - the network level; and level 4 - the backbone level. All levels have some communication degree among each other. In other words, the forecasts obtained from level 1 are shared and correlated to the forecasts of the other levels. Lower levels work as sensors to higher levels; consequently feedback about the UIT trends may be exchanged from one level to another.

Level 1 concerns the trend analysis about incidents, alerts and diagnosis reported independently by the hosts' security devices (antivirus, antispyware, host-based IDPS and other anomaly detector systems). For each security device, individual forecasts may be provided, e.g. the trend about spam for next hour or the day of tomorrow, or the trend about virus infection etc. The next step of the IFS level 1 is to help the hosts' security devices to determine whether or not they should adopt countermeasures to stop UIT

Level 2 involves correlation of forecasts about the hosts' security devices. At this level, the analysis lays on two databases: a) All the historical data generated from each one of the hosts' security devices are processed individually by the IFS first level, then stored in a database; b) The network flow may also be recorded for further forecasting analysis. The next step for the IFS level 2 is to query and to analyze the trends (forecasts) of such databases. After analyzing it, IFS level 2 returns a feedback to IFS level 1. It is important to notice that the databases of IFS level 1 work as sensors for IFS level 2.

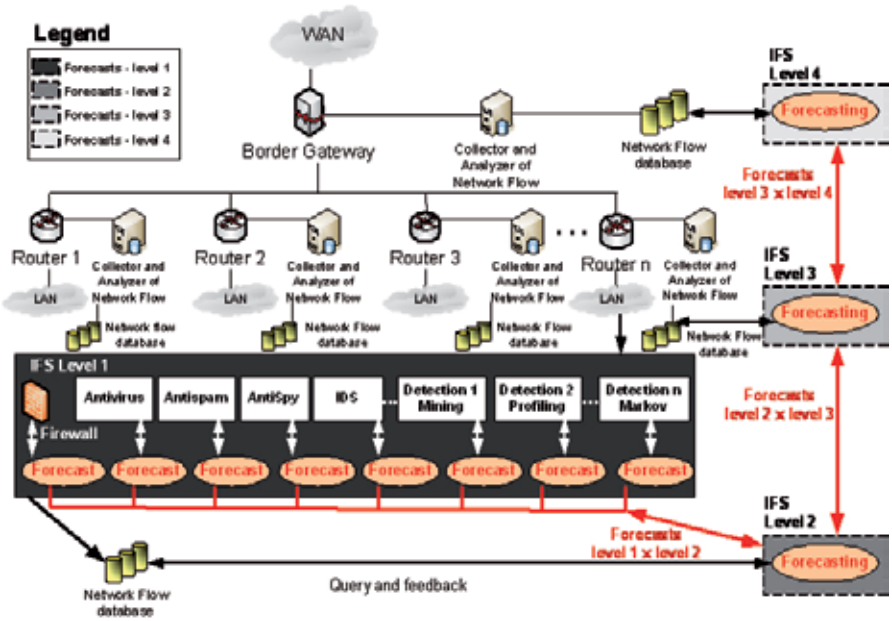

Fig. 6. DIFS Architecture - adapted from (Pontes & Guelfi, 2009)

The implementation of IFS level 3 happens at the gateway of the LAN. IFS level 3 is analogous to IFS level 2, as it queries databases generated by IFS levels 1 and 2. Likewise IFS level 1, some security devices may be installed at the gateway (as firewall, regular IDPS, etc) and they may also be analyzed. The steps for analysis at this level are: a) Network security devices record UIT in databases; IFS level 3 queries the databases provided by the lower levels and current level; b) IFS level 3 analyzes the provided databases to define trends; c) IFS level 3 provides feedback of the trend analysis to the security devices; d) IFS level 3 may also give feedback for the lower levels. It is important to notice that IFS level 1 and level 2 databases work as sensors for IFS level 3. The sensor elements may be more numerous at IFS level 3.

IFS level 4 is the major level. It considers the structure of the backbone providers (an ISP, for instance). In the same way IFS level 3 and level 2, different security devices are linked to the backbone level. The steps for IFS level 4 to work are: a) Backbone security devices record UIT in database; b) IFS level 4 queries the databases provided by the lower and current level; c) IFS level 4 analyzes the provided databases to define the trends; d) IFS level 4 provides feedback of the trend analysis to the current level; e) IFS level 4 may also give feedback for the lower levels. Similarly to lower levels, IFS level 4 uses the same concept of sensors: lower databases and the entire lower IFS levels are sensors for IFS level 4. An important note is: the IFS level 4 may be shared and correlated among various backbone providers. To correlate forecasts of IFS level 4 means to provide the most realistic and integrated trend about UIT, as it may spread sensors along the network (Lajara et al, 2007).

It is important to notice that for the IFS we implemented a two stage system (Pontes et al, 2011), intending to improve the forecasting results by the use of correlation. Fig. 7 presents the sequence of activities done by the system:

1. The first task is the multi-correlation, running the EAS, to filter FP and tracing sophisticated. During this step, OS's logs, IDPS's logs, network traffic and other logs are analyzed by the EAS. According to Fig. 4, diverse logs and network traffic represent the Entry 1 for the two stage system.

2. The second task is done by the IFS, applying forecasting techniques over the EAS' generated data (historical series, without a considerable amount of FP). Several forecasting techniques may be adopted in this stage (e.g. EWMA, Fibonacci sequence, Markov chains). As illustrated by Fig. 7, EAS' generated data is the Entry 2 for the two stage system. Sep 2 of the two stage system considers just data from Entry 2.

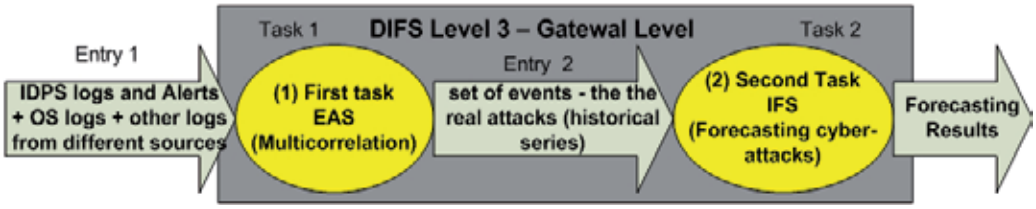

Fig. 7. Sequence of Steps: (1) EAS Filtering – (2) IFS (Pontes et al, 2011)

4. Proof of concept

In this section we are going to describe two of the prototypes we have prepared and analysed. In the first one (Pontes et al, 2009), for the proof of concept, levels 1, 2 and 3 of the DIFS were implemented in three sites geographically divided (A, A' and A''). The following hardware and services were used: a) 1 Pentium core 2 quad 2.0 GHz, 8GB RAM; b) 2 Pentium core 2 duo 1.8 GHz, 4GB RAM; c) 10 virtual machines (Ubuntu 8.04) 512MB RAM; d) 4 virtual machines (WindowsXP) 512MB RAM; e) Windows Vista (host for the virtual machines); VMware Player 2.51; Snort; Netfilter/Iptables; MySQL; OpenVPN.

Likewise (Haslum et al, 2008), in this prototype the simulation of UIT was divided in just in four types: 1) Denial of service (DoS): Ping of Death and SYN Flood are examples of this kind of UIT; 2) Remote to local (R2L): SQL injection is an example of this kind of UIT, where typical vulnerabilities that are exploited is buffer overflow and pure environment sanitation; 3) User to root (U2R): SQL injection is also example of this kind of UIT; 4) Probe (Scanning): Nmap, IPswep, Satan are examples of software for scanning. During eight weeks, we simulate usual network traffic and UIT among hosts in each site. Normal network traffic and UIT were also simulated among sites. H-IDPS (NIST SP800-94, 2007) was installed in each one of the hosts. N-IDPS (NIST SP800-94, 2007) was installed at the gateway. Fig. 8 illustrates the sites, hosts with normal activities and infected hosts. Infected hosts inflict UIT to the hosts of each site and to hosts from other sites, as pointed by arrows. In this prototype, the propagation of UIT was in the following sequence: from site A to site A', from site A and A' to site A", from site A, A' and A" to site A. For this prototype, IFS was developed in JAVA and it runs in the three levels of DIFS. The IDPS Snort was used to analyze the network traffic. All classified UIT is lately recorded in a MySQL database. IFS collects data from the database, analyzes them and next, when a particular threshold of UIT is exceeded, a warning is sent to the IFS collaborators.

For the second prototype (Pontes et al, 2009), the two stage system was implemented and employed in a wired LAN, specifically in a computer working as gateway for the Internet (level 3 of the DIFS). Elements of level 1 (logs from the OS) were used in the. Although level 3 of the DIFS was approached, level 1, 2 and 4 were disregarded in the second prototype. The reason for implementing only level 3 is the representativeness of the gateway level: (a) the simulated cyber-attacks and the real network traffic have just one path to reach the Internet: throughout

the gateway; (b) at the gateway level it was possible to assure timestamp conditions for correlation processes, as the IDPS is set at the same machine, the EAS and the gateway.

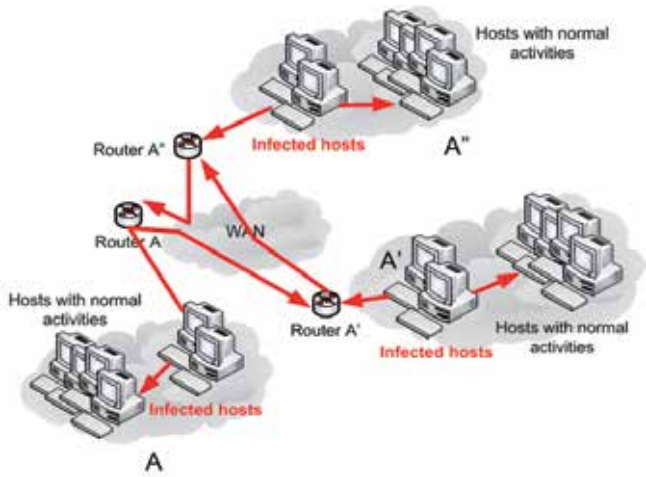

Fig. 8. DIFS Prototype – adapted from (Pontes & Guelfi, 2009)

Fig 9 illustrates the LAN for the tests, which is based on the diversity: diverse machines, settings, protocols and services are executed; further more there are several OS and free access to the Internet. Virtualized OSs (Linux Fedora), using VMWare, the host operational systems with Windows 7 and Windows XP are used in the prototype.

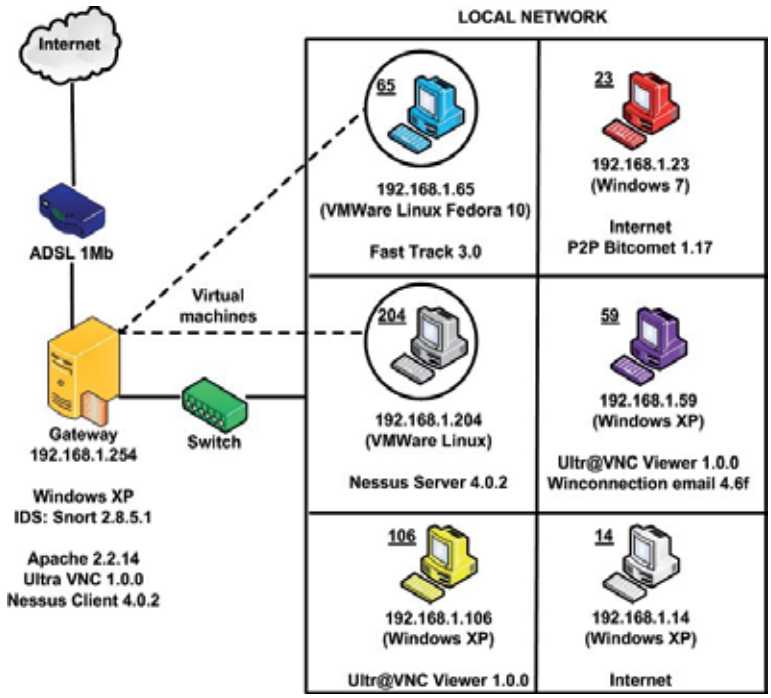

Fig. 9. Environment for Tests of the TSS – Computers, OSs and Services (Pontes et al, 2011)

The computer working as gateway (DIFS level 3) was able to register all alerts of the Network IDPS and logs from its own OS. Table 2 details services used in the two stage system, as the source machines for each service and the reached destiny for each service. In the environment for the tests, multi-correlation was done between alerts from an IDPS with the OS' logs.

Services	Source machine	Destiny
Internet browser	14 and 23	Internet
Remote access (VNC)	59 and 106	Gateway
Peer-to-peer (Bitcomet)	59	Internet
E-mail server (Winconnection)	59	Internet
Complete attack test (Fast-Track)	65	Gateway
Complete attack test (Nessus)	204	Gateway

Table 2. Services in the Prototype (Pontes et Al, 2011)

Table 3 presents applications which were used in the prototype. EAS was developed by the authors, in Visual FoxPro. Finally, Table 3 shows the elapsed time for the prototype. Both simulation of normal network traffic and simulation of cyber-attacks were referred in the prototype. Normal network traffic was brought up as well. Unlike (Pontes et al, 2008), (Pontes & Guelfi, 2009a), (Pontes & Guelfi, 2009b), (Pontes & Zucchi, 2010) Cyber-attacks concern the following types: (1) AWStats - allows remote attackers to execute arbitrary commands via shell; (2) SNMP: remote attackers can cause a DoS or gain privileges via SNMPv1 trap handling (SNMP AGENTX/TCP REQUEST is an example of this kind of attack); (3) P2P: multiple TCP/IP and ICMP implementations allow remote attackers to cause a DoS (reset TCP connections) via spoofed ICMP error messages.

Features	Applications	Time (m)	Details
EAS	Visual FoxPro		
IDPS	Snort	19	13113 signatures
logs Detection	Procmon	19	752851 logs
Graphs	Graphviz		

Table 3. Experiment Applications (Pontes et Al, 2011)

The following hardware were used for our prototype: gateway - Intel Core 2 Duo 2.66 GHz, 3 GB RAM – Windows XP Professional; number 65 – VMWare Workstation 6.0.2 768 MB RAM – Fedora 10 (Fast Track); number 204 - VMWare Workstation 6.0.2 512 MB RAM – Fedora 10 (Nessus Server 4.0.2); number 14 – Intel Core 2 Duo 2.5 GHz, 4 GB RAM – Windows XP Professional (browser's Internet access); number 23 – Intel Pentium 4 3.2 GHz, 4 GB RAM – Microsoft Windows 7 (browser's Internet accesss, Bitcomet 1.17); number 59 – Intel Pentium 4 3.06 GHz, 1 GB RAM – Windows XP Professional (Winconnection E-mail Server 4.6f, Ultr@VNC Viewer 1.0); number 106 – Intel Pentium 4 2,4 GHz, 2 GB –Windows XP Prof. (Ultr@VNC Server 1.0).

It is important to notice that the cyber-attacks considered in this prototype are, in matter of fact, a set of events (alerts and logs) classified as a single and more elaborated attack. In our earlier works (Pontes et al, 2008), (Pontes & Guelfi, 2009a), (Pontes & Guelfi, 2009b), (Pontes & Zucchi, 2010), forecasting techniques considered just individual events in the cyber-security context. Consequently in this paper forecasting techniques are differently

employed, considering the DIFS architecture, as the prototype deals with more refined sets of attacks. Details regarding the EAS and the IFS tasks are not reported in this chapter due space limitations, but the reader may consult (Silva & Guelfi, 2010), (Silva, 2010) and (Pontes et al, 2008), (Pontes & Guelfi, 2009a), (Pontes & Guelfi, 2009b), (Pontes & Zucchi, 2010) for more information relating to EAS and IFS, respectively.

5. Results

Table 4 depicts the results of forecasting UIT in the first prototype. The UIT hit 4.320 thresholds from site A to site A′ and, gradually, it increased with propagation of the UIT among the three sites. The total amount of the UIT thresholds among the three sites was about 16.416. In Table 4, correct forecasts are the number of times that it was possible to foresee the increasing and/or decreasing UIT's phases, without any delay. The correct predictions' rates were about 60,71%. Forecast with delay are the number of the times the increasing and decreasing thresholds were identified lately. In this prototype, forecasts' rates with delay were about 34,74%. During the prototype tests, sometimes it was not possible to identify thresholds for of UIT decreasing or increasing. The rate for the times we could not predict was about 4,95%.

	A →A′	**A →A′ →A″**	**A →A′ →A″ →A**
Overall UIT thresholds	4.320	8.208	16.416
Correct forecast	2.623	4.984	9.967
Forecast with delay	1.483	2.818	5.635
Times not predict	214	406	814

Table 4. Results of Forecasting the UIT Propagation Using EWMA and Fibonacci Sequence (Pontes et al, 2009)

Table 5 depicts the results of forecasting UIT with only one forecasting technique (Fibonacci sequence) to the same experiments. The correct predictions' rates were among 5,21% and 7,55%. Forecasts with delay were among 3,92% and 4,68%.

	A →A′	**A →A′ →A″**	**A →A′ →A″ →A**
Overall UIT thresholds	4.320	8.208	16.416
Correct forecast	326	534	855
Forecast with delay	195	384	643
Times not predict	3.799	7.290	14.918

Table 5. Results of Forecasting the UIT Propagation Using Only Fibonacci Sequence (Pontes et al, 2009)

In the second prototype, for the first step (EAS), results are achieved by analyzing consecutive graphs and tables from each phase. Quantity of alerts and correlations are independently accounted, according to the registered route (source and destination). In case the alerts and correlation regards the gateway, whether for source or destination), they are registered as Gateway; the alerts and correlation which disregard the gateway are registered as Non-Gateway. Table 6 summarizes the prototype and some results. Correlation shows a range of attack strategies. In each strategy a number of different alerts are connected sequentially as they were a single attack. A peer-to-peer (P2P) attack performed on machine 23 was chosen for the analysis of forecasting (Fig. 10, Fig. 11, Fig. 12 and Fig. 13).

	Values		Total
Detected alerts	2554 Gateway	1588 Non-gateway	4142
Alert types			137
Isolated alerts	29 (all in FP1)	21 FP / 8 TP	72,41% FP
Correlated alerts	14 FP1 = 21.08%	55 FP3 = 44.72%	
% FP	21.08 (FP1)	44.72% (FP3)	54.22%
% TP	45.78%	10.52% of all TP alerts were isolated	

Table 6. Prototype Results (Pontes et al, 2009)

Fig. 10 depicts the amount of FP which was detected, considering a preliminary correlation without FP filters. Notice there are 17 alerts (nodes) with 69 correlations among them (connections between alerts represented by arrows). Fig. 10 denotes the first scenario for comparisons: the DIFS level 3 work\ing without EAS.

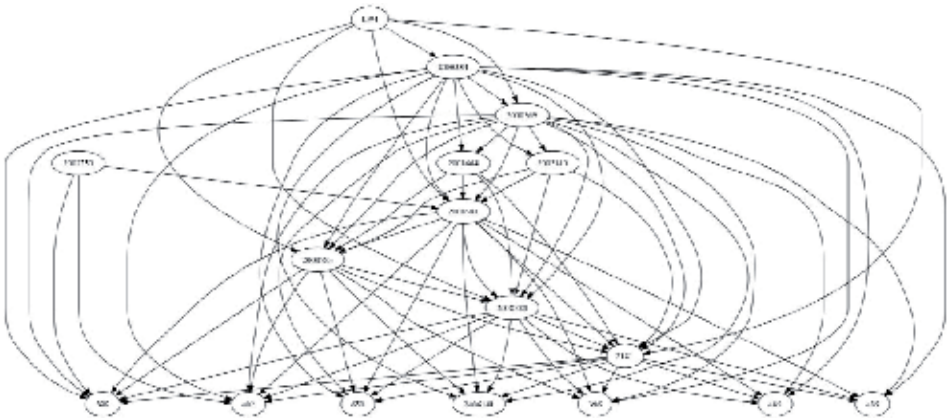

Fig. 10. P2P Graph Attack (TP + FP alerts) (Pontes et al, 2009)

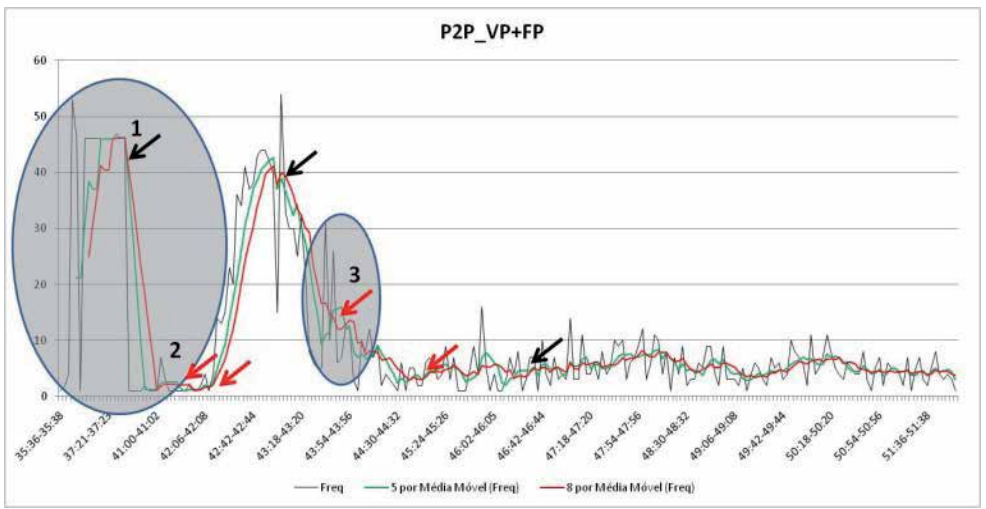

Fig. 11. True Positives + False Positves for P2P Attack (Pontes et al, 2009)

Fig. 11 illustrates the forecasting for cyber-attacks before the use the EAS, specifically for P2P events. Thus Fig. 11 takes into account the same scenario of Fig. 10. The ellipse spots the high volume of FP at the beginning of the experience with the prototype, consequently it is possible to notice three false thresholds for the forecasting, as shown by points (1), (2) and (3). Forecasting was done by the use of diverse EWMA.

Fig. 12 represents the graph after applying EAS filtering. Notice there are just 8 alerts (nodes) with 22 correlations among them (connections between alerts represented by arrows). Fig. 12 denotes the second scenario for comparisons: the DIFS level 3 (gateway level) working with the EAS filtering. As a result by the use of EAS, it was possible to track FP, filtering them, in order to improve forecasts, as the false thresholds for the predictions were eliminated as well.

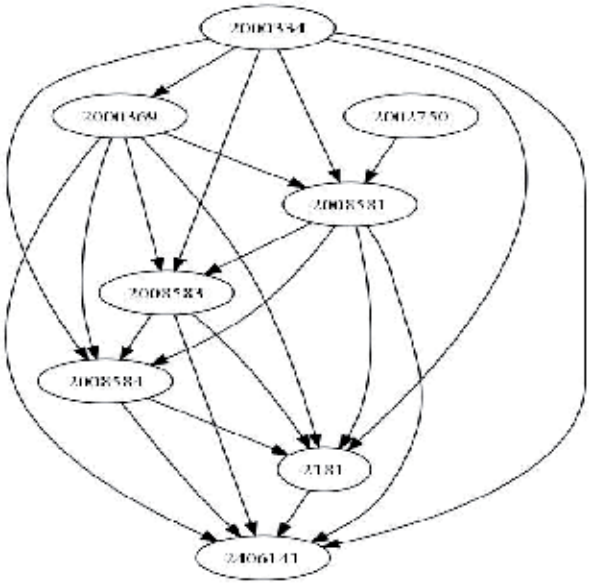

Fig. 12. P2P Graph Attack (only TP alerts) (Pontes et al, 2009)

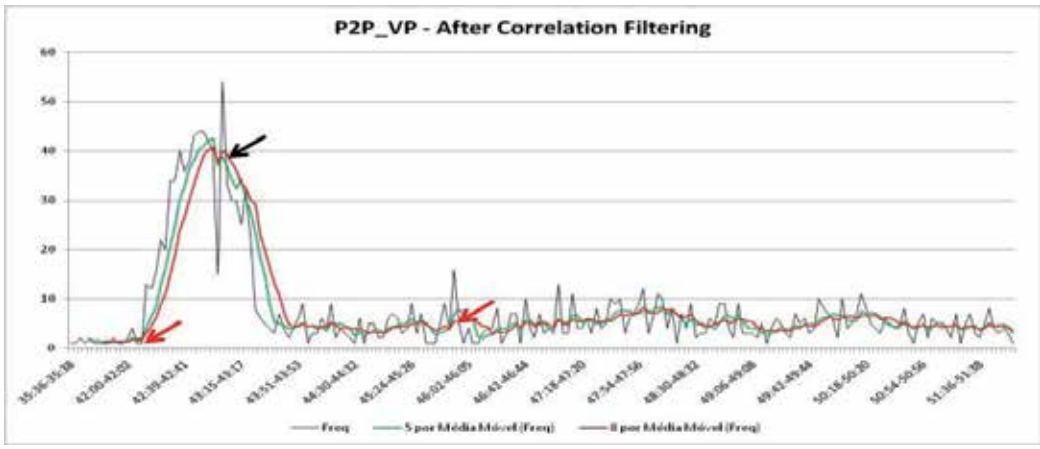

Fig. 13. True Positives for the P2P Attack – After the Correlation Filtering (Pontes et al, 2009)

Fig. 13, in the next page, depicts the application of forecasting techniques (diverse EWMA), i.e. the IFS, after the employment of EAS filtering. In Fig. 13 it is possible to verify two thresholds pointing out the increasing of events (as indicated by the red arrows, and one threshold point out the decreasing of events (as shown by black arrow). Notice there is no significant occurrence of alerts at the beginning of the experiment and two false thresholds regarding forecasts were eliminated. It is also important to observe that the second ellipse with the FP were eliminated after the EAS filtering, hence, another false threshold was wipe out as consequence. More details regarding results can be found in (Pontes et al 2011).

6. Conclusion

As a conclusion, this chapter has introduced the Distributed Intrusion Forecasting System (DIFS) (Pontes et al, 2009), approaching cyber attacks and UIT in the cyber space context. The DIFS also presented the two stage system with the EAS implemented for making the multi-correlation (step 1) (Pontes et al, 2009), afterwards the application of the forecasting techniques over the generated data by the EAS (step 2). The forecasting model presented in this chapter could be analogously employed for earthquake prediction, due the following aspects: a) DIFS, with the Two Stage System and the EAS, was able to track in advance the increasing and decreasing rates of cyber attacks and UIT; hence such methodology may be employed as an early warning system; b) DIFS considers just frequency and temporal characteristics (timestamp) of events (UIT and cyber attacks), thus this approach can be similarly used in other areas.

Even though only 4,95% of the thresholds for UIT's increasing and decreasing were not detectable, the value of the outcome is still questionable, as this early warning system still has 34,74% of warnings being lately reported. The use of two forecasting techniques represented better results if compared to the use of only one prediction technique. The reason for the accuracy using two forecasting techniques, according to (Pretcher and Frost, 2002), is due to the fact Fibonacci sequence depends on EWMA for marking the first wave. Thus, it was possible to observe just some of the trends drew by the Fibonacci sequence. Another characteristic for predictions with Fibonacci sequence is forecasts in the long term (2, 3 days): EWMAs don't have this feature, so, predictions using only EWMA lack in long term predictions. Employing both of the techniques aggregates the positive of either techniques, making the forecast more accurate.

For the EAS, it was suggested a standard to define causes and consequences within the PC-correlation method combined with multi-correlation criteria, correlation analysis (ascending/descending) and identification of FP alerts through tables and graphs. It was done an experiment with a prototype, in a LAN, with diverse machines and OS, which used a gateway to get access to the Internet. The obtained results from the tests in our prototype indicate that level 3 of DIFS was improved, as some FPs were treated and predictions concerning cyber-attacks were more accurate. It is possible to come to this conclusion by verifying that, despite high FP rates of FP1 (21.08%) and FP3 (44.72%) – see Table III -; during the whole experiment, no TP alert was correlated exclusively as result of an FP alert.

As a suggestion for improving the work, it is suggested to automate analysis' processes that require user interpretation (table correlation and mapping) for using the EAS in real time.

The accuracy of the results can be improved whether the multi-correlation is extended to entire LAN. Regarding the forecast's result, among the suggestions for future works there are the aggregation of the fractal approaches (according to (Mandelbrot & Hudson, 2006)), and the use of other kinds of forecasting techniques (as Markov chains and neural networks) to follow (Armstrong, 2002)'s advices. It is also suggested to extend the employment of the EAS for the

four levels of DIFS, so levels 1, 2 and 4 may be approached in future works. The EAS/DIFS has not yet undergone extensive training enough to be used in commercial applications.

7. References

A. A. A. Silva, "A security event analisys system to identify false positive alerts and evaluate isolated alerts creating multi-correlation criteria". IPT; São Paulo, SP, Brasil, 2010, 107 f. Masters Dissertation in Computer Engeneering.

Abad, Cristina et al. "Log correlation for intrusion detection a proof of concept".. p. 10. In the 19th IEEE ACSAC 2003. University of Illinois as Urbana-Champaign; 2003, ISBN 0-7695-2041-3, pp. 8-12.

Andersson, L.; Davies, E.; Zhang, L.; 2007 "Report from the IAB workshop on Unwanted Traffic March 9-10, 2006", RFC 4948, IETF. 2006

Alampalayam, P.; Kumar, A. "predictive security model using data mining", in proc IEEE Globcom, 2004.

Armstrong, J. S.. Principles of Forecasting: A Handbook for Researchers and Practitioners, (2002). Springer (Ed), ISBN 0792379306, USA, 2002

Bleier, T.; Freund, F. (2005). Earthquake [earthquake warning systems], In IEEE Spectrum. Vol 42, Issue 12, (05 December 2005) , pp. 22, ISSN 0018-9235.

Chung, Y.; Kim, I.; Lee, C.; Im, E. G.; Won, D. "Design of on-line intrusion forecast system with a weather forecasting model", In the Springer ICCSA 2006.

Cisar, P.; Cisar, S. M. "EWMA Statistic in Adaptive Threshold Algorithm", In the IEEE INES, 2007, pp 51-54.

Feitosa, E. L.; Souto, E. J.; Sadok, D. "Tráfego Internet não Desejado: Conceitos, Caracterização e Soluções". in Proc. VIII SBSeg, SBC. 2008 pp. 91-137.

Gula, Ron. Correlating IDS Alerts with Vulnerability Information. Chief Technology Officer – Tenable Network Security; Columbia, MD, EUA, 2007. p. 10.

Haslum, K.; Abraham, A.; Knapskog, S., (2008). Fuzzy Online Risk Assessment for Distributed Intrusion Prediction and Prevention Systems, Proceedings of IEEE UKSIM 2008 10th International Conference on Computer Modeling and Simulation, pp. 216-223, ISBN 0-7695-3114-8, Cambridge, UK, April 1-3, 2008

Holliday, James R.; Nanjo, Kazuyoshi Z.; Tiampo, Kristy F.; Rundle, John B.; Turcotte, Donald L.; (2005). Earthquake forecasting and its verification, Nonlinear Processes in Geophysics,.

IC3 - Internet Crime Complaint Center, "2009 Internet Crime Report" Bureau of Justice Assistance and National White Collar Crime Center, 2010, [Online]. Available: www.ic3.gov, 2010.

Ishida, C.; Arakawa, Y.; Sasase, I. "Forecast Techniques for Predicting Increase or Decrease of Attacks Using Bayesian Inference", In the IEEE PACRIM, 2005, pp 450-453.

Jemilli, F., Zaghdoud, M.; Ahmed, M. B. "DIDFAST.BN :Distibuted intrusion detection and forecasting multiagent system using bayesian network", In the IEEE ICTTA, 2006, pp 3040-3044.

King, Samuel; Chen, Peter; Mao, Z. Morley; Lucchetti, Dominic G. "Enriching intrusion alerts through multi-most causality". In the 12th NDSS 2005, University of Michigan, USA, 2005. p. 13.

Lai-Chenq, C. "A high-efficiency intrusion prediction technology based on markov chain", In the IEEE CISW, 2007.

Lajara, R., Alberola, J., Pelegri, J., Sogorb, (2007) Ultra Low Power Wireless Weather Station, Proceedings of IEEE SENSOR COMM International Conference on Sensor

Technologies and Applications, pp. 469-474, ISBN 978-0-7695-2988-2, Valencia, Spain, October 14-20, 2007

Leu, F.; Yang, W.; Chang, W. "IFTS : Intrusion Forecast and Traceback based on Union Defense Environment", In the IEEE ICPADS, 2005.

Lorenz, E. N. "Designing chaotic models", Journal of the Atmospheric Sciences: Vol. 62, No. 5, ISSN 1520-0469, 2005, pp. 1574–1587.

Mandelbrot, B.; Hudson, R. L. "The behavior of markets: a fractal view of risk, ruin and reward", John Willey, 2006.

Manikopoulos, Constantine; Papavassiliou; Symeon, Network Intrusion and Fault Detection: A Statistical Anomaly Approach. In IEEE Communications Magazine 40, 2002, pp. 76-82 New Jersey Institute of Technology, NJ, EUA, 2002. p. 7.

McPherson, D.; Labovitz, C. "5th Worldwide Infrastructure Sec. Report", 2010, [Online]. Available: http://seclists.org/funsec/2010/q1/295 /, 2010.

Mizoguchi, Fumio, Anomaly Detection using Visualization and Machine Learning. In the IEEE 9th International WET ICE, 2000, pp. 76-82. Science University of Tokyo – Information Media Center; Noda, Japan, 2000. p. 6.

Morin, Benjamin; Debar, Hervé. Correlation of Intrusion Symptoms: An Application of Chronicles. France Télécom R&D; In the 6th International Conference on RAID, 2003, PP. 94-112. Springer-Verlag - Berlin Heidelberg , 2003, G. Vigna, E. Jonsson, and C. Kruegel (Eds.).

Ning, Peng; Cui, Yun. "An intrusion alert correlator based on prerequisites of intrusions". Technical Report TR-2002-01 North Carolina State University; Raleigh, NC, USA, 2002. p. 16.

Ning, Peng; Cui, Yun; Reeves S., Douglas; Analyzing Intensive Intrusion Alerts via Correlation. North Carolina State University; In the 5th International Symposium on RAID, 2002, p. 21. Raleigh, NC, EUA, .

NIST – National Institute of Standards and Technology, (2007). Guide to Intrusion Detection and Prevention Systems (IDPS), In: NIST SP 800-94, December, 2010, Available from: <http://csrc.nist.gov/publications/>

NIST/SEMATECH, e-Handbook of Statistical Methods, 2009, www.itl.nist.gov/.

Pietraszek, Tadeusz; Tanner, Axel. Data mining and Machine Learning – Towards Reducing False Positives in Intrusion Detection. IBM Zuurich Research Laboratory, Ruschlikon, Suécia, 2005. Information Security Technical Report, Vol. 10, ed. 3, pp 169-183.

Pontes, E.; Guelfi, A. E., "Third generation for intrusion detection: applying forecasts and ROSI to cope with unwanted traffic". In Proceedings of 4th IEEE ICITST 09, London, UK, November 2009, ISBN 978-1-4244-5647-5, pp. 1-6.

Pontes, E.; Guelfi, A. E.; Alonso, E. "Forecasting for return on security information investment: new approach on trends in intrusion detection and unwanted traffic". In IEEE Journal Latin America Transactions, 2009, Vol 7, ISSN 1548-0992, pp 438-445.

Pontes, E.; Guelfi, A., (2009). IFS – Intrusion forecasting system based on collaborative architecture, Proceedings of the IEEE ICDIM 2009 4th International Conference on Digital Information Management, pp. 1-4, ISBN 978-1-4244-4253-9, Ann Arbor, Michigan, USA, Nov 1-4, 2009

Pontes, E.; Zucchi, W. L. "Fibonacci sequence and EWMA for intrusion forecasting system". In 5th ICDIM 2010, Lakehead University, Thunder Bat, Canada, July 2010, ISBN 978-1-4244-7571-1, pp. 1-6.

Pontes, E.; Guelfi, A. E., Silva, A. A. A., Kofuji, S. T. "Applying Multi-Correlation for Improving Forecasting in Cyber Security". In 6th ICDIM 2011, Melbourne University, Thunder Bat, Canada, July 2010, ISBN 978-1-4244-7571-1, pp. 1-6.

Prechter, R. R. Jr; Frost, A. J "Elliott Wave Principles", John Wiley, 2002.

Ramasubramanian, P.; Kannan, A. "Quickprop neural network ensemble forecasting framework for database intrusion prediction system", In the Springer 7th ICAISC, 2004, pp 9-18.

Reeves S., Douglas; Ning, Peng; Cui, Yun. "Constructing attack scenarios through correlation of intrusion alerts". In the 9th ACM CCCS, North Carolina State University; CCS'02, Washington, DC, USA., 2002. p. 10.

Roberts, S. W. "Control Chart Tests Based On Geometric Moving Average", Technometrics, pages 239-251,1959.

Silva, A. A. A.; "A security event analisys system to identify false positive alerts and evaluate isolated alerts creating multi-correlation criteria". IPT; São Paulo, SP, Brasil, 2010, 107 f. Masters Dissertation, Computer Engineering Department.

Silva, A. A. A.; Guelfi, A. E. "Sistema para identificação de alertas falso positivos por meio de análise de correlacionamentos e alertas isolados", In the 9th IEEE I2TS 2010, Rio de Janeiro, Brazil, 2010.

Sindhu, S.S.S.; Geetha, S.; Sivanath, S.S.; Kannan, A. "A neuro-genetic ensemble short term forecasting framework for anomaly intrusion prediction", In the IEEE ADCOM, 2006, pp 187-190.

Su, You-Po; Zhu, Qing-Jie (2009). Application of ANN to Prediction of Earthquake Influence, Proceedings of IEEE ICIC '09 Second International Conference on Information and Computing Science, pp. 234 – 237, ISBN 978-0-7695-3634-7, Manchester, UK, May 21-22, 2009

Valdes, Alfonso; Skinner, Keith; Probabilistic Alert Correlation. SRI International; In the 2001 International Workshop on the RAID, 2001, pp. 54-68. Springer-Verlag Berlin Heidelberg , 2001, W. Lee, L. Me, and A. Wespi (Eds).

Viinikka, J.; Debar, H.; Mé, L.; Séguier, R. "Time Series Modeling for IDS Alert Management", A In the CM ASIAN ACM Symposium on Information, Computer and Communications Security, 2006.

Wong, W.; Guan, X., Zhang, X.; Yang, L. "Profiling program behavior for anomaly intrusion detection based on the transition and frequency property of computer audit data", In the ELSEVIER Computer & Security, 2006.

Ye, N.; Li, X.; Chen, Q.; Emran, S. M.; Xu, M. "Probabilistic techniques for IDS based on computer audit data", In the IEEE Transactions on Systems, Man and Cybernetics, pages 266-274, IEEE, 2001.

Ye, N.; Vilbert, S.; Chen, Q. "Computer intrusion detection through EWMA for autocorrelated and uncorrelated data", In the IEEE Transactions on Reliability, pages 75-82, IEEE, 2003.

Yin, Q.; Shen, L.; Zhang, R.; Li, X "A new intrusion detection method based on behavioral model", In the IEEE WCICA, 2004, pp 4370-4374.

Zhay, Yan; Ning, Peng; Iyer, Purush; Reeves, Douglas S. "Reasoning about complementary intrusion evidence", In 20th Annual CSAC. North Carolina State University;USA, 2004. pp. 39-48.

Zhay, Yan; Ning, Peng; Xu, Jun "Integrating IDS alert correlation and os-level dependency tracking". Technical Report TR-2005-27 North Carolina State University , 2006, S. Mehrotra et al. (Eds.): ISI 2006, LNCS 3975, pp. 272–284, 2006.

Zhengdao, Z.; Zhumiao, P.; Zhiping, Z. "The Study of Intrusion Prediction Based on HSMM", In the IEEE Asia-Pacific Services Computing Conference, 2008, pp 1358-1363.

Zuckerman, E.; Roberts, H.; McGrady, R.; York, J.; Palfrey, J. "distributed denial of service attacks against independent media and human rights sites", 2010, [Online]. Available: http://www.soros.org, 2010.

6

Identification of Simultaneous Similar Anomalies in Paired Time-Series

R. G. M. Crockett
University of Northampton
United Kingdom

1. Introduction

Changes in radon and other soil-gas concentrations, and other parameters, before and after earthquakes have been widely reported (Asada, 1982; Chyi *et al.*, 2001; Climent *et al.*, 1999; Crockett *et al.*, 2006a; Crockett & Gillmore, 2010; Igarishi *et al.*, 1995; Kerr, 2009; Koch & Heinicke, 1994; Planinic *et al.*, 2000; Plastino *et al.*, 2002; Wakita, 1996; Walia *et al.*, 2005; Walia *et al.*, 2006; Zmazek *et al.*, 2000). However, in the majority of such radon cases, changes in magnitude in single time-series have been reported, often large changes recorded using integrating detectors, and the majority of radon time-series analysis is reported for single time-series (e.g. Baykut *et al.*, 2010; Bella & Plastino, 1999; Finkelstein *et al.*, 1998). With a single time-series, recorded at a single location, there is no measure of the spatial extent of any anomaly and, to a great extent, only anomalies in magnitude can be investigated. With two, or more, time-series from different locations, it is possible to investigate the spatial extent of anomalies and also investigate anomalies in time, i.e. frequency and phase components, as well as anomalies in magnitude.

The aim of this chapter is to present techniques, developed and adapted from techniques more familiar in the field of signal analysis, for investigating paired time-series for simultaneous similar anomalous features. A paired radon time-series dataset is used to illuminate these techniques. This is not to imply that the techniques are restricted to radon time-series: it is simply that the investigation at the University of Northampton of these techniques in the context of earthquake precursory phenomena has been conducted on radon datasets. This work commenced in the autumn of 2002, following the Dudley earthquake of 23 September which was felt in Northampton and which occurred approximately three months into a radon monitoring programme being conducted as part of another project (Crockett *et al.*, 2006a; Phillips *et al.*, 2004).

1.1 UK earthquakes

The UK is not generally regarded as a seismically active region. In general, across the UK as a whole, in any given year there might be a few earthquakes of magnitude up to 3 or 4 and every 5-10 years there might be an earthquake of magnitude 5 or thereabouts (e.g. Bolt, 2004; Musson, 1996). This is simultaneously an advantage and disadvantage to this research. It is an advantage in that with so few earthquakes there is very little seismic 'noise' in any radon, or other, dataset. It is a disadvantage in that with so few earthquakes, long intervals can

elapse between events and there is an element of luck in obtaining suitably paired time-series to investigate for potential earthquake-related anomalies.
Indeed, in 2002, luck played a major role in stimulating this research. During the latter part of 2002 the University of Northampton Radon Research Group had two hourly-sampling radon detectors deployed for a period which included the Dudley earthquake and also an unusual earthquake swarm in the Manchester area. Subsequently, 5.5 years then elapsed until another UK earthquake of similar magnitude occurred at Market Rasen in February 2008. Again, the University of Northampton had two hourly-sampling radon detectors deployed and, although that paired time-series was shorter in duration, it was still possible identify simultaneous similar anomalies (Crockett and Gillmore, 2010).

1.2 Magnitude anomalies, probability of occurrence

An anomaly in magnitude is, expressed straightforwardly, a magnitude that occurs infrequently, at low probability, often determined according to user-defined probability criteria in a given context. One commonly used criterion assumes that the magnitudes are normally distributed and defines an anomalous magnitude as being one that lies more than a specified number of standard deviations from the arithmetic mean. For example, in any normally-distributed data, an interval of two standard deviations either side of the mean includes 95.45% of the data and any data lying outside this interval can be defined as anomalous, occurring only 4.55% of the time (2.28% at each tail of the distribution). This straightforward type of criterion is clearly satisfactory for normally distributed data but becomes increasingly less robust with divergence of data from normal distributions, indicating the use of more rigorous probability criteria.

1.2.1 Standardised data, Standardised Radon Index (SRI)

Where the data are not normally distributed, or not sufficiently close to normally distributed in a given context, account must be taken of the specific probability distribution. In some cases, it is possible to map onto a normal distribution, via an equiprobability mapping, and then use the mapped-onto distribution to investigate magnitude anomalies. This is essentially the approach taken with, for example, Standardised Precipitation Indices (SPIs) as described by McKee *et al.* (1993) which are a representation of (precipitation) data in terms of standard normal variables, i.e. standard deviations around a zero mean. Alternatively, where the data are lognormally distributed, as is generally the case with radon datasets, or for example, square-root or cube-root normally distributed (Fu *et al.*, 2010), it is possible to define magnitude anomalies in terms of the normal distributions of the logarithms, square-roots or cube-roots of the data respectively, again a representation of the data in terms of standard normal variables. This is the premise underpinning the Standardised Radon Indices (SRIs) proposed by Crockett & Holt (2011). SRIs are determined from the normally-distributed logarithms of lognormally distributed radon data, a representation of the data in terms of standard normal variables. Thus, a given magnitude of SRI is determined by the probability of occurrence of a given magnitude of radon concentration within a dataset.
In addition to transforming radon data, or other data by extension, such that the familiar normal-distribution definitions of magnitude anomaly can be used reliably, SRIs also allow radon time-series to be compared more fully than by considering relative magnitude as obtained by normalising the data, e.g. scaling the data to unit mean value. Such

normalisation does not account for different radon responses to identical stimuli as might arise from differences in emission properties of rocks, soils, groundwater etc. SRIs, in standardising according to probability of occurrence, allow comparison of different radon datasets having different, possibly non-linear, responses to changes in radon emission in response to identical stimuli. In the case of paired time-series, as being considered herein, if values in the time-series have the same probabilities of occurrence they will have the same SRI even if their (relative) magnitudes are different.
Whilst not the focus of this chapter, this technique is discussed briefly, with an example, in Section 3.

1.3 Quality of data, validity of comparison

In any application of any of the correlation and coherence techniques described herein, the durations and sampling intervals of the paired time-series must be equal. Ideally, the two time-series should be sampled at the same times so as to avoid a built-in time-difference between pairs of data. Where there is such a time difference, it might be possible to pre-process the time series, e.g. via a moving average, to minimise its significance, although this must be balanced against the resultant loss of high-frequency content. Under some circumstances where the sampling intervals are different but one is a multiple of the other, it can be possible to aggregate shorter-interval data to correspond to longer-interval data.
In the following sections, it is implicitly assumed that differences between the paired time-series do not arise from different monitoring equipment responses. Where both time-series are of the same parameter or process recorded using the same equipment, this is generally a safe assumption. However, where this is not the case, e.g. the same parameter or process recorded using different equipment for each time-series or different parameters or processes (recorded using different equipment), it will generally be necessary to pre-process the time-series to minimise such differences. In such cases, filtering or spectral decomposition techniques can be used. In particular, Empirical Mode Decomposition (EMD), in decomposing a time-series into separate components (Intrinsic Mode Functions) according to frequency content, has shown promise (Crockett & Gillmore, 2010; Feng, 2011; Huang *et al.*, 1998; Rilling *et al.* 2003).

2. Correlation and coherence

Correlation and coherence are techniques for comparing time-series (more generally, waveforms, signals). In brief, correlation compares shape, i.e. envelope, and is a time-domain technique; coherence compares composition, i.e. frequency (harmonic) content, and is a frequency-domain technique. Neither technique directly compares scale, i.e. neither directly detects magnitude anomalies.
Correlation is a relatively familiar and straightforward technique, widely used in various forms to compare datasets in general. However, correlation can be misleading, particularly if used in isolation as sole means of comparison. For example, consider a pair of identical time-series, such as two equal-frequency sinusoids in the simplest case. If the two sinusoids are exactly in-phase, then their correlation coefficient will be 1 (maximum positive correlation) because both time-series are always changing in the same sense (positively or negatively) at the same time. Conversely, if they are exactly, i.e. a half-cycle, out-of-phase

then their correlation coefficient will be –1 (maximum negative correlation) because one time-series is always changing in the opposite sense to the other. Depending on their phase difference, their correlation coefficient will be between or equal to these two limiting values. However, if they are a quarter-cycle out of phase, their correlation coefficient will be zero. This is because in consecutive quarter-periods the time-series are alternately changing in the same or opposite sense, yielding alternate quarter-periods of positive and negative correlation, equal in magnitude, which sum to zero over a complete period. Thus, whilst a zero, or small, correlation coefficient can indicate a real lack of similarity between two time-series, it can be misinterpreted if there is no information with regard to their frequency content (and phase relationship).

This leads to the less familiar coherence technique. Coherence measures common frequency content, with or without phase information depending on the exact definition. Strictly, the coherence coefficient (i.e. "coherence") measures similarity of frequency content only, irrespective of relative phase, but the overall coherence analysis readily yields a phase-difference for each frequency considered for the coherence coefficient. In the hypothetical case of paired equal-frequency sinusoids considered above, the coherence would be maximal, i.e. coherence coefficient of 1, in all cases irrespective of the phase difference, although the coherence-derived phase-difference would vary exactly as the actual phase-difference. If there is no common frequency content, the coherence is zero.

Correlation is a time-domain technique, coherence is a frequency-domain technique: they are related via their Fourier transforms. Before considering correlation and coherence, therefore, a brief review of Fourier transforms – discrete Fourier transforms – will be given.

2.1 Fourier transform and Discrete Fourier Transform (DFT)

For a continuous function of time, $x(t)$, of infinite duration its continuous Fourier transform is:

$$X(f) = \int_{-\infty}^{\infty} x(t) e^{-2\pi i f t} dt \,, \tag{1}$$

and it is a frequency-domain representation of it (its spectrum). The inverse transform is:

$$x(t) = \int_{-\infty}^{\infty} X(f) e^{2\pi i f t} df \,. \tag{2}$$

In practice, time-series are neither continuous nor infinite, and so the Discrete Fourier Transform (DFT) is used, generally via a Fast Fourier Transform (FFT) algorithm. Subject to constraints arising from the finite and discrete nature of the time-domain function $x(t)$, its DFT, $X(f)$, is a frequency-domain representation of it comprising a spectrum of discrete frequencies on a finite frequency interval. Thus, the forward DFT, $x(t) \to X(f)$, is:

$$X_n = \frac{1}{N} \sum_{k=0}^{N-1} x_k e^{-\left(\frac{2\pi i}{N}\right) nk} \text{, for } x(t) = x_0, x_1, ..., x_{N-1};\ x_k = x(t_k)\ ;\ N \text{ samples} \,, \tag{3}$$

The inverse DFT (IDFT), $X(f) \to x(t)$, is:

$$x_k = \sum_{n=0}^{N-1} X_n e^{\left(\frac{2\pi i}{N}\right)nk} \text{, for } X(f) = X_0, X_1, ..., X_{N-1};\ X_n = X(f_n)\ ;\ N \text{ elements .} \quad (4)$$

For further information on and fuller descriptions of Fourier transforms and their properties see, for example, Riley, 1974; Gabel & Roberts, 1986; Proakis & Manolakis, 2006.

2.2 Correlation analysis

Covariance and correlation are measures of similarity of shape, correlation is normalised covariance and so is independent of scale (e.g. Cramer, 1946; Mood *et al.* 1974). Generalising from the simple case outlined above, the correlation coefficient between two datasets (or samples) will be +1 or –1 if they have the same shape, in-phase or out-of-phase/sign-inverted respectively. The magnitude of the correlation coefficient will reduce according to differences in shape and, as noted above, mismatch in phase.

More formally, in summary, for the comparison of two N-sample time-series, $\{x_i\},\{y_i\}$, e.g. to ascertain if they contain similar features possibly occurring with a lag between them, there is lagged covariance, $\sigma_{xy}(k)$, and lagged cross-correlation, $R_{xy}(k)$, i.e.:

$$\sigma_{xy}(k) = \sum_{n=1}^{N} (x_n - \mu_x)(y_{n-k} - \mu_y) \text{, for } k \le N \text{ ,} \quad (5)$$

$$R_{xy}(k) = \frac{\sigma_{xy}(k)}{\sigma_x \sigma_y} . \quad (6)$$

The straightforward unlagged covariance and (cross-) correlation of two time-series are (5) and (6) evaluated at zero-lag, i.e.:

$$\sigma_{xy} = \sigma_{xy}(0) = \sum_{n=1}^{N} (x_n - \mu_x)(y_n - \mu_y) \text{ ,} \quad (7)$$

$$R_{xy} = R_{xy}(0) = \frac{\sigma_{xy}(0)}{\sigma_x \sigma_y} . \quad (8)$$

Where, in equations (5) – (8):

x_i, y_i are the i^{th} members of time-series $\{x_i\},\{y_i\}$ respectively

μ_x, μ_y are the mean values of $\{x_i\},\{y_i\}$ respectively

σ_x, σ_y are the standard deviations of $\{x_i\},\{y_i\}$ respectively

For the comparison of a time-series against lagged versions of itself, e.g. to find the period(s) of any cyclic features, there is (lagged) autocovariance, $\sigma_{xx}(k)$, and (lagged) autocorrelation $R_{xx}(k)$, i.e.:

$$\sigma_{xx}(k) = \sum_{n=1}^{N} (x_n - \mu_x)(x_{n-k} - \mu_x) \text{ ,} \quad (9)$$

$$R_{xx}(k) = \frac{\sigma_{xx}(k)}{\sigma_{xx}(0)} = \frac{\sigma_{xx}(k)}{\sigma_{xx}} \text{ ,} \quad (10)$$

which are (5) and (6) with both time-series the same, and clearly both have their maximum values (i.e. autocorrelation is +1) at zero lag.

2.2.1 Rolling/sliding correlation

Whilst lagged cross-correlation reveals any lag between two time-series and cross-correlation of whole time-series gives an overall measure of similarity, neither reveals any time-dependence of similarity during the time-series, i.e. sections where the time-series correlate to greater or lesser extents. One means of achieving this is to window the paired time-series, starting at the beginning, cross-correlate across the window, roll/slide the window forwards a number of samples and repeat the cross-correlation, repeating the roll/slide-and-correlate procedure until the end of the time-series is reached. This yields a time-series of correlation coefficients which reveals those sections of the paired time-series which are varying exactly in phase (R = 1), those which are varying exactly out-of-phase (R = –1) and all intermediate values. This can be repeated for different window-durations and, for example, the results presented as a contour plot to reveal the time-duration relationships of any periods of significant cross-correlation between the time-series, analogous to the more familiar spectrogram representation of time-frequency relationships in single time-series, and to cross-coherence, as described below (e.g. Crockett *et al.*, 2006a).

2.3 Coherence (cross-spectral) analysis

Coherence (cross-coherence, magnitude-squared coherence) can be useful in that it measures the similarity of two signals, i.e. time-series in this context, in terms of their frequency composition (Brockwell & Davis, 2009; Penny, 2009; Proakis & Manolakis, 2006; Venables & Ripley, 2002). It is a normalised measure of power cross-spectral density and is a frequency-domain measure of correlation of the two signals (time-series).

2.3.1 Power spectral density

The concept of "signal power" is not itself useful in this context but the terminology is established and is retained herein for reasons of simplicity. In signals which transmit energy, power, it is significant and is determined by the square of the amplitude.

The power spectral density is obtained via the Discrete Fourier Transform and is the proportion of the total power content, i.e. square-of-magnitude, carried at given frequencies. As defined by the Wiener-Khintchine Theorem (Proakis & Manolakis, 2006), the power spectral density, G_{xx}, of a signal (time-series) is the Fourier transform of the autocovariance, i.e.:

$$G_{xx}(k) = \sum_{n=0}^{N-1} \sigma_{xx}(n) e^{-i\frac{2\pi}{N}nk} \quad . \tag{11}$$

Also, the power cross-spectral density, G_{xy}, of two signals (time-series) is the Fourier transform of their cross-covariance, i.e.:

$$G_{xy}(k) = \sum_{n=0}^{N-1} \sigma_{xy}(n) e^{-i\frac{2\pi}{N}nk} \quad . \tag{12}$$

2.3.2 Coherence (magnitude-squared coherence)

The coherence (coherence-coefficient), C_{xy}, is the cross-spectral density (complex) normalised by the product of the individual spectral densities (real), i.e.:

$$C_{xy}(k) = \frac{\left|G_{xy}(k)\right|^2}{G_{xx}(k)G_{yy}(k)}, \tag{13}$$

and the phase difference, Φ_{xy}, is given by:

$$\tan(\Phi_{xy}(k)) = \frac{\mathrm{Im}(G_{xy}(k))}{\mathrm{Re}(G_{xy}(k))}. \tag{14}$$

The coherence, C_{xy}, is real and varies between zero, i.e. no common components of the signals (time-series) at frequency k, and 1, i.e. equal proportional components of the signals (time-series) at frequency k.

2.4 Summary

This section has outlined the mathematics of correlation and coherence and also summarised their strengths and weaknesses. Both techniques have their strengths and weaknesses but complement each other. Correlation compares shape (envelope), effectively in-phase periodic features, but gives no information regarding frequency content and so can be misleading with regard to out-of-phase features. Conversely, coherence compares periodic structure (frequency composition and phase difference) and so informs with regard to similarity of composition and structure, accounting for phase difference, but not with regard to overall shape. Thus, used in combination, a much more complete comparison can be obtained than by using either in isolation.

3. Case-study: July – November 2002

The techniques outlined above have been investigated, developed and adapted using primarily one paired time-series dataset: this is a radon dataset comprising two hourly-sampled time-series spanning 5.5 months from late June to mid December 2002. This period also included the M_L=5 Dudley (UK) earthquake of 23 September (22 September GMT), which was widely felt by people in Northampton (and elsewhere in the English Midlands), and the Manchester (UK) earthquake swarm of 21-29 October, which wasn't felt in Northampton but was widely felt in southern parts of NW England and northern parts of the English Midlands. Such events are unusual for the UK and, the Dudley earthquake in particular, were the stimulus for the original investigation (Crockett *et al.*, 2006a).

In effect, this is an investigation of three time-series, one of earthquake incidence and two of hourly-sampled radon concentrations, for common radon responses to earthquake stimuli. The hypothesis for this investigation is that a big disturbance, such as an earthquake, occurring at a relatively large distance compared to the detector separation could be expected to produce simultaneous similar radon anomalies (Crockett *et al.*, 2006a). Conversely, any anomalies which are neither simultaneous nor similar are more likely to arise from stimuli local to individual monitoring locations. This hypothesis is appropriate under the circumstances for the radon time-series considered herein, as described below.

However, under different circumstances, e.g. where the detector separation is greater in comparison to the distance from the stimulus, or where one detector location is significantly closer to the stimulus than the other, the analysis might have to modified appropriately to account for a time lag, e.g. moving one time-series relative to the other in the time domain as indicated by lagged cross-correlation. Also, where the individual time-series arise from different monitored substances or processes (e.g. radon and another soil-gas or rock property), pre-processing as indicated in section 1.3 (or otherwise) might be appropriate.

3.1 The time-series

The radon data were collected using Durridge RAD7s, operated 2.25 km apart in Northampton (Phillips *et al.*, 2004; Crockett *et al.*, 2006a,b). A central 20-week extract, 14 July – 30 November 2002, of the 5.5-month paired time-series is shown in Figure 1.

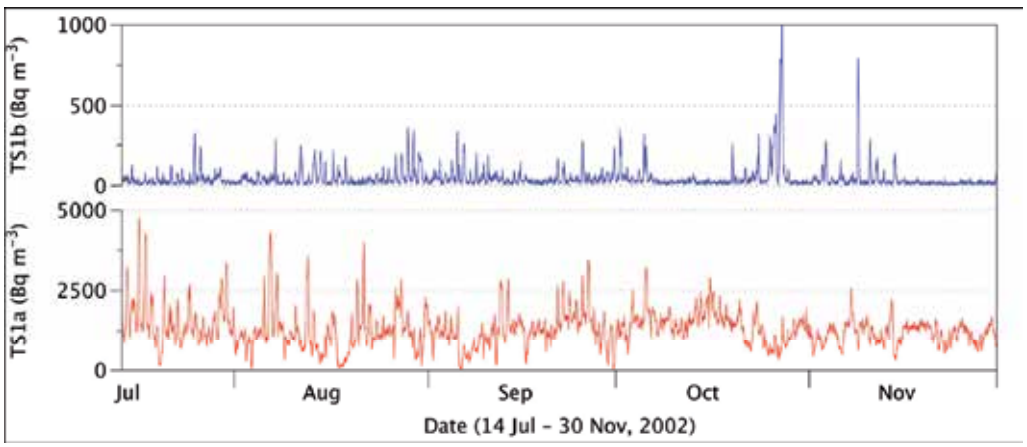

Fig. 1. The paired radon time-series, central 20-week period.

In summary, both time-series are lognormally distributed, with correlation coefficients to lognormal distributions of > 0.91, although TS1a recorded radon levels typically 30-40 times greater than TS1b (Crockett *et al.*, 2006a). Both time-series are characterised by weak, noisy, non-stationary 24 h cycles having short autocorrelation times, *ca.* 1-2 days, as shown in the spectrograms and autocorrelograms in Figures 2 and 3 respectively. There is also weak evidence of 7 day cycles, typical of anthropogenic influences, and in TS1b there is evidence of some longer-period variations, durations *ca.* 15 and 30 days, which are possibly attributable to lunar-tidal influences (Crockett *et al.*, 2006a, 2006b). With the exception of rainfall, behind which TS1a and TS1b lag by 14 and 10 days respectively, there are no observed meteorological dependencies (Crockett *et al.*, 2006a).

The spectrograms are for 6 day windows, stepped at 1 day intervals. This window duration gives the best balance between resolution in the time and frequency domains in light of the durations of the periods of high correlation and coherence discussed below.

The earthquake data for the monitoring period, for earthquakes occurring within 250 km of Northampton, are presented in Table 1 (BGS (http://www.bgs.ac.uk) 2003; USGS/ANSS (http://quake.geo.berkeley.edu/anss), 2011). The next nearest earthquakes during this period occurred at distances greater than 420 km, i.e. there is a distance interval of 170 km between the earthquakes listed and the next nearest earthquakes. As well as the Dudley and Manchester earthquakes, there were other earthquakes of interest, these being an English

Channel earthquake on 26 August and a North Sea earthquake on 22 November (not of identified interest in previous stages of this research).

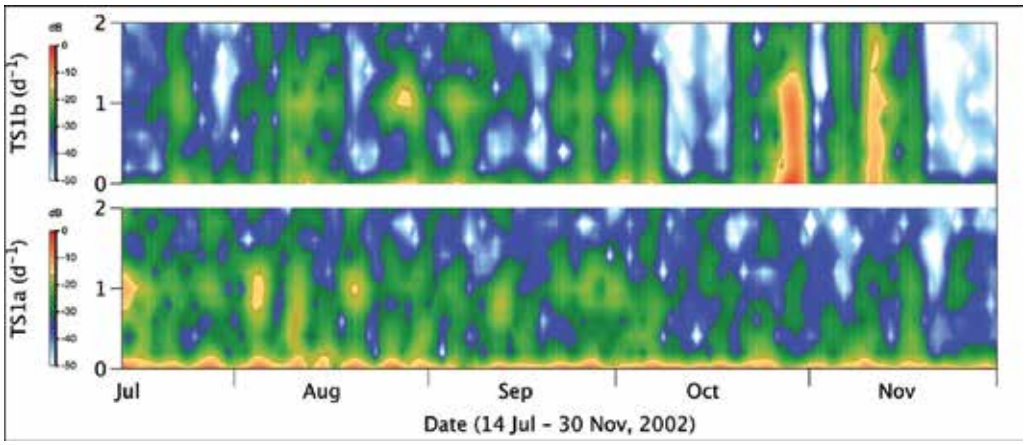

Fig. 2. Spectrograms of the radon time-series, central 20-week period. The amplitude is calibrated in dB, from maximum 0 dB (red) to –50 dB (blue-white). The vertical axes are cycles per day.

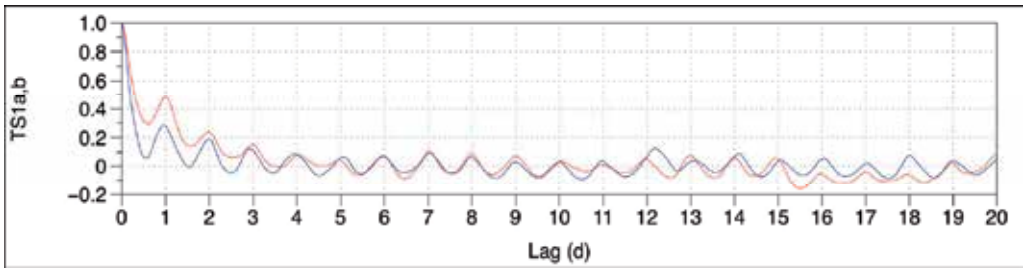

Fig. 3. Autocorrelograms of the radon time-series, central 20-week period (TS1a in red, TS1b in blue).

Date / Time (GMT)	Lat.	Lon.	Depth (km)	Mag. (M_L)	Dist. (km)	Location
26/08/2002 23:41	50.048	-0.009	4.0	3.0	247	Eng. Channel
22/09/2002 23:53	52.520	-2.150	9.4	5.0	94	Dudley
23/09/2002 03:32	52.522	-2.136	9.3	3.2	93	Dudley
21/10/2002 07:45	53.475	-2.000	5.0	3.7	161	Manchester
21/10/2002 11:42	53.478	-2.219	5.0	4.3	169	Manchester
22/10/2002 12:28	53.473	-2.146	4.2	3.5	165	Manchester
23/10/2002 01:53	53.477	-2.157	5.0	3.3	166	Manchester
24/10/2002 08:24	53.485	-2.179	3.7	3.8	168	Manchester
29/10/2002 04:42	53.481	-2.198	5.0	3.1	168	Manchester
22/11/2002 01:40	52.921	2.430	10.0	3.4	237	North Sea

Table 1. Earthquakes ($M_L \geq 3$) within 250km of Northampton, July – December 2002.

3.2 Correlation results

The rolling/sliding windowed correlation, for windows of duration 1-10 days, is shown contour-plotted in the upper plot of Figure 4 (vertical axis is window duration), with the radon time-series and earthquake timings also shown in the lower plot. In this and subsequent figures the time-series are shown normalised to unit mean, to assist visual comparison. This is a simple scaling of amplitudes: in terms of the waveforms of the time-series, the shape and phase are preserved unaltered by this normalisation.

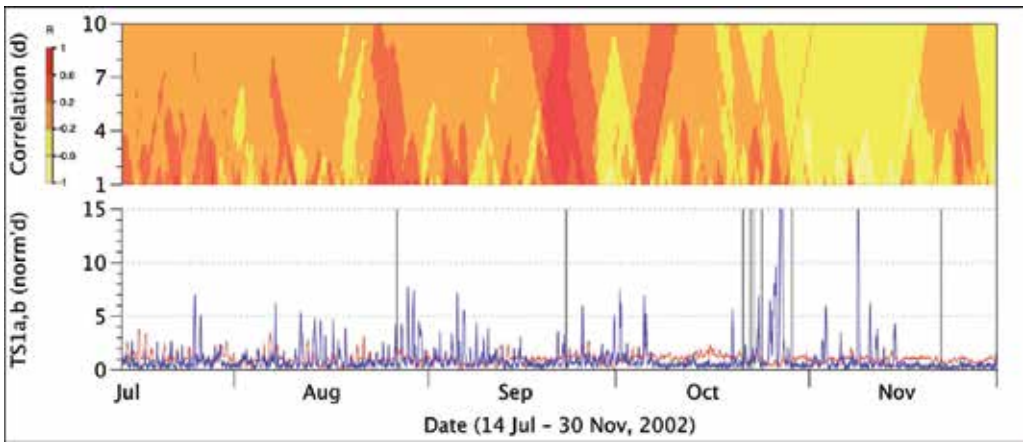

Fig. 4. Rolling/sliding windowed cross-correlation shown contour-plotted (upper plot, strong red and pale yellow areas indicate high positive and negative correlation respectively) with time-series and earthquake incidence (lower plot, TS1a and TS1b in red and blue respectively, earthquake timings as vertical black lines).

Figure 4 (upper) shows two distinct periods of high positive correlation (i.e. red); around (i) 21-23 September, across window durations of up to 10 days, and (ii) 25-27 August, across window durations of up to 5-6 days. The correlation coefficient for the whole period is $R = -0.08$ and the mean values of the correlation coefficient across all ten window durations is $|R| \leq 0.036$. Therefore, the paired time-series typically do not correlate and periods of high correlation are anomalous: e.g. the maximum values of the correlation coefficient for 1-5 day windows occur less than 5% of the time and do so predominantly in these two periods. The more significant of these two periods, 21-23 September, corresponds temporally to the Dudley earthquake of 22 September. The other period, 25-27 August, corresponds temporally to the English Channel earthquake of 26 August. Each period lasts *ca.* 5-7 days and, in each, correlation peaks prior to the earthquakes by *ca.* 1 day. There is no similar period of high positive correlation at the time of the Manchester or North Sea earthquakes.

3.3 Coherence results

The coherence, for windows of duration 6 days stepped at 1 day intervals, is shown in Figure 5. The corresponding phase coherence is shown in Figure 6 (phase difference of TS1b relative to TS1a). In these (upper) figures, the coherence information is contour-plotted to show the variation in coherence (Fig. 5) and phase-difference (Fig. 6) at frequencies of 0-3 cycles per day (vertical axes). The 6 day window duration corresponds to the window

duration used for the spectrograms and also to the durations of the two periods of high positive correlation.

In both coherence and phase-coherence, it is the 24 h cycles, as revealed by the spectrograms and autocorrelograms, which are the focus as these constitute the main frequency component in each time series and, thus, the main frequency at which the time-series could cohere. The figures also show coherence and phase-coherence for 12 h cycles, i.e. twice the frequency of the main cycles, because coherence at this frequency also reveals some information. There is no significant coherence information outside this frequency range.

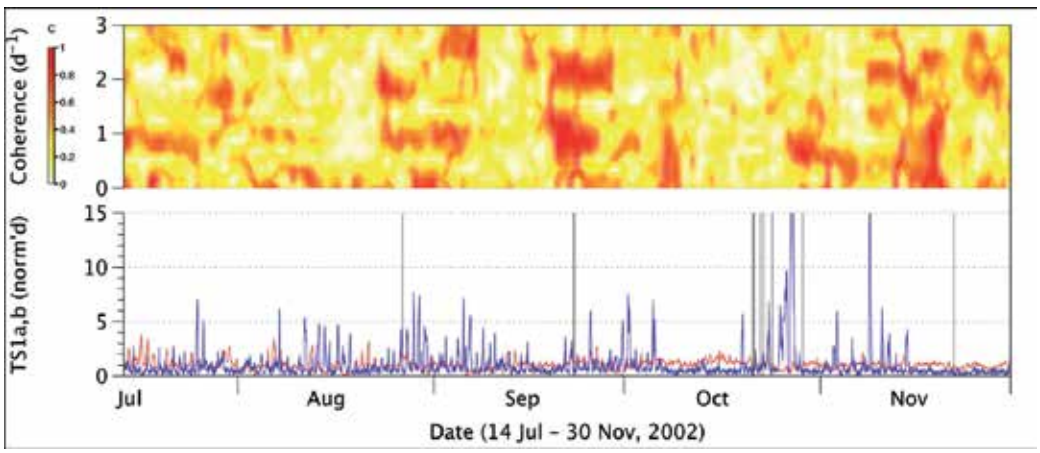

Fig. 5. Coherence shown contour-plotted (upper plot, strong red and pale yellow areas indicate high and low coherence respectively) with time-series and earthquake incidence (lower plot, TS1a and TS1b in red and blue respectively, earthquake timings as vertical black lines).

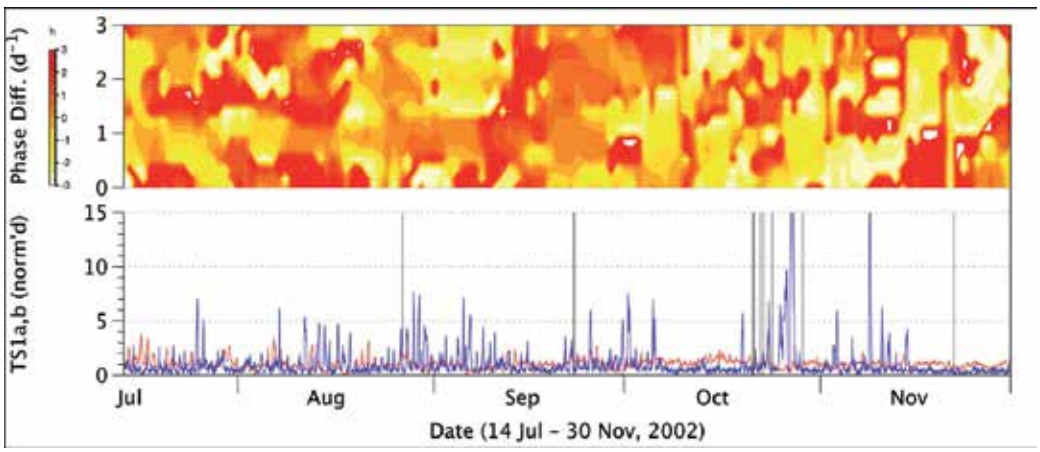

Fig. 6. Phase coherence shown contour-plotted (upper plot, strong red and pale yellow areas indicate positive and negative phase difference respectively, mid-orange indicates small phase difference) with time-series and earthquake incidence (lower plot, TS1a and TS1b in red and blue respectively, earthquake timings as vertical black lines).

Figure 5 (upper) shows two conspicuous periods of high coherence (i.e. red) for both 24 h and 12 h cycles; i.e. late August, late September, and another less conspicuous period in mid-late November. The late August and late September periods correspond to the periods of high positive correlation shown in Figure 4 and correspond temporally to the English Channel and Dudley earthquakes respectively. The mid-late November period occurs a few days before the North Sea earthquake of 22 November. Additionally, there is a period of high coherence for 24 h cycles in late October, which corresponds temporally to the end of the Manchester earthquake swarm, and also a period of high coherence for 24 h cycles in late July with no apparent correspondence to any recorded earthquakes in the region.
Figure 6 (upper) shows two periods where the time-series are in phase (i.e. approximately zero phase difference, medium orange) for both 24 h and 12 h cycles, one in late August and the other in late September. These two periods confirm the two periods of high correlation: if the principal periodic content (24 h) and a principal harmonic (12 h) are in phase then there will be underlying in-phase similarities in the envelopes, giving rise to (high) positive correlation. However, across the time-series as a whole, the daily maxima typically occur at *ca.* 18:00 and 16:00 GMT for TS1a and TS1b respectively, i.e. typically the time-series are not in-phase. This is confirmed directly in Figure 6, which shows variations in phase-difference throughout the period, and also confirmed by the short autocorrelation times shown in Figure 3 and the small average cross-correlation coefficients shown in Figure 4.

3.4 Summary of results

The rolling/sliding windowed correlation, as reported in the initial investigation (Crockett *et al.* 2006a), reveals strong evidence that the two radon time-series correlate positively at the time of the Dudley earthquake, and also evidence that they correlate positively at the time of the English Channel earthquake, but that in general they do not correlate. These results are confirmed by the coherence results, both coherence coefficients and phase-difference.
Seven day details from the time-series are shown in Figure 7, for the period around the Dudley earthquake and Figure 8, for the period around the English Channel earthquake.

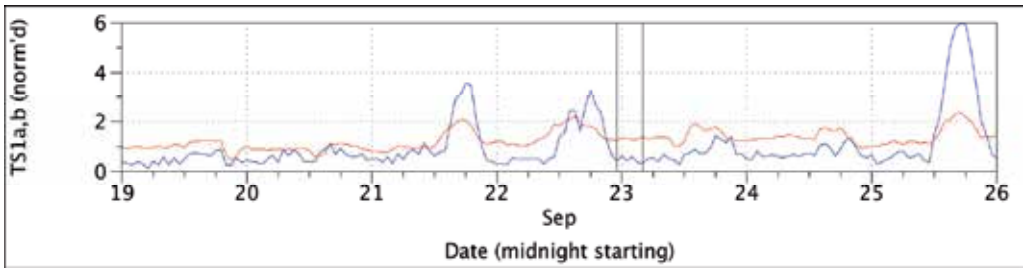

Fig. 7. Late September Anomalies (TS1a in red, TS1b in blue, earthquake timings as vertical black lines).

The two periods are similar in showing the daily maxima, i.e. spikes of *ca.* 6 h duration, occurring simultaneously (i.e. in-phase), and are dissimilar to the remainder of the time-series. Some of these simultaneous maxima occur before the earthquakes – and are potentially earthquake precursory phenomena.
It is clear from these figures, however, that the relative magnitudes of these daily maxima are 2-4 times greater in TS1b than TS1a, indicating that the radon emission characteristics in

the two locations are different. The reasons for this will be differences in the rocks and soils at the two locations and possibly different ventilation characteristics in the two basements where the RAD7s were placed. However, if the time-series are represented in terms of SRIs, effectively standard normal variables, then these different responses are (partially) equalised in terms of probability of occurrence. This is shown in Figure 9 for the September anomalies.

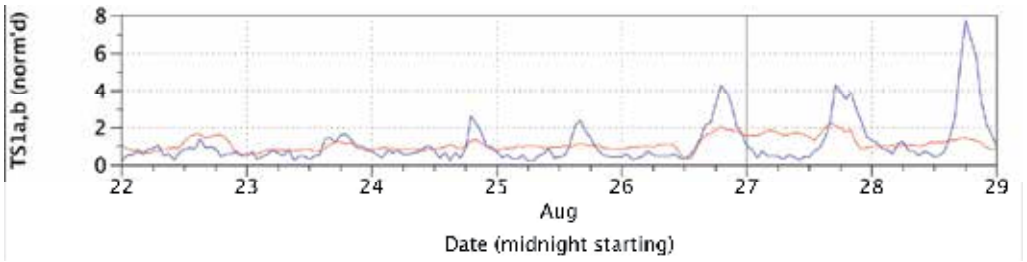

Fig. 8. Late August Anomalies (TS1a in red, TS1b in blue, earthquake timing as a vertical black line).

Figure 9 shows that these simultaneous daily maxima are more similar in probability than in relative magnitude. In SRIs, these maxima have magnitudes *ca.* 1.5-2.5, i.e. 1.5-2.5 standard deviations from the mean. Thus, some of these would 'pass' a plus-or-minus 2 standard deviations criterion for magnitude anomaly whilst others would not, and none would 'pass' a plus-or-minus 3 standard deviations criterion. Therefore, what the correlation and coherence analyses have identified are anomalies in the time domain, i.e. anomalies in frequency composition and phase, rather than in the magnitude domain.

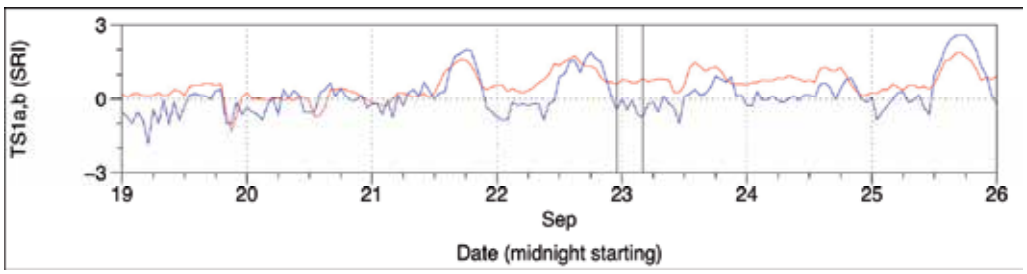

Fig. 9. Late September Anomalies (TS1a in red, TS1b in blue, earthquake timings as vertical black lines).

The late September and late August periods are identified as time-domain anomalies by correlation, coherence and phase-coherence (at 24 h and 12 h cycles), and these periods temporally correspond to the Dudley and English Channel earthquakes. The mid-late November period of coherence (at 24 h and 12 h cycles), but without significant correlation or phase-coherence, is another time-domain anomaly, which has similarities to (coherence) and differences from (correlation, phase-coherence) the late September and late August time-domain anomalies. This mid-late November anomaly occurs a few days prior to the 22 November earthquake but any temporal association with that earthquake is weakened by the absence of corresponding correlation or phase-coherence information. The two periods of 24 h coherence (without 12 h coherence) are clearly ambiguous: the late October period

corresponds temporally to the later Manchester earthquakes but the late July period does not correspond temporally to any recorded earthquake in the region.
Noting the relative magnitudes and proximities of the Manchester earthquakes compared to the English Channel earthquake, it is perhaps surprising the there is no similarly well-defined time-domain anomaly in the radon time-series at the time of Manchester earthquakes. The reasons for this are not currently understood but there are essentially two possibilities. First, any such temporal correspondence between earthquake and time-domain anomalies in the radon time-series is coincidental, as discussed below. Second, the temporal correspondence is not coincidental but the natures of the geologies at and between Northampton and Manchester are such that any earthquake-related radon-stimuli are blurred and attenuated. For information on geology see, for example, Boulton, 1992; Hains & Horton, 1969; Poole *et al.*, 1968; Smith *et al.*, 2000 and Toghill, 2003. However, having also identified time-domain radon anomalies which temporally correspond to the Market Rasen earthquake of 27 February 2008 (Crockett & Gillmore, 2010), the second reason is arguably more probable but more data are required, both earthquake and radon, to investigate this more fully.
In these data, another potential geophysical explanation is possible: i.e. lunar-tidal influences, which have been reported for TS1b in terms of cyclic variations in radon concentration (Crockett *et al.*, 2006b). Tidal influences might account for the periods of 24 h coherence which temporally correspond to tidal maxima associated with the full moons of 24 July, 22 August, 21 September and 20 November, but not the absence of any coherence around the 21 October full moon. This potential explanation is further weakened by the absence of (a) consistent coherence around the new-moon maxima and (b) consistent correlation or phase coherence around both sets of maxima. Also, a tidal-maximum explanation does not account for the anomalies in the February 2008 time-series, which temporally correspond to the Market Rasen earthquake but not a tidal maximum. Lastly, despite the apparent similarities in timing, it is unknown whether there is any lunar-tidal influence on the English Channel, Dudley, Manchester and North Sea earthquakes and no such influence has been reported for UK earthquakes in general.

4. Conclusions

Both correlation and coherence show when two, or more, time-series behave similarly in the time domain, according to shape (correlation) or frequency composition (coherence). Thus, these techniques allow the identification of time-domain anomalies, i.e. periods in time when the common behaviour of two, or more, time-series changes from the typical to the anomalous. In the radon data used to illustrate the techniques, the paired time-series typically neither correlate nor cohere but do so anomalously for short periods. In other data, the emphasis might be different, e.g. the time series might typically both correlate and cohere but contain anomalous periods where they do not or, the time-series might typically cohere at some frequencies but contain anomalous periods where the cohering frequencies change.
Correlation does not imply causality, is not proof of causality: at most, correlation might be evidence to support causality. In the dataset analysed above, despite the clear temporal correspondence of the late September and late August time-domain anomalies to earthquakes, and the temporal correspondence of the mid-late November less well-defined time-domain anomaly to another earthquake, this is all that is shown, i.e. temporal

correspondence. The analysis does not prove that the anomalies are related to the earthquakes, i.e. does not demonstrate that an earthquake-stimulus radon-response relationship exists, but such analysis does provide necessary evidence towards the demonstration that such a relationship might exist.
With regard to magnitude anomalies, care must be taken to apply criteria used for identifying anomalies correctly dependent upon the probability distribution(s) of the data being investigated. Noting the simplicity and familiarity of the normal distribution, and associated *de facto* standard criteria for determining anomalies, a technique such as the SRI which maps data onto standard normal variables is useful, but this technique is also useful in effectively equalising different, generally non-linear radon-emission characteristics and facilitating comparison in terms of probability of occurrence.

5. Acknowledgements

The author gratefully acknowledges members of the University of Northampton Radon Research Group for the collection of the data and also DEFRA (UK) for funding the research under which the 2002 data were collected (EPG 1/4/72, RW 8/1/64). The author also acknowledges UNESCO / IUGS / IGCP Project 571 for facilitating preparation and dissemination of earlier stages of this and related research.
The data-analysis was performed using the open-source R (http://www.r-project.org)) and Scilab (http://www.scilab.org) software packages, with the EMD and Seewave R libraries.

6. References

Asada, T. (1982). *Earthquake Prediction Techniques: Their Application in Japan*, University of Tokyo Press, Japan.

Baykut, S., Akgul, T. & Seyis, C. (2010). Observation and removal of daily quasi-periodic components in soil radon data, *Rad. Meas.*, Vol.45, No.7, pp. 872-879, doi:10.1016/j.radmeas.2010.04.002.

Bella, F. & Plastino, W. (1999). *Radon time series analysis at LNGS, II*, LNGS Annual Report 1999, Gran Sasso National Laboratory, Italy, pp.199-203.

Bolt, B.A. (2004). *Earthquakes* (5th edition). W.H. Freeman & Co, New York, USA. ISBN 0-7167-5618-8.

Boulton, G.S. (1992). Quaternary, In: *Geology of England and Wales*, Duff, P.McL.D. & Smith, A.J. (Eds.),The Geological Society, London, pp.413-444.

Brockwell, P.J. & Davis, R.A (2009). *Time Series: Theory and Methods*, Springer. ISBN 978-1-4419-0319-8.

Chyi, L., Chou, C-Y., Yang, F. & Chen, C-H. (2001). *Continuous Radon Measurements in Faults and Earthquake Precursor Pattern Recognition*, Western Pacific Earth Sciences, Vol.1, No.2, pp.227-246.

Climent, H., Tokonami, S. & Furukawa, M. (1999). Statistical Analysis Applied to Radon and Natural Events, *Proc. Radon in the Living Environment*, Athens, Greece, April 1999, pp.241-253.

Cramer, H. (1974, repub. 1999). *Mathematical Methods of Statistics*, Princeton University Press, ISBN 978-06-910-0547-8.

Crockett, R.G.M., Gillmore, G.K., Phillips, P.S., Denman, A.R. & Groves-Kirkby, C.J. (2006a). Radon Anomalies Preceding Earthquakes Which Occurred in the UK, in Summer and Autumn 2002. *Science of The Total Environment*, Vol.364, pp. No.1-3, pp.138-148. doi:10.1016/j.scitotenv.2005.08.003.

Crockett, R.G.M., Gillmore, G.K., Phillips, P.S., Denman, A.R. and Groves-Kirkby, C.J. (2006b). Tidal Synchronicity of Built Environment radon levels in the UK. *Geophys. Res. Lett.* Vol.33, No.5, L0538, doi:10.1029/2005GL024950.

Crockett, R.G.M. & Gillmore, G.K. (2010). Spectral-decomposition techniques for the identification of radon anomalies temporally associated with earthquakes occurring in the UK in 2002 and 2008. *Nat. Hazards Earth Syst. Sci.*, 10, 1079–1084, doi:10.5194/nhess-10-1079-2010.

Crockett, R.G.M. & Holt, C.P. (2011). Standardised Radon Index (SRI): a normalisation of radon datasets in terms of standard normal variables. *Nat. Hazards Earth Syst. Sci.*, 11, 1839-1844, doi:10.5194/nhess-11-1839-2011.

Feng, Z. (2011). The seismic signatures of the 2009 Shiaolin landslide in Taiwan, *Nat. Hazards Earth Syst. Sci.*, Vol.11, 1559-1569, doi:10.5194/nhess-11-1559-2011.

Finkelstein, M., Brenner, S., Eppelbaum, L. & Ne'eman, E. (1998). Identification of Anomalous Radon Concentrations Due to Geodynamics Processes by Elimination of Rn Variations Caused by Other Factors. *Geophys. J. Int.*, Vol.133, No.5, pp.407-412, doi:10.1046/j.1365-246X.1998.00502.x.

Fu, G., Viney, N.R. & Charles, S.P. (2010). Evaluation of various root transformations of daily precipitation amounts fitted with a normal distribution for Australia. *Theor. Appl. Climatol.* Vol.99, No.1-2, pp.229–238, doi:10.1007/s00704-009-0137-6.

Gabel, R.A. & Roberts, R.A. (1986). *Signals and Linear Systems* (3rd edition), Wiley. ISBN 978-04-718-2513-5

Hains, B.A. & Horton, A. (1969). *British Regional Geology Central England.* (3rd edition), HMSO.

Huang. N.E., Shen. Z., Long. S.R., Wu, M.L., Shih, H.H., Zheng, Q., Yen, N.C., Tung, C.C., Liu, H.H. (1998). The empirical mode decomposition and Hilbert spectrum for nonlinear and nonstationary time series analysis. *Proc. Roy. Soc. A*, Vol.454, No.1971, pp.903–995, doi:10.1098/rspa.1998.0193.

Igarashi, G., Saeki, S., Takahata, N., Sumikawa, K., Tasaka, S., Sasaki, Y., Takahashi, M. & Sano, Y. (1995). Ground-Water Radon Anomaly Before the Kobe Earthquake in Japan, *Science*, Vol.269, pp.60-61, DOI: 10.1126/science.269.5220.60.

Kerr, R.A. (2009). After the Quake, in Search of the Science – or even good prediction. *Science*, Vol.324, No.5925, p.322, doi:10.1126/science.324.5925.322.

Koch, U. & Heinicke, J. (1994). Radon Behaviour in Mineral Spring Water of Bad Bramburgh (Vogtland, Germany) in the Temporal Vicinity of the 1992 Rörmond Earthquake, the Netherlands, *Geologie en Mijnbouw*, Vol.73, pp.399-406.

McKee, T.B., Doesken, N.J. & Kleist, J. (1993). The relationship of drought frequency and duration to time scales. Preprints, *8th Conference on Applied Climatology*, pp.179–184. January 17–22, Anaheim, California.

Meyer, L.L. (1977). *California Quake*, Sherbourne Press, Nashville, USA.

Mood, A.M., Graybill, F.A. & Boes, D.C. (1974). *Introduction to the Theory of Statistics* (3rd edition), McGraw-Hill. ISBN 978-00-708-5465-9

Musson, R. (1996). British earthquakes and the seismicity of the UK. *Geoscientist*, Vol. No.2, pp. 24-25.

Penny, W.D. (2009). Signal Processing Course, April 2011, Available from http://www.fil.ion.ucl.ac.uk/~wpenny/course/course.html

Planinic, J., Radolic, V. & Culo, D. (2000). Searching for an Earthquake Precursor: temporal variations of radon in soil and water, *Fizika B*, Vol.9, No.2, pp.75-82. ISSN 1330–0008.

Plastino, W., Bella, F., Catalano, P. & Di Giovambattista, R. (2002). Radon groundwater anomalies related to the Umbria-Marche, September 26, 1997, Earthquakes, *Geofisica Internacional*, Vol.41, No.4, pp.369-375. ISSN 0016-7169.

Phillips, P.S., Denman, A.R., Crockett, R.G.M., Groves-Kirkby, C.J. & Gillmore, G.K. (2004). *Comparative analysis of weekly vs. three-monthly radon measurements in dwellings*. DEFRA commissioned research for radioactive substances division. Report DEFRA/RAS/03.006. ISBN 1-900868-44-x.

Poole, E.G., Williams, B.J. & Hains, B.A. (1968). *Geology of the Country around Market Harborough*. Institute of Geological Sciences Memoirs of the Geological Survey of Great Britain, England and Wales, HMSO.

Proakis, J.G. & Manolakis, D.K. (2006). Digital Signal Processing (4th Edition), Prentice Hall. ISBN 978-01-318-7374-2

Riley, K.F. (1974 [and subsequent editions]). *Mathematical Methods for the Physical Sciences: An Informal Treatment for Students of Physics and Engineering*, Cambridge University Press, ISBN 978-05-210-9839-7.

Rilling, G., Flandrin, P. & Goncalves, P. (2003). On Empirical Mode Decomposition and its Algorithms, *IEEE-EURASIP Workshop on Nonlinear Signal and Image Processing NSIP-03,* Grado (I)

Smith, K.A., Gillmore, G.K. & Sinclair, J.M. (2000). Sediments and Ostracoda from Courteenhall, Northamptonshire, U.K. and their implications for the depositional environment of the Pleistocene Milton Formation, *Proc. Geologists' Association*, Vol.111, No.3, pp.253-263, doi:10.1016/S0016-7878(00)80018-8.

Toghill, P. (2003). *The Geology of Britain: an Introduction*, Airlife, Wiltshire, UK. ISBN 1-84037-404-7.

Venables, W.N. & Ripley, B.D. (2002). *Modern Applied Statistics with S.* (4th Edition), Springer. ISBN 0-387-95457-0 and online complement http://www.stats.ox.ac.uk/pub/MASS4/

Wakita, H. (1996). Geochemical Challenge to Earthquake Prediction, Proc. *USA National Academy Science*, Vol.93, No.9, pp.3781-3786.

Walia, V., Virk, H.S., Yang, T.F., Mahajan, S., Walia, M. & Bajwa, B.S. (2005). Earthquake prediction studies using radon as a precursor in N-W Himalayas, India: A case study. *Terrestrial, Atmospheric and Oceanic Sciences*, Vol.16, No.4, pp.775-804. ISSN 1017-0839.

Walia, V., Virk, H.S. & Bajwa, B.S. (2006). Radon precursory signals for some earthquakes of magnitude > 5 occurred in N-W Himalaya. *Pure and Applied Geophysics*, Vol.163, No.4, pp.711-721. ISSN 0033-4553.

Zmazek, B., Vaupotic, J., Zivcic, M., Premru, U. & Kobal, I. (2000). Radon Measurements for Earthquake Prediction in Slovenia, *Fizika B*, Vol.9, No.3, pp.111-118. ISSN 1330-0016 / 1333-9133.

7

Radon as Earthquake Precursor

Giuseppina Immè and Daniela Morelli
Dipartimento di Fisica e Astronomia Università di Catania - INFN Sezione di Catania
Italy

1. Introduction

Earthquake predictions are based mainly on the observation of precursory phenomena. However, the physical mechanism of earthquakes and precursors is at present poorly understood, because the factors and conditions governing them are so complicated. Methods of prediction based merely on precursory phenomena are therefore purely empirical and involve many practical difficulties.

A seismic precursor is a phenomenon which takes place sufficiently prior to the occurrence of an earthquake. These precursors are of various kind, such as ground deformation, changes in sea-level, in tilt and strain and in earth tidal strain, foreshocks, anomalous seismicity, change in b-value, in microsismicity, in earthquake source mechanism, hypocentral migration, crustal movements, changes in seismic wave velocities, in the geomagnetic field, in telluric currents, in resistivity, in radon content, in groundwater level, in oil flow, and so on. These phenomena provide the basis for prediction of the three main parameters of an earthquake: place and time of occurrence and magnitude of the seismic event.

The most important problem with all these precursors is to distinguish signals from noise. A single precursor may not be helpful, the prediction program strategy must involve an integral approach including several precursors.

Moreover, in order to evaluate precursory phenomena properly and to be able to use them confidently for predictive purposes, one has to understand the physical processes that give rise to them. Physical models of precursory phenomena are classified in two broad categories: those based on fault constitutive relations, which predict fault slip behavior but no change in properties in material surrounding the fault, and those based on bulk rock constitutive relations, which predict physical property changes in a volume surrounding the fault. Nucleation and lithospheric loading models are the most prominent of the first type and the dilatancy model is of the second type.

During the past two decades efforts have been made to measure anomalous emanations of geo-gases in earthquake-prone regions of the world, in particular helium, radon, hydrogen, carbon dioxide. Among them radon has been the most preferred as earthquake precursor, because it is easily detectable.

Radon is found in nature in three different isotopes: ^{222}Rn, member of ^{238}U series, with an half life of 3.8 days, ^{220}Rn (also called thoron), member of ^{232}Th series, with an half life of 54.5 s and ^{219}Rn, member of ^{235}U series, with an half life of 3.92 s.

Owing to his longer half-life, the most important of them is ^{222}Rn, produced by ^{226}Ra decaying. After his production in soil or rocks, ^{222}Rn can leave the ground crust either by

molecular diffusion or by convection and enters the atmosphere where his behavior and distribution are mainly governed by meteorological processes.
The radon decay products are radioactive isotopes of Po, Bi, Pb and Tl and they are easily attached to aerosol particles present in air. In table 1 are shown the principal decay characteristics of ^{222}Rn and ^{220}Rn, including properties of their respective parent radionuclides and their short-lived decay products.

Radionuclide	Half-life	Radiation	E_α(MeV)	E_γ(MeV)
^{226}Ra	1600 y	α	4.78(94.3%) 4.69 (5.7%)	0.186 (83,3%)
^{222}Rn	3.824 d	α	5.49(100%)	
^{218}Po	3.05 m	α	6.00(100%)	
^{214}Pb	26.8 m	β, γ		0.295 (19%) 0.352 (36%)
^{214}Bi	19.7 m	β, γ		0.609 (47%) 1.120 (15%) 1,760 (16%)
^{241}Po	164 μs	α	7.69 (100%)	
^{224}Ra	3.66 d	α	5.45 (6%) 5.68 (94%)	0.241(3.9%)
^{220}Rn	55 s	α	6.29 (100%)	
^{216}Po	0.15 s	α	6.78 (100%)	
^{212}Pb	10.64 h	β, γ		0.239 (47%) 0.300 (3.2%)
^{212}Bi	1.01 h	α, β, γ	6.05 (25%) 6.09 (10%)	0.727 (11.8%) 1.620 (2.8%)
^{212}Po	298 ns	α	8.78 (100%)	
^{208}Tl	3.05 m	β, γ		0.511 (23%) 0.583 (86%) 0.860 (12%) 2.614 (100%)

Table 1. Principal decay Characteristics of ^{222}Rn and ^{220}Rn

The release of radon from natural minerals has been known since 1920's (*Spitsyn, 1926*) but its monitoring has more recently been used as a possible tool for earthquake prediction, because the distribution of soil-gas radon concentration is closely related to the geological structure, fracture, nature of rocks and distribution of sources. Therefore, surveying of radon concentration can prospect fracture trace, earthquake forecast, environment monitoring, etc.

2. Radon production and transport

The production of ^{222}Rn depends on the activity concentrations of ^{226}Ra in the earth's crust, in soil, rock and water.

When radium decays in a mineral substance, the resulting radon atoms must first emanate from the grains into the air-filled pore space. The fraction of radon that enters the pores, commonly known as *emanation fraction*, consists of two components due to recoil and diffusion mechanisms. Since the diffusion coefficient of gases in solid materials is very low, it is assumed that the main portion of the emanation fraction comes from the recoil process. From the alpha decay of radium, radon atoms possess sufficient kinetic energy (86 keV) to move from the site where radon is generated. The range of ^{222}Rn is between 20 to 710 nm in common materials, 100 nm for water and 63 μm for air. (*Sabol et al., 1995*)

The emanation fraction can be strongly influenced by water content in the material, increasing with soil moisture, up to saturation in the normal range of soil moisture content. A representative estimate of the fraction of radon that leaves solid grains is 25%.

The increase in the emanation fraction can be explained by the lower recoil range of radon atoms in water than in air. A radon atom entering a pore that is fully or partially filled with water has a very good chance of being stopped by the water in the pore. Generally, the presence of water increases the emanation fraction, but this trend may show a saturation effect or the effect may even later reverse as the water content becomes greater.

In addition to the moisture effect, dependence of the emanation fraction on grain size and temperature has also been observed. Small grain size soils, such as clay, display maximum emanation at about 10%-15% water content. The ratio of the maximum emanation fraction to that of a dry sample also decreases as the grain size increases. A rise in temperature also causes an increase in the emanation fraction, which is probably due to the reduced adsorption of radon.

Different types of soil show different emanation fractions for ^{222}Rn, which are generally in the range 0.01-0.5 (*Sabol et al., 1995*).

Some emanated radon atoms, after their penetration trough the pore of a material, may finally reach the surface before decaying. Radon behaves as a gas and its movement in material follows some well-known physical laws. There are essentially two mechanisms of radon transport in material: (1) molecular diffusion and (2) forced advection.

In diffusive transport, radon flows in a direction opposite to that of the increasing concentration gradient. Fick's law describes this process. Expressions for the radon fluence rate, in Bq m^{-2} s^{-1} , can be derived for specified geometric conditions.

If one assumes the earth as a semi-infinite homogeneous material, with density ρ and porosity ε, the fluence rate J_D of radon emerging at the earth surface can be given by (*Sabol et al., 1995*):

$$J_D = C_{Ra}\lambda_{Rn} f \rho \left[\frac{D_e}{\lambda_{Rn}\varepsilon}\right]^{0.5} \quad (1)$$

where C_{Ra} is the activity concentration of ^{226}Ra in earth material (Bq/kg); λ_{Rn} is the decay constant of ^{222}Rn (2.1×10^{-6} s^{-1}); f and D_e are the emanation fraction and the effective diffusion coefficient for earth material (m^2/s) respectively.

After crossing soil-air interface radon exhales into the atmosphere. The exhalation rate, that is the amount of radon activity released from the surface, depends on meteorological parameters. In particular the exhalation of radon is positively correlated with moisture content, temperature and wind speed and negatively with pressure, so that these factors

must be considered in the determination of exhalation rates in environmental measurements. Since the main mechanism governing the entry of radon into the atmosphere from the surface of the earth is diffusion, the radon fluence rate can be calculated by using appropriate parameters in equation (1). Representative values of these parameters and C_{Ra} = 40 Bq m^{-3} yield J_D= 0.026 Bq m^{-2} s^{-1} which is quite close to the average value experimentally obtained for some regions (*Sabol et al. ,1995*).

2.1 Theory of radon diffusion

In order to understand how radon anomalies could be correlated to geodynamic events radon transport mechanisms in soil must be considered. Different models to describe radon diffusion have been proposed. In this section we will give a brief review.

2.1.1 Plate sheet model

One of the most reliable models to describe radon diffusion is the plane sheet model. The molecular diffusion is considered in only one direction and, for any stable element, can be described by Fick's second law as follows (*Gauthier et al.,1999*):

$$\frac{\partial C}{\partial t} = D\frac{\partial^2 C}{\partial z^2} \tag{2}$$

where C is the concentration of the element and D the diffusion coefficient along z. This equation admits a solution C(z, t) which is constrained by the initial and boundary conditions (C = C_0 at t = 0 and –a < z < a; C = 0 at t > 0 and z = +a):

$$C(z,t) = \frac{4C_0}{\pi}\sum_{n=0}^{\infty}\left\{\left(\frac{(-1)^n}{2n+1}\right)\times\cos\left(\frac{(2n+1)\pi z}{2a}\right)\times\exp\left(\frac{-D(2n+1)^2\pi^2 t}{4a^2}\right)\right\} \tag{3}$$

where a is the half-width of the slab.

In order to take into account radioactivity, equation (3) has to be modified for radon by adding a production term from its parent ^{226}Ra and a decay term, which leads to:

$$\frac{\partial C_{Rn}}{\partial t} = \lambda_{Ra}\, C_{Ra} - \lambda_{Rn} C_{Rn} + D\frac{\partial^2 C_{Rn}}{\partial z^2} \tag{4}$$

where C_{Ra} and C_{Rn} represent the concentrations (in atoms · g^{-1}) and λ_{Ra} and λ_{Rn} the decay constants of ^{226}Ra and ^{222}Rn, respectively.

Defining the function $K(z, t)$ as:

$$K(z,t) = \left(C_{Rn}(z,t) - \left(\frac{\lambda_{Ra}}{\lambda_{Rn}}C_{Ra}\right)\right)\exp(\lambda_{Rn}t) \tag{5}$$

and introducing $K(z, t)$ in equation (4) gives:

$$\frac{\partial K}{\partial t} = D\frac{\partial^2 K}{\partial z^2} \tag{6}$$

which is the Fick's second law expressed for the function K(z, t). Nevertheless the solution of equation (6) cannot be merely obtained by combining the solution of the general Fick's second law (2) with the substitution (5) because the two functions *K(z, t)* and C_{Rn} *(z, t)* do not admit the same initial and boundary conditions. These conditions are for C_{Rn} *(z, t)* :

$$\begin{aligned} &C_{Rn}(z,0) = C_{RnEq} = \frac{\lambda_{Ra}}{\lambda_{Rb}} C_{Ra} && \text{for } -a < z < a, t = 0 \\ &C_{Rn}(z,t) = 0 && \text{for } z = -a, z = a \end{aligned} \tag{7}$$

(the atmosphere is considered as a reservoir of concentration *C* = 0) which means for *K(z, t)*:

$$\begin{aligned} &K(z,0) = 0 && \text{for } -a < z < a, t = 0 \\ &K(z,t) = -C_{RnEq} \exp(\lambda_{Rn} t) && \text{for } z = -a, z = a \end{aligned} \tag{8}$$

Fick's law is usually solved for plane sheet geometry by separation of variables but this method is unsuccessful for such initial and boundary conditions. Several studies have been done for heat conduction in a slab having an initial zero temperature and surfaces maintained at the temperature *f(t) = V exp(vt)* (*Gauthier et al.,1999*), obtaining:

$$\begin{aligned} K(z,t) = -C_{RnEq} \exp(\lambda_{Rn} t) \frac{\cosh\left(z\sqrt{\frac{\lambda_{Rn}}{D}}\right)}{\cosh\left(a\sqrt{\frac{\lambda_{Rn}}{D}}\right)} + \\ + \frac{4C_{RnEq}}{\pi} \sum_{n=0}^{\infty} \frac{(-1)^n \exp\left(\frac{-(2n+1)^2 \pi^2 D t}{4a^2}\right)}{(2n+1)\left[1 + \left(\frac{4\lambda_{Rn} a^2}{(2n+1)^2 \pi^2 D}\right)\right]} \cos\frac{(2n+1)\pi z}{2a} \end{aligned} \tag{9}$$

and therefore, combining with (6):

$$\begin{aligned} C_{Rn}(z,t) = C_{RnEq} - C_{RnEq} \frac{\cosh\left(z\sqrt{\frac{\lambda_{Rn}}{D}}\right)}{\cosh\left(a\sqrt{\frac{\lambda_{Rn}}{D}}\right)} + \\ + \frac{4C_{RnEq}}{\pi} \sum_{n=0}^{\infty} \frac{(-1)^n \exp\left(-\left(\frac{(2n+1)^2 \pi^2 D}{4a^2} + \lambda_{Rn}\right) t\right)}{(2n+1)\left[1 + \left(\frac{4\lambda_{Rn} a^2}{(2n+1)^2 \pi^2 D}\right)\right]} \cos\frac{(2n+1)\pi z}{2a} \end{aligned} \tag{10}$$

By multiplying by λ_{Rn} both sides of the equation (10), one obtains the activity of C_{Rn} (z, t) given in equation:

$$C_{Rn}(z,t) = C_{Ra} - C_{ra}\frac{\cosh\left(z\sqrt{\frac{\lambda_{Rn}}{D}}\right)}{\cosh\left(a\sqrt{\frac{\lambda_{Rn}}{D}}\right)} + \\ + \frac{4C_{Ra}}{\pi}\sum_{n=0}^{\infty}\frac{(-1)^n \exp\left(-\left(\frac{(2n+1)^2\pi^2 D}{4a^2} + \lambda_{Rn}\right)t\right)}{(2n+1)\left[1+\left(\frac{4\lambda_{Rn}a^2}{(2n+1)^2\pi^2 D}\right)\right]}\cos\frac{(2n+1)\pi z}{2a} \tag{11}$$

where C_{Rn} and C_{Ra} represent the activity of ^{222}Rn and ^{226}Ra, respectively.

2.1.1 Infinite source model

In another earth model an infinite source C_0 is overlain by an overburden of thickness h, where no radon source exists. In this case the radon transportation equation in the overburden, where radon production rate is zero, can be written as (*Wattanikorn et al,1998*):

$$\frac{d^2C}{dz^2} + \frac{v}{D}\frac{dC}{dz} - \frac{\lambda_{Rn}}{D}C = 0 \tag{12}$$

where C is the radon concentration at depth z, v is the gas flow velocity; D is the diffusion coefficient of radon, and λ_{Rn} is the decay constant. The solution of (12) is:

$$C_{Rn} = C_{Rn0}\exp\left[\frac{v(h-z)}{2D}\right]\frac{\sinh\left[\left(\sqrt{\left(\frac{v}{2D}\right)^2 + \frac{\lambda_{Rn}}{D}}\right)z\right]}{\sinh\left[\left(\sqrt{\left(\frac{v}{2D}\right)^2 + \frac{\lambda_{Rn}}{D}}\right)h\right]} \tag{13}$$

3. Radon measurements

In general Radon measurements can be performed in continuous, integrating or discrete mode, regarding the time duration of measurement, and by using passive devices, when Radon enters the detection system by natural diffusion, or active technique, when gas is pumped in the device, that require electric power.

Some types of the most used detectors for in-soil radon measurements are the following:

a. **Solid State nuclear track detectors**: the most used SSNTD are Cr-39 type or LR-115 one. They are particularly sensitive to alpha particles that, passing trough, produce tracks visible in optical microscope after chemical etching. The main advantages of this kind of detectors, especially for the first type, is that they are cheap, are sensitive only to alpha particles, are unaffected by humidity, low temperature, moderate heating and light. Moreover these passive devices don't need electrical power supply.
b. **Electret detector**: an electret is a dielectric material that exhibits a permanent electrical charge. The particles from Radon decay produce ions within the device that determine

changing in the total charge of the electret. This kind of detector offers several advantages: possibility to store information over relatively long period, independence from moisture in its envelop and ease to read. The main problems are linked to its response curve that does not cover efficiently the very low and very high doses and its sensitivity also to gamma radiations.

c. **Activated charcoal**: this type of detectors is based on the capability of the charcoal to adsorb Radon gas. The analysis is carried out by means of the gamma spectrometry of the Radon products. However with this kind of device measurements can be performed only for 3 – 5 days and they are affected by humidity.
d. **Thermoluminescent detector**: Radon is allowed to enter the detection device volume containing the TLD. A metallic plate, placed at short distance in front of the TLD, can be electrically charged for a better collection efficiency. Radon daughters deposited on the plate decay producing energy storage in the TLD. After appropriate exposition, the TLD is recovered and read out in a TLD apparatus.
e. **Scintillation detector**: the most widely used is the ZnS(Ag) scintillation cell for grab sampling. It is a metal container internally coated with silver activated zinc solphide. Light photons are detected, resulting from the interaction of the alpha particles from radon decaying. For counting the photons, the scintillation cell is coupled to a photomultiplier.

In the last years active devices have been used for continuous measurements of in soil Radon gas. They use prevalently detectors as ionization chamber or silicon detectors. The devices have a probe placed in the soil at a certain depth, the gas Radon enters into the detection chamber or by means of a pump with a fixed flow rate or they can be placed inside the soil and the gas enters into the detection chamber via natural diffusion. This kind of measurements need power supply, not always available in active fault areas, but in the last years the detection systems have been implemented with solar panels, overcoming the problem. These devices have more performance respect to the previous ones because they allow continuous measurements and on-line reading by means of remote data transfer and so they allow to monitor continuously the Radon temporal trend.

Accordingly, the choice among the different possibilities can be guided by the particular interest in radon measurements, whether in time-dependent or in space-dependent variations of the concentrations. In particular, spot measurements (with portable detectors) of soil–gas Radon are useful for the quick recognition of high emission sites to be later monitored for Radon variations in time. SSNTD allow for the temporal monitoring of a relatively large number of sites, but cannot distinguish short-term changes due to their long integration times. Continuous monitoring probes are optimal for defining detailed changes in soil–gas Radon activities, but are expensive and can thus be used to complete the information acquired with SSNTD in a network of monitored sites.

4. Origin and mechanisms of radon anomalies

Most of the researchers define radon anomaly as the positive deviation that exceeds the mean radon level by more than twice the standard deviation.

The origin and the mechanisms of the radon anomalies and their relationship to earthquakes are yet poorly understood, although several in-situ and laboratory experiments have been performed and mathematical modelings have been proposed. The radon observed in case of anomalies correlated with geophysical events may be considered as having two possible

origins. Either it is produced in depth origin or, once produced locally, it is displaced by other interstitial fluids whose motion is triggered by geodynamical events. Both possibilities have been discussed so far but the local origin hypothesis seems to be the most reliable, sustained by experiments too. In order to relate radon anomalies to earthquake occurrence, several scenarios have been proposed. Accordingly to the dilatancy-diffusion model (*Scholz, 1973; Planinic et al, 2001*) the radon anomalies could be related to mechanical crack growth in the volume of dilatancy or to changes in groundwater flow. Consequently either opening of new cracks, widening or closing of old cracks or redistribution of open and closed cracks can happen. In dry rocks opening or closing of cracks will lead to significant changes of the diffusion coefficient of radon. Volumetric changes in the rock will also lead to a subsurface gas flow and therefore to an additional radon transport. If the new open cracks are filled with water the increased water-rock interface leads to an increase in the transfer of radon from the rock matrix to the water. If water filled cracks close, the water will be compressed to another subsurface volume where the emanation from the rock to the water may be different. All these effects result in pressure and water level variations of the relevant aquifer. This also can lead to changes in the mixing ratios for the water which can be observed at the earth's surface. Finally gas flows can also move some groundwater and again all previously discussed mechanisms which are consequences of the redistribution of water in the earth's crust can take effects. This scenario has the drawback that an unreasonably large change in stress or strain is required far away from the epicentre.

An alternative mechanism is the stress corrosion theory, first proposed by *Anderson and Grew (1977)*. It attributes the radon anomalies to slow crack growth controlled by stress corrosion which should precede any mechanical cracking in wet environment. According to the mechanism of stress corrosion radon anomalies may depend on strain rate and local conditions such as rock type, porosity, elasticity, pattern of micro-cracks, degree of saturation, temperature, stress intensity factor and hygroscopic properties.

If the local parameters of the rocks are assumed to be responsible for the radon anomalies an explanation is needed to justify how very small changes in the stress field can produce such effects. From the theory of the earthquake preparation process it could be derived that in a region where the stress reaches a level which is not very far away from rock failure, very small changes in the stress fields result in considerable changes in certain rock parameters. If this theory holds, earthquake sensitivity could be expected only in areas which are highly pressed, for example near fault zone systems, not necessarily seismic active.

According to another kind of mechanism, the compression mechanism proposed by *King (1978)*, the anomalous radon concentration may be due to an increase in crustal compression, impending an earthquake, that squeezes out the soil-gas into the atmosphere at an increased rate. Radon anomalies have been observed at large distance from the earthquake epicentre, resulting from changes in the immediate vicinity of recording station, rather than at the distant focal region. This is accomplished if it is assumed that changes in stress or strain are propagated from the rupture zone to the radon station, leading to variations also in porosity, emanating power or flow rate of the local groundwater, near the radon monitoring station.

When the diffusion constant of radon in a soil of average porosity and moisture content is considered, the calculation shows that radon cannot be detected at a distance larger than a few meters. When radon is pumped by an upward moving carrier, whose motion is of the order of a few microns per second, it of course increases its concentration near the

monitoring station while the underground is depleted in radon. Since the half-life of radon is of 3.82 d, it would take a time larger than what is observed actually for those lower parts to supply by radioactive decay only. A much longer radon gas column than the few meters involved by mere diffusion should be involved. However, the most of the radon would decay away before reaching the detection system. The motion of pore fluids would first of all increase the radon concentration temporarily and then exhaust the available resources for further increase.

4.1 Radon anomaly shapes

When radon concentrations are measured in continuous mode for a long time and with a time resolution of at least one hour, it is possible to classify the observed radon anomalies according to different trends. Typically two shapes can be considered that *Friedman, 1991* classified group A and group B anomalies. Probably the physical process is different for the two groups of anomalies.

The group A shows a very slow increase (or decrease) of the radon concentration with a rate less than 0.1% per hour. This kind of anomaly can be linked to a continuous increase in stress, until the rock fracture occurency.

The second group B is characterized by a fast increase (or decrease) in the radon concentration with a rate of about 1% per hour. Often a fast increase is followed by a rather constant radon concentration. Sometimes anomaly spikes with fast radon change immediately followed by a fast change in the opposite direction. These two kind of B anomalies could be linked to different physical processes or simply to different time scales (*Friedmann, 1991*).

The B-type anomalies can be a local effect, which depends on certain local parameters, or they can be an epicentral effect. In this case the epicentral area must be supposed as origin of the fast change in stress.

For spike anomalies the maximum velocity of the radon concentration change is:

$$V = \frac{1}{\delta C}\left(\frac{dC_{Rn}}{dt}\right)_{\max} \geq \frac{1}{\tau} \tag{14}$$

where C_{Rn} is radon concentration

δC_{Rn} the difference between radon concentration before and after the fast change

τ the time of the fast change (in hours)

From data of V and the epicentral distance d a very rough correlation can be found for d>70km, according to a relation of the form:

$$log(V) = -2log(d) + 4 \qquad [V] = hours^{-1},\ [d] = km \tag{15}$$

Thus by considering V from an observed anomaly a rough estimation of the distance from the epicentre can be made.

5. Forecasting relations

Earthquake prediction means to forecast place, time and magnitude of an earthquake. From the analysis of a wide variety of radon data available from different countries and

earthquakes with M<3, *Rikitake* proposed an empirical relation between the time interval t between radon anomaly and earthquake occurrence and magnitude of an earthquake (*Rikitake, 1976*):

$$Log\ t = 0.76M - 1.83 \tag{16}$$

The relation was modified by *Fleischer* depending on the time interval: (*Rikitake, 1976*):

$$Log\ t = M - 2.16 \quad \text{for } 0{,}1<t<7 \text{ days} \tag{17}$$

$$Log\ t = 0.62M - 1.0 \quad \text{for } t> 7 \text{ days} \tag{18}$$

Starting from the radon diffusion equation and analyzing radon data from many countries , *Ramola et al (1988)* proposed an empirical relation to predict the magnitude of strong earthquakes (M>5) :

$$M = 2log(\lambda_{Rn}\Delta C_{Rn}/KT) - 15.26 \tag{19}$$

where ΔC_{Rn} is the anomalous variation of radon concentration, T rise time for radon anomaly and K is a constant (3.96×10^{-17}).

Several models were suggested in the past to evaluate the size of the area subject to changes in the tensional state. The models are based on assumption of homogeneity and isotropy of the ground or little heterogeneity around the focal zone.

In particular, *Dobrovolsky et al.(1979)* proposed some relations, taking into account an ellipsoidal inclusion with a 30% of heterogeneity with respect to the surrounding ground. He obtained the following relations that connect the magnitude M and the maximum distance R that the deformation can reach with the amplitude of the deformation E:

$$\begin{aligned} E &= \frac{10^{1.5M-9.18}}{R^3} && M < 5.0 \\ E &= \frac{10^{1.3M-8.19}}{R^3} && M \geq 5.0 \end{aligned} \tag{20}$$

On the basis of these relationships deformations that can generate an anomaly were evaluated to be of the order of 10^{-8} (*Hauksson, 1981*).

Since radon anomalies seem to have a local origin, it is important to consider a relationship between the magnitude and the distance to the epicentre.

If the maximum possible distance d between the epicentre of a forthcoming earthquake and the spring which can be influenced by this earthquake is proportional to the volume of the pre-stressed lithosphere or to the energy of the earthquake respectively, a relation holds of the form (*Friedmann, 1991*):

$$M = a \bullet log(d) + b \quad a,b = const \tag{21}$$

From known relations between magnitude M and the volume of the focal zone the a-value can be determined to be about 2. *Dobrovolsky et al.(1979)* observed that precursory phenomena are not observed beyond the distance d, thus to estimate roughly the radius of the effective precursory manifestation zone, they proposed the formula:

$$d = 10\ exp\ 0.43\ M \tag{22}$$

where d is in km and M is the magnitude of the earthquake. It means that a magnitude 5 earthquake will be detected by means of precursory phenomena at a distance not greater than 142 km.
By collecting and analyzing radon anomaly data *Hauksson et and Goddard (1981)* found a similar relation. It is important that all these relations do not differ by more than 30% in d for $M \geq 4$. But the most interesting result is that all observed precursors are limited by a straight line which coincides practically with a computed deformation of 10^{-8}. Summarizing the results in only one formula it is possible to estimate the magnitude-limit Mmin for the possibility of detecting a precursor anomaly at a distance d (in Km) to be

$$M \geq Mmin = (2.3 \pm 0.2)\log(d) - (0.4 \pm 0.3) \tag{23}$$

The constants in (23) may differ for different areas, however it is a good over all approximation. Of course we can expect that certain directions from the future epicentre are favored compared to others. The limit (23) must be seen as the limit for the favored directions.
Another relation was proposed by *Martinelli, 1992* for which:

$$M = 2.4\log d - 0.43 - 0.4 \tag{24}$$

While precursor time t (in days) related to the magnitude M and the epicentral distance d (in km) can be estimated as follows:

$$\log dt = 0.63M + (-)\ 0.15 \tag{25}$$

Long term series analyses have revealed a relation between the amplitude and duration of the gaseous anomaly and the magnitude M of the expected earthquake (*Barsukov et al., 1984*):

$$M = K\sqrt{S} \tag{26}$$

where K is a correction factor and S is the area of the peak anomaly, thus the shape of the peak is a diagnostic parameter for the forthcoming seismic event.

6. Radon anomalies and earthquakes: Some cases

Several radon investigations have been carried out all over the world. Measurements of this gas both in soil and in groundwater have shown that spatial and temporal variations can provide information about geodynamical events.
In the following we report some examples of studies among the numerous ones performed around the world with the purpose to relate abnormal radon emission to seismic events.
The pioneering work on radon investigation in groundsoil was performed at an active fault zone for two years (*Hatuda, 1953*). Radon concentration in soil gas was measured and anomalous radon concentrations were reported before the strong earthquake (M=8) of Tonankai (December 1944, Japan).
Some years later Tanner (*Tanner, 1959*) evidenced the importance of the influence of the meteorological parameters on radon measurements and in 1964 he suggested that radon could be used as tracer to discover uranium deposits or to predict earthquakes (*Tanner, 1964*).

The first evidence of radon in groundwater as precursor of earthquakes was observed in Tashkent (*Ulomov, 1967*). The author observed that the radon concentration in a spring near Tashkent increased constantly before the M=5.2 earthquake on April 15, 1966.
Afterward many studies have been performed about radon anomalies and earthquakes.
In the following some examples are reported on ground radon monitoring in the most seismic regions in the world.

6.1 Japan

As already cited, studies performed by *Hatuda (Hatuda 1953),* at an active fault zone evidenced anomalous radon concentration before the strong earthquake (M=8) of Tonankai.
Radon anomalies were recorded before the Nagano Prefecture earthquake (M= 6.8) on September 14, 1984 (*Hirotaka et al., 1988*). The authors observed a gradual increase in radon counts three months before the quake and a remarkable increase two weeks before the shock.
For about twenty years an extensive network of groundwater radon monitoring has been operated mainly by the University of Tokyo and the Geological Survey of Japan for the purpose of earthquake prediction in eastern Japan. In figure 1. a significant example of radon anomaly is reported (*Igarashi et al., 1995)*. The authors performed radon concentration analysis in a well 17 m deep from November 1993 to March 1995 and observed stable radon concentration of 20 Bq/l at the end of 1993. The radon concentration started to increase gradually from October 1994 reaching 60 Bq/l on November 1994, three times that in the same period one year before. Furthermore, a sudden increase of radon concentration, recorded on 7 January was followed by a sudden decrease on 10 January, 7 days before an earthquake of magnitude 7.2. After the earthquake, the radon concentration returned to the pre-October 1994 levels. The main result of this example is that it is possible to observe strange behavior before an anomaly. This, for instance, as in this case, must be preceded by a continuous increasing in the background level till its manifestation. Naturally it depends on the geodynamical evolution of the area

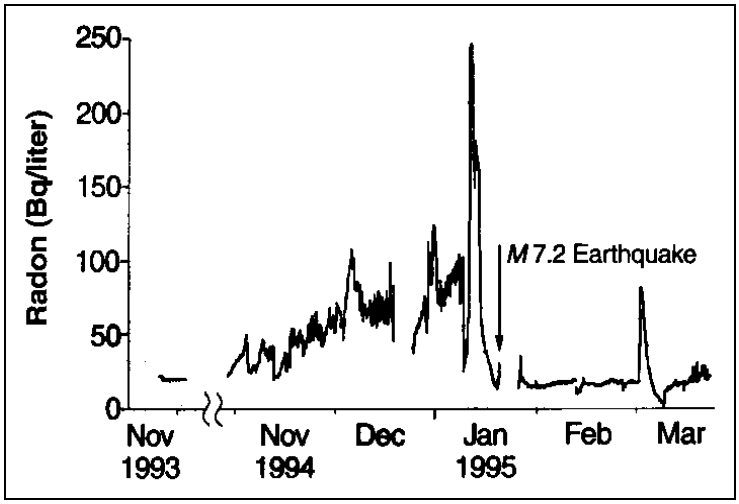

Fig. 1. Radon concentration data at the well in the southern part of Nishinomiya city, Japan [From . *Igarashi et al., 1995*]

6.2 India

In Bhatsadam, Maharashtra, India, major earthquakes occurred during August 1983 - July 1984. In that region radon concentration was measured by *Rastogi et al.(1986).* They found an increase in radon concentration during March–April 1984 when seismicity was high enough. Precursory phenomena of radon in earthquake sequence were observed by *Rastogi et al. (1987)* and by other groups at the Osmansagar reservoir, Hederabad, India during January–February, 1982 (*Rastogi et al.,1987*). An earthquake with a magnitude of 3.5 occurred on January 14, 1982 with subsequent seismic events. There was an increase of radon concentration in soil gas during February due to those high seismic activities.

Singh et al. (1991) performed a daily radon monitoring in soil-gas in Amritsar from 1984 to 1987. They recorded radon anomalies before different earthquakes: June 1988 (M=6.8); April, 26, 1986 (M=5.7); July 1986 (M=3.8); Kangra earthquake March 1987 (M=7) and May 1987 (M= 5).

Virk and Singh (1994) carried out daily measurements of radon in soil-gas and groundwater at Palampur since 1989 and radon anomaly was recorded simultaneously in both soil- gas and groundwater. Weekly integrated data also showed abnormal radon behaviour during first week of October, 1991 at different recording stations. These recorded anomalies were correlated with an earthquake of magnitude 6.5 occurred in Uttarakashi area in October 1991.

6.3 Syria

Al-Hilal et al. (1998) recorded groundwater radon data for two years, during 1993 and 1994 at monthly intervals, from two selected monitoring sites of the northern extension of the Dead Sea Fault System. The results showed that measured radon concentrations fluctuate around the mean value, showing some variations with peak values, about two or three times the mean value, preceding some seismic events. It is possible to consider those anomalies related to changes in crustal strain and thereby to indicate a probable relation with the local seismicity. Nevertheless, the authors conclude that this does not necessarily means that it is possible to relate univocally these radon peaks to seismic event occurrence, but rather, it may indicate the possibility of using groundwater radon variations as a useful tool.

6.4 Turkey

In soil radon gas was monitored by *Friedmann et al. (1988)* in a network of five monitoring sites along 200 km at the North Anatolian Fault Zone, Bolu. They observed an increase in radon concentration during the strong earthquake (M=5.7) on July 5, 1983. In order to search some relation between earthquakes and radon concentration variations, more recently *Inceoz et al (2006)* performed a radon investigation at the North and East Anatolian fault system. They found that radon anomaly was quite significant in particular over the fault line but not away from this line.

Also the Aksehir fault zone was investigated, by *Baykara and Dogru (2006)* and *Yalim et al. (2007),* trough radon measurements in well water. Although the observed radon levels could be related to several seismic activity that at the fault region occurred with high magnitude, the authors did not infer correlation between seismic activity and radon concentration.

Radon concentration in thermal water was investigated by *Erees et al. (2006,2007)* at two thermal springs at the Denizli basin site and significant radon anomalies were observed before earthquakes with magnitude between 3.8 and 4.8.

6.5 Italy

In the last ten years systematic studies on Radon as precursor of geophysical events have been carried out on Mt. Etna since 2001 (*Immè et al, 2005; Immè et al. 2006a, Immè et al, 2006b; La Delfa et al. 2007; La Delfa et al., 2088; Morelli et al. 2006, Morelli et al., 2011*). In particular two sites were investigated among the cropping up structural discontinuities, which lie along the NE-SW direction through the volcano. One site (*Biancavilla*) is in the SW flank, while the other one (*Vena*) is in the NE flank (circles in fig.2). Continuous monitoring was performed by using active systems with time resolution of 10 min. Capillary probes inserted into the soil at one meter depth, allowed to reduce influence from the meteorological parameters that were measured too.

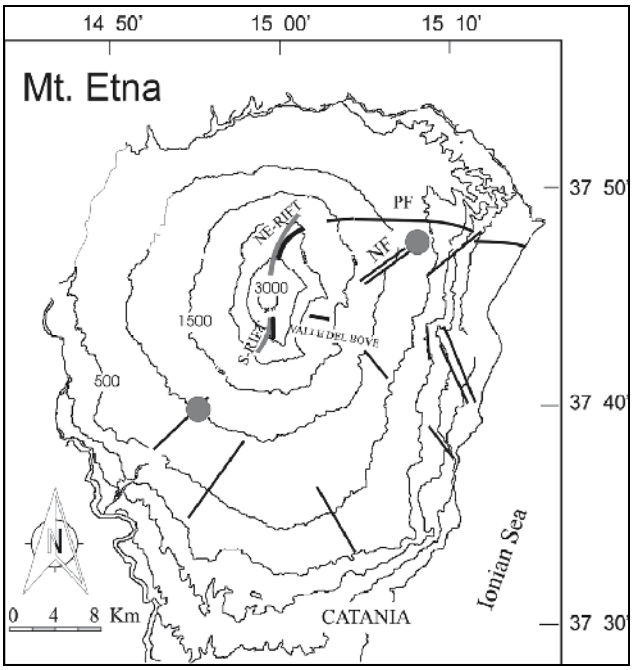

Fig. 2. Mt. Etna map– Circles indicate the sites where devices for continuous in soil gas Radon monitoring were positioned

Several studies conducted in tectonic areas evidenced relation to earthquakes of magnitude bigger than 3 (*Igarashi et al., 1995; Virk et al., 1994, Al-Hilal et al., 1998*). The etnean area is characterized by a big number of earthquakes, up to about thousands per day before an eruptive period (*Benina et al,1984; Patanè et al, 1995*), but with low magnitude (< 3) and rarely they exceed magnitude 4. Moreover Mt. Etna has a very complex structure, due to the occurrence of both tectonic and volcanic phenomena. Major results have been obtained respect to a possible link between radon concentration and volcanic activity. Nevertheless, some relations were also observed with seismic events as reported by *Immè et. al, 2005*, the data are referred to the period 2001-2002. Radon concentration values started to increase the 27th of October 2002, reached the maximum the 1st of November 2002 and the minimum the 3rd of November 2002. During this period several earthquakes of magnitude higher than 3 occurred, some of them reached values up to M= 4.5 (29/10/02 time 09:02:00 epicentral area of *Santa Venerina*).

It was observed that, as well as the radon raises the earthquake daily rate and strain release raise, correspondently at the eruption beginning.
A radon anomaly was recorded before the November 3rd event (M= 3.5), with epicentral zone close (less than 1 km) to the *Vena* Station (NE station), also associated to evident soil fractures.

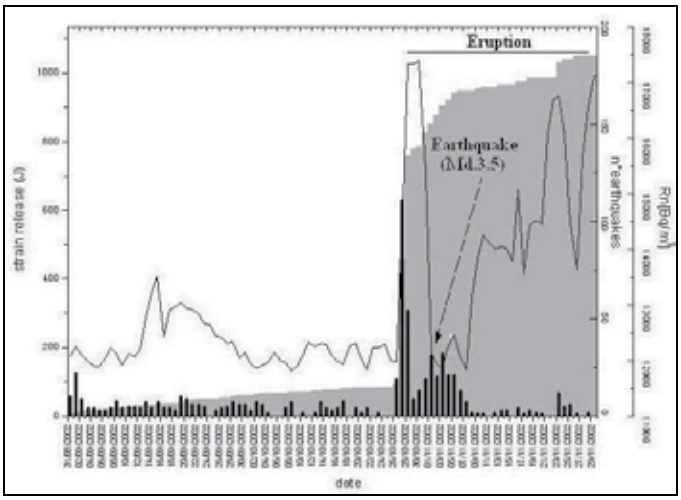

Fig. 3. Radon concentration (black line), daily earthquakes rate (black column bar) and strain release (grey histogram) measured in the period between 1st September 2002 and 30th November 2002 (Vena station).[*Immè et al., 2005*]

More recently a systematic radon investigation was extended to fault systems, in particular the Pernicana fault, one of the more active etnean fault, was chosen as first monitoring area. In particular, two different horizontal profiles, orthogonally to the main fault plane, were investigated. The first one was located at 1400m asl, the second one at 1370m asl (*Giammanco et al, 2009*). Each profile consisted of ten measurement points where CO_2 efflux values were also measured. Concentrations of ^{222}Rn were obtained by means of three different methodologies: passive, spot and continuous. The pattern of soil ^{222}Rn values measured in the two profiles is clearly similar: higher values were generally recorded on the up thrown side of the fault and the lowest values occurred generally close to the main fault plane. Differently to radon, higher CO_2 emissions were recorded on the fault plane. This behavior can be justified by the in-soil gas transport mechanism. In particular, along the main fault plane, advective transport of deep gases (CO_2, Rn) occurs because of the high ground fracturation and permeability. Near the surface, dilution of radon by CO_2 prevails, thus producing lower radon values.
This kind of investigations is useful to study the dynamics of the faults and the possible earthquake mechanisms.

7. Conclusion

From many years a lot of efforts have been done in order to improve in-situ radon data monitoring and analysis, technical methodologies and mathematical modeling, with the aim to reinforce the link between ground radon concentration anomalies and geodynamical

events. Measurements of radon gas in soil and in ground water have been carried out all over the world and the results seem to indicate the radon as a good indicator of crustal activity such as earthquakes. However, the current literature describing the possible correlation between radon levels and earthquake activity uses such qualifying and caution words as possible, apparent, limited, could, sometimes, may be, and so on.

It is clear that in some cases there are precursor changes in radon levels, but that the causal relationship or mechanism relating these to earthquake activity is not yet well understood. Thus, even if some results seem to suggest that geodynamical events could influence radon concentrations, however, because of the complexity of its transport mechanism, the correlation needs more investigations in order to clearly and firmly established it.

Further contributions can be obtained from more extended continuous data recording, in particular near active faults, and from the comparison with other earthquake precursors.

8. References

Al-Hilal, M., Sbeinati, M.R. and Darawcheh, R. (1998) Radon variation and microearthquakes in western Syria. *Applied Radiation and Isotopes* Vol.49, Nos.1-2, pp. 117-123

Anderson, O.L., and Grew, P.C. (1977) Stress corrosion theory of crack propagation with application to geophysics. *Rev. Geophys. Space Phys.,* Vol. 15, 77-104.

Antsilevich, M.G. (1971). An attempt to forecast the moment of origin of recent tremors of the Tashkent earthquake through observations of the variation of radon. *Izvestiâ Akademii nauk Uzbekskoj* SSR 188-200.

Barsukov, V.l., Varshal, G.M., Garanin, A.B., and Serebrennikov, V.S. (1984). Hydrochemical Precursors of Earthquakes. *Earthquake Prediction, UNESCO, Paris,*169-180.

Baykara, O., Dogru, M. (2006). Measurements of radon and uranium concentration in water and soil samples from East Antolian active fault systems (Turkey). *Radiation Measurements* 41 (3), 362–367.

Benina, A., Imposa, S., Gresta, S., Patanè, G. (1984). Studio macrosismico e strutturale di due terremoti tettonici avvenuti sul versante meridionale dell'Etna, *Atti III convegno annuale del GNGTS;* 931-946

Dobrovolsky, I.P., Zubkov, S.I., Achkin, V.I. (1979). Estimation of the size of earthquakes preparation zone. *Paleoph.,*Vol.117, 1025-1044.

Erees, F.S., Yener, G., Salk, M., Ozbal, O. (2006). Measurements of radon content in soil gas and in the thermal waters in Western Turkey. *Radiation Measurements,* 41, 354–361.

Erees, F.S., Aytas, S., Sac, M.M., Yener, G., Salk, M. (2007). Radon concentrations in thermal waters related to seismic events along faults in the Denizli Basin, Western Turkey. *Radiation Measurements*, 42, 80–86.

Friedmann, H., Aric, K., Gutdeutsch, R., King, C.Y., Altay, C., Sav, H. (1988). Radon measurements for earthquake prediction along the North Anatolian Fault Zone: a progress report. *Tectonophysics* 152 (3–4), 209–214.

Friedmann, H. (1991) Selected problems in Radon measurement for earthquake prediction *Proceedings of the Second workshop on Radon Monitoring in Radioprotection, Environmental and/or Earth Science*, Furlan, G. and Tommasino, L. (Ed.) World Scientific.307-316.

Gauthier, P-J. and Condomines, M. (1999). ^{210}Pb - ^{226}Ra radioactive disequilibria in recent lavas and radon degassing: inferences on the magma chamber dynamics at Stromboli and Merapi volcanoes. *Earth and Planetary Science Letter,* Vol. 172, 111-126.

Giammanco, S., Immè, G., Mangano, G., Morelli, D., Neri, M. (2009). Comparison between different methodologies for detecting Radon in soil along an active fault: the case of the Pernicana fault system, Mt. Etna(Italy). *Applied radiation and Isotopes* 67, 178 -185.

Hauksson, E. (1981). Radon content of groundwater as an earthquake precursor: evaluation of worldwide data and physical basis. *Journal of geophysical research,* Vol. 86, 9397-9410.

Hauksson, E., Goddard J.G (1981). Radon earthquake precursor studies in Iceland. *J. Geophys. Res.* , Vol.86, No. B8, 7037-7054

Hatuda, Z. (1953). Radon content and its change in soil air near the ground surface. *Memoirs of the College of Science*, University of Kyoto, Series B 20, 285–306.

Hirotaka, U., Moriuchi, H., Takemura, Y., Tsuchida, H., Fujii, I., Nakamura, M. (1988). Anomalously high radon discharge from the Atotsugawa fault prior to the western Nagano Prefecture earthquake (m 6.8) of September 14, 1984. *Tectonophysics* 152 No 1–2, 147–152.

Igarashi, G., Saeki, S., Takahata, N., Sumikawa, K., Tasaka, S., Sasaki, Y., Takahashi, M., Sano ,Y. (1995). Ground-water radon anomaly before the Kobe earthquake in Japan *Science* Vol. 269, 60-61.

Imamura, G. (1947). Report on the observed variation of the Tochiomata hot spring immediately before the Nagano earthquake of july 15, 1947*, Kagaku*, 11, 16-17

Immè, G., La Delfa, S., Lo Nigro, S., Morelli D., Patanè, G. (2005). Gas Radon emission related to geodynamic activity of Mt. Etna. *Annals of Geophysics*, 48 N.1, 65-7.

Immè, G., La Delfa, S., Lo Nigro, S. , Morelli D., Patanè, G. (2006a) Soil Radon concentration and volcanic activity of Mt. Etna before and after the 2002 eruption. *Radiation Measurements* Vol.41, 241-245.

Immè, G., La Delfa, S., Lo Nigro, S., Morelli D., and Patanè, G. (2006b). Soil Radon monitoring in NE flank of Mt. Etna (Sicily), *Applied Radiation and Isotopes,* Vol.64, 624-629.

Inceoz, M., Baykara, O., Aksoy, E., Dogru, M. (2006). Measurements of soil gas radon in active fault systems: a case study along the North and East Anatolian fault systems in Turkey. *Radiation Measurements* 41 (3), 349–353.

King, C.Y. (1978). Radon emanation on San Andreas Fault. *Nature*, Vol. 271, 576-519.

La Delfa, S., Immè, G., Lo Nigro, S., Morelli, D., Patanè, G., Vizzini, F. (2007) Radon measurements in the SE and NE flank of Mt. Etna (Italy). *Radiation Measurements*, Vol. 42, 1404-1408

La Delfa, S., Agostino, I., Morelli, D., Patanè, G. (2008). Soil Radon concentration and effective stress variation at Mt Etna (Sicily) in the period January 2003-April 2005 *Radiation Measurements* 43 1299- 1304.

Martinelli, G. (1992). Fluidodynamical and chemical features of radon 222 related to total gases: implications on earthquakes prediction topics. IAEA-TECDOC-726 Isotopic and geochemical precursors of earthquakes and volcanic eruptions *Proceedings of an Advisory Group Meeting held in Vienna, 9-12 September 1991*, 48-62.

Morelli, D., Immè, G., La Delfa, S. , Lo Nigro, S., Patanè, G. (2006). Evidence of soil Radon as tracer of magma uprising at Mt. Etna. *Radiation Measurements* Vol. 41, 721-725

Morelli, D., Immè, G., Altamore, I., Cammisa, S. , Giammanco, S. , La Delfa, S. , Mangano, G., Neri, M., Patanè, G. (2011). Radionuclide measurements, via different methodologies, as tool for geophysical studies on Mt. Etna. *Nuclear Instruments and Methods in Physics Research A,* DOI NIMA 10.1016/j.nima.2011.01.172

Patanè, G., Coco, G., Corrao, M., Imposa, S. Montalto, A. (1995): Source parameters of seismic events at Mount Etna Volcano, Italy, during the outburst of the 1991-1993 eruption. *Phys. earth and Planet. Inter.*, 89, 149-162

Planinic, J., Radolic, V., Lazanin, Z. (2001). Temporal variation of radon in soil related to earthquakes. *Applied Radiation and Isotopes* ,Vol. 55, 267-272.

Ramola, R.C., Sing, S. and Virk, H.S. (1988). The correlation between radon anomalies and magnitude of earthquakes. *Nucl. Tracks Radiat. Meas.* ,Vol. 15, 689-692.

Rastogi, B.K., Chadha, R.K., Raju, I.P., (1986). Seismicity near Bhatsa reservoir, Maharashtra, India. *Physics of the Earth and Planetary Interiors* 44 (2), 179–199.

Rikitake, T., (1976). Earthquake prediction developments in solid earth. *Geophysics.,* Vol.9 357

Sabol, J. and Weng, P.-S. (1995). *Introduction to radiation protection dosimetry*. World Scientific, Singapore

Scholz, C.H., Sykes, L.R. and Aggarwal, Y. P.(1973). Earthquake prediction a physical basis. *Science*, Vol. 181, 803-810.

Shiratoi, K., (1927). The variation of radon activity of hot spring . Science Reports of the Tohoku Imperial University, Series 3 (16), 1725-1730.

Spitsyn, V. I., (1926). Collection of studies on radium and radioactive ores, 264

Tanner, A.B. (1959). Meterological influence on radon concentration in drill holes. *Mining Engineering,* Vol.11, 706-708.

Tanner, A.B. (1964). Radon migration in the ground : a supplementary review. The natural radiation environment. In Lowder, W.M. (Ed.). symposium proc. Houston, Texas, April 10-13, 1963. University of Chicago Press. Chicago, III, 161-190.

Singh, M., Ramola, R. C., Singh, B. , Singh S. and Virk, H.S.(1991). Radon anomalies: correlation with seismic activities in northern India. *Proceedings of the Second workshop on Radon Monitoring in Radioprotection, Environmental and/or Earth Science*, Furlan, G. and Tommasino, L. (Ed.) World Scientific.,354-375.

Ulomov, V.I., Zakharovc, A, I. and Ulomova, N.V. (1967). Tashkent earthquake of April 26, 1966, and its aftershocks. *Akad Nauk SSSR, Geophysic* 177, 567-570

Virk, H. S. and Singh, B. (1994). Radon recording of Uttarkashi earthquakes. *Geophysical Research Letters*, Vol.21, No.8, pp.737-740

Wattananikorn, K., Kanaree, M. and Wiboolsake, S. (1998). Soil gas radon as an earthquake precursor: some considerations on data improvement. *Radiation Measurements* Vol. 29, No.6, pp.593-598.

Yalim, H.A., Sandikcioglu, A., Unal, R., Orhun, O., (2007). Measurements of radon concentrations in well waters near the Aksehir fault zone in Afyonkarahisar, Turkey. *Radiation Measurements* 42, 505–508.

8

Application of Recurrent Radon Precursors for Forecasting Local Large and Moderate Earthquakes

Ming-Ching T. Kuo
National Cheng Kung University
Taiwan

1. Introduction

Measurement of radon-222 in groundwater has been frequently used in earthquake prediction (Igarashi et al. 1995; Liu et al. 1985; Noguchi & Wakita 1977; Teng, 1980; Wakita et al. 1980; Kuo et al. 2006, 2010a, 2010b). According to a worldwide survey (Hauksson 1981; Toutain & Baubron 1999), more than 80 % of radon (Rn-222) anomalies associated with earthquakes show increases in radon concentration precursor to a rupture while a few anomalies manifested decreases in radon. The purpose of this chapter is to provide a practical guide of monitoring groundwater radon for the early warning of local disastrous earthquakes. In this chapter, methods of monitoring groundwater radon including procedures of sample collection and radon determination will be addressed. The following sections outline suitable geological conditions to consistently catch precursory declines in groundwater radon, in-situ radon volatilization mechanism for interpreting anomalous decreases in groundwater radon prior to earthquakes, and mathematical model for quantifying gas saturation developed in newly created cracks preceding an earthquake. Case studies are provided to illustrate the application of recurrent radon precursors for forecasting local large and moderate earthquakes.

2. Sample collection radon determination

Accurate sampling for radon measurements depends on appropriate monitoring wells. Because radon concentration in groundwater relates to emanation rates of geological layers, representative sampling must be from properly constructed wells. A submersible pump is commonly used in monitoring wells for groundwater sampling except artesian wells. Every sampling starts with flushing the stagnant water in the well and especially in the screen zone. Inadequate purging can be a major source of error, because the water sample is a mixture of stagnant water from the well bore, pore water from the filter gravel and groundwater influenced by the natural emanation rate of the aquifer. Fig. 1 shows the radon concentration in the well discharge during continuous sampling in a monitoring well. During the first period of flushing, the radon concentration of the water samples is practically zero and then increases rapidly to 529 pCi/L. The mean radon concentration measured for this monitoring well was 529 ± 19 pCi/L (eleven samples). A minimum of 3 well-bore volumes was purged before taking samples for radon measurements.

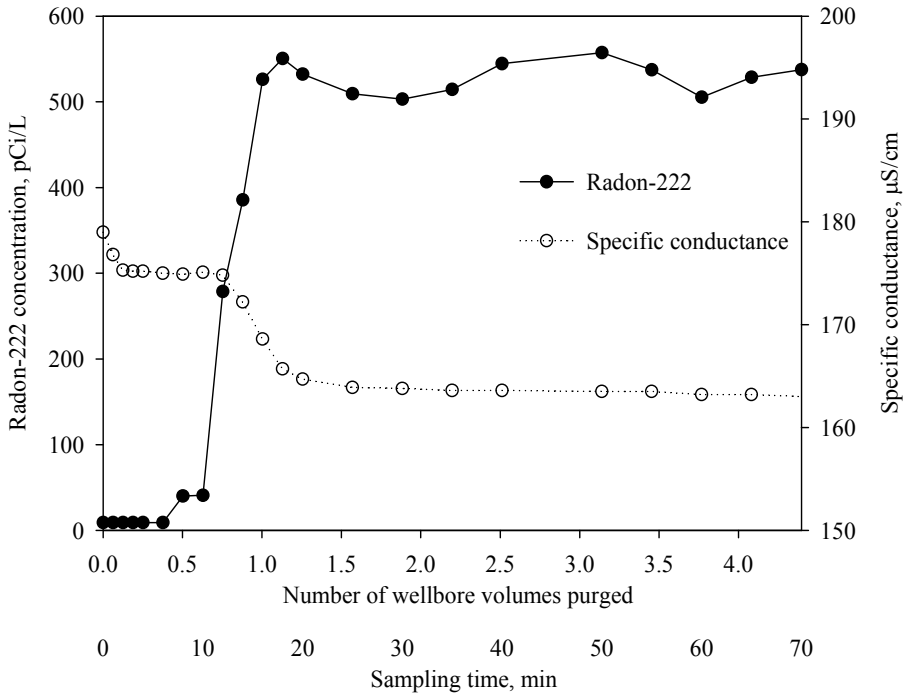

Fig. 1. Radon concentration and electrical conductivity in the well discharge during continuous sampling in a deep observation well

A 40-ml glass vial with a TEFLON lined cap was used for sample collection. After collecting a sample, the sample vial was inverted to check for air bubbles. If any bubbles were present, the sample was discarded and the sampling procedure repeated. The date and time of sampling was recorded and the sample stored in a cooler. The maximum holding time before analysis was 4 days.

For the determination of the activity concentration of radon-222 in groundwater, a modified method described by Prichard and Gesell (1977) was adopted. Radon was partitioned selectively into a mineral-oil scintillation cocktail immiscible with the water sample (Noguchi 1964). The sample was dark-adapted and equilibrated, and then counted in a liquid scintillation counter (LSC) using a region or window of the energy spectrum optimal for radon alpha particles (Lowry 1991).

Radon concentrations were determined by drawing a 15-ml sample directly from a field sample into a clean syringe. Care was taken to prevent aeration of the samples in the process. The samples were then injected beneath a 5-ml layer of mineral-oil-based scintillation solution in 24-ml vials. The vials were vigorously shaken to promote phase contact, dark-adapted and held for at least three hours to ensure equilibrium between radon-222 and its daughters, and then assayed with a liquid scintillation counter. The results were corrected for the amount of radon decay between sampling and assay.

The results of the measurements were determined in units of counts per minute (cpm). It was essential to ensure that only the activity of radon-222 was measured. Using the TRI-CARB software of Packard 1600TR, it was possible to view the alpha spectrum (Fig. 2). The peaks of radon-222 (5.49 MeV), polonium-218 (6.00 MeV) and polonium-214 (7.69 MeV) can be distinguished.

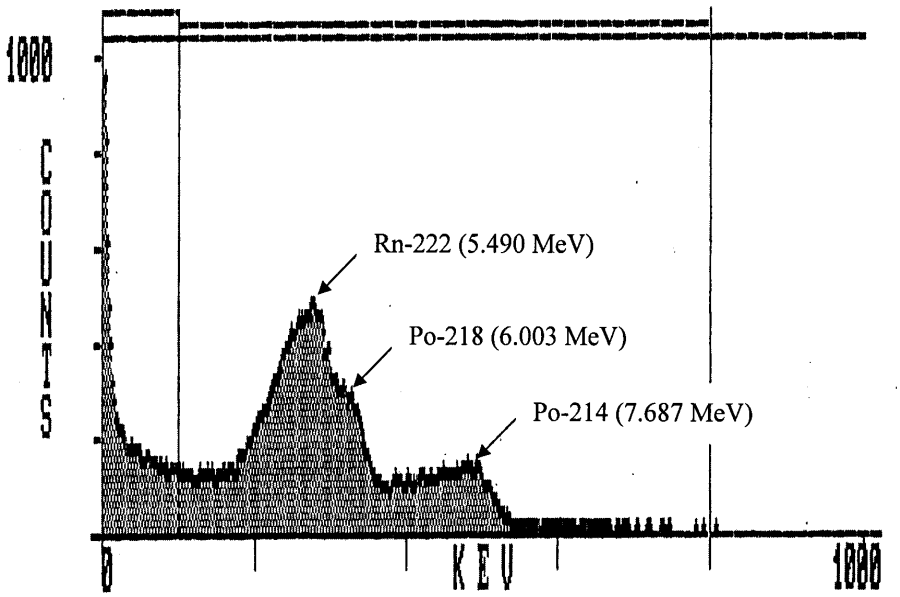

Fig. 2. Alpha spectrum of radon-222 and its daughter nuclides represented by TRI-CARB software

A calibration factor for the LSC measurements of 7.1 ± 0.1 cpm/pCi (Fig. 3) was calculated using an aqueous Ra-226 calibration solution, which is in secular equilibrium with Rn-222 progeny. For a count time of 50 min and background less than 6 cpm, a detection limit below 18 pCi/L was achieved using the sample volume of 15-ml (Prichard et al. 1992).

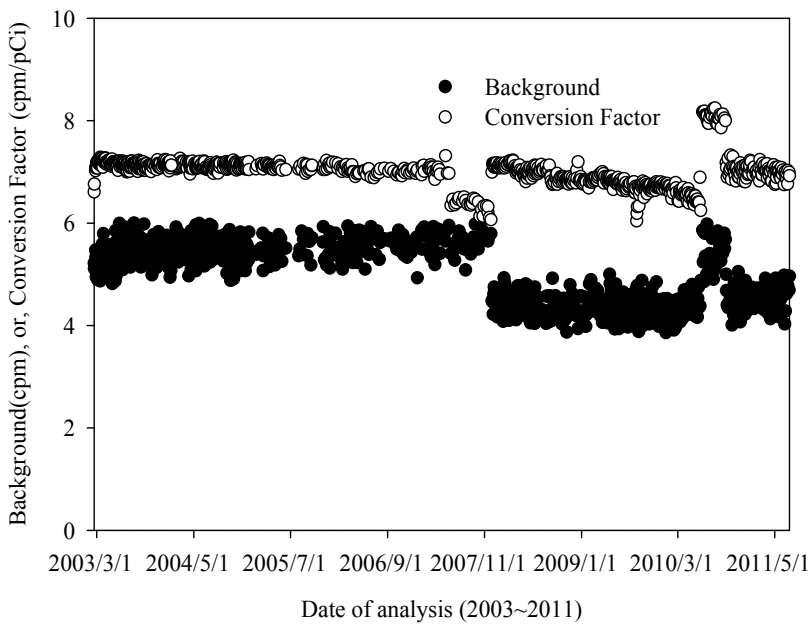

Fig. 3. Calibration factor and background for LSC measurements

Verification of radon-222 as the radioisotope responsible for activity in the well water tested was obtained by the repeated counting of three samples from two wells. The half-life of 3.841 days experimentally determined for samples from Well Liu-Ying (I) located in Tainan Plain, Taiwan compares favorably with the accepted value of 3.825 days as shown in Fig. 4. When the counting vials are lack of tightness, radon will escape from counting vials and the half-life times experimentally determined for samples will be apparently shorter. Fig. 4 also shows an example of such a case from Well Wen-Tsu (II) located in Choshui River Alluvial Fan, Taiwan.

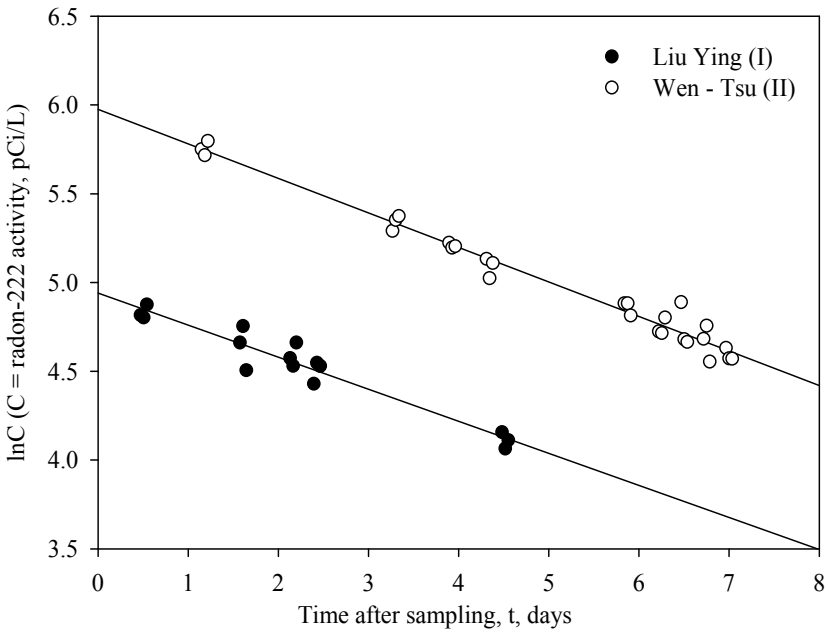

Fig. 4. Measurement of half life from semi-logarithmic decay curve

3. Suitable geological conditions to catch recurrent radon precursors

The 2003 Chengkung earthquake of magnitude (M) 6.8 on December 10, 2003 was the strongest earthquake near the Chengkung area in eastern Taiwan since 1951. The Antung radon-monitoring well (D1, Fig. 5) was located 20 km from the epicenter. Approximately 65 days prior to the 2003 Chengkung earthquake, precursory changes in radon concentration in ground water were observed. Specifically, radon decreased from a background level of 780 pCi/L to a minimum of 330 pCi/L (Fig. 6). Both geological conditions near the Antung hot spring and the vapor-liquid phase behavior of radon were investigated to explain the anomalous decrease of radon precursory to the 2003 Chengkung earthquake.

The production interval of the well ranges from 167 m to 187 m below ground surface and is pumped more or less continuously for water supply purposes. Discrete samples of geothermal water were collected for analysis of radon (Rn-222) twice per week. Liquid scintillation method was used to determine the activity concentration of radon-222 in ground water (Noguchi 1964; Prichard et al. 1992). The radon concentration was fairly stable (780 pCi/L in average) from July 2003 to September 2003 (Fig. 6). Sixty-five days before the magnitude (M) 6.8 earthquake (December 10, 2003), the radon concentration of ground

water started to decrease and continued to decrease for 45 days. Twenty days prior to the earthquake, the radon concentration reached a minimum value of 330 pCi/L and before starting to increase. Just before the earthquake, the radon concentration recovered to the previous background level of 780 pCi/L. The main shock also produced a sharp anomalous coseismic decrease (~300 pCi/L). After the earthquake, some irregular variations were observed, which we interpret as an indication that the strain release by the main shock was not complete and that some accumulation and release of strain continued in the region.

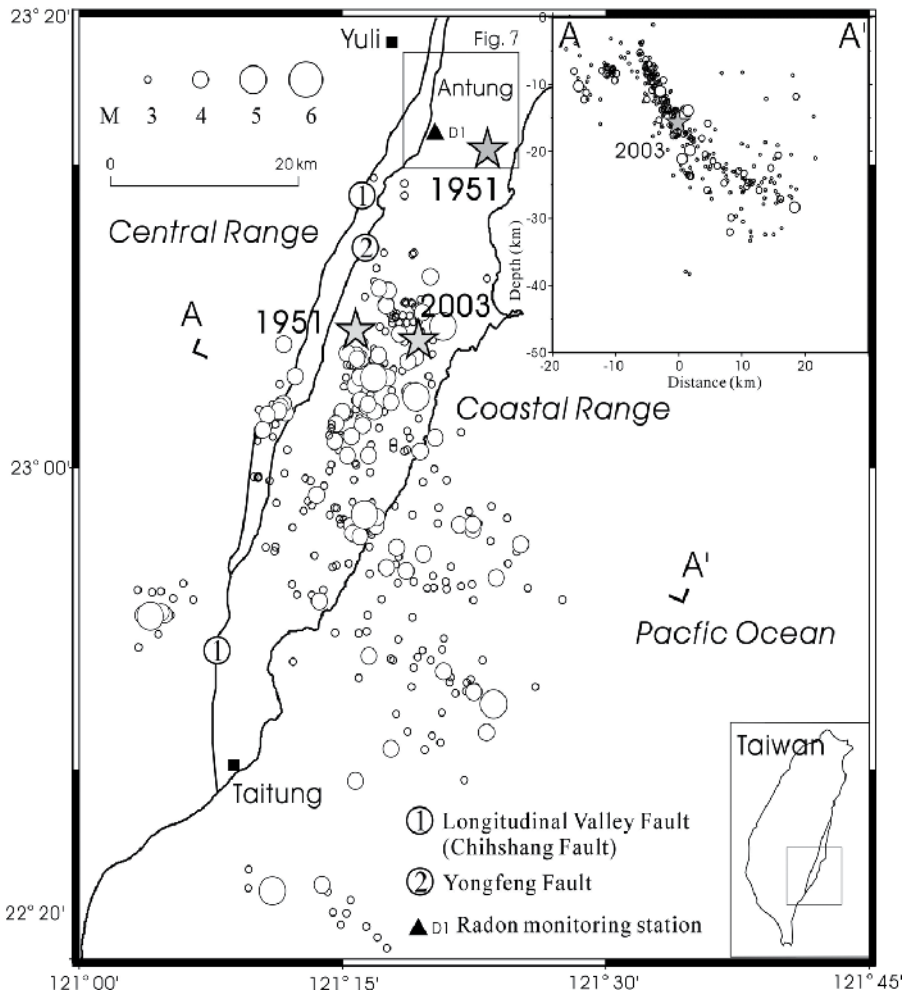

Fig. 5. Map of the epicentral and hypocentral distributions of the mainshock and aftershocks of the 2003 Chengkung earthquake and 1951 mainshocks (star: mainshock, open circles: aftershocks).

The Antung hot spring (Fig. 7) is in a unique tectonic setting located at the boundary between the Eurasian and Philippine Sea plates near the Coastal Range. Four stratigraphic units are present. The Tuluanshan Formation consists of volcanic units such as lava and volcanic breccia as well as tuffaceous sandstone. The Fanshuliao and Paliwan Formations

consist of rhythmic sandstone and mudstone turbidites. The Lichi mélange occurs as a highly deformed mudstone that is characterized by penetrative foliation visible in outcrop. The Antung hot spring is situated in a brittle tuffaceous-sandstone block surrounded by a ductile mudstone of the Paliwan Formation (Chen & Wang 1996). Well-developed minor faults and joints are common in the tuffaceous-sandstone block displaying intensively brittle deformation. It is possible that these fractures reflect deformation and disruption by the nearby faults. Hence, geological evidence suggests the tuffaceous-sandstone block displays intensively brittle deformation and develops in a ductile-deformed mudstone strata. Ground water flows through the fault zone and is then diffused into the block along the minor fractures.

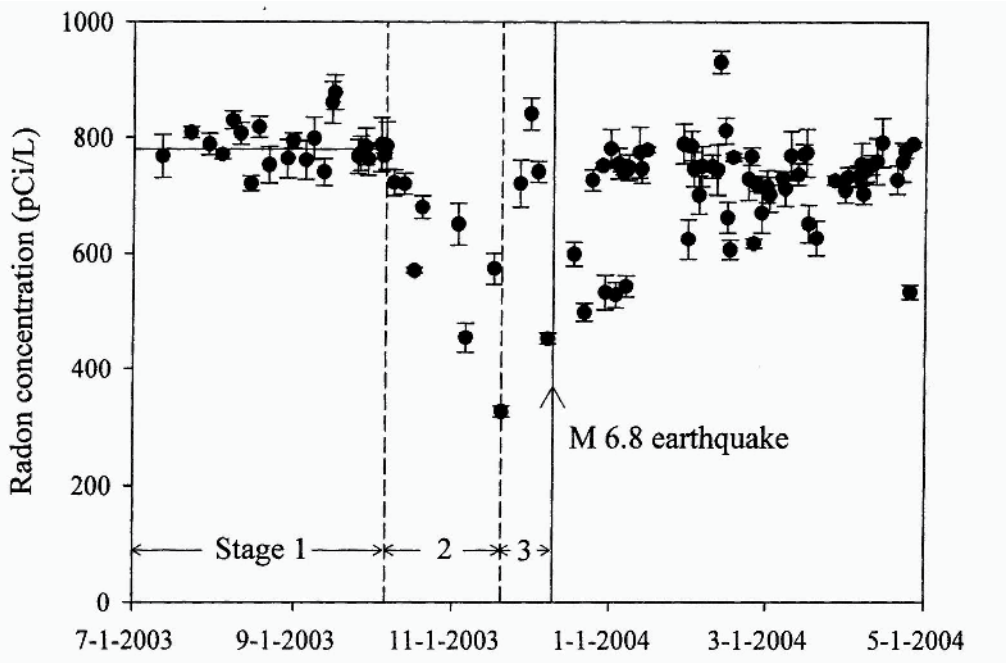

Fig. 6. Radon concentration data at the monitoring well (D1) in the Antung hot spring. Stage 1 is buildup of elastic strain. Stage 2 is dilatancy and development of cracks and gas saturation. Stage 3 is influx of ground water and diminishment of gas saturation.

Under geological conditions such as those of the Antung hot spring, we hypothesized that when regional stress increases, dilation of the rock mass occurs at a rate faster than the rate at which pore water can flow into the newly created pore volume (Brace et al. 1966; Scholz et al. 1973). During this stage (Stage 2 in Fig. 6), gas saturation and two phases (vapor and liquid) develop in the rock cracks. Meanwhile, the radon in ground water volatilizes and partitions into the gas phase and the concentration of radon in ground water decreases. Thus, the sequence of events for radon data prior to the 2003 Chengkung earthquake (Fig. 6) can be interpreted in three stages. From July 2003 to September 2003 (Stage 1), radon was fairly stable (around 780 pCi/L). During this time, there was an accumulation of tectonic strain, which produced a slow, steady increase of effective stress. Sixty-five days before the magnitude (M) 6.8 earthquake, the concentration of radon started to decrease and reached a

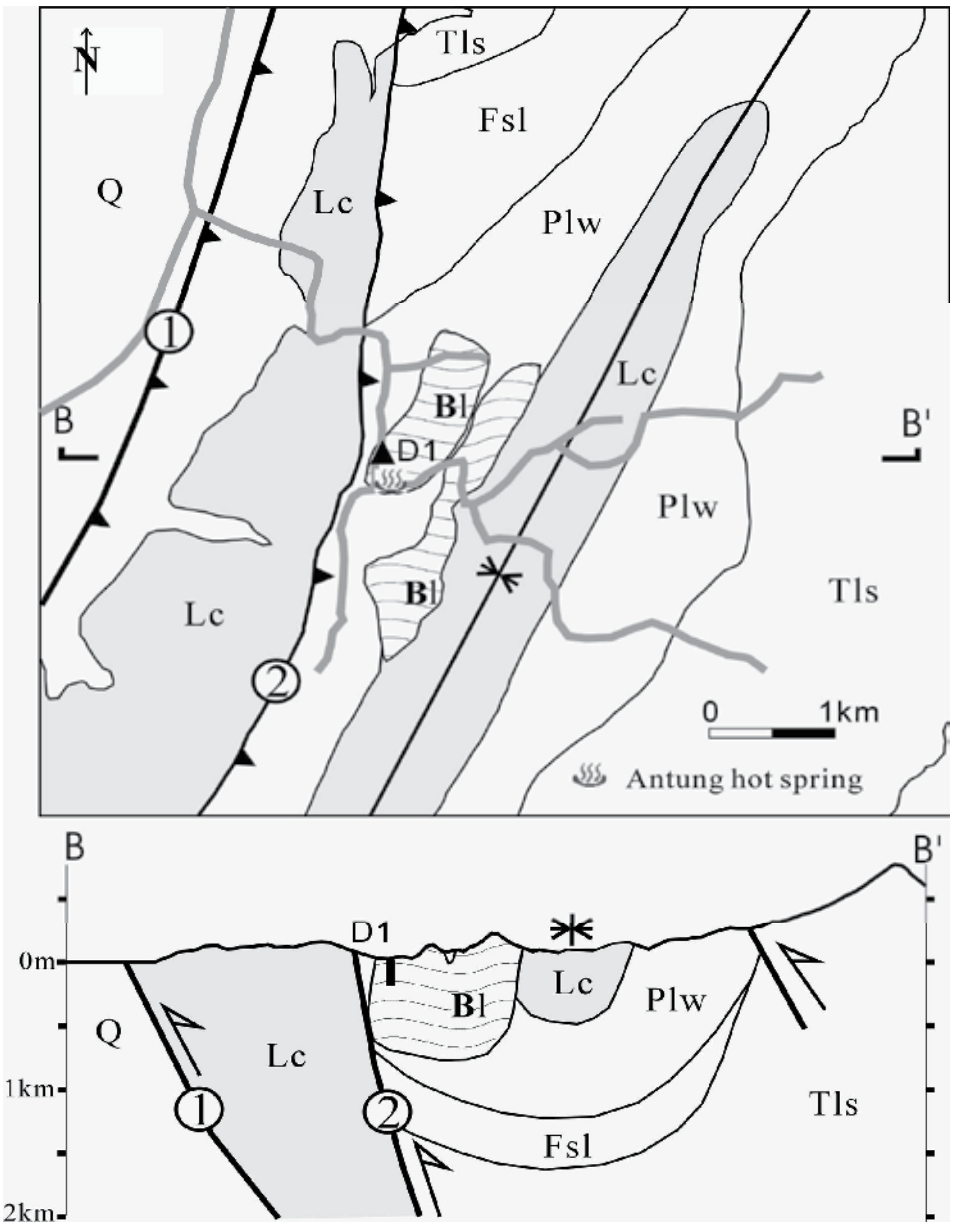

Fig. 7. Geological map and cross section near the radon-monitoring well in the area of Antung hot spring (Q: Holocene deposits, Lc: Lichi mélange, Plw: Paliwan Formation, Fsl: Fanshuliao Formation, Tls: Tuluanshan Formation, Bl: tuffaceous fault block, D1: radon-monitoring well, : Chihshang, or, Longitudinal Valley Fault, : Yongfeng Fault). See Fig. 6 for map location.

minimum value of 330 pCi/L twenty days before the earthquake. During this 45-day period (Stage 2), dilation of the rock mass occurred and gas saturation developed in cracks in the

rock and radon volatilized into the gas phase. Stage 3 started at the point of minimum radon concentration when water saturation in cracks and pores began to increase and radon increased and recovered to the background level. The main shock produced a sharp coseismic anomalous decrease (~300 pCi/L). After the earthquake, some irregular variations were observed, which we attribute to strain release as some accumulation and release of strain continued in the region.

4. In-situ radon volatilization mechanism

Radon partitioning into the gas phase can explain the anomalous decreases of radon precursory to the earthquakes (Kuo et al., 2006). To support the hypothesis of radon volatilization from ground water into the gas phase, radon-partitioning experiments were conducted to determine the variation of the radon concentration remaining in ground water with the gas saturation at formation temperature (60 ℃) using formation brine from the Antung hot spring. Five levels of gas saturation were investigated, specifically S_g = 5 %, 10 %, 15 %, 20 %, and 25 % where S_g is gas saturation. Triplicate experiments were conducted for each level of gas saturation. Every experiment started with 40-ml of formation brine. Five levels of headspace volume at 2 ml, 4 ml, 6 ml, 8 ml, and 10 ml were then created above the liquid phase for five levels of gas saturation at 5 %, 10 %, 15 %, 20 %, and 25 %, respectively. Two-phase equilibrium was achieved for each experiment in 30 minutes at the formation temperature (60 ℃).

A kinetic study of radon volatilization from ground water into the gas phase was conducted to determine the time required to reach equilibrium. In the kinetic experiment, formation brine from the Antung hot spring with an initial radon concentration of 479 ± 35 pCi/L was used. Every sample started with 40-ml formation brine and a headspace volume at 6 ml was then created above the liquid phase. A total of five samples were prepared. The radon concentration remaining in ground water was determined at various volatilization times (i.e., 2 min, 5 min, 15 min, 30 min, and 60 min). The time required to reach equilibrium for radon volatilization was only about 5 minutes.

Data from the vapor-liquid two-phase equilibrium radon-partitioning experiments (Fig. 8) were regressed with the two-phase partitioning model to determine Henry's coefficient as follows.

$$C_0 = C_w (H \times S_g + 1) \quad (1)$$

where C_0 is initial radon concentration in groundwater precursory to each radon anomaly, pCi/L; C_w is the radon minimum in groundwater observed in well D1 during an anomalous decline, pCi/L; S_g is gas saturation, fraction; H is Henry's coefficient for radon at formation temperature (60 ℃), dimensionless. Fig. 8 shows the regressed line with H = 12.8 and R^2 = 0.9919 (regression coefficient). Henry's coefficient for radon at 60 ℃ determined for the Antung formation brine (12.8) is higher than the value (7.91) for water at 60 ℃ (Clever, 1979). Fig. 8 can be used to estimate the amount of gas saturation required for various decreases in concentration of radon. For example, the anomalous decrease of radon concentration from 780 pCi/L to 330 pCi/L required a gas saturation of 10 % in cracks in the rock.

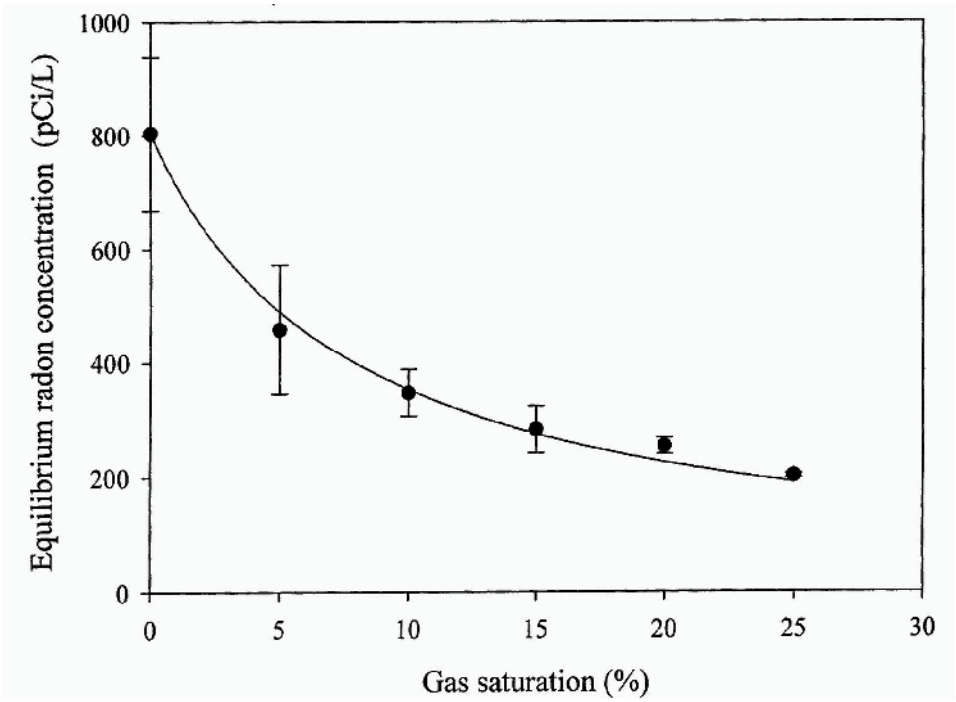

Fig. 8. Variation of radon concentration remaining in ground water with gas saturation at 60 °C using formation brine from the Antung hot spring.

5. Case study

We have monitored groundwater radon since July 2003 at well D1 at the Antung hot spring that is located about 3 km southeast of the Chihshang fault (Fig. 9). The Chihshang fault is part of the eastern boundary of the present-day plate suture between the Eurasia and the Philippine Sea plates. The Chihshang fault ruptured (Hsu, 1962) during two 1951 earthquakes of magnitudes M = 6.2 and M = 7.0. The annual survey of geodetic and GPS measurements has consistently revealed the active creep of the Chihshang fault that is moving at a rapid steady rate of about 2-3 cm/yr during the past 20 years (Angelier et al., 2000; Yu & Kuo, 2001; Lee et al., 2003).

Fig. 10 shows the radon concentration data since July 2003 at the monitoring well (D1) in the Antung hot spring. Radon-concentration errors are ±1 standard deviation after simple averaging of triplicates. Recurrent groundwater radon anomalies were observed to precede the earthquakes of magnitude M_w = 6.8, M_w = 6.1, M_w = 5.9, and M_w = 5.4 that occurred on December 10, 2003, April 1, 2006, April 15, 2006, and February 17, 2008 at the Antung D1 monitoring well. We consider the M_w 5.9 earthquake that occurred on April 15, 2006 triggered by stress transfer in response to the 2006 M_w 6.1 Taitung earthquake. All the three recurrent anomalous decreases observed at Antung follow the same v-shaped progression and are marked with green inverted triangles in Fig. 10. Environmental records such as atmospheric temperature, barometric pressure, and rainfall were examined to check whether the radon anomaly could be attributed to these environmental factors. The

atmospheric temperature, barometric pressure, and rainfall are periodic in season. It is difficult to explain such a large radon decrease by these environmental factors. There was also no heavy rainfall responsible for the radon anomaly.

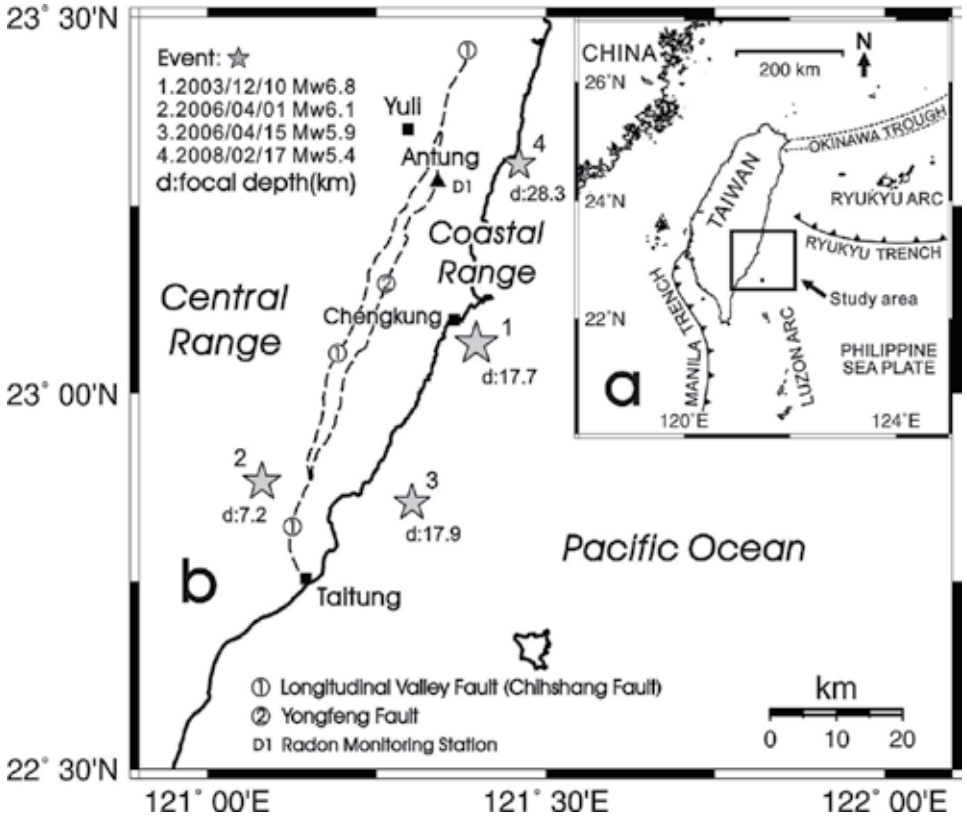

Fig. 9. Map of the epicenters of the earthquakes that occurred on December 10, 2003, April 1 and 15, 2006, February 17, 2008 near the Antung hot spring. (a) Geographical location of Taiwan. (b) Study area near the Antung hot spring.

The box-and-whisker plot is used on the right-hand side in Fig. 10. It shows the median (50th percentile, 764 pCi/L) as a center bar, and the quartiles (25th and 75th percentiles, 692 pCi/L and 849 pCi/L) as a box. The whiskers (456 pCi/L and 1077 pCi/L) cover all but the most extreme values in the data set. Based on the box-and-whisker plot, the threshold concentration of anomalous radon minima at the Antung D1 monitoring well is estimated as 456 pCi/L. The radon minimum recorded prior to the 2008 M_w = 5.4 Antung earthquake is close to the threshold concentration and can be easily masked by the noisy background. On

the other hand, the radon anomalous minima, recorded precursory to strong earthquakes ($M_w > 6.0$), the 2003 M_w = 6.8 Chengkung and 2006 M_w = 6.1 Taitung earthquakes, are low enough to be clearly distinguished from the background noise.

The radon minima, measured prior to local moderate earthquakes, are easily masked by the noisy background. Fig. 10 also shows the large background variation in radon data following the 2003 M_w = 6.8 Chengkung, 2006 M_w = 6.1 Taitung, and 2008 M_w = 5.4 Antung earthquakes. Four local earthquakes with magnitudes (M_w) of 5.5, 5.2, 6.2, and 5.2 occurred on 12/11/2003, 1/1/2004, 5/19/2004, and 9/26/2005, respectively. Based upon their magnitudes and locations, we consider these as aftershocks and induced events of the 2003 Chengkung earthquake. The large scatter in radon data between the 2003 M_w = 6.8 Chengkung and 2006 M_w = 6.1 Taitung earthquakes can be related to these aftershocks. The 2006 Mw 6.1 Taitung earthquake also triggered the Mw 5.9 earthquake that occurred on April 15, 2006. One local earthquake of magnitude M_w = 4.9 that occurred on 6/4/2006 can be considered as an aftershock of the 2006 M_w = 6.1 Taitung earthquake. The M_w = 4.9 aftershock also caused a large scatter in radon data following the 2006 M_w = 6.1 Taitung earthquake. The large background variation in radon data following the 2008 M_w = 5.4 Antung earthquake can also be attributed to local earthquakes, such as a local earthquake of magnitude M_w = 5.3 that occurred on 12/2/2008.

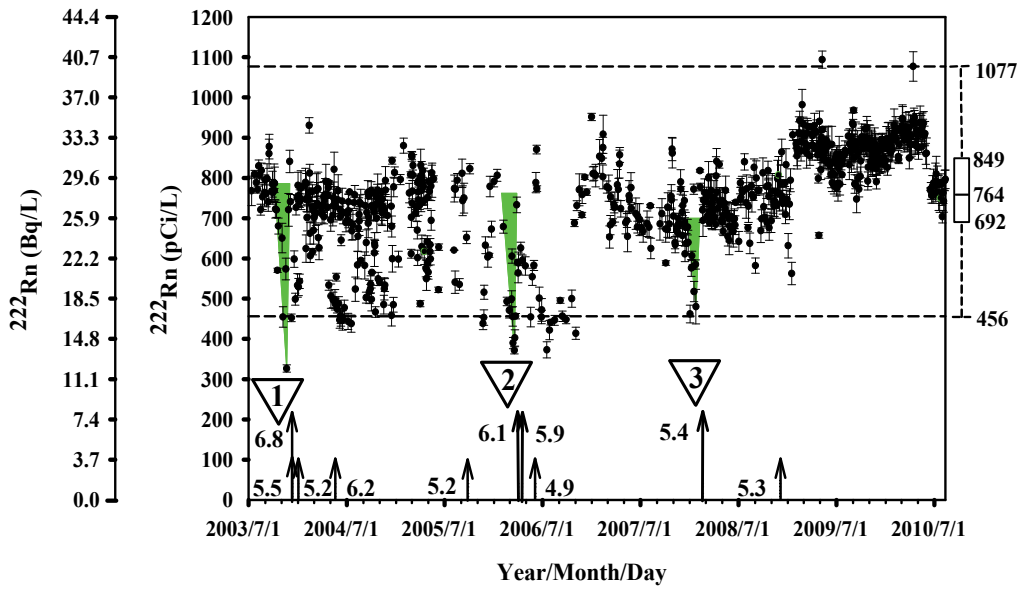

Fig. 10. Radon concentration data at well D1 in the Antung hot spring (open inverted triangles: anomalous radon minima; green inverted triangles: v-shaped pattern; long arrows: mainshocks; short arrows: aftershocks; earthquake magnitude M_w shown beside arrows).

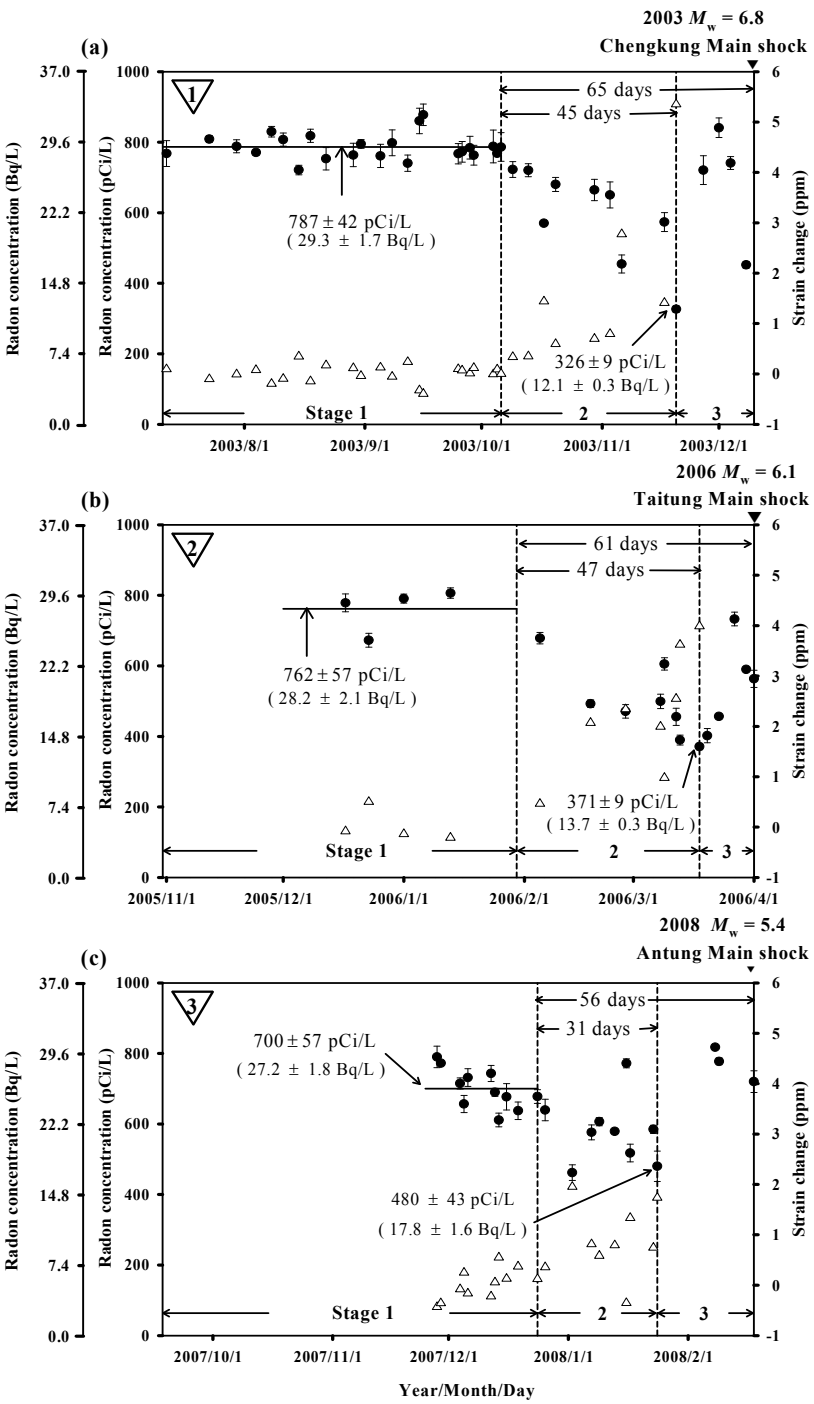

Fig. 11. Observed radon anomalies at well D1 prior to (a) 2003 Chengkung, (b) 2006 Taitung, and (c) 2008 Antung earthquakes. Stage 1 is buildup of elastic strain. Stage 2 is development of cracks. Stage 3 is influx of ground water.

The observed v-shaped pattern prior to the three main shocks clearly progresses in a sequence of three stages (Kuo et al. 2006). The sequence of events for radon anomalies prior to the 2003 M_w = 6.8 Chengkung, 2006 M_w = 6.1 Taitung, and 2008 M_w = 5.4 Antung earthquakes were characterized into three stages in Figs. 11a, 11b, and 11c, respectively (Kuo et al. 2006, 2010a). During Stage 1, the radon concentration in ground water was fairly stable; there was an accumulation of tectonic strain and a slow, steady increase of regional stress. The Antung hot spring is a fractured aquifer with limited recharge surrounded by ductile mudstone (Chen & Wang 1996). When the regional stress increased under these geological conditions, dilation of brittle rock masses occurred at a rate faster than the rate at which ground water could recharge into the newly created rock cracks (Brace et al. 1966; Nur 1972; Scholz et al. 1973). During this stage (Stage 2 in Fig. 11), gas saturation and two phases (vapor and liquid) developed in the rock cracks. The radon in ground water volatilized into the gas phase and the radon concentration in ground water decreased. Stage 3 started at the point of minimum radon concentration when the water saturation in cracks and pores began to increase again. During this stage (Stage 3 in Fig. 11), the radon concentration in groundwater increased and recovered to the previous background level before the main shock.

Figs. 11a, 11b, and 11c show that during Stage 2 prior to the 2003 M_w = 6.8 Chengkung, 2006 M_w = 6.1 Taitung, and 2008 M_w = 5.4 Antung earthquakes the radon concentration in ground water kept decreasing for a significantly long period of 45, 47, 31 days, respectively. Combining the use of box-and-whisker plot, the v-shaped radon pattern shown in Figs. 10 and 11 prior to the 2003 M_w = 6.8 Chengkung, 2006 M_w = 6.1 Taitung, and 2008 M_w = 5.4 Antung earthquakes can be clearly distinguished from other scattering radon data which appear to be related to smaller local earthquakes and aftershocks.

As shown in Fig. 11, radon decreased from background levels of 787 ± 42, 762 ± 57, and 700 ± 57 pCi/L to minima of 326 ± 9, 371 ± 9, and 480 ± 43 pCi/L prior to the 2003 M_w = 6.8 Chengkung, 2006 M_w = 6.1 Taitung, and 2008 M_w = 5.4 Antung earthquakes, respectively. Kuo et al. (2010b) recognized that the observed precursory minimum in radon concentration decreases as the local earthquake magnitude increases. Kuo et al. (2010b) also proposed an empirical correlation for local applications as follows.

$$C_w = 1063 - 110M_w \tag{2}$$

where C_w is the radon minimum in groundwater observed in well D1 during an anomalous decline, pCi/L; M_w is the earthquake magnitude. Eq. (2) did not take the initial stable radon concentration in groundwater precursory to each radon anomaly into account. Our observations in well D1 indicate that the initial stable radon concentration in groundwater precursory to each radon anomaly does vary occasionally. Eq. (2) will be improved by taking into account the initial stable radon concentration in groundwater precursory to each radon anomaly.

Based on radon phase behavior and rock dilatancy, Kuo et al. (2006, 2010a) developed a mechanistic model correlating the observed decline in radon with the volumetric strain change. The model consists of two parts, i.e., the radon-volatilization model and the rock-dilatancy model. The radon-volatilization model can be expressed as follows.

$$C_0 = C_w (H \times S_g + 1) \quad (1)$$

where C_0 is initial radon concentration in groundwater precursory to each radon anomaly, pCi/L; C_w is the radon minimum in groundwater observed in well D1 during an anomalous decline, pCi/L; S_g is gas saturation, fraction; H is Henry's coefficient for radon at formation temperature (60 ℃), dimensionless. The radon-volatilization model correlates the radon decline to the gas saturation for a given fracture porosity.

The rock-dilatancy model can be expressed as follows.

$$d\varepsilon \cong \phi S_g \quad (3)$$

where $d\varepsilon$ is volumetric strain, fraction; ϕ is initial fracture porosity before rock dilatancy, fraction; S_g is gas saturation, fraction. The rock-dilatancy model correlates the volumetric strain to the gas saturation for a given fracture porosity.

Combining the radon volatilization and rock dilatancy models, equations (1) and (3), the groundwater radon concentrations can be correlated to the strain changes associated with earthquake occurrences as follows.

$$d\varepsilon \cong \frac{\phi}{H} \left(\frac{C_0}{C_w} - 1 \right) \quad (4)$$

where $\left(\frac{C_0}{C_w} - 1 \right)$ is normalized radon decline, dimensionless. The Henry's coefficients (H) at formation temperature (60 ℃) is 7.91 for radon (Clever, 1979). Given an average fracture porosity of 0.00003 for the Antung hot spring, Eq. (4) can be used to calculate the crust strain.

Using the radon minima precursory to the 2003, 2006, and 2008 quakes, the calculated crust –strain and observed dimensionless radon-decline are plotted as a function of earthquake magnitude in Fig. 12. The best-fitting straight line is obtained by means of the least-square method with a high value of the sample correlation squared regression coefficient (i.e., R^2 = 0.9802). The regressed equations are as follows.

$$d\varepsilon = 2.5893 M_w - 12.0948 \quad (5)$$

$$\left(\frac{C_0}{C_w} - 1 \right) = 0.6827 M_w - 3.189 \quad (6)$$

where C_0 is initial radon concentration in groundwater precursory to each radon anomaly, pCi/L; C_w is the radon minimum in groundwater observed in well D1 during an anomalous decline, pCi/L; M_w is the earthquake magnitude; $d\varepsilon$ is volumetric strain, fraction. Eq. (6) would be quite useful locally in predicting earthquake magnitude nearby the Chihshang fault from the radon minimum observed in well D1 during an anomalous decline.

Three precursory radon minima associated with nearby large and moderate earthquakes have been recorded from the same monitoring well (D1). The same v-shaped pattern

recognized in all the three recurrent radon anomalies and the threshold concentration are useful for the early warning of potentially disastrous earthquakes ($M_w > 6.0$) in the southern segment of coastal range and longitudinal valley of eastern Taiwan.

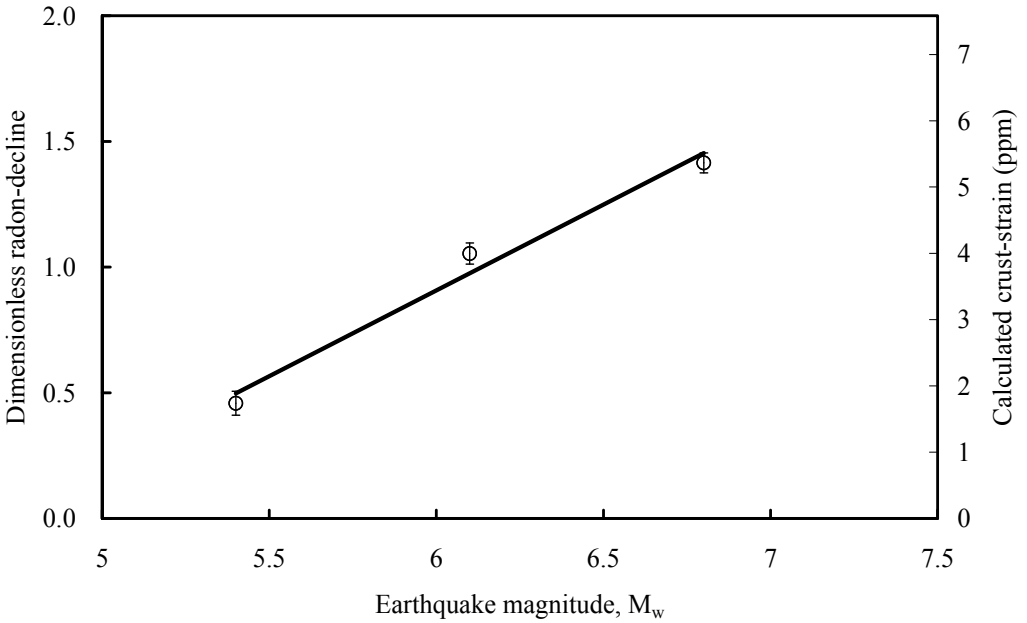

Fig. 12. Calculated crust-strain ($d\varepsilon$) and observed radon-decline ($\frac{C_0}{C_w} - 1$) at well D1 that occurred on December 10, 2003, April 1, 2006, February 17, 2008 as a function of earthquake magnitude (M_w). Radon-concentration errors are ±1 standard deviation.

6. Conclusions

Since July 2003, we have recorded three recurring radon anomalies (precursory to the 2003 M_w = 6.8 Chengkung, 2006 M_w = 6.1 Taitung, and 2008 M_w = 5.4 Antung earthquakes) at well D1, located at the Antung hot spring. The local geological conditions near the Antung hot spring with well D1 situated in a fractured aquifer surrounded by ductile mudstone and the in-situ volatilization of groundwater radon were attributed for causing the recurrent radon anomalies precursory to the nearby large and moderate earthquakes. The following conclusions can be drawn from this study.

1. Radon anomalous declines in groundwater consistently recorded prior to local large and moderate earthquakes near the Antung hot spring in eastern Taiwan provide the reproducible evidence to catch radon precursors under suitable geological conditions.
2. "A low-porosity fractured aquifer surrounded by ductile formation in a seismotectonic environment" is a suitable geological site to consistently catch precursory declines in groundwater radon and dissolved gases prior to local large and moderate earthquakes.
3. Radon partitioning into the gas phase (the mechanism of in-situ radon volatilization) may explain the radon anomalous declines in groundwater consistently recorded prior to local large and moderate earthquakes near the Antung hot spring in eastern Taiwan
4. The observed precursory minimum in radon concentration decreases as the earthquake magnitude increases. The observed relationship between radon minima and earthquake magnitude provides a possible means to forecast local disastrous earthquakes.

7. Acknowledgments

Supports by the National Science Council (NSC-96-2116-M-006-012, NSC-96-2738-M-006-004, NSC-97-2745-M-006-001, NSC-98-2116-M-006-016, and NSC-99-2116-M-006-019) and Central Geological Surveys (98-5226904000-05-02 and 99-5226904000-05-02), Radiation Monitoring Center, and Institute Earth Sciences of Academia Sinica of Taiwan are appreciated.

8. References

Angelier, J.; Chu, H. T.; Lee, J. C. & Hu, J. C. (2000). Active faulting and earthquake hazard: The case study of the Chihshang fault, Taiwan. *Journal of Geodynamics*, Vol. 29, pp. 151-185, ISSN 0264-3707

Brace, W. F.; Paulding, B. W. Jr. & Scholz, C. (1966). Dilatancy in the fracture of crystalline rocks. *Journal of Geophysical Research*, Vol. 71, pp. 3939-3953, ISSN 2156–2202

Chen, W. S. & Wang, Y. (1996). Geology of the Coastal Range, eastern Taiwan, In: *Geological Series of Taiwan 7*, F. C. Chien, Central Geological Survey, ISBN 957-00-6978-3, Taiwan

Clever, H. L. (1979). Krypton, Xenon and Radon-Gas Solubilities, In: *Solubility Data Series 2*, H. L. Clever & R. Battino, Pergamon Press, ISBN 0-08-022352-4, Oxford, UK

Hauksson, E. (1981). Radon content of groundwater as an earthquake precursor: Evaluation of worldwide data and physical basis. *Journal of Geophysical Research*, Vol. 86, pp. 9397-9410, ISSN 2156–2202

Hsu, T. L. (1962). Recent faulting in the Longitudinal Valley of eastern Taiwan. *Memoir of the Geological Society of China*, Vol. 1, pp. 95-102, ISSN 0578-1825

Igarashi, G.; Saeki, S.; Takahata, N.; Sumikawa, K.; Tasaka, S.; Sasaki, Y.; Takahashi, M. & Sano, Y. (1995). Ground-water radon anomaly before the Kobe earthquake in Japan. *Science*, Vol. 269, pp. 60-61, ISSN 1095-9203

Kuo, M. C. Tom; Fan, K.; Kuochen, H. & Chen, W. (2006). A mechanism for anomalous decline in radon precursory to an earthquake. *Ground Water*, Vol. 44, pp. 642-647, ISSN 1745-6584

Kuo, T.; Lin, C.; Chang, G.; Fan, K.; Cheng, W. & Lewis, C. (2010a). Estimation of aseimic crustal-strain using radon precursors of the 2003 M 6.8, 2006 M 6.1, and 2008 M 5.0 earthquakes in eastern Taiwan. *Natural Hazards*, Vol. 53, pp. 219-228, ISSN 1573-0840

Kuo, T.; Su, C.; Chang, C.; Lin, C.; Cheng, W.; Liang, H.; Lewis, C. & Chiang, C. (2010b). Application of recurrent radon precursors for forecasting large earthquakes (M_W > 6.0) near Antung, Taiwan. *Radiation Measurements*, Vol. 45, pp. 1049-1054, ISSN 1350-4487

Liu, K. K.; Yui, T. F.; Yeh, Y. H.; Tsai, Y. B. & Teng, T. L. (1985). Variations of radon content in groundwaters and possible correlation with seismic activities in northern Taiwan. *Pure and Applied Geophysics*, Vol. 122, pp. 231-244, ISSN 1420-9136

Lee, J. C.; Angelier, J.; Chu, H. T.; Hu, J. C.; Jeng, F. S. & Rau, R. J. (2003). Active fault creep variations at Chihshang, Taiwan, revealed by creep meter monitoring, 1998-2001. *Journal of Geophysical Research*, Vol. 108, pp. 2528-2548, ISSN 2156–2202

Lowry, D. (1991). Measuring low radon levels in drinking water supplies. *Journal American Water Works Association*, Vol. 83, pp. 149-153, ISSN 1551-8833

Noguchi, M. (1964). Radioactivity measurement of radon by means of liquid scintillation fluid. *Radioisotope*, Vol. 13, pp. 362-366, ISSN 0033-8303

Noguchi, M. & Wakita, H. (1977). A method for continuous measurement of radon in groundwater for earthquake prediction. *Journal of Geophysical Research*, Vol. 82, pp. 1353-1357, ISSN 2156–2202

Nur, A. (1972). Dilatancy, pore fluids, and premonitory variations of ts/tp traval times. *Bulletin of the Seismological Society of America*, Vol. 62, pp. 1217-1222, ISSN 1943-3573

Prichard, H. M. & Gesell, T. F. (1977). Rapid measurements of 222Rn concentrations in water with a commercial liquid scintillation counter. *Health Physics*, Vol. 33, pp. 577-581, ISSN 1538-5159

Prichard, H. M.; Venso, E. A. & Dodson, C. L. (1992). Liquid-Scintillation analysis of 222Rn in water by alpha-beta discrimination. *Radioactivity and Radiochemistry*, Vol. 3, pp. 28-36, ISSN 1045-845X

Scholz, C. H.; Sykes, L. R. & Aggarwal, Y. P. (1973). Earthquake prediction: A physical basis. *Science*, Vol. 181, pp. 803-810, ISSN 1095-9203

Teng, T.L. (1980). Some recent studies on groundwater radon content as an earthquake precursor. *Journal of Geophysical Research*, Vol. 85, pp. 3089-3099, ISSN 2156–2202

Toutain, J. P. & Baubron J. C. (1999). Gas geochemistry and seismotectonics: a review. *Tectonophysics*, Vol. 304, pp. 1–27, ISSN 0040-1951

Wakita, H.; Nakamura, Y.; Notsu, K.; Noguchi, M. & Asada, T. (1980). Radon anomaly: A possible precursor of the 1978 Izu-Oshima-kinkai earthquake. *Science*, Vol. 207, pp. 882-883, ISSN 1095-9203

Yu, S. B. & Kuo, L. C. (2001). Present-day crustal motion along the Longitudinal Valley Fault, eastern Taiwan. *Tectonophysics*, Vol. 333, pp. 199-217, ISSN 0040-1951

9

Radon as an Earthquake Precursor – Methods for Detecting Anomalies

Asta Gregorič, Boris Zmazek, Sašo Džeroski,
Drago Torkar and Janja Vaupotič
Jožef Stefan Institute, Ljubljana
Slovenia

1. Introduction

Radon is one of many geophysical and geochemical phenomena that can be considered to be an earthquake precursor. Due to the non-linear dependence of earthquakes' initial conditions, the question about the predictability of earthquakes often arises (Geller, 1997). The successful prediction of earthquakes is yet to be accomplished, in terms of their magnitude, location and time, and much effort has been spent on this goal.

The term "earthquake precursor" is used to describe a wide variety of geophysical and geochemical phenomena that reportedly precede at least some earthquakes (Cicerone et al., 2009). The observation of these types of phenomena is one recent research activity which has aimed at reducing the effects of natural hazards. Among the different precursors, geochemistry has provided some high-quality signals, since fluid flows in the Earth's crust have a widely recognised role in faulting processes (Hickman et al., 1995). The potential of gas geochemistry in seismo-tectonics has been widely discussed by Toutain and Baubron (1999).

In the late 1960s and early 1970s, reports from seismically active countries such as the former USSR, China, Japan and the USA (Ulomov & Mavashev, 1967; Wakita et al., 1980) indicated that concentrations of radon gas in the earth apparently changed prior to the occurrence of nearby earthquakes (Lomnitz, 1994). The noble gas radon (^{222}Rn) originates from the radioactive transformation of ^{226}Ra in the ^{238}U decay chain in the Earth's crust. Since radon is a radioactive gas, it is easy and relatively inexpensive to monitor instrumentally, and its short half-life (3.82 days) means that short-term changes in radon concentration in the earth can be monitored with a very good time resolution. Radon emanation from grains depends mainly on their ^{226}Ra content and their mineral grain size, its transport in the earth being governed by geophysical and geochemical parameters (Etiope & Martinelli, 2002), while exhalation is controlled by hydrometeorological conditions. The stress-strain developed within the Earth's crust before an earthquake leads to changes in gas transport and a rise of volatiles from the deep earth up to the surface (Ghosh et al., 2009; Thomas, 1988), resulting in anomalous changes in radon concentration. The mechanism of observed radon anomalies is still poorly understood, although several theories have been proposed (Atkinson, 1980; King, 1978; Lay et al., 1998; Martinelli, 1991). Over the past three decades, the occurrence of anomalous temporal

changes of radon concentrations has been studied by several authors specialising in soil gas (King, 1984, 1985; Kuo et al., 2010; Mogro-Campero et al., 1980; Planinić et al., 2001; Ramola et al., 2008; Ramola et al., 1990; Reddy & Nagabhushanam, 2011; Walia et al., 2009a; Walia et al., 2009b; Yang et al., 2005; Zmazek et al., 2005; Zmazek et al., 2002b) and groundwater (Barragán et al., 2008; Favara et al., 2001; Gregorič et al., 2008; Heinicke et al., 2010; Kuo et al., 2006; Ramola, 2010; Singh et al., 1999; Zmazek et al., 2002a; Zmazek et al., 2006). However, radon anomalies are not only controlled by seismic activity but also by meteorological parameters like soil moisture, rainfall, temperature and barometric pressure (Ghosh et al., 2009; Stranden et al., 1984). This makes it complicated and, for small earthquakes, often impossible to differentiate between those anomalies caused by seismic events and those caused solely by atmospheric changes. Therefore, the application of theoretical and empirical algorithms for removing meteorological effects is necessary (Choubey et al., 2009; Ramola et al., 2008; Ramola et al., 1988; Torkar et al., 2010; Zmazek et al., 2003). In this chapter, the different approaches to distinguishing between those anomalies in radon time series caused by seismic activity and those caused solely by hydrometeorological parameters are presented and discussed.

2. Radon migration in the Earth's crust

Only a fraction of the radon atoms created by radioactive transformation from radium are able to emanate from mineral grains and enter into the void space, filled either by gas or water. Radon ascends towards the surface mainly through cracks or faults, on a short scale by diffusion and, for longer distances, by advection - dissolved either in water or in carrier gases. Gas movement should be ascribed to the combination of both processes. Diffusive movement is driven by a concentration gradient and is described by Fick's law. Considering gas diffusion in porous media, it is necessary to take into account that the volume through which gas diffuses is reduced and the average path length between two points is increased, thus altering the diffusion coefficient (Etiope & Martinelli, 2002). Nevertheless, the velocity of radon transport in the earth is quite low ($\leq 10^{-3}$ cm/s) and the concentration of radon is reduced by radioactive decay to the background level before even 10 m are traversed (Etiope & Martinelli, 2002; Fleischer, 1981). Diffusion is only important in capillaries and small-pored rocks. On the other hand, the velocity and space scales of advective movements are much higher than those of diffusive ones. Advective transport is driven by pressure gradients, following Darcy's law. The amount of radon itself is, however, too small to form a macroscopic quantity of gas which can react to pressure gradients. Therefore, it must be carried by a macroscopic flow of carrier gases (Kristiansson & Malmqvist, 1982). A gas mixture formed by carrier gases (e.g., CO_2, CH_4, and N_2) and rare gases (e.g., He, Rn) can be referred to as "geogas" (Etiope & Martinelli, 2002; Kristiansson & Malmqvist, 1982). In dry, porous or fractured media, gas flows through an interstitial or fissure space (gas-phase advection) whereas in saturated, porous media gas can dissolve and then be transported in three ways: by groundwater (water-phase advection), by displacing water (gas-phase advection) or by forming a bubble flow by means of buoyancy in aquifers and water-filled fractures. The bubble movement has been theoretically and experimentally recognised as a fast gas migration mechanism governing the distribution of carrier and trace gases over wide areas on the Earth's surface (Vàrhegyi et al., 1992).

2.1 External effects on radon in soil gas and water

Radon concentration in soil, gas or water is not only controlled by geophysical parameters, but it also changes due to other external effects. Meteorological effects – such as soil humidity, rainfall, temperature, barometric pressure and wind – control radon concentrations in soil gas. These parameters change the physical characteristics of soil and rock, thus influencing the rate of radon transport and, consequently, perturbing eventual radon variations caused by geophysical processes originating in the deeper parts of the Earth's crust. Shallow soil levels are more affected by changing meteorological conditions than deeper ones. Radon concentrations with no larger variations present are usually observed at depths of 0.8 m or deeper. Besides the effects of meteorological parameters on radon in soil gas, considerable variations in the gas composition of thermal springs have been shown to be the result of fluctuations of local hydrologic regimes (Klusman & Webster, 1981).

The significant influence of barometric pressure has been discussed by several authors, who clearly pointed out an inverse relationship between barometric pressure and radon concentration in soil gas (Chen et al., 1995; Clements & Wilkening, 1974; Klusman & Webster, 1981). A decrease in barometric pressure, with the values of other environmental parameters remaining constant, generally causes an increase in radon exhalation from the ground, whereas during periods of rising pressure, air with low radon concentration is forced into the ground, thus diluting radon. Temperature-related fluctuations of soil gas radon concentration have also been proven to be very important. Klusman & Jaacks (1987) found an inverse relationship between soil temperature and radon concentration. They suggested that lower air temperatures as compared with soil temperatures during winter months promoted an upward movement of radon by convection, whereas during the summer, lower soil temperatures as compared with air temperatures and an inversion layer below the level of sampling reduces the upward flux and observed concentration. In general, the behaviour of soil gas migration in different types of soil is seasonally dependent (King & Minissale, 1994; Washington & Rose, 1990). In systems where gas movement is driven by diffusion or slow advection processes, radon activity in soil might be controlled by soil moisture and rainfall through the opening of cracks in the surface (Pinault & Baubron, 1996; Toutain & Baubron, 1999). On the other hand, barometric pressure has the major influence on radon concentrations in soils in advective systems, which display generally higher gas flows. However, micro-scale soil heterogeneities in permeability, porosity and lithology can cause significant heterogeneities in the response of radon concentration to changes of atmospheric parameters (King & Minissale, 1994; Neznal et al., 2004). Numerous and often divergent results in studies related to the effect of external factors on soil gas radon concentration suggest that no general predictive model for excluding meteorological effects can be proposed, and studies of radon in soil gas need a simultaneous record of meteorological parameters.

3. Anomalous radon concentration and seismicity

Both mechanisms of radon transport – diffusion and advection – depend on both soil porosity and permeability, which at the same time vary as a function of the stress field (Holub & Brady, 1981). However, migration by diffusion is negligible, where a component of advective long-distance transport exists (Etiope & Martinelli, 2002). The high permeability

of the bedrock and soil in areas of crustal discontinuities, such as fractures and fault zones, promotes intense degassing fluxes, which causes higher soil gas radon concentrations on the ground surface above active fault zones. Although several measurements, experiments and models have been performed, the understanding of the mechanism of radon anomalies and their connection to earthquakes is still inadequate (Chyi et al., 2010; King, 1978; Ramola et al., 1990). Before the earthquake stress in the Earth's crust builds up causing a change in the strain field; the formation of new cracks and pathways under the tectonic stress leads to changes in gas transport and a rise in volatiles from the deep layers to the surface. In fact, fluids play a widely recognised role in controlling the strength of crustal fault zones (Hickman et al., 1995). Anomalous changes of radon concentration are closely linked to changes in fluid flow and, therefore, also to highly permeable areas along fault zones. Large faults are not discrete surfaces but rather a braided array of slip surfaces encased in a highly fractured and often hydrothermally altered transition – or "damage" – zone. Episodic fracturing and brecciation are followed by cementation and crack healing, leading to cycles of permeability enhancement and reduction along faults (Hickman et al., 1995).

Several mechanisms have been proposed, which could explain the relationship between radon anomalies and earthquake. Two models of earthquake precursors are discussed by Mjachkin et al. (1975), with a common principle: at a certain preparation stage, a region of many cracks is formed. According to the dilatancy-diffusion model (Martinelli, 1991; Mjachkin et al., 1975), the increase in tectonic stress causes the extension and opening of favourably-oriented cracks in a porous, cracked, saturated rock. Water flows into the opened cracks, drying the rock near each pore and finally resulting in a decrease of pore pressure in the total earthquake preparation zone. Water from the surrounding medium diffuses into the zone. The increased water-rock surface area, due to cracking, leads to an increase in radon transfer from the rock matrix to the water. At the end of the diffusion period, the appearance of pore pressure and the increased number of cracks leads to the main rupture. According to the crack-avalanche model (Mjachkin et al., 1975), the increasing tectonic stress leads to the formation of a cracked focal rock zone, with slowly altering volume and shape. At a certain stage – when the whole focal zone becomes unstable – the cracks quickly concentrate near the fault surface, triggering the main rupture. An alternate mechanism for earthquake precursory study, based on stress-corrosion theory, has been proposed by Anderson and Grew (1977). According to them, the observed radon anomalies are due to slow crack growth controlled by stress corrosion in a rock matrix saturated by ground waters. King (1978) has proposed a compression mechanism for radon release, whereby anomalous high radon release may be due to an increase of crustal compression before an impending earthquake, that squeezes out soil gas into the atmosphere at an increasing rate.

Toutain and Baubron (1999) observed that gas transfer within the upper crust is affected by strains less than 10^{-7}, much smaller than those causing earthquakes. According to Dobrovolsky (1979), the radius of the effective precursory manifestation zone depends on the earthquake magnitude and can be calculated using the empirical equation:

$$R_D = 10^{0.43 \times M_L} \quad (1)$$

Where R_D is the strain radius in km and M_L is the magnitude of the earthquake. Considering the Earth's crust to be an anisotropic medium, this law can be modified according to the

effective sensitivity to the impending earthquake. The ideal circle with its theoretical radius can be transformed into an ellipse or characterised by shadow areas where no precursory phenomena are observable due to crustal anisotropy, discontinuities or loose contacts along some faults, which prevent further stress transfer (İnan & Seyis, 2010; Martinelli, 1991).
Although radon anomalies can be studied in soil gas and thermal waters, thermal waters could be much more representative of the geologic environment and could be more reactive to stress/strain changes acting at depth than soil gases. The disadvantage of soil gases lie in weak gas concentrations, generally due to the thickness of the sedimentary cover and the high level of atmospheric perturbations (Toutain & Baubron, 1999).

4. Methods for detecting anomalies in radon time series

An anomaly in radon concentration is defined as a significant deviation from the mean value. Due to the high background noise of radon time series, it is often impossible to distinguish an anomaly caused solely by a seismic event from one resulting from meteorological or hydrological parameters. For this reason, the implementation of more advanced statistical methods in data evaluation is important (Belyaev, 2001; Cuomo et al., 2000; Negarestani et al., 2003; Sikder & Munakata, 2009; Steinitz et al., 2003). In our research, radon has been monitored in several thermal springs (Gregorič et al., 2008; Zmazek et al., 2002a; Zmazek et al., 2006) and in soil gas (Zmazek et al., 2002b) and different approaches to distinguishing radon anomalies were applied.

4.1 Standard deviation

A very common practice in determining radon anomalies is the use of standard deviation. The average radon concentration is calculated for different periods with regard to the nature of yearly cycles of radon concentration. In the case of radon in soil gas, the mean value of radon concentration is calculated separately for four seasons (spring, summer, autumn and winter) based on the air and soil temperature.

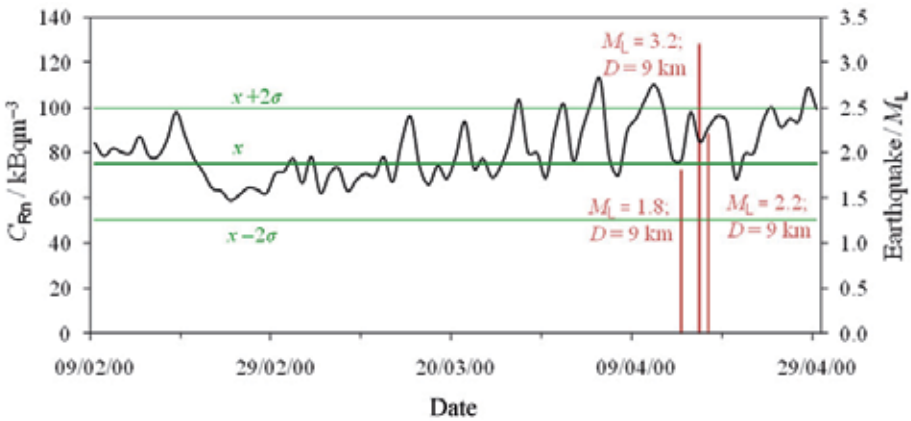

Fig. 1. Continuous radon concentration recorded in soil gas at Krško basin. Straight lines represent the mean value and two standard deviations of the radon concentration. Local seismicity is expressed in terms of local magnitude (M_L) and the distance between the measuring location and the earthquake epicentre (D). Radon anomalies are C_{Rn} values outside the ±2σ region.

In contrast to soil gas, radon in ground or spring water is greatly influenced by the hydrologic cycle, which has to be considered during the data analysis. To define the mean and standard deviation, anomalously high and low values – which may cause unnecessary high deviation and perturb the real anomalies – have to be neglected. The periods when radon concentration deviates by more than ±2σ from the related seasonal value are considered as radon anomalies that are possibly caused by earthquake events and not by meteorological parameters (Ghosh et al., 2007; Gregorič et al., 2008; Virk et al., 2002; Zmazek et al., 2002b). Fig. 1 shows an anomalous radon concentration, exceeding 2σ above the average value, which appeared approximately 10 days before the occurrence of three earthquakes with magnitudes from 1.8 to 3.2.

4.2 Relationship between radon exhalation and barometric pressure

An inverse relationship exists between the time derivative of radon concentration in soil gas and the time derivative of barometric pressure (as was discussed previously in section 2.1). A decrease in barometric pressure causes an increase in radon exhalation from the ground, whereas during periods of rising pressure, air with low radon concentration is forced into

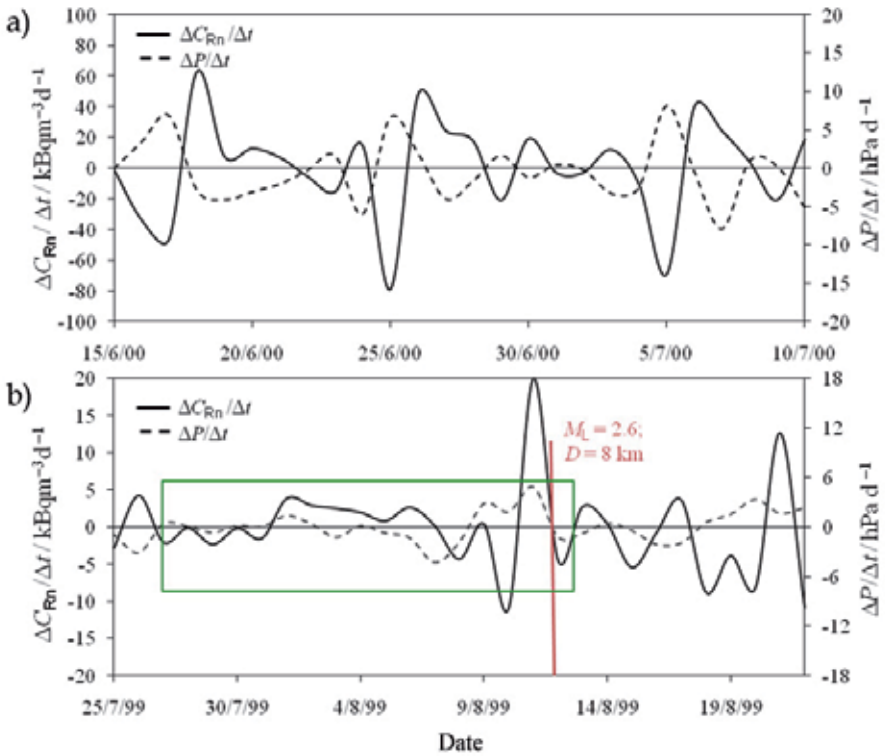

Fig. 2. The time gradient of radon concentration in soil gas and the time gradient of barometric pressure during two periods at the Krško basin: a) the period without local seismic activity, b) the seismically active period, whereby the radon anomaly 14 days before the earthquake is marked by the green rectangle. The earthquake is expressed in terms of local magnitude (M_L) and the distance between the measuring location and the earthquake epicentre (D).

the ground, thus diluting the radon concentration. Therefore, deviations from this rule during these periods – when the time gradient of barometric pressure, $\Delta P/\Delta t$, and the time gradient of radon concentration, $\Delta C_{Rn}/\Delta t$, in soil gas have the same sign – can be considered to be radon anomalies (Zmazek et al., 2002b). A clear negative correlation between the time gradient of radon concentration and the time gradient of barometric pressure can be seen in Fig. 2a, when no seismic activity is present. The radon anomaly, characterised by positive correlation of time gradients, is marked in Fig. 2b. Anomalous behaviour in radon concentration started 14 days before the earthquake with a local magnitude of 2.6, and ended a few days after the earthquake.

4.3 Machine learning methods

Machine learning methods have been successfully applied to many problems in the environmental sciences (Džeroski, 2002). In the case of radon as an earthquake precursor, it must be considered – as discussed in section 2.1 – that the variation in radon concentration is controlled not only by geophysical phenomena in the Earth's crust, but also by the environmental parameters associated with the radon monitoring sites. With machine learning methods, a model for the prediction of radon concentration can be built, taking into account various environmental parameters (e.g., barometric pressure, rainfall, and air and soil temperature). The aim is to identify radon anomalies which might be caused by seismic events. The application of artificial neural networks (Negarestani et al., 2002, 2003; Torkar et al., 2010), regression and model trees (Džeroski et al., 2003; Sikder & Munakata, 2009; Zmazek et al., 2003; Zmazek et al., 2006) and some other methods (Sikder & Munakata, 2009; Steinitz et al., 2003) have proven to be useful means of extracting radon anomalies caused by seismic events.

4.3.1 Artificial neural networks

An artificial neural network (ANN) is a well-known computational structure inspired by the operation of the biological neural system (Jain et al., 1996) and it is a well-established tool, being used widely in signal processing, pattern recognition and other applications. An ANN consists of a set of units (neurons, nodes), and a set of weighted interconnections among them (links). The organisation of neurons and their interconnections defines the net topology. The inputs are grouped in an input layer, the outputs in an output layer and all the other units in so-called hidden layers. The algorithm repeatedly adjusts the weights to minimise the mean square error between the actual output vector and the desired network output vector. The universal approximator functional form of ANNs is well-suited for the requirements of modelling the non-linear dependency of radon concentrations on multiple variables. Among a number of various topologies, training algorithms and architectures of ANNs, the traditional multilayer perceptron (MLP) with a conjugate gradient learning algorithm was chosen in the case of analysing the soil gas radon concentration time series at the Krško basin (Torkar et al., 2010). The series was first split into seismically non-active periods (NSA) and seismically active periods (SA), adjusting the duration of the seismic window from 0 to 10 days before and after the earthquake and with the purpose of investigating the influence of a complete earthquake event on radon concentration (the preparation phase, the earthquake itself and aftershocks). The ANN of the MLP type was trained with each of the NSA datasets, which were divided into three sets: the training set (60%), the cross-validation set (15%) and the test set (25%). The ANN was trained with the

training and cross-validation set, while the test set was used to verify its performance. The topology of the ANN generated for each NSA dataset is shown in Fig. 3.

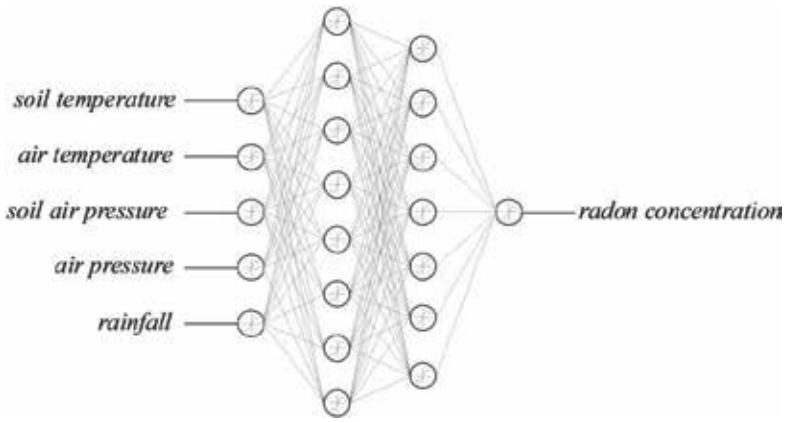

Fig. 3. The ANN topology for learning radon concentration dependency on environmental parameters.

In the testing phase, the correlation between the measured (m-C_{Rn}) and predicted (p-C_{Rn}) radon concentration in NSA periods was compared to the correlation between the measured and predicted radon concentration in the entire dataset (NSA and SA). The difference between the correlation coefficients might indicate a period of seismically induced radon anomaly. The ratio between the measured and predicted values (m-C_{Rn}/p-C_{Rn})–1 represents the discrepancy between both values (Fig. 4).

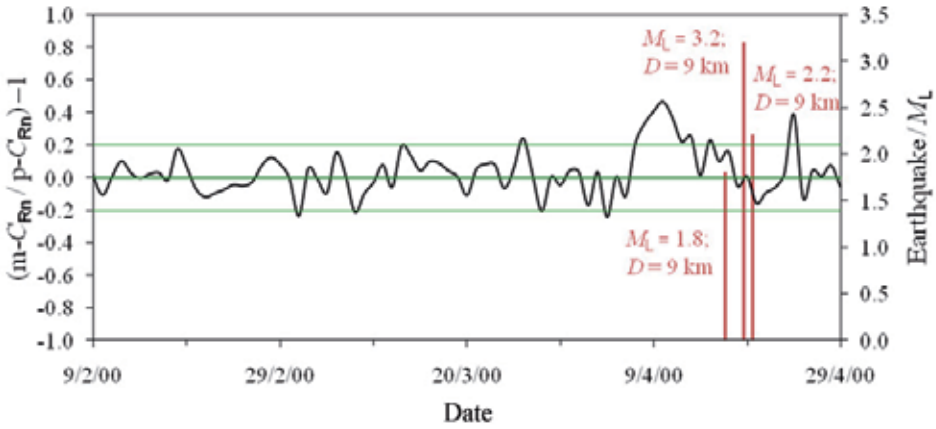

Fig. 4. The ratio between the measured and predicted radon concentration (m-C_{Rn}/p-C_{Rn})–1 using an ANN in the case of soil gas radon in the Krško basin for a seismic window of ±7 days. A radon anomaly, possibly caused by a seismic event, is observed when the signal exceeds the threshold value of 0.2.

A radon anomaly is held to be when the absolute value of signal (m-C_{Rn}/p-C_{Rn})–1 exceeds the predefined threshold of 0.2. The ANN in this case performed the best in the case of a seismic window of ±7 days (indicating the length of the period of pre- and post-seismic changes).

4.3.2 Decision trees

Decision trees are machine-learning methods for constructing prediction models from data. The models are obtained by recursively partitioning the data space and fitting a simple prediction model within each partition. As a result, the partitioning can be represented graphically as a decision tree, where each internal node contains a test on an attribute, each branch corresponds to an outcome of the test, and each leaf node gives a prediction for the value of the class variable (Džeroski, 2001; Loh, 2011). Regression trees are designed for dependent variables that take continuous or ordered discrete values. Like classical regression equations, they predict the value of a dependent variable (called the class) from the values of a set of independent variables (called attributes).

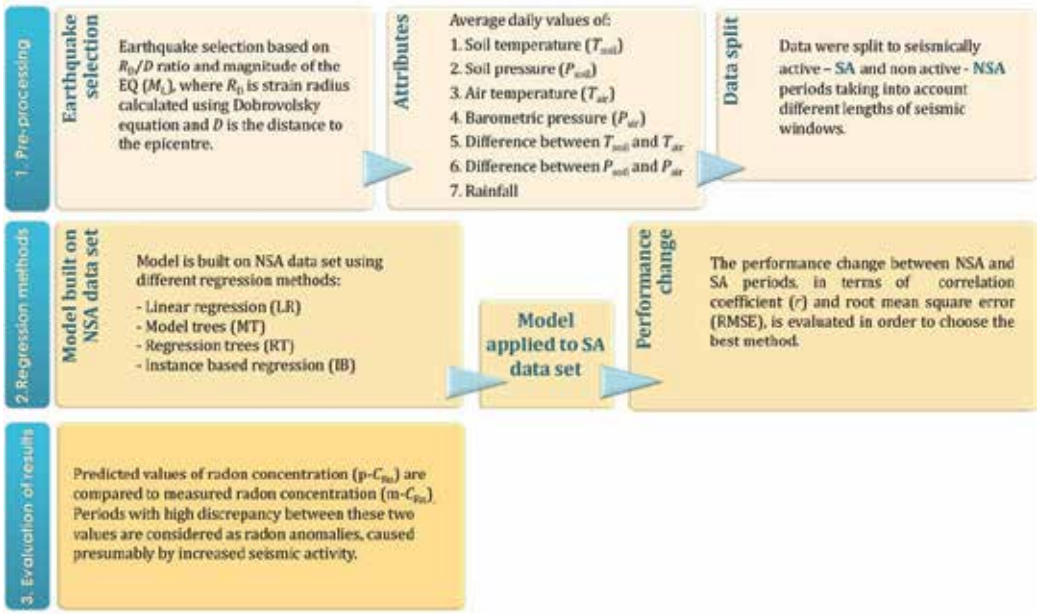

Fig. 5. A schematic description of the different stages of radon data series analysis with machine learning methods.

The model in each leaf can be either a linear equation or just a constant; trees with linear equations in the leaves are also called model trees. Tree construction proceeds recursively, starting with the entire set of training examples. At each step, the most discriminating attribute is selected as the root of the sub-tree and the current training set is split into subsets according to the values of the selected attribute. For continuous attributes, a threshold is selected and two branches are created, based on that threshold. The attributes that appear in the training set are considered to be thresholds. Tree construction stops when the variance of the class values of all examples in a node is small enough. These nodes are called leaves and are labelled with a model for predicting the class value. An important mechanism used to prevent the tree from over-fitting data is tree pruning.
Regression (RT) and model trees (MT), as implemented with the WEKA data mining suite (Witten & Frank, 1999), were used for predicting radon concentration from meteorological parameters in the case of radon time series in soil gas at the Krško basin (Zmazek et al., 2003; Zmazek et al., 2005) and in the thermal spring water in Zatolmin (Zmazek et al., 2006).

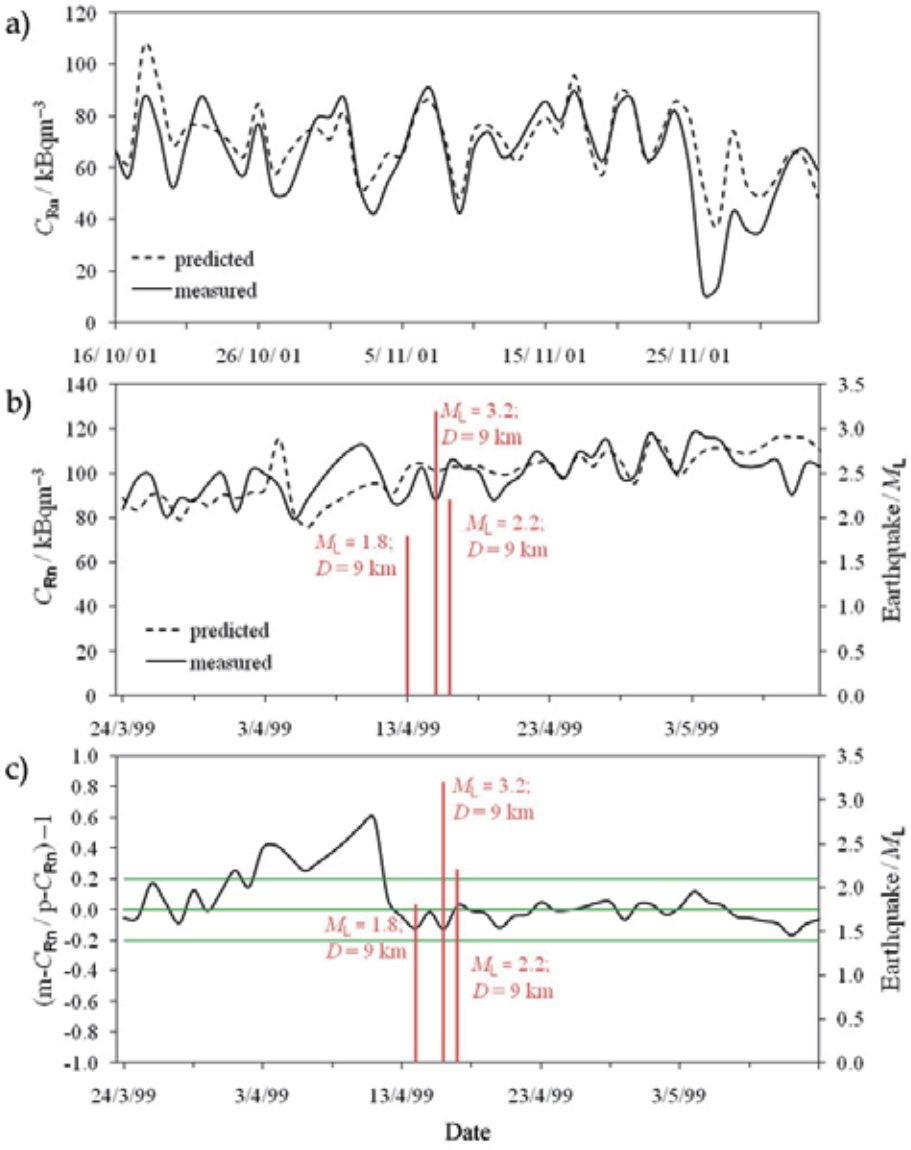

Fig. 6. Measured and predicted radon concentration using model trees in the case of soil gas radon at the Krško basin for a seismic window ±7 days; a) low discrepancy in the period without seismic activity; b) high discrepancy starting 10 days before a group of earthquakes; c) the ratio between the measured and predicted radon concentration (m-C_{Rn}/p-C_{Rn})–1 for the same SA period. A radon anomaly, possibly caused by earthquakes, is observed when the signal exceeds the threshold value of 0.2 (marked by the green lines).

As presented in Fig. 5 the first stage of data analysis comprises the selection of attributes – i.e. environmental parameters – and the partitioning of the whole data set to the periods with and without seismic activity, SA and NSA respectively. After inspecting the correlation changes between radon concentration and barometric pressure, a seismic window of ±7

days was chosen. The performance was estimated with 10-fold cross-validation in order to evaluate the predictability of the radon concentration in the NSA periods. The model built on the NSA data set was then applied to the SA data set and the performance change was determined using two different measures, the correlation coefficient (r) and the root mean square error (RMSE). For the purposes of prediction, the measured performance in NSA periods should be higher than the performance in SA periods. In these periods, when the discrepancy between the measured and predicted radon concentration is low, no seismic activity is anticipated (Fig. 6a), while in the periods with a higher discrepancy, a radon anomaly can be ascribed to increased seismic activity, rather than to the effect of atmospheric parameters (Fig. 6b). This discrepancy is clearly shown in form of the ratio between both values (m-C_{Rn}/p-C_{Rn})–1, as shown in Fig. 6c. A radon anomaly is held to be when the absolute value of the signal (m-C_{Rn}/p-C_{Rn})–1 exceeds the predefined threshold of 0.2. Besides regression trees, other machine learning methods were also tested (e.g., linear regression and instance-based regression). However, model trees have been shown to outperform other approaches.

4.4 Comparison of the results

The results of all of the approaches used for the identification of radon anomalies caused by seismic events in the case of soil gas radon at the Krško basin are shown in Fig. 7 for the period of 1/9 – 30/12/2000. Among all of the approaches – and although not very exact – the ±xσ method (I) is the most frequently used. The threshold of anomalous concentrations (e.g., ±1σ, ±2σ, ±3σ) should be chosen in order to minimise the number of false anomalies (FA: anomalies in seismically non-active periods) and so as not to miss the correct ones (CA). Generally, a range of ±2σ from the related seasonal mean value is chosen. Furthermore, a cyclic behaviour of radon concentration has to be taken into account in order to accurately define the period of standard deviation and the calculation of the mean value. For this purpose different methods of time series analyses – for example, Fourier transform (Ramola, 2010) – can be applied.

In the case shown in Fig. 7a, three radon anomalies exceeding 2σ above the mean value may be noticed. The first, in the beginning of September, cannot be assigned to a seismic event (FA). About a week before a weak earthquake of local magnitude M_L=1.1, 5 km away from the measurement location – which is the first of five earthquakes over a period of 2 months – the second anomaly is observed. And finally, the third one can be noticed soon after a weak earthquake 6 km away (M_L=1).

The first of the anomalies mentioned above as FA is also visible by applying the method of pressure gradients (II) (Fig. 7b). A positive correlation between the time gradient of radon concentration and the time gradient of barometric pressure is considered to be a radon anomaly, and corresponds to the anomaly observed through method (I) which preceded the first earthquake (M_L=1.1). A radon anomaly can also be noticed a few days before the last earthquake, as with the analysis of method (I). Additionally, the anomalous behaviour of the radon concentration as regards the gradient approach is observed during the period starting a few days before the earthquake with M_L=2.7 and lasting until the earthquake with M_L=1.

More often than not, swarms of anomalies are observed over longer periods, with a higher number of anomalies in a swarm observed for approach (II) than for approach (I). As an additional criterion, a threshold of $\Delta P/\Delta t > 2$ hPa d^{-1} is introduced by this approach in order to optimise the identification of anomalies caused by seismic events. However, by increasing the threshold value above 2 hPa d^{-1}, the ratio between correct and false anomalies cannot be significantly improved (Zmazek et al., 2005).

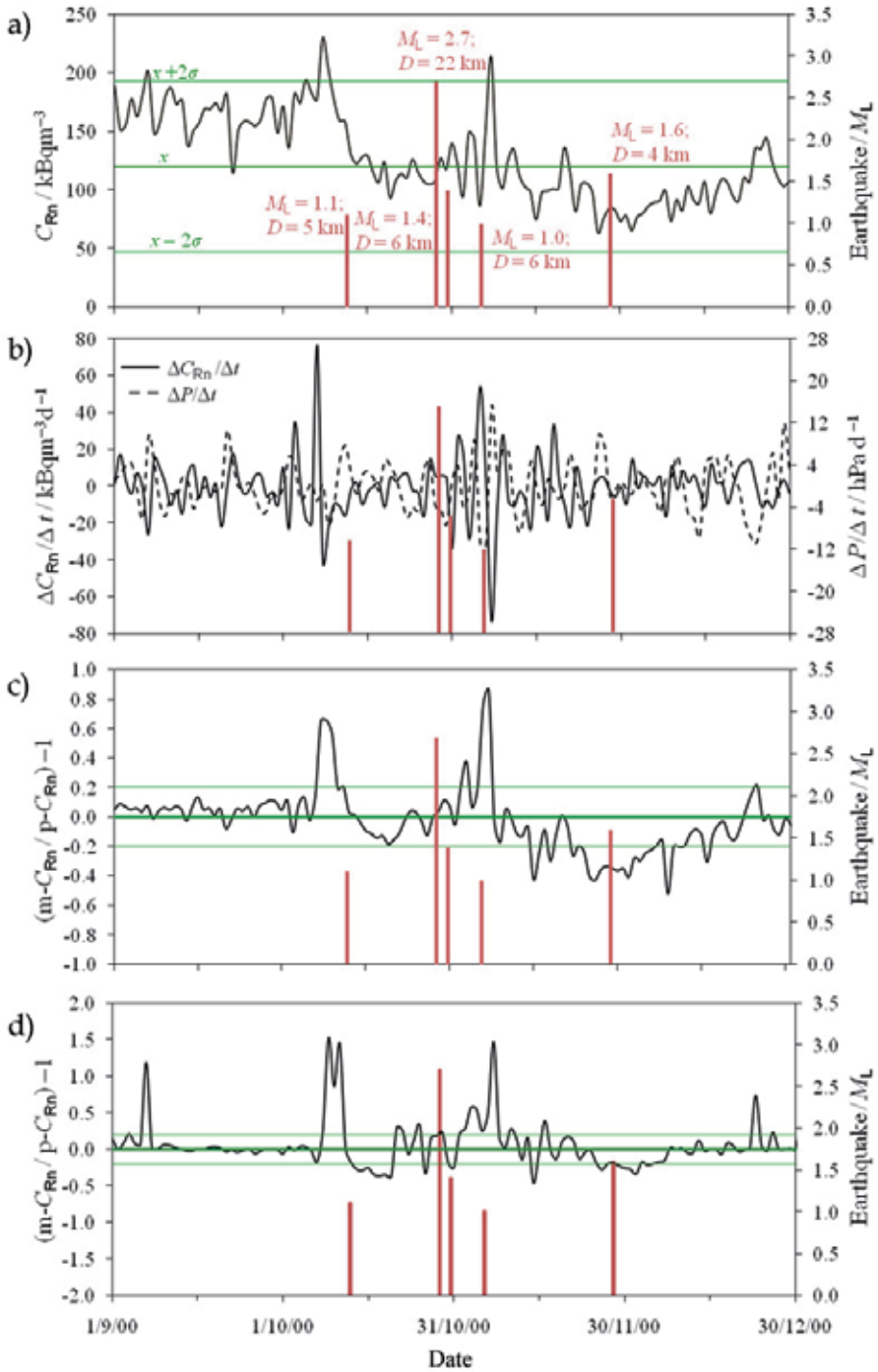

Fig. 7. A comparison of different approaches for the identification of radon anomalies: a) standard deviation (I); b) the relationship between radon exhalation and barometric pressure (II); c) artificial neural networks (III); and d) model trees (IV).

Both machine learning approaches, artificial neural networks (III) and decision trees (IV) give promising results, with a low number of false anomalies. The two distinctive anomalies – observed in Fig. 7c and Fig. 7d, for ANN and MT, respectively – confirm the anomalies identified by approaches (I) and (II). Additionally, a relatively long negative anomaly was observed using the ANN approach at the end of November, accompanying the earthquake with M_L=1.6. On the other hand, the same negative anomaly is only weakly expressed using the MT approach. A FA observed at the beginning of September using approaches (I) and (II) was also noticed using the MT approach but not by the ANN approach. Approaches (III) and (IV) do not appear to greatly depend upon the choice for the threshold of (m-C_{Rn}/p-C_{Rn})–1 and can, therefore, be used with less hesitation.

5. Conclusion

Since the appropriate interpretation of field measurements plays an important role in any research, the purpose of this work was to combine and evaluate the different approaches applied by our research group for differentiating the radon anomalies caused by increased seismic activity from those caused solely by environmental parameters. The application of four different approaches – standard deviation from the related mean value (I), the correlation between time gradients of barometric pressure and radon concentration (II), artificial neural networks (III) and decision trees (IV) – was presented. Radon anomalies based on approach (I) have been less successful in predicting earthquakes than those based on the other three approaches. Secondly, approaches (I) and (II) greatly depend upon the values of the ±xσ and $\Delta P/\Delta t$ thresholds, respectively, while the dependence of approaches (III) and (IV) on the threshold of (m-C_{Rn}/p-C_{Rn})–1 is very weak. The number of false anomalies for approach (II) points to the disturbance of radon exhalation by other environmental parameters and not just by barometric pressure. The assumption that radon exhalation is only directly influenced by barometric pressure is further suggested by different forms of radon transport at compression and dilatation zones (Ghosh et al., 2009). Promising results are achieved by applying approaches (III) and (IV), which make it possible to simultaneously incorporate all of the available environmental parameters. Furthermore, in using these techniques, the relation between radon concentration and environmental parameters does not necessarily have to be presumed linear. And finally, in taking into account the scale of the earthquake magnitudes observed during the time of radon measurements, one may speculate that the performance of the applied approaches would be better in the case of stronger earthquakes.

6. Acknowledgement

This study was done within the program P1-0143: Cycling of substances in the environment, mass balances, modelling of environmental processes and risk assessment.

7. References

Anderson, O.L., & Grew, P.C. (1977). Stress-corrosion theory of crack-propagation with applications to geophysics. *Reviews of Geophysics,* Vol. 15, No. 1, pp. 77–104

Atkinson, B.K. (1980). Stress corrosion and the rate-dependent tensile failure of a fine-grained quartz rock. *Tectonophysics,* Vol. 65, No. 3–4, pp. 281–290

Barragán, R.M., Arellano, V.M., Portugal, E., & Segovia, N. (2008). Effects of changes in reservoir thermodynamic conditions on ^{222}Rn composition of discharged fluids: study for two wells at Los Azufres geothermal field (Mexico). *Geofluids,* Vol. 8, No. 4, pp. 252–262

Belyaev, A.A. (2001). Specific features of radon earthquake precursors. *Geochemistry International,* Vol. 39, No. 12, pp. 1245–1250

Chen, C., Thomas, D.M., & Green, R.E. (1995). Modeling of radon transport in unsaturated soil. *Journal of Geophysical Research-Solid Earth,* Vol. 100, No. B8, pp. 15517–15525

Choubey, V.M., Kumar, N., & Arora, B.R. (2009). Precursory signatures in the radon and geohydrological borehole data for M4.9 Kharsali earthquake of Garhwal Himalaya. *Science of the Total Environment,* Vol. 407, No. 22, pp. 5877–5883

Chyi, L.L., Quick, T.J., Yang, T.F., & Chen, C.H. (2010). The experimental investigation of soil gas radon migration mechanisms and its implication in earthquake forecast. *Geofluids,* Vol. 10, No. 4, pp. 556–563

Cicerone, R.D., Ebel, J.E., & Britton, J. (2009). A systematic compilation of earthquake precursors. *Tectonophysics,* Vol. 476, No. 3–4, pp. 371–396

Clements, W.E., & Wilkening, M.H. (1974). Atmospheric-pressure effects on Rn-222 transport across earth-air interface. *Journal of Geophysical Research,* Vol. 79, No. 33, pp. 5025–5029

Cuomo, V., Di Bello, G., Lapenna, V., Piscitelli, S., Telesca, I., Macchiato, M., & Serio, C. (2000). Robust statistical methods to discriminate extreme events in geoelectrical precursory signals: Implications with earthquake prediction. *Natural Hazards,* Vol. 21, No. 2–3, pp. 247–261

Dobrovolsky, I.P., Zubkov, S.I., & Miachkin, V.I. (1979). Estimation of the size of earthquake preparation zones. *Pure and Applied Geophysics,* Vol. 117, No. 5, pp. 1025–1044

Džeroski, S. (2001). Data mining in a nutshell, In: *Relational data mining*, Džeroski, S., Lavrač, N. (Eds.), pp. 3–27, Springer, Berlin

Džeroski, S. (2002). Environmental sciences, In: *Handbook of data mining and knowledge discovery*, Klösgen, W., Żytkow, J. (Eds.), pp. 817–830, Oxford University Press, Oxford

Džeroski, S., Todorovski, L., Zmazek, B., Vaupotič, J., & Kobal, I. (2003). Modelling soil radon concentration for earthquake prediction. *Discovery Science, Proceedings,* Vol. 2843, pp. 87–99

Etiope, G., & Martinelli, G. (2002). Migration of carrier and trace gases in the geosphere: an overview. *Physics of the Earth and Planetary Interiors,* Vol. 129, No. 3–4, pp. 185–204

Favara, R., Grassa, F., Inguaggiato, S., & Valenza, M. (2001). Hydrogeochemistry and stable isotopes of thermal springs: earthquake-related chemical changes along Belice Fault (Western Sicily). *Applied Geochemistry,* Vol. 16, No. 1, pp. 1–17

Fleischer, R.L. (1981). Dislocation model for radon response to distant earthquakes. *Geophysical Research Letters,* Vol. 8, No. 5, pp. 477–480

Geller, R.J. (1997). Earthquake prediction: a critical review. *Geophysical Journal International,* Vol. 131, No. 3, pp. 425–450

Ghosh, D., Deb, A., & Sengupta, R. (2009). Anomalous radon emission as precursor of earthquake. *Journal of Applied Geophysics,* Vol. 69, No. 2, pp. 67–81

Ghosh, D., Deb, A., Sengupta, R., Patra, K.K., & Bera, S. (2007). Pronounced soil-radon anomaly - Precursor of recent earthquakes in India. *Radiation Measurements,* Vol. 42, No. 3, pp. 466–471

Gregorič, A., Zmazek, B., & Vaupotič, J. (2008). Radon concentration in thermal water as an indicator of seismic activity. *Collegium Antropologicum,* Vol. 32, pp. 95–98

Heinicke, J., Italiano, F., Koch, U., Martinelli, G., & Telesca, L. (2010). Anomalous fluid emission of a deep borehole in a seismically active area of Northern Apennines (Italy). *Applied Geochemistry,* Vol. 25, No. 4, pp. 555–571

Hickman, S., Sibson, R., & Bruhn, R. (1995). Introduction to special section: Mechanical involvement of fluids in faulting. *Journal of Geophysical Research,* Vol. 100, No. B7, pp. 12831–12840

Holub, R.F., & Brady, B.T. (1981). The effect of stress on radon emanation from rock. *Journal of Geophysical Research,* Vol. 86, No. NB3, pp. 1776–1784

İnan, S., & Seyis, C. (2010). Soil radon observations as possible earthquake precursors in Turkey. *Acta Geophysica,* Vol. 58, No. 5, pp. 828–837

Jain, A.K., Jianchang, M., & Mohiuddin, K.M. (1996). Artificial Neural Networks: A Tutorial. *Computer,* Vol. 29, No. 3, pp. 31–44

King, C.Y. (1978). Radon emanation on San Andreas Fault. *Nature,* Vol. 271, No. 5645, pp. 516–519

King, C.Y. (1984). Impulsive radon emanation on a creeping segment of the San-Andreas fault, California. *Pure and Applied Geophysics,* Vol. 122, No. 2–4, pp. 340–352

King, C.Y. (1985). Radon monitoring for earthquake prediction in China. *Earthquake Prediction Research,* Vol. 3, No. 1, pp. 47–68

King, C.Y., & Minissale, A. (1994). Seasonal variability of soil-gas radon concentration in central California. *Radiation Measurements,* Vol. 23, No. 4, pp. 683–692

Klusman, R.W., & Jaacks, J.A. (1987). Environmental influences upon mercury, radon and helium concentrations in soil gases at a site near Denver, Colorado. *Journal of Geochemical Exploration,* Vol. 27, No. 3, pp. 259–280

Klusman, R.W., & Webster, J.D. (1981). Preliminary analysis of meteorological and seasonal influences on crustal gas emission relevant to earthquake prediction. *Bulletin of the Seismological Society of America,* Vol. 71, No. 1, pp. 211–222

Kristiansson, K., & Malmqvist, L. (1982). Evidence for nondiffusive transport of $^{222}_{86}$Rn in the ground and a new physical model for the transport. *Geophysics,* Vol. 47, No. 10, pp. 1444–1452

Kuo, T., Fan, K., Kuochen, H., Han, Y., Chu, H., & Lee, Y. (2006). Anomalous decrease in groundwater radon before the Taiwan M6.8 Chengkung earthquake. *Journal of Environmental Radioactivity,* Vol. 88, No. 1, pp. 101–106

Kuo, T., Su, C., Chang, C., Lin, C., Cheng, W., Liang, H., Lewis, C., & Chiang, C. (2010). Application of recurrent radon precursors for forecasting large earthquakes (Mw > 6.0) near Antung, Taiwan. *Radiation Measurements,* Vol. 45, No. 9, pp. 1049–1054

Lay, T., Williams, Q., & Garnero, E.J. (1998). The core-mantle boundary layer and deep Earth dynamics. *Nature,* Vol. 392, pp. 461–468

Loh, W.-Y. (2011). Classification and regression trees. *Wiley Interdisciplinary Reviews: Data Mining and Knowledge Discovery,* Vol. 1, No. 1, pp. 14–23

Lomnitz, C. (1994). *Fundamentals of Earthquake Prediction*, John Wiley & Sons, New York

Martinelli, G. (1993). Fluidodynamical and chemical features of radon 222 related to total gases: implications for earthquake predictions, *Proceedings of IAEA Meeting on isotopic and geochemical precursors of earthquakes and volcanic eruptions*, Vienna, September 1991

Mjachkin, V.I., Brace, W.F., Sobolev, G.A., & Dieterich, J.H. (1975). Two models for earthquake forerunners. *Pure and Applied Geophysics,* Vol. 113, No. 1, pp. 169–181

Mogro-Campero, A., Fleischer, R.L., & Likes, R.S. (1980). Changes in subsurface radon concentration associated with earthquakes. *Journal of Geophysical Research,* Vol. 85, No. NB6, pp. 3053–3057

Negarestani, A., Setayeshi, S., Ghannadi-Maragheh, M., & Akashe, B. (2002). Layered neural networks based analysis of radon concentration and environmental parameters in earthquake prediction. *Journal of Environmental Radioactivity,* Vol. 62, No. 3, pp. 225–233

Negarestani, A., Setayeshi, S., Ghannadi-Maragheh, M., & Akashe, B. (2003). Estimation of the radon concentration in soil related to the environmental parameters by a modified Adaline neural network. *Applied Radiation and Isotopes,* Vol. 58, No. 2, pp. 269–273

Neznal, M., Matolin, M., Just, G., & Turek, K. (2004). Short-term temporal variations of soil gas radon concentration and comparison of measurement techniques. *Radiation Protection Dosimetry,* Vol. 108, No. 1, pp. 55–63

Pinault, J.L., & Baubron, J.C. (1996). Signal processing of soil gas radon, atmospheric pressure, moisture, and soil temperature data: A new approach for radon concentration modeling. *Journal of Geophysical Research-Solid Earth,* Vol. 101, No. B2, pp. 3157–3171

Planinić, J., Radolić, V., & Lazanin, Ž. (2001). Temporal variations of radon in soil related to earthquakes. *Applied Radiation and Isotopes,* Vol. 55, No. 2, pp. 267–272

Ramola, R.C. (2010). Relation between spring water radon anomalies and seismic activity in Garhwal Himalaya. *Acta Geophysica,* Vol. 58, No. 5, pp. 814–827

Ramola, R.C., Prasad, Y., Prasad, G., Kumar, S., & Choubey, V.M. (2008). Soil-gas radon as seismotectonic indicator in Garhwal Himalaya. *Applied Radiation and Isotopes,* Vol. 66, No. 10, pp. 1523–1530

Ramola, R.C., Singh, M., Sandhu, A.S., Singh, S., & Virk, H.S. (1990). The use of radon as an earthquake precursor. *Nuclear Geophysics,* Vol. 4, No. 2, pp. 275–287

Ramola, R.C., Singh, S., & Virk, H.S. (1988). A model for the correlation between radon anomalies and magnitude of earthquakes. *Nuclear Tracks and Radiation Measurements,* Vol. 15, No. 1–4, pp. 689–692

Reddy, D.V., & Nagabhushanam, P. (2011). Groundwater electrical conductivity and soil radon gas monitoring for earthquake precursory studies in Koyna, India. *Applied Geochemistry,* Vol. 26, No. 5, pp. 731–737

Sikder, I.U., & Munakata, T. (2009). Application of rough set and decision tree for characterization of premonitory factors of low seismic activity. *Expert Systems with Applications,* Vol. 36, No. 1, pp. 102–110

Singh, M., Kumar, M., Jain, R.K., & Chatrath, R.P. (1999). Radon in ground water related to seismic events. *Radiation Measurements,* Vol. 30, No. 4, pp. 465–469

Steinitz, G., Begin, Z.B., & Gazit-Yaari, N. (2003). Statistically significant relation between radon flux and weak earthquakes in the Dead Sea rift valley. *Geology,* Vol. 31, No. 6, pp. 505–508

Stranden, E., Kolstad, A.K., & Lind, B. (1984). Radon exhalation - moisture and temperature dependence. *Health Physics,* Vol. 47, No. 3, pp. 480–484

Thomas, D. (1988). Geochemical precursors to seismic activity. *Pure and Applied Geophysics,* Vol. 126, No. 2, pp. 241–266

Torkar, D., Zmazek, B., Vaupotič, J., & Kobal, I. (2010). Application of artificial neural networks in simulating radon levels in soil gas. *Chemical Geology,* Vol. 270, No. 1–4, pp. 1–8

Toutain, J.P., & Baubron, J.C. (1999). Gas geochemistry and seismotectonics: a review. *Tectonophysics,* Vol. 304, No. 1–2, pp. 1–27

Ulomov, V.I., & Mavashev, B.Z. (1967). On forerunners of strong tectonic earthquakes. *Doklady Akademii Nauk SSSR*, No. 176, pp. 319–322

Vàrhegyi, A., Hakl, J., Monnin, M., Morin, J.P., & Seidel, J.L. (1992). Experimental study of radon transport in water as test for a transportation microbubble model. *Journal of Applied Geophysics,* Vol. 29, No. 1, pp. 37–46

Virk, H.S., Sharma, A.K., & Sharma, N. (2002). Radon and helium monitoring in some thermal springs of North India and Bhutan. *Current Science,* Vol. 82, No. 12, pp. 1423–1424

Wakita, H., Nakamura, Y., Notsu, K., Noguchi, M., & Asada, T. (1980). Radon anomaly - possible precursor of the 1978 Izu-Oshima-Kinkai earthquake. *Science,* Vol. 207, No. 4433, pp. 882–883

Walia, V., Lin, S.J., Hong, W.L., Fu, C.C., Yang, T.F., Wen, K.L., & Chen, C.H. (2009a). Continuous temporal soil-gas composition variations for earthquake precursory studies along Hsincheng and Hsinhua faults in Taiwan. *Radiation Measurements,* Vol. 44, No. 9–10, pp. 934–939

Walia, V., Yang, T.F., Hong, W.L., Lin, S.J., Fu, C.C., Wen, K.L., & Chen, C.H. (2009b). Geochemical variation of soil-gas composition for fault trace and earthquake precursory studies along the Hsincheng fault in NW Taiwan. *Applied Radiation and Isotopes,* Vol. 67, No. 10, pp. 1855–1863

Washington, J.W., & Rose, A.W. (1990). Regional and temporal relations of radon in soil gas to soil-temperature and moisture. *Geophysical Research Letters,* Vol. 17, No. 6, pp. 829–832

Witten, I.H., & Frank, E. (1999). *Data Mining: Practical Machine Learning Tools and Techniques with Java Implementations*., Morgan Kaufmann, San Francisco

Yang, T.F., Walia, V., Chyi, L.L., Fu, C.C., Chen, C.H., Liu, T.K., Song, S.R., Lee, C.Y., & Lee, M. (2005). Variations of soil radon and thoron concentrations in a fault zone and prospective earthquakes in SW Taiwan. *Radiation Measurements,* Vol. 40, No. 2–6, pp. 496–502

Zmazek, B., Italiano, F., Živčić, M., Vaupotič, J., Kobal, I., & Martinelli, G. (2002a). Geochemical monitoring of thermal waters in Slovenia: relationships to seismic activity. *Applied Radiation and Isotopes,* Vol. 57, No. 6, pp. 919–930

Zmazek, B., Todorovski, L., Džeroski, S., Vaupotič, J., & Kobal, I. (2003). Application of decision trees to the analysis of soil radon data for earthquake prediction. *Applied Radiation and Isotopes,* Vol. 58, No. 6, pp. 697–706

Zmazek, B., Todorovski, L., Živčić, M., Džeroski, S., Vaupotič, J., & Kobal, I. (2006). Radon in a thermal spring: Identification of anomalies related to seismic activity. *Applied Radiation and Isotopes,* Vol. 64, No. 6, pp. 725–734

Zmazek, B., Živčić, M., Todorovski, L., Džeroski, S., Vaupotič, J., & Kobal, I. (2005). Radon in soil gas: How to identify anomalies caused by earthquakes. *Applied Geochemistry,* Vol. 20, No. 6, pp. 1106–1119

Zmazek, B., Živčić, M., Vaupotič, J., Bidovec, M., Poljak, M., & Kobal, I. (2002b). Soil radon monitoring in the Krško Basin, Slovenia. *Applied Radiation and Isotopes,* Vol. 56, No. 4, pp. 649–657

10

Changes in Apparent Resistivity in the Late Preparation Stages of Strong Earthquakes

Du Xuebin et al.*
Lanzhou Base of Institute of Earthquake Science, CEA, Lanzhou China

1. Introduction

In China, a large-scale observation network that is comprised of a number of apparent resistivity (for short, AR) stations has been established for the purpose of earthquake (EQ) monitoring and prediction since the 1966 Ms7.2 Xingtai EQ in Hebei Province. Presently, over 70 AR stations are in observation in seismically active belts in densely populated areas and nearby some of large, medium-sized cities. The 2008 Ms8.0 Wenchuan great EQ in Sichuan province occurred in the AR station network that was located in the border area of both Sichuan and Gansu provinces. In the 1970s-1980s, more than 110 AR stations had been in observation, and in those years, several great earthquakes (EQs) occurred nearby AR stations, such as the 1976 Ms7.8 Tangshan EQ in Hebei province, the 1976 Ms7.2 Songpan-Pingwu EQ in Sichuan province, the 1976 Ms7.4 Longling EQ in Yunnan province, and the 1988 Ms7.6 Lancang-Gengma EQ in Yunnan Province. At an AR station, two horizontally perpendicular observation channels or three channels, more one horizontally skewed channel (a NE or NW channel, as illustrated in Fig.1a), are employed, and for each channel, an AR observation configuration with a symmetry four-electrode array is installed (Fig.1b). For most stations, the current electrode spacing $\overline{AB} = 1000 \sim 2000\text{m}$.

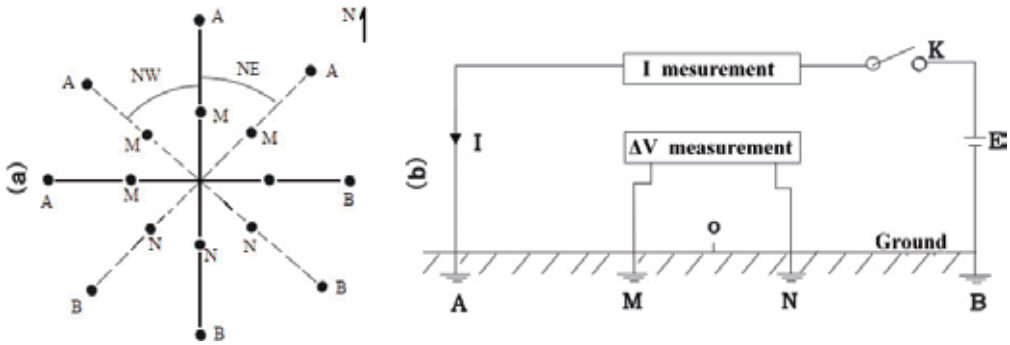

Fig. 1. The observation channels (a) and symmetric four-electrode resistivity array for a channel (b) at a geo-electrical station

* An Zhanghui[1], Yan Rui[3], Ye Qing[2], Fan Yingying[1], Liu Jun[1], Chen Junying[1] and Tan Dacheng[1]
[1]*Lanzhou Base of Institute of Earthquake Science, CEA, Lanzhou, China*
[2]*China Earthquake Networks Center, China Earthquake Administration, Beijing, China*
[3]*Earthquake Administration of Beijing Municipality, Beijing, China*

Some of the AR stations have continuously observed for more than 40 years, and a lot of AR data are observed. Using these data we can understand whether the earthquake-related AR changes are recorded or not, which is an issue that should be seriously discussed because the precursory anomalies before EQs have been strongly debated. In this chapter we try to study the issue from two respects: (1) the EQ case research on AR changes recorded before EQs, and (2) the theoretical analysis on anisotropic AR changes related to the maximum principal compression stress (P – axis) azimuth of focal mechanism solution, nearby an EQ focal region in the late preparation stages of a strong EQ. This chapter will help objectively evaluate and comprehend the AR precursory changes related to EQs.

2. EQ case research

Before several great EQs with magnitude of Ms≥7.0 and some moderate EQs, obvious AR anomalies, which include the medium-term anomalies that start to appear about 2-3 years to several months before EQs and the imminent anomalies that start to appear about 3 months to several days preceding EQs, are recorded at geo-electrical stations nearby the epicentral areas, in China. Some of the anomalies are ascertained after EQs, whereas some are discerned before EQs. More interestingly, two groups of EQs with magnitude of Ms 6 nearby AR stations are actually forecasted on a one-year time scale using medium-term AR anomalies, for which the expected EQ magnitudes and forecasted locations are all right.

2.1 AR changes ascertained after EQs

2.1.1 Reappearing AR anomalies before two great EQs

In 1976, three great EQs with magnitude of Ms ≥ 7.2 occurred in the mainland Chinese, such as the July 28 Ms7.8 Tangshan EQ in Hebei province, the Aug. 16 Ms7.2 Songpan-Pingwu EQs in Sichuan province, and the May 29 Ms7.4/7.3 Longling EQ in Yunnan province. Of the EQs, the Tangshan EQ and Songpan-Pingwu EQ occurred in a local AR station network, and significant AR changes were ascertained after the EQs. As shown in figure 2[1], obviously drop AR changes were recorded at station Changli-Houtuqiao (CLH) in Hebei province, before the Ms7.8 Tangshan EQ (80 km from CLH station) and at station Wudu-Hanwang(WDH) in Gansu province, before the Songpan-Pingwu Ms7.2 EQ (105 km from WDH station), respectively. On those days, the two stations were in normal operation. It can be seen from raw AR daily mean curves of the two stations that AR changes fell all during about 40 days before the occurrence of the two great EQs, which were notable short-term anomalies proceeding the two EQs. Especially, during about 20 days before the two EQs AR changes started to fall by a larger margin, which were imminent anomalies before the impending EQs. Then, immediately after the occurrence of the two EQs, the drop changes started to rise. Based on the two AR anomalies corresponding to the two EQs, we can discuss two problems as follows:

The first problem is on the repeatability of AR anomalies before the two EQs. The Ms7.8 Tangshan EQ occurred in Hebei Province, in east China, and the M7.2 Songpan-Pingwu EQ occurred in north Sichuan province, in western China. The distance between the two EQ epicenters were beyond 1500 km; and the two stations were located in different tectonic units (station CLH was nearby the Cangdong fault belt in the Beijing-Tianjin-Tangshan area, in east China, and station WDH was nearby the Bailong river fault belt in South Gansu province, in western China). The underground geo-electrical structure of the two stations was very different. Nevertheless, the drop AR changes of the two stations before the two

great EQs and their recovery AR changes immediately after the two events had a similar changeable pattern in appearance. Therefore, the anomalous AR changes were believed to be the anomalies related to the two great EQs.

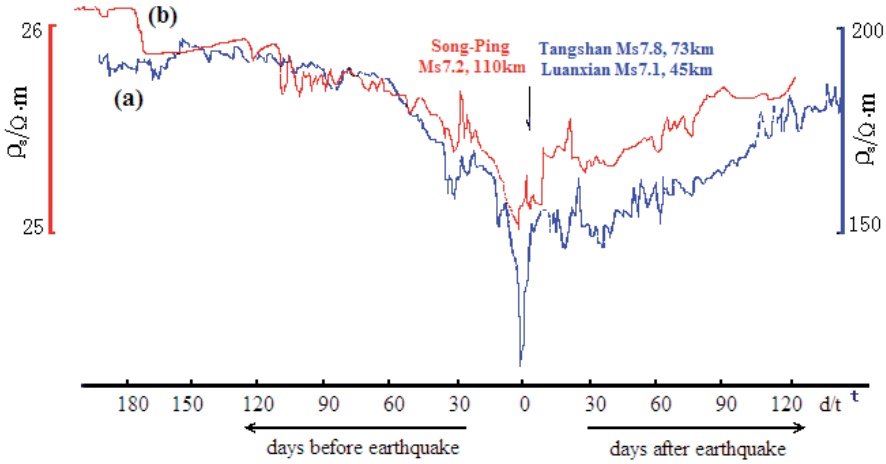

Fig. 2. AR changes observed at CLH station before the 1976, Ms7.8 Tangshan EQ (a), and at WDH station before the 1976, Ms7.2 Songpan-Pingwu EQ (b)

The second problem is on the drop pattern of the two AR anomalies. It is obvious from figure 2 that the AR changes have a notable drop pattern during the imminent stage of the two impending great EQs. In general, the underground medium is abundant with water and the medium resistivity is susceptible to water, therefore, we believed that the changes of underground water resulted in these drop AR changes before the two impending EQs. Figure 3 are the raw AR daily-mean curve at CLH station and the raw curve of water level

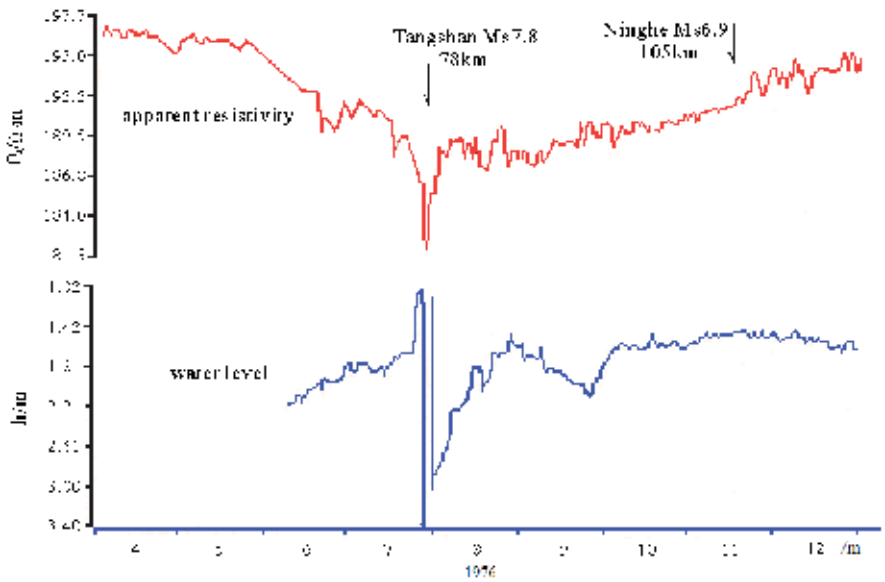

Fig. 3. The AR change observed at CLH station and the water level change observed at Longjiadian station

observed at underground water station[2], Longjiadian station which was about 20 km from station CLH and nearby the Cangdong rupture zone. We can notice from figure 3 that immediately before and after the occurrence date of the EQ, the drop AR change at station CLH was well corresponding to the rise change in water level at station Longjiadian. The opposite changeable patterns between electric and water are quite significant, which indicated that the water in the underground medium nearby the focal region played an important role in AR changes.

It can be seen from figure 3 that nothing was recorded before the Ms6.9 Ninghe aftershock (Nov. 15, 1976) at the geo-electrical and water stations, a possible reason for which was explained by associating with the mainly active faults in/nearby the focal region and the focal mechanism of the aftershock by Du *et al*.[3-4].

2.1.2 AR anomalies corresponding to the Ms8.0 Wenchuan EQ

On May 12, 2008, a great EQ of Ms8.0 struck the Wenchuan county and its adjacent area in Sichuan province of China, and within one month following it, more than thirty Ms5.0~6.4

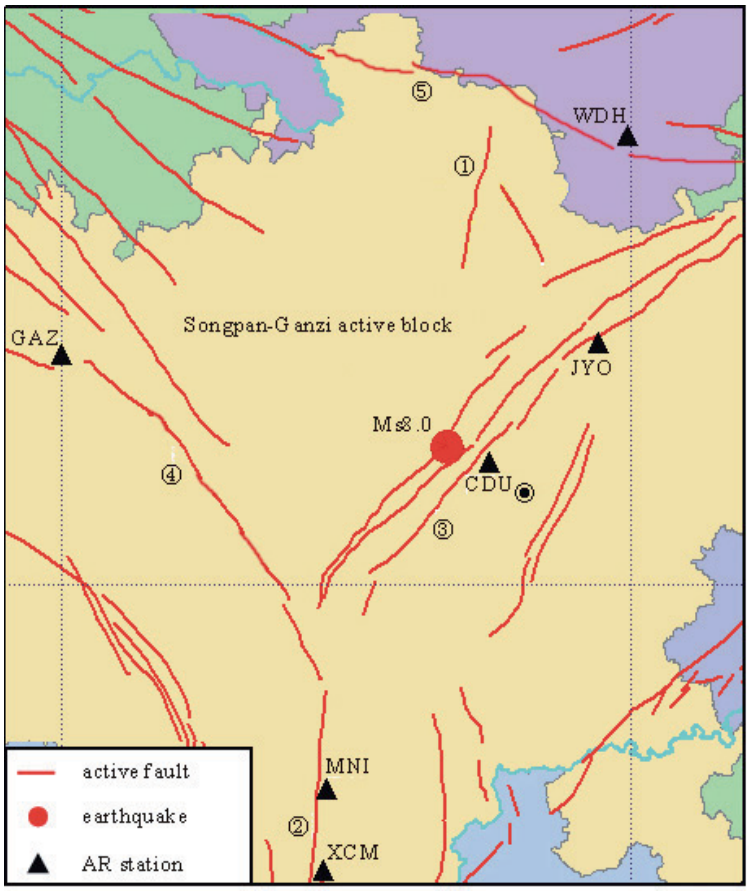

①Minjiang river fault, ②Anning river fault, ③Doujiang Weir–An county fault, ④Xianshui river fault, ⑤White Dragon River fault

Fig. 4. Distributions of station, epicenter and fault.

aftershocks occurred along the NE-strike fault belt beyond 300 km long, from the Wenchuan county to the Ningqiang county in Shaanxi province. There were six AR stations within 400 around the main epicenter, which were Chengdu station (CDU, 35km), Jiangyou station (JYO, 150 km), Ganzi station (GAZ, 331 km), Mianning station (MNI, 260) and Xichang station (XCM, 360 km) in Sichuan province, and WDH station (300 km) in Gansu province (Fig.4).

2.1.2.1 Medium-term AR anomalies before the EQ

Significant AR anomalies were recorded at four stations in the medium-term stage before the Ms 8.0 Wenchuan EQ as follows.

1. Locally concentrated anomalies

The anomalies were recorded at CDU, JYO, GAZ and WDH during the medium-term stage before the EQ, which were in the range of 400km from the main epicenter (Fig.5, Fig.6).

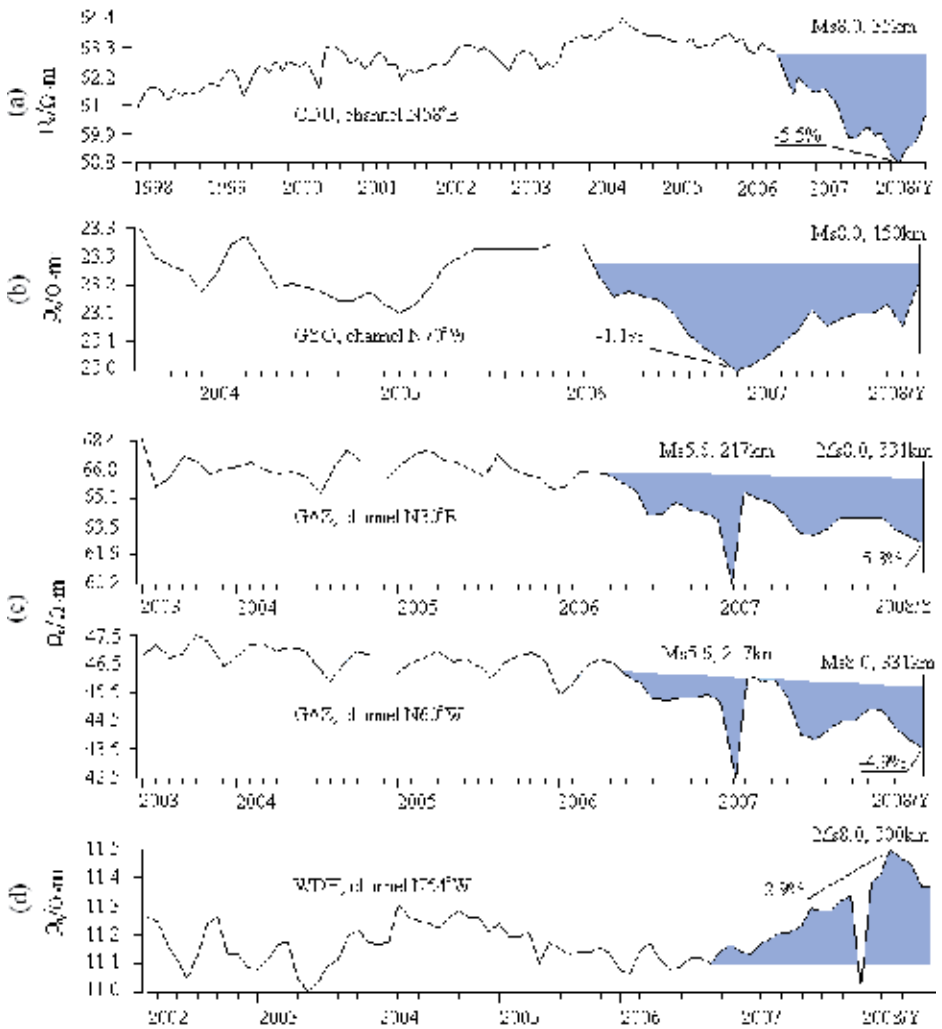

Fig. 5. AR monthly mean changes observed at four stations that were located along the Songpan-Ganzi active block before the M8.0 Wenchuan EQ

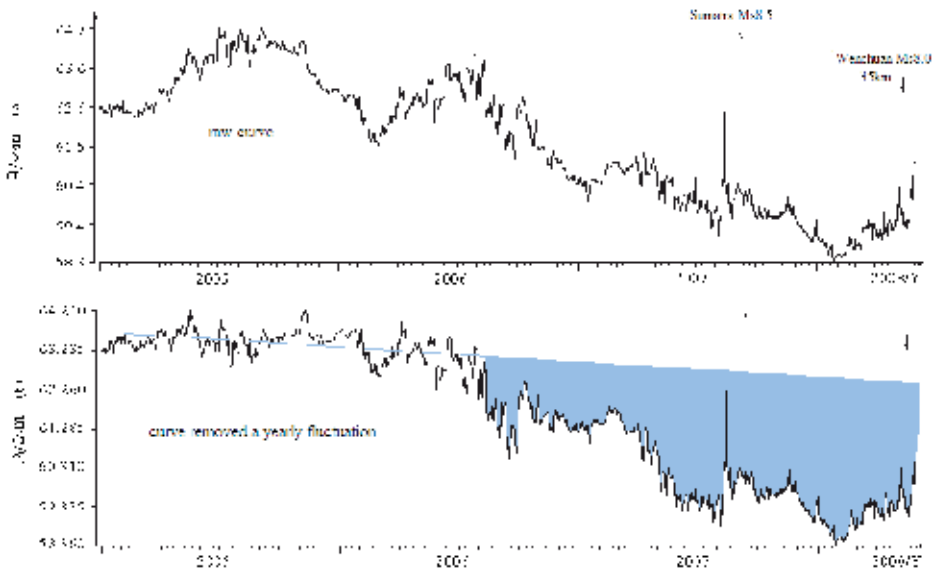

Fig. 6. AR daily mean changes observed at CDU station before the M8.0 Wenchuan EQ

Furthermore, the spatial distribution of the anomalies was tectonically relevant to the Songpan-Ganzi active block. The main shock and its aftershocks occurred along the Longmen mountain nappe structure of the block. Accordingly, the anomalies were recorded at the four stations along the bordering faults around the block (Fig.4), whereas such anomalies were not recorded at the two stations MNI and XCM, which were located along the Anning river fault, beyond the block. This situation is similar to that which was observed before the 1976 Ms7.8 Tangshan EQ when anomalies appeared mostly at the stations along NE- and NW-striking conjugate faults in the Beijing-Tianjin-Tangshan areas.

According to previous statistical studies on numerous EQ cases[5-6] by other Chinese scholars, the spatially distribution of medium-term AR anomalies is about 300~400 km before an EQ with magnitude of Ms ≥ 7.0. According to paper[7], for Ms>6.0 EQs most AR anomalies distribute in the range of 400 km from epicenters and there is commonly no obvious difference between the ranges for Ms>6.0 EQs and Ms ≥ 7.0 EQs. The results show that an epicentral distance of 400km can be used as a reference for identifying medium-term AR anomalies related to Ms>6.0 EQs. Du *et al*.[8] studied the relationship between the spatial distribution of medium-term anomalies of other precursor observations in China, such as AR, groundwater chemical components and water level, geo-stress and geo-deformation, and the mainly active fault around the epicentral region, as a result, it was believed that the anomalies usually appeared nearby the faults around EQ focal areas.

The spatial distribution of the medium-term AR anomalies before the Wenchuan great EQ, which were concentrated in the range of 400 km from the main epicenter and along the bordering faults around the Songpan-Ganzi active block, was in accordance with the foregoing research results.

2. Synchronous medium-term AR anomalies

These AR anomalies started to appear from about Aug. 2006 at CDU, JYO, GAZ and WDH. In other wards, they appeared synchronously before the main shock at the four stations which were located along the bordering faults of the Songpan-Ganzi active block. The

behavior was similar to previous research results. According to Du et al.[8], the medium-term AR anomalies along a actively geological structure around an EQ focal area usually started to appear synchronously or quasi-synchronously. In fact, the medium-term anomalies in observation of groundwater chemical components and water level, geo-stress and geo-deformation along a same structure also have such behavior as seen in AR observation[8].

3. Mostly drop-type AR anomalies

The drop-type anomalies were recorded at stations CDU, GAZ and JYO. Only at station WDH, was a rise-type anomaly recorded, yet this was not isolated. Stations WDH and Tianshui (TSE), in Gansu province, were all located to the north of the main epicenter, and station TSE was to the north of station WDH, which was nearby the NWW-striking western Qinling rupture belt and was 452 km from the main epicenter. At station TSE, a rise anomaly beyond 1% appeared during two months period preceding the main shock, which was the most prominent AR change in the last ten years at the station. The phenomenon of mostly drop-type AR anomalies coincided with previous researches, and the spatial distribution of the medium-term anomalies at the four stations well tallied, in the range of -400 km, with that before EQs with magnitude Ms>7.0.

For change of patterns, a drop-type or rise-type change, of the medium-term AR anomalies which were processed by using the normalized variation rate method (NVRM)[9,7], Du et al.[10,7] got the following statistic results: for Ms ≥ 7.0 EQs, about 100% of the anomalies in the range of 150 km from epicentral areas are negative (a drop-type pattern) and about 71% of the anomalies in the range of 400 km are still negative. The reasons on the change patterns of the anomalies was theoretically explained by papers[10, 7].

4. Large-amplitude anomalies

At station CDU, which was the nearest station to the EQ epicenter, the anomaly amplitude reached up to -5.5%. At stations GAZ and WDH, which were farther away from the EQ epicenter than station CDU, the anomaly amplitudes reached up to -5.3%－-4.9% and 2.9%, respectively. The mean of the anomaly amplitudes was larger than that before the1976 M7.8 Tangshan EQ, and the anomaly amplitudes of the three stations decreased with the increase of epicentral distance. The anomaly recorded at JYO was small in amplitude, only -1.1%, although it was nearby the main EQ epicenter area (according to an investigation after the EQ, the measuring instrument at the station was not in good operation at that time, with a fixed error).

The relationship between AR anomaly amplitude and EQ magnitude has been studied by numerous scholars[5-7]. The anomaly amplitude before the Wenchuan great EQ was in accordance with the previous researches.

5. Anisotropic AR changes

Two observation channels, along N58^{o}E and N49^{o}W directions, are employed at station CDU. The anomaly amplitude recorded through the N58^{o}E channel was -5.5%, whereas no anomaly was recorded through the N49^{o}W channel. According to previous works[2,11], this anisotropic AR changes roughly indicated that the underground media here had been under the action of the maximum compressive stress in the NW-SE direction during the period from about Aug. 2006 to the occurrence of the main shock. At station GAZ, two channels, along N30^{o}E and N60^{o}W directions, are employed. The anomaly amplitude recorded

through the N30°E channel was -5.3%, and that recorded through the N60°W channel was -4.9%. This indicated that the media here had been under the maximum compressive stress in the NWW-SEE direction during the period. The maximum compressive stress directions that were revealed by the AR changes at the two stations basically corresponded to the P-axis azimuth of the main shock[12]. Station JYO was near the northern aftershock area of the great EQ, and two channels, along the N70°W and N10°E directions, are employed at the station. The comparison between anomaly amplitudes recorded through the two channels was still credible as the measuring instrument at the station had just a fixed error. The anomaly amplitude recorded through the N70°W channel was -1.1% and no anomaly was recorded through the N10°E channel. This indicated that the media here had been under the maximum compressive stress close to the NS direction during the period, which well corresponded to the P-axis azimuths of most strong aftershocks in the northern aftershock area.

In summary, the behaviors of these medium-term AR anomalies, such as their spatial distribution within 400 km, their tectonic relevance to the Songpan-Gazi active block, and their amplitude attenuation with increasing distance, as well as their synchronous, mostly descending, large-amplitude and anisotropic changes, strongly support that these anomalies are indeed related to the focal processes of the main shock and strong aftershocks. Such locally concentrative AR anomalies as recorded at the four stations have not been succeeded in identifying in areas beyond 400 km from the EQ epicenter.

2.1.2.2 Short-term AR anomalies before the EQ

During the short-term period before the occurrence date of the great EQ, no obvious anomaly, like these recorded at station CLH (72km) in Hebei province before the 1976 M7.8 Tangshan EQ and at station WDH (110 km) before the 1976 M7.2 Songpan-Pingwu EQs (Fig.2), was recorded at the six stations within 400 km from the EQ epicenter. Upward AR changes commenced at station CDU from March 2008 and at station JYO from April 2008 (Fig.5a-b and Fig.6). The patterns consisting of an initial medium-term drop change followed by a short-term rise change before the EQ are consistent with these of the electrical resistivity change within an EQ focal area that are forecasted by DD model[13-14]. In fact, such patterns appeared often nearby epicentral areas of previous strong EQs[9, 2,7]. However, the rise change, upon which the main shock occurred, did not satisfy the anomaly criterion in amplitude, so no sufficient precursory information could be confidently detected in the period when approaching the EQ.

Du *et al*[3, 15] studied the spatial distribution characteristics of imminent AR anomalies before the moderate, strong EQs that occurred in the continent of China. As a result, it was got that the spatial distribution of the anomalies was influenced by mainly active faults around EQ focal areas and focal mechanisms. The influences include: (1) the anomalies appear mostly along or nearby the faults; (2) most anomalies are distributed in the two areas that are symmetrical about an epicenter and that azimuthally tie to the P- or T-axis areas that correspond to the focal fault movement; (3) If there is an active fault between a station and an epicentral area, and the fault strike is along or close to the azimuth of the foregoing P- or T-axis, then, no imminent anomaly is usually recorded at the station in the period when approaching the EQ, or an anomaly is generally weak in amplitude.

For example, in the Songpan-Pingwu area in Sichuan Province, three EQs with magnitude of Ms7.2, Ms6.7 and Ms7.2 occurred successively within 8 days in August 1976 at almost the same location (Fig.7), under the action of the compressive stresses in the NE direction (for the previous Ms7.2 EQ) and near to the EW direction (for the following Ms6.7/7.2 EQs)[16].

And the P-axis azimuths of the three EQs were 63°, 101° and 95°, respectively, resulting in an right-lateral movement of the NNW-striking Huya fault (i.e., the focal fault) when the previous Ms7.2 EQ occurred, and then an left-lateral movements of the fault when the following Ms6.7 and Ms7.2 EQs occurred[16]. At that time, three stations were in observation within a range of ~190 km from the three epicenters: station Songpan (SPN, 45km, and it was abandoned shortly afterwards) in Sichuan Province and station Lixian (LXN, 190 km, and abandoned in the 1990s) and station WDH (110 km), in Gansu Province. There were obvious differences between AR changes recorded at station SPN and those recorded at station LXN (Fig. 8). Station SPN was located on the west side of the Minjiang River fault (MRF) with the NNE strike, whereas the epicenters were to the east of the fault. As a result, no imminent AR anomaly was recorded at station SPN when approaching the occurrence date of the first Ms7.2 EQ, though the station was only 45 km from the epicenter, whereas at LXN station, a drop anomaly with amplitude of -0.8% was recorded during 4 days before the EQ in despite of being 190 km away. Contrarily, for the subsequent Ms6.7 and Ms7.2 EQs, a drop anomaly with amplitude of -3.5% was clearly captured at station SPN during 3–4 days before them. This anomaly amplitude was much greater than that recorded at station LXN before the first Ms7.2 EQ. No imminent anomaly appeared at station LXN for the latter EQs. At station WDH, which was located between station LXN and the three epicenters and was near to the north side of the White Dragon River fault (WDRF) with the EW strike, the AR changes recorded before the three events were similar to those seen at station LXN.

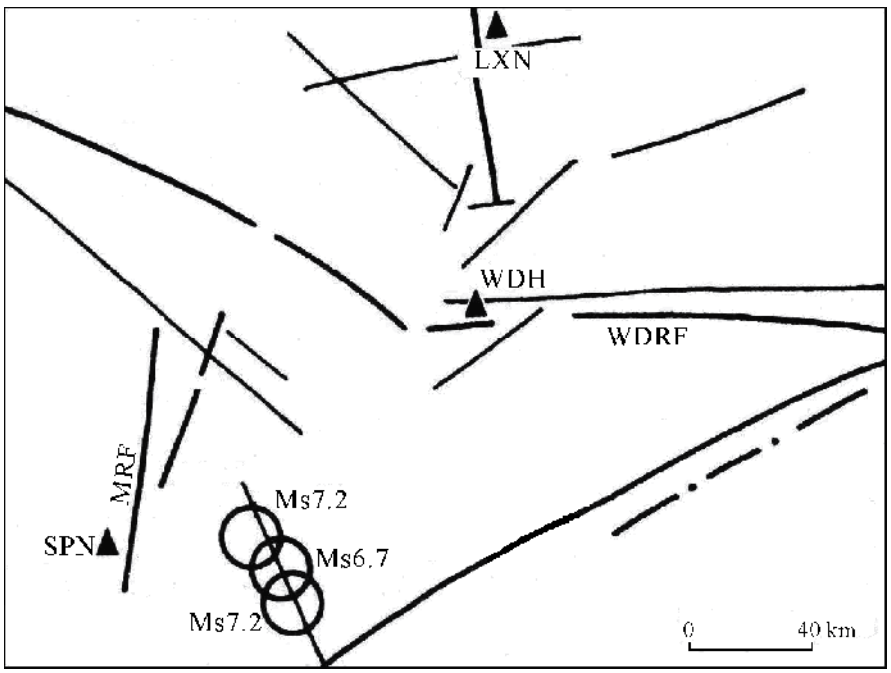

Fig. 7. Distribution of epicenters, active faults and AR stations

According to papers[4, 17], imminent anomalies recorded at underground water level and water chemistry stations before the moderate, strong EQs which occurred in the continent of China also demonstrated such spatial distribution as AR imminent anomalies, which was related to mainly active faults of epicentral areas and EQ focal mechanisms. From loading

experiments of rock sample[18], the crust medium nearby active faults are susceptive to stress disturbances during the loading processes, therefore, the AR and underground-water anomalies which is related to the geo-stress changes are easy recorded nearby the faults. Paper [19] calculated the strain distribution in a geologic body model with a fault using the elasto-plastic 2-D finite element method, and then the calculated strain values are converted into relative AR changes. It can be seen from the spatially non-uniform distribution of these calculated AR changes that the spatial distribution of AR changes which are related mainly active faults around epicentral areas and EQ focal mechanisms, as described in papers [3,15,7], can be well explained. In fact, the spatially non-uniform distribution of imminent anomalies in observation of underground water level and water chemistry, as described in papers [4, 17], can be well explained based on the calculated strain distribution by paper [19] also.

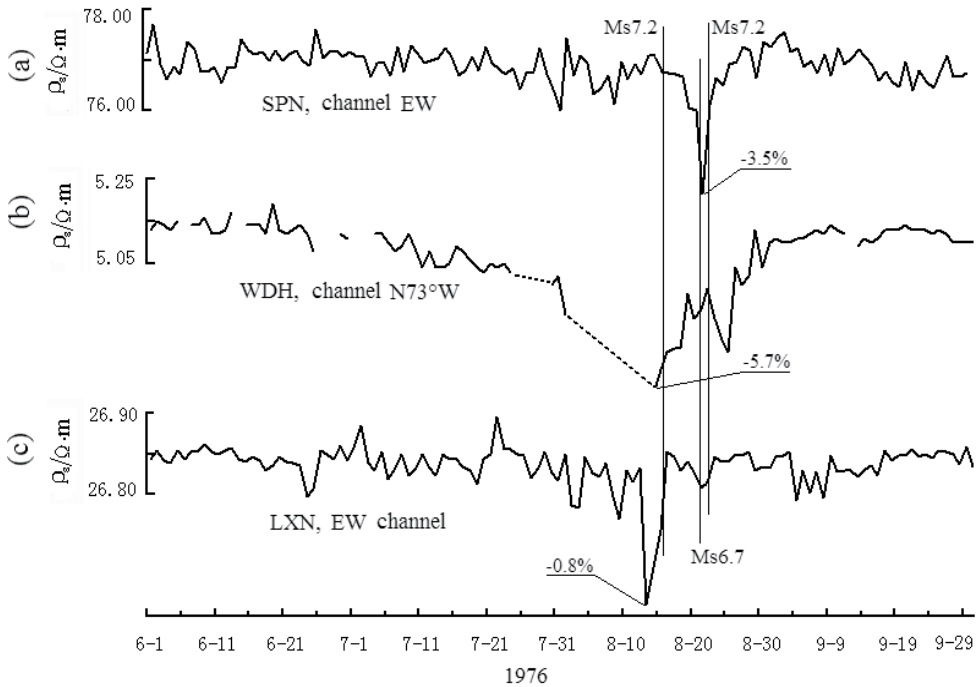

Fig. 8. AR daily-mean curves of SPN (a), WDH (b) and LXN (c) stations

Based on the above-mentioned research works, the lack of imminent AR anomalies before the Wenchuan great EQ can be roughly explained. The main shock and strong aftershocks occurred to the west of the NE-striking Doujiang Weir-An county fault; station GAZ was located on the southwestern side of the NW-striking Xianshui River fault, and station WDH was located on the northern side of the NWW-striking WDRF (Fig.4 and Fig.7). Hence, the reason why no anomaly was recorded at stations GAZ and WDH during the period when approaching the great EQ can be explained. The reason why no anomaly was seen at stations MNI and XCM can be explained also. Stations CDU and JYO were located to the east of the Doujiang-Weir-An county fault, near the main epicenter and in the area liable to record the anomaly related to the main shock, but at the two stations only weak upward changes were recorded during the period. The reason for this remains to be explained and requires additional research.-A possible reason is affected by secondary faults nearby the two stations.

2.2 Medium-term AR anomalies discerned before EQs

On Oct. 25, 2003, two EQs with magnitude of Ms6.1 and Ms5.8 occurred in Minle-Shandan area in Gansu province of China. This year, on Jul. 21, one Ms 6.2 EQ occurred in the Dayao area in Yunnan province, and on Oct. 6, a Ms6.1 EQ occurred also in Dayao area. In fact, the medium-term AR anomalies were well discerned before the two groups of strong EQs, and the EQ locations and magnitudes were successfully forecasted on a one-year time scale, in Nov. of 2002.

Within the range of ~400 km from the epicenters of the Ms 6.1/5.8 Minle- Shandan EQs, there were 6 AR stations, such as Shandan (SHD), Wuwei (WWE), Jayuguan (JYG), Lanzhou (LZL), Linxia (LNX) and Dingxi (DGX) stations, which are all set by China Earthquake Administration (CEA). Of 6 stations, the previous 5 stations, not including DGX station, were in good observation at that time. Of the 5 stations, reliable medium-term AR anomalies, drop-type AR changes, appeared at station SHD during the end of 2002. This station has always kept an observational environment which is up to the technical requirement of seismic geo-electrical station in the long-term observation. Figure 9 shows AR normalized variation rate curves of three channels of this station from Aug. of 1988 to Oct. of 2002, based on monthly AR averages, which are processed by the normalized variation rate method (NVRM)[9,7] in Nov. of 2002. It can be seen from the curves that notable medium-term or short-term AR anomalies which were up to the identification criterion for NVRM anomaly, beyond the threshold value of ± 2.4, appeared before several EQs with magnitude of $Ms \geq 5.0$ around the station from 1990 to 2001. In 2002, two drop-type AR anomalies appeared again through channels EW and NW of the station, and a rise-type anomaly did through channel NS. These anomalies were new, following the rise-type anomalies of three channels in the end of 2001 which corresponded to the Nov. 2011 Kunlunshan mountain Ms8.1 EQ far—one type of anomalies which had nothing with the focal process of the great EQ[20, 7-8]. According to the past EQ cases of the station where AR anomalies corresponded to EQs around and the research results in papers [8,10], Du *et al*. forecasted in Nov. 2002 that one strong EQ will occur nearby the station in 2003 year.

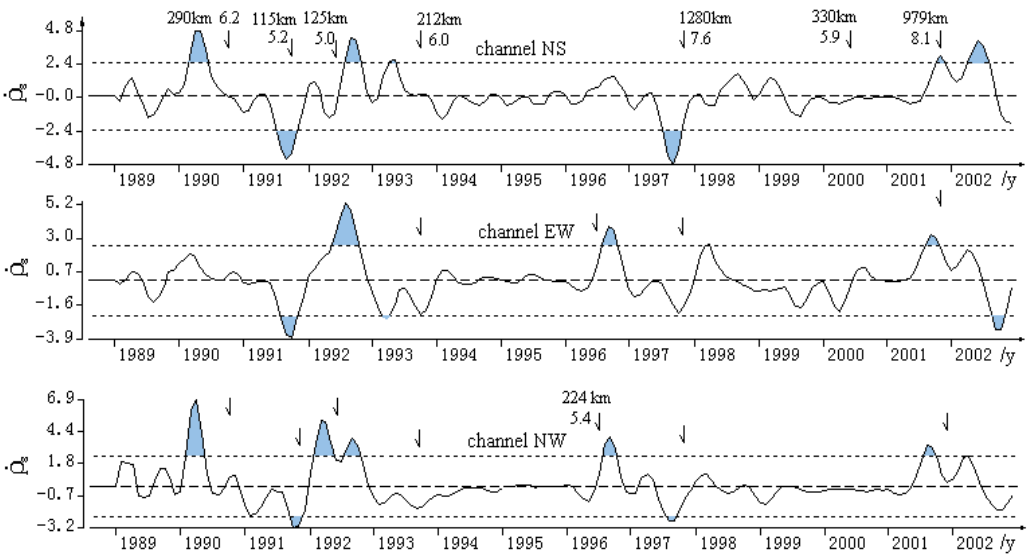

Note: these curves were drown in Nov. of 2002

Fig. 9. NVRM curves of AR changes of SHD station (from Aug. of 1988 to Oct. of 2002)

In Nov. of 2002, Du *et al*. also detected that AR anomalies appeared at Panzhihua (PAH) and Yuanmou (YNM) in Yunnan province. The AR data, monthly mean data, observed by the two stations were processed using NVRM. Figure 10 gives the NVRM curves of PAH station which were reprocessed in 2004. This station was settled in 1970s, around which many EQs with magnitude of Ms ≥ 5.0 have occurred since then, accordingly, at this station AR anomalies have been recorded before the EQs. According to the previous EQ monitoring efficiency of the station, Du *et al*. forecasted in Nov. of 2002 that the AR upward anomaly of 2002 at this station, as seen in figure 10 (the lower curve in the figure), possibly indicated an future strong EQ nearby the station. Besides, at YNM station which was close to the PAH station, AR upward anomalies appeared in the end of 2002 also. Thus, the credibility for the expected EQ was increased.

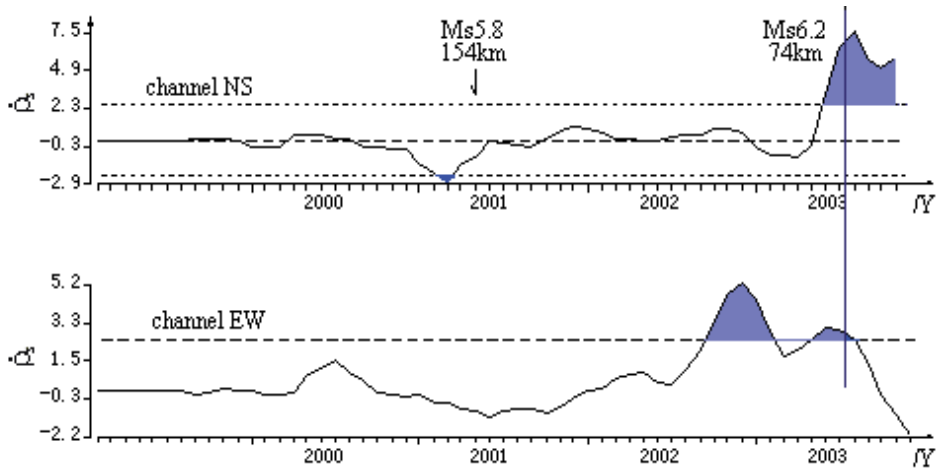

Note: these curves were drown in Nov. of 2004

Fig. 10. NVRM curves of AR changes of PAH station (from Jan. of 199 to Dec. of 2003)

Apart from these above-mentioned, Du *et al*. processed the observation data of other AR stations in the continent of China in Nov. of 2002, as a result, in other places some AR anomalies appeared in 2002 also. Thus, Du *et al*. submitted an EQ forecast view to CEA, a formal written report in Nov. of 2002. In the report, Du *et al*. believed that several EQs probably occurred in 2003 year within 4 regions with the maximal radius being less than 100 km and the minimal radius being less than 60 km, and expected EQ magnitudes were Ms6.0±, Ms≥6.0, Ms5~6 and Ms≥5 (Fig.11), respectively. As a result, the EQs as expected in this report indeed occurred in the former two regions in 2003. It is the case that the Oct. 25, 2003, Ms6.1 and 5.8 Minle~Shandan EQs just occurred in the forecast region with magnitude of Ms6.0±, in Gansu province; and the Jul. 21 Ms6.2 and Oct. 10 Ms6.1, 2003, Dayao EQs just occurred in the forecast region with magnitude of Ms≥6.0, in Yunnan province (Fig.11). In figure 11, the two forecast regions were marked in green color, painted in Nov. 2002, and the two solid circles in red are the locations of occurrence of the two groups of EQs. In other two forecast regions with magnitude of Ms5~6 and Ms≥5, the expected EQs did not occur, and still nearby the forecast region with magnitude of Ms 5~6, in Shanxi province, one Ms5.1 EQ happened in Nov. 2003. The former two strong EQs are successfully predicted, which locations and magnitudes are properly estimated and which occurred in 2003 year, a one-year time scale prediction, therefore, it is reasonable to believe that the AR changes

related to the two strong EQs were truly recorded before the occurrence of the two EQs. In 2005, the case for forecasting the two strong EQs was in public reported in paper [21].

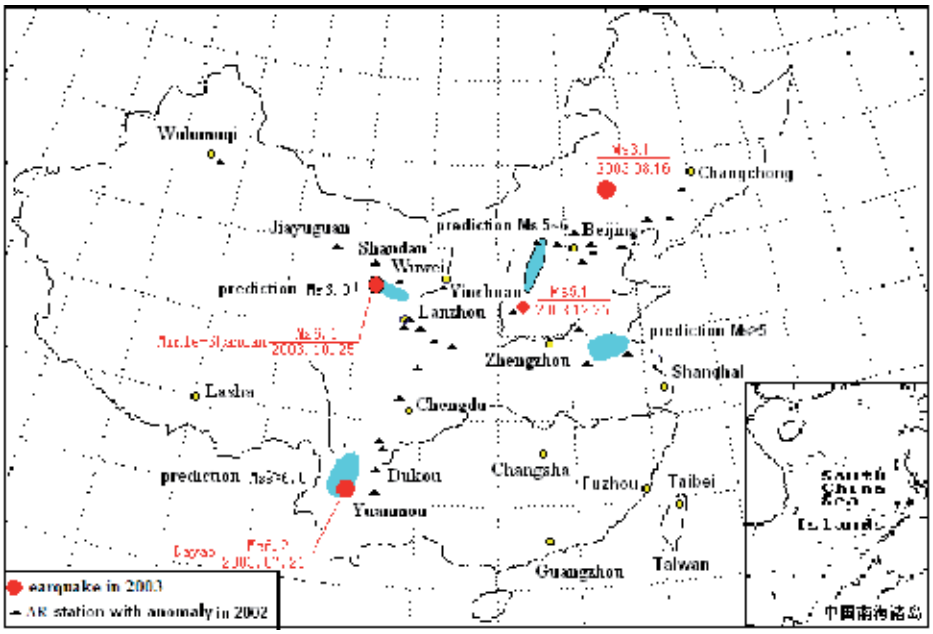

Note: (1) Red solid circles are EQ epicenters that occurred in 2003; (2) Green areas are forecast areas where EQ will occur in 2003; (3) Black solid triangles are AR stations where AR anomaly appeared in 2002

Fig. 11. Distributions of epicenters, AR stations and forecast areas

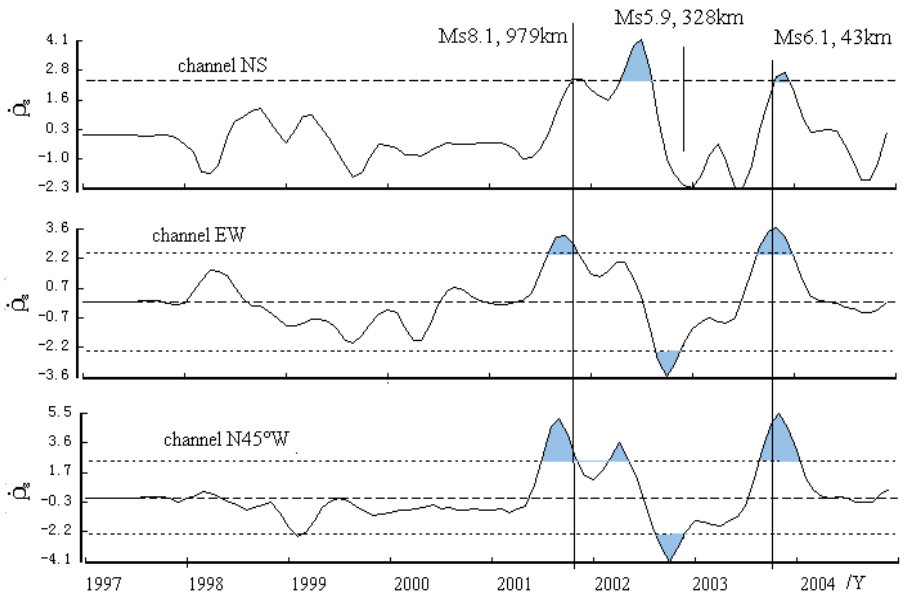

Note: these curves were drown in 2004

Fig. 12. NVRM curves of AR changes of SHD station (from 1997 to 2004)

After the Ms6.1 and 5.8 Shandan-Minle EQs, Du *et al* again processed the AR data observed at SHD station (43 km) from the two epicentral areas 1997 to 2004 using NVRM, as a result, it can be seen from figure 12 that the medium-term drop-type to short-term rise-type AR changes are similar to the AR changes in the focal area as foretold by the DD model (Dilatancy-Diffusion Model)[13-14] in appearance, a pattern consisting of an initial medium-term fall followed by a short-term rise.

People may ask why the May 12, 2008, Ms8.0 EQ was not forecasted in the medium-term period before the great EQ, which just occurred around/nearby 6 AR stations in this area? In fact, authors had no time to process and analyze the AR data observed at the 6 AR stations in those days, and the AR changes of the stations were analyzed and studied only after the great EQ[7].

3. Anisotropic AR changes related to strong EQ

Kraev studied the calculating method of AR in a homogeneous anisotropy medium[22]. Later, Brace *et a*l.[23], Chen *et al*.[24] and Lu *et al*.[25] reported that during the loading process of most rock (soil) samples, AR changes showed the directional changes which were associated with the maximum loading direction. In recent years, people try to explore related-earthquake anisotropic AR changes, which would have an important significance to understand the stress status in/nearby the EQ focal region, to explain the reason of related-earthquake AR changes and to forecast an EQ. However, it is very difficult to detect the anisotropic changes from actual EQ cases. Such researches were reported only in China because China has long made a lot of fixed-site AR observations. Qian *et al*.[26] and Du *et al*.[9, 11] reported that the anisotropic AR changes that were associated with the maximum compressional stress (P-axis) azimuths of EQ focal mechanism solutions, and Du *et al*.[2, 27] try to explain the anisotropic AR changes in theory.

3.1 Analysis of EQ cases on anisotropic AR changes

The studied EQ cases are picked out according to the following three principles: ①strong EQs with magnitude of Ms ≥ 5.5, ②EQs nearby AR stations, and ③AR changes in the later stages of EQ preparation. From the formula to estimate the focal body radius *L*[29], *Ms=3.3+2.1 Log L*, for Ms5.5 EQ *L* is no more than 15 km, for Ms 6～7 EQ *L* is no more than 60 km and for Ms7.8 EQ *L* is about 140 km. According to Du *et al*.[7, 10], AR anomalies within tens km for Ms 6~6.9 EQs and within 150 km for Ms ≥ 7.0 EQs are mostly characterized by drop-type changes in the medium-term stages of EQ preparation. The underground medium commonly contains rich water, so the concentrative range of the drop-type AR changes is well coincident with the focal body radius *L*. This indicates how we pick out the EQs nearby stations.

It is very important in study of anisotropic AR changes to distinguish the precursory AR anomaly related to strong EQs from observational AR data. Therefore, NVRM is usually used to process data. Du *et al*.[11] have studied anisotropic AR changes, using NVRM, recorded at 41 stations before 27 Ms ≥ 5.5 EQs that occurred in the Chinese mainland. The results show that for over 95% of the stations, the anisotropic AR changes appeared during the later stages of EQ preparation, which were obviously related to the P-axis azimuth of EQ focal mechanism solution. The behaviors of these anisotropic changes are that the AR change recorded through the channel perpendicular (or almost perpendicular) to the azimuth is a maximum in amplitude, whereas that recorded through the channel along (or close to) the azimuth is a minimum.

For example, the two observation channels, N20°E and N70°W channels, are installed at station PGU that had epicentral distances of 111 and 140 km for the 1976 Ms7.8 Tangshan EQ and Ms7.1 Luanxian aftershock; the P-axis azimuths of the two events were 75° and 297°, respectively, roughly in the EW direction. As a result, the medium-term drop-type and short-term rise-type AR changes recorded through N20°E channel (with a near NS direction) prior to the EQs were greater in amplitude than those through N70°W channel (with a near EW direction) (Fig.13). As another example, three channels, NS, EW and N45°W channels, are installed at station SHD that had an epicentral distance of 43 km for the 2003 Ms6.1 Minle- Shandan EQ; the P-axis azimuth of this EQ was 65°. As a result, the medium-term drop-type and short-term rise-type AR changes recorded through N45°W channel prior to the EQ were greater in amplitude than those through EW channel (Fig. 12).

It is obvious that the relationship between the anisotropic AR changes and the P-axis azimuth from actual EQ cases agrees well with the relationship between the directional AR changes and the maximum loading direction in most experiments of water-bearing rock (or soil) samples. This proves that such AR changes are just related to the EQ preparation process.

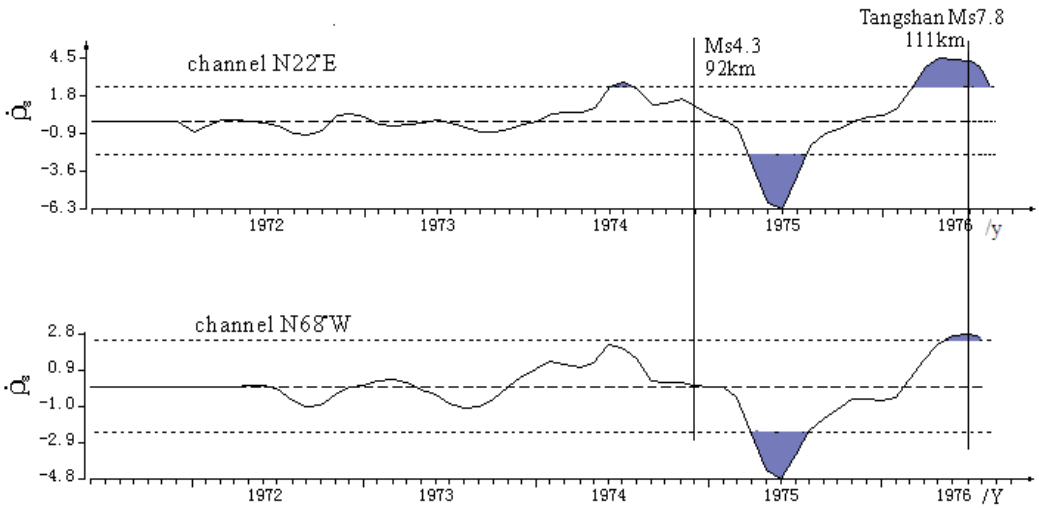

Fig. 13. NVRM curves of AR changes of station PGU for the 1976 Ms 7.8 Tangshan EQ

3.2 Theoretical analysis on anisotropic AR changes

According to DD model, the micro cracks inside the underground medium fast and nonlinearly develop immediately before the main rupture within an EQ focal area, their strikes align predominately in a certain direction and underground water fast come in them. Barsukov[29] interpreted a larger amplitude change in resistivity on the assumption that the micro crocks are tortuously linked each other, and underground water comes in them, as a result, the conductive aisles inside the medium are formed. Mei *et al*.[30] deduced that in the later preparation stages of strong EQs a number of micro-cracks inside the medium of an EQ focal region is increased sharply. The fact that in the medium-term statges before moderate, strong EQs of the Chinese mainland, for larger-magnitude EQs the AR anomaly amplitude increases fast, whereas the anomaly duration increases more slowly[10] supports Mei's deduction. According to Crampin *et at*.[31], the maximum compressional stress inside the

near-surface crust is commonly horizontal, and because of hydrostatic pressure of rock the horizontal cracks are closed and the erect cracks are developed, with the normal of the erect cracks being usually mostly horizontal and the strikes of the cracks being predominantly along in the direction of the maximum compressional stress axis. As a result, this forms an EDA medium with conductive fluid. According to the above-mentioned discussions, we presume that in the later preparation stages of strong EQs there probably exist two physical behaviors inside the medium in and nearby the focal area: (a) the erect micro-cracks is well developed, their number is non-linearly increased, and their strikes are predominantly along the direction of the maximum compressional stress axis. (b) in above-mentioned processes, the macro-cracks are linked each other and the underground water with low resistance comes fast in them. This forms the conductive aisles in the medium. As the result of its sensitivity to water, the electrical resistivity of the medium, therefore, undergoes significant changes.

Based on the two physical behaviors, we approximately regard the medium in/nearby the EQ focal region as a homogeneous azimuthal anisotropic medium. We establish a Descartes coordinate system $o-x_1x_2x_3$ on the ground where x_1, x_2 and x_3 are three electrical principal axes, respectively, which x_2 is along the horizontal loading direction (this means the P-axis direction of EQ focal mechanism solution in study of EQ cases), x_1 is horizontal and perpendicular to the direction and x_3 is downwards vertical to the ground surface. ρ_1, ρ_2 and ρ_3 are true resistivity (TR) along the three axes, respectively, and $\rho_1 > \rho_2 = \rho_3$. φ is the angle between ground observation channel X and the axis x_1. Another ground observation channel Y is perpendicular to channel X. Based on the calculating formula for the relative AR changes ($\Delta\rho_s/\rho_s$) in the anisotropic medium by Du *et al*.[2] (after referring to paper [22]), we can get the relation of relative AR changes ($\Delta\rho_{sx}/\rho_{sx}$ and $\Delta\rho_{sy}/\rho_{sy}$) of observational channels X and Y to relative TR changes ($\Delta\rho_1/\rho_1$ and $\Delta\rho_2/\rho_2$) in two horizontal principal axes directions. When $\varphi = 0^\circ$ (here, channel X is perpendicular to the loading direction and channel Y is along the direction) the relation is as follows:

In x_1 direction (perpendicular to the maximum loading direction)

$$\frac{\Delta\rho_{sx}}{\rho_{sx}} = \frac{\Delta\rho_2}{\rho_2} \quad . \tag{1}$$

In x_2 direction (along the loading direction)

$$\frac{\Delta\rho_{sy}}{\rho_{sy}} = \frac{1}{2}\left(\frac{\Delta\rho_1}{\rho_1} + \frac{\Delta\rho_2}{\rho_2}\right). \tag{2}$$

According to most loading experiments of rock (soil) samples, following two inequalities are generally true:

$$\text{When } \frac{\Delta\rho_s}{\rho_s} < 0, \qquad \frac{\Delta\rho_{sx}}{\rho_{sx}} < \frac{\Delta\rho_{sy}}{\rho_{sy}}; \tag{3}$$

$$\text{When } \frac{\Delta\rho_s}{\rho_s} > 0 \qquad \frac{\Delta\rho_{sx}}{\rho_{sx}} > \frac{\Delta\rho_{sy}}{\rho_{sy}}. \tag{4}$$

From formulas (1) ~ (3), we can get that the TR changes along the two principal axes satisfy the following inequality:

$$\frac{\Delta\rho_2}{\rho_2} < \frac{\Delta\rho_1}{\rho_1}. \tag{5}$$

Let the AR variation rate $\dot{\rho}_s = \Delta\rho_s / \Delta t$ (Δt is a time interval). When the underground medium change from homogeneous ($\rho_{sx} = \rho_{sy}$) into anisotropic ($\rho_{sx} \neq \rho_{sy}$), we can obtain the inequality of $\dot{\rho}_{sx} < \dot{\rho}_{sy}$ from inequality (3), in which $\dot{\rho}_{sx}$ is the AR variation rate of channel X and $\dot{\rho}_{sy}$ is that of channel Y. From the inequality and formulae (1) and (2) as well as the calculating formula for ρ_s in the anisotropic medium, the following inequality is obtained[11]:

$$\dot{\rho}_2 < \frac{\lambda^2}{2\lambda - 1}\dot{\rho}_1. \tag{6}$$

Where $\dot{\rho}_1$ and $\dot{\rho}_2$ are TR variation rates along two electrical principle axes, and a true anisotropic coefficient $\lambda = \sqrt{\rho_2 / \rho_1}$ ($0 < \lambda < 1$). In the case of $0.5 < \lambda < 1.0$ (viz., $1 < \rho_1/\rho_2 < 4$), we get the following inequality:

$$\dot{\rho}_2 < \dot{\rho}_1. \tag{7}$$

If the AR changes along the loading direction and perpendicular to the direction are all increased the sigh ">"will replace "<" in inequalities (5) and (7), from inequality (4). According to inequalities (5) and (7) and their derivation conditions, we can have the following understandings: anisotropic TR changes in which the change along the loading direction is more prominent than that perpendicular to the direction cause anisotropic AR changes in which the change perpendicular to the direction is more prominent than that in the direction. It is obviously that there are a difference of 90° between the directions of both the most prominent AR change (perpendicular to the loading direction) and the most prominent TR change (along the loading direction). This result distinctly explained the relationship between the most loading direction and the anisotropic AR changes when approaching the main rupture of most rock (or soil) samples and theoretically supported the research results from actual EQ cases.

3.3 A Reason for anisotropic AR changes

From the TR relationship among three principal axes in the anisotropic medium, $\rho_1 > \rho_2 = \rho_3$, we assume the shape of a single micro crack as a schistose ellipsoid that takes ρ_1 axis as its rotation axis, and whose radius is a in x_2 direction, b in x_3 direction and c in x_1 direction and a=b>c (an erect crack). And then, we assume that the resistivity in saturated-water cracks (water is rich within the underground medium) is ρ_f, that of framework is $\rho_\circ$ and the crack ratio is ν. Using Kraev's result[22] we have the approximate formulae of $\Delta\rho/\rho$ versus $\Delta\nu/\nu$:

$$\left.\begin{aligned}\frac{\Delta\rho_1}{\rho_1} &\approx \frac{\rho_f-\rho_\circ}{\rho_\circ/\nu+\rho_f}\cdot\frac{\Delta\nu}{\nu}\\ \frac{\Delta\rho_2}{\rho_2} &\approx \frac{\rho_f-\rho_\circ}{\rho_f/\nu+\rho_\circ}\cdot\frac{\Delta\nu}{\nu}\end{aligned}\right\}. \tag{8}$$

In generally, $\rho_\circ >> \rho_f$. From formulae (8), $\Delta\rho_1/\rho_1 <0$ and $\Delta\rho_2/\rho_2 <0$ when $\Delta\nu/\nu > 0$, and they will decrease with $\Delta\nu/\nu$ going bigger, which could be why most AR anomalies in/nearby the epicenter region in the late preparation stages of strong EQs are commonly a drop-type pattern; And $\Delta\rho_1/\rho_1 >0$ and $\Delta\rho_2/\rho_2 >0$ when $\Delta\nu/\nu < 0$, and they increase with $\Delta\nu/\nu$ decreasing. This is coincident with the physical analysis. Because $\nu << 1$, in formulae (8) $\left|\frac{\rho_f-\rho_\circ}{\rho_\circ/\nu+\rho_f}\right| < \left|\frac{\rho_f-\rho_\circ}{\rho_f/\nu+\rho_\circ}\right|$, so for $\Delta\nu/\nu > 0$ and $\Delta\nu/\nu < 0$ cases $\frac{\Delta\rho_2}{\rho_2}\Big/\frac{\Delta\rho_1}{\rho_1} >1$ all the time when the AR changes of channels X and Y, $\Delta\rho_{sx}/\rho_{sx}$ and $\Delta\rho_{sy}/\rho_{sy}$, are all increased or decreased. This is coincident with the physical meaning of inequality (5). Let $\dot\rho_i = \Delta\rho_i/\Delta t$ ($i = 1, 2$), the equation, $\frac{\dot\rho_2}{\dot\rho_1} \approx \frac{\rho_\circ\rho_f}{(\rho_\circ\nu+\rho_f)^2}$, can be deduced. Thus we get that $\dot\rho_2/\dot\rho_1 >1$ all the time. This is coincident with the physical meaning of inequality (7).

In general, it can be seen that anisotropic TR changes is obviously associated with ρ_f, $\rho_\circ$ and ν, which is clear in theory, and anisotropic AR changes arise from anisotropic TR changes. Therefore, the reason for AR changes and their anisotropic changes as well as their pattern (drop-type or rise-type) are clear in theory also.

4. Conclusions

1. The AR changes related to the late preparation process of strong EQs are indeed recorded in china. The two proofs are as follows: (a) Reappearing AR changes are observed before two great EQs. (b) Two strong EQs are successfully predicted using AR changes observed at stations nearby on an one-year time scale, which three elements, such as locations, magnitudes and year 2003, are all right.
2. Of 41 stations in or nearby the epicentral areas of 27 strong EQs, for over 95% stations the anisotropic AR changes are related to the maximum compressional stress directions of the EQ focal mechanism solutions. Their behaviors are: the most prominent AR change appears perpendicular or nearly perpendicular to the direction. The relationship between the anisotropic changes and the direction is well coincident with the directional AR changes in the loading process of most rock (soil) samples. And the relationship can be explained in theory. Therefore, we can confirm that the anisotropic AR changes which are directly associated with the later preparation processes of strong EQs are truly recorded nearby epicentral regions.
3. The reasons for AR changes and their anisotropic changes as well as their pattern (drop-type or rise-type) are clear. The compressional action along the maximum compressional stress direction plays an important role in/nearby the EQ focal region in the later preparation stages of strong EQs. This caused that the micro cracks in the underground medium develop fast in number, and their strikes are predominant along the direction, as a result, conductive aisles in the medium are linked each other and

underground water comes fast in. The physical processes induce the TR changes which drop-type pattern occurs in a medium dilatancy stage and rise-type pattern does in a closure stage of micro cracks, and also induce the anisotropic TR changes in which the most prominent change appears along the maximum compressional stress direction.

4. In a homogeneous anisotropic medium, the AR change is in agreement with the TR change in drop-type or rise-type pattern, hence, a drop-type pattern of AR change appears in a medium dilatancy stage and a rise-type pattern appears in a closure stage of micro cracks. Because of the directional discrepancy with 90° angle between the most prominent TR change and the most prominent AR change, the anisotropic AR changes, in which the most prominent change appears perpendicular or nearly perpendicular to the maximum loading direction, just appear.

5. References

[1] Gui X T, Guan H P, Dai J A. The short-term and immediate anomalous pattern recurrences of the apparent resistivity before the Tangshan and Songpan earthquake of 1976. Northwestern Seismological Journal (in Chinese, with an English abstract), 1989, 11(4): 71~75

[2] Du X B, Li N, Ye Q, et al. A possible reason for the anisotropic changes in apparent resistivity near the focal region of strong earthquake. Chinese J Geophys (in Chinese), 2007, 50(6): 1802~1810. http://www.agu.org/wps /cjg, Chinese J Geophys (in English), 2007, 50(6): 1555~1565

[3] Du X B, Zhao H Y, Chen B Z, et al. On the relation of the imminent sudden change in earth resistivity to the active fault and generating-earthquake stress field. Acta Seismolgic Sinica, 1993, 6: 663~673

[4] Du X B, Liu Y W, Ni M K. On the spatial characteristic of the short-term and imminent anomalies of underground water behaviors before strong earthquake. Acta Seismologic Sinica, 1997, 10: 523~533

[5] Qian F Y, Zhao Y L, Yu M M. Anomalous changes in geoelectric resistivity before earthquakes (in Chinese). Sci China Ser B, 1982, 12: 831~839

[6] Qian J D, Chen Y F, Jin A Z. The Application of Geoelectrical Resistivity Method in Earthquake Prediction (in Chinese). Beijing: Seismological Press, 1985. 48~132, 226~266

[7] Du X B. Two types of changes in apparent resistivity in earthquake prediction. Science in China-Series D, 2011, 54(1): 145~156 / doi: 10.1007/s11430-010-4031-y

[8] Du X B, Ren G J, Xue S Z. Study on many kinds of precursory anomalies and trial prediction of strong earthquakes in the continent of China (in Chinese, with an English abstract). Northwestern Seismol J, 1999, 21: 113~122

[9] Du X B, Ruan A G, Fan S H, et al. Anisotropy of the apparent resistivity variation rate near the epicentral region for strong earthquake. Acta Seismologic Sinica, 2001, 14(3): 303~314

[10] Du X B, Xue S Z, Hao Z, et al. On the relation of moderate-short term anomaly of earth resistivity to earthquake. Acta Seismologic Sinica, 2000, 13: 393~403

[11] Du X B, Ma Z H, Ye Q, et al. Anisotropic changes in earth resistivity associated with strong earthquakes. Progress in Geophysics (in Chinese, with an English abstract), 2006, 21(1): 93~100.

[12] Lu H F, Jia D, Wang L S, et al. On the triggering mechanics of Wenchuan earthquake (in Chinese). Geol J Chin Univ, 2008, 14: 133~138

[13] Nur A. Dilatancy, pore fluids, and premonitory variations of ts/tp travel times. Bull Seismol Soc Amer, 1972, 62: 1217~1222
[14] Scholz C H, Sykes L R, Aggarwal Y P. Earthquake prediction: A physical basis. Science, 1973, 181: 803~810
[15] Du X B, Yan Z D, Zou M W, et al. Process of source dynamics of the Jingtai earthquake (M=6.2). Acta Seismologic Sinica, 1994, 7: 379~388
[16] Seismological Bureau of Sichuan Province. The Songpan Earthquake in 1976 (in Chinese). Beijing: Seismological Press, 1979. 4~5, 86~91, 103
[17] Du X B, Zhang X J, Zhang H, et al. The spatial characteristics of the short-term and imminent anomalies of water radon before earthquake in the mainland of China. Acta Seismologic Sinica, 1996, 9: 461~470
[18] Ma J, Ma S L, Liu L Q. The stages of anomalies before an earthquake and the characteristics of their spatial distribution (in Chinese). Seismol Geol, 1995, 17: 363~371
[19] Zheng G. L., Du X. B., Chen J. Y., et al. Influence of active faults on erathquake-related anomalies of geo-electric resistivity (in Chinese, with an English abstract). Acta Seismol Sinic, 2011, 33: 187~197
[20] Du X B, Tan D C. On the temporal and spatial clusters of one-year scale anomalies of earth-resistivity and the relation to seismicity (in Chinese, with an English abstract). Earthquake Research in China, 2000, 6: 283~292
[21] Ye Q, Du X B, Chen J Y, *et al*. One-Year Prediction for the Dayao and Minle-Shandan Earthquakes in 2003 (in Chinese, with an English abstract). Journal of seismological research, 2005, 28(13): 226~230
[22] A.P.Kraev., 1951.Geoelectrics Principle. Moscow State's technological and theoretical liber press of Soviet Union, 10~50
[23] W.F. Brace., 1968. Electrical resistivity changes in saturated rocks during fracture and fractional sliding, J. Geophys. Res., Vol. 73, 1433~1444
[24] Chen D Y, Chen F, Wang L H, 1983. Study of rock resistivity under uniaxial press-Anisotropy of resistivity. Acta Geophysica Sinica, Vol. 26 (Supp.): 783~792
[25] Lu Y Q, Qian J D, Liu J Y. An experimental study on the precursory features of apparent resistivity and acoustic emission of large scale of granite specimen during the process of slowly dilatancy rupturing (in Chinese, with an English abstract). Northwestern Seismol J, 1990, 12: 35~41
[26] Qian F Y, Zhao Y L, Huang Y N. Anisotropic parameters calculation of earth resistivity and seismic precursory examples · Acta Seismologica Sinica, 1996, 9(4): 617~627
[27] Du X B, Ye Q, Ma Z H, et al. The detection depth of symmetric four-electrode resistivity observation in/near the epicentral region of strong earthquakes (in Chinese, with an English abstract). Chin J Geophys, 2008, 51: 1943–1949. http://www.agu.org/wps /cjg, Chinese J Geophys (in English), 2008, 51(6): 1220~1228
[28] Guo Z J, Qin F Y. 1979. Physics of Earthquake Source (in Chinese). Beijing: Seismological Press, 100~170
[29] O.M. Barsukov, 1979.A possible cause of electrical precursors to earthquake. Earth's Physics, Vol. 8, 85~90
[30] Mei S R, Fen D Y, Zhang G M, 1993. Introduction of Earthquake Research in China. Beijing: Seismological press, 302~307
[31] Crampin S, Evan R, Atkins B.K., 1984. Earthquake prediction: a new physical basis. Geophys. J.R.astr.soc, Vol.76, 147~156

11

Are There Pre-Seismic Electromagnetic Precursors? A Multidisciplinary Approach

Konstantinos Eftaxias
University of Athens, Faculty of Physics, Department of Solid State Section, Panepistimiopolis Zofrafos, Athens Greece

1. Introduction

In recent years, the wind prevailing in the scientific community does not appear to be favourable for earthquake (EQ) prediction research, in particular for the research of short term prediction [1]. Sometimes the arguments were extended to the extreme claim that any precursory activity is impossible [2]. Considering the difficulties associated with such factors as the highly complex nature, rarity of large EQs and subtleties of possible preseismic signatures, the present negative views are not groundless. It is difficult to prove associations between any two events (possible precursor and EQ) separated in time. To a certain extent, the aforementioned negative views were due to the fact that in the last decades the study of seismic precursors was expected to lead in a relatively short period of time to EQ prediction. However, the EQs are nothing but physical phenomena, and science should have some predictive power on their future behaviour of any physical system. In spite of this scepticism of the scientific community, the research towards the possible prediction of EQs in the future continues. This is attempted now with a more critical view taking into account new ideas and performing detailed theoretical, laboratory, field, and numerical investigations. Significant progress has been made in the research of precursory pattern changes of seismicity (e. g., Wyss and Martirosyan,[3]; Huang et al. [4]; Huang [5]) and the intermediate-term prediction of large EQs world-wide is already in the statistically proven stage (e g., Kossobokov et al. [6]). More recently, even the efforts to shorten the lead time to the "short-term" range are being made (e. g., Keilis-Borok et al.[7]). Some significant new waves have been rising in EQ science!

An EQ is a sudden mechanical failure in the Earth's crust, which has heterogeneous structures. The use of basic principles of fracture mechanics is a challenging field for understanding the EQ preparation process. A key fundamental question in strength considerations of materials is: *when does it fail?* Thus, a vital problem in material science and in geophysics is the identification of precursors of macroscopic defects or shocks. It is reasonable to expect that EQ's preparatory process has various facets which may be observed before the final catastrophe. *The science of EQ prediction should, from the start, be multidisciplinary!*

The present contribution focuses on fracture induced electromagnetic (EM) fields, which allow a real-time monitoring of damage evolution in materials during mechanical loading. Crack propagation is the basic mechanism of material failure. EM emissions in a wide frequency

spectrum ranging from kHz to MHz are produced by opening cracks, which can be considered as the so-called precursors of general fracture. The radiated EM precursors are detectable both at a laboratory [8-16] and geological scale [17-37].

Data collection: Since 1994, a station has been installed and operated at a mountainous site of Zante island $(37.76^{o}N - 20.76^{o}E)$ in the Ionian Sea (western Greece). The main aim of this station is the detection of kHz-MHz EM precursors. Six loop antennas detect the three components (EW, NS, and vertical) of the variations of the magnetic field at 3 kHz and 10 kHz respectively; three vertical $\lambda/2$ electric dipoles detect the electric field variations at 41, 54 MHz, and 135 MHz respectively. These frequencies were selected in order to minimize the effects of the sources of man-made noise in the mountain area of the Zante Island. Moreover, two *Short Thin Wire Antennas*, oriented at EW and NS directions of length of 100 m, respectively, have been also installed. The aim of the last installation is the detection of ultra-low-frequency $(< 1Hz)$ EM precursors rooted in a preseismic lithosphere-atmosphere-ionosphere-coupling. All the EM time series were sampled at 1 Hz. Such an experimental setup helps to specify not only whether or not a single EM anomaly is preseismic in itself, but also whether a sequence of EM disturbances at different frequencies, which are emerged one after the other in a short time period, could be characterized as preseismic one. Clear such EM precursors have been detected over periods ranging from approximately a week to a few hours prior to catastrophic EQs that occurred in Greece or Italy (e.g., [21,22,25-37]). We emphasize that the detected precursors were associated with EQs: (i) occurred in land (or near coast-line); (ii) were strong, i.e., with magnitude 6 or larger; and (iii) were shallow. Recent results indicate that the recorded EM precursors contain information characteristic of an ensuing seismic event (e.g., [21,22,25-37]).

An important feature, observed both at laboratory and geophysical scale, is that it the MHz radiation precedes the kHz one [25,27-29,35,36]. Studies on the small (laboratory) scale reveal that the kHz EM emission is launched in the tail of pre-fracture EM emission from 97% up to 100% of the corresponding failure strength [25 and references therein]. At the geophysical scale the kHz EM precursors are emerged from a few days up to a few hours before the EQ occurrence. The association of MHz, kHz EM precursors with the last stages of EQ generation is justified.

The origin of EM emissions. The origin of EM emissions from fracture is not completely clear, and different attempts have been made in order to explain it [8, 32 and references therein]. A relevant attempt is related to the "capacitor model" [32]. In many materials, emission of photons, electrons, ions and neutral particles are observed during the formation of new surface. The rupture of inter-atomic (ionic) bonds also leads to intense charge separation, which is the origin of the electric charge between the micro-crack faces. On the faces of a newly created micro-crack the electric charges constitute an electric dipole or a more complicated system. The motion of a crack has been shown to be governed by a dynamical instability causing oscillations in its velocity and structure of the fractured surfaces. It is worth mentioning that laboratory experiments show that more intense fracto-emissions are observed during the unstable crack growth. Due to the crack strong wall vibration, in the stage of the micro-branching instability, it behaves as an efficient EM emitter [32].

Are there credible EM earthquake precursors? This is also a question debated in the science community. Despite fairly abundant circumstantial evidence, EM precursors have not been

adequately accepted as real physical quantities [1]. There may be legitimate reasons for the critical views. The degree to which we can predict a phenomenon is often measured by how well we understand it. However, many questions about fracture processes remain standing. Especially, many aspects of EQ generation still escape our full understanding. Kossobokov [38] states that *"No scientific prediction is possible without exact definition of the anticipated phenomenon and the rules, which define clearly in advance of it whether the prediction is confirmed or not"*. We bear in mind that whether EM precursors to EQ exist is an important question not only for EQ prediction but also for understanding the physical processes of EQ generation. The comprehensive understanding of EM precursors in terms of physics is a path to achieve more sufficient knowledge of the last stages of the EQ preparation process and thus more sufficient short-term EQ prediction. A *seismic* shift in thinking towards basic science will lead to a renaissance of strict definitions and systematic experiments in the field of EQ prediction.

2. A proposed strategy for the study of MHz and kHz EM precursors

This chapter concentrates, in an appropriately critical spirit, on asking 3 crucial questions:

(i) How can we recognize an EM observation as a pre-seismic one?

(ii) How can we link an individual EM precursor with a distinctive stage of the earthquake preparation?

(iii) How can we identify precursory symptoms in EM observations which signify that the occurrence of the prepared EQ is unavoidable?

We shall attempt to approach the above mentioned questions in the simplest and most intuitive way, rather than emphasize mathematical rigor. In any case, the readers should be aware that this attempt refers to a *snap-shot* of a rapidly moving field.

One wonders whether necessary and sufficient criteria, have yet been established, that permit the characterization of an EM anomaly as a real EM precursor. One of the main purposes of this contribution is to suggest a procedure for the designation of observed kHz / MHz EM anomalies as seismogenic ones.

As it is said, an important feature, observed both at laboratory and geophysical scale, is that the MHz radiation precedes the kHz one [25, 28, 29 and references therein]. The remarkable asynchronous appearance of these precursors indicates that they refer to different stages of EQ preparation process. Moreover, it implies a different mechanism for their origin. Scientists ought to attempt to link the available various EM observations, which appear one after the other, to the consecutive processes occurring in Earth's crust.

The following *two stage model of EQ generation by means of pre-fracture EM activities* has been proposed: The pre-seismic MHz EM emission is thought to be due to the fracture of the highly heterogeneous system that surrounds the family of large high-strength entities distributed along the fault sustaining the system, while the kHz EM radiation is due to the fracture of the aforementioned large high-strength entities themselves [e.g.,28-30,32-36,39]. In the frame of the above mentioned two stage model, the identification of MHz and kHz EM precursors requires different methods of analysis.

2.1 Focus on MHz EM precursors

Fracture process in heterogeneous materials *can be attributed to phase transition of second order* [40,41,42]. This crucial property should be hidden in a seismogenic MHz EM activity [28,29,34,39]. The temporal evolution of a MHz EM precursor, which behaves as a second order phase transition, reveals transition from the phase from non-directional almost symmetrical cracking distribution to a directional localized cracking zone that includes the backbone of strong asperities (*symmetry breaking*) [29]. The identification of the time interval where the *symmetry breaking* is completed indicates that the fracture of heterogeneous system in the focal area has been obstructed along the backbone of asperities that sustain the system: *The siege of strong asperities begins [29]. However, the prepared EQ will occur if and when the local stress exceeds fracture stresses of asperities*. Consequently, the appearance of a really seismogenic MHz EM anomaly does not mean that the EQ is unavoidable (see Section 3).

2.2 Focus on kHz EM precursors

It has been suggested that the lounge of the kHz EM activity shows the fracture of asperities sustaining the fault [28,29,32-36]. This fracture is characterised by a non-equilibrium instability, thus acquiring a self-regulating character and to a great degree the property of irreversibility. The latter, is one of the most important components of prediction reliability. An associated fracto-EM precursor should show persistent behaviour and evolve as a phase transition far from equilibrium without any footprint of an equilibrium phase transition. Two questions effortlessly arise:

(i) *How can we recognize an observed kHz EM anomaly as a seismogenic one?*

(ii) *How does it indicate that the impending EQ is unavoidable?*

What follows concentrates on the above aforementioned two questions.

2.2.1 Statistical analysis of the kHz candidate EM precursors

An anomaly in a recorded time series is defined as a deviation from normal (background) behaviour. Concerning the development of a quantitative identification of kHz EM precursors, tools of information theory and concepts of entropy rooted in extensive and nonextensive statistical mechanics can be used in order to identify changes in the statistical pattern. A significant change is expected in the time series of the EM precursor, namely the appearance of entropy "drops" or information "peaks", revealing that the underlying fracto-EM mechanism is characterized by a high order of organization. The catastrophic fracture of asperities should be also characterized by a positive feedback mechanism. This means that the kHz EM precursors should show persistent behaviour (see Section 5.2.1).

2.2.2 Analysis in terms of universal structural patterns of fracture and faulting

From the early work of Mandelbrot [43], the aspect of self-affine nature of faulting and fracture is widely documented from field observations, laboratory experiments, and studies of failure precursors on the small (laboratory) and large (EQ) scale. The activation of a single fault should behave as a "reduced image" of the regional seismicity, and a "magnified image" of the laboratory seismicity. Moreover, fracture surfaces were found to be self-affine following the fractional Brownian motion (fBm) model over a wide range of length scales, while, the spatial

roughness of fracture surfaces has been interpreted as a universal indicator of surface fracture, weakly dependent on the nature of the material and on the failure mode [27-30,35,36 and references therein]. Such universal structural patterns of fracture and faulting process should be included into an EM precursor which is rooted in the activation of a single fault. Therefore, an important pursuit is to examine whether universal patterns of fracture and faulting are hidden in the observed candidate kHz EM precursors (see Section 5).

2.2.3 Analysis by means of fractal electrodynamics

EQ's occur on a fractal structure of faults. An active crack or rupture, can be simulated by a "radiating element" [32]. The idea is that a fractal geo-antenna can be formed as an array of line elements having a fractal distribution on the focal area as the critical point is approached. The recently introduced Fractal Electrodynamics [44, 45], which combines fractal geometry with Maxwell's equations, offers a new possibility for the exploration of the kHz EM anomalies (see Section 7).

2.2.4 The science of EQ prediction should, from the start, be multi-disciplinary

EQ's preparatory process has various facets which may be observed before the final catastrophe. The science of EQ prediction should, from the start, be multidisciplinary. A candidate preseismic kHz-MHz EM activity should be consistent with other EM precursors (SES [46], EM precursors rooted in lithosphere-atmosphere-ionosphere coupling [47]) and precursors which are imposed by data from other disciplines such as: Seismology, Infrared Remote Sensing [48], Synthetic Aperture Radars Interferometry [49]. The sequential appearance of different precursors in a relative short time interval supports the seismogenic origin of each of them, increases the probability that a significant EQ is coming, and leads to higher estimation accuracy of its parameters, namely, magnitude, time and position (see Section 8). The EQ generation is a cooperative phenomenon and its prediction needs the cooperation of scientists!

2.2.5 Analysis in terms of complex systems

The field of study of complex systems holds that their dynamics is founded on universal principles that may be used to describe various crises [50,51]. The presence of common pathological symptoms in candidate kHz EM precursors on one hand and other catastrophic events (e.g., epileptic seizures, magnetic storms and solar flares), which clearly distinguish the catastrophic event from the corresponding normal state, strongly supports the seismogenic origin of the detected kHz EM anomalies (see Section 8.4).

The burden of this section was to describe a plausible scenario for the study of kHz EM precursors, without obvious internal inconsistencies and without violating the laws of physics. In the next sections we present results gained from previous studies applying the framework of analysis described above.

3. The precursory MHz EM activity as a second order phase transition phenomenon

In natural rocks at large length scales there are long-range anti-correlations, in the sense that a high value of a rock property, e.g. threshold for breaking, is followed by a low value and

vice versa. Failure nucleation begins to occur at a region where the resistance to rupture growth has the minimum value. An EM event is emitted during this fracture. The fracture process continues in the same weak region until a much stronger region is encountered in its neighborhood. When this happens, fracture stops, and thus the emitted EM emission ceases. The stresses are redistributed, while the applied stress in the focal area increases. A new population of cracks nucleates in the weaker of the unbroken regions, and thus a new EM event appears, and so on. Therefore, the associated precursory MHz EM activity should be characterized by antipersistent behaviour and the interplay between the heterogeneities and the stress field should be responsible for this behaviour. This crucial feature is included in the recorded MHz EM precursors.

Physically, the presence of anti-persistency implies a set of EM fluctuations tending to induce stability to the system, essentially the existence of a non-linear negative feedback mechanism that “kicks" the opening rate of cracks away from extremes. The existence of such a mechanism leads to the next step: it has been proposed that the fracture of heterogeneous materials can be described in analogy with a continuous second order phase transition in equilibrium [40,41]. Thus, a seismogenic MHz EM activity, which is rooted in the fracture of the highly heterogeneous system that surrounds the family of large high-strength asperities, should be described as critical phenomenon. This critical signature is also hidden in the recorded MHz EM precursors [28-29,34-36,39]. The relevant analysis is based on the recently introduced Method of Critical Fluctuations (MCF) [52,53].

3.1 The method of critical fluctuations

The MCF, which constitutes a statistical method of analysis for the critical fluctuations in systems that undergo a continuous phase transition at equilibrium, has been recently introduced [52,53]. The authors have shown that the fluctuations of the order parameter ϕ, obey a dynamical law of intermittency which can be described in terms of a 1-d nonlinear map. The invariant density $\rho(\phi)$ for such a map is characterized by a plateau which decays in a super-exponential way (see Fig. 1 in [52]). For small values of ϕ, this critical map can be approximated as

$$\phi_{n+1} = \phi_n + u\phi_n^z + \epsilon_n \tag{1}$$

The shift parameter ϵ_n introduces a non-universal stochastic noise: each physical system has its characteristic “noise”, which is expressed through the shift parameter ϵ_n. For thermal systems the exponent z is introduced, which is related to the isothermal critical exponent δ by $z = \delta + 1$.

The plateau region of the invariant density $\rho(\phi)$ corresponds to the laminar region of the critical map where fully correlated dynamics take place [29 and references therein]. The laminar region ends when the second term in Eq. (1) becomes relevant. However, due to the fact that the dynamical law (1) changes continuously with ϕ, the end of the laminar region cannot be easily defined based on a strictly quantitative criterion. Thus, the end of the laminar region should be generally treated as a variable parameter.

Based on the foregoing description of the critical fluctuations, the MCF develops an algorithm permitting the extraction of the critical fluctuations, if any, in a recorded time series. The

important observation in this approach is the fact that the distribution $P(l)$ of the laminar lengths l of the intermittent map (1) in the limit $\epsilon_n \to 0$ is given by the power law [53]

$$P(l) \sim l^{-p_l} \tag{2}$$

where the exponent p_l is connected with the exponent z via $p_l = \frac{z}{z-1}$. Therefore the exponent p_l is related to the isothermal exponent δ by

$$p_l = 1 + \frac{1}{\delta} \tag{3}$$

with $\delta > 0$.

Inversely, the existence of a power law such as relation (2), accompanied by a plateau form of the corresponding density $\rho(\phi)$, is a signature of underlying correlated dynamics similar to critical behavior [52,53].

We emphasize that it is possible in the framework of universality, which is characteristic of critical phenomena, to give meaning to the exponent p_l beyond the thermal phase transitions [53].

The MCF is directly applied to time series or to segments of time series which appear to have a cumulative stationary behaviour. The main aim of the MCF is to estimate the exponent p_l. The distribution of the laminar lengths, l, of fluctuations included in a stationary window is fitted by the relation:

$$P(l) \sim l^{-p_2} e^{-p_3 l} \tag{4}$$

If p_3 is zero, then p_2 is equal to p_l. Practically, as p_3 approaches zero, then p_2 approaches p_l and the laminar lengths tend to follow a power-law type distribution. So, we expect a good fit to Eq. (4) with $p_2 > 1$ and $p_3 \approx 0$ if the system is in a critical state [50]. In terms of physics this behaviour means that the system is characterized by a "strong criticality", e.g., the laminar lengths tend to follow a power-law type distribution: during this critical time window the opening cracks (EM-emitters) are well correlated even at large distances [50].

We stress that when the exponent p_2 is smaller than one, then, independently of the p_3-value, the system is not in a critical state. Generally, the exponents p_2, p_3 have a competitive character, namely, when the exponent p_2 decreases the associated exponent p_3 increases (they are mirror images of each other). To be more precise, as the exponent p_2 ($p_2 < 1$) is close to 1 and simultaneously the exponent p_3 is close to zero, then the system is in a sub-critical state. As the system moves away from the critical state, then the exponent p_2 further decreases while simultaneously p_3 increases, reinforcing in this way the exponential character of the laminar length distribution: the EM fluctuations show short range correlations. In this way, we can identify the deviation from the critical state [50,52,53].

3.2 Application of the MCF method

On 13 May 1995 (8:47:13 UT) the Kozani-Grevena EQ (40.17°N, 21.68°E) occurred with magnitude $M = 6.6$. Fig. 1 shows the associated 41 MHz EM time series [25,28,29]. The data are sampled at 1 Hz.

A critical window (CW) has been identified including 23000 points (Fig. 1a) starting almost 11 hours before the time of the EQ occurrence. The corresponding distribution of the amplitude $P(\psi)$ of the emerged EM pulses in this CW is shown in Fig. (1c). It is characteristic the appearance of the plateau region in the top of distribution, as it is provided for the invariant density of critical map [52]. The laminar lengths l follow a power-law distribution $P(l)$. This feature indicated that the underlying fracture mechanism is characterized by fluctuations which are extended at many different time scales as well as the presence of long-range correlations. We note that the amplitude ψ_i of the preseismic MHz EM time series behaves as a kind of the order parameter [29]. Therefore, in the CW the fluctuations of the amplitude ψ_i of the recorded EM time series have an intermittent behaviour similar to the dynamics of the order parameter's fluctuations of a thermal critical system at the critical point. It is for this reason that this window is characterized as *critical window*.

A thermal phase transition is associated with a *symmetry breaking*. To gain inside into the temporal evolution of fracture, as the EQ is approaching, we elucidate the evolution of the *symmetry breaking* with time by making an analogy to a thermal continuous phase transition [29]. In the latter, the distribution of the fluctuations of the order parameter with temperature reveals the progress of the *symmetry breaking*. This distribution is almost a δ function at high temperature and evolves to a Gaussian with mean value zero as the system approaches the critical point. At the critical point, a characteristic plateau in the distribution appears, and the *symmetry breaking* emerges as the temperature further decreases. Below the critical temperature the distribution becomes again Gaussian, but its mean shifts to higher values associated with the *symmetry breaking*. As temperature approaches to $0^{\circ}K$, where the *symmetry breaking* is completed, it becomes a δ function again. We look for these characteristic features in the preseismic time series, with stress taking on the role of temperature [29].

Let us look specifically at the precursor under study. Figs. (1b-1e) exhibit the distribution of the recorded EM fluctuations in successive time windows. As is was mentioned, the distribution of the amplitude (order parameter) in Fig. (1c) indicates the appearance of the CW. Fig. (1b) shows the distribution before the emergence of CW: the laminar lengths, l, do not follow a power-law-type distribution $P(l)$. The system is characterized by a spare almost symmetrical distributed in space random cracking with short-range correlations.

During the CW the sort-range correlation evolve to long-range; the corresponding distribution (Fig. 1c) might be considered as a precursor of the impending *symmetry breaking*. The *symmetry breaking* is readily observable in the subsequent time interval (Fig. 1d). The cracking is restricted in the narrow zone that includes the backbone of strong asperities distributed along the activated fault sustaining the system [29]. The distribution of the order parameter in Fig. (1e) is very similar to that of Fig. (1b). However, here there is an upward shift of the values to the range of the second lobe of the distribution in Fig. (1d). The laminar lengths does not follow a power-law distribution $P(l)$. The appearance of this window indicates that the *symmetry breaking* in the underlying fracto-EM process has been almost completed [29]. *The siege of strong asperities begins* [29]. However, the prepared EQ will occur if and when the local stress exceeds fracture stresses of asperities. The lounge of the kHz EM activity shows the fracture of asperities sustaining the fault [28,29,32-36]. Indeed, a very strong kHz EM burst appeared a few hours later and after that face the EQ occurred [29].

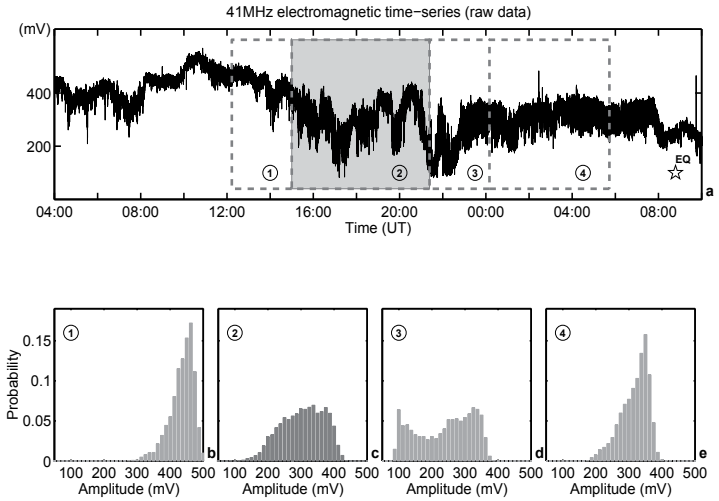

Fig. 1. The upper part shows the 41 MHz EM time series associated with the Kozani-Grevena EQ. The lower part elucidates the evolution of symmetry breaking with time.

4. How can we recognize a kHz EM anomaly as a pre-seismic one?

An anomaly in a recorded time series is defined as a deviation from normal (background) behaviour. In order to develop a quantitative identification of EM precursors, tools of information theory and concepts of entropy are used in order to identify statistical patterns. Entropy and information are seen to be complementary quantities, in a sense: entropy "drops" have as a counterpart information "peaks" in a more ordered state. The seismicity is a critical phenomenon [41,54] , thus, it is expected that a significant change in the statistical pattern, namely the appearance of entropy "drops" or information "peaks", represents a deviation from normal behaviour, revealing the presence of an EM anomaly.

It is important to note that one cannot find an optimum organization or complexity measure. Thus, a combination of some such quantities which refer to different aspects, such as structural or dynamical properties, is the most promising way.

Several well-known techniques have been applied to extract EM precursors hidden in kHz EM time series:

(i) *T*-entropy: It is based on the intellectual economy one makes when rewriting a string according to some rule [55].

(ii) Approximate entropy: It provides a measure of the degree of irregularity or randomness within a series of data. More precisely, this examines the presence of similar epochs in time series; more similar and more frequent epochs lead to lower values of approximate entropy [35 and references therein].

(iii) Fisher Information: It represents the amount of information that can be extracted from a set of measurements [56].

(iv) Correlation Dimension: It measures the probability that two points chosen at random will be within a certain distance of each other, and examines how this probability changes as the distance is increased [57].

(v) R/S analysis: It provides a direct estimation of the Hurst Exponent which is a precious indicator of the state of randomness of a time-series [58].

(vi) Detrended Fluctuation Analysis: It has been proven useful in revealing the extent of long-range correlations in time series [59, 60].

(vii) Shannon n-block entropies (conditional entropy, entropy of the source, Kolmogorov-Sinai entropy): They measure the uncertainty of predicting a state in the future, provided a history of the present state and the previous states [61-65].

(viii) Tsallis entopy: One of the crucial properties of the Boltzmann-Gibbs entropy in the context of classical thermodynamics is extensivity, namely proportionality with the number of elements of the system. The Boltzmann-Gibbs (B-G) entropy satisfies this prescription if the subsystems are statistically (quasi-) independent, or typically if the correlations within the system are essentially local. In such cases the energy of the system is typically extensive and the entropy is additive. In general, however, the situation is not of this type and correlations may be far from negligible at all scales. Inspired by multifractals concepts, Tsallis [66, 67] has proposed a generalization of the B-G statistical mechanics. He introduced an entropic index q which leads to a nonextensive statistics. The value of q is a measure of the nonextensivity of the system: $q = 1$ corresponds to the standard, extensive, B-G statistics. The order of organization of the nonextensive systems is measured by the Tsallis entropy.

The application of all the above mentioned multidisciplinary statistical procedure [30,33,35,36,68-71] sensitively recognizes and discriminates the candidate EM precursors from the EM background: they are characterized by significantly higher organization in respect to that of the EM noise in the region of the station. However, we should keep in mind that though a sledge hammer may be wonderful for breaking rock, it is a poor choice for driving a tack into a picture frame!

5. Focus on the possible seismogenic origin of the detected kHz EM anomaly by means of universally holding scaling laws of fracture

As it is mentioned in the previous Section, all the applied techniques reveal that the kHz EM anomaly is characterized by a significant lower complexity (or higher organization). Importantly this anomaly is also characterized by strong persistency [28,29]. The simultaneous appearance of both these two crucial characteristics implies that the underlying fracture process is governed by a positive feedback mechanism which is consistent with an anomaly being a precursor of an ensuing catastrophic event.

However, we suggest that any multidisciplinary statistical analysis by itself is not sufficient to characterize an emerged kHz EM anomaly as a pre-earthquake one. Much remains to be done to tackle systematically real pre-seismic EM precursors.

As it is mentioned in Section 2.2, the Earth's crust is extremely complex. However, despite its complexity, there are several universally holding scaling relations. Such universal structural patterns of fracture and faulting process should be included into an EM precursor which is rooted in the activation of a single fault. Therefore an important pursuit is to investigate whether universal features of fractures and faulting are included in the recorded kHz EM precursors.

5.1 The activation of a single fault as a self-affine image of the regional and laboratory seismicity

The self-affine nature of faulting and fracture predicts that the activation of a single fault is a reduced / magnified image of the regional/ laboratory seismicity, correspondingly (see Section 2.2.2). A fracto-EM precursor rooted in the activation of a single fault should be consistent with the above mentioned requirement.

5.1.1 The activation of a single fault as a "reduced self-affine image" of the regional seismicity

A model for EQ dynamics coming from a non-extensive Tsallis formulation [66,67] has been recently introduced by Sotolongo-Costa and Posadas, [72]. Silva et al. [73] have revised this model. The authors assume that the mechanism of relative displacement of fault plates is the main cause of EQs. The space between fault planes is filled with the residues of the breakage of the tectonic plates, from where the faults have originated. The motion of the fault planes can be hindered not only by the overlapping of two irregularities of the profiles, but also by the eventual relative position of several fragments. Thus, the mechanism of triggering EQs is established through the combination of the irregularities of the fault planes on one hand and the fragments between them on the other hand. This nonextensive approach leads to a Gutenberg-Ricter (G-R) type law for the magnitude distribution of EQs:

$$\log(N_{>m}) = \log N + \left(\frac{2-q}{1-q}\right) \log\left[1 - \left(\frac{1-q}{2-q}\right)\left(\frac{10^{2m}}{\alpha^{2/3}}\right)\right] \tag{5}$$

where N is the total number of EQs, $N(>m)$ the number of EQs with magnitude larger than m. Parameter α is the constant of proportionality between the EQ energy, ε and the size of fragment. The entropic index q describes the deviation of Tsallis entropy from the traditional Shannon one. The proposed non-extensive G-R type law (5) provides an excellent fit to seismicities generated in various large geographic areas, each of them covering many geological faults. We emphasize that the q-values are restricted in the narrow region from 1.6 to 1.8 [72-74]. Notice, the magnitude-frequency relationship for EQs do not say anything about a specific activated fault (EQ). A kHz EM precursors refers to the activation of a specific fault. Thus, we examine whether the kHz EM activity also follows the Eq. (5).

Definition of the "Electromagnetic earthquake": We regard as amplitude A of a candidate "fracto-EM fluctuation" the difference $A_{fem}(t_i) = A(t_i) - A_{noise}$, where A_{noise} is the background (noise) level of the EM time series. We consider that a sequence of k successively emerged "fracto-EM fluctuations" $A_{fem}(t_i)$, $i = 1, \ldots, k$ represents the EM energy released, ε, during the damage of a fragment. We shall refer to this as an "electromagnetic earthquake" (EM-EQ). Since the squared amplitude of the fracto-EM emissions is proportional to their energy, the magnitude m of the candidate "EM-EQ" is given by the relation

$$m = \log \varepsilon \sim \log\left(\sum \left[A_{fem}(t_i)\right]^2\right) \tag{6}$$

The Eq. (5) provides an excellent fit to the pre-seismic kHz EM experimental data incorporating the characteristics of nonextensivity statistics into the distribution of the

detected precursory "EM-EQs" [32,33,36,75]. Herein, $N(> m)$ is the number of "EM-EQs" with magnitude larger than m, $P(> m) = N(> m)/N$ is the relative cumulative number of "EM-EQs" with magnitude larger than m, and α is the constant of proportionality between the EM energy released and the size of fragment. The best-fit q parameter for this analysis has been estimated to be approximately 1.8 [32,33,36,75].

It is very interesting to observe the similarity in the q-values associated with the non-extensive Eq. (5) for: (i) seismicities generated in various large geographic areas, and (ii) the precursory sequence of "EM-EQs". This finding indicates that the statistics of regional seismicity could be merely a macroscopic reflection of the physical processes in the EQ source, as it has been suggested by Huang and Turcotte [76].

5.1.2 The activation of a single fault as a "magnified self-affine image" of the laboratory seismicity

Rabinovitch et al. [77] have studied the fractal nature of EM radiation induced in rock fracture. The analysis of the prefracture EM time series reveals that the cumulative distribution of the amplitudes also follows a power law with exponent $b = 0.62$. A similar statistical analysis of kHz EM precursor associated with the Athens EQ reveals that this also follows the power law $N(> A) \sim A^{-b}$, where $b = 0.62$ [78].

In seismology, a well known scaling relation between magnitude and the number of EQs is given by the Gutenberg-Richter (G-R) relationship:

$$\log N(> M) = \alpha - bm \tag{7}$$

where, $N(> M)$ is the cumulative number of EQs with a magnitude greater than M occurring in a specified area and time and b and α are constants.

Importantly, the Gutemberg-Ricther law also holds for acoustic emission events in rock samples [79]. Laboratory experiments by means of acoustic emissions also show a significant decrease in the level of the observed b-values immediately before the global fracture [79]. Characteristically, Ponomarev et al. [80] have reported a significant fall of the observed b-values from ~ 1 to ~ 0.6 just before the global rupture. Recently, Lei and Satoh [81], based on acoustic emission events recorded during the catastrophic fracture of typical rock samples under differential compression, suggest that the pre-failure damage evolution is characterized by a dramatic decrease in b-value from ~ 1.5 to ~ 0.5 for hard rocks. There are increasing reports on premonitory decrease of b-value before EQs: foreshock sequences and main shocks are characterized by a much smaller exponent compared to aftershocks [82]. We emphasise the sequence of kHz EM-EQs associated with the Athens EQ also follows the Gutenberg-Richter law with $b = 0.51$ [32].

The above mentioned results verify that the activation of a single fault behaves as a magnified self-affine image of the laboratory seismicity and reduced image of the regional seismicity.

5.2 Signatures of fractional-Brownian-motion nature of faulting and fracture in the candidate kHz EM precursor

Fracture surfaces were found to be self-affine following the fractional Brownian motion model (see Section 2.2.2) [27-30,35,36 and references therein]. This universal feature should be

included into an kHz EM precursor. If a time series is a temporal fractal then a power-law of the form $S(f) \propto f^{-\beta}$ is obeyed, with $S(f)$ the power spectral density and f the frequency. The spectral scaling exponent β is a measure of the strength of time correlations. The goodness of the power-law fit to a time series is represented by a linear correlation coefficient, r. Based on a fractal spectral analysis, which has been performed by means of wavelets, it has been shown [27-30,35,36] that the emergent strong kHz EM precursors follow the law $S(f) \propto f^{-\beta}$; the coefficient r takes values very close to 1, i.e., the fit to the power-law is excellent. This result shows the fractal character of the underlying processes and structures.

The β exponent takes high values, i.e., between 2 and 3. This finding reveals that:

(i) The EM bursts have long-range temporal correlations, i.e. strong memory: the current value of the precursory signal is correlated not only with its most recent values but also with its long-term history in a scale-invariant, fractal manner.

(ii) The spectrum manifests more power at lower frequencies than at high frequencies. The enhancement of lower frequency power physically reveals a predominance of larger fracture events. This footprint is also in harmony with the final step of EQ preparation.

(iii) Two classes of signal have been widely used to model stochastic fractal time series, fractional Gaussian (fGn) and fractional Brownian motion (fBm) model [83]. The fGn-model the scaling exponent β lies between -1 and 1, while the fBm regime is indicated by β values from 1 to 3. The estimated β exponent successfully distinguishes the candidate precursory activities from the EM noise [27-31,35,36]. Indeed, the β values in the EM background are between 1 and 2 indicating that the time profile of the EM series during the quiet periods is qualitatively analogous to the fGn class. On the contrary, the β values in the candidate EM precursors are between 2 and 3, suggesting that they belong to the fBm class.

In summary, the fBm nature of faulting and fracture is included in the kHz EM precursors.

5.2.1 Persistent behaviour of the detected kHz EM precursors

The β exponent is related to the Hurst exponent H by the formula [83, 84]:

$$\beta = 2H + 1 \tag{8}$$

with $0 < H < 1$ ($1 < \beta < 3$) for the fractional Brownian motion (fBm) model. The exponent H characterizes the persistent / anti-persistent properties of the signal. The range $0.5 < H < 1$ ($2 < \beta < 3$) indicates persistency, which means that if the amplitude of the fluctuations increases in a time interval it is likely to continue increasing in the next interval. We recall that we found β values in the candidate EM precursors to lie between 2 and 3. The H values are close to 0.7 in the strong segments of the kHz EM activity [27-31,35,36]. This means that the EM fluctuations are positively correlated: the underlying dynamics is governed by a positive feedback mechanism. External influences would then tend to lead the system out of equilibrium. The system acquires a self-regulating character and, to a great extent, the property of irreversibility, one of the important components of prediction reliability. Sammis and Sornette [85] have recently presented the most important positive feedback mechanisms.

It is expected that a positive feedback mechanism results in a finite-time singularity. The kHz EM time series under study shows such a behaviour by means of the "cumulative Benioff type EM energy release". A clear finite-time singularity of this type has been reported in [27,28,78].

Remark: The estimated Hurst exponents through the R/S analysis are in harmony with those estimated from the fractal spectral analysis via the hypothesis that the time series follows the fBm-model [35,36]. This fact supports the hypothesis that the profile of kHz EM precursors follow the persistent fBm-model. The last hypothesis has been further verified by a DFA-analysis [35,36].

5.3 Footprints of universal roughness value of fracture surfaces in the kHz EM activity

The Hurst exponent, H, specifies the strength of the irregularity ("roughness") of the fBm surface topography: the fractal dimension is calculated from the relation $D = (2 - H)$ [83].

The Hurst exponent $H \sim 0.7$ has been interpreted as a universal indicator of surface fracture, weakly dependent on the nature of the material and on the failure mode [86-90]. Importantly, the surface roughness of a recently exhumed strike-slip fault plane has been measured by three independent 3D portable laser scanners [91]. Statistical scaling analyses show that the striated fault surface exhibits self-affine scaling invariance that can be described by a scaling roughness exponent, $H_1 = 0.7$ in the direction of slip. In Section 5.2.1 we showed that the "roughness" of the profile of the kHz EM precursors, as it is represented by the Hurst exponent, is distributed around the value 0.7. This result has been verified by means of both fractal spectral analysis and R/S analysis [35,36]. Thus, the universal spatial roughness of fracture surfaces nicely coincides with the roughness of the temporal profile of the recorded kHz EM precursors.

6. Interpretation of precursory kHz EM activity in terms of Intermittent Criticality

The Intermittent Criticality (IC)-viewpoint of EQ dynamics is based on the hypothesis that a large regional EQ is the end result of a process in which the stress field becomes correlated over increasingly long scale-lengths, which set the size of the largest EQ that can be expected at any given time. The largest event on the fault network cannot occur until regional criticality has been achieved and stress is consequently correlated at all length scales up to the size of the region. The growth of the spatial correlation length obeys a power law with a singularity in the critical point [92-102]. This large event destroys, after its occurrence, the criticality on its associated network, creating a period of relative quiescence, after which the process repeats by rebuilding correlation lengths towards criticality and the next large event. In contrast to self-organized criticality, in which the system is always at or near criticality, intermittent criticality implies time-dependent variations in the activity during a seismic cycle. Before the large EQ, the growing correlation length manifests itself as an increase in the frequency of intermediate-magnitude earthquakes. This is commonly referred to as the "accelerating moment release model", and has been discussed by a number of authors [97,98]. Briefly, IC-approach includes self-organized criticality, growing spatial correlation length, and accelerating energy release.

A kHz EM anomaly can be interpreted as an EM confirmation of the IC-hypothesis. Indeed, a power-law type increase in the rate of EM energy release as the global instability approaches is observed [27,28,78]. The recorded acceleration of the EM emission leading up to EM large event and "EM shadow" following this is in harmony with the IC-hypothesis. Notice, the rate of seismic energy release computed around the epicenter of the EQ follows a similar

power-law type increase [27,28,78]. This experimental fact supports the hypothesis that both the seismicity and the preseismic EM activity represent two cuts in the same underlying fracture mechanism. Moreover, the spectral scaling exponent β (see Section 5.2) is a measure of the strength of time correlations. The β-values are significantly shifted to higher values as the EQ is approaching [27,28,78], namely, the correlation length in the time series increases as the catastrophic event approaches. Consequently, the two basic signatures predicted by the IC-model are included in the candidate kHz EM precursors.

7. Interpretation of MHz-kHz EM precursors in terms of fractal electrodynamics

Recently, the research area known as "fractal electrodynamics" has been established. This term was first suggested by Jaggard [44,45] to identify the newly emerging branch of research, which combines fractal geometry with Maxwel's theory of electrodynamics. From the laboratory scale to the geophysical scale, fault displacements, fault and fracture trace length, and fracture apertures follow a power-law distribution. Thus a fault shows a fractal pattern: a network of line elements having a fractal distribution in space is formed as the event approaches. However, an active crack or rupture can be simulated as a radiating element. The idea is that a *Fractal EM Geo-Antenna* can be formed as an array of line elements having a fractal distribution on the ground surface as the significant EQ is approached. This idea has been tested in [27]: the precursors are governed by characteristics (e.g., scaling laws, temporal evolution of the spectrum content, broad-band spectrum region, and accelerating emission rate) predicted by fractal electrodynamics. Notice, the fractal tortuous structure can significantly increase the radiated power density, as compared to a single dipole antenna. The tortuous path increases the effective dipole moment, since the path length along the emission is now longer than the Euclidean distance, and thus the possibility to capture these preseismic radiations by aerial antennas.

The fractal dimension of the *fractal EM geo-antenna* associated with the Athens EQ is $D = 1.2$ [27]. Seismological measurements as well as theoretical studies [101,102 and references therein] suggest that a surface trace of a single major fault might be characterized by $D = 1.2$. We clarify that the exponent D does not describe the geometrical setting of the rupture faults but it only gives the distribution of rupture fault lengths irrespective of their positions. More information is needed for a full geometrical interpretation of the faults, e.g. the position of the rupture centers.

8. The science of EQ prediction should, from the start, be multi-disciplinary

As it was mentioned in Introduction, EQ's preparatory process has various facets which may be observed before the final catastrophe, thus, a candidate preseismic EM activity should be consistent with other EM precursors or precursors that are imposed by data from other disciplines (Seismology, Infrared Remote Sensing, Synthetic Aperture Radars Interferometry e.t.c.).

8.1 Seismic electric signals

A well documented type of precursory signals is the so-called seismic electric signals (SES) [103]. They are transient low frequency $(< 1Hz)$ electric signals and are consistent with the "pressure stimulated currents model", which suggests that, upon a gradual variation of the pressure (stress) on a solid, transient electric signals are emitted, from the reorientation of

electric dipoles formed due to disorder in the focal area, when approaching a critical pressure. Field and laboratory experience coincide to the point that the transient SES tend to appear earlier in respect to the MHz-kHz EM precursors. In a recent paper, Varotsos et al. [54] report that the occurrence time of a main shock is specified in advance by analyzing in "natural time" the seismicity subsequent to the initiation of the SES activity. This analysis identifies the time when the seismicity approaches the critical state. The authors conclude that, from the time of that critical state, "the main shock was found empirically to follow usually within a few days up to one week". It is important to note that: (i) MHz / kHz EM precursors are emerged from approximately a week up to a few hours before the EQ occurence, namely, when the earth crust is in critical state by means of seismicity. (ii) MHz EM precursors can also be attributed to a phase transition of second order, as it happens for the seismicity preceding main shocks. Bear in mind that, in the frame of the proposed two stage model, MHz EM precursors are rooted in fracture of heterogeneous regime which surrounds the activated fault. The finally emerged kHz EM precursors indicate that the occurrence of the prepared EQ is unavoidable. This scheme, namely, the appearance of SES following by kHz-MHz EM precursory radiations, has been reported before EQs that occurred in Greece [21,25,30,104]. We note that, using Fisher Information and entropy metrics, it has been found that both the organization of the seismicity around the activated fault and the organization of the kHz EM precursors significantly increase as the EQ approaches [105].

8.2 EM anomalies rooted in preseismic LAI-coupling

A class of precursors is rooted in anomalous propagation of EM signals over epicentral regions due to a pre-seismic Lithosphere-Atmosphere-Ionosphere (LAI)coupling [1 and references therein]. During quiet periods, the daily EM data present a main bay-like behaviour. The records refer to the Earth-ionosphere waveguide propagation of natural EM emissions. Any change in the lower ionosphere due to an induced pre-seismic LAI-coupling may result in significant changes in the signal propagation-received at a station. Therefore, the emergence of an ionospheric EM anomaly is recognized by a strong perturbation of the characteristic bay-like morphology in the chain of daily data. Pulinets et al. [106] have reported that ionospheric precursors within 5 days before the seismic shock are registered in 100% of the cases for EQs with magnitude 6 or larger. Such anomalies have been recorded in Greece [21, 27, 104]. *Importantly, these anomalies were followed by well documented preseismic sequence of MHz and kHz EM activities, while SES appeared earlier*. The EM precursors sourced in the preseismic LAI-coupling and the MHz/kHz EM precursors appear during the last days before the main shock, namely, when the earth crust was in critical state by means of seismicity.

8.3 Precursors imposed by data from other disciplines

As it was emphasized in Introduction, EQ's preparatory process has various facets which may be observed before the final catastrophe. On September 7, 1999 the catastrophic Athens (Greece) EQ with a magnitude $M_w = 5.9$ occurred. The following sequence of well documented different precursors have been observed [26,29,30,104]:

1. A clear SES activity was recorded.

2. MHz EM anomalies were simultaneously recorded at 41, 54, and 135 MHz on August 29, 1999. These anomalies can be attributed to a phase transition of second order by means of the analysis reported in Section 3.

3. Two stong burst-like EM anomalies at 3 and 10 kHz were simultaneously recorded before the EQ occurrence. The first and second anomaly lasted for 12 and 17 hours, respectively, with a cessation of 9 hours. The second anomaly ceased about 9 hours before the EQ. This preseismic activity obeys all the requirements of the Section 2.2.

4. Infrared remote sensing makes use of satellite infrared sensors to detect infrared radiation emitted from the Earth's surface before EQs. A clear increase in the thermal infrared radiation (TIR) over the area around the Athen's EQ epicentre recorded during the last days before the EQ. The appearance of TIR emissions enhances the consideration that the fracture process has been extended up to the surface layers of the crust in the case of this EQ.

5. Synthetic aperture radars (SAR) are space-borne instruments that emit EM radiation and then record the strength and time delay of the returning signal to produce images of the ground. By combining two or more SAR images of the same area, it is possible to generate elevation maps and surface change maps with unprecedented precision and resolution. This technique is called SAR interferometry. SAR interferometry is becoming a new tool for active tectonics by providing both mm-precision surface change maps spanning periods of days to years and m-precision, high-resolution topographic maps for measuring crustal strain accumulated over longer periods of time. The fault modelling of the Athens EQ, based on information obtained by radar interferometry (ERS-2 satellite), predicts two faults: the main fault segment is responsible for 80% of the total energy released, with the secondary fault segment for the remaining 20%. A recent seismic data analysis carried out by Kikuchi, using the now standard methodology, also indicates that a two-event solution for the Athens EQ is more likely than a single event solution. According to Kikuchi, there was probably a subsequent ($M = 5.5$) EQ after about 3.5 s of the main event ($M = 5.8$). On the other hand, two strong impulsive kHz EM bursts were emerged in the tail of the preseismic EM emission. The first burst contains approximately 20% of the total EM energy received during the emergence of the two bursts, and the second the remaining 80%. The aforementioned surprising correlation in the energy domain between the two strong preseismic kHz EM signals and two faults activated, strongly supports beyond any analysis the hypothesis that the two strong EM bursts reveal the nucleation of the impending EQ.

6. A precursory power-law-type acceleration of the seismic energy release has been observed in the case of Athens EQ. The apparent onset of precipitous power-law behaviour began approximately 20 days before the EQ and culminated with the main event appearance, disappearing soon afterward.

The aforementioned observed phenomena, support the proposal that *"the science of EQ prediction should, from the start, be multi-disciplinary!"*

8.4 Universality among various geophysical and biological catastrophic events

In the last 20 years, the study of complex systems has emerged as a recognized field in its own right, although, a good definition of what a complex system is has proven elusive. Is there a common factor in the seemingly diverse complex phenomena? The answer is yes-they happens in systems consisting of many similar units interacting in a relatively well-defined manner; the field of study of complex systems holds that their dynamics is founded on universal principles that may be used to describe phenomena that are otherwise quite different in nature. When one considers a phenomenon or a thing that is "complex", one generally associates it with something that is *hard to separate, analyze or to solve*. Instead,

we refer to a complex system as one whose phenomenological laws, which describe the global behaviour of the system, are not necessarily directly related to the microscopic laws that regulate the evolution of its elementary parts. The main features of this collective bahaviour are that an individual unit's action is dominated by the influence of its neighbours, the unit behaves differently from the way it would behave on its own; and such systems show ordering phenomena as the units simultaneously change their behaviour to a common pattern [107-109]. Generally, topological disorder within the complex system introduces new, surprising effects, the laws that describe their behaviour are qualitatively different from those that governs its units. Therefore, the description of the entire system's behaviour requires a qualitatively new theory. Interesting principles have been proposed in an attempt to provide such a unified theory. These include self-organization, intermittent criticality, simultaneous existence of many degrees of freedom, self-adaption, rugged energy landscapes, and scaling (for example, power-law dependence) of the parameters and the underlying network of connections.

Empirical evidence has been mounting that supports the possibility that a number of systems arising in disciplines as diverse as physics, biology, engineering, and economics may have certain quantitative features that are intriguingly similar. Picoli et. al. [110] reported similarities between the dynamics of geomagnetic signals and heartbeat intervals. de Arcangelis et al. [111] presented evidence for universality in solar flare and earthquake occurrence. Kossobokov and Keilis-Borok [112] have explored similarities of multiple fracturing on a neutron star and on the Earth, including power-law energy distributions, clustering, and the symptoms of transition to a major rupture. Sornette and Helmstetter [113] have presented occurrence of finite-time singularities in epidemic models of rupture, EQs, and starquakes. Abe and Suzuki [114] have shown that internet shares with EQs common scale-invariant features in its temporal behaviours. Peters et al. [115] have shown that the rain events are analogous to a variety of nonequilibrium relaxation processes in nature such as EQs and avalanches. Fukuda et al. [116] have shown similarities between communication dynamics in the Internet and the automatic nervous system.

A corollary in the study in terms of complexity is that transferring ideas and results from investigators in hitherto disparate areas will cross-fertilize and lead to important new results. Considering the rarity of large surface EQs which occurs on land and subtleties of possible preseismic EM signatures, the study of EM precursors by means of complexity offers new possibilities for their exploration.

Importantly, the strong analogies between the dynamics of EQ and neurobiology have been realized by numerous authors [117-123]. In general, authors have suggested that EQ's dynamics and neurodynamics can be analyzed within similar mathematical frameworks [117-127]. Characteristically, driven systems of interconnected blocks with stick-slip friction capture the main features of EQ process. These models, in addition to simulating the aspects of EQs may also represent the dynamics of neurological networks [117 and references therein]. Hopfield [118] proposed a model for a network of N integrate-and-fire neurons. In this model, the dynamical equation of k^{th} neuron equation 28 in [118] is based on the Hodgekin-Huxley model for neurodynamics and represents the same kind of mean field limit that has been examined in [123], in connection with EQs.

Recently, it has been shown that a unified approach to catastrophic events-from the normal state of earth / brain to EQ by means of preseismic kHz EM emission/epileptic seizure exists.

The appearance of common "pathological" symptoms, i.e, high organization, persistency, and acceleratin energy release accompanies the emergence of kHz EM precursors and seizures [124-126]. More recently, Osorio et al. [127] have shown that a dynamical analogy supported by five scale-free statistics , namely, the Gutenberg-Richter distribution of event sizes, the distribution of interevent intervals, the Omori and inverse Omori laws, and the conditional waiting time until the next event, is shown to exist between seizures and EQs.

Strong analogies between the dynamics of kHz EM precursors and that and magnetic storms have been realized. The appearance of common "pathological" symptoms, i.e, high organization, persistency, and accelerating energy release accompanies the emergence of these two crises [128-131]. Moreover, the Tsallis-based energy distribution function (Eq. 5) is able to describe solar events and magnetic storms, as well. The best-fit for this analysis is given by a q-parameter value equal 1.82 and 1.84, correspondingly [131]. It is very interesting to observe the similarity in the q-values for: (i) seismicities generated in various large geographic areas, (ii) the precursory sequence of "EM-EQs" associated with the activation of a single fault,(iii) solar flares, and (iv) magnetic storms. This experimental evidence could be considered as an indication of universality among various geophysical processes. A unified theory may exist for the ways in which the above mentioned different systems organize themselves to produce a large geological or biological crisis.

9. Conclusions

As mentioned in Introduction, a key question debated in the scientific community is: Are there credible EM earthquake precursors? Despite fairly abundant circumstantial evidence, EM precursors have not been adequately accepted as real physical quantities, and there may be legitimate reasons for the critical views. In this contribution we propose a strategy for the study of MHz and kHz EM precursors which concentrates in an appropriately critical spirit, on asking 3 crucial questions:

(i) How can we recognize an EM observation as a pre-seismic one?

An anomaly in a recorded time series is defined as a deviation from normal (background) behaviour. In order to develop a quantitative identification of EM precursors, tools of information theory and concepts of entropy are used in order to identify statistical patterns. Entropy and information are seen to be complementary quantities, in a sense: entropy "drops" have as a counterpart information "peaks" in a more ordered state. The seismicity is a critical phenomenon [41,54], thus, it is expected that a significant change in the statistical pattern, namely the appearance of entropy "drops" or information "peaks", represents a deviation from normal behaviour, revealing the presence of an EM anomaly. Several well-known techniques have been applied to extract EM precursors hidden in kHz EM time series: T-entropy, Approximate entropy, Fisher Information, Correlation Dimension, R/S analysis, Detrended Fluctuation Analysis, Shannon n-block entropies (conditional entropy, entropy of the source, Kolmogorov-Sinai entropy), Tsallis entopy. It is important to note that one cannot find an optimum organization or complexity measure. Thus, a combination of some such quantities which refer to different aspects, such as structural or dynamical properties, is the most promising way. The application of all the above mentioned multidisciplinary statistical procedure [30,33,35,36,69-71] sensitively recognizes and discriminates the candidate kHz EM precursors from the EM background: they are characterized by significantly higher

organization / lower complexity in respect to that of the EM noise in the region of the station. Importantly this pre-seismic EM emission is also characterized by strong persistency [28,29]. The simultaneous appearance of both these two crucial characteristics, i.e., higher organization and persistency, implies that the underlying fracture process is governed by a positive feedback mechanism which is consistent with an anomaly being a precursor of an ensuing catastrophic event.

However, we suggest that any multidisciplinary statistical analysis by itself is not sufficient to characterize an emerged kHz EM anomaly as a pre-earthquake one. Much remains to be done to recognise systematically real pre-seismic EM precursors. The Earth's crust is clearly extremely complex. However, despite its complexity, there are several universally valid scaling relations. From the early work of Mandelbrot, much effort has been put to statistically characterise the resulting fractal surfaces in fracture processes. Fracture surfaces were found to be self-affine following the fractional Brownian motion (fBm) model over a wide range of length scales. Moreover, the spatial roughness of fracture surfaces has been interpreted as a universal indicator of surface fracture, weakly dependent on the nature of the material and on the failure mode. The Hurst Exponent H specifies the strength of the irregularity ("roughness") of the surface topography and the value of $H \sim 0.7$ has been interpreted as a universal indicator of surface fracture, weakly dependent on the nature of the material and the failure mode. Therefore, an important pursuit is to make a quantitative comparison between fractal patterns possibly hidden in an emergent kHz EM anomaly on one hand and universal fractal patterns of fracture surfaces on the other hand: an EM precursor associated with the last stage of EQ generation should behave as a persistent fBm temporal fractal, while the "roughness" of its profile, as it is represented by the Hurst exponent, should be characterized by the value $H \sim 0.7$. These two universal features of fracture are hidden in the recorded kHz EM precursors (see Section 5).

The self-affine nature of faulting and fracture predicts that the activation of a single fault is a reduced / magnified image of the regional/laboratory seismicity, correspondingly [76]. A fracto-EM precursor rooted in the activation of a single fault should be consistent with the above mentioned requirement. The sequence of kHz "electromagnetic earthquakes" rooted in the activation of a single fault satisfies the aforementioned requirement.

(ii) How can we link an individual EM precursor with a distinctive stage of the earthquake preparation?

An important feature, observed both at laboratory and geophysical scale, is that the MHz radiation precedes the kHz one. The remarkable asynchronous appearance of these precursors indicates that they refer to different stages of EQ preparation process. Moreover, it implies a different mechanism for their origin. Scientists ought to attempt to link the available various EM observations, which appear one after the other, to the consecutive processes occurring in Earth's crust.

The following *two stage model of EQ generation by means of pre-fracture EM activities* has been proposed: The pre-seismic MHz EM emission is thought to be due to the fracture of the highly heterogeneous system that surrounds the family of large high-strength entities distributed along the fault sustaining the system, while the kHz EM radiation is due to the fracture of the aforementioned large high-strength entities themselves [e.g.,28,29,31,34,39].

The temporal evolution of a MHz EM precursor, which behaves as a phase transition of second order (see Section 3), reveals transition from the phase from non-directional almost symmetrical cracking distribution to a directional localized cracking zone that includes the backbone of strong asperities (*symmetry breaking*). The identification of the time interval where the *symmetry breaking* is completed indicates that the fracture of heterogeneous system in the focal area has been obstructed along the backbone of asperities that sustain the system: *The siege of strong asperities begins*. However, the prepared EQ will occur if and when the local stress exceeds fracture stresses of asperities. As it is mentioned, the lounge of the kHz EM activity shows the fracture of asperities sustaining the fault.

(iii) How can we identify precursory symptoms in EM observations which signify that the occurrence of the prepared EQ is unavoidable?

This is a crucial question. Our results suggest that the appearance of a really seismogenic MHz EM anomaly does not mean that the EQ is unavoidable [28, 29]. The interplay between the heterogeneities and the stress field could be responsible for the observed antipersistent pattern of the precursory MHz EM time series [28, 29]. Indeed, in natural rock at large length scales there are long-range anticorrelations, in the sense that a high value of a rock property, e.g., threshold for breaking is followed by a low value and vice versa. The antipersistent character of the MHz EM time series may reflect the fact that in heterogeneous media, volumes with a low threshold for breaking alternate with much stronger volumes. Crack growth in a heterogeneous medium continues until a much stronger region is encountered. When this happens, crack growth stops while another crack nucleates in a weaker region and so on. Antipersistent behavior implies a set of fluctuations tending to induce stability within the system, i.e., a nonlinear negative feedback, which "kicks" the opening cracks away from extremes. Consequently, heterogeneity could account for the appearance of a stationary-like behavior in the antipersistent MHz part of the prefracture EM time series and thus enable the fracture in highly heterogeneous systems to be described via an analogy with thermal continuous phase transition of second order (see Section 3).

On the contrary, the lounge of the kHz EM activity is the sign of EQ generation. Accumulated evidence support the hypothesis that the kHz EM emission is originated during the fracture of asperities distributed along the activated fault sustaining the system (see Sections 4-7).

The burden of this contribution was to describe a plausible scenario for the study of EM precursors which includes a rather strict set of criteria for characterizing a sequence of MHz - kHz EM emissions as a seismogenic one. We emphasize that this scenario has already been applied to precursors associated with significant, i.e., EQs with magnitude larger than 6, surface EQs that occurred on land or near the coast-line in Greece and Italy. It seems to provide a coherent framework which ties together the observed phenomenology of MHz and kHz EM precursors, without obvious internal inconsistencies and without violating the laws of physics.

It might be difficult for someone to accept that such anomalies are indeed seismogenic. However it is even more difficult to prove that they are not. How possible would it be to find a non seismogenic EM emission that meets the criteria for such a multidisciplinary scheme?

One of the largest controversial issues of the materials science community is the interpretation of scaling laws on material strength. In particular, an important open question is whether the spatial and temporal complexity of earthquake and fault structures emerges from geometry or from the chaotic behaviour inherent to the nonlinear equations governing the dynamics of these phenomena. The observed scaling laws associated with EQs have led a variety of researchers to the conclusion that these events can be regarded as a type of generalized phase transition, similar to the nucleation and critical phenomena that are observed in thermal and magnetic systems [132]. In spite of this prevailing view, other scientists propose a different argument, purely based on geometry. They conclude that as happened for relativity, geometry could again hold an unexpected and fundamental role [133].

Our analysis suggests that we should discriminate two distinct cases: (i) The scaling laws associated with the fracture of the backbone of asperities of a single fault could be a product of the fractal scaling of asperities. Geometry holds a fundamental role of the emergence of fractal scaling laws in phenomena associated with the fracture of asperities. The observed precursory kHz EM emission is such a phenomenon. (ii) The scaling laws associated with the fracture of highly heterogeneous component that surrounds the family of asperities could be attributed to a phase transition of second order. Recent results support the concept that seismicity which preceeds of a significant seismic event is a critical phenomenon, it can be attributed to a phase transition of second order [134]. Moreover, it has been found empirically that main shocks occur a few days up to one week after the appearance of criticality. We recall that the MHz EM precursors also behave as a phase transition of second order, and also emerge from approximately one week up to a few hours before the EQ occurrence. These findings verify that the seismicity and the precursory MHz EM activity are two faces of the same coin. Notice, the persistent kHz EM emission, which is emerged in the tail of the preseismic preseismic EM activity, is a nonequilibrium process without any footprint of an equilibrium thermal phase transition. This process indicates that the system acquires a self-regulating character and to a great degree the property of irreversibility, which is one of the important components of predictive capability. The above mentioned findings suggest reconsidering the interpretation of scaling laws on material strength.

The absence of any EM activity during the EQ occurrence and aftersocks period constitutes a puzzling feature in the study of seismogenic EM precursors. A catastrophic decrease in the elastic modulus just before the final rupture is expected. The appearance of an EM gap in all the frequency bands just before the EQ occurrence might be considered as a hallmark that the expected decrease in the elastic modulus has occurred [28, 29]. So, the existence of a quiescent period may constitute the last clue that a significant seismic event is forthcoming with a considerable probability. On the basis of our study, drawing on both field observations and laboratory experiments on rock fracture, we make the following suggestion concerning the initial and final times for the crucial last stage of the EQ preparation process. The initial point corresponds to the appearance of persistent kHz EM emission. The final point corresponds to the onset of a quiescent period when all precursory EM activities cease. This analysis may point to a possible way of estimating the time to global failure. Certainly, further work in this direction is needed.

Irreversible deformation of rocks is accompanied by the Kaizer effect: if the heterogeneous material is loaded, then unloaded before fracture, and loaded again, only a small number of micro-fractures are detected before attaining the previous load. Micro-fracturing activity increases dramatically as soon as the largest previously experienced stress level are exceeded

indicating the beginning of further damage in rocks. The existence of Kaiser effect in geological scale can justify the systematically observed absence of EM emission during the aftershocks period. The stress during the aftershocks period does not exceed the maximum previously reached stress level associated with the main shock occurrence.

The described here results seem to be tolerable, whether the presented ideas will prove to be corrects or disappear as others have remain for the future. However, if we accept the presented suggestions, the absence of EME after the EQ occurrence supports the hypothesis that the launched EQ was the main shock. In any case, the complexity of EQ preparation process is enormous, and thus a huge amount of research is needed before we begin to understand it. There are many outstanding answers that we do not know. Yet it is certain that we have begun to place most of the right questions. And this is perhaps a sign of a latent solution. The Greek poet and Nobel Laureate George Seferis has referred to what the ancient Greek spirit is all about:

"The birthplace of this idea is found at the dawn of Greek history. Aeschylus, the ancient Greek playwright, formulated it once and for all: He who steps beyond moderation is a hubrist, i.e. arrogant, and hubris is the greatest evil that can fall upon us. Greek Tragedy throughout is full of symbols of this idea. And the symbol that moves me above all others, this symbol I find in the Persians. Xerxes, the old legend tells us, was defeated because he was a hubrist; because he committed this extraordinary deed: he lashed at the sea...".

For the purpose of this chapter, it would mean committing hubris for scientists who have dedicated themselves to the prognosis of earthquakes to think that they can defeat "Eggelados".

10. References

[1] Uyeda, S., Nagao, T., and Kamogawa, M.: Short-term earthquake prediction: Current status of seismo-electromagnetics, Tectonophysics 470 205–213, 2009.

[2] Geller, R., Jackson, D., Kagan, Y., Mulargia, F.: Earthquakes cannot be predicted, Science 275, 1616–1617, 1997.

[3] Wyss, M., Martirosyan, A.: Seismic quiescence before the M7, 1988, Spitak earthquake, Armenia. Geophys. J. Int. 134, 329–340, 1998

[4] Huang, Q.: Search for reliable precursors: a case study of the seismic quiescence of 2000 western Tottori prefecture earthquake. J. Geophys. Res. 111, B04301, 2006.

[5] Huang, Q., Sobolev, G.A., Nagao, T.: Characteristics of the seismic quiescence and activation patterns before the M = 7.2 Kobe earthquake, January 17, 1995, Tectonophysics 237, 99–116, 2001.

[6] Kossobokov, V.G., Romashkova, L.L., Keilis-Borok, V.I., Healy, J.H.: Testing earthquake prediction algorithms: statistically significant real-time prediction of the largest earthquakes in the Circum-Pacific, 1992–1997, Phys. Earth Planet. Inter. 111, 187–196,

[7] Keilis-Borok, V., Shebalin, P., Gabrielov, A., Turcotte, D.: Reverse detection of short term earthquake precursors. Phys. Earth Planet. Inter. 145, 75–85, 2004.

[8] Bahat, D., Rabinovitch, A., and Frid, V.: Tensile Fracturing in Rocks , Springer, New York, 2005.

[9] Ogawa, T., Oike, K. and Miura, T.; Electromagnetic radiation from rocks. J. Geophys. Res. 90, 6245–6249, 1985.

[10] OŠKeefe, S. G. and Thiel, D. V.; A mechanism for the production of electromagnetic radiation during fracture of brittle materials. Phys. Earth Plant. Inter. 89, 127–135, 1995.
[11] Lolajicek, T. and Sikula, J.: Acoustic emission and electromagnetic effects in rocks. In: Progress in Acoustic Emission VIII. Proceedings of the 13th International Acoustic Emission Symposium, 30 November, 1996. (Kishi, T., Mori, Y., Higo, H. and Enoki, M., Eds). Japanese Society for NDI, Nara, Japan: 311–314: 1996.
[12] Panin, V., Deryugin, Ye., Hadjicontis, V., Mavromatou, C., and Eftaxias, K.: Scale levels of strain localization and fracture mechanism of LiF single crystals under compression, Physical Mesomechanics, 4, 21-32, 2001.
[13] Frid, V., Rabinovitch, A. and Bahat, D.: Fracture induced electromagnetic radiation. J. Phys. D. Appl. Phys. 36, 1620–1628, 2003.
[14] Mavromatou, C., Hadjicontis, V., Ninos, D. Mastroyiannis, D., Hadjicontis, E., and Eftaxias, K.: Understanding the fracture phenomena in inhomogeneous rock samples and ionic crystals, by monitoring the electromagnetic emission during the deformation, Physics and Chemistry of the Earth, 29, 353 – 357, 2004.
[15] Fukui, K., Okubo, S. and Terashima, T.: Electromagnetic radiation from rock during uniaxial compression testing: the effects of rock characteristics and test conditions. Rock Mech. Rock Eng. 38, 411–423, 2005.
[16] Lacidogna, G., Carpinteri, A., Manuello, A., Durin, G., Sciavi, A., Niccolini, G., and Agosto, A.: Acoustic and electromagnetic emissions as precursor phenomena in failure processes, Strain 47,1-9, 2011, doi: 10.1111/j.1475-1305.2010.00750.x
[17] Warwick, J. W., Stoker. C, and Meyer, T. R.: Radio emission associated with rock fracture: possible application to the great Cjilean earthquake of May 22, 1960, J. Geophys. Res. 87, 2851-2859, 1982.
[18] Gokhberg, M. B., Morgunov, V. A., Yoshino, T. and Tozawa, I.: Experimental measurement of electromagnetic emissions possibly related to earthquakes in Japan. J. Geophys. Res. 87, 7824–7828, 1982
[19] Hayakawa, M. and Fujinawa, Y.: Electromagnetic Phenomena Related to Earthquake Prediction, Terrapub, Tokyo, 1994.
[20] Hayakawa, M.: Atmospheric and Ionospheric Electromagnetic Phenomena Associated with Earthquakes, Terrapub, Tokyo, 1999.
[21] Eftaxias, K., Kopanas, J., Bogris, N., Kapiris, K., Antonopoulos, G. and Varotsos P.: Detection of electromagnetic earthquake precursory signals in Greece, Proc. Japan Acad., 76(B), 45-50, 2000.
[22] Eftaxias, K., P. Kapiris, J. Polygiannakis, N. Bogris, J. Kopanas, G. Antonopoulos, A. Peratzakis and V. Hadjicontis.: Signatures of pending earthquake from electromagnetic anomalies. Geophys. Res. Let., 28, 3321-3324, 2001.
[23] Hayakawa, M. and Molchanov, O.: Seismo Electromagnetics, Terrapub, Tokyo, 2002.
[24] Nagao, T., Enomoto, Y., Fujinawa, Y. etăal.: Electromagnetic anomalies associated with 1995 Kobe earthquake. J. Geodyn. 33, 401–411, 2002.
[25] Eftaxias, K., Kapiris, P., Dologlou, E., Kopanas, J., Bogris, N., Antonopoulos, G., Peratzakis, A., and Hadjicontis, V.: EM anomalies before the Kozani earthquake: A study of their behaviour through laboratory experiments, Geophys. Res. Lett., 29, 69/1-69/4, 2002.
[26] Eftaxias, K., Kapiris, P., Polygiannakis, J., Kopanas, J., Antonopoulos, G., and Rigas, D.: Experience of short term earthquake precursors with VLF-VHF electromagnetic emissions, Natural Hazards and Earth System Sciences, 3, 217-228, 2003.

[27] Eftaxias, K., Frangos, P., Kapiris, P., Polygiannakis, J., Kopanas, J., Peratzakis, A., Skountzos, P., and Jaggard, D.: Review-Model of Pre-Seismic Electromagnetic Emissions in Terms of Fractal-Electrodynamics, Fractals, 12, 243 – 273, 2004.

[28] Kapiris, P., Eftaxias, K., Chelidze, T.: Electromagnetic Signature of Prefracture Criticality in Heterogeneous Media, Physical Review Letters, 92(6), 065702, 2004.

[29] Contoyiannis, Kapiris, P., and Eftaxias, K.: A Monitoring of a Pre-Seismic Phase from its Electromagnetic Precursors, Physical Review E, 71, 061123-1 – 061123-14, 2005.

[30] Karamanos, K., Dakopoulos, D., Aloupis, K., Peratzakis, A., Athanasopoulou, L., Nikolopoulos, S., Kapiris, P., Eftaxias, K.: Study of pre-seismic electromagnetic signals in terms of complexity. Physical Review E. 74, 016104-1/21, 2006.

[31] Eftaxias, K., Sgrigna, V., and Chelidze, T., (Eds): Mechanical and Electromagnetic Phenomena Accompanying Preseismic Deformation: from Laboratory to Geophysical Scale, Tectonophysics, 431, 1-301, 2007.

[32] Papadimitriou, K., Kalimeri, m., and Eftaxias, K.: Nonextensivity and universality in the earthquake preparation process, Physical Review E, 77, 36101, 2008.

[33] Kalimeri, M., Papadimitriou, K., Balasis, G., and Eftaxias, K.: Dynamical complexity detection in pre-seismic emissions using nonadditive Tsallis entropy, Physica A, 387, 1161-1172-, 2008.

[34] Contoyiannis, Y., and Eftaxias, K.: Tsallis and Levy statistics in the preparation of an earthquake, Nonlinear Processes in Geophysics, 15, 379–388, 2008.

[35] Eftaxias, K., Athanasopoulou, L., Balasis, G., Kalimeri, M., Nikolopoulos, S., Contoyiannis, Y., Kopanas, J., Antonopoulos, G., and Nomicos, C.: Unfolding the procedure of characterizing recorded ultra low frequency, kHZ and MHz electromagetic anomalies prior to the L'Aquila earthquake as pre-seismic ones. Part I, Nat. Hazards Earth Syst. Sci.., 9, 1953–1971, 2009.

[36] Eftaxias, K., Balasis, G., Contoyiannis, Y., Papadimitriou, C., Kalimeri, M., Kopanas, J., Antonopoulos, G., and Nomicos, C.: Unfolding the procedure of characterizing recorded ultra low frequency, kHZ and MHz electromagnetic anomalies prior to the L'Aquila earthquake as pre-seismic ones. Part II, Nat. Hazards Earth Syst. Sci. 10, 275–294, 2010.

[37] Eftaxias, K., Maggipinto, T., Meister, C-V., and Katz. O (Eds).: Progress in the research on earthquakes precursors, Natural Hazard and Earth System Sciences (Special Issue), 2011.

[38] Kossobokov, V.: Testing earthquake prediction methods: the West Pacific short-term forecast of earthquakes with magnitude $MwHRV > 5.8$, Tectonophysics, 413, 25–31, 2006

[39] Contoyiannis, Y., Nomicos, C., Kopanas, J., Antonopoulos, G., Contoyianni , L.,and Eftaxias, K.: Critical features in electromagnetic anomalies detected prior to the L'Aquila earthquake, Physica A 389 , 499-508, 2010.

[40] Herrmann, H. J., and Roux, S.: Statistical Physics for the Fracture of Disordered Media, Elsevier, Amsterdam, 1990.

[41] Sornette, D.: Critical Phenomena in Natural Sciences, Chaos, Fractals, Self-organization and Disorder: Concepts and Tools, Second edition, Springer Series in Synergetics, Heidelberg, 2004.

[42] Contoyiannis, Y., Diakonos, F., Kapiris, P., Peratzakis, A., and Eftaxias, K.: Intermittent Dynamics of Critical Pre-seismic Electromagnetic Fluctuations, Physics and Chemistry of the Earth, 29, 397 – 408, 2004.

[43] Mandelbrot, B.: The Fractal Geometry of Nature, W. H. Freema, New York, 1982.
[44] Jaggard, D.: On fractal electrodynamics, in Recent Advances in Electromagnetic Theory, eds. H. Kritikos and D. Jaggard, Springer-Verlag, New York, 183–224, 1990.
[45] Jaggard, D., and Frangos, P.: Surfaces and superlattices, in Frontiers in Electrodynamics, eds. D. Werner and R. Mittra, IEEE Press,1–47, 2000.
[46] Varotsos, P.: The Physics of Seismic Electric Signals, TerraPub, Tokyo, 2005.
[47] Pulinets, S. and Boyarchuk, K.: Ionospheric Precursors of Earthquakes, Springer, 2005.
[48] Ouzounov, D., and Freund, F.: Mid-infrared emission prior to strong earthquakes analyzed by remote sensing data. Advances in Space Research, 33, 268–273, 2004.
[49] Rosen, P., Hensley, S., Joughin, I., Li, F., Madsen, S., Rodriguez, E., and Goldstein, R.: Synthetic Aperture Radar Interferometry, Proceedings of the IEEE, 88, 333-382, 2000
[50] Stanley, H.: Scaling, universality, and renormalization: Three pillars of modern critical phenomena, Rev. Mod. Phys., 71, S358– S366, 1999.
[51] Bar-Yam, Y.: Dynamics of complex systems. Reading, Mass., Addison-Wesley, 1997.
[52] Contoyiannis, Y. and Diakonos, F.: Criticality and intermittency in the order parameter space, Phys. Lett. A, 268, 286–272, 2000.
[53] Contoyiannis, Y., Diakonos, F., and Malakis, A.: Intermittent dynamics of critical fluctuations, Phys. Rev. Lett., 89, 35701– 35704, 2002.
[54] Varotsos, P., Sarlis, N., Skordas, E., Uyeda, S., and Kamogawa, M.: Natural time analysis of critical phenomena, PNAS, July 12, 108 , 11361–11364, 2011.
[55] Titchener, M., Nicolescu, R., Staiger, L., Gulliver, A., and Speidel,U.: Deterministic Complexity and Entropy, Fund. Inform., 64, 443–461, 2005.
[56] Fisher, R.: Theory of statistical estimation, Proc. Camb. Phil. Soc. 22, 700–725, 1925.
[57] Grassberger, P. and Procaccia, I.: Characterization of strange attractors, Phys. Rev. Lett., 50, 346–349, 1983.
[58] Hurst, H.: Long term storage capacity of reservoirs, Trans. Am. Soc. Civ. Eng., 116, 770–808, 1951.
[59] Peng, C., Mietus, J., Hausdorff, J., Havlin, S., Stanley, H., and Goldberger, A.: Long-range anticorrelations and non-Gaussian behavior of the heartbeat, Phys. Rev. Lett., 70, 1343–1346, 1993.
[60] Peng, C., Havlin, S., Stanley, H., and Goldberger, A.: Quantification of scaling exponents and crossover phenomena in nonstationary heartbeat timeseries, Chaos, 5, 82-87, 1995.
[61] Shannon, C. E.: A mathematical theory of communication, The Bell System Tech. J., 27, 379–423, 623-656, 1948.
[62] Ebeling, W. and Nicolis, G.: Word frequency and entropy of symbolic sequences: A dynamical Perspective, Chaos, Solitons & Fractals, 2, 635–650, 1992.
[63] Ebeling, W.: Prediction and entropy of nonlinear dynamical systems and symbolic sequences with LRO, Physica D, 109, 42–52, 1997.
[64] Ebeling, W., Steuer, R., and Titchener, M.: Partition-based entropies of deterministic and stochastic maps, Stochastics and Dynamics, 1, 45–61, 2001.
[65] Ebeling,W.: Entropies and predictability of nonlinear processes and time series, edited by: Sloot, P. M. A., et al., ICCS 2002, LNCS, 1209–1217, 2002
[66] Tsallis, C.: Possible generalization of Boltzmann-Gibbs statistics, J. Stat. Phys., 52, 479–487, 1988.
[67] Tsallis, C.: Introduction to Nonextensive Statistical Mechanics, Approaching a Complex Word, Springer, 2009.

[68] Karamanos, K. Peratzakis, A., Kapiris, P., Nikolopoulos, S., Kopanas, J., and Eftaxias, K.: Extracting pre-seismic electromagnetic signatures in terms of symbolic dynamics, Nonlinear Processes in Geophysics, 12, 835-848, 2005.
[69] Nikolopoulos, S., Kapiris, P., Karamanos K., and Eftaxias, K.: A unified approach of catastrophic events, Natural Hazards and Earth System Sciences, 4, 615-637, 2004
[70] Eftaxias, K., Kapiris, P., Balasis, G., Peratzakis, A., Karamanos, K., Kopanas, J., Antonopoulos, G., and Nomicos, C.: A Unified Approach to Catastrophic Events: From the Normal State to Geological or Biological Shock in Terms of Spectral Fractal and Nonlinear Analysis, Natural Hazards and Earth System Sciences, 6, 205-228, 2006.
[71] Eftaxias, K., Minadakis, G., Athanasopoulou. L., Kalimeri. M., Potirakis, S., and Balasis, G.: Are Epileptic Seizures Quakes of the Brain? An Approach by Means of Nonextensive Tsallis Statistics (submitted)
[72] Sotolongo-Costa, O. and Posadas, A.: Fragment-asperity interaction model for EQ, Phys. Rev. Lett., 92, 048501, 2004.
[73] Silva, R., Franca, G., Vilar, C., and Alcaniz, J.: Nonextensive models for earthquakes, Phys. Rev. E, 73, 026102, 1–5, 2006.
[74] Telesca, L.: Tsallis-Based Nonextensive Analysis of the Southern California Seismicity Entropy, 13(7), 1267-1280, 2011.
[75] Eftaxias, K.: Footprints of nonextensive Tsallis statistics, self-affinity and universality in the preparation of the L'Aquila earthquake hidden in a pre-seismic EM emission, Physica A 389, 133-140, 2009.
[76] Huang, J., and Turcotte, D.: Fractal distributions of stress and strength and variations of b–value, Earth Planet. Sci. Lett., 91, 223-230, 1988.
[77] Rabinovitch, A., Frid, V., and Bahat, D.: Gutenberg-Richter-type relation for laboratory fracture-induced electromagnetic radiation, Phys. Rev. E, 65, 11 401/1-11 401/4, 2001.
[78] Kapiris, P., Balasis, G., Kopanas, J., Antonopoulos, G., Peratzakis, A., and Eftaxias, K.: Scaling Similarities of Multiple Fracturing of Solid Materials, Nonlinear Proc. Geoph., 11, 137–151, 2004.
[79] Scholz, C.: The frequency-magnitude relation of macrofracturing in rocks and its relation to earthquakes, Bull. Seismo. Soc. Am., 58, 399–415, 1968.
[80] Ponomarev, A. Zavyalov, A., Smirnov, V., and Lockner, D.: Physical modelling of the formation and evolution of seismically active fault zones, Tectonophysics, 277, 57–81, 1997.
[81] Lei, X., and Satoh, T.: Indicators of critical point behavior prior to rock failure inferred from pre-failure damage, Tectonophysics, 431, 97–111, 2007.
[82] Hainzl, S., Zoller, G., and Scherbaum, F.: Earthquake clusters resulting from delayed rupture propagation in finite fault segments, Geophys. Res. Lett., 108, 2013-2016, 2003.
[83] Heneghan C., and McDarby, G.: Establishing the relation between detrended fluctuation analysis and power spectral density analysis for stochastic processes, Phys. Rev. E, 62, 6103–6110, 2000
[84] Turcotte., D.: Fractals and chaos in geology and geophysics, Cambridge University Press, 1997.
[85] Sammis, C. and Sornette, D.: Positive feedback, memory, and the predictability of EQ, P. Natl. Acad. Sci. USA, 99, 2501–2508, 2002.
[86] Ponson, L., Bonamy, D., and Bouchaud, E.: Two-dimensional scaling properties of experimental fracture surfaces, Phys. Rev. Lett., 96, 35506-1/4, 2006.

[87] Mourot, G., Morel, S., Bouchaud, E., and Valentin, G.: Scaling properties of mortar fracture surfaces, Int. J. of Fracture, 140, 39–54, 2006.
[88] Lopez, J., and Schmittbuhl, J.: Anomalous scaling of fracture surfaces, Phys. Rev. E, 57, 6405-6408, 1998.
[89] Zapperi, S., Kumar, P., Nukala, V., and Simunovic, S.: Crack roughness and avalanche precursors in the random fuse model, Phys. Rev. E, 71, 26106/1–10, 2005.
[90] Hansen, A., and Schmittbuhl, J.: Origin of the universal roughness exponent of brittle fracture surfaces:stress-weighted percolation in the damage zone, Phys. Rev. Lett., 90, 45504–45507, 2003.
[91] Renard, F., Voisin, C., Marsan, D., and Schmittbuhl, J.: High resolution 3D laser scanner measurements of a strike-slip fault quantity its morphological anisotropy at all scales, Geophys. Res. Lett., 33, L04305, 2006.
[92] Sornette, D., Helmstetter, A.: Occurrence of finite-time singularities in epidemic models of rupture, earthquakes and starquakes, Phys. Rev. Lett. 89 (15), 158501, 2002.
[93] Sornette, D., Sammis, C.: Complex critical exponents from renormalization group theory of earthquakes: Implications for earthquake predictions, J. Phys. I 5, 607–619, 1995.
[94] Sornette, D., Vanneste, C.: Dynamics and memory effects in rupture of thermal fuse networks, Phys. Rev. Lett. 68, 612–615, 1992.
[95] Sornette, D., Vanneste, C., Knopoff, L.: Statistical model of earthquake foreshocks, Phys. Rev. A 45, 8351–8357.
[96] Bowman, D., Ouillon, G., Sammis, C., Sornette, A., and Sornette, D.: An observational test of the critical earthquake concept, J. Geophys. Res., 103, 24359-24372, 1998.
[97] Bowman, D. and King, G.: Accelerating seismicity and stress accumulation before large Earthquakes, J. Geophys. Res. Lett., 28(21), 4039–4042, 2001.
[98] Bufe, C. and Varnes, D.: Predictive modelling of the seismic cycle of the greater San Francisco Bay region, J. Geophys. Res., 98, 9871–9883, 1993.
[99] S. C. Jaume and L. R. Sykes, Evolving towards a critical point: a review of accelerating seismic moment/energy release prior to large and great earthquakes, Pure Appl. Geophys. 115 (1999) 279–305.
[100] Sahimi, M.: Flow phenomena in rocks: from continuum models to fractals, percolation, cellular automata, and simulated annealing, Rev. Mod. Phys., 65, 1393–1534, 1993.
[101] Sahimi, M., Robertson, M., and Sammis, C.: Fractal distribution of earthquakes hypocenters and its relation to fault patterns and percolation, Phys. Rev. Lett., 70, 2186–2189, 1993.
[102] Sornette, D.: Self-organized criticality in plate tectonics, in: Spontaneous Formation of Space-Time Sructures and Criticality, edited by Riste, T. and Sherrington, D., 57–106, Kluwer Academic Publishers, 1991.
[103] Varotsos, P.: The Physics of Seismic Electric Signals, TerraPub, Tokyo, 2005.
[104] Kapiris, P., Nomicos, K., Antonopoulos, G., Polygiannakis, J., Karamanos, K., Kopanas, J., Zissos, A., Peratzakis, A., and Eftaxias, K.: Distinguished seismological and electromagnetic features of the impending global failure: did the 7/9/1999 M5.9 Athens earthquake come with a warning? Earth Planets and Space, 57, 215-230, 2005.
[105] Potirakis, S., Minadakis, G., Eftaxias, K.: Fisher information measure, Tsallis entropy, Symbolic dynamics, Fracture induced electromagnetic emissions, Physica A, (in press).

[106] Pulinets, S., LegenŠka, A., Gaivoronskaya, T., and Depuev, V: Main phenomenological of ionospheric precursors of strong earthquakes, J. Atmos. Sol.-Terr. Phy., 65, 1337–1347, 2003.
[107] Vicsek, T.: A question of scale, Nature, 411, 421 pp., 2001.
[108] Vicsek, T.: The bigger picture, Nature, 418, 131 pp., 2002.
[109] Stanley, H.: Exotic statistical physics: Applications to biology, medicine, and economics, Physica A, 285, 1-17, 2000.
[110] Picoli, S., Mendes, R., Malacarne, L., Papa, A.: Similarities between the dynamics of geomagnetic signal and heartbeat intervals, Europhysics Letters, 80, 50006/1Ů6, 2007.
[111] de Arcangelis, L., Godano, C., Lippiello, E., and Nicodemi, M.: Universality in Solar Flare and Earthquake Occurrence, Phys. Rev. Lett., 96, 051102/1–4, 2006.
[112] Kossobokov, V., Keillis-Borok, V., and Cheng, B.: Similarities of multiple fracturing on a neutron star and on Earth, Phys. Rev. E, 61, 3529–3533, 2000.
[113] Sornette, D.: Predictability of catastrophic events: material rupture, earthquakes, turbulence, financial crashes and human birth, Proceedings of the National Academy of Sciences USA, 99, 2522–2529, 2002.
[114] Abe, S., and Suzuki, N.: Statistical similarities between internetquakes and earthquakes, Physica D 193, 310-314, 2004.
[115] Peters, O., Hertlein, C., and Christensen, K.: A complexity view of rainfall, Phys. Rev. Lett. 88, 018701, 2002.
[116] Fukuda, K., Nunes, L., and Stanley, H.: Similarities between communication dynamics in the Internet and the automatic nervous system, Europhys. Lett., 62, 189–195, 2003.
[117] Herz, A. and Hopfield, J.: Earthquake cycles and neural reverberations: Collective oscillations in systems with pulse-coupled threshold elements, Phys. Rev. Lett., 75, 1222-1225, 1995.
[118] Hopfield, J.: Neurons, dynamics and computation, Phys. Today, 40, 40-46, 1994.
[119] Usher, M., Stemmler, M., and Olami, Z.: Dynamic pattern formation leads to $1/f$ noise in neural populations, Phys. Rev. Lett., 74, 326–329, 1995.
[120] Corral, A., Perez, C., and Diaz-Guilera, A.: Self-organized criticality induced by diversity, Phys. Rev. Lett., 78(8), 1492–1495, 1997.
[121] Plenz, D.: When inhibition goes incognito: feedback interaction between spiny projection neurons in striatal function, TRENDS in Neurosciences, 26(8), 436–443, 2003.
[122] Zhao, X. and Chen, T.: Type of self-organized criticality model based on neural networks, Phys. Rev. E, 65, 026114-1–026114-6, 2002.
[123] Rundle, J., Tiampo, K., Klein, W., and Sa Martins, J.: Selforganization in leaky threshold systems: the influence of near mean field dynamics and its implications for EQs, neurology, and forecasting, PNAS, 99, 2514–2521, 2002.
[124] Nikolopoulos, S., Kapiris, P., Karamanos, K., and Eftaxias, K.: A unified approach of catastrophic events, Natural Hazards and Earth System Sciences, 4, 615-637, 2004.
[125] Li, X., Polygiannakis, J., Kapiris, P., Peratzakis, A., Eftaxias, K., and Yao, X.: Fractal spectral analysis of pre-epileptic seizures in terms of criticality, Journal of Neural Engineering 2, 1-6, 2005.
[126] Kapiris, P., Polygiannakis, J., Yao, X., and Eftaxias, K.: Similarities in precursory features in seismic shocks and epileptic seizures. Europhysics Letters 69, 657-663, 2005.
[127] Osorio, I., Frei, M., Sornette, D., Milton, J., and Lai, Y.: Epileptic seizures: Quakes of the brain? Phys. Rev. E. 82, 021919, 2010.

[128] Balasis, G., Daglis, I., Kapiris, P., Mandea, M., Vassiliadis, D., and Eftaxias, K.: From pre-storm activity to magnetic storms: a transition described in terms of fractal dynamics, Ann. Geophys. 24, 3557-3567, 2006.
[129] Balasis, I. Daglis, Papadimitriou, C., Kalimeri, M., Anastasiadis, A., and Eftaxias, K.: Investigating dynamical complexity in the magnetosphere using various entropy measures, Journal of Geophysical Research, 2009.
[130] Balasis, G., Daglis, I., Papadimitriou, C., Kalimeri, M., Anastasiadis, A., and Eftaxias, K.: Dynamical complexity in Dst time series using non-extensive Tsallis entropy, Geophysical Research Letters, L14102, doi:10.1029/2008GL034743, 2008.
[131] Balasis, G., Daglis, I., Anastasiadis, A., Papadimitriou, C., Mandea, M., and Eftaxias, K.: Universality in solar flare, magnetic storm and earthquake dynamics using Tsallis statistical mechanics, Physica A, 390, 341-346, 2011.
[132] Rundle, J., Turcotte, D., Shcherbakov, R., Klein, W., and Sammis, C.: Statistical physics approach to understanding the multiscale dynamics of earthquake fault systems, Reviews of Geiophysics, 41, 5/1-5/30, doi:10.1029/2003RG000135, 2003.
[133] Carpinteri, A., and Pugno, N.: Are scaling laws on strength of solids related to mechanics or to geometry?, Nature materials, 4, 421-423, 2005.
[134] Varotsos, P., Sarlis, N., and Skordas, E.: Natural Time Analysis: The New View of Time (Springer, Berlin), 2011.

12

The Effect of Marmara (Izmit) Earthquake on the Chemical Oceanography and Mangan Enrichment in the Lower Layer Water of Izmit Bay, Turkey

Nuray Balkis
Istanbul University, Marine Science and Management Institute, Istanbul Turkey

1. Introduction

Dissolved oxygen (DO) content of the marine environment is a crucial parameter for life and water quality as well as playing an important role in biogeochemical processes, and respiration of plants and animals, and decomposition of organic matter by bacteria are the primary processes that consume dissolved oxygen content of water and pore-water in sediments. If the oxygen concentration of water falls below about 2 mg/1, living organisms become stressed and the consequent conditions lead to hypoxia. Persistent hypoxia and increased oxygen uptake accompanies release of hydrogen sulfide. Anoxia occurs in estuaries where high loads of organic matter and/or nutrients are supplied, and in semienclosed water bodies where water mixing and tidal exchanges are strongly restricted.

In recent years, aquatic ecosystems have been contaminated by heavy metals; which are of agricultural, industrial, domestic, mining and also natural origins (Ayas and Kolankaya 1996; Han et al., 2002). They are potentially toxic to the aquatic environment; if they exceed natural limits, they will be harmful to the aquatic organisms' environments and human health (Forstner and Witmann, 1981). Organisms need some metals such as Fe, Cu, Zn, Co, Se, Ni and Mn in certain amounts; however, exceeding these amounts may cause toxic effects for these organisms. Some metals such as Hg, Cr, Pb and Cd are toxic to organisms and marine habitat. These metals are dissolved in sea water or suspended in solid materials and absorbed through the gills or skin of marine organisms; they also accumulate in the bodies of organisms through the food chain (Forstner and Witmann, 1981). Mussels, in particular, have been used as biological indicator organisms to monitor marine pollution by toxic heavy metals and potentially toxic chemicals due to their properties of inhabitation (Pempcowiac et al., 1999; Hu 2000).

Izmit Bay (Figure 1) is a semi-enclosed water body and situated in the NE of Marmara Sea. It has been subjected to pollution problems (Orhon et al., 1984; Tuğrul et al., 1989; Morkoç et al., 1996), including eutrophication of the water and inputs of toxic industrial and domestic effluents. Total organic matter load of industrial discharges has been reduced to 80% within the last 10 years, whereas domestic organic loads have been increased in two fold (Morkoç et al., 1996, 2001). The earthquake with a magnitude of 7.4 was occurred at 17th of August 1999, destroying the eastern Marmara Region. The epicenter of the earthquake was found to

be in a small city (Gölcük) located on the southern coast of Izmit Bay. This seismic event caused the destruction of wastewater discharge systems and also dispersal of refined petroleum products onto the sea surface from the subsequent refinery fire. The surface waters of the Bay were partly covered by the thick petroleum layers and partly by a film (Güven et al., 2000, Ünlü et al., 2000). Petroleum layer covering the surface water reduced the transfer of oxygen from air/sea interface and also caused the subsequent death of living organisms. Increasing effluent discharges into the Bay produced an exceptional plankton bloom. Coupling of such factors leading to oxygen deficiency at the sea floor caused the formation of anoxic conditions. Okay et al., (2001) investigated ecological changes in Izmit Bay, however their data is limited with the September 1999.

This paper presents the results of one-year monitoring program performed in Izmit Bay after the Earthquake, with the purposes of describing the abrupt changes in chemical oceanography and understanding the mechanism of H_2S generation in the Bay which has not been occurred before. Furthermore, the factors controlling metal distributions in water column and surface sediments of the Bay were discussed in this study.

1.1 Study area

Izmit Bay is an elongated semi-enclosed water body with a length of 50 km, width varying between 2 to 10 km (Figure 1) and has an area of 310 km^2. The bathymetry of the Bay constitutes three sub-basin separated by shallow sills from each other. The eastern basin is relatively shallow (at about 30 m) whereas the central basin has two small depressions with depths of 160 and 200 m. The western basin deepens in westward from 150 m to 300 m and connects the Bay to the Marmara Sea. Izmit Bay is oceanographically an extension of Marmara Sea, having a permanent two-layered water system. The upper layer is originated from less saline Black Sea waters (18.0-22.0 psu), whereas the lower layer originated from the Mediterranean Sea waters is more saline (37.5-38.5 psu) (Ünlüata et al., 1990). The permanent stratification occurs at about 25 m in the Marmara Sea (Beşiktepe et al., 1994), however it is highly variable in Izmit Bay (Oğuz and Sur, 1986) (Figure 2). The thickness of the upper layer changes seasonally from 9 to 18 m spring and autumn, respectively (Oğuz and Sur, 1986; Algan et al., 1999). The upper layer enters into the Bay in spring and summer, corresponding to the freshwater inflow changes in the Black Sea, while the lower layer flows to the Marmara Sea from the Bay. However, the upper layer flows towards the Marmara Sea in autumn and winter (Oğuz and Sur, 1986). Vertical mixing of the two layers is restricted and occurs at shallow depths. An intermediate layer develops throughout the year in the water column of the Bay with varying thickness (DAMOC, 1971; Baştürk et al., 1985; Tuğrul et al., 1989; Oğuz and Sur, 1986; Altıok et al., 1996). The upper layer of Izmit Bay, in general, is saturated with DO (Tuğrul and Morkoç, 1990). DO concentrations in the lower layer of Izmit Bay has been found to be 2.5-3.0 mgl^{-1} in winter and spring periods and 0.7-1.5 mgl^{-1} in summer, in previous studies (Morkoç, et al., 1996). The minimum DO concentrations have been measured locally in the central basin (0.1-0.2 mgl^{-1}) and in the eastern basin (0.5 mgl^{-1}) during spring-summer period (Tuğrul and Morkoç, 1990). Izmit Bay and its surroundings is one of the most industrialized and populated area of Turkey, receiving more than 300 industrial and domestic effluents (Morkoç et al., 1996). Industrial effluents discharges a total of 163,000 m^3/day wastewater, 24 tons/day BOD and 19,5 tons/day TSS to Izmit Bay (Morkoç et al., 2001). The eastern basin receives the highest inputs compare to other basins of the Bay. Based on the previous studies, no DHS has been measured in Izmit Bay (Morkoç et al., 1988; Tuğrul et al., 1989; Morkoç et al., 1996).

Industrial loads have been reduced by treatment and waste minimization within the last 10 years, but domestic wastes has doubled, due to the increasing population in the Bay. Therefore, the total (domestic + industrial) discharge load into the Bay during the last 10 years has not changed significantly (Morkoç, et al., 2001). The dissolved oxygen content of Izmit Bay decreased dramatically from 1984 to 1999 and reached to a minimum value at 20 m throughout the Bay (Okay et al., 2001). Ergin et al., (1991) suggested that the surface sediments in İzmit Bay are uncontaminated by anthropogenic pollution. However Yaşar et al., (2001) investigated that the heavy metal concentrations are highest in the eastern and central basins. The western basin was also found generally unpolluted with respect to heavy metals by Yaşar et al., 2001.

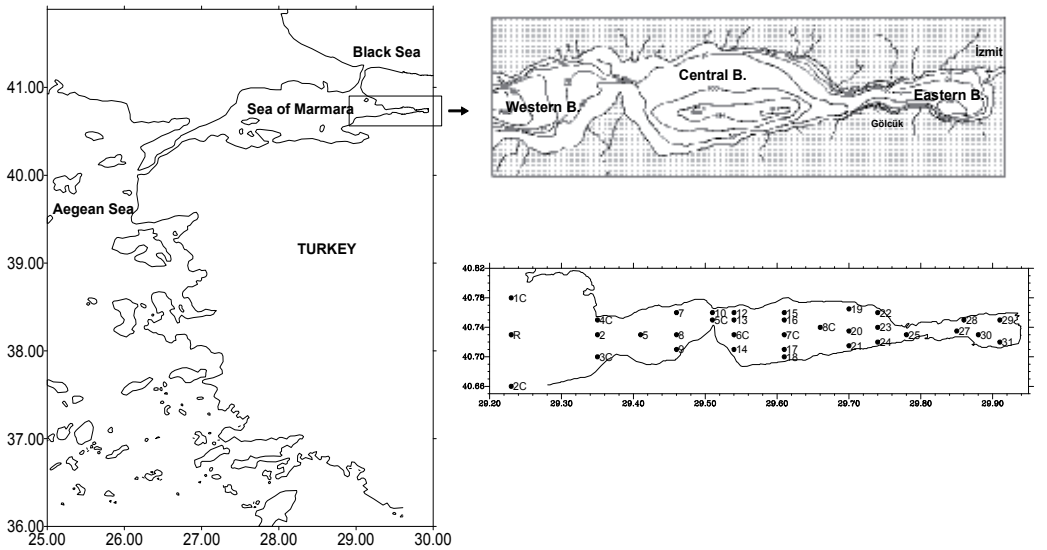

Fig. 1. The location (left) and bathymetry (above) of the study area. The location of sampling station in İzmit Bay (below).

2. Material and methods

2.1 Sampling sites

The water samples were collected from 32 stations in İzmit Bay, including one station located off the western basin (R), on board the R/V Arar (Figure 1). Station (R) represents the characteristics of the Marmara Sea and hence, provides a comparison between the Bay and the Marmara Sea. The sampling stations in İzmit Bay represent the various depths of three basins, with a minimum of 17 m and maximum of 200 m. Sampling was carried out with a Rosette sampler assembled to the Sea Bird CTD System at about 10 m depth intervals through the upper and the lower layers. Sampling period includes August 1999, immediately after the Earthquake and performed monthly in 1999 and in February, May and August during 2000.

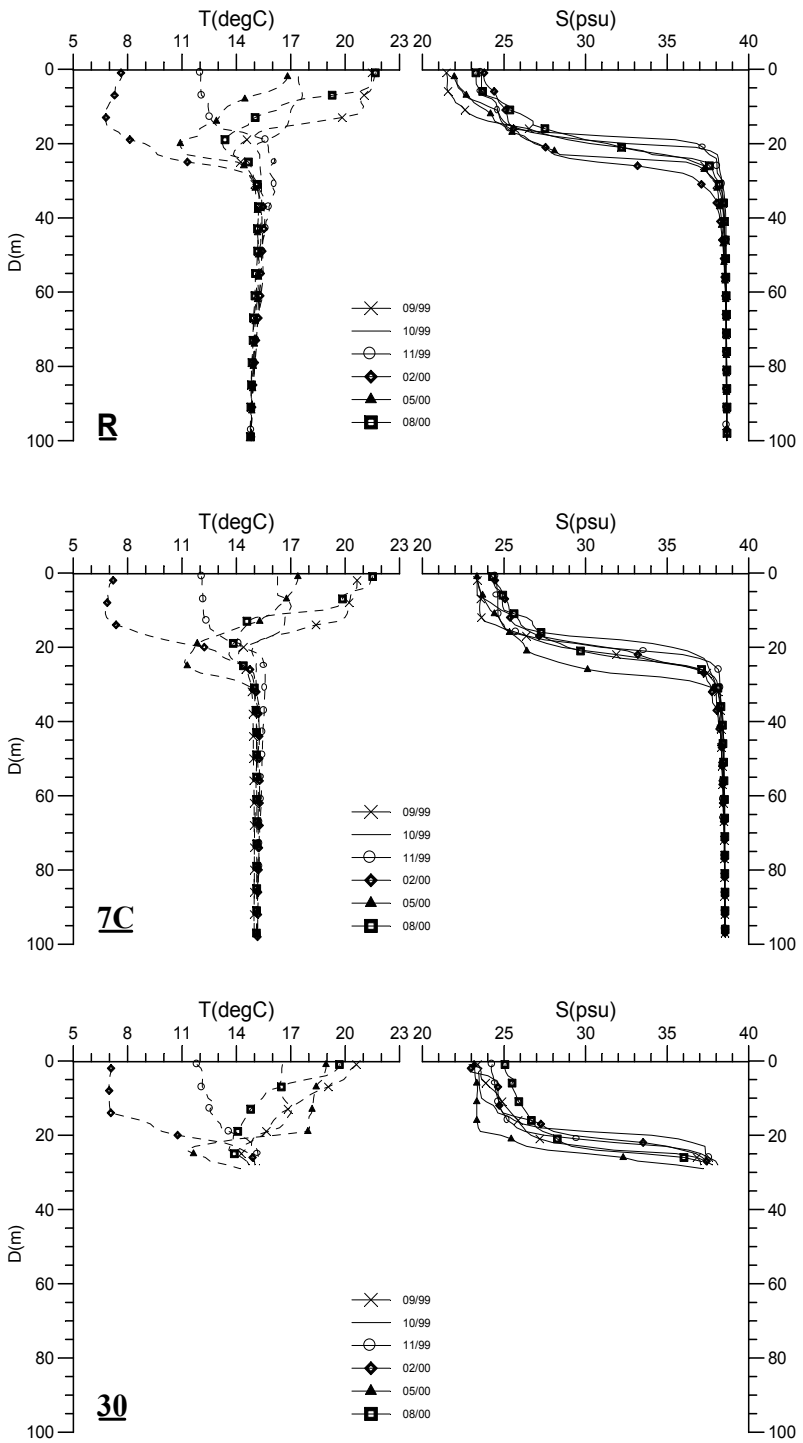

Fig. 2. Depth profile of salinity and temperature distribution along the water column of some selected station from İzmit Bay (from Güven et al., 2000).

2.2 Analytical methods

Samples for DO determinations were drawn first from the Niskin bottles of Rosette to prevent any biological activity and gas exchanges with the atmosphere. DO determination was carried out by Winkler method (Greenberg et al., 1985) on board from all the stations (Figure 1). The precision of method was estimated at ± 1.9 % .

Dissolved hydrogen sulfide (DHS) was measured only at stations where DO concentrations are lower than the detection limit of the method (0.03 mgl^{-1}) (Figure 1), in all the sampling periods, except August and September 1999. DHS contents were measured by an iodometric titration method (Strickland and Parsons, 1972).

pH values measured along the water column at all stations with a WTW 526 pH-meter equipped with a temperature-compensation adjustment on board.

The water samples were filtered through 0.45 µm filters using metal clean tecniques (Bruland et al., 1979). The samples were stored in polyethylene bottles (LDPE) that were acid cleaned using methods described Patterson and Settle (1976). After collection, the samples were acidified to a pH between 1.5 and 2.0 using HNO_3. Dissolved heavy metal concentrations (Fe, Mn, Pb, Cu and Cd) were measured by atomic absorption spectrophotometer (AAS) following preconcentration with ammonium 1-pyrrolidinedithiocarbamate (APDC) in an organic extraction (Bruland et al., 1985). The blanks for the metals analyzed were: Fe, 010 ± 0.05 mg/l; Mn, 0.10 ± 0.02 mg/l; Cu, 0.15 ± 0.08; Cd, 0.05 ± 0.03 mg/l; Pb, 0.20 ± 0.30 mg/l.

The surface sediments total carbonate contents were determined by a gasometric-volumetric method (Loring & Rantala, 1992). Total organic carbon (C_{org}) was analyzed by the Walkey-Blake method, which involves titration after a wet combustion of the sample (Gaudette, 1974; Loring & Rantala, 1992). Al, Fe, Mn, Cu, Zn, Co and Cr contents were determined by atomic absorption spectrophotometer (AAS) after a "total" digestion, involving HNO_3 + $HClO_4$ + HF acid mixture.

The sequential selective extraction analyses were carried out using 1M Na-acetate (pH=5 adjusted by acetic acid) for the dissolution of carbonate phase, 0.04M hydroxylamine hydrochloride (HAHC) in 25% acetic acid for dissolving Fe-Mn-oxyhydroxides, 0.02M nitric acid + 30% hydrogen peroxide (pH=2) for extracting organic matter, and HNO_3 + $HClO_4$ + HF mixture for the total extraction of the residual (lithogenous) fraction (Tessier et al., 1979).

Reference Material	Element	Measured value (this study) ppm	Certified value or range ppm
SL-1	Fe	62	65-7-69.1
IAEA405	Al	63500	72700-83100
SL-1	Cr	98	95-113
SL-7	Mn	634	604-650
CRM-142	Cu	25	27.5
CRM-142	Zn	92	92.4
CRM-142	Co	13	7.9

Table 1. Accuracy of ASS analyses used in this study, as determined by Analysis of AQCS (SL-1 and SL-7), IAEA405 and BCR (CRM 142) reference materials.
SL-1 and SL-7 are lake sediment and CRM 142 is a light sandy soil.

The precision of the "total" metal analyses and the different selective extraction steps is better than 10% and 15%, respectively, at 95% significance level. The accuracy of the analyses were checked by analyzing the AQCS (lake sediment SL-1 and SL-7), IAEA405 and BCR (light sandy soil CRM 142) reference materials (Table 1). The metal values were normalized to eliminate the grain-size effects using metal/Al ratios (e.g., Loring & Rantala, 1992).

3. Results

3.1 Dissolved Oxygen (DO)

The vertical changes of DO in water column are shown by selecting some of the stations from each of the three (western-central-eastern) basins where the variations are significant (Figure 3). In station (R), DO concentrations are between 7.4-10.7 mgl^{-1} for the upper layer, and 1.1-1.5 mgl^{-1} in the lower layer during the sampling period between August 1999 to August 2000 (Figure 3), which are similar to vertical DO concentrations of the Marmara Sea (Ünlüata and Özsoy, 1986; Ünlüata et al., 1990; Doğan et al., 2000). Depth profile of DO concentration in İzmit Bay displays a sharp decrease at about 20 m below the surface in the western and the central basins, following the water stratification during late summer and autumn (Güven et al., 2000) (Figure 3). In February the gradual decline of DO occurs at about 30 m water depth.

DO concentration of the water column in the eastern basin indicates a more gentle profile, probably due to the vertical mixing of the two layers (Oğuz and Sur, 1986; Altıok et al., 1996) in shallow depths. DO concentration of the upper layer in İzmit Bay varies in a range between 4.5 to 12.1 mgl^{-1} during August 1999-2000 (Figure 4a and b). Saturated DO occurs in the upper layer locally at the eastern basin in October 1999 (Figure 4a, 5). The saturation concentration of DO (SDO) values are determined by the solubility oxygen in sea water as a function of the concurrently measured values of temperature and salinity (Figure 2, 5 and 6). The highest DO concentrations were measured in February 2000 (Figure 4b), whereas the lowest DO concentrations were measured in September 1999 after the earthquake. The distribution of DO concentration in the upper layer is almost homogeneous in August and September 1999. From October 1999 to February 2000, DO concentration of the upper layer significantly increases. The increase of DO concentration occurred subsequently following the maximum phytoplankton bloom in October (Güven et al., 2000). DO concentrations range between 7.9-14.5 mgl^{-1} in October 1999, displaying the highest value in the eastern basin (Figure 4a and 5). The distribution of DO concentration in the upper layer becomes almost homogeneous with a range of 9.0-10.4 mgl^{-1} in December 1999 and slightly increases (10.19-12.12 mgl^{-1}) in February 2000. DO concentrations in the upper layer decrease (6.69-10.57 mgl^{-1}) in spring (May-2000, Figure 4b) and are lower in the eastern basin compare to the central and the western basins of İzmit Bay. In August 2000, DO concentrations lie between 5.0 and 9.4 mgl^{-1}, being relatively high in the central basin.

DO content of the lower layer is significantly lower than that of the upper layer, throughout the sampling period (Figure 3). In August 1999, after the earthquake DO concentrations of the lower layer ranges between 0.0-1.46 mgl^{-1}. DO concentration below the detection limits (<0.03 mgl^{-1}) was measured in areas where the water depth is deeper than 100 m and also in the eastern basin (Figure 7a and b). The lowest DO concentration ranges were measured in September 1999. The deficiency of DO is mostly accompanied with the presence of DHS and

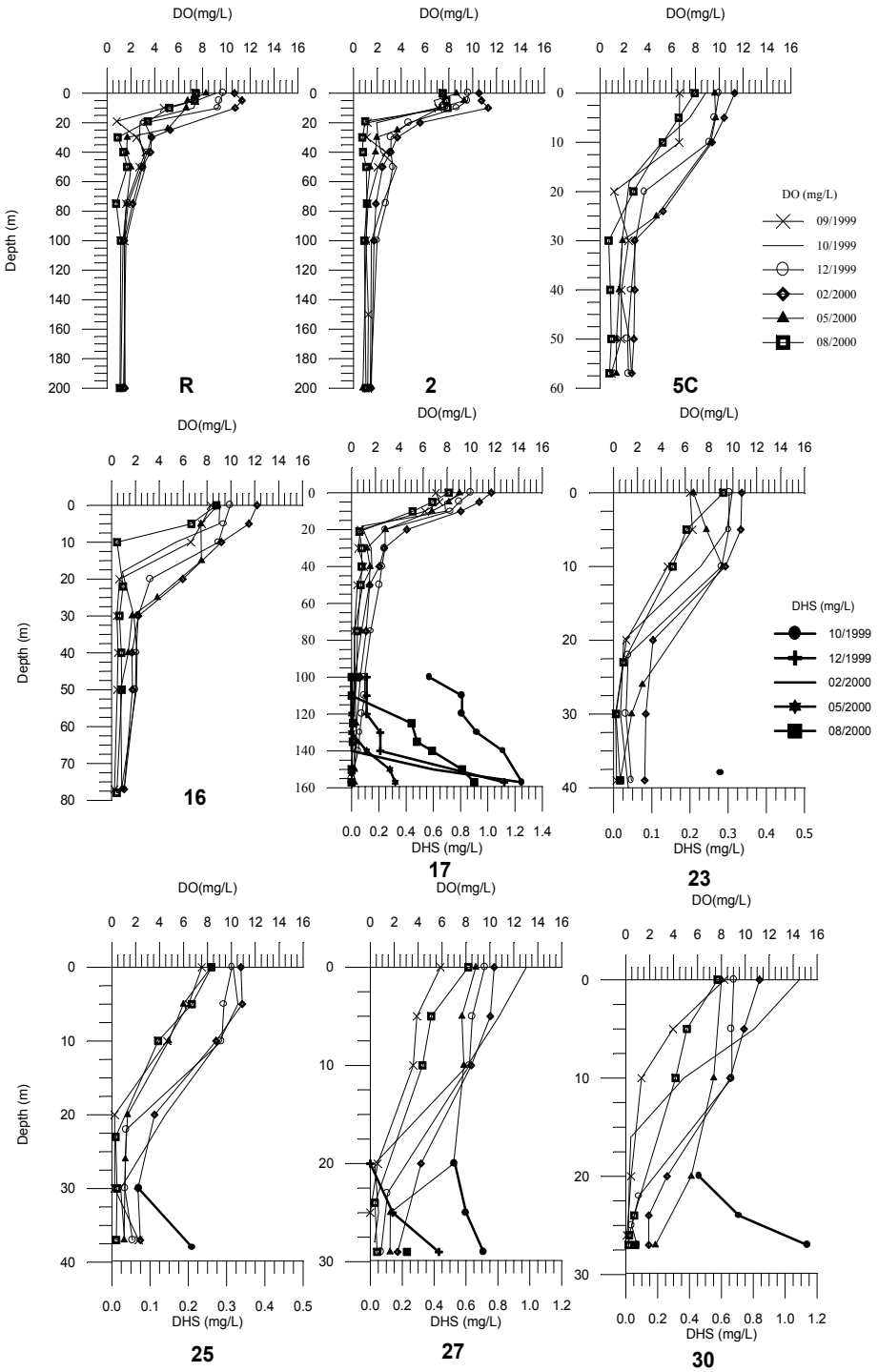

Fig. 3. Vertical distribution of DO and DHS along the water column in various stations of İzmit Bay.

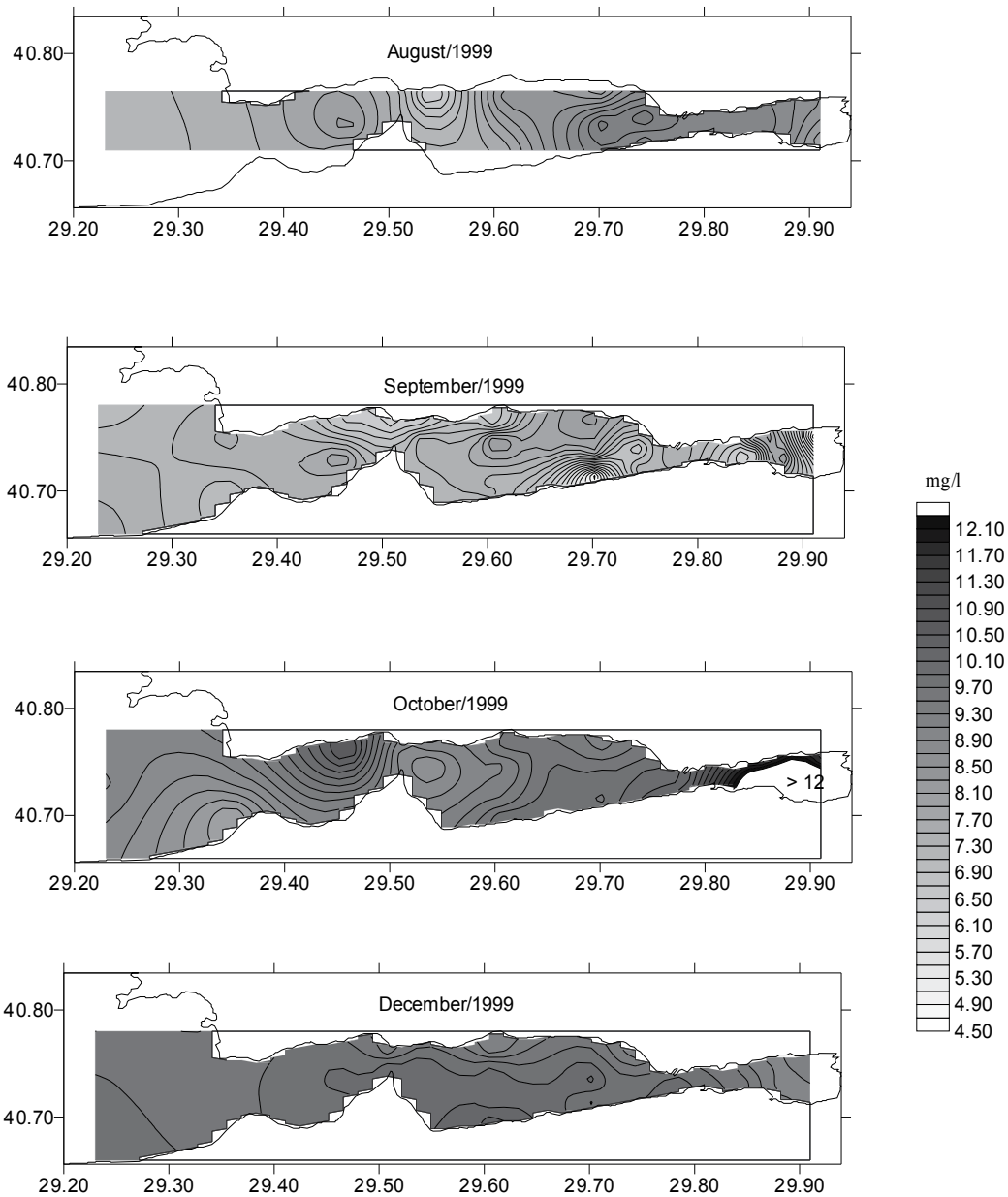

Fig. 4a. Spatial distribution of DO (mgl^{-1}) in the upper layer of İzmit Bay during August to December 1999.

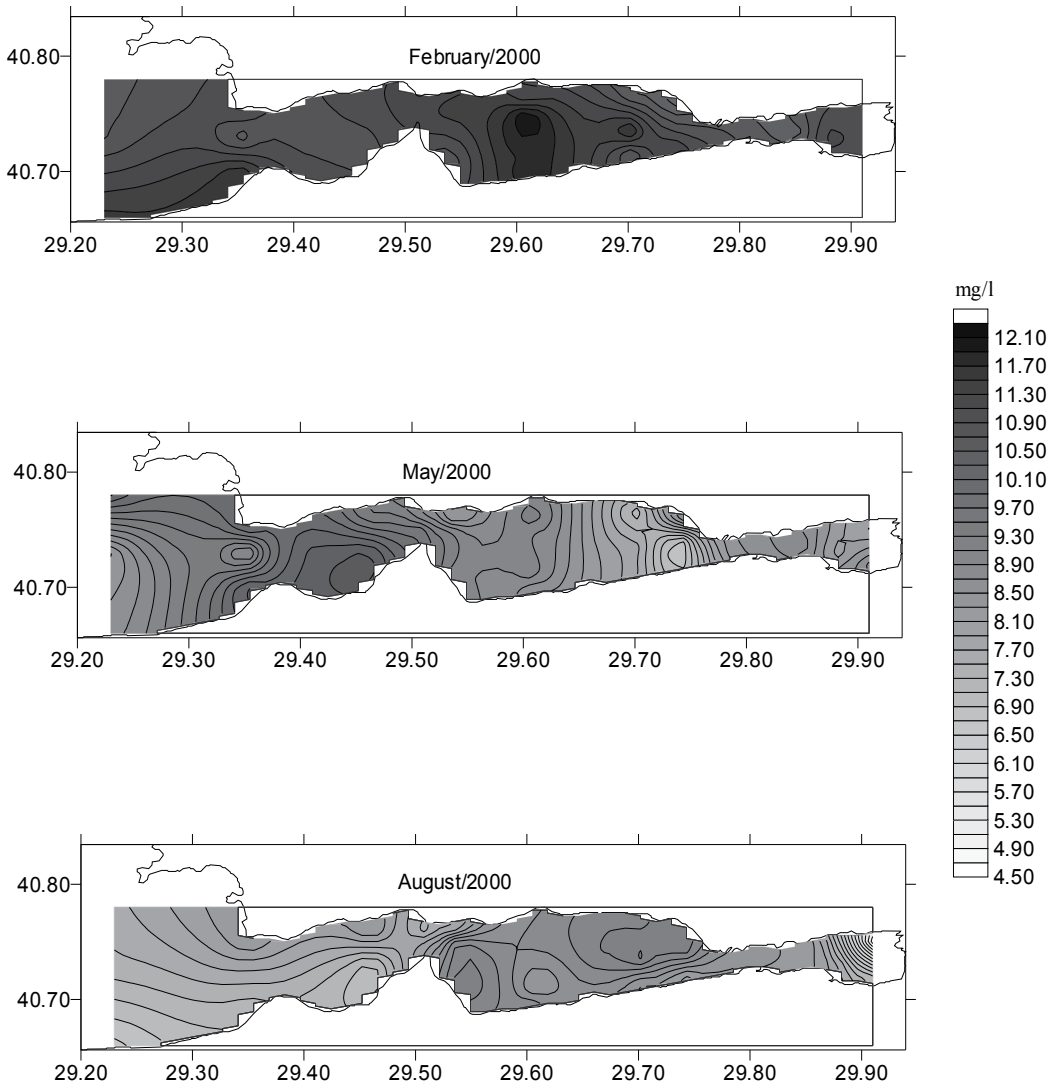

Fig. 4b. Spatial distribution of DO (mgl^{-1}) in the upper layer of İzmit Bay during February to August 2000.

is discussed below. The local anoxic conditions continue in September and October 1999 (Figure 7a), mainly in the central basin with DO concentration range of 0.0-3.4 mgl^{-1} and 0.0-7.9 mgl^{-1}, respectively. In December 1999, DO concentration of the lower layer generally increases (0.0-8.3 mgl^{-1}), but in only one station (17) no DO was lower than the detection limits (Figure 7a). The distribution pattern of DO concentration in the lower layer displays similar behavior in February and May 2000 (Figure 7b) with ranging between 0.0-8.2 mgl^{-1} and 0.0-8.8 mgl^{-1}, respectively. Relatively higher DO concentrations are close to the northern coast of İzmit Bay (Figure 7a and 7b). DO concentration of the lower layer decrease in August 2000, ranging between 0.0-3.6 mgl^{-1}.

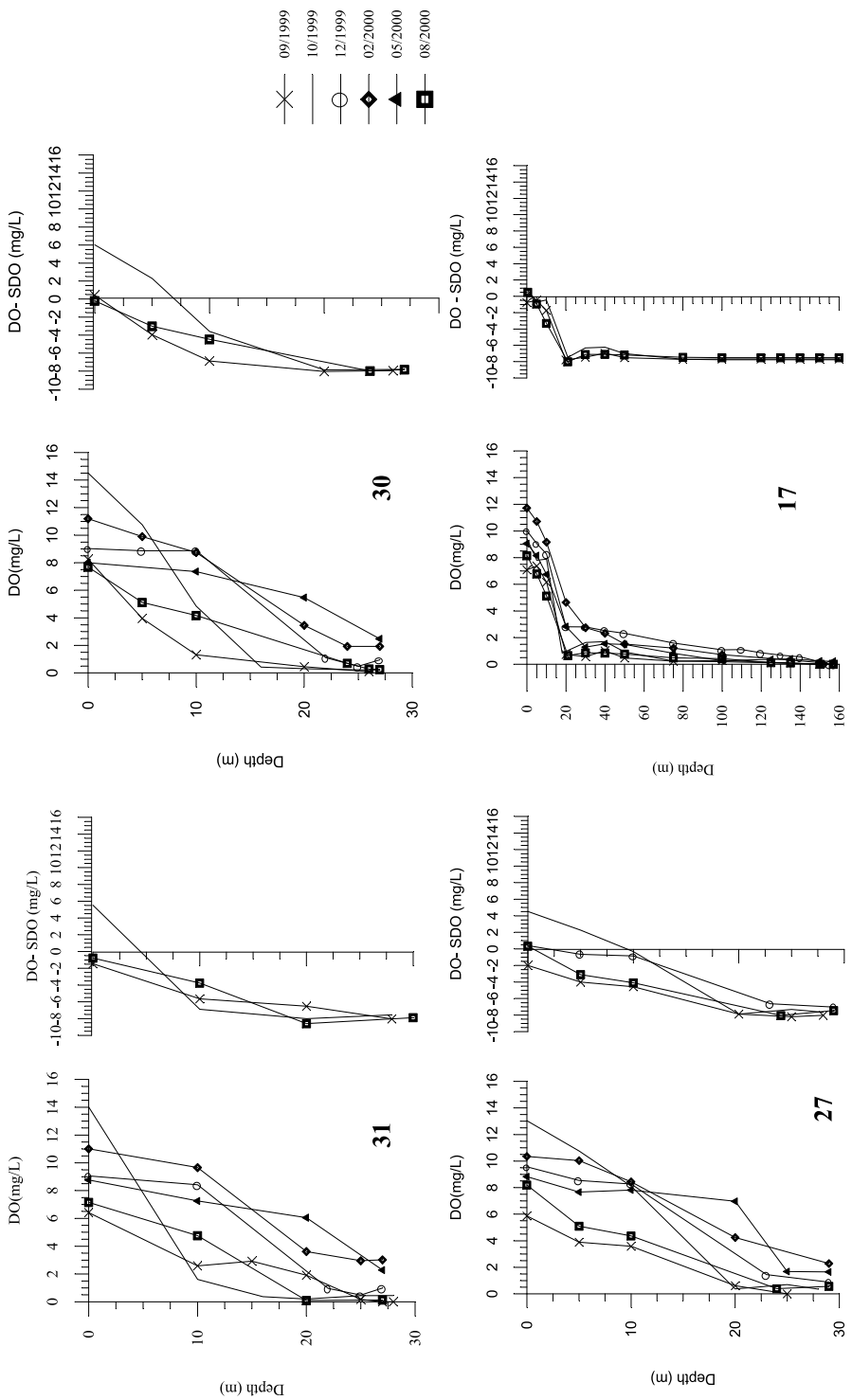

Fig. 5. Oxygen deficiency profiles in some selected stations of İzmit Bay.

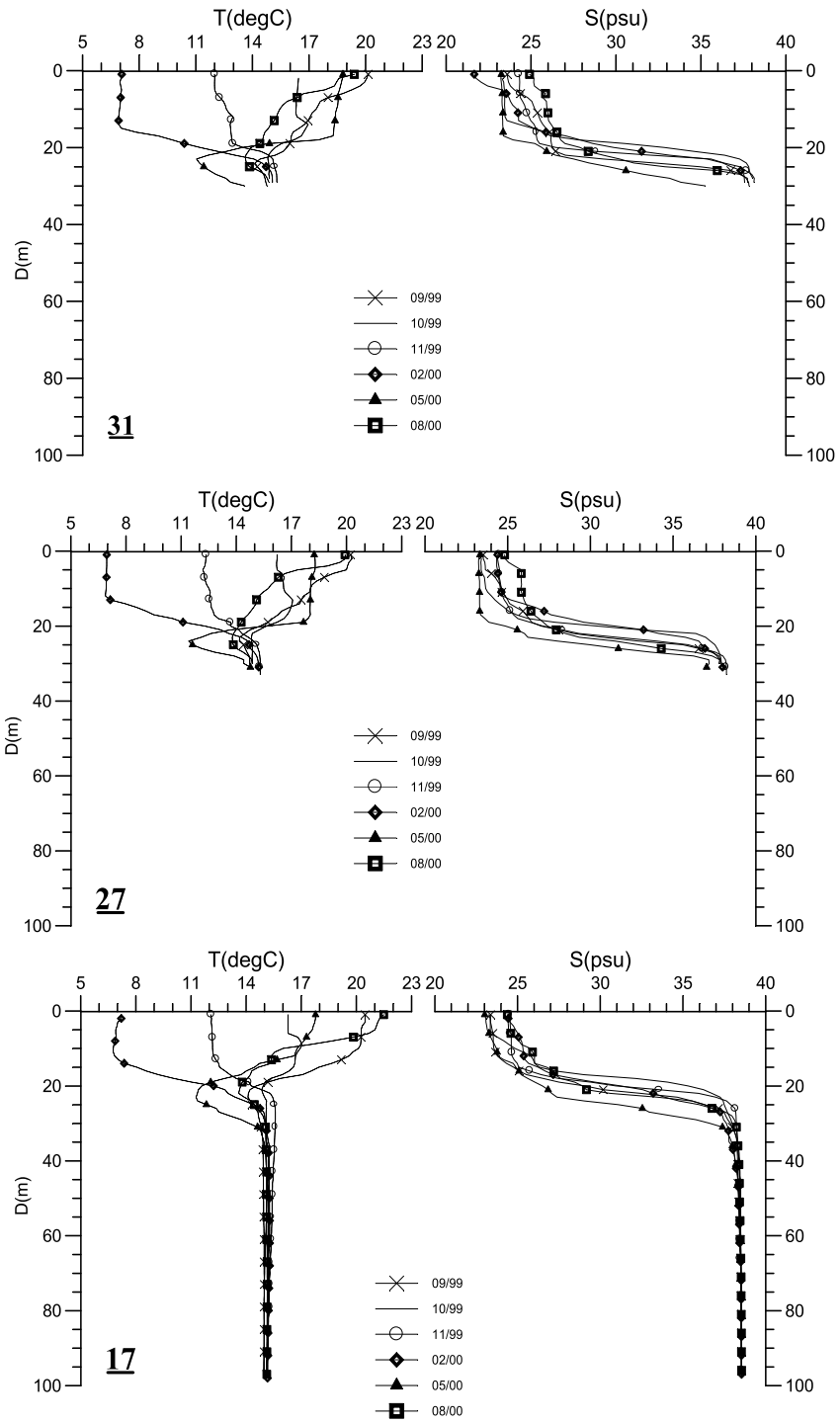

Fig. 6. Depth profile of salinity and temperature distribution along the water column of some selected stations from İzmit Bay (from Güven et al., 2000).

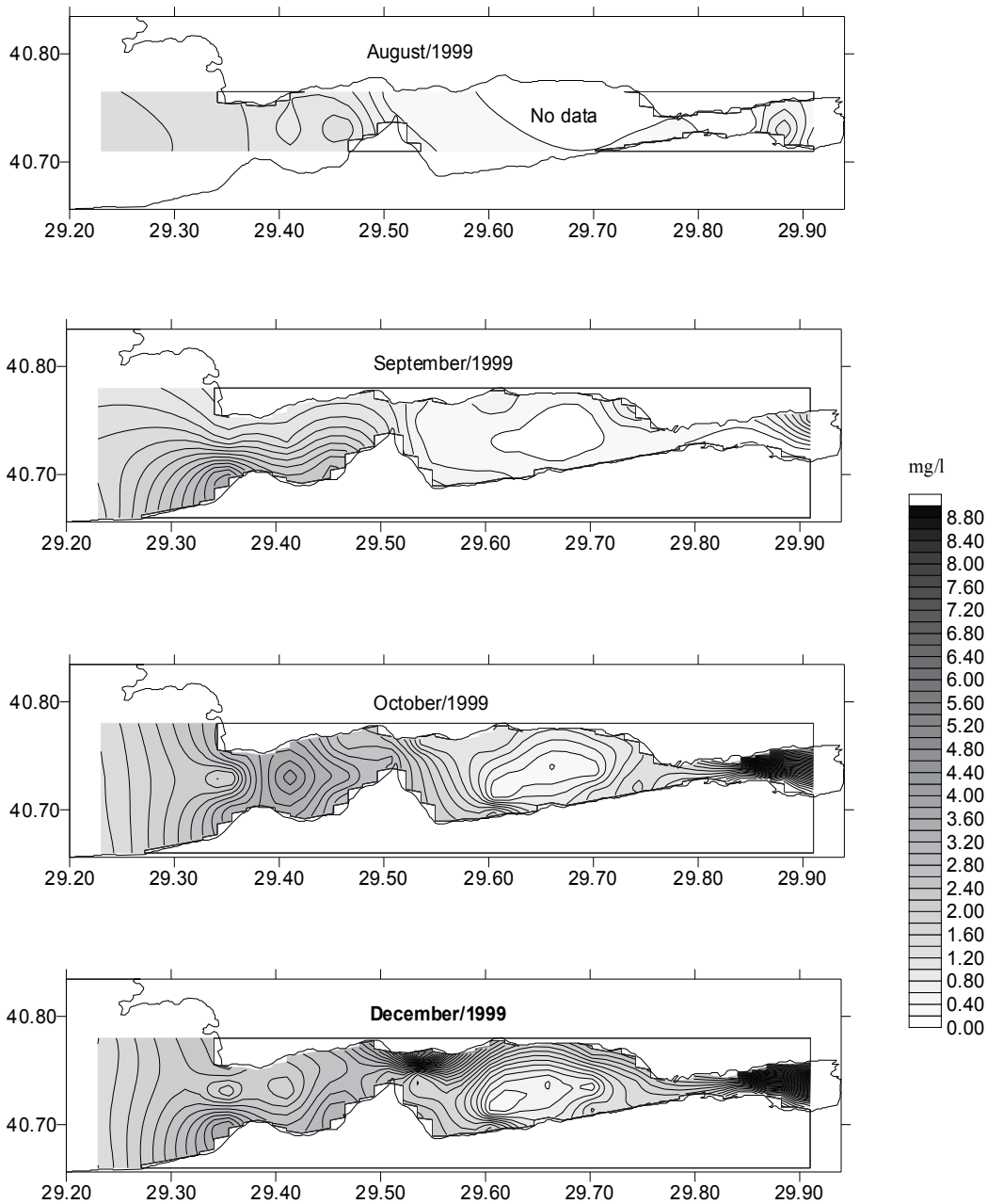

Fig. 7a. Spatial distribution of DO (mgl^{-1}) in the lower layer of İzmit Bay during August to December 1999

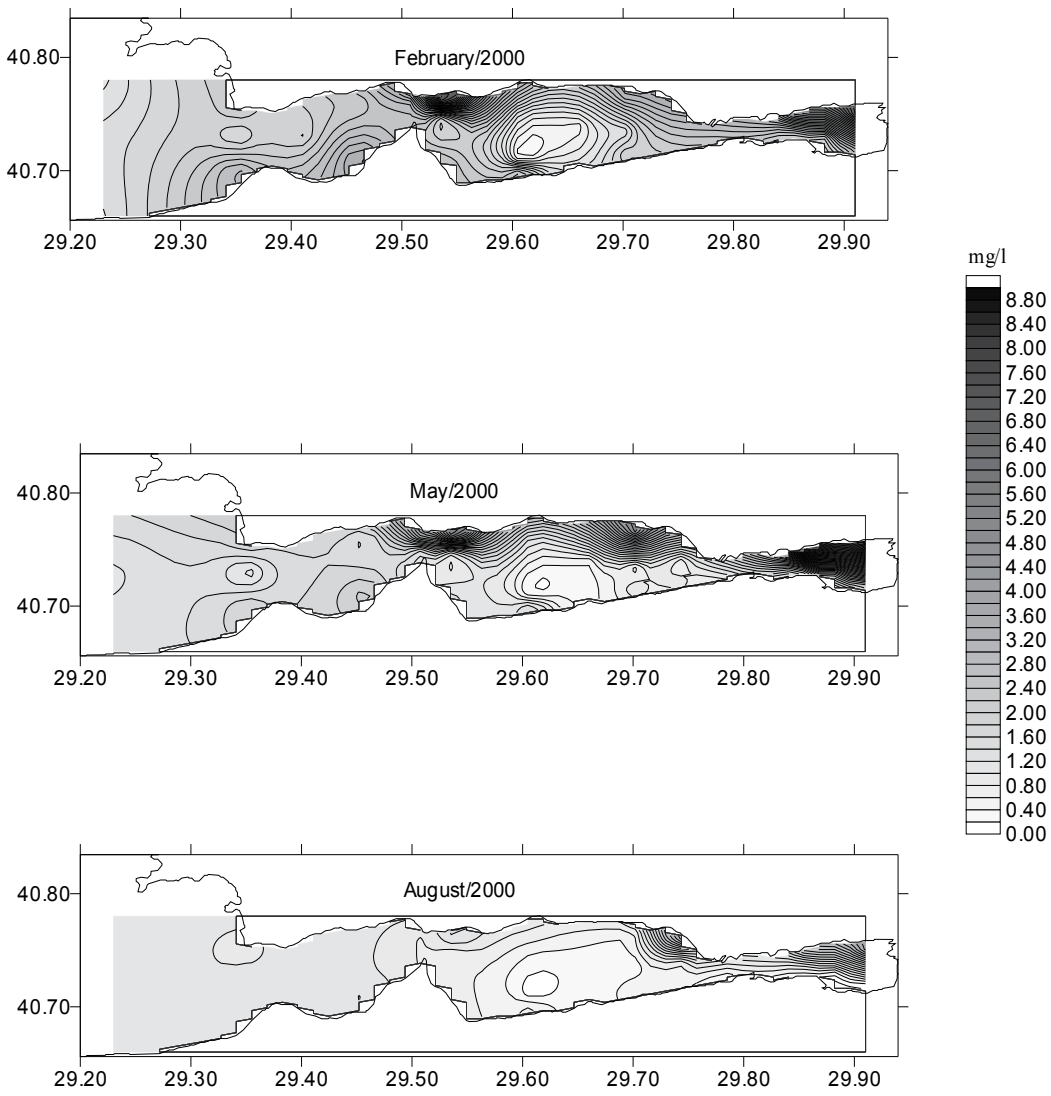

Fig. 7b. Spatial distribution of DO (mgl^{-1}) in the lower layer of İzmit Bay during February to August 2000.

3.2 Dissolved Hydrogen Sulfide (DHS)

The presence of DHS is limited with certain stations and in the lower layer. DHS formation develops both in the shallow area of the eastern basin (maximum 30 m) and relatively deep areas of the central basin. DHS is detected in stations 27, 29, 30 and 31 in the eastern basin, and 8C, 17, 19, 20, 23 and 24 in the central basin (Figure 1, Table 1). In the station 25 situated at the connecting small strait between the eastern and the central basin, measurable DHS exists in the lower layer. DHS concentrations vary in between 0.06-1.25 mgl^{-1}, reaching to their maximum in the lower layer of station 17. No DHS data available for the sampling period of August 1999 after the Earthquake. DHS concentration in October 1999 reaches to 1.14 mgl^{-1} in the eastern basin (station 30) (Figure 3). In general, DHS appears at a water

depth of 20 m in the shallow parts of the eastern basin, with the exception of station 29 where DHS exists up to 10 m to the surface. In December, DHS formation occurs only in stations 27 and 29 and disappears in the other stations. During winter and spring sampling period, no DHS is detected in the eastern basin. Low DHS concentration (0.06 and 0.23 mgl^{-1}) is found in stations 27 and 30 in August 2000.

The central basin							
Station	Water depth (m)	Sampling depth (m)	October 1999	December 1999	February 2000	May 2000	August 2000
25	40	30	0.07	*	*	*	*
		38	0.21	*	*	*	*
27	31	20	0.53	*	*	*	*
		25	0.60	0.14	*	*	*
		29	0.71	0.40	*	*	0.23
29	18	10	0.43	*	*	*	*
		15	0.50	*	*	*	*
		17	0.85	0.24	*	*	*
30	29	20	0.45	*	*	*	*
		24	0.71	*	*	*	*
		27	1.14	*	*	*	0.06
31	30	20	0.28	*	*	*	*
		25	0.28	*	*	*	*
		27	0.36	*	*	*	*
The eastern basin							
17	160	100	0.57	0.11	*	*	*
		110	0.81	0.11	*	*	*
		120	0.81	0.11	*	*	0.43
		130	0.92	0.21	*	*	0.48
		140	1.11	0.21	*	0.11	0.59
		150	-	-	0.60	0.28	0.81
		152	-	-	0.89	-	-
		157	1.25	1.12	1.25	0.32	0.90
8C	116	100	0.64	*	*	*	*
		114	0.93	*	*	*	*
19	29	25	0.40	*	*	*	*
20	106	75	0.28	*	*	*	*
		80	0.40	*	*	*	*
		90	0.43	*	*	*	*
		102	0.71	0.32	*	*	*
23	43	38	0.28	*	*	*	*
24	57	53	0.28	*	*	*	*

(*) No detectable DHS

Table 2. DHS concentrations in the lower layer of the eastern and the central basins of İzmit Bay.

DHS is continuously detected in station 17 from the central basin in all the sampling periods, being highest in October 1999 and lowest in May 2000. The occurrence of DHS corresponds to depth interval of 100-160 m (bottom) during October and December 1999. In February 2000, DHS concentration is limited with the lower 10 m water column, increasing to 1.25 mgl^{-1} at the bottom. The thickness of DHS formation layer slightly increases to 20 m in May 2000, however the concentrations are reduced compare to February 2000 (Figure 3, Table 2). In August 2000, both concentration and thickness of DHS formation of the lower layer in station 17 increase. In spite of continuous presence of DHS in station 17, it occurs solely in October 1999 in the other stations of the central basin, and never reaches to 1 mgl^{-1} (Figure 3, Table 1). DHS is detected mainly at the very close to bottom (2 m above the sea floor) of the lower layer in most of the stations in the central basin, however the lower 25 m and 15 m of the water column in station 20 and 8C, respectively, contain DHS.

3.3 pH

The highest pH values were measured in October 1999 and May 2000 throughout the water column in İzmit Bay, and were particularly high in the eastern basin (Figure 8 and 9). The lowest pH values, on the other hand, correspond to sampling period of August 2000. pH values significantly decrease from 8.5 to 7.1 mainly in the eastern basin and to a lesser degree in the central basin, during the formation of DHS.

3.4 Metals

3.4.1 Water column

Iron concentrations range between <4 mg/l and 21 mg/l along the water column in İzmit Bay (Table 3). The highest values are measured after the Earthquake (October-1999). High dissolved Fe concentrations indicate reduction of Fe-oxides by bacteria during mineralization of organic carbon in the sediment and diffusion into bottom waters (Nealson, 1982; Lovley and Phillips, 1988; Nealson and Myers, 1990). Fe values are decrease in May and August 2000 where Fe limitation is thought to control phytoplankton productivity.

Manganese concentrations vary between <1 and 123 mg/l in water column of the Bay (Table 3). The values increased in lower layer water and near the sediment-water interface in eastern and central basins. This was attributable to the degradation of settling organic carbon (Nealson, 1982; Nealson and Saffarini, 1994; Nealson and Myers, 1990). Manganese oxides were reduced to dissolved Mn^{+2}, which diffused from the sediment into the water column occurring the anoxic conditions. The lowest Mn values are obtained in December 1999 and February 2000. In these periods, oxygen-rich waters of Marmara Sea (Mediterranean originating) flow into the Bay. Thus, Mn-oxides are occurred and flocculated in water column with reoxidation of dissolved Mn in more oxygenated waters.

Lead concentrations range between <0.8 and 1.8 mg/l in the Bay waters (Table 3). The highest values are suggested that atmospheric and anthropogenic inputs.

Copper concentrations vary between <0.4 and 7.4 mg/l along the water column of the Bay (Table 3). The high values shows that Cu was mainly affected by redox reactions involving Mn and Fe in bottom waters of the eastern and central basins. The lowest Cu concentrations are measured in occurring the extreme phytoplankton blooms periods especially in these regions.

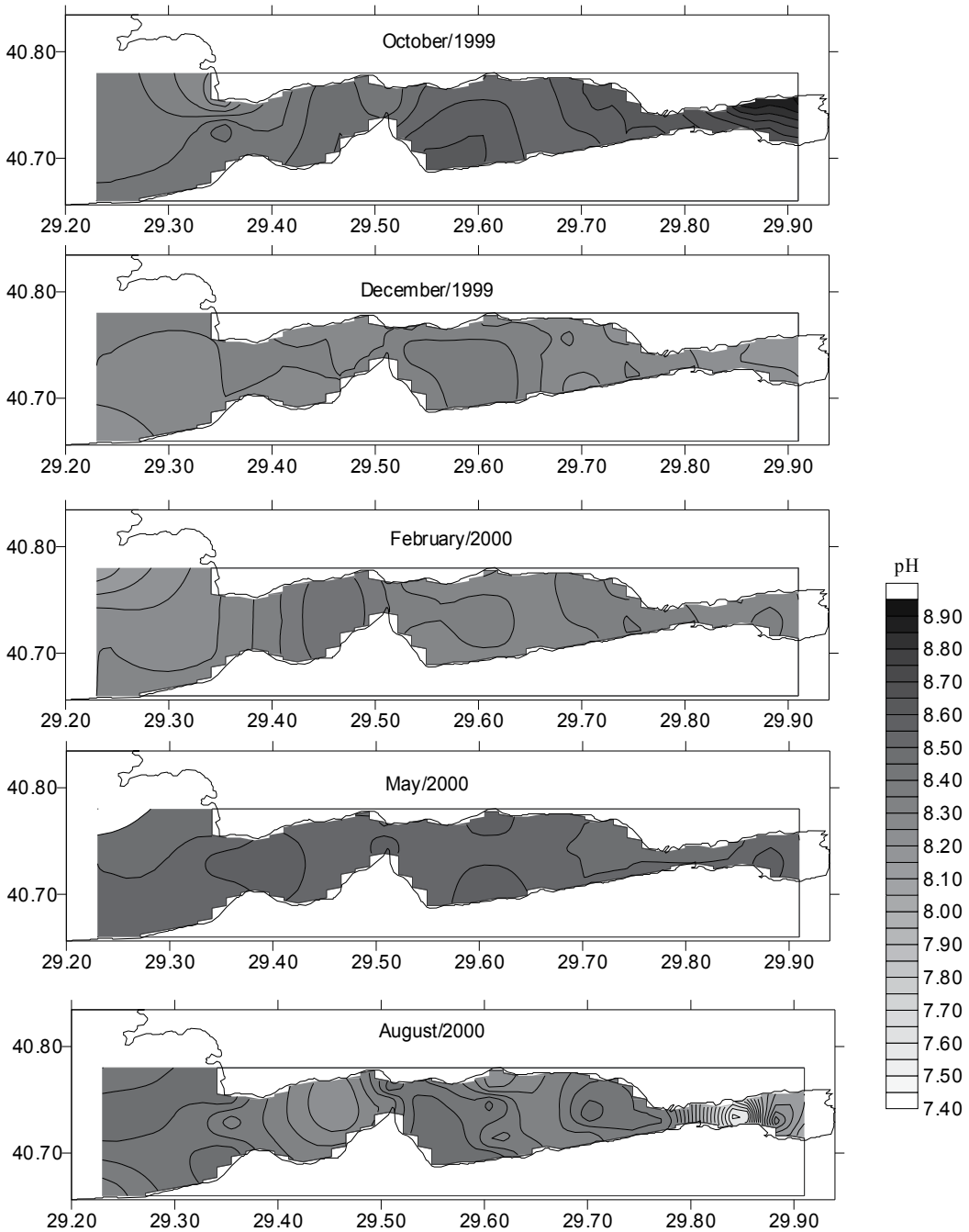

Fig. 8. Spatial distribution of pH values in the upper layer of İzmit Bay.

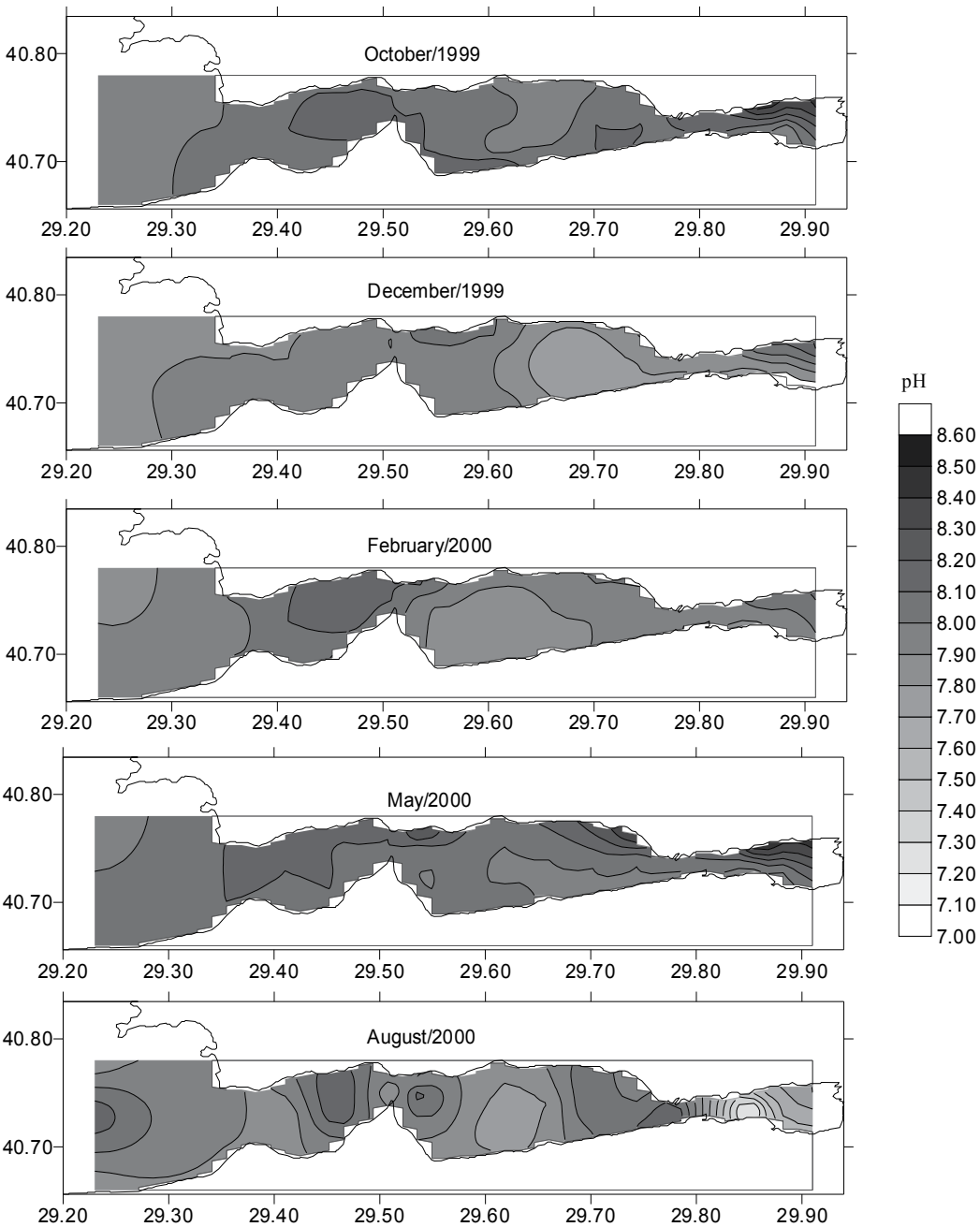

Fig. 9. Spatial distribution of pH values in the lower layer of İzmit Bay.

Element	October 1999	December 1999	February 2000	May 2000	August 2000
Fe	7-15	<4-4	<4-13	<4	<4
Mn	<1-4	1-7	2-4	4-12	<1-13
Pb	<0.8-1	<0.8-0.9	0.9-1	<0.8-2	<0.8-1
Cu	0.5-0.7	0.5-0.9	0.4-0.8	<0.4-0.6	<0.4-0.8
Cd	<0.1	<0.1	<0.1	<0.1	<0.1

Table 3. Metal concentrations along the water column of the Izmit Bay (µg/l).

Cadmium concentrations are lower than the detection limit of the method (<0.01 mg/l) along the water column of the Bay (Table 3). Since the domestic and industrial waste-water system has been damaged by the earthquake, causing the extreme phytoplankton bloom (Okay et al., 2001). This element is incorporated into organic matter by phytoplankton during periods of primary production (Sunda and Huntsman, 1995). Therefore, the relatively low residence time could be the result of biological uptake.

3.4.2 Surface sediments

3.4.2.1''Total'' metal distributions

The Iron concentrations range between 2.4 % and 11.8 % and are generally above the shale average value of 4.7 % (Krauskopf, 1979) (Table 4). The highest values are measured in southern shelf and eastern basin of the İzmit Bay. The Fe distribution in the Bay sediments is controlled mainly by the riverine and anthropogenic inputs on this land-locked system.

Element	Average shale (Krauskopf, 1979)	Gulf of Izmit min - max	Gulf of Izmit mean - SD
Cu (µg/g)	50	11- 42	23 ± 8.87
Zn (µg/g)	90	84 - 306	149 ± 57
Fe (%)	4.7	4.6 - 7.1	6.1 ± 0.6
Mn (µg/g)	850	139 - 494	327 ± 89
Co (µg/g)	20	6 - 20	12 ± 3.93
Cr (µg/g)	100	34 - 77	58 ± 11
Al (%)	9.2	2.3 - 11.4	7.4 ± 2.5
CaCO3	6.0[a]	13 -42	13.4 ± 9.9
Corg (%)	0.8[a]	0.6 - 6.2	3.0 ± 1.6

[a] From Mason and Moore (1982, p.153)

Table 4. Range of metal concentrations of bulk surface sediments from different parts of the Marmara Sea

Manganese concentrations are in general, lower than the average abundance of this element in shale (<850 µg/g). The values increase in western basin of the Bay. Here, Mn^{+2} form of this redox sensitive element derived from the early diagenesis of the sediments, is believed to have been oxidized and flocculated by the oxygen-rich lower layer waters of the Marmara Sea (Mediterranean originating).

The Copper, Cobalt and Chromium concentrations are in general, below the shale average values of 50, 20 and 100 μg/g (Krauskopf, 1979) (Table 3). The highest values in eastern basins surface sediments shows that the anthropogenic inputs from the industrialized regions in here. The Cu values show high correlation with the C_{org} content (r=0.81, Table 4).

Element	Al (%)	Fe (%)	Mn (μg/g)	Cu (μg/g)	Zn (μg/g)	Co (μg/g)	Cr (μg/g)	CaCO3 (%)	Corg (%)
Al (%)	1	+0.22	-0.13	+0.17	+0.17	+0.39	+0.30	-0.57	+0.1
Fe (%)		1	-0.03	+0.37	+0.44	+0.14	+0.54	- 0.32	+0.22
Mn (μg/g)			1	-0.28	-0.32	-0.12	+0.08	+ 0.1	-0.20
Cu (μg/g)				1	+0.89	+0.55	+0.66	- 0.39	+0.81
Zn (μg/g)					1	+030	+0.61	-0.28	+0.78
Co (μg/g)						1	+0.39	-0.56	+0.46
Cr (μg/g)							1	-0.59	+0.55
Corg (%)								1	-0.1
CaCO3 (%)									1

Table 5. Corelation coefficient of matrix geochemical parameters of sediments.

Zinc concentrations range between 84 μg/g and 306 μg/g and are above the shale average value of 4.7 % (Krauskopf, 1979) (Table 4). The high values seem to have been controlled mainly by the anthropogenic inputs from the eastern region similar to the other elements. This element shows a high correlation with the C_{org} and Cu contents (r=0.78, and 0.89 respectively) (Table5).
Al, Fe, Mn, Co and Cr values do not show any significant correlation with the C_{org} content (Table 5).

3.4.2.2 Selective extraction analysis

Sequential exraction analysis were performed to determined the anthropogenic and /or natural inputs on metal distributions in the bay surface sediments. Metal contents of the geochemical phases were given in Table 6.
The highest values of Al, Fe, Zn, Co, and Cr varied between 2.2 % with 10.9 %, 3.8 % with 5.4 %, 18 % with 98 %, 4 % with 9 %, and 12 % with 51 % in the residual phase, respectively. In contrast, the highest values of Cu and Mn ranged from 6 % to 26 % in organic phase and from 32 % to 276 % in the Fe-Mn oxyhydroxide phase, respectively. While Fe and Cr values were generally lower than the detection limit of the methods (<0.05 and 0.08 μgL-1) in the exchangeable and carbonate phases, Al contents were also detected in the organic and residual (lithogenous) phases. Zn and Mn showed the highest values in Fe-Mn-oxyhydroxide phase, but Cu those in the organic phase along the bay. In addition, Cu, Zn, Mn and Co levels were relatively high in all geochemical phases.

Element	Exchangable phase	Carbonate phase	Fe-Mn-oxyhydroxide phase	Organic phase	Residual phase
Cu (ppm)	0.3-1.1	0.3-1	1.3-4.5	6-26	4-14
Zn (ppm)	0.1-2.3	0.8-37	15-121	14-46	18-98
Fe (%)	<0.05	<0.05	0.1-0.6	0.5-1.1	3.8-5.4
Mn (ppm)	1-13	6-51	32-276	32-241	32-176
Co (ppm)	0.1-1.3	0.1-2.2	0.3-3.7	0.2-9	4-9
Cr (ppm)	<0.08-4.5	<0.08	1.4-24	2-23	12-51
Al (%)	<0.03	<0.03	<0.03	0.1-0.4	2.2-10.9

Table 6. Metal distributions in different geochemical phases (%).

4. Discussion

DO concentrations of the water column were low in August 1999, after the earthquake, compare to that of other sampling periods. The low DO content was determined in all the stations of İzmit Bay, and particularly in the lower layer waters of the eastern and the central basins, being lower than the detection limit of the method (0.03 mgl^{-1}) (Figure 7b). The negative DO–SDO value along the water column suggested that the oxygen utilization was resulted from the decomposition of organic matter (Figure 5). The limited air-water exchange of free oxygen caused by the spreading petroleum from the refinery fire to the sea surface might be one of the main reason for lowering of DO content in water column. The highest oil concentration was determined in surface water of south of the central basin as 179.2 mgl^{-1} in August 1999 (Güven et al., 2000, Ünlü et al., 2000). The oil concentrations of the surface water are more than 500 μgl^{-1} in almost half of the western and central basins after the earthquake. In spite of high oil pollution levels of the surface water, the oil concentrations in the lower layer are between 13-55 μgl^{-1}in the Bay exception of north of the central basin in August 1999. This oil pollution level decreased to 10.5 mgl^{-1} in September 1999 and 3.3 mgl^{-1} in October 1999. The upper layer flows westward to Marmara Sea, while the lower layer flows into the Bay transporting oxygenated Mediterranean originated Marmara Sea waters in September and October 1999 (Güven et al., 2000). This current system provided the removal of the petroleum layer at the sea surface from İzmit Bay to the Marmara Sea and consequently DO concentrations increased in the water column accompanied by phytoplankton bloom (Figure 4a). Phytoplankton bloom was intense in the eastern basin (2,553,000 cell/l, Güven et al., 2000) and possibly the reason for the saturated DO content in this part of the Bay (Figure 5). Since the domestic and industrial wastewater system has been damaged by the earthquake, the nutrient input into the Bay increased, causing the extreme phytoplankton bloom (Okay et al., 2001). In spite of high DO concentrations of the upper layer, DHS is found in the lower layer of the eastern and the central basins (Figure 3). This striking condition clearly indicates the excess organic load that rapidly depositing at the bottom of

the Bay. Although no DHS data is available for the previous sampling period (August and September 1999), the establishment of this anoxic condition at the bottom might have started to develop earlier than October 1999. Earlier studies related to the ocenographic features of the Bay have never determined anoxic conditions in the water column (Morkoç, et al., 1988; Tuğrul et al., 1989; Morkoç et al., 1996).

The Marmara Sea water flows as the upper layer into the Bay in December 1999 and the current system is towards the interior of the Bay, whereas the lower layer flows out of the Bay (Güven et al., 2000). The available DHS formation in the eastern and the central basins is reduced or completely disappears in this month by the outflow of the lower layer (Table 2). This current system becomes reversed in February 2000, entering the lower layer and out-flowing the upper layer. The significant increase of DO concentrations of the upper layer in February 2000 might possibly indicate the replenishment of water column in İzmit Bay with oxygenated waters. This is in agreement with the vertical and spatial distribution of DO concentrations in February (Figures 3 and 4b). The thickness of the upper layer increases to 25-30 m suggesting the entrance of waters into the Bay. DO content of the both the upper and the lower layer slightly decreases in May 2000, together with increasing alkalinity (Figures 4b, 7b, 8 and 9). The reducing DO content in this month might be related with the water influx enriched with nutrients into İzmit Bay from the Black Sea (via the Marmara Sea) that receives increasing amount of freshwater inflow during spring (Oğuz and Sur, 1986; Tuğrul and Polat, 1995). In August 2000, DO concentration of the water column is significantly reduced (Figures 4 and 6), suggesting the enhanced consumption of DO by decomposition of high organic materials that possibly from the subsequent death of blooming phytoplanktons. In the eastern basin, the lowest pH is found in this month, supporting the increasing decomposition processes and the formation of DHS (Figure 9).

The formation of DHS leading to anoxia at the lower layer of İzmit Bay occurs in the eastern basin where the depths are shallower than 30 m and also locally in the deep site of the central basin where circulation is restricted (Table 2). After the Earthquake, in the central and the eastern basins, the formation of DHS is resulted from the spreading petroleum from the refinery fire to the surface waters and accumulation of high amounts of organic load from the damaged wastewater systems, and resuspension of bottom sediments releasing the DHS in the anoxic part of the sediment column. This is in agreement with the low DO concentrations of the water column in İzmit Bay during August and September 1999 (Figures 4a, 7a). The removal of anoxia at the bottom of the eastern and the central basins occurred in December 1999 by the replacing of water layers with the oxygenated Marmara Sea waters. DHS exists in the lower layer consistently throughout the sampling period in station 17 (Table 2), however its thickness varies. The reduced bottom current velocities (Algan et al., 1999) and topographic restriction of this small depression might be the reasons for the presence of DHS, by preventing the circulation.

In August 2000, DHS forms again in the eastern basin in low concentrations (Table 2). This re-occurrence of DHS is related with the extreme phytoplankton bloom. A high amount of organic matter produced from their death consumes oxygen for decomposition in the sediment. High decomposition rates might have led the depletion of DO in the overlying water column and consequent formation of DHS. The seasonal circulation pattern and timing of blooms in İzmit Bay were not different than the present as indicated by the

previous studies (Oğuz and Sur, 1986; Tuğrul et al., 1989; Morkoç et al., 1996). DO content has never been fallen below 0.5 mgl^{-1}, and no DHS has been detected in İzmit Bay. Therefore, the re-occurrence of DHS a year after the Earthquake might indicate that İzmit Bay has not been completely return to its regular chemical oceanography. This may be explained by the fact that the amount of organic and possible inorganic wastes into İzmit Bay must have been considerably high and/or must have continued to discharge after the Earthquake. Increasing nutrients, phytoplankton blooms, rapid sedimentation of death organisms and decomposition processes constituted a successive cycle in İzmit Bay and intensified by the Earthquake at 17th August 1999. However, decomposition processes within this cycle might not be completed within a year.

The highest pH values found (8.9) at the upper layer compare to other months in the eastern basin confirms the increasing biological activity in October 1999 (Figure 8). During the respiration of phytoplanktons, dissolved CO_2 content of water column increases and consequently CO_3^{-2} and HCO_3^- anions increase. Increasing carbonate causes enhancement of alkalinity. The pH values become 7.9 at the lower layer (Figure 9) where the anoxic conditions are developed (Figure 3) and indicate the decomposition of organic matter.

Total metal contents in the İzmit Bay sediments increase towards to eastern basin. The eastern basin receives the highest inputs compare to other basins of the Bay (Morkoç et al., 2001). Ergin et al., (1991) suggested that the surface sediments in İzmit Bay are uncontaminated by anthropogenic pollution. However Yaşar et al., (2001) investigated that the heavy metal concentrations are highest in the eastern and central basins. The western basin was found generally unpolluted with respect to heavy metals in this study, also.

Selective extraction studies indicate that the metals are mainly found in the lithogenous, Fe-Mn-oxvhydroxide and organic fractions (Table 6). The results show that the main source of high metal concentrations in the İzmit Bay sediments is of anthropogenic origin. The highest metal values in these fractions are found in eastern basin sediments similar to total metal distributions.

5. Conclusions

Izmit Bay have been polluted by increasing industrial activities and domestic discharges since early 1980. However this abrupt event caused short-time drastic changes in the water column. Earthquake at 17 August 1999 initiated a fast variation in the chemical oceanography of polluted Izmit Bay. This variation includes the consumption of DO and formation of DHS in the lower layer. The refinery fire and damaged municipal waste effluents caused the reduction of DO in water column by preventing the oxygen transfer from air/ water contact and increasing organic wastes, respectively, and as a result DHS was formed. The increasing wastewater into the Bay stimulated the phytoplankton blooms that causes locally saturated DO concentrations in the eastern basin, however anoxic conditions were prevailing in the lower layer during autumn 1999. The changing circulation pattern during winter provided replenishment of the water column in Izmit Bay and removal of DHS. However, DHS formation established again in August 2000.

The distribution of total metals (Fe, Pb, Cu, Zn, Co, Cr and Cd) in both the water-column and surface sediments showed the influences of terrestrial anthropogenic inputs in the bay. The Mn enrichment in the lower-layer water of the central and eastern basins

originated from the occurring anoxic conditions after the Marmara (Izmit) earthquake. Selective extraction studies indicated that the metals were mainly found in the lithogenous, Fe-Mn-oxvhydroxide and organic fractions. The results underlined that the main source of high metal levels in Izmit Bay sediments is of anthropogenic origin. These conclusions reached by the selective extraction studies were supported by the "total" metal distributions along the bay.

6. Acknowledgements

The Captain, crew, scientists and technicians on board RV *Arar* of Institute of Marine Sciences and Management of Istanbul University, for their help during the collection of water samples. This work was supported by the Turkish Ministry of Environment.

7. References

Algan, O., Altıok, H.. and Yüce, H., 1999. Seasonal Variation of Suspended Particulate Matter in Two-layered İzmit Bay, Turkey. Estuarine, Coastal and Shelf Science 49, 235-250.

Altıok, H., Legovich, T. and Kurter, A., 1996. A case study of circulation and mixing processes in two-layered water system: İzmit Bay. Eight International Biennial Conference on Physics of Estuaries and Coastal Seas, Extended Abstracts, 8-12 September 1996, Netherlands Centre for Coastal Research, pp. 92-96.

Ayas, Z., & Kolankaya, D., 1996. Accumulation of some heavy metals in various environments and organisims at Göksu Delta, Türkiye, 1991-1993. Bulletin of Environmental Contamination and Toxicology, 56, 65-72.

Baştürk, Ö., Tuğrul, S., Sunay, M., Balkaş, T., Morkoç, E., Okay, O.S. and Bozyap, A., 1985. Determination of oceanographic characteristics and assimilation capacity of İzmit Bay. NATO TU-WATERS Project, Technical Report. Kocaeli, Turkey. TÜBİTAK-MRC Publication.

Beşiktepe, Ş.T., Sur, H.İ., Özsoy, E., Latif, M.A., Oğuz, T. and Ünlüata, Ü., 1994. The circulation and hydrography of the Marmara Sea. Progress in Oceanography 34: 285-334.

Bruland, K. W., Franks, R. P., Knauer, G.A., Martin, J. H., 1979. Sampling and analytical methods for the determination of copper, cadmium, zinc and nickel at the nanogram per liter level in seawater. *Anal. Chim. Acta* 105, 233-245.

Bruland, K. W., Coale, K. H., Mart, L., 1985. Analysis of seawater for dissolved cadmium, copper and lead: an inter comparison of voltametric and atomic adsorption methods. *Mar. Chem*. 17, 285-300.

DAMOC, 1971. Master plan and feasibility report for water supply and sewerage for Istanbul region. Prepared by the DAMOC Consortium for WHO, Los Angles, CA, Vol. III, Part II and III.

Doğan, E., Sur, H.İ., Güven, K. C., Polat, Ç., Kıratlı, N., Yüksek, A., Uysal, A., Algan, O., Balkıs, N., Ünlü, S., Altıok, H., Gazioğlu, C., Taş, S., Aslan, A., Yılmaz, N. and Cebeci, M., 2000. Su Kalitesi İzleme Çalışması. Technical Report. İSKİ. Deniz Bilimleri ve İşletmeciliği Enstitüsü, Istanbul Üniversitesi. (in Turkish).

Ergin, M., Saysam, C., Baştürk, Ö., Erdem, E. and Yörük, R., 1991. Heavy metal concentrations in surface sediments from the two coastal inlets (Golden Horn Estuary and İzmit Bay) of the northeastern Sea of Marmara. Chemical Geology, 91: 269-285.

Förstner, U. & Witmann, G.T.W., 1981. Metal pollution in the environment (p. 486). Berlin Heidelberg New York: Springer.

Greenberg, A.G., Trussel R.R., Clesceri, L.S., Franson, M.A.H., editors. Standard methods for the examination of water and wastewater, American Water Work Association (APHA, AWWA and WPCF). 16 th ed. Washington, 1985.

Güven, K.C., Sur, H.İ., Okuş, E., Yüksek, A., Uysal, A., Balkıs, N., Kıratlı, N., Ünlü, S., Altıok, H., Taş, S., Aslan, A., Yılmaz, N., Müftüoğlu, A. E., Gazioğlu, C., and Cebeci, M. 2000. İzmit Körfezi'nin Oşinografisi. 17 Ağustos 1999 Depremi sonrası İzmit Körfezi'nde Ölçme ve İzleme Programı. Technical Report. T. C. Çevre Bakanlığı. Deniz Bilimleri ve İşletmeciliği Enstitüsü, Istanbul Üniversitesi. (in Turkish).

Han, X.F., Banin, A., Su, Y., Monts, L.D., Plodinec, J.M. & Kingery, L. W., 2002. Industrial age anthropogenic inputs of heavy metals into the pedosphere. Naturwissen-schaften, 89, 497-504.

Hu, H., 2000. Exposure to metals. Prim. Care, 27: 983-996.

Krauskopf, K. B., 1979. *Intoduction to Geochemistry*, (617 pp). Tokyo: McGraw-Hill Kogakusha.

Loring, D.H., & Rantala, R.T.T., 1992. Manuel for the geochemical analyses of marine sediments and suspended particulate matter. *Earth-Science Reviews,* 32, 235-283.

Lovley, D.R., Pihillips, E.J.P., 1988. Novel mode of microbial energy metabolism: organic carbon oxidation coupled to dissimilatory reduction of iron and manganese. Applied "Environmental Microbiology 54, 1472-1480.

Morkoç, E., Tuğrul, S. and Okay, S.O., 1988. Determination of Limiting Nutrients by Using Algal Bioassay Technique. Wastewater treatment and disposal studies. NATO-TU-WATERS, First Annual Report. TÜBİTAK-MRC Publications, Kocaeli, Turkey.

Morkoç, E., Okay, S.O. and Geveci, A.1996. Towards a Clean İzmit Bay. Technical Report. TÜBİTAK-MRC Publications, Kocaeli, Turkey.

Morkoç, E., Okay, S.O., Tolun, L., Tüfekçi, V., Tüfekçi, H., and Legoviç, T., 2001. Towarsd a clean İzmit Bay. Environmental International 26: 157-161.

Nealson, K.H., 1982. Microbiological oxidation and reduction of Iron: Holland, H.D., Schidlowski, M. (Eds.), Mineral Deposits and Evolution of the Biosphere. Dahlem Konferenzen, Springer, Berlin, pp. 51-56.

Nealson, K.H., Myers, C.R., 1990. Iron reduction by bacteria: potential role in the genesis of banded iron formation. American Journal of Science 290A, 34-45.

Nealson, K.H., Myers, Saffarani, D., 1994. Iron and manganese in anaerobic respiration: environmental significance, physiology and regulation. Annual Review in Microbiology 48, 31-343.

Oğuz, T. and Sur, H.İ., 1986. A numerical modelling study of circulation in the Bay of İzmit: Final Report. TÜBİTAK-MRC, Chemistry Department Publication, Kocaeli, Turkey, No. 187. 97 pp.

Okay, S.O., Legoviç, T., Tüfekçi, V., Egesel, L. and Morkoç, E., 1996. Environmental impact of land-based pollutants on İzmit Bay (Turkey): short-term algal bioassays and simulation of toxicity distribution in the marine environment. Archives of Environmental Contamination and Toxicology 31, 459-465.

Okay, S.O., Tolun, L., Telli-Karakoç, F., Tüfekçi, V., Tüfekçi, H.. and Morkoç, E., 2001. İzmit Bay (Turkey) Ecosystem after Marmara Earthquake and Subsequent Refinery Fire: the Long-term Data. Marine Pollution Bulletin, 42, 361-369.

Orhon, D., Gönenç, E., Tünay, O. and Akkaya, M., 1984. The prevention and removal of water pollution in the İzmit Bay : determination of technological aspects. Technical Report. İstanbul, Turkey: İTU-Civil Eng. Publ., 1984.

Sunda, W.G., Huntsman, S.A., 1995. Cobalt and zinc interreplacement in marine phytoplankton: biological and geochemical implications. Limnol. Oceanogr. 40, 1404-1417.

Strickland, J.D.H. and Parsons, T.R., 1972. A Practical handbook of seawater analysis 2nd. Ed., Oxford press, Ottawa, Bull. Fish. Bd. Can.

Pempcowiac, J., Sikora, A., Biernacka, E., 1999. Specification of heavy metals in marine sediments, their bioaccumulation by musssels. Chemosphere, 39: 313-321.

Tessier, A., Campbell, P. G. C., & Bisson, M., 1979. Sequental extraction procedure for the speciation of particulate trace metals. *Analyt. Chem.,* 51, 844-850.

Tuğrul, S., Sunay, M., Baştürk, Ö. and Balkaş, T.I., 1986. The İzmit Bay case study. In: G. Kullenberg (Ed.), The Role of Oceans as a Waste Disposal Option., pp. 243-275. Reidel, Dordrecht.

Tuğrul,S., Morkoç, E. and Okay, S.O., 1989. The Determination of Oceanographic Characteristics and Assimilation Capacity of the İzmit Bay. Wastewater treatment and disposal studies. NATO TU-WATERS, Technical Report. TÜBİTAK- MRC, Kocaeli-Turkey.

Tuğrul, S. and Morkoç, E., 1990. Transport and water quality modeling in the Bay of İzmit. NATO TU-WATERS Project, Technical Report. TÜBİTAK-MRC Publ. Kocaeli, Turkey.

Tuğrul, S. and Polat, Ç., 1995. Quantitative comparison of the influxes of the nutrients and organic carbon into the Sea of Marmara both from anthropogenic sources and from the Black Sea. Water Science and Technology, 32: 115-121 pp.

Ünlüata, Ü., and Özsoy, E., 1986. Oceanography of the Turkish Straits-First Annual Report, Volume II, Health of the Turkish Straits, I. Oxygen Deficiency of the Sea of Marmara, Institute of Marine Sciences, METU, Erdemli, İçel, Turkey, 81 pp.

Ünlüata, Ü., Oğuz, T., Latif, M.A. and Özsoy, E., 1990. On the Physical Ocenography of the Turkish Straits. In: Pratt, L. J., (Ed.), The Physical Oceanography of Sea Straits. Kluwer Academic Publishers, Netherland, pp. 25-60.

Ünlü, S., Güven, K. C., Okuş, E., Doğan, E. and Gezgin, T. (2000). Oil Spill Tüpraş Refinery Following Earthquake occured in 17 Aug 1999. Second International Conference, Oil Spills in the Mediterranean and Black Sea Regions, pp. 1-11, Istanbul, Turkey.

Yaşar, D., Aksu, A.E., Uslu, O., 2001. Anthropogenic Pollution in İzmit Bay: Heavy Metal Concentrations in Surface Sediments. Turk. J. Engin. Environ. Sci., 25, 299-313.

Part 3

Earthquake Observatories

13

Newly-Proposed Methods for Early Detection of Incoming Earthquakes, Tsunamis & Tidal Motion

Samvel G. Gevorgyan
Center on Superconductivity & Scientific Instrumentation, Chair of Solid State Physics, Faculty of Physics, Yerevan State University; Institute for Physical Research, National Academy of Sciences; Precision Sensors/Instrumentation (PSI) Ltd. Armenia

1. Introduction

During a last decade scientists and engineers step-by-step are developing a Single-layer Flat-Coil-Oscillator (**SFCO**)-based *new measurement technology*, and looking for its effective use in a research, and elsewhere. It was introduced in 1997 by our group in Armenia [1-2] and then improved by an integrated research group in Kyushu University, Japan, during next 4 years (1998-2002) [3-4] – allowing to reveal fine physical effects related with the basic properties of high-T_c superconductors (**HTS**) [5-8]. Starting with 2004 the method passed further development in Armenia, and was then applied for creation of a new *absolute*-position sensor of *nano*-scale resolution [9]. Advantages of the *SFCO* method-based position sensor become more evident when applied to the *quasi*-static Seismometry – to study slow movements of ground. Due to these, the *SFCO measurement technology* (in a whole [1-4]), and its first application as a novel seismic detector of slow movements (in particular [9-10]) appeared among the Top six World Security Technologies at the 2008 year's "*Global Security Challenge*" competition – details on "**GSC-2008**" forum see in: http://www.globalsecuritychallenge.com. In this Chapter, we discuss principle of operation, and test data of such a new *absolute*-position sensor, installed (for validation) in a well-known seismometer, as an additional pick-up component – showing its advantages compared to traditional technique. We discuss also wide potential of this new method, as a real-time measurement technique for early detection of incoming earthquakes, tsunamis and tidal motion. We also outline prosperous future of such a sensor.

To sense what are advantages of the flat-coil-based this unique method, let's remember: oscillators are among the most of precise measuring instruments, because the frequency is possible to measure with a very high accuracy. Among them, those at *MHz* frequencies, having volume pick-up coils (mainly, solenoid-shaped), activated by a *low*-power (*backward*) tunnel diodes (**TD**) (see [2, 11-12] and references therein), are of special interest. Replacement of such a standard coil by the unusual, single-layer flat (open-faced) one, as a detecting circuit in a stable-frequency and amplitude *TD*-oscillator, enabled to make coil's filling factor close to the maximal possible value (the *unit*) for flat objects, resulting in strong enhance-

ment of the resolution of measurements by 3–4 orders of magnitude (especially, in studies of thin, plate-like *HTS* materials [1, 3-8]). For comparison, typical values of the filling factor for solenoid coils are 10^{-4}–10^{-3} for the said samples. Advantages of the *SFCO* technique become more evident at slow movements of the objects, positioned near the coil face. Just therefore, this method has been very soon applied for the creation of a *nano*-scale *absolute*-shift position sensor, which one may successfully use in many areas: for example, for the *quasi*-static (*slow*-movement) Seismometry [9-10], in various security systems. Why this problem is so urgent? Basically, there are two types of seismic sensors, acting presently [13]: *inertial seismometers*, which measure ground motion relative to some inertial reference (*suspended inert mass*), and *strain-meters* (or *extensometers*), which detect shift between two points of the ground. Although strain-meters are conceptually simpler than inertial seismometers, their technical realization is much more difficult. Besides, as ground motion relative to the suspended inert mass is usually larger than differential motion within a test tube of reasonable dimensions, inertial seismometers usually are more sensitive to earthquakes. At low (and especially, at *super*-low) frequencies, however, it becomes hard to maintain the hanging reference fixed, and for detection of *quasi*-static deformations and *low*-order free oscillations of the earth's crust, tidal motion (*moon movement*), and for observation of mechanical vibrations of buildings, bridges, etc., the strain-meters may take noticeable lead over inertial seismometers. We describe in this Chapter how to overcome such lack of acting seismographs/accelerometers/vibrometers by the use of the recently offered by us flat-coil-based, super-broadband, nano-scale-resolution position sensor [9-10]. The more so, because further development of such a highly sensitive sensor technology may contribute also to on-time tracking (*prediction*) of potential incoming tsunamis, and monitoring of the state and zone borders as well.

2. Flat coil-based *absolute*-position sensor for *nano*-scale resolution, *super*-broadband Seismometry

And so, a new class *super*-broadband, *nano*-scale resolution position sensor is developed and tested by our group. It can be used, in particular, as an additional sensor in presently acting seismographs. It enables to extend *frequency*-band (theoretically, up to "zero"), and enhance *absolute*-resolution (*sensitivity*) of seismographs available on the market (*by at least an order of magnitude*). It allows transferring of the mechanical vibrations of constructions, buildings, bridges & ground with amplitudes over *1nm* into detectable signal in a *frequency*-range starting practically from the *quasi*-static movements ("zero"!). It is based on detection of position changes of a vibrating normal-metallic plate placed near the coil face – being used as a pick-up circuit in a stable *TD*-oscillator. Frequency of the oscillator is used as a detecting parameter, and the measuring effect is determined by a distortion of the *MHz*-range testing field configuration near the coil face by a vibrating plate, leading to magnetic inductance changes of the coil, with a resolution *1-10pH* (*depending on operation temperature of a technique*). This results in changes of test oscillator frequency. Below, we discuss work-principle, and test data of such a new position sensor, installed in a known Russian *SM-3* seismometer (for validation) as an additional pick-up element – showing its advantages compared to traditional techniques. We also discuss potentials of this novel *absolute*-position sensor, operating down to liquid–^{4}He temperatures, and in high magnetic fields – as a real-time measurement element for early detection of earthquakes, incoming tsunamis, tidal motion, and for tracking borders. We discuss also possible design of seismic detectors based on this sensor. Besides,

we outline perspective future of such an unprecedented sensor – involving substitution of a normal-conducting pick-up coil by a superconductive one, and replacement of a tunnel diode by the *S/I/S hetero*-structure – as much less-powered active element in a detecting oscillator, compared to the tunnel diode. These may improve stability of oscillators, created by the use of *SFCO* method, and thus, enhance the resolution of seismic devices, and tsunami detectors as well – by at least another 2-3 orders of magnitude. Such improvements may enable to reveal and study *quasi*-static deformations and *low*-order free oscillations of earth's crust, precursor to earthquakes. It may also permit to study features of the tidal motion and tsunami waves. Such a sensor may be also used as a *position/vibration* sensing element in *micro*- and *nano*-electronics (in probe microscopy), in security systems, and in medicine as well.

2.1 Traditional inertial seismometer

A *Traditional inertial seismometer* converts ground motion into electrical signal, but its properties cannot be described by a single-scale parameter, such as the output volts per millimetre of the ground motion [13] (*as occur in case of the absolute*-position *sensors*). Its response to ground motion depends not only on the amplitude of motion (*how large it is*) but also on its time-scale (*how fast it is*). So, the suspended (*hanging*) seismic mass has to be kept in place by certain restoring force (*electromagnetic*, *mechanical*, *else nature*). But, when ground motion is slow, the mass will move with the body of a seismometer, and the output signal even for a large motion will thus be negligibly smaller. Such a system is so a high-pass filter for ground shifts. This must be taken into account if the ground motion is reconstructed from the recorded signal. So, creation of seismic detectors, which may give large output both for fast and slow motion (*regardless of the rate of motion – as absolute-position sensors behave themselves*), still remains among the prime important problems in the Seismology (*and not only*…).

2.2 Principle of operation of new seismic detector

To this end, a prototype of the *SFCO* method-based position sensor has been created and installed by us in a setup of the Russian seismometer of *SM-3* type (Fig.1a). In such a *"hybrid SM-3"* device (Fig.1b) a flat coil serves as a pick-up in a stable *16MHz*–oscillator, driven by a *low*-power Russian tunnel diode of the *AI-402B* model. Actually, 2 similar flat-coil oscillators are mounted in *SM-3*. One is used as a position detector, the other – to detect background at all times (*bottom* and *top* oscillators in Fig.1b respectively). Let-in *SM-3* position sensor is extra to its own *vibro*-sensor one, based on excitation of the electromotive force (**EMF**) in a solenoid coil (Figs. 1a and 1c). In case of the *SFCO*-based sensor, measuring effect is proportional to changes of mutual distance between the coil and metallic plate vibrating parallel to the coil face (*d* in Fig.1c). This results in the changes of the *test*-oscillator frequency.

So, new seismic detector converts ground motion into shift of a flat-coil-oscillator frequency – *due to ground shaking*. The measuring signal appears as a result of the coil motion (fixed on seismograph's body – Figs. 1b-1c and 2) relative to metallic plate (fixed on hanging pendulum (Fig.1c), or membrane (Fig.2)), positioned near the coil. Figures. 1c and 2 schematically illustrate *SFCO* sensor-based novel seismic detectors' possible designs: F_S is the shock force, and *d* – amplitude of vibration of a pendulum (see Fig.1c) or membrane (Fig.2), caused by it.

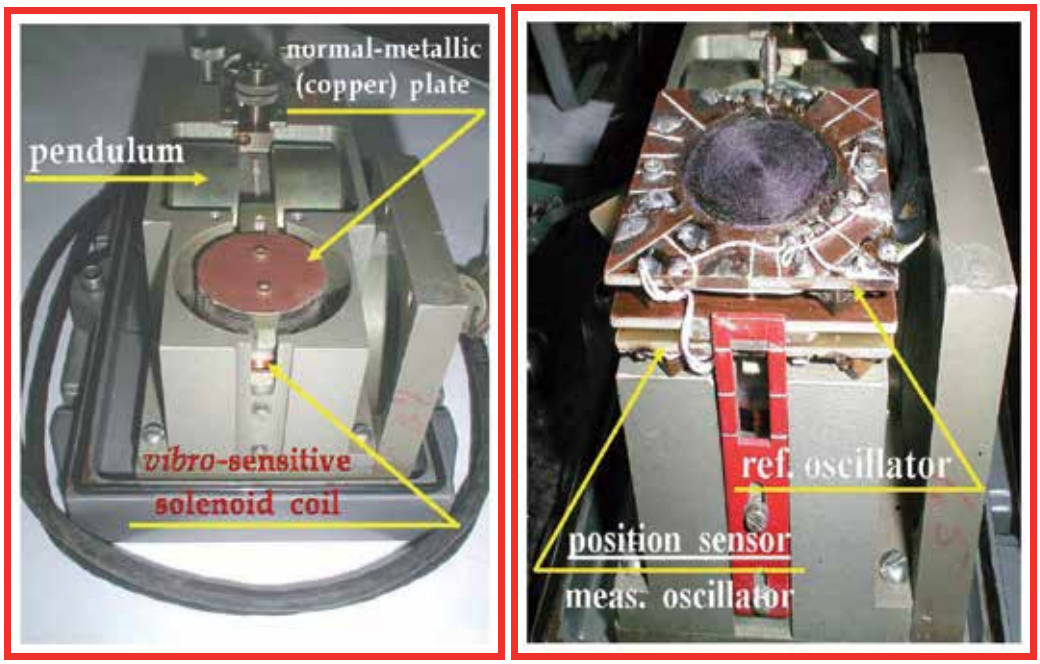

a) b)

Fig. 1. a) Top view of the *original Russian SM-3 seismograph*, with the light metallic (*copper*) plate additionally screwed on its vibrating pendulum (*schematics see in* Fig.1c). Initially, the *SM-3* device is designed to detect vibrations in a frequency range from *0.5Hz*, and up to *50Hz*.
b) Front-view of the *original Russian SM-3 seismograph*, with additionally installed package with 2 flat-coil-based oscillators – named as the *"hybrid SM-3"* seismograph.

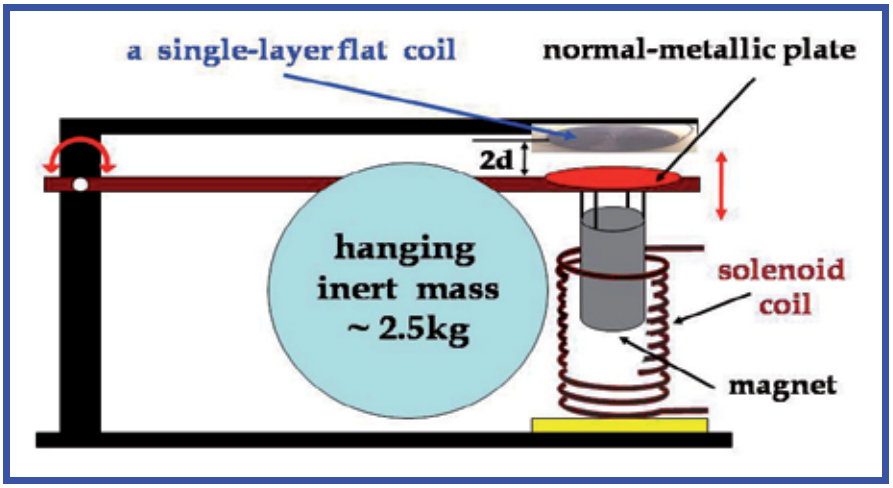

Fig. 1. c) Mechanical schematics of the *"hybrid SM-3"* seismograph – advanced by the use of *SFCO* method-based highly sensitive, *super*-broadband position sensor: *d* is the amplitude of vibration of a pendulum, caused by the ground shaking.

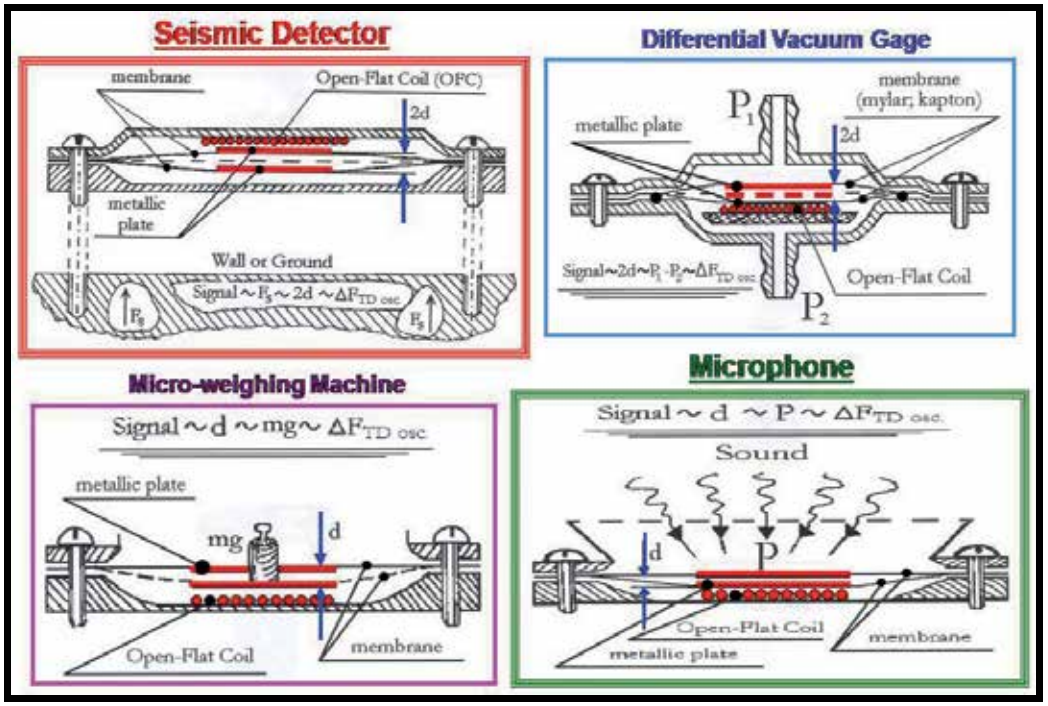

Fig. 2. Mechanical schematics of the *SFCO* sensor-based fully novel 4 techniques: seismic detector, differential vacuum gage, microphone, as well as micro-weighing machine: F_S is the shock force, d – the amplitude of flapping of a membrane, caused by the ground shaking.

2.3 Flat-coil based measurement technology: Its advantages

A single-layer flat-coil-oscillator test method (the **SFCO** technique [1-2] – it is introduced by our group in 1997, its electrical scheme is shown in Fig.3) is a fine research instrument for doing *MHz*-range, sensitive measurements. It can be used for determination of too much little changes of distances with Δd*~1-10Å* absolute and $\Delta d/d \sim 10^{-5}$-10^{-6} relative resolution (depending on a model and working temperature of the *TD*-oscillator [3-4]. It is also a sensitive radio-frequency (**RF**) *Q*-meter – to study absorption as small as $10^{-9}W$ in thin flat materials (for example, in plate-like high-T_c superconductors [5-7]). The *SFCO* method can operate down to the liquid–^{4}He temperatures. Presently, it is tested by us up to *12T* magnetic fields [7]. The method differs from the known "*LC*-resonator" technique (see, for example, [14]) by replacement of the volume-shaped testing coil by the unusual single-layer flat (open-faced) one. Additionally, it is driven by the *stable*-frequency, *low*-power tunnel diode.

Advantages of the *SFCO* method-based sensor become more evident when applied to *quasi*-static Seismometry – to study slow movements of ground. In this regards, Fig.4 compares responses of the *SFCO* position sensor and the *EMF*-based *world*-best *SM-24 ST vibro*-sensor (geophone.com) – against the same vibrations. The vertical size of the blacked-out region in this Figure shows advantages of our novel *SFCO*-sensor for different values of vibration frequencies. One may conclude from the Fig.4, that advantages of the *SFCO* method-based new sensor become much more evident at *super*-slow vibrations (*movements*), with F< *10Hz*.

Both the frequency and amplitude of the oscillator are used as testing parameters in a *SFCO* technique. The measuring effects are determined by a distortion of the coil testing field

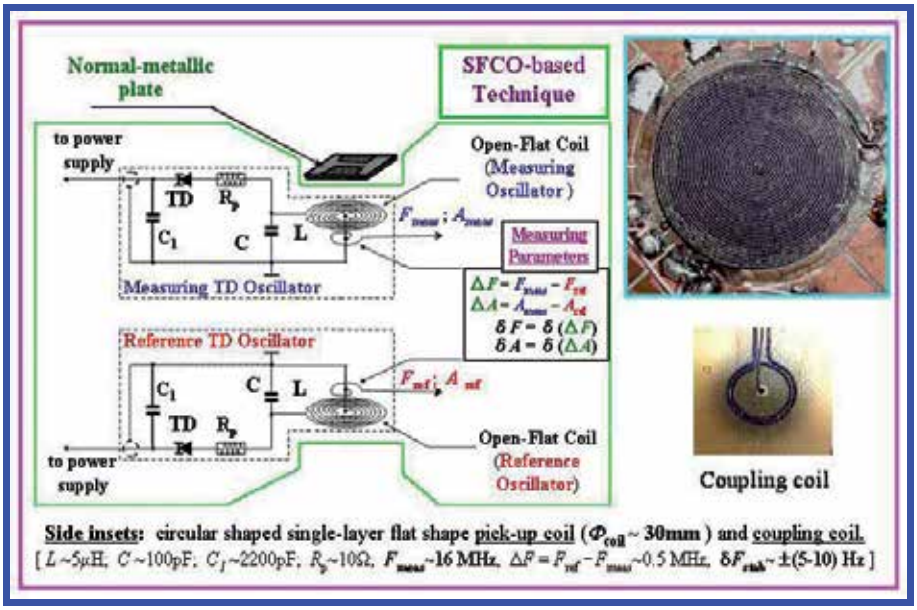

Fig. 3. Electrical schematics of the new seismic detector, based on *SFCO* technique (single-layer flat-coil-oscillator, driven by the *stable*-frequency, *low*-power tunnel diode (**TD**).

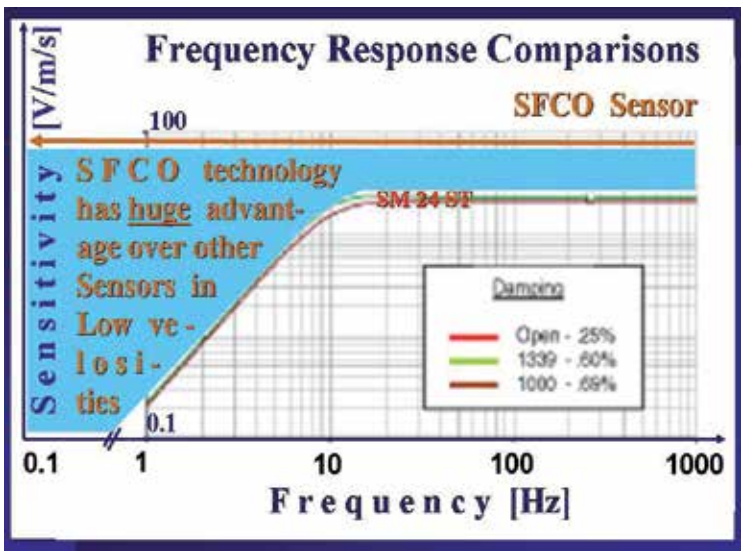

Fig. 4. Comparision of the *SFCO*-based *absolute*-position sensor with an electro-motive-force (**EMF**)-based *world*-best *SM-24 ST vibro*-sensor (geophone, see: www.geophone.com).

configuration near its flat face, and by the absorption of the same field's power by an object under test (*due to external influences*). These finally result in the changes of test oscillator frequency and/or amplitude, respectively. Compared with the traditional (*volume*-coil) method, in a flat-coil technique testing *RF*-field is densely distributed near the coil face. Besides, due to flat shape, even a little shift of the position of a *normal*-conducting plate, placed near the coil, may

lead to strong distortion of the field distribution around the coil. These features, and the stability of *TD*-oscillators ($\Delta F_{stability}$~*1–10Hz*, $\Delta F/F$~10^{-7}–10^{-6} – depending on the model & temperature – see [2, 11-12]) enabled us to reach 6 orders relative resolution in *SFCO* technique [3-4], permitting to effectively use it in a basic research [5-8], as well as in some modern technical applications [9-10]. In the last case, frequency of the oscillator is mainly used as a testing parameter, and the measuring effect is determined by a distortion of the *MHz*-range testing field configuration near the coil face by the vibrating copper plate, leading to the magnetic inductance changes of the coil, with a resolution ~ *1-10pH* (*depending on operation temperature of a technique*), resulting in the changes of test oscillator frequency.

2.4 Reconstruction of ground motion from recorded frequency-shift of *TD*-oscillator

Since electro-motive force based traditional *vibro*-sensors (included, the own sensor of *SM-3*) and suggested by us position sensors are various nature devices, with different outputs (*EMF*-based sensor converts ground motion into output volts, while flat-coil-based novel sensor converts the same motion into the shift of test-oscillator frequency), there are no direct ways to compare them properly, except that one may compare their responses over the respective noises during the same shaking. And so, we tried to detect and compare signal-to-noise (**S/N**) ratios for these two (*different principle of operation*) sensors, during the same experiment – against the same *1-2Hz* time-scale weak vibration.

In this regard, note that for correct reconstruction of the ground motion from the recorded frequency shift there is need to properly calibrate the *SFCO* method-based this non-traditional technique. The problem here is much complicated compared with the cylindrical (*solenoid*)-coil based technique, since even for the simplest case of a weakly vibrating thin conducting plate near the flat coil the calibration data are dependent on the used plate's diameter. For comparison, in case of cylindrical (*solenoid*) coil-based similar technique one needs calibration for only one (*given volume*) cylindrical sample, placed in the homogeneous testing field area inside the coil. Then, the obtained *calibration*-data can be expanded and used for any other shape and volume samples, provided that they are positioned anywhere inside the almost homogeneous-field area, near the cylindrical coil center [14].

So, below we discuss briefly the method, and results of calibration of the tested flat coil's *RF*-field configuration, by the use of a normal-conducting (*copper*) plate enabling correct transfer of the measured shifts of frequency δF, to the changes of distance δd, from the coil face d. One of possible ways to do that seems the calibration by moving the *given*-size *disk*-shaped copper plate towards the coil's face, up to the given distance, d, and back. This strongly changes the coil's testing field configuration (*and thereby*, *oscillator frequency*), and enables the empirical estimation of the so-called *G*-factor – as the coefficient for the coil's inductance (*resonant frequency*) modulation. Changing the position of the metallic object, we could experimentally determine the value of the *G*-factor as the relation between the resonant frequency modulation δF and the change in position δd. Figure 5 presents and illustrates the results of such calibration of the created position sensor (*let-in the SM-3 seismic device*) – which we realized. As is seen, the empirically determined $G(d)$-factor (*which actually is the absolute resolution of the technique*) for the given area metallic plate depends on the position d, near the flat coil. *G*-factor enables correct transferring of the measured shifts in frequency to the linear changes in distance by the formula: $\delta d \equiv -G(d) \times \delta F$, important for the proper reconstruction of the ground motion from the recorded *frequency*-shifts. Figure 5 shows that *G*-factor depends strongly on distance from the coil face. Namely, sensitivity (*absolute*

resolution) drops exponentially with an increasing distance – due to sharp drop of a testing field density. $G_{\mathbf{w}} \sim 1Å/Hz$ in Fig.5 is a typical value of a geometric factor achieved for the $F_{meas} \sim 16MHz$ operating frequency and $\Phi_{coil} \sim 30mm$ coil oscillator on $d \sim 1.1mm$ distance from the coil face, at liquid–^{4}He temperatures (*typical stabilities reached for TD-oscillators at low temperatures are* $\delta F_{stability} \sim \pm$ (**1-2**) *Hz* – see Fig.6b) [3-4, 15]. At the room temperatures, the noise level of the tested flat-coil sensor (*let-in the SM-3 seismic device*) is a little bit worse – close to ± (**5-10**) *Hz*.

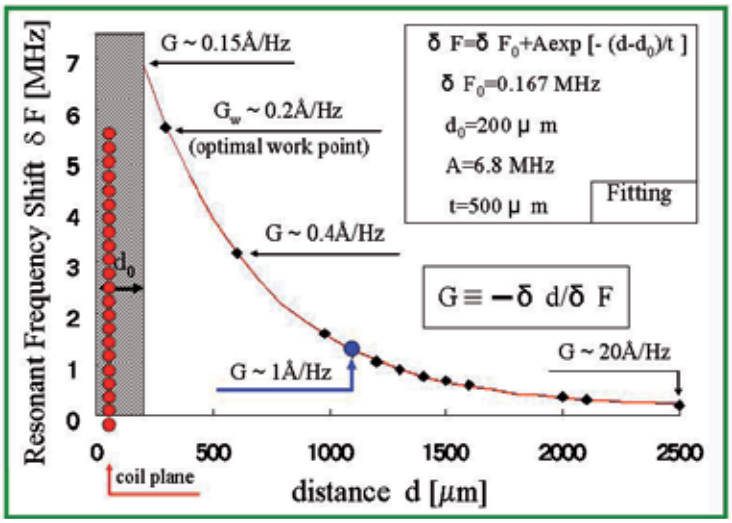

Fig. 5. *SFCO* technology-based position sensor sensitivity vs. the distance from the coil flat face: testing *RF*-field's density vs. the distance from the open-flat coil's face in a *SFCO* position sensor.

Note that such a low noise level of the tested sensing system is due to changes in inductance caused by all internal factors in the system's electronics, and mechanics. To be sure in this matter fully, we fixed mechanically (*for a long time*) the pendulum of the *"hybrid SM-3"* (see Figs. 1a - 1c), and tried to detect noise level of the measuring oscillator. Its stability was close to ± (**5-10**) *Hz* at room temperatures, during an hour. And so, distance *d* can be taken as a unique factor to determine inductance changes in measurements (*due to vibration of a copper plate near the coil face*) in the range of resolution corresponding to the frequency shift of about ± (**5-10**) *Hz*, at room temperatures. Hence, for the $\Phi_{coil} \sim 30mm$ coil sensor, installed in *"hybrid SM-3"* (*with the copper plate, vibrating near the coil face, at a distance* $d \sim 1.1mm$), we reached a resolution $\delta d = G \times \delta F_{stab} \sim 1Å/Hz \times \pm$ (**5-10**) $Hz \sim \pm 1nm$ at the room temperatures (see Fig.5).

2.5 Novel seismic detector based on SFCO measurement technology (test-results, discussion, future perspectives)

2.5.1 Test-results

Thus, because there is no other reasonable ways for direct comparison of the said 2 different nature (*principle of work*) sensors we tried to compare their responses over respective noises, during the same shaking. So, we detected, and below compare, the signal-to-noise ratios for above sensors – during the same experiment, against the same *1-2Hz* time-scale weak vibration. Comparative-test data of such an experiment are shown in Fig.6. In our tests, the *"hybrid SM-3"* was fixed to the glazed-tile floor of a laboratory room, situated on the 2-nd floor.

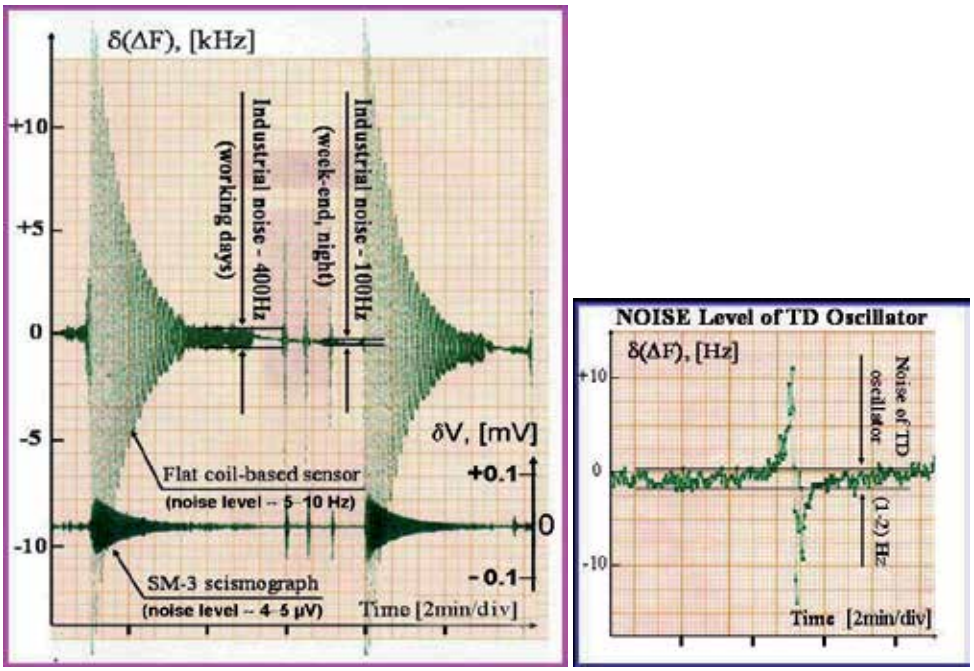

a) b)

Fig. 6. a) Comparative-test data of the flat-coil-oscillator based *absolute*-position sensor (left vertical scale – $\delta(\Delta F)$, [kHz]) and *EMF*-based *vibro*-sensor (right vertical scale – δV, [mV]) – both installed in the same *"hybrid SM-3"* seismic device. Room-temperature noise levels of both sensors are also pointed out in the figure (~ *5-10Hz* and ~ *4-5μV*, respectively).
b) Noise level (*stability*) of a tested *TD*-oscillator at liquid–^{4}He temperatures, permitting to estimate an extreme resolution one may reach in *"hybrid SM-3"* seismic device, supposing that its *SFCO* novel position sensor is cooled down to 4K. Note, that the room-temperature noise level of the tested *SFCO* sensor is a little larger – close to ±(*5-10*)*Hz*. The room-temperature noise of the *SM-3*'s *EMF*-based own *vibro*-sensor is about ~ *4-5μV* – see Fig.6a.

First, from data shown in Fig.6a one may conclude that, as detected by a *SFCO* position sensor, the level of background vibrations of a laboratory floor is near ±*400Hz* – during workdays. Taking into account the above said value of about *1*Å/*Hz* for the *G*-factor at *d~1.1mm work*-distance from the coil (see Fig.5) such level of background vibrations corresponds to the amplitude of vibration of the laboratory floor of about ±*40nm*. Besides, Fig.6a indicates that background vibrations of our laboratory building were almost 4 times stronger at workdays, compared to weekends and nights. Even such shakings at nights, however, almost *50* times exceeds the measured noise level (of about ±*1-2Hz* – Fig.6b) one may get in created *"hybrid SM-3"* seismic device – provided that its *SFCO* position sensor is cooled down to 4K. Background shakings of the laboratory room might be caused by the industrial pumping of an environment, and besides, by the vibration of earth's crust. Background shakings might be caused also by rocking during the tests of a technical nature. In this regard, note that a fine signal, seen in Fig.6b, detected by our *SFCO* method-based new sensor, is an evidence of its high abilities. The signal is result of beating of the measuring *TD*-oscillator with a little signal "coming" from the close-located broadcasting station. An acting seismic station is un-

der creation in Yerevan State University, based on created *"hybrid SM-3"* new seismographs, capable of providing LabVIEW environment-based data acquisition and processing (Fig.7).

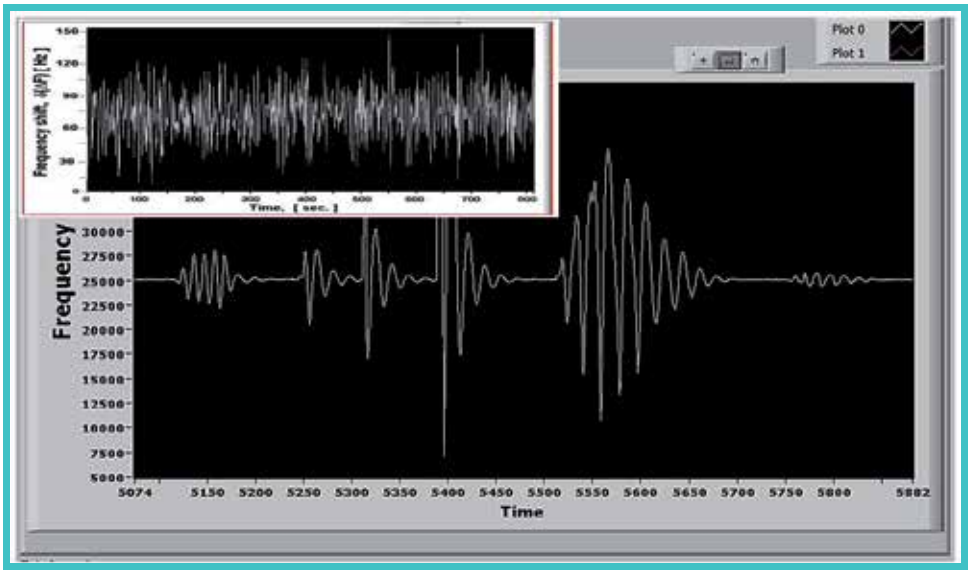

Fig. 7. LabVIEW signals of our new *SFCO absolute*-position sensor-based inertial seismic detector (the *"hybrid SM-3"* seismograph) for different amplitude shakings, ranging from ±25 to ±250nm, at the background vibration of about ±5nm (see inset on *top left*). Background-vibration LabVIEW signals of the *SFCO*- sensor based new inertial seismic detector. Experiments were conducted at the night time-period, to achieve as low as possible noise level at room temperature in a technique caused by the industrial rocking of an environment and vibration of the earth's crust.

2.5.2 Discussion

Comparison of signal-to-noise ratios (at F~1Hz), for new sensor (*flat-coil based SFCO sensor* – $(s/n)_{flat\text{-}coil}$ is about 16kHz/(5-10Hz) ≅ 1600-3200) and for *SM-3* sensor ($(s/n)_{EMF\text{-}sensor}$~150μV /(4-5μV) ≅ 30-35) – both operating in the same *"hybrid SM-3"* seismograph – permits to conclude that the *SFCO* sensor is more sensitive by about 50-100 times (see Figs. 6a and 8). Besides, since the *SFCO* sensor allows detecting of *absolute*-position shifts (see Fig.4, low frequencies), it may enable to detect very beginnings of *quasi*-static deformations and oscillating processes in earth crust – at very low frequencies – in contrast to the traditional *EMF*-based sensors, being used practically in all acting inertial seismometers of a different design. This is the case since *EMF*-sensor may not detect slowly passing processes – due to minor voltage arising in solenoid pick-up coils during the slow movements of a pendulum (Fig.1c). So, in order to effectively detect *quasi*-static deformations by the *SFCO* technology-based *absolute*-position sensor, one should build and use a properly vibrating mechanical pendulum (*with a mass as heavy as possible*, and *with as weak as possible restoring force of the mechanical part of pendulum*) – something like to what is the case in Russian *SM-3* detector, but with less friction against the motion of a freely hanging pendulum. *EMF*-based sensor may not detect slow processes, at any case, since it is a velocity sensor. This all may become crucial for detection of low-order free oscillations of the earth crust, and for observation of the peculiari-

ties of a few-hour duration tidal motion & tsunami shaping. That is why one should use the *SFCO absolute*-position sensing technology (in this, or another modification of a sensor – *see schematics of different sensors in Fig.2, to be used depending on the application*) to reveal in advance, and study origins of formation of earthquakes, tsunami waves, and tidal motion – *impossible, in principle, for other methods*. We believe this offer holds considerable potential for meeting advanced technical needs of the seismic & tsunami services supported by governments of practically all countries positioned in the seismically active regions of the world.

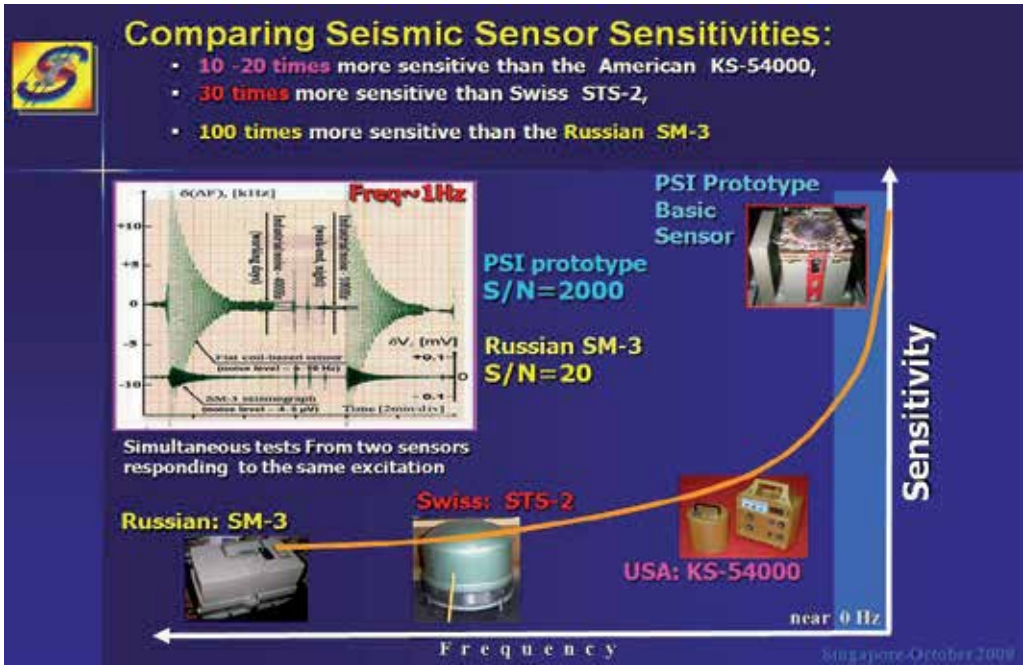

Fig. 8. Comparision of *"hybrid SM-3"* seismic detector (based on a *SFCO* technology *absolute*-position sensor), with the *EMF* principle of operation based other word-wide detectors.

In this connection, we bring in a next Fig.8 comparative data, related with the *SFCO absolute*-position sensor technology-based *"hybrid SM-3"* and the *EMF*-based word-wide seismic detectors. Comparison is again made at vibration with F~1Hz. Taking into account huge advantages of the *SFCO* position sensor technology over the other sensor technologies (especially, at vibrations with F < *10Hz* – see Fig.4) much higher sensitivity of the said *"hybrid SM-3"* detector (having inside integrated *SFCO* sensor, as the additional sensing element) becomes evident. As to the vibration frequencies below the 1Hz, the *EMF*-based all seismic sensors loss their row sensitivity at al (sensitivity, without long-time and expensive integrating electronics) – see Fig8 and Fig.4.

2.5.3 Future perspectives

There are many ways how to even more enhance the resolution of such new *absolute*-position sensors, and, as a result, capabilities of the presently acting *inertial seismometers* – even by the several orders of magnitude. For that purpose, the pick-up flat coil, and/or the active element of the measuring oscillator should be made of superconductive material (high-T_c or low-T_c – for better stability). In other words, one of the relatively easier ways relates with

the replacement of the normal-metallic coil by the superconductive one. This may improve the tunnel diode oscillator stability by at least 1-2 orders of magnitude [2]. The next improvement relates with the substitution of the tunnel diode by the superconductive *S/I/S* hetero-structure – as much more less-powered active element (*compared to tunnel diodes*) for the measuring oscillator of the *SFCO absolute*-position sensor, with a few orders of magnitude less steep of its *I-V* curve's negative differential resistance [16]. This may raise the oscillator stability by another 2-3 orders of a value [2]. Even these two modernizations are enough in order to enhance the stability of the measuring and reference oscillators of such a technique (Fig.3) and hence, to increase the signal-to-noise ratio (*sensitivity*) of the *SFCO* technology-based seismic detectors – by at least 3-4 orders of a value. As follows from the Fig.5, the *absolute*-resolution of such a new sensor drops exponentially when a normal-conducting plate moves away from the coil face. This property of *SFCO* sensors makes easy adjustment of the sensitivity (*resolution*) of such a new position sensor, for various practical usages in future.

3. Areas for specific application of SFCO *absolute*-position sensors

Besides the usage of the SFCO technology - based *absolute*-position sensors in seismic predicttion & protection, they might be also effectively applied in: *security systems*; *geophysics & town-planning; micro- & nano-electronics; military science, engineering & intelligence;* etc.:

Fig. 9-10. The *SFCO*-sensor based *Early Warning Security System* can secure the runway and specific underwater perimeter with the invisible and totally passive security net, and can detect over the ground and underground, as well as underwater moving intruders.

in security systems: The new (**SFCO**) technology *absolute*-position sensor-based ultra-sensitive seismic detectors and vacuum gages may give rise to many markets & applications, and bring to products that can serve both military & civilian applications. Early warning security systems (**EWSS**) are natural applications that can serve to protect State & Federal borders, provide Ports security & control, as well as Civilian applications of perimeter security

Fig. 11. The *SFCO*-sensor based *Early Warning Security System* can secure the ground and underground, as well as specific underwater perimeter with the invisible and totally passive security net, and identify the location of underwater moving intruders.

controls such as security of oil pipelines, airports, and private properties. The new technology sensors may also enable detection and recognition of various mobile targets (*walking or crawling man*, *vehicles*, *tanks*, *or other human activities*) approaching any zone (*military camps, state properties, banks, or other critical high priority infrastructures*) or borders without the need of physical line of sight.

Figures 9 through 11 are pictorial depictions of systemic applications to real world security scenarios, showing the flexibility and versatility of this new technology rendering one of the highest quality EWSS for military or civilian applications, covering detection for underground movements, over the ground movements, and underwater movement.

in geophysics and town-planning: for gas and oil prospecting, and also to reveal too much weak vibrations and slow bending (*twist*) of the buildings, constructions and bridges, as well as for permanent monitoring of old bridges aging;

in micro- and nano-electronics: for creation of *New Generation* microscopes with long-range action "*magnetic-field*" probes.

Our recent research shows [17-18], that flat coil based *TD*-oscillators can be activated also with their internal capacitances (*without an external capacitance C in their resonant circuits* – see **Fig.3**). That is the result of relatively high value of internal capacitances of single-layer flat coils compared to their parasitic capacitances with respect to the surrounding radiotechnical environment. This opens one more exotic area for flat-coil oscillator application. Namely, a "*needle-like*" testing magnetic field of such a flat coil (see **Fig.12a**), used as a pick-up in such a stable *TD*-oscillator, enables a novel method (*new approach*) for surface probing, based on replacement of short-range, solid-state probes of acting microscopes (*such as needles or cantilevers of tunneling* [19-20] *and atomic-force* [21] *microscopes*, *probes of the near-field microscopes*, etc.) by the long-range action non-solid-state ones. Such an unusual probe shows strong dependence of a detected signal on the size of the spatial-gap between the probe and the surface of the object – crucial for the probe microscopy (**PM**) [22]. This opens an opportunity for creating of the "*magnetic-field*" probes with a *RF* power applied to the sample lying in the range of 1nW to 5μW. The gap between such a "*probe-formative*" flat coil and the object can be larger than 100μm [18], compared with the 1nm gap of the acting probe microscopes [22]. In our tests we reached a lateral resolution ~ 1μm even for the relatively large diameter ($2R_{coil}$ ~ 14mm) flat-coil technique [18].

Such a *SFCO*-probe may also "*notice*" and distinguish details of the relief of the normal-metallic object – with about 10μm spatial-resolution, presently (**Fig.12**). In order to demonstrate that, we performed an experiment with one-dimensional (**1D**) metallic grid made of 6 copper wires (see **Fig.12a**): each wire was ~20-30μm in dia. and was positioned with an average interval of about 200μm between the wires. Copper wires distort the coil *RF*-field configuration when they move (*or*, *when the coil moves relative to the grid*), leading to changes of the oscillator frequency or/and amplitude. The effect is maximum when each wire reaches to the coil center. **Fig.12b** illustrates detected dependence of the oscillator frequency shift, $\delta(\Delta F)$, vs. the lateral position of the metallic-comb relative to the flat-coil face (*relative to "magnetic-field" probe*). Average distance between the detected 6 vertical neighboring peaks on the curve in **Fig.12b** is ~200μm – just in agreement with the experimental setup in **Fig.12a**. That is why, we believe, that *SFCO*-probe may also in future distinguish (*both by amplitude and frequency of the TD-oscillator*) details of the relief of the magnetic or metallic 2D grids, in *sub*-micrometer scales. For such high lateral resolution, there is need to work out and create the *SFCO* method-based advanced "*magnetic-field*" probe, with a lithographically made single-

layer flat coil of about 1mm in diameter [23] – *as an effective needle-type probing instrument with better than* 100nm *predicted lateral resolution*. Such a radically new probe will have considerably *large work-distances* (more than 100μm) *between the probe and surface of the object*, which enables a "visual" control of the local area of probing of the object, and, if needed, application of test perturbations (for example, exposition to laser radiation).

in military science, engineering and Intelligence: to detect onset and amount of attacking soldiery of enemy arm-forces in the absence of direct visibility, and to reveal and detect low-powered nuclear weapon tests. Besides, to solve the perimeter or/and zone-security problems for the intelligence group(s), as well as for the special mission unit(s).

In a precision sensor industry: for creation of non-contact acceleration sensors (*the pickups*) of *super*-high resolution.

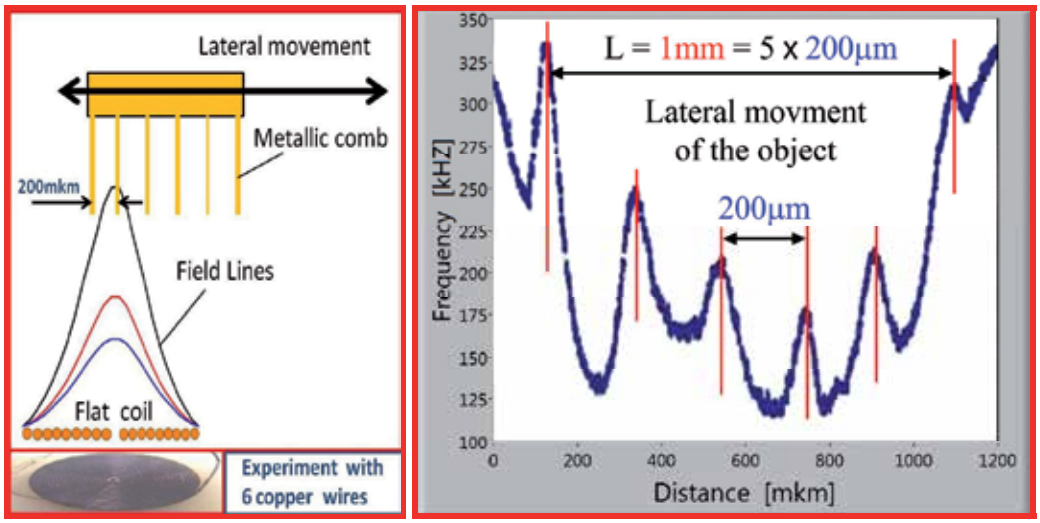

a) b)

Fig. 12. Dependence of the *SFCO* technique's *TD* oscillator frequency shift $\delta(\Delta F)[kHz]$ (**b**) on the lateral position of the *1D* grid-shaped metallic object (**a**) relative to the "*probe-formative*" flat coil face.

in a basic research: for high-precision measurements of the Casimir Force and very little friction related with it. Besides, high- and/or low-T_c superconductive coil-based 3D analogue of such a new, ultra-sensitive *SFCO*-position sensor seems to be very useful also for the *sub*-Angstrom *spatial*-resolution gravity-wave detection.

4. Conclusion

A new class super-broadband nano-scale-resolution position sensor appeared quite recently. It can be used, in particular, as an additional sensor in seismographs. It enables to extend the frequency-band (up to "zero"), and enhance the absolute-resolution (*sensitivity*) of the vibrometers and seismographs, available on the market, by 10-100 times, depending on the model of the base product (such as the American KS-1/KS-54000 and FBA-23, the European GS-13 and STS-1/STS-2, and the Russian SM-3 – presented and discussed above *SFCO*-sensor was installed just inside the SM-3 seismometer, and compared with its own sensor).

The new position sensor allows transferring of mechanical vibrations of the constructions, buildings & the ground (earth crust) with amplitudes over 1nm, into detectable signal in a frequency range starting practically from quasi-static movements ("zero"!). Such high is the achieved resolution, because due to much higher precision one may measure the frequency of oscillator, compared with the inductance or capacitance of its resonant circuit (even, if use more sensitive AC-bridge technique), oscillators are most suitable sensors for high-precision detection. This is why a very similar position sensor, based on the inductance-change detection of a lithographically made single-layer flat geometry coil, enables three orders less resolution in absolute position sensing [24]. Operation of the new sensor is based on detection of the position changes of a vibrating normal-metallic plate placed near the single-layer flat geometry coil – being used as a pick-up in a stable tunnel diode oscillator. The frequency of the oscillator is used as a detecting parameter in such a sensor, and the measuring effect is determined by a distortion of the *MHz*-range testing field configuration near the flat coil face by a vibrating plate, leading to the magnetic inductance changes of the coil, with a resolution ~10 pH. This results in changes of measuring oscillator frequency.

5. Acknowledgment

This Chapter was written thanks to study results supported by the Armenian **NFSAT** (*National Foundation of Science and Advanced Technologies*) and the U.S. **CRDF** (*Civilian Research and Development Foundation*) under the Grants ## ISIPA 01-04, GRASP 30/06 and UCEP 07/07. Our research was partially supported also by the state sources of Armenia in frames of the task program on "new materials" (code #041027), as well as in frames of State R&D projects ## 301-0046 and 72-103. The author is also grateful to his staff (YSU, IPR–NAS, and PSI Ltd.) for assistance and useful discussions.

This Chapter was prepared and written also thanks to the information and illustrative material given by the chief executive officer (CEO) of the *Precision Sensors/Instrumentation* (**PSI**) *Ltd.*, Mr. Levon P. Thorose, and by leading specialists of this Company.

6. References

[1] Gevorgyan, S.G.; Movsisyan, A.A.; Movsesyan, G.D.; Shindyan, V.A. & Shirinyan, H.G. (1997). On the Possibility of the Creation of Radically New Type Detectors of Particles & Radiation Based on High-T_c Superconductors. *Modern Physics Letters B*, Vol.11, No.25, pp. 1123-1131.

[2] Gevorgyan, S.G.; Movsesyan, G.D.; Movsisyan, A.A.; Tatoyan, V.T. & Shirinyan, H.G. (1998). Modeling of Tunnel Diode Oscillators & Their Use for Some Low Temperature Investigations. *Review of Scientific Instruments*, Vol.69, No.6, pp. 2550-2560.

[3] Gevorgyan, S.G.; Kiss, T.; Movsisyan, A.A.; Shirinyan, H.G.; Hanayama, Y.; Katsube, H.; Ohyama, T.; Takeo, M.; Matsushita, T. & Funaki, K. (2000). Highly Sensitive Open-Flat Coil Magnetometer for the $\lambda(H,T)$ Measurements in Plate-Like High-T_c Cuprates. *Review of Scientific Instruments*, Vol.71, No.3, pp. 1488-1494.

[4] Gevorgyan, S.G.; Kiss, T.; Ohyama, T.; Movsisyan, A.A.; Shirinyan, H.G.; Gevorgyan, V.S.; Matsushita, T.; Takeo, M. & Funaki, K. (2001). Calibration of the Open-Flat Coil-based Tunnel Diode Oscillator Technique (OFC magnetometer) for Quantitative Extraction of Physical Characteristics of Superconductive State. *Physica C: "Superconductivity and its Applications"*, Vol.366, No.1, pp. 6-12.

[5] Gevorgyan, S.G.; Kiss, T.; Ohyama, T.; Inoue, M.; Movsisyan, A.A.; Shirinyan, H.G.; Gevorgyan, V.S.; Matsushita, T. & Takeo, M. (2001). New Paramagnetic Peculiarity of the Superconductive Transition Detected by a Highly Sensitive OFC magnetometer. *Superconductor Science and Technology*, Vol.14, No.12, pp. 1009-1013.

[6] Gevorgyan, S.G.; Kiss, T.; Shirinyan, H.G.; Movsisyan, A.A.; Ohyama, T.; Inoue, M.; Matsushita, T. & Takeo M. (2001). The Possibility of Detection of Small Absorption in HTS Thin Films by Means of the Highly Sensitive OFC Magnetometer. *Physica C: "Superconductivity and its Applications"*, Vol.363, No.2, pp. 113-118.

[7] Gevorgyan, S.G.; Kiss, T.; Inoue, M.; Movsisyan, A.A.; Shirinyan, H.G.; Harayama, T.; Matsushita, T.; Nishizaki, T.; Kobayashi, N. & Takeo, M. (2002). Peculiarities of the Magnetic Phase Diagram in Small-size Untwinned $YBa_2Cu_3O_y$ Crystal Constructed by Highly Sensitive OFC-magnetometer. *Physica C: "Superconductivity and its Applications"*, Vol.378-381 (P1), pp. 531-536.

[8] Gevorgyan, S.; Shirinyan, H.; Manukyan, A.; Sharoyan, E.; Takeo, M.; Polyanskii, A.; Sarkisyan, A. & Matsushita, T. (2004). Flat Coil-based Tunnel Diode Oscillator Enabling to Detect Real Shape of the Superconductive Transition Curve & Capable of Imaging the Properties of HTSC Films with High Spatial-resolution. *Nuclear Instruments & Methods in Physics Research A* (NIM-A), Vol.520, No.1-3, pp. 314-319.

[9] Gevorgyan, Samvel; Gevorgyan, Vardan. & Karapetyan, Gagik. (2008). A Single-layer Flat-coil-oscillator (SFCO) based Super-broadband Position Sensor for Nano-scale-resolution Seismometry. *Nuclear Instruments & Methods in Physics Research A*, Vol.589, No.3, pp. 487-493.

[10] Gevorgyan, S.G.; Gevorgyan, V.S.; Shirinyan, H.G.; Karapetyan, G.H. & Sarkisyan, A.G. (2007). A Radically New Principle of Operation Seismic Detector of Nano-scale Vibrations. *IEEE Transactions on Applied Supercond.*, Vol.17, No.2, pp. 629-632.

[11] Van Degrift, C.T. (1975). Tunnel Diode Oscillator for 0.001 ppm Measurements at Low Temperatures. *Review of Scientific Instruments*, Vol.46, No.5, pp. 599-607.

[12] Van Degrift, C.T. & Love, D.P. (1981). Modeling of Tunnel Diode oscillators. *Review of Scientific Instruments*, Vol.52, No.5, pp. 712-723.

[13] Bath, M. (1973). Introduction to Seismology, *John Wiley & Sons, NY.*

[14] Sharvin, Y.V. & Gantmakher, V.F. (1960). Dependence of the Superconductive Penetration Depth on the Value of Magnetic Field. Value. *Journal of Experimental and Theoretical Physics (Soviet JETP).* Vol.39, p. 1242.

[15] Gevorgyan, S.; Kiss, T.; Movsisyan, A.; Shirinyan, H.; Ohyama, T.; Takeo, M.; Matsushita, T. & Funaki, K. (2000). Advantages of λ Measurement in Flat Geometry High-T_c Cuprates by an Open-Flat Coil Magnetometer Demonstrating Its Wide Possibilities For Detection. *Nuclear Instruments & Methods in Physics Research A* (NIM-A), Vol.444, No.1-2, pp. 471-475.

[16] Giaever, I. (1960). Electron Tunneling Between Two Superconductors. *Physical Review Letters*, Vol.5, No.10, pp. 464-466.

[17] Muradyan S.T., Gevorgyan S.G. (2008) Investigation of TD-oscillators activated on the internal capacitance of their coils. *Journal of Contemporary Physics* (NAS of Armenia), Allerton Press, Inc., Vol.43, No.2, pp. 97-100.

[18] Gevorgyan S.G., Muradyan S.T., Kurghinyan B.K., Qerobyan M.I. (2011) Needle-like Properties of the probing RF field of "*magnetic-field*" probes based on the single-

layer flat coils. *Proceedings of the Yerevan State University*, Physical and Mathematical Sciences, No.3(226), pp. 47-51.

[19] Binning G. and Rohrer H. (1980) "Scanning Tunneling Microscope". *U.S. Patent 4,343,993*, Aug.10, 1982. Field: Sep.12.

[20] Binning G. et al. (1982) *Appl. Phys. Lett.*, Vol.40, p.178.

[21] Binning R., Quate C., et al. (1986), *Phys. Rev. Lett*., Vol.56, p.930.

[22] Bikov V.A. (2000) "Topical review on Probe Microscopes". *Russian Doctoral Degree Dissertation*, Moscow – in Russian.

[23] Spiral Chip Inductors (U.S. Microwaves production – *www.usmicrowaves.com*).

[24] Roger A. (1996). Coil-based Micromachined Sensor Measures Speed & Position for Automotive Applications. *Electronic Design*, December 16, pp. 34-37.

14

Earth Observation for Earthquake Disaster Monitoring and Assessment

Huadong Guo, Liangyun Liu, Xiangtao Fan, Xinwu Li and Lu Zhang
Key Laboratory of Digital Earth Science, Center for Earth Observation and Digital Earth, Chinese Academy of Sciences, Beijing China

1. Introduction

China is a country where earthquakes and many other disasters happen often. After earthquakes, roads are damaged, traffic is blocked off, secondary disasters occur frequently, weather conditions become adverse, and communications are interrupted, which makes it difficult to gather data from stricken regions. And the big problem for recovery operations is that there is no accurate information about the situation. Earth observation technology, which has many advantages including high-speeds, maneuverability, and macro- to micro-level observation, has shown its importance for gathering information about stricken regions and making reasonable recovery decisions.

Optical Earth observation technology can provide vivid images for target interpretation and disaster information extraction. Maneuverable, flexibile airborne optical observation technology can especially provide real-time surface images, which also obtains information about collapsed houses, broken roads, geological disasters, barrier lakes and so on. It plays an important part in disaster mitigation activities (Guo et al., 2010a). Synthetic aperture radar (SAR) not only has the capability of all-weather monitoring, but also is sensitive to geometric shape and movement, which becomes an efficient tool to analyze and evaluate recent earthquakes (Guo et al., 2000; Guo et al., 2010b). Multi-mode SAR data can provide many kinds of information for disaster research. Wide-mode SAR images and In-SAR images are important methods for detecting terrain deformation. Wide-mode SAR images can analyze the faulted zone and lithologic characteristics in stricken regions from a macro-level, because it acquires large-scale image (Guo et al., 2000). In-SAR images yield information about surface deformation size and spatial distribution acquired from two-scene repeat-pass data (Massonnet & Feigl, 1998). Polarimetric SAR images, due to the sensitivity to target structures, can be used to extract the distribution of collapsed buildings.

After the Wenchuan and Yushu earthquakes, some departments took full advantage of airborne and satellite remote sensing technology, or unmanned aerial vehicles, to obtain images of the disaster area, which played a very important role in disaster emergency monitoring and disaster assessment and reconstruction (Guo et al., 2010ab; Singh et al., 2010; Liou et al., 2010). Besides monitoring targets directly affected by the disaster, such as collapsed buildings (Lei 2009), remote sensing can observe secondary damage such as barrier lakes, collapse, landslide, debris flow et al. (Cui et al, 2008; Wang et al, 2008; Liu et al., 2009; Huang et al., 2009; Ge et al., 2009; Xu et al., 2009; Han et al., 2009; Zhuang et al., 2010; Zhang et al., 2010; Xu et al., 2010).

The Chinese Academy of Sciences (CAS) immediately arranged a cooperative data acquisition program of airborne and satellite remote sensing data after Wenchuan and Yushu earthquakes and obtained 17 categories of more than 500 scenes of satellite images and high-resolution optical and microwave airborne remote sensing data. 8.7 TB of high-resolution data were freely provided initially to 16 ministries and 28 units, and an additional 3.5 TB were later downloaded from the network. At the same time, a study on remote sensing monitoring methods for post-earthquake secondary geological disasters was carried out, which played an important role in the disaster response. This paper focuses on three aspects, including optical Earth observation technology for monitoring secondary geological disasters, multi-mode radar Earth observation for post-earthquake deformation analysis, and an earthquake disaster simulation evaluation system using the results of seismic disaster remote sensing.

2. Detecting geological disasters using optical technology for Earth observation

Optical technology for Earth observation can provide visual images for disaster target interpretation and disaster information extraction. Airborne optical technology is one of the main instruments for Earth observation, with its mobility and flexibility to provide real-time disaster remote sensing and surface images. With disaster mitigation work done to remotely sense secondary disasters after the Wenchuan earthquake, including barrier lake breaches, road damage, and landslides and debris flows, we analyze and discuss technical methods and applications of optical technology for Earth observation in monitoring secondary geological disasters.

2.1 Extracting background information from the disaster area in Wenchuan

The Wenchuan earthquake occurred in the Longmen mountain fault zone. Longmen mountain runs in the general northeast to southeast direction, about 500km from Guangyuan to Ya'an. Longmen mountain is one of China's typical nappe structures, a tectonic rock sheet along a imbricated thrust to the basin mainly formed in the Mesozoic and early Cenozoic (Wang et al, 2001). The Wenchuan earthquake occurred in the crustal brittle-ductile transition zone, and was a shallow earthquake with a focal depth of 10 km to 20 km and longer duration, so its destructiveness was huge (Bi et al, 2008).

After the Wenchuan earthquakes, CAS urgently arranged airborne and satellite data coordinate acquisition plans and obtained 41 scenes of post-disaster, high-resolution satellite data, and 105 scenes of pre-disaster and concurrent high-resolution archive satellite data. An optical remote sensing airplane carrying an advanced ADS40 aviation camera obtained high-resolution (0.5 - 0.8 m) optical pictures of the disaster area totaling 5 TB with a coverage area of 23,000 km^2.

2.2 Remote sensing monitoring and analysis of barrier lakes after the Wenchuan earthquake

High-resolution ADS40 optical images of the disaster area were used to analyze the barrier lake for the first time. In the coverage area, 51 barrier lakes were detected, some with a bead-like distribution. The location, area, water level and height, and area of the dam body were detected according to a monitoring algorithm of barrier lake risk factors and 1:50,000 DEM data. The risk conditions, geology, and distribution of the 51 major barrier lakes were evaluated to support urgent relief work. The research indicated that the distribution of barrier lakes and spatial features of the earthquake fracture zone were identical.

2.2.1 Barrier lake volume detection algorithm

The water level and area of the barrier lakes were first estimated using high-resolution airborne images. The capacity of the barrier lake was then calculated using elevation contours, and the calculation was based on DEM data with a resolution of 25 m, which were interpolated from a 1:50,000-scale topographical map.

The method to calculate the reservoir capacity involves the following steps:

The water surface area was derived from high-resolution airborne images. Then the water surface elevation (h_s) was acquired by overlapping the water surface with the DEM data, since the elevation of the water surface is a constant. If there is some small shift between the orthorectified ADS40 image and the DEM data, the interpreted water surface should be adjusted slightly to ensure all interpreted water surfaces' borderline is located at the same altitude. Meanwhile, the elevation of the midline of the river (h_r) was directly recorded from the 1:50,000-scale topographic map. Therefore, the elevation difference and the water level could be calculated.

The capacity of the barrier lake was calculated by an integral approach. The capacity V at the water elevation of H is:

$$V(H) = \sum_{i=1}^{n} S_i \times \Delta h \tag{1}$$

where Δh is the integration interval, n is the equally parted cells number of the elevation drop from the water surface elevation (h_s) to the elevation of the midline of the river, (h_r), $\Delta h = (h_s - h_r)/n$ is the integration interval of each cell, and S_i is the water surface area at the elevation of $h_r - (i-1)\Delta h$, which can be automatically derived from the DEM data. The capacity and area of all the 51 barrier lakes were calculated by this method. According to their capacities, the barrier lakes were clustered into three types: Type I (large-sized) with a capacity over 3,000,000 m³; Type II (medium-sized) with a capacity between 1,000,000 and 3,000,000 m³; and Type III (small-sized) with a capacity less than 1,000,000 m³

2.2.2 Risk assessment of the barrier lakes

Barrier lakes formed in an earthquake will result in extreme flooding when they burst. Therefore, the risk assessment of barrier lakes becomes very important. The dimensionless blockage index (DBI) was introduced by Casagli and Ermini (Ermini et al, 2003; Liu et al., 2009) to evaluate the stability of a dam:

$$\mathrm{DBI} = log(\frac{A_B \times H_d}{V_d}) \tag{2}$$

where V_d is the volume of the dam, which is the dominant parameter of stability since it determines the gravity of the dam; A_b is the area of the basin, which is the primary parameter of instability since it determines the runoff in the basin; and H_d is the height of the dam, which is an important parameter for evaluating the stability of the barrier lake when confronted with overflow. The smaller the DBI value, the more stable the barrier lake. It is difficult to calculate the dam volume with the remote sensing image without in-situ measurement. An approximate estimation of dam volume is to multiply the dam area with its height, and thus Eq. (2) can be written as:

$$DBI \approx \log\left(\frac{A_b \times H_d}{H_d \times S_d}\right) = \log\left(\frac{A_b}{S_d}\right) \tag{3}$$

where S_d is the dam area.

2.2.3 Detection results of quake lakes in the Wenchuan earthquake

We interpreted the barrier lake surface and the dam area from the high spatial resolution ADS40 airborne images and located the position of the landslide forming the barrier lake. The basin area of the barrier lake was then extracted with the DEM and hydrological data. Therefore, the reservoir capacity and DBI of the barrier lake could be calculated according to Eqs. (1) and (3). The monitoring information of barrier lakes within airborne remote sensing data coverage shows that:

i. Generally, the slope of the landslided are steep, and most of them are over 20 degrees. This condition causes the formation of barrier lakes.
ii. DBI values can reliably reflect the stability of the barrier lakes. A lower DBI value indicates a more stable barrier lake, but the risk of a secondary disaster is higher if breaches and overflows occur. According to the overflow time of the two barrier lakes located at Xiaojia Bridge, Anxian County, and Tangjiashan, Beichuan County, the barrier lakes in the Wenchuan earthquake could survive for more than 30 days if the DBI were smaller than 4.0.
iii. The Wenchuan earthquake generated 10 large-sized and 14 medium-sized barrier lakes. Therefore, immediate attention should be paid to those barrier lakes with serious and continuous breaches.

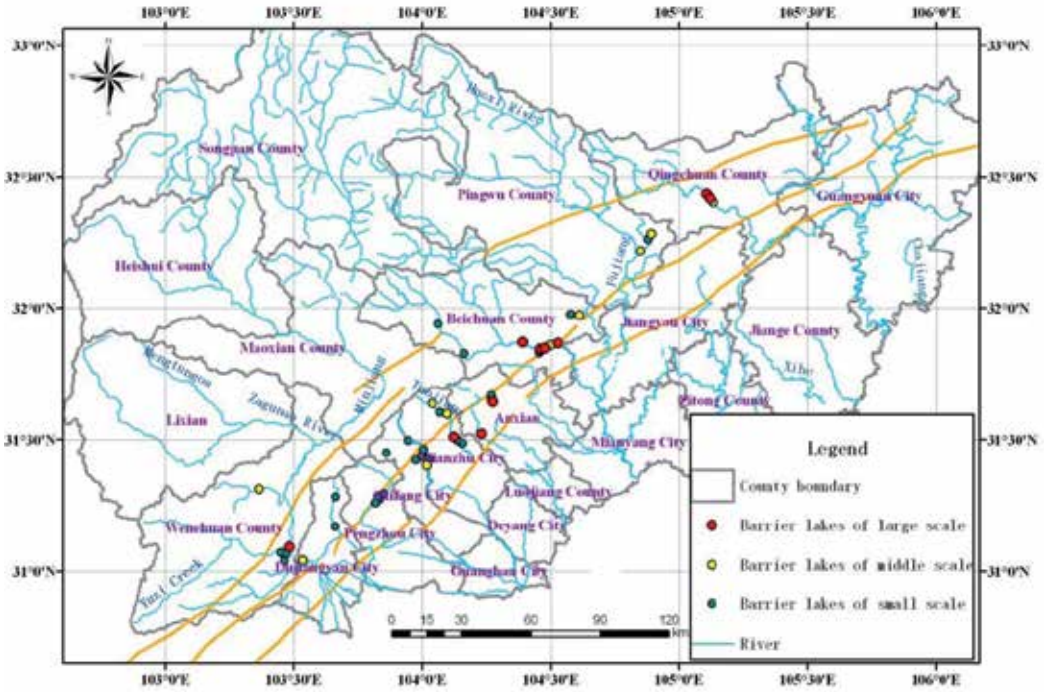

Fig. 1. Distribution map of barrier lakes caused by the Wenchuan earthquake (Liu et al., 2009)

2.2.4 Geological conditions and spatial distribution of the barrier lakes

The Wenchuan earthquake triggered many geological hazards, including collapses and landslides along river valleys. Some of the large masses of land fell into the river valleys and formed a number of barrier lakes. Figure 1 shows the distribution of 51 barrier lakes through the interpretation of remote sensing images. From the distribution map, the barrier lakes were apparently along the Yingxiu-Beichuan fault, and the distribution was consistent with the direction of the fault zone. There were a series of high-risk barrier lakes distributed along the rivers such as the Jianjiang River's upstream in Beichuan County, the Mianyuan River's upstream in Mianzhu City, and the Pingshui River in Shifang City.

2.3 Remote sensing monitoring and analysis of roads damaged by Wenchuan earthquake

High-resolution ADS40 optical airborne remote sensing images and other data were used to analyze and locate some national and provincial highways in seriously damaged areas. The process included analyzing qualitatively, orientatively and quantitatively different factors and classes of blocked and damaged roads from landslip, debris flows, river bank collapse, barrier lakes, earthquake disruption and ground fissuring. These monitoring and analysis results may give transportation department powerful information support.

2.3.1 Road blockage and damage conditions in badly stricken areas

The main remote sensing road blockage and damage condition detection focuses on national and provincial highways. There are 5 national and provincial highways in the badly stricken

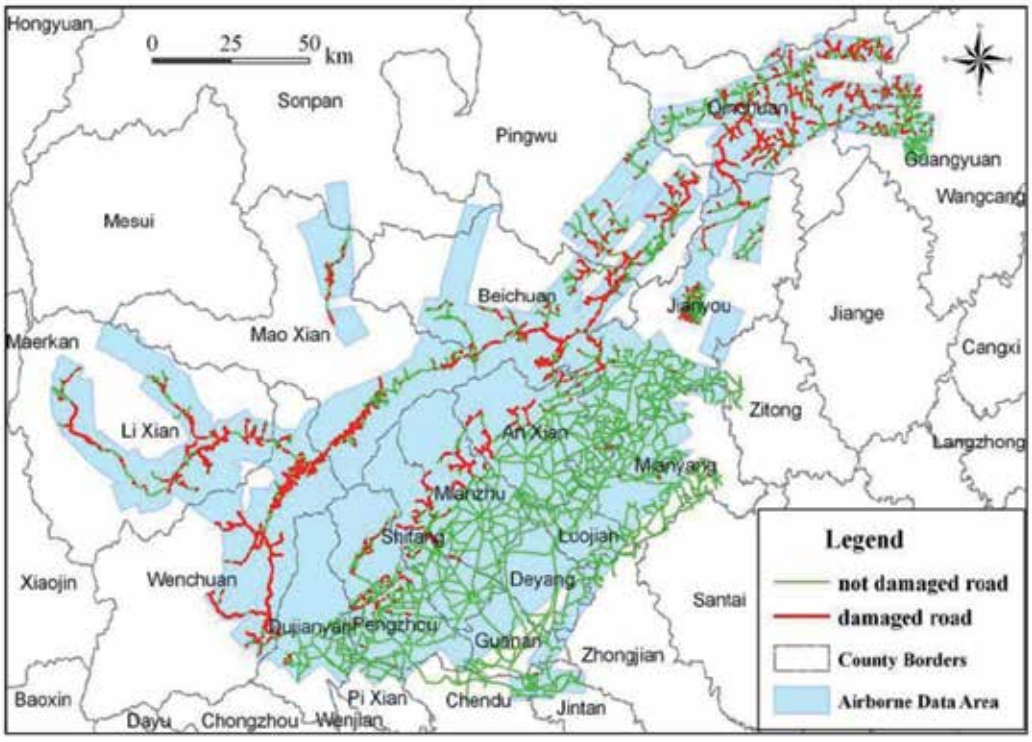

Fig. 2. Map of damaged roads after the Wenchuan earthquake

area, with an overall length of 573.82 km. This includes 3 national roads with a total length of 394.07 km: National Highway 213 (239.563 km) from Xuankou Town, Wenchuan County to Minjiang Village, Mao County, National Highway 212 (31.814 km) from Baolun town, Guangyuan City to Lijia Ping, Qingchuan County, National Highway 317 (122.692 km) from Siboguo Village, Li County to Wenchuan County. It also includes 2 provincial highways with a total length of 179.75 km: Provincial Road 105 (50.85 km) from Anchang Town, An County to Beichuan County and Provincial Road 302 (128.90 km) from Mao County, Jiangyou City.

The Wenchuan earthquake caused more than five national and provincial road blockages and damage, including 808 points in total with a total length of 170.17 km, which accounted for 29.66% of the total length of paths in the badly stricken area, in which, National Road 213 was most seriously damaged, then National Road 317 and Provincial Road 105. Damage to the others was comparatively light. The conditions of damaged roads is described in Figure 2.

2.3.2 Damage level and distribution condition of hard-hit areas

The blocked roads were obviously segmented and the worst parts appeared to have a cluster distribution. Outside of the observed areas, the roads were light damaged and without major disasters such as landslips.

2.3.3 Category, scale and causation of damaged paths

According to remote sensing monitoring and analysis, the blockage paths of the worst-damaged places were caused by geological disasters such as landslips, falling debris, mud-rock flows and ground fissures. The distribution of these disasters was related to the break structure, drape structure, and rock broken under stress.

Fracture tectonic belt was the most important role in road damage. The magnitude-8 earthquake happened on the fault zone of Longmen Mountain, which is composed of many approximately parallel disruptions oriented towards the northeast with a length of more than 500 km and 50 km in width. The Yingxiu-Beichuan fault and Wenchuan-Maoxian fault were the most important parts of the Longmen Mountain fault zone, and the most serious damage to National Road 213 was along these two fault zones.

The background of the badly stricken area's geological structure is very complex with a long evolutionary history. The rocks in hard-hit areas were squeezed extremely because of the long-term activities of well-developed faults and fold faults. These broken rocks provide a large amount of material for potential falling, mud-rock flows (with fragment flows) and landslips. This material slipped rapidly under the force of gravity and piled up on the lower roads and caused blockage in the harder-hit area.

In addition, the earthquake's power is the reason that roads in harder-hit area were blocked and damaged. When the earthquake occurred, there were both southeast-direction thrust extrusion and dextral shear in the Longmen Mountain Fault Zone (Chen Yuntai etc., 2008), which made steep mountains, high-angle clockwise slope and extremely broken rock strata lose their balance and dependence. Then under the action of gravity, broken rock rapidly slid downward, or collapsed and accumulated in low-lying areas on the highway, which damaged and blocked the road.

2.4 Secondary geological disaster analysis of Wenchuan earthquake

Using high-resolution ADS40 optical aviation remote sensing images and comprehensive, conventional data, we evaluated secondary geological disasters, such as collapses,

landslides, and debris flows. Using investigations by remote sensing and field survey results combined with the Ministry of Land and Resources, PRC emergency investigation data, a secondary geological hazards information acquisition model was established. It allowed for the monitoring and rapid extraction of secondary geological disaster data. Researchers studied the characteristics and distribution of secondary geological disasters, completed the interpretation of 11 heavily-damaged area's geologic disasters and their geological background, and analyzed the geological hazards' distribution, intensity, scale and distribution regularity. The study revealed that the development of secondary geological disasters had obvious clustering. In the area, seismic geological hazards were along the Longmen Mountain Fault Zone and mainly caused by the Beichuan-Yingxiuwan fracture control.

2.4.1 Remote sensing information extraction method for secondary geological disasters

The special weather conditions in Wenchuan make the ratio of vegetation coverage higher. The study on vegetation destruction in this area shows the severity of geological disasters and supports the job of disaster evaluation and post-disaster reconstruction.

First, remote sensing data were acquired from before and after the earthquake. Extracting the information map of vegetation was done with standardized resolution and registration. Second, high spatial resolution images were used to check causes of vegetation change including geological disasters, human destruction, agricultural changes and so on. The third step was to remove the vegetation change information caused by non-geological disasters and make a classification according to remote sensing image identification of secondary geological disasters. Last, statistics were calculated and analysis conducted to make a difference map.

i. Standardize resolution and make registration

In order to reduce the extraction difference of vegetation caused by different spatial resolutions, we standardized the spatial resolution of the images by two-dimensional cubic convolution before the vegetation information extraction. Then map-to-map control points were adopted and registered by a polynomial method. Because the registration method uses vegetation information difference extraction before and after the disaster, the registration precision should be controlled within 1 pixel.

ii. extract vegetation information

According to the special vegetation spectrum, we can efficiently extract the vegetation information from pre- and post-disaster images. The formula is as follows:

$$NDVI = \frac{R_{NIR} - R_R}{R_{NIR} + R_R} \tag{4}$$

where NDVI is vegetation index, R_{NIR} is reflectivity of near infrared wave, and R_R is reflectivity of infrared wave. Comparing the results with a real vegetation coverage map to fix the threshold, we can extract the vegetation coverage map and change it into a vector diagram.

iii. extracting the vegetation information difference from geological disasters

Based on the extraction of a vegetation information vector graph, the difference between the two figures can be extracted by doing differential operation. The high spatial resolution data can be used to correct elements caused by the difference and then reject the difference in

vegetation information caused by non-geological factors. Finally, according to remote sensing image identification of secondary geological disasters, they can be classified.

2.4.2 Secondary geological disaster remote sensing monitoring results

The overall results of monitoring secondary geological disaster are shown in Figure 3, where the red stands for landslides, blue for debris flows, and green for collapses. As can be seen from the figure, the landslide occurred mainly in Beichuan, Pingwu and Qingchuan counties; debris flow occurred mainly in Wenchuan, Maoxian and Li counties; and collapse occurred mainly in Wenchuan and Beichuan counties. According to statistics, the total disaster area is about 29,000 square kilometers, and the secondary geological disaster area is 2,250 square kilometers (7.8% of the total).

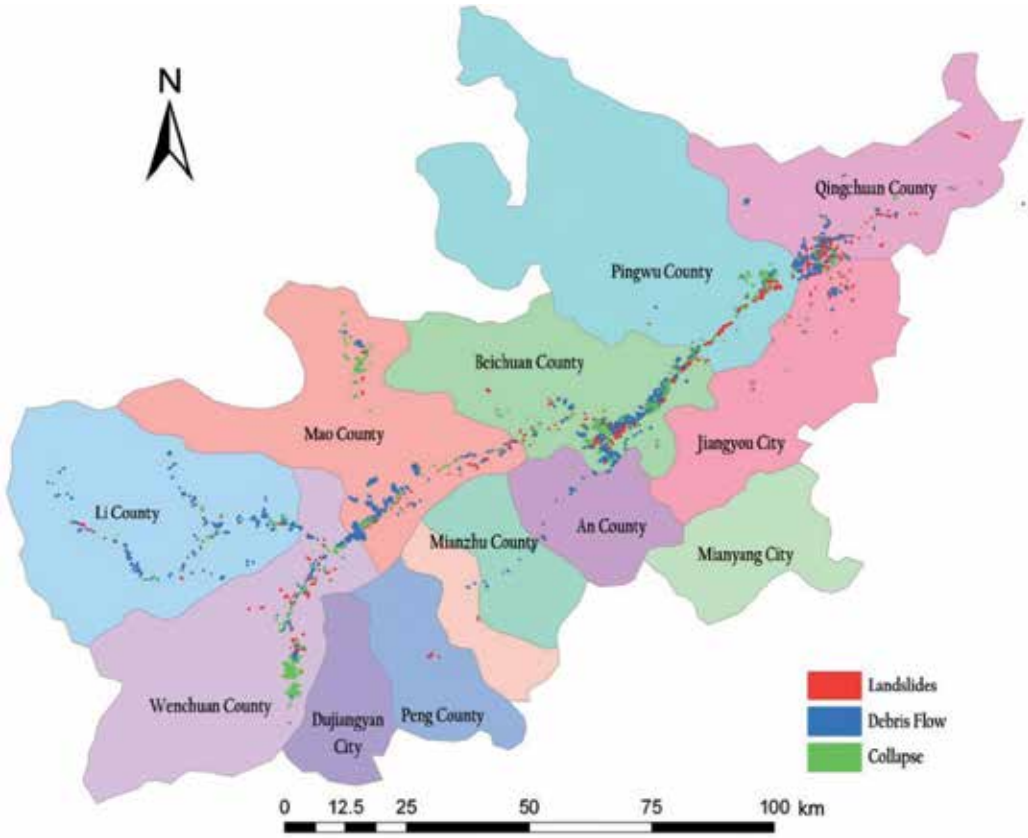

Fig. 3. Map of secondary geological disasters occurring in the heavily-hit areas of the Wenchuan earthquake

3. Multi-mode radar imaging technology for monitoring earthquake deformation

Synthetic aperture radar (SAR) multi-mode data can provide a variety of types of information for earthquake research. We take Yushu earthquake, which occurred in Yushu

County, Qinghai Province, China, on April 14, 2010, as the research object and use RADARSAT-2 and ALOS-PALSAR repeat-pass SAR interferometry data to analyze earthquake deformation characteristics.

3.1 Yushu earthquake area background and data acquisition

The Yushu earthquake occurred in the Garzê-Yushu Fault Zone. The fault strike runs in a northwest direction for a length of nearly 500 km, and has a fracture width from 50 to several hundred meters. From analysis of the plate tectonics, it can be concluded that the source of this earthquake was in the Qinghai-Tibetan Plateau, located in the north of the collision zone in the Himalayas, which was formed by the subduction of the Indian plate toward the Eurasian continent. Because of this plate subduction, lateral sliding of the internal blocks of the Qinghai-Tibetan Plateau occurred, which caused the northward shift of the plateau and its internal blocks and finally, the formation of strike-slip fault systems with different scales at the edge of the blocks. Zhang et al. (2010) inverted the moment tensor solution using wave-form data from global stations. From this solution and the background of the fault tectonics, it can be concluded that the fault with a trend of 119° and a dip of 83° was the earthquake rupture. The breaking process was determined based on teleseismic data from the 35 global stations. Two active regions on the fault surface were identified. One was located near the micro-epicenter, and the other was located to the southeast at a distance of 10 to 30 km. The latter had the greater slip, 2.4 m, and was a near vertical sinistral strike-slip fault.

The study uses SAR data including RADARSAT-2 wide-mode data and ALOS PALSAR repeat-pass data. The RADARSAT-2 wide-mode data was acquired on April 21, 2010, with a spatial resolution of 40 meters and an incident angle of 21 degrees. ALOS PALSAR data, including two pre-earthquake and post-earthquake scenes, were acquired on January 15, 2010, and April 17, 2010, respectively. Table 1 shows the PALSAR data parameters for repeat-pass SAR interferometry.

Sensor	Date	Orbit	Frame	Perpendicular baseline (m)	Temporal baseline (d)
PALSAR	2010-1-15	487	650	700.5	92
PALSAR	2010-4-17	487	650		

Table 1. PALSAR parameters for SAR interferometry

3.2 The method of extracting earthquake geological characteristics and surface deformation information from SAR data

Ground-fissuring phenomena are often a reflection of different lithological characteristics. SAR image brightness and texture structure can reflect the degree of fissuring. In addition, radar waves are sensitive to the linear structure (Guo, 1996, 1997), so using SAR imagery can help interpret tectonic information.

Interferometric SAR is an important means of extracting surface deformation because it can measure it precisely in three-dimensional space, including small deformations of the surface, and can achieve high spatial resolution observation of surface changes in large areas. Interferometric SAR images of the same area at different times by SAR sensor were obtained at different time SAR complex images. Then we process SAR images acquired at different times to obtain an interferogram. SAR interferograms show electromagnetic wave

transmission path length variation from the SAR antenna to the target in two images. Electromagnetic wave transmission path length changes are generally subject to the following three factors: satellite position changes, surface changes, and atmospheric changes. Product by the satellite position changes is terrain interferometry phase, which produced by surface changes is the atmospheric phase. Generally speaking, the SAR interference phase can be expressed as type (5).

$$\Phi_{IFG} = W\left\{\Phi_{topo} + \Phi_{defo} + \Phi_{atm} + \Phi_{noise}\right\} \tag{5}$$

where $W\{\}$ is a phase winding operator, and deformation interference phase in type (5) Φ_{defo} represents monitoring surface deformation ability of SAR interferometry. In order to obtain the deformation interference phase information, the atmosphere in the mathematical model of SAR interference measurement will be classified as noise signal, which directly considers the SAR interferometry phase as the terrain interferometry phase and deformation interference phase (Rosen, 2000), and then the removal of the terrain interferometry phase can obtain surface deformation information.

3.3 Multi-mode SAR data and the Yushu earthquake area evaluation results

3.3.1 Yushu earthquake area lithology and SAR image fraction analysis results

To further analyze the regional earthquake geology, wide-swath RADARSAT-2 SAR data were acquired on April 21, 2010, with HH polarization, a spatial resolution of 40 m, and an incident angle of 21°. Combined with geological data, the study area can be divided into A to E regions (Figure 4).Because radar waves are sensitive to the linear structure (Guo, 1996,

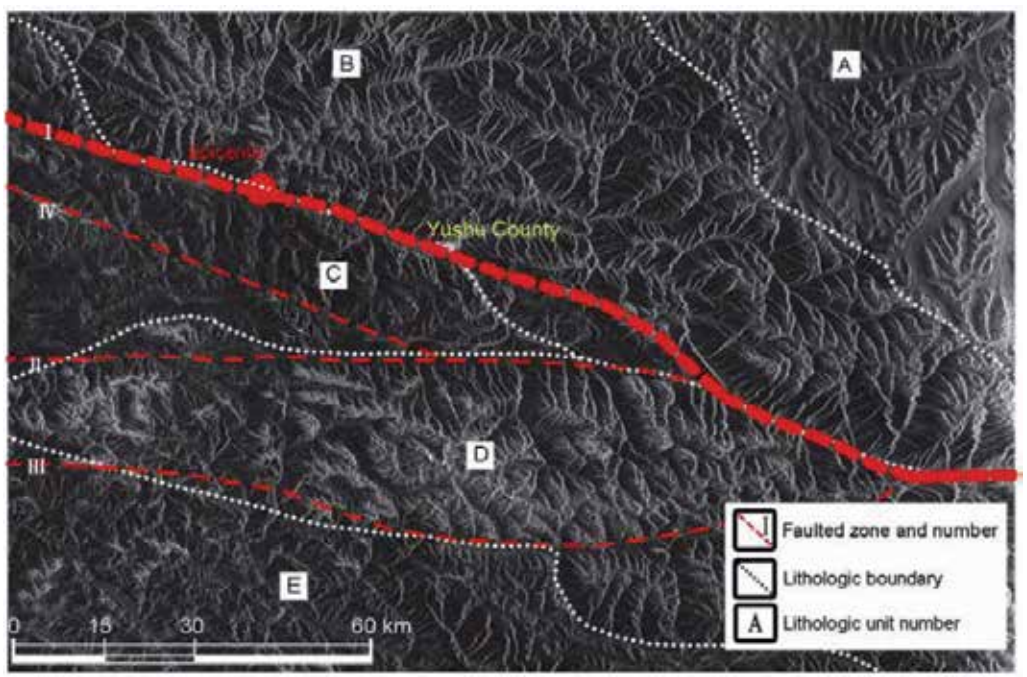

Fig. 4. Geological analysis from RADARSAT-2 HH polarization wide-swath SAR imagery. (from Guo et al., 2010b)

1997), based on the SAR image interpretation and existing research results of active tectonic plates (Deng, 2007), four main faults of this area have been interpreted as follows: the main faults I and IV are oriented in a northwest-southeast direction; fault IV developed in the limestone areas of the map; and faults II and III are distributed in an east-west direction. According to the structural composition of the faults and existing active tectonics results, the main fault I is a strike-slip sinistral fracture.

3.3.2 Yushu earthquake area InSAR deformation extraction analysis result

Using Doris InSAR data processing software and SRTM3 DEM data with 90 m resolution, the two-pass differential interferometry method was used to process the ALOS PALSAR data. We then get the seismic deformation interference phase image shown in Figure 5.

The radar interferogram clearly shows the spatial distribution of the surface deformation field caused by the Yushu earthquake. The coseismic deformation field within the image is about 82 km long and about 40 km wide along the fault. From the distribution of the interferometric fringes caused by the Yushu seismic deformation field, we can see that the distribution of the coseismic deformation is centered on the Garzê-Yushu fault zone, which is the triggered fault (Figure 4, the main fault I), and is parallel to this fault. From the distribution pattern of the interferometric fringes, we can see that the direction and density of the interferometric phase change are different for the two sides of the fault. From the southernmost point A to the fault direction, the interferometric fringe phase indicates an increasing trend from south to north. To the north of the fault, the interferometric fringe phase shows a decreasing trend from north to south. From the whole interferometric phase distribution, the change in the line of sight is left-lateral, revealing significant seismogenic fault sinistral strike-slip properties. It corresponds with the result of wide swath SAR image interpretation.

The seismogenic fault is in a northwest-southeast direction. Along the seismogenic fault zone, there are two major areas with large surface deformation, shown as ① in Figure 5(b) and ② in Figure 5(c). Position ① corresponds with the instrumental epicenter calculated by the National Earthquake Network, and ② corresponds with the macroscopic epicenter. From enlarged views of the interferogram of the instrumental epicenter area in Figure 5(b) and macroscopic epicenter regions in Figure 5(c), we can also see that the radar interferometric fringes change intensely around the instrumental epicenter, while the central region of the macroscopic epicenter has an apparent decorrelation due to the large surface deformation. Both of the two regional seismic fault slip dislocations are relatively large, but that of the latter region, which is close to the city of Yushu, will inevitably lead to stronger tremors for the city of Yushu and the surrounding area, where rupture has been the predominant cause of enormous casualties and economic losses.

PALSAR operates in the L-band, and a color change cycle in the interferogram represents 11.8 cm in the line of sight. According to the interferometric fringes analysis, on the north of the fault, the maximum sinking displacement in the line of sight is 11.8×3=35.4 cm. Since the surface near the epicenter was damaged during the earthquake, the coherence of the corresponding region in the two radar images is very low and cannot form effective interferometric fringes. Therefore, it is reasonable to conclude that one fringe remains on

each side of the fault in the low coherence area, and the cross-fault displacement in the line of sight should not be less than 11.8×8=94.4 cm.

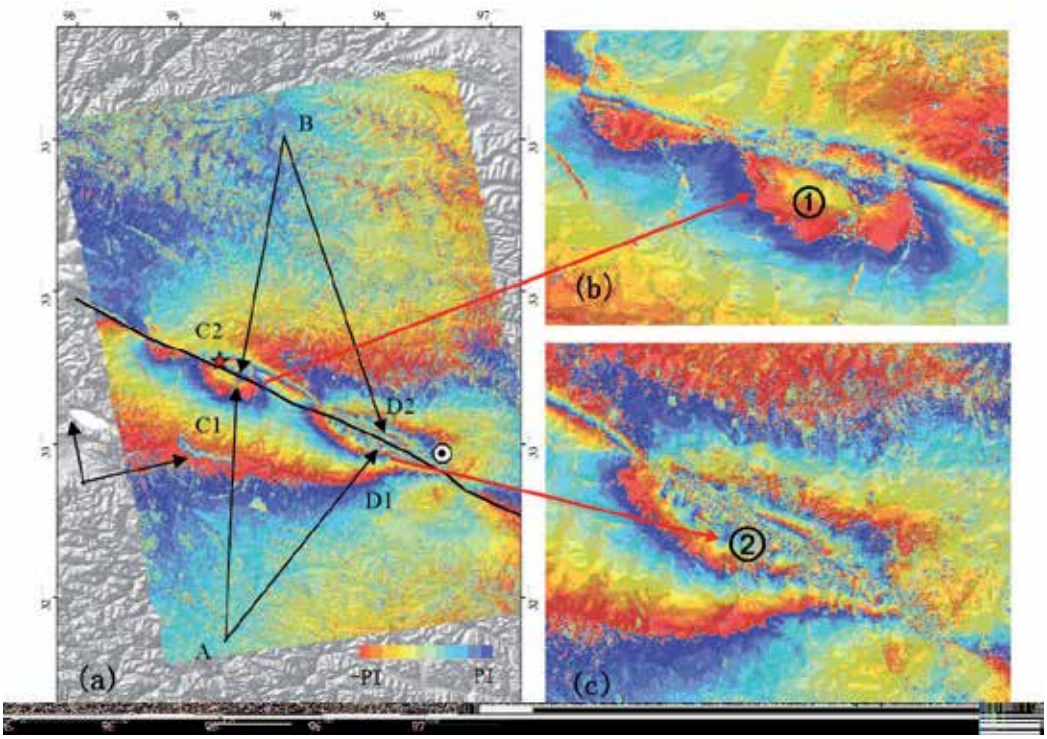

Fig. 5. Coseismic deformation map from ALOS PALSAR data, (a) Differential interferometric phase map; (b) Differential interferometric phase of instrumental epicenter; (c) differential interferometric phase of macro epicenter. A, B, C1, C2, D1 and D2 in (a) represent the different positions and in (b) and in (c) are two large deformation areas (from Guo et al., 2010b).

3.4 Extraction and analysis of collapsed buildings from polarimetric SAR

Large-scale earthquakes severely damage people's lives and property. Fast, accurate, and effective collapsed buildings a monitoring and evaluation after earthquake using remote sensing provides an important scientific basis and decision-making support for government emergency command and post-disaster reconstruction.

RADARSAT-2 polarimetric SAR data (FQ mode, ascending) on April 21, 2010 from Yushu County were used to extract the distribution of collapsed buildings. The resolution of the image is about 8 m and the incidence angle is 21°. From this polarimetric SAR data, the H-α–ρ method (Guo et al., 2010b) was used to extract the spatial distribution of building collapse caused by the earthquake in the Yushu urban area. At the same time, for comparison and analysis, a manual interpretation map obtained from the high-resolution airborne optical image was also collected and shown in Figure 6. From the collapsed buildings extraction result, the reasons for the severe earthquake damage to buildings are also discussed and assessed.

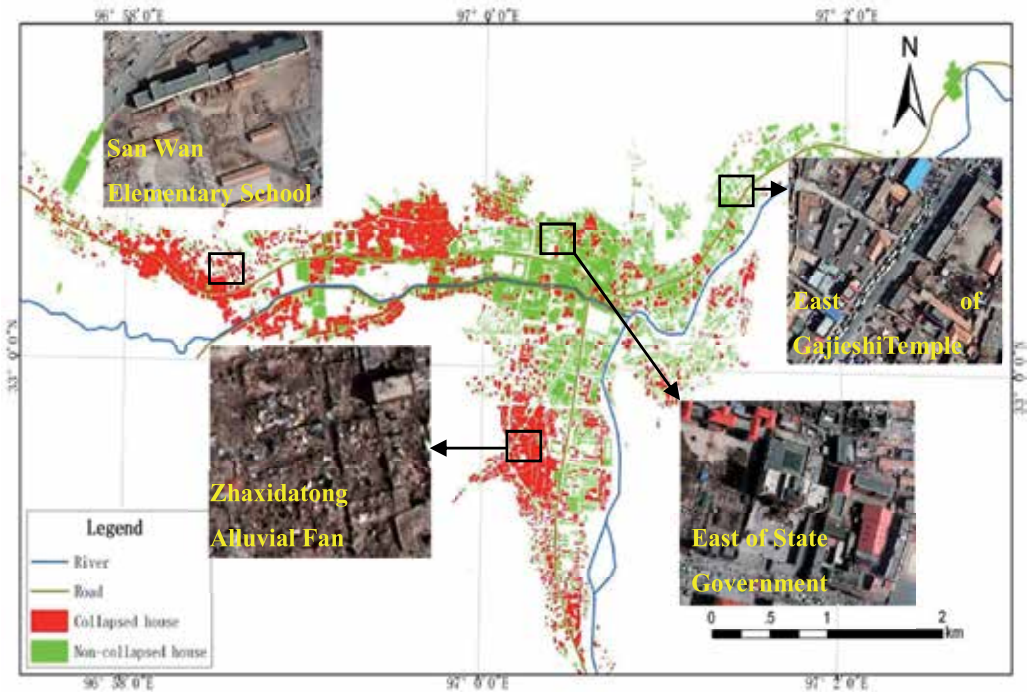

Fig. 6. Spatial distribution of collapsed buildings interpreted from airborne images and sample images for typical regions.

3.4.1 *H–α–ρ* method

From the RADARSAT-2 polarimetric data (FQ mode) and the polarimetric decomposition model, a new *H–α–ρ* method that uses only one post-earthquake SAR image was proposed to identify collapsed buildings. This method mainly utilizes three important polarimetric parameters to extract the collapsed buildings. These parameters are *H*, *α* and *ρ*, Where *H* is entropy, representing the random level of target scattering, *α* is the averaged scattering type and *ρ* is the circle polarization correlation coefficient which is very sensitive to artificial objects. *H* and *α* are obtained by using Cloude's *H–α* decomposition(Cloude, 1996,1997).The *ρ* of uncollapsed buildings is high while that of collapsed buildings is low. However, *ρ* is also related to the surface roughness. For a low roughness surface, the *ρ* is also high. Therefore, it is necessary to remove the disadvantaged influence of the bare soil surface before this parameter can be used for building identification(Ainsworth etc al.,2008). The circular polarization correlation coefficient ρ can be expressed as Eq. 6(F.Mattia, 1997),

$$\rho_{RRLL} = \frac{< S_{RR} S_{LL}^{*} >}{\sqrt{< |S_{RR}|^2 >< |S_{LL}|^2 >}} \tag{6}$$

Where $S_{RR} = iS_{HV} + \frac{1}{2}(S_{HH} - S_{VV})$, $S_{LL} = iS_{HV} - \frac{1}{2}(S_{HH} - S_{VV})$. For the Yushu urban area, three main land cover types were categorized: collapsed buildings, uncollapsed buildings, and bare soil surface. The basic process using *H–α–ρ* method to identify the collapsed buildings is as follows: 1) the extraction of the bare soil surface. *H* and *α* are obtained using

the $H–\alpha$ decomposition theorem, then, the bare soil surface was extracted with H<0.5 and α<42° (Cloude, 1996,1997). 2) Using statistical analysis, the ρ, which can discriminate between uncollapsed and collapsed buildings, is determined. From the high- resolution optical data, typical areas of collapsed and uncollapsed buildings are selected from the radar image to analyze the statistical characteristics of ρ, and the appropriate threshold value of ρ is obtained. 3) From the threshold value of ρ, the separation of collapsed and uncollapsed buildings is conducted, and the distribution map of collapsed buildings is obtained.

3.4.2 Result and analysis of collapsed building extraction

Figure 7 shows the collapsed building distribution of the Yushu urban area extracted by the $H–\alpha–\rho$ method. The rate of building collapse is about 58%. To verify the result, two test sites were selected as follows: (a) a severely damaged area, and (b) an almost undamaged area. Comparing the extraction results with the manual interpretation results from the airborne optical image with a resolution of 0.33 m shown as a' and b' in the lower left corner, we can see that the result of the collapsed buildings' extraction is consistent with the result from the optical manual interpretation. Furthermore, to verify the effectiveness of this method, the recognition rates of collapsed buildings and uncollapsed buildings are analyzed from two sample regions (more than 10000 pixels) from a and b test sites, respectively. From the statistical analysis, the recognition rate for collapsed buildings is 88% and that for uncollapsed buildings is 80%. It should be noted that the polarimetric SAR could play a more important role in the collapsed building extraction if the weather conditions were unsuitable for obtaining optical data.

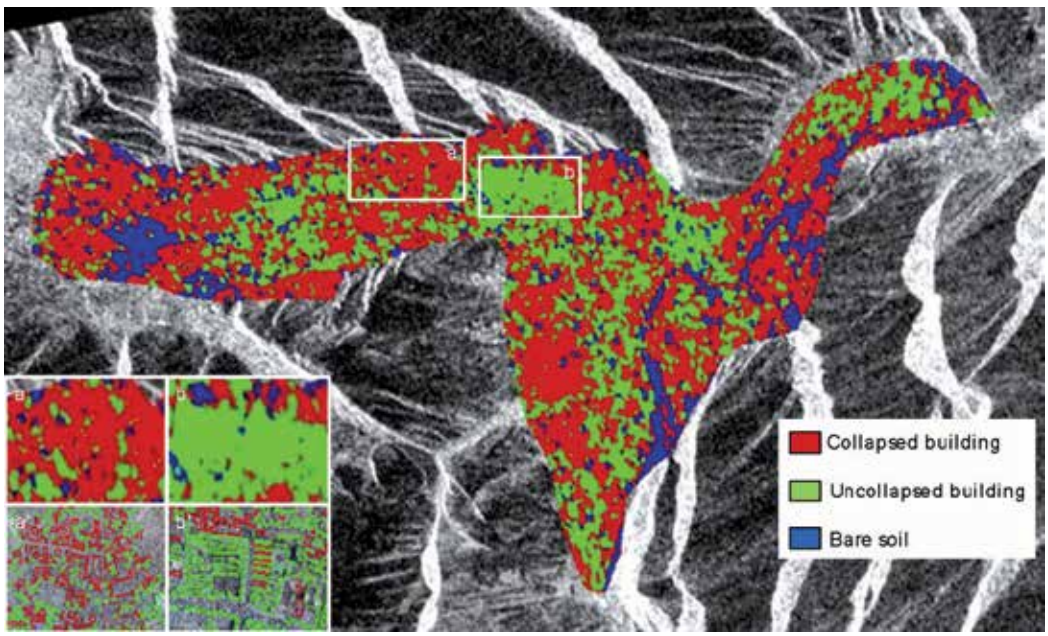

Fig. 7. Collapsed buildings distribution of Yushu County extracted with the $H–\alpha–\rho$ method from polarimetric SAR data, a and b in the lower left corner are the detailed images of the two test sites, a' and b' show the corresponding manual interpretation results from the airborne optical image(from Guo et al., 2010b).

From the collapsed building distribution, it is clear that the degree of collapse is related to the distance from the main fault. The buildings, which were constructed in the alluvial zone, had very poor earthquake resistance because their foundations were weak and most were built of earth and wood.

4. The foundation of an earthquake condition simulation and evaluation system

Based on remote sensing image two-dimensional spatial information systems, interpretation and analysis has been the main means of seismic disaster assessment. Although two-dimensional spatial information systems have the macroscopic and overall characteristics, it also has inevitable defects in the earthquake disaster assessment (Xiao et al, 2001, Li et al, 2007), such as in accurate expression of three-dimensional information, an inability to record non-uniform three-dimensional spatial entities, and a lack of a basis for uneven spatial entity description of lake water, landslides, collapsed buildings and so on. Therefore, it is necessary to establish an evaluation system based on three-dimensional spatial information of earthquake disaster information for analysis.

For the Wenchuan and Yushu earthquakes, using three-dimensional simulation and evaluation with advanced Earth observation technology, we established realistic 3D terrain model using the relatively sophisticated disaster assessment model and successfully created an earthquake disaster simulation and evaluation system. Based on multi-sensor, multi-temporal, and multi-resolution remote sensing images and 1: 50,000 scale DEM data, we produced technology for large 3D terrain modeling and interactive real-time rendering. The 3D simulation system provides a more intuitive disaster analysis method for major collapse, landslide, and debris flow disasters. Using red-blue 3D imaging techniques to get airborne remote sensing stereo images and reconstruct three-dimensional scenes, we can efficiently extract data on damage to housing and improve the disaster analysis accuracy using red and blue stereo glasses. In a 3D environment, not only can the geo-spatial relationship between objects be shown, but also the topological relations between spatial objects. Practice has proven that this kind of three-dimensional assessment is more efficient and reliable.

4.1 Three-dimensional terrain modeling and visualization

We use 1: 50,000 topographic vector data of the disaster area for error analysis and to eliminate gross errors of contour and control point data. We use a difference algorithm for vector contour data to obtain high-resolution DEM raster data. In order to rebuild 3D virtual scenes, we use a merging method of aerial remote sensing images and Landsat TM images to generate the terrain texture. In severe disaster areas, we acquired high-resolution data, TM images. Then combined with DEM data, the aerial remote sensing data can be corrected precisely. Finally, the merging of aviation data and TM data yield the an image of the entire area, which is then mapped to the three-dimensional terrain model to form a virtual 3D environment.

The complicated terrain of earthquake-stricken areas and large data of three-dimension model after overlaying images and DEM have brought challenges for real-time rendering. This paper proposes a multi-resolution triangular grid dynamic geographic model based on computing vision, established a simplified algorithm based on multi-resolution vision. Using a multi-resolution scene model algorithm, this paper resolves the real-time interactive roaming difficulty of large-scale three-dimensional terrain data. First, according to the

amount of data and resolution of images, the magnitude n is established. According to the given format, a model file of different resolutions is generated, and then when modeling real-time rending, a series of irregular grids is used to imitate the terrain. According to their distance from the point of view and complexity of the terrain, we choose the relevant resolution terrain model within sight of the study area that is the closest to the view point. The more complex the terrain is, the higher the terrain series are, the more triangle grids in the drawing area, the more sophisticated the display terrain, and the higher the resolution. Conversely, if the view point is farther away or the terrain is flat, the series of the topography of the area shows will be lower, the number of mesh triangles will be fewer, the terrain rougher, and the resolution lower. Thus, minimizing the number of triangles and reducing memory consumption can make the images and models have identical effects or gaps in a given range, closest to the real terrain.

In this paper we take the improved adaptive quaternary tree to construct layers of details. The quaternary tree index and the grading mode of organization management for large-scale three-dimensional scenes can provide the chance for real-time interactive roaming analysis. In order to ensure the smoothness of scene rendering, we adopt a pre-loaded cache before the scene into the visible range. Then based on real-time rendering of the scene's rectangular range and the quaternary tree index, we can access related scenes' serial numbers quickly, which can be pre-loaded into memory. The scheduling management strategy can improve the rendering efficiency significantly, achieve real time, interactive terrain rendering, and improve the efficiency of disaster evaluation and analysis in the 3D environment.

4.2 Three-dimensional terrain modeling and visualization

Exposed areas along the river valley include a regional north-east-trending thrust fault. The area exhibits many faults and tectonites, which are weak and vulnerable and form the detachment surfaces. Due to the earthquake's physical destruction combined with heavy rain, a large number of landslides, mud-rock flows, and other geological disasters occurred. Our system provides a qualitative and quantitative analysis and monitoring of these secondary disasters. A 3D system for the analysis of secondary disasters has the following advantages:

1. The three-dimensional system can reproduce the true disaster scene, and secondary disasters can be observed directly, including landslides and debris flows and their causes, occurrence and trends (Figure 8a).
2. Using DEM data, the analysis of landslide height and volume can give quantitative estimates of damage due to the scope and extent of landslides.
3. The visual angle can rotate in a 3D system; providing omnidirectional observation of the target, which has obvious advantages in making decisions about rescue routes and strategies.

One example is a statistical analysis of the secondary disaster in Chenjiaba. High-resolution aerial remote sensing images from May 28 were integrated into the system. The system gives information on landslides and mud-rock flows in the area from Beichuan County, Zhixin Village, to Pingwu County Yaogouli. The study identifies the Chenjiaba section landslide debris and other secondary geological disasters as the most serious. The system also marks the distribution of the disaster and builds disaster level categories. There is a total of 135 landslides, covering an area of 508 square kilometers, 38 dilapidations, covering 75.6 square kilometers, and 9 mud-rock flows covering an area of 23.9 square kilometers.

The overlap rate between two adjacent high-resolution images of the disaster area from airborne remote sensing is high. Using this characteristic and remote sensing image processing, the images can generate red and blue stereopairs. Through red and blue stereo glasses, they can show the 3D Spatial Information of buildings in the disaster area intuitively and greatly improve the identification and extraction efficiency of housing damage information. The identification accuracy of semi-damaged buildings increases to more than 10%.

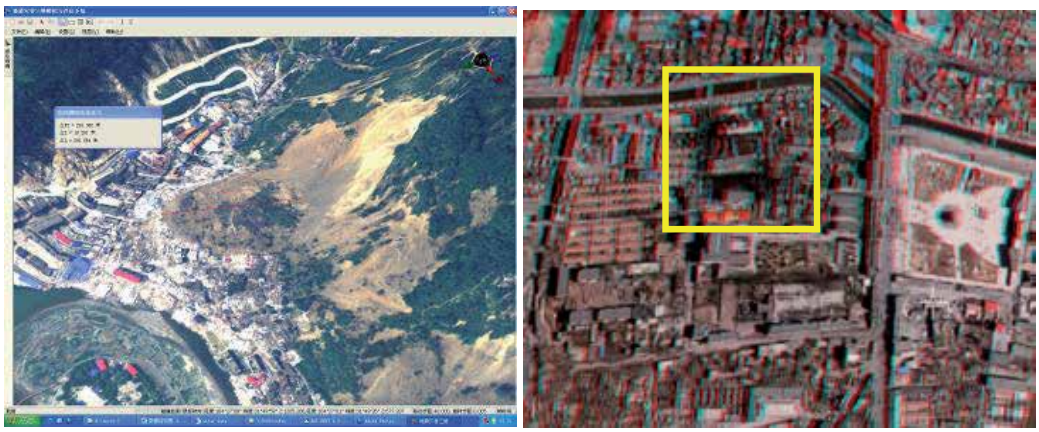

(a) (b)

Fig. 8. (a) 3D analysis of secondary geological disasters in the Wenchuan earthquake, (b) 3D view in red-blue mode for damaged building extraction.

5. Conclusion

Remote sensing monitoring of the Wenchuan and Yushu earthquakes' secondary geological disaster shows that high-resolution optical remote sensing, which can extract the seismic secondary disaster remote sensing characteristics accurately and monitor and evaluate the information of spatial distribution, damage degree and so on of earthquake secondary geological disasters has some advantages, such as intuition, large information and quantification. SAR has the advantages of all-weather data acquisition. The Yushu earthquake multi-mode SAR remote sensing monitoring study has proven that multi-mode SAR is effect and has important potential in earthquake disaster analysis and evaluation. Three-dimensional computing technology for measuring secondary geological disasters is an important technology, which not only improves the calculation and simulation accuracy of secondary geological disasters, but also can promote collaboration on three-dimensional simulation technology and auxiliary mitigation and provide analysis platforms for interactive operation in secondary geological disasters.

In addition, quantitative and reliable evaluation of secondary earthquake disaster depends on high-resolution Earth observation technology. But at present the automatic disaster monitoring algorithms and software for high-resolution Earth observation images still cannot meet actual needs, and 3D interactive analysis platform technology is still not mature. Meanwhile, secondary geological disaster monitoring relies heavily on traditional man-machine interactive visual interpretation technology.

6. Acknowledgement

The authors would like to thank all of the team members who participated in the Wenchuan Earthquake Disaster Reconstruction, Monitoring and Assessment Using Remote Sensing Technology.

This work was supported by the National Basic Research Program of China (2009CB723906, 2009CB723902) and National Natural Science Foundation of China (60972141).

7. References

Ainsworth T L, Schuler D L, Lee J S. Polarimetric SAR characterization of man-made structures in urban areas using normalized circular-pol correlation coefficients. Rem Sens Environ, 2008, 112: 2876–2885

Chen Yuntai, Xu Lisheng, Zhang Yong et al., Report on the Wenchuan large earthquake source of May 12, 208, http://www.csi.ac.cn/Sichuan

Cloude S R, Pottier E. A review of target decomposition theorems in radar polarimetry. IEEE Trans Geosci Rem Sens, 1996, 34: 498–518

Cloude S R, Pottier E. An entropy based classification scheme for land applications of polarimetric SAR. IEEE Trans Geosci Rem Sens, 1997, 35: 68–78

Cui Peng, Wei Fangqiang, He Siming et al. 2008. Mountain disasters induced by the earthquake of May 12 in Wenchuan and the disasters mitigation. JOURNAL OF MOUNTAIN SCIENCE, 26(3):.280-282(In Chinese)

Deng Qidong, Ran Yongkang, Yang Xiaoping. 2007. Active tectonic map of China. Beijing: Earthquake Press (In Chinese)

Ermini L. and Casagli N. 2003. Prediction of the behavior of landslide dams using a geomorphological dimensionless index. Earth Surface Processes and Landforms, 28(1): 31-47.

F.Mattia, T.Le Toan, J. C.Souyris, G.D.Carolis, N.Floury,and F.Posa, The effect of surface roughness on multifrequency polarimetric SAR data . *IEEE Trans Geosci Rem. Sens.*, vol. 35, no. 4, pp. 954−966, July 1997

Fu Bihong, Shi Pilong, Zhang Zhilong. 2008. Spatial characteristics of the surface rupture rroduced by the MS 8.0 Wenchuan earthquake using high-resolution remote sensing imagery. ACTA GEOLOGICA SINICA, 82(12): 1679-1687(In Chinese)

Ge Yong, Xu Jun, Liu Qingsheng, et al. 2009. Image interpretation and statistical analysis of vegetation damage caused by the Wenchuan earthquake and related secondary disasters. Journal of Applied Remote Sensing, 3, 031660.

Guo H D, Liao J J,Wang C L et al. 1997. Use of multifrequency,multipolarization shuttle imaging radar for volcano mapping in the kunlun mountains of western China. Remote Sensing of Environment, 59:364-374.

Guo H D, Zhu L P,Shao Y et al. 1996. Detection of structural and lithological features underneath a vegetation canopy using SIR-C/X-SAR data in Zhao Qing test site of southern China. Journal of Geophysical Research, 101(E10): 23101-23108.

Guo Huadong, Liu Hao, Wang Xinyuan, et al. 2000. Subsurface old drainage detection and paleoenvironment analysis using spaceborne radar images in Alxa Plateau, Science in China Series D: Earth Sciences, 43(4): 439-448.

Guo Huadong, Liu Liangyun, Lei Liping, et al. 2010a. Dynamic analysis of the Wenchuan Earthquake disaster and reconstruction with 3-year remote sensing data, International Journal of Digital Earth, 3(4):355–364.

Guo Huadong, Wang Xinyuan, Li Xinwu, et al.. 2010b. Yushu earthquake synergic analysis using multimodal SAR datasets. Chinese Science Bullet, 55(31): 3499-3503.

Guo Huadong. 2000. Radar for Earth observation: Theory and Applications, Beijing: Science Press(In Chinese)

Han Yongshun, Liu Hongjiang, Cui Peng, et al. 2009, Hazard assessment on secondary mountain-hazards triggered by the Wenchuan earthquake. Journal of Applied Remote Sensing, 3, 031645.

Huang Xiaoxia, Wei Chenjie, and Li Hongga. 2009. Remote sensing analysis of the distribution and genetic mechanisms of transportation network damage caused by the Wenchuan earthquake. Journal of Applied Remote Sensing, 3, 031650.

Jin Feng, Shen Xuhui, Hong Shunying, Ouyang Xinyan. 2008. The application of remote sensing in the earthquake science research. Remote Sensing for Land&Resources, (2): 5—8(In Chinese)

Lei Liping, Liu Liangyun, Zhang Li, et al. 2009. Assessment of spatial variation of the collapsed houses in Wenchuan earthquake with aerial images. Journal of Applied Remote Sensing, 3, 031670.

Li ping, Tao xiaxin, Yan shiju. 2007. 3S-based quick evaluation of earthquake damage, Journal of natural Disasters, 16(3):110-113 (In Chinese)

Liou Yuei-An, Kar Sanjib K.; Chang Liyu. 2010. Use of high-resolution FORMOSAT-2 satellite images for post-earthquake disaster assessment: a study following the 12 May 2008 Wenchuan Earthquake. International Journal of Remote Sensing, 31(13):3355 – 3368.

Liu Liangyun, Wu Yanhong, Zuo Zhengli, et al.. 2009. Monitoring and assessment of barrier lakes formed after the Wenchuan earthquake based on multitemporal remote sensing data. Journal of Applied Remote Sensing. 3, 031665.

Massonnet D., Feigl K. 1998. Radar interferometry and its application to changes in the Earth's surface. Reviews of Geophysics, 36(4):441-500.

Paul Rosen, Scott Hensley, Ian R. Joughin, et al. 2000. Synthetic aperture radar interferometry. Proceedings of the IEEE, 88(3):333–382

Ramesh P. Singh. 2010. Satellite observations of the Wenchuan Earthquake, 12 May 2008. International Journal of Remote Sensing, 31(13):3335 – 3339.

Wang Erqi, Zhou Yong, et al. 2001. Geologic and geomorphic origins of the east Himalayan gap. Chinese Journal of Geology (SCIENTIA GEOLOGICA SINICA), 36(1):122-128(In Chinese)

Wang Shixin, Zhou Yi, Wei Chengjie, ShaoYun, Yan Fuli. 2008. Risk Evaluation on the secondary disasters of dammed lakes using remote sensing datasets，in the‘Wenchuan Earthquake. Journal of Remote Sensing, 12(6):900-907(In Chinese)

Xiao lebin, Zhong ershun, Liu jiyuan, Song guanfu, 2001, A Disussion on Basic Problems of 3D GIS, Journal of Image and Graphics, 6(9): 842-848. (In Chinese)

Xu Min, Cao Chunxiang, Zhang Hao, et al. 2010. Change detection of an earthquake-induced barrier lake based on remote sensing image classification. International Journal of Remote Sensing, 31(13): 3521 – 3534.

Xu Weihua, Dong Rencai, Wang Xuezhi, et al. 2009. Impact of China's May 12 earthquake on Giant Panda habiat in Wenchuan County. Journal of Applied Remote Sensing, 3, 031655.

Zhang Wenjiang, Lin Jiayuan, PengJian, et al. 2010. Estimating Wenchuan Earthquake induced landslides based on remote sensing. International Journal of Remote Sensing, 31(13): 3495 – 3508.

Zhang Yong, Xu Lisheng, Chen Yuntai, et al. 2010. Fast inversion of rupture process for 14 April 2010 Yushu, Qinghai, earthquake. Acta Seismologica Sinica, 32(3): 361-365(In Chinese)

Zhuang JianQi, Cui Peng, Ge YongGang, et al. 2010. Probability assessment of river blocking by debris flow associated with the Wenchuan Earthquake. International Journal of Remote Sensing, 31(13):3465 – 3478.

15

Earthquake Observation by Social Sensors

Takeshi Sakaki and Yutaka Matsuo
The University of Tokyo
Japan

1. Introduction

Many studies have examined observation and detection of earthquakes using physical sensors. These systems require highly accurate physical sensors located over a broad area, necessitating great expense to set up the supporting infrastructure.

Social media have garnered much attention recently and the number of social media users has been increasing. Social media are kinds of media for social interaction among users. Users create contents for themselves and exchange them on social media. Social media include many kinds of forms, including weblog, wikis, videos and microblogs. One of the biggest characteristics of social media is *user-generated contents*.

Social media users often make posts about what happened around them: live performance, sports events and natural disaster, including earthquake. Figure 1 depicts the graph of tweet counts and the sizes of earthquake on March 11th 2011, the day of the Great Eastern Japan Earthquake. It is apparent that tweet counts and earthquake occurrences are correlated. It means that when earthquakes occurs, social media users make posts about those earthquakes.

Along with the popularization of social media, new methods for earthquake observation are appearing. These method use information about earthquakes posted on the internet by users. For example, the web site *Did You Feel It?*, operated by the United States Geological Survey (USGS), gathers earthquake information from web-site users through a

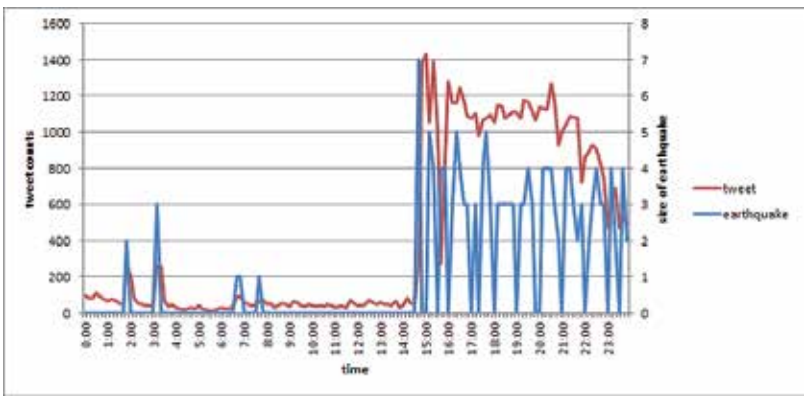

Fig. 1. Size of earthquakes and change of tweet counts on the day of the Great Eastern Japan Earthquake

questionnaire format(Intensity, 2005). From the Twitter web-site, *Toretter* extracts tweets that refer to earthquakes and estimates the location of an earthquake's epicenter using location information included with those tweets(Sakaki et al., 2010)

These methods treat social media users as sensors. We designate these virtual sensors as *social sensors*, which entail no costs. Unfortunately, such sensors provide a signal that is extremely noisy because users sometimes misunderstand phenomena, sleep, and are not near a computer.

We introduce these methods and explain a process for earthquake detection by analyzing social sensor information. We introduce current studies and services for earthquake observation using *social sensors* . Moreover, we explain *Toretter* as an example and describe its mechanisms.

2. Overview of earthquake observation by social sensors

We explain the basic idea of *social sensors* and introduce internet service users as social sensors to observe earthquakes.

2.1 Earthquake observation services performed by social sensors

We introduce four earthquake observation services that use information from internet users. In this chapter, we examine Toretter as an example. We explain its detailed mechanisms in the next chapter.

Did You Feel It?

The web site *Did You Feel It?*, which is operated by United States Geological Survey (USGS), is shown in Fig. 2. Through the internet, it gathers earthquake information from users who experienced those earthquakes directly (Intensity, 2005).

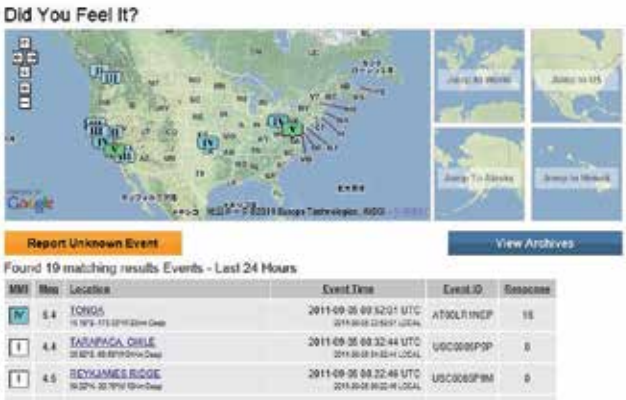

Fig. 2. Screenshot of *Did You Feel It*?

TED

The USGS also manages the Twitter Earthquake Detector (TED), which gathers tweets referring to earthquake occurrences from Twitter. They acquire location information and photographs attached to tweets and show this information related to maps(Survey, 2009).

iShake

The iShake project has developed a smartphone application (Fig. 3) that uses a phone to measure acceleration during an earthquake and report those data to researchers for processing (CITRIS, 2011). This project, conducted by UC Berkeley, is designed to create a system that moves beyond *Did You Feel It?*. Data from smartphone applications can complement data obtained from ground monitoring instruments, thereby improving the resolution and accuracy of earthquake intensity maps.

Fig. 3. Screenshot of *iShake*.

Toretter

Toretter extracts tweets referring to earthquakes and estimates the location of the earthquake epicenter using location information of those tweets(Sakaki et al., 2010). A temporal model and spatial model for earthquake detection are defined by social sensors. Then methods are proposed to detect earthquakes and to estimate the location of an earthquake epicenter automatically.

The Toretter mechanism is shown in Fig. 4.

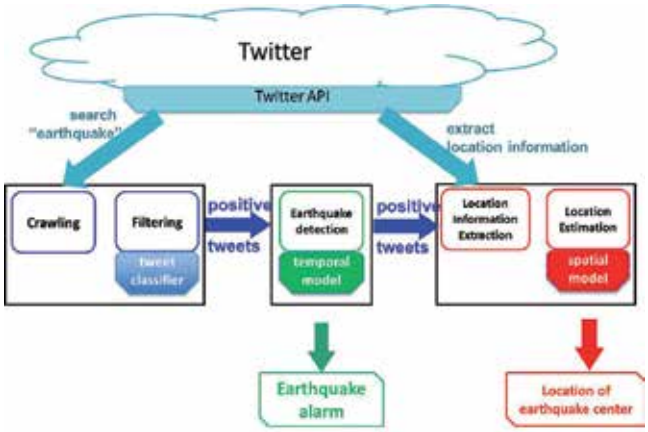

Fig. 4. Image of the Toretter mechanism.

First it collects tweets referring to earthquakes by crawling with the Twitter API and filtering the tweet messages using a tweet classifier. Second it tries to detect an earthquake from collected tweets based on a temporal model for earthquake detection. Finally, it extracts location information for each tweet from Twitter. The system uses that information and a particle filter to estimate the earthquake epicenter based on a spatial model for social sensors.

In this chapter, we explain methods of earthquake observation using social sensors according to the Toretter mechanism. We explain this entire process in the following section.

2.2 Overview of social sensors

We introduce the mode of *social sensors* and describe their features in comparison to physical sensors.

2.2.1 Basic idea of social sensors

Many methods and infrastructure can be used to observe events and natural phenomena using physical sensors: heavy traffic, air pollution, astronomical events, weather phenomena, and earthquakes are some examples. The basic mechanisms of such observations by physical sensors are presented on the right side of Fig. 5. First, a target event for observation occurs. Second, some sensors for the target event respond with a positive signal. Third, a central server collects signals from sensors and analyzes them. Finally, the server detects the target event or produces some observation values as output.

If users of social media observe an event, then similarly to physical sensors, they make posts about the event. For example, some Twitter users might post "Oh earthquake!" or "pouring rain, thunder & lightning " or "It's a double rainbow! & the moon is out. Beautiful!". These actions by users are analogous to the response of physical sensors to a stimulus: the users and sensors send a signal when an event occurs. Therefore, a user of social media is a sensor of a kind. We designate such sensors as social sensors.

An observation system incorporating social sensors is depicted on the left side of Fig. 5. First, an event occurs. Second, social media users make posts about the event. Third, the posts are collected at a central server and analyzed. Finally, the server detects the event or produces some observation value. This whole process corresponds to a process of observation by physical sensors, presented for comparison in Fig. 5

Methods for observing phenomena by physical sensors can be adapted to social sensors. Actually, some services based on social media use methods of observation resembling methods used with physical sensors.

Regarding Twitter users as social sensors, we can work with the following assumption.

1. Each Twitter user is regarded as a sensor. A sensor detects a target event and makes a report probabilistically.
2. Each tweet is associated with a time and location, which is a latitude–longitude pair.

2.2.2 Features of social sensors

Social sensors differ from physical sensors in some points. We describe features of social sensors in comparison to physical sensors.

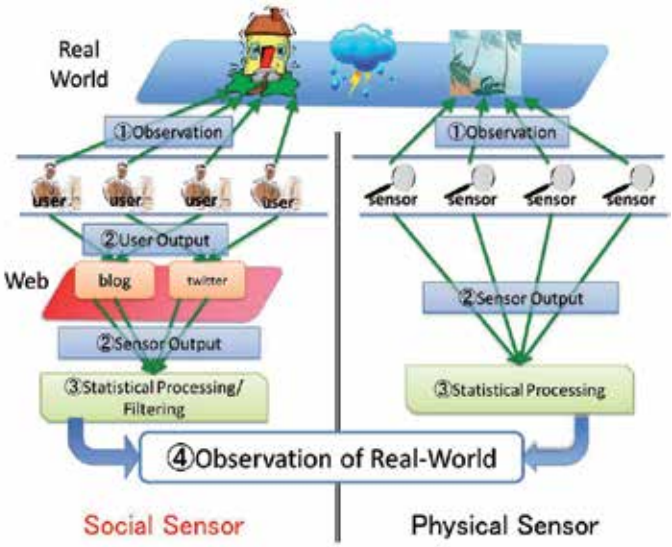

Fig. 5. Correspondence between event observation by social sensors and by physical sensors.

Social sensors are uncontrollable. They sometimes become inoperable because some users are not on-line; maybe they are sleeping or busy doing something else. They also function improperly more often than physical sensors because users misinterpret events more often than physical sensors. Therefore, it is necessary to know that social sensors are noisier than physical sensors and that their signals must be analyzed more carefully.

Social sensors, which are users of social media, are located over a wide area. They can give responses to events of many kinds, ranging from natural phenomena, such as earthquakes and hurricanes, to events related to human activities, such as heavy traffic, live performances, and elections. The extremely numerous social sensors all over the world present the possibility of responding to events of many kinds. In other words, detection of target events can be done with no cost to set up sensors. However, when using social media systems such as Twitter, which incorporate these social sensors, it is necessary to filter the signals (tweets) posted by social sensors (Twitter users) according to the event that is to be observed. Using some method, it is necessary to extract tweets referring to a target event. We summarize the features of social sensors and physical sensors in Table 1.

We explain these methods in the next section.

3. Tweet collection

In the first step portrayed in Fig. 4, it is necessary to collect tweets referring to an earthquake from Twitter. This process includes two steps: crawling tweets from Twitter and filtering out

features	physical	social
accuracy	high accuracy	noisy
versatility	target events only	event of any kind
cost	high	very low
processing	simple	complex

Table 1. Features of physical sensor and social sensors.

tweets that do not refer to the earthquake. For crawling and filtering tweets, we recommend using script programming languages, such as Python, PERL, and Ruby.

3.1 Crawling tweets from Twitter

To collect tweets or some user information from Twitter, one must use the Twitter Application Programmers Interface (API). Twitter API is a group of commands that are necessary to extract data from Twitter. Twitter has APIs of three kinds: Search API, REST API, and Streaming API. In this section, we introduce Search API and Streaming API, which are necessary to crawl tweets from Twitter. We explain REST API later because REST API is necessary to extract location information from Twitter information.

Additionally, it is known that Twitter API specifications are subject to change. When using Twitter API, it is necessary to know the latest details and requirements. They are obtainable from Twitter API documentation[1].

3.1.1 Twitter Search API

The Twitter Search API extracts tweets from Twitter, including search keywords or those fitting other retrieval conditions, in chronological order. It is possible to use language, date, location and other conditions as retrieval conditions.

When searching tweets including *earthquake* posted from 1 Aug 2011 to 5 Aug 2011, one might access the following URL:

http://search.twitter.com/search.json?q=earthquake&since=2011-09-01&until=2011-09-05

tweet time	user	tweet text
2011-09-04 04:47:10	user 1	The truth of 311 seismic terror.http://t.co/R9I6U9w 911 #earthquake #fukushima #japan #CNN #tsunami #prayforJapan
2011-09-04 04:47:09	user 2	FML! What did I say?! @..... RT @.... 24 HOUR EARTHQUAKE WARNING for San Diego, - 6.0+ likely - hey @....
2011-09-04 04:47:08	user 3	ML 2.3 SOUTHERN GREECE: Magnitude ML 2.3Region SOUTHERN GREECEDate time 2011-09-04 04:37:42.0 UTCLocation ...

Table 2. Search results of keyword *earthquake* after the conversion.

It is possible to obtain results in Fig. 6, as described in JavaScript Object Notation (JSON) format, which is a text-based open standard designed for human-readable data. It is possible to convert this result in Fig. 6 into Table 2 by parsing the result using a script programming language. Parameters that are often used to collect tweets are shown in Table 3 (This table is referred to Twitter API Documentation[2]).

[1] https://dev.twitter.com/docs
[2] https://dev.twitter.com/docs/api/1/get/search

Fig. 6. Search results from Twitter Search API.

name	explanation	required	value
q	search keywords	required	-
rpp	the number of tweets to return per page	optional	up to 100
result type	search result of type	optional	mixed/recent/popular
until	tweets before the given date	optional	before today
since	tweets after the given date	optional	after 5 days ago
lang	restricts tweets to the given language	optional	jp/en/all/others

Table 3. Search conditions of Twitter Search API.

Some points must be considered when using Twitter Search API:

- It is possible to collect tweets posted only during the prior five days. It is not possible to search tweets posted six days ago.
- It is only possible to collect the latest 1500 tweets at one time.
  (Technically speaking, it is possible to access one page with a request and track pages back to the 15th page. One page includes 100 tweets at most. Therefore it is possible to acquire the latest 1500 tweets at one time.)
- One is limited to API requests.
  (No limit is published, but it is possible to access the Twitter Search API at least 500 times per hour.)

Therefore, we recommend the collection of tweets every 10 min or more often because it is impossible to crawl all tweets including *earthquake* if those tweets are posted at 2000 tweets per hour and one uses Twitter Search API every hour. Actually, tweets including *earthquake* were posted at more than 5000 per hour when the earthquake occurred on March 11, 2011.

Toretter requests the API command *search* 15 times every 5 min to collect the latest tweets each time: 180 command executions per hour.

3.1.2 Twitter Streaming API

The Twitter Streaming API extraction is defined in Twitter API documentation as follows:

The Twitter Streaming API enables high-throughput near-real-time access to various subsets of public and protected Twitter data.

Twitter Streaming API provides some methods shown in Table 4, of which *filter* method can be used to crawl tweets related to earthquakes.

command	explanation
filter	returns public statuses that match one or more filtering conditions.
firehose	returns all public statuses. A few companies have permission to access this command.
link	returns all statuses containing http: and https:.
retweet	returns all retweets
sample	returns a random sample of all public statuses.(ratio is about 1%)

Table 4. Streaming API methods.

Filter method returns public statuses that match one or more filtering conditions. All conditions of *filter* are presented in Table 5. It is possible to use the parameter *track* to collect tweets because keywords can be set as a condition value of *track*.

command	explanation
follow	returns public statuses that reference the given set of users.
track	returns public statuses that include specified keywords.
locations	returns public statuses that posted from a specific set of bounding boxes to track.

Table 5. Conditions of *filter* methods.

When using a *filter* command with the parameter keyword, *earthquake*, it is necessary to create a file called *tracking* that contains *track=earthquake*. Then one can access the following URL:

https://stream.twitter.com/1/statuses/filter.json

Streaming API also returns results in the form of JSON, shown in Fig. 6. Therefore, it is possible to parse those results in the same way as results obtained with Search API.

It is possible to collect tweets including *earthquake* in real time. Some points must be considered when using Twitter Streaming API:

- The prepared server must have sufficiently high specifications to process all data received from Twitter.
- It is impossible to use some characters in Twitter Streaming API
  (e.g., Japanese characters can not be used in Twitter Streaming API).

Using Toretter, we want to detect earthquakes in Japan. For that purpose, it is necessary to collect tweets including *earthquake* in Japanese. However, Japanese characters cannot be used in Twitter Streaming API. Therefore, Toretter uses the Twitter Search API to crawl tweets. To collect tweets of languages other than English, it is necessary to check whether that language is supported by the Twitter Streaming API.

tweet	real-time
SYF News: Magnitude 7.0 earthquake shakes Vanuatu; no tsunami alert	no
HOLY **** EARTHQUAKE	yes
Powerful earthquake rocks Vanuatu, no tsunami warnings (Newkerala)	no
AAAAAAAAAH earthquake !	yes
Holy ****, that earthquake scared the **** outta me	yes
a year on after our very first earthquake... and the shakes are still happening	no

Table 6. Sample tweets and relevance of real-time earthquake detection.

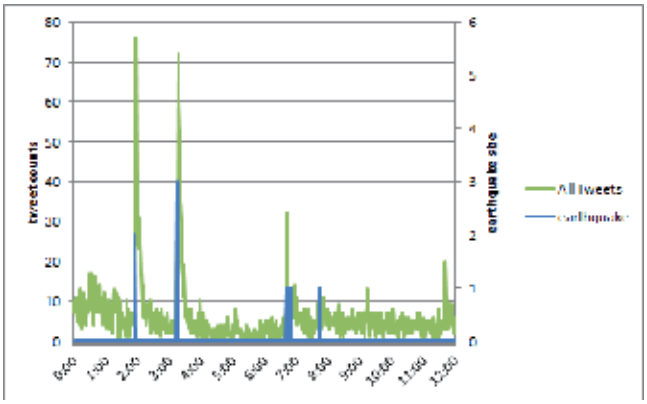

Fig. 7. Size of earthquakes and change of tweet counts on February 11, 2011

3.2 Filtering tweets using machine learning

We collected data from tweets including keywords related to earthquakes, such as *earthquake*, *shake*. Sample tweets are presented in Table6.

Those tweets include not only tweets that users posted immediately after they felt earthquakes, but also tweets that users posted shortly after they heard earthquake news, or perhaps they misinterpreted some sense of shaking from a large truck passing nearby. Figure 7 presents sizes of earthquakes and counts of Japanese tweets including the keyword *earthquake* on February 11, 2011. When the seismic activity reached its peak, the graph of tweets invariably showed a peak. However, when the graph of tweet counts showed a peak, the seismic activity did not necessarily show a peak. Some "false-positive" peaks of the graph of tweet counts arise from mistakes by users or some news related to earthquakes. Therefore, we must filter tweets to extract those posted immediately after the earthquake. We designate tweets posted by users who felt earthquakes as *positive* tweets, and other tweets as *negative* tweets.

Here, we describe the creation of a classifier to categorize crawled tweets into *positive* tweets and *negative* tweets, using Support Vector Machine: a supervised learning method.

3.2.1 Supervised learning

Supervised learning, a machine learning method, solves classification problem and regression problems analyzing training data. It is often used for spam mail filtering and gender estimation of Web users.

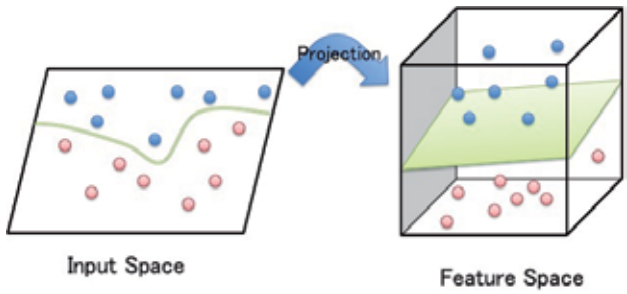

Fig. 8. Mechanism of Support Vector Machine.

Toretter uses Support Vector Machine (SVM), an extremely effective supervised learning method.

3.2.1.1 Support Vector Machine

SVM is a method used to create a classifier for two-class pattern classification. The SVM projects each training sample as points (as presented on the left side of Fig. 8) into multi-dimensional feature space. It creates a hyperplane that has the largest distance to the nearest training sample points of each class (as presented on the right side of Fig. 8). One must input positive samples and negative samples into SVM, which creates a classifier for two classes by searching the hyperplane.

To study them in detail, several books are useful (Bishop, 2006).

3.2.1.2 Process of creating a classifier using machine learning

Figure 9 depicts the process of supervised learning, which has three steps. We explain this process using an example of creation of a spam filter along the lines of Fig. 9

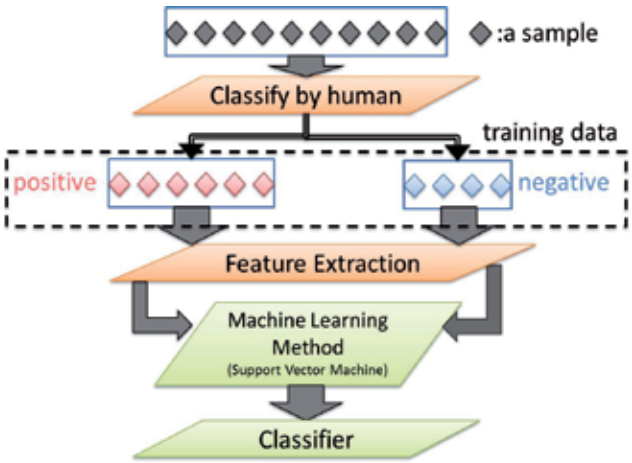

Fig. 9. Process of Machine Learning.

First, we prepare both sample collections of spam mails as positive samples and those of other mails as negative samples. Those must be classified manually by humans.

Second, we extract various features from samples. We must select effective features for classification. Effective features are those which positive samples seem to have and which negative samples do not seem to have, or vice versa. For example, all words included in samples are often used to create spam filters because we can infer that spam messages include words such as "Free!", "50% off!", and "Call now!" with high probability.

Third, we input both positive samples and negative samples with feature information and create a classifier for those samples. If inputting a new mail into the classifier, then it outputs a positive value or a negative value. If the output is positive, the new mail is regarded as a spam message.

3.2.2 Creation of sample data for the classifier

Positive samples and negative samples must be created manually. There are two points of consideration.

First, this process is very sensitive. One must classify positive tweets and negative tweets accurately. Therefore, it is necessary to acquire records of actual earthquakes. One must choose positive tweets referring to these earthquake records to classify them precisely.

Second, one must prepare equal numbers of positive tweets and negative tweets. The number of samples needed depends on the task. Generally, it is said that sample data must comprise 300–500 samples. Actually, one should increase the number of samples until finding the classification which provides sufficient performance.

3.2.3 Extraction of features from sample data

Next, one must select features of tweets for machine learning. In the spam mail filter example, words included in sample mails are chosen as features. Toretter uses features of three kinds. We explain them in detail and use the following sentence for explanation.

Oh! Earthquake happened right now!

Keyword features all words included in a tweet.
example sentence → Oh, earthquake, happened , right, now

Statistical features number of words in a tweet message and the position of the search keyword within a tweet
example sentence → number of words: *five*, the position of the search keyword: *second*

Context features words before and after a search keyword.
example sentence → *Oh*, *happened*

Statistical features are the most effective in these three features according to results of our earlier research(Sakaki et al., 2010). It is guessed that this is true because people who came across an earthquake were surprised and in an emergency situation so that they tend to post short tweets such as "Oh! earthquake!" and "It's shaking".

Of course, these features can differ depending on language, country, and culture. Therefore, effective features should be chosen when creating a filter for tweets.

feature ID	feature	feature ID	feature
0	I	1	am
2	in	3	Japan
4	earthquake	5	right
6	now		
7	*number of words in tweets*		
8	*position of search keyword*		
9	*word before keywords* is Japan		
10	*word after keywords* is right		

Table 7. Sample features for SVM-Light.

3.2.4 Applying machine learning

Some machine learning methods can create a classifier for any problem: Naive Bayes classifier, Neural Networks, Decision Tree, and Support Vector Machine. In this chapter, Support Vector Machine is used for our explanation because it is said that SVM is a superior method for classification problems and regression problems, and many SVM software packages exist. We treat SVM-Light, which is a popular SVM tool, as an example in this chapter.

Creating a classifier demands three steps.

3.2.4.1 Create training data from tweets

First, it necessary to convert tweet data into a training data file format for SVM-Light. The training data file format of SVM-Light is

<target> <feature>:<value> <feature>:<value> ... <feature>:<value> # <info>
-1 1:0.43 3:0.12 9284:0.2 # abcdef

In this file format, each line corresponds to a single tweet. **<target>** expresses a polar of each tweet. $+1$ means positive and -1 means negative. **<feature>** expresses a feature ID of each feature and **<value>** expresses the weight of each feature in the tweet. Each feature should be assigned to each feature ID. For example, if one assigns each feature to each feature ID, as in Table 7, then a tweet conversion into a training data for SVM-Light as shown below.

I am in Japan, earthquake right now $\rightarrow$ +1 0:1 1:1 2:1 3:1 4:1 5:1 6:1 7:7 8:5 9:1 10:1

You must run the following command to create a classifier for tweets after converting positive tweets collected into a training data file *training data file*.

svm_learn *"training data file" "model file"*

svm_learn is a command in SVM-Light to create a model file for classifier. After running *svm_learn*, it is possible to obtain *model file* as an output of *svm_learn*. It is possible to classify the tweet command *svm_classify* with this model file. When classifying new tweets into a positive class and negative class, each tweet is converted into *test data* in the same format as *training data*. Then the following command is executed.

svm_classify *"test data file" "model file" "output file*

It is possible to obtain polars of each tweet in the *output file* New tweets are classifiable into a positive class and negative class by the classifier for tweets as described.

SVM-Light(Joachims, 2008), LIBSVM(Chih-Chung & Chih-Jen, 2011), and Classias(Okazaki, 2009) have compatibility such that the process we explain here is applicable to LIBSVM and Classias. (Toretter uses Classias for SVM tools.)

4. Earthquake detection from a time-series data using a probabilistic model

The second step of Fig. 4 detects an earthquake from positive tweets.

First, it is difficult to believe these tweets directly because some users misinterpret shaking caused by something other than an earthquake. Some ill-willed users post positive tweets to deceive others. This closely resembles physical sensors, and sometimes produces a wrong value. Therefore, we must process positive tweets to detect earthquakes with high accuracy, similarly to treating physical sensors.

Figure 10 depicts the sizes of earthquakes and counts of positive tweets filtered by SVM on Feb 11 2011. These two graphs are correlated: whenever an earthquake occurs, a peak appears in the graph of positive tweet counts. Therefore, we can detect earthquakes by detecting the peaks of positive tweet counts.

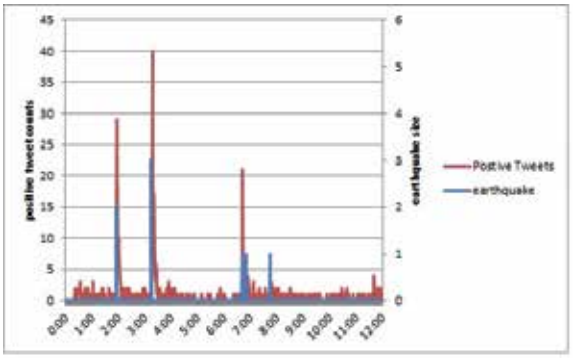

Fig. 10. Sizes of earthquakes and changes of filtered tweet counts Feb 11 2011.

Many methods have been used to detect peaks from time-series data for purposes such as burst detection(Kleinberg, 2002; Zhu & Shasha, 2003) and anomaly detection(Cheng et al., 2008; Krishnamurthy et al., 2003). Toretter uses a static rule *5 tweets in 5 min* that is calculated using an exponential function. We explain this method hereinafter.

4.1 Temporal model

To detect an earthquake using physical sensors, we must calculate the probability of earthquake occurrence based on signals from those sensors. Similarly, we must calculate the probability of earthquake occurrence from signals of social sensors. In this subsection, we explain the temporal model we use to calculate this probability.

Figure 11 presents graphs of positive tweet counts during earthquakes. In Fig. 11, the green line shows an exponential function. As shown here, the green line resembles the red line,

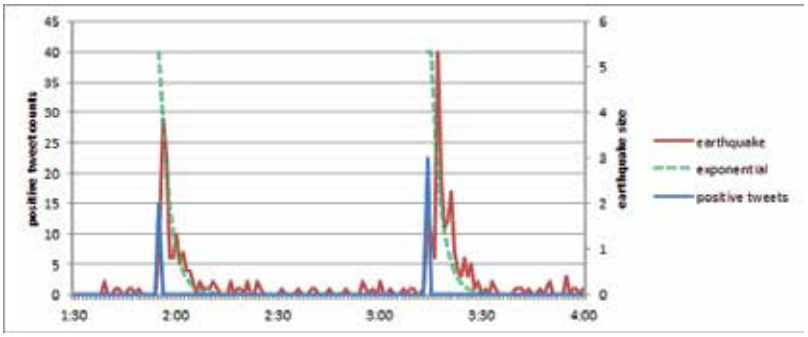

Fig. 11. Number of Tweets and Exponential Curve.

the graph of positive tweet counts. It can be inferred from these graphs that this frequency distribution of positive tweets is an exponential distribution, as expressed by the following equation(Sakaki et al., 2010).

$$f(t\lambda) = ke^{-\lambda t} \tag{1}$$

We express the number of sensors producing positive value at time t in $n(t)$. Here, $n(t)$ is equal to the number of positive tweets at time t. If n_0 sensors produce positive value at $t = 0$, then we can calculate the number of sensors for which the response is a positive value at time t using the following equation.

$$n(t) = n_0 \cdot e^{-\lambda t} \tag{2}$$

Therefore, we can calculate N_{t_a}, the number of sensors that produce a positive value from time 0 to time t_a, as presented below.

$$\begin{aligned} N_{t_a} &= \sum_{t=0}^{t_a} n(t) \\ &= n_0 \sum_{t=0}^{t_a} e^{-\lambda t} \\ &= n_0 \frac{1 - e^{-\lambda(t_a+1)}}{1 - e^{-\lambda}} \end{aligned} \tag{3}$$

We define the false-positive ratio of a sensor as p_f. In this case, we assume that we have n sensors and that all n sensors have the same false-positive ratio equally. The probability of all n sensors producing a false alarm is p_f^n. Therefore, the probability of earthquake occurrence can be estimated as

$$P(n) = 1 - p_f^n. \tag{4}$$

From Eq. 3, Eq. 4, we can calculate the probability of earthquake occurrence at time t_a.

$$\begin{aligned} p_{occur}(t) &= 1 - p_f^{N_{t_a}} \\ &= 1 - p_f^{n_0\left(1-e^{-\lambda(t_a+1)}\right)/\left(1-e^{-\lambda}\right)} \end{aligned} \tag{5}$$

4.2 Setup the condition for detection trigger

In the Toretter system, we detect an earthquake when *five positive tweets arrive in 5 min*, which means *five sensors produce positive signals in 5 min*. In this subsection, we explain how to determine this condition.

We set $\lambda = 0.34, p_f = 0.35$ (taken from our earlier research) to Equation (5) , by which we can calculate the probability of earthquake occurrence. When obtaining n_0 positive tweets, and given that we would like to make an alarm with false-positive ratio less than 1%, we can calculate t_{wait} as

$$t_{wait} = -\frac{1}{0.34} log\left(1 - \frac{1.264}{n_0}\right) - 1. \tag{6}$$

If we set $t_{wait} = 5$, then we can calculate $n_0 = 4.1$ from Eq. 6. Therefore, the trigger for earthquake detection is set as *five positive tweets come in 5 min* in Toretter. The trigger used for detection of earthquake calculation can be determined using an exponential function, as described in this section.

5. Location estimation from tweets

In this section, we explain a means to estimate the location of an earthquake epicenter by analyzing tweets. First, we introduce the kinds of location information to be acquired from tweets. Next, we explain methods to estimate the location of the earthquake epicenter.

5.1 Extracting location information from tweets

Two kinds of information are applicable for location estimation from tweets: using location information in the Twitter user profile or using *geotag* attached to tweets.

5.1.1 Location information in user profiles

The twitter user profile includes the location information of users. Of course, not all users make their location information public on the internet, but a sufficient number of users do so (This number varies among countries.).

For earthquake detection, we collect positive tweets. We extract the location information of users who post those positive tweets for earthquake epicenter location estimation. Twitter REST API must be used to extract location information of users from Twitter.

Twitter REST API is one Twitter API included among all methods to use basic functions of Twitter. Many methods of using REST API exist. We use the *users/show* method to obtain user information. To extract user information of Twitter user *TwitterAPI*, it is necessary to access the following URL.

http://api.twitter.com/1/users/show.json?screen_name=TwitterAPI
&include_entities=true

It is possible to obtain results in Fig. 12, which is described in JSON format, in the same manner as that used for Twitter Search API. It is possible to know from the result in Fig. 12 that Twitter user TwitterAPI resides in *San Francisco, CA*.

Some points to consider when using Twitter REST API are the following:

```
[
  profile_sidebar_fill_color: "a9d9f1",
  protected: false,
  id_str: "6253282",
  notifications: false,
  profile_background_tile: false,
  screen_name: "twitterapi",
  name: "Twitter API",
  display_url: null,
  listed_count: 9143,
  location: "San Francisco, CA",
  expanded_url: null,
  show_all_inline_media: false,
  contributors_enabled: true,
  following: false,
  geo_enabled: true,
  utc_offset: -28800,
  profile_link_color: "0094C2",
  description: "The Real Twitter API. I tweet about API changes, service
  about Twitter and our API. Don't get an answer? It's on my website.",
  profile_sidebar_border_color: "0094C2",
  url: http://dev.twitter.com,
  time_zone: "Pacific Time (US & Canada)",
```


Fig. 12. User information extraction from Twitter Search API.

- Some users do not register their location information, or register non-location data, such as *in a dream*, *anywhere*. Such non-location data should be ignored.
- API requests are limited.
  (The limit is published: it is possible to access the Twitter Search API about 150 times per hour without authorization.)

It is possible to access REST API 150 times per hour. This limit is sufficient to extract user information for location estimation of an earthquake epicenter because the earthquake-related tweets posted in the 5 min after an earthquake are most often fewer than 100. To expand the limit, one must register with Twitter and obtain an authorization called OAuth, according to the Twitter API Documentation[3].

Moreover one must convert location information acquired from Twitter into a latitude–longitude pair because human beings can understand places expressed by the names of places, such as *San Francisco*, but a computer can not understand where that place is. One must treat location information in the format of a latitude–longitude coordinate pair. At present, some web services can convert geographical names into a latitude–longitude coordinate pairs, such as the Google Maps API and Yahoo Maps API. Here we explain the Google Maps API.

To convert *San Francisco* into a a latitude–longitude coordinate pair, one can access the following URL.

http://maps.google.com/maps/api/geocode/json?address=San%20Francisco&sensor=false&language=en

Results are obtainable as in Fig. 13, which is described in JSON format, in the same manner as Twitter API. It is possible to convert *San Francisco* into $latitude = 37.7749295$, $longitude = -122.4194155$.

Location information related to an earthquake can be acquired as described above.

[3] https://dev.twitter.com/docs/auth

Fig. 13. Result of geographical name converted using Google Maps API.

5.1.2 Geotags attached to each tweet

Some tweets have an attached geotag, which includes a latitude–longitude pair acquired from GPS. If positive tweets related to an earthquake include tweets with attached geotags, then it is possible to use these geotag data for location estimation. Geotag data can be extracted using the Twitter Search API. Therefore, GPS data can be obtained if stored when using crawl for those tweets by the Twitter Search API.

Geotag data are more accurate than location information of the Twitter user profile because they are acquired from GPS. Nevertheless, it is unusual that positive tweets referring to an earthquake include a sufficient number of tweets with attached geotags to estimate the earthquake epicenter location. Actually, a combination of location information of Twitter users and geotag should be used.

5.2 Location estimation using Bayesian filtering

If one can obtain sufficient location information from positive tweets, then estimating the location of the earthquake epicenter can be done using the information. Nevertheless, that information is often inaccurate. Alternatively if they are precise, then users might still be posting far from the earthquake epicenter. Therefore, it is preferred that the location of the earthquake epicenter be estimated probabilistically.

Several methods can be used to estimate the location of events from sensor readings using Bayesian Filters: Kalman filters, Multihypothesis tracking, Grid-based approaches, Topological approaches, and Particle filters.

We use particle filters as an example for explanation. Particle filters have high performance in belief, accuracy, robustness, and variety according to an evaluation by Fox et al. (Fox et al., 2003). Moreover particle filters work better to detect earthquakes from Twitter in the experiments by Sakaki et al. (Sakaki et al., 2010).

5.2.1 Spatial model

Each tweet is associated with a location. We describe a method that can estimate the location of an event from sensor readings. To define the problem of location estimation, we consider the evolution of the state sequence $\{x_t, t \in \mathbf{N}\}$ of a target, given

$$x_t = f_t(x_{t-1}, u_t), \;\; f_t : \mathcal{R}_t^n \times \mathcal{R}_t^n \to \mathcal{R}_t^n,$$

where f_t is a possibly nonlinear function of the state x_{t-1}. Furthermore, u_t is an i.i.d. process noise sequence. The objective of tracking is to estimate x_t recursively from measurements, as

$$z_t = h_t(x_t, n_t), \;\; h_t : \mathcal{R}_t^n \times \mathcal{R}_t^n \to \mathcal{R}_t^n,$$

where h_t is a possibly nonlinear function, and where n_t is an i.i.d. measurement noise sequence. From a Bayesian perspective, the tracking problem is to calculate, recursively, some degree of belief in the state x_t at time t, given data z_t up to time t.

Presuming that $p(x_{t-1}|z_{t-1})$ is available, the prediction stage uses the following equation.

$$p(x_t|z_{t-1}) = \int p(x_t|x_{t-1})p(x_{t-1}|z_{t-1})dx_{t-1}$$

Here we use a Markov process of order one. Therefore, we can assume that

$$p(x_t|x_{t-1}, z_{t-1}) = p(x_t|x_{t-1}).$$

In the update stage, Bayes' rule is applied as

$$p(x_t|z_t) = p(z_t|x_t)p(x_t|z_{t-1}) / p(z_t|z_{t-1}),$$

where the normalizing constant is

$$p(z_t|z_{t-1}) = \int p(z_t|x_t)p(x_t|z_{t-1})dx_t.$$

To solve the problem, several methods of Bayesian filters are proposed such as Kalman filters, multi-hypothesis tracking, grid-based and topological approaches, and particle filters. For this study, we use particle filters, both of which are widely used in location estimation.

Additionally, we must consider the nonuniform distribution of Twitter users when we apply Bayesian filters to *social sensors* because *social sensors* are arranged non-uniformly to a greater degree than normal physical sensors are.

5.2.2 Location estimation using a particle filter

A particle filter is a Bayes filter that approximates a state probabilistically. It is a sequential Monte Carlo method. For location estimation, we maintain a probability distribution for the location estimation at time t, designated as the belief $Bel(x_t) = \{x_t^i, w_t^i\}, i = 1 \ldots n$. Each x_t^i is a discrete hypothesis related to the location of the object. The w_t^i are non-negative weights, called *importance factors*, which sum to one.

The Sequential Importance Sampling (SIS) algorithm is a Monte Carlo method that forms the basis for particle filters. The SIS algorithm consists of recursive propagation of the weights and support points as each measurement is received sequentially.

We use a more advanced algorithm with re-sampling. We use weight distribution $D_w(x, y)$, which is obtained from the Twitter user distribution to assess the biases of user locations[4] . The algorithm is shown as follows:

1. **Initialization**: Calculate the weight distribution $D_w(x, y)$ from Twitter users' geographic distribution in Japan.
2. **Generation**: Generate and weight a particle set, which means the N discrete hypothesis.
   (a) Generate a particle set
   $$S_0 = (s_0^0, s_0^1, s_0^2, \ldots, s_0^{N-1})$$
   and allocate them evenly on the map, as
   $$particle\ s_0^k = (x_0^k, y_0^k, w_0^k)$$
   $x, longitude; y, latitude; w, weight$
   (b) Weight them based on weight distribution $D_w(x, y)$.
3. **Re-sampling**
   (a) Re-sample N particles from a particle set S_t using weights of respective particles and allocate them on the map. We allow re-sampling of more than that of the same particles.
   (b) Generate a new particle set S_{t+1} and weight them based on weight distribution $D_w(x, y)$.
4. **Prediction**: Predict the next state of a particle set S_t from Newton's motion equation.
   $$\begin{aligned}(x_t^k, y_t^k) &= (x_{t-1}^k + v_{x_{t-1}}\Delta t + \frac{a_{x_{t-1}}}{2}\Delta t^2,\\ &\qquad y_{t-1}^k + v_{y_{t-1}}\Delta t + \frac{a_{y_{t-1}}}{2}\Delta t^2)\\ (v_{x_t}, v_{y_t}) &= (v_{x_{t-1}} + a_{x_{t-1}}, v_{y_{t-1}}, a_{y_{t-1}})\end{aligned}$$
   $$a_{x_t} = \mathcal{N}(0; \sigma^2),\ \ a_{y_t} = \mathcal{N}(0; \sigma^2).$$
5. **Weighing**: Re-calculate the weight of S_t by measurement $m(m_x, m_y)$ as follows.
   $$\begin{aligned}dx_t^k &= m_x - x_t^k,\quad dy_t^k = m_y - y_t^k\\ w_t^k &= D_w(x_t^k, y_t^k) \cdot \frac{1}{(\sqrt{2\pi}\sigma)}\\ &\qquad \cdot exp\left(-\frac{({dx_t^k}^2 + {dy_t^k}^2)}{2\sigma^2}\right)\end{aligned}$$
6. **Measurement**: Calculate the current object location $o(x_t, y_t)$ by the average of $s(x_t, y_t) \in S_t$.
7. **Iteration**: Iterate Steps 3, 4, 5, and 6 until convergence.

[4] We sample tweets associated with locations and obtain a user distribution that is proportional to the number of tweets in each region.

6. Evaluation and application

In this section, we explain how to evaluate results of experiments and describe points that should be considered when applying these methods.

6.1 Selection of the target area

Three conditions must be met to apply methods for earthquake observation from social media.

The first is that a sufficient number of people use Twitter in a targeted area. The second one is that several earthquakes occur each year for a target area. The third one is that infrastructure should be set up in a target area.

These three conditions are needed in each step of earthquake detection and location estimation. A sufficient number of tweets and a certain number of earthquakes are needed to create a classifier for tweets and to estimate the locations of earthquake epicenters. Accurate logs of earthquakes are also necessary to calculate the false-alarm probability of social sensors and to evaluate the earthquake detection system performance.

If creating a classifier and setting a trigger for earthquake detection in an area and applying them in another area, then the third condition is not indispensable. However, the first condition and the second condition are necessary in both areas.

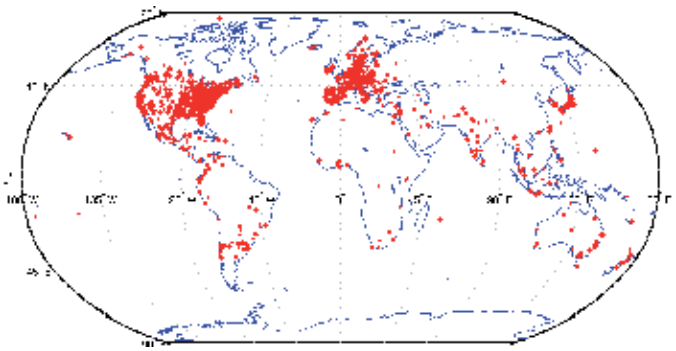

Fig. 14. Twitter user map.

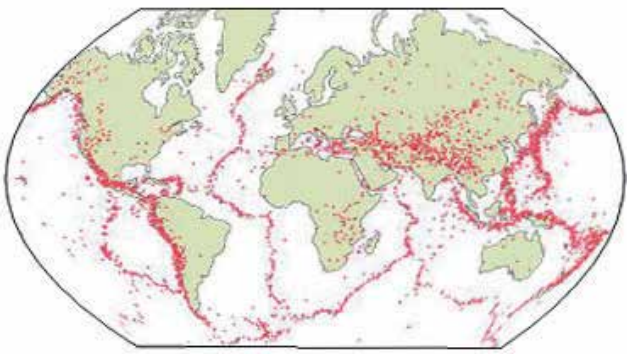

Fig. 15. Earthquake map.

Figure 14 depicts the Twitter user distribution map and Fig. 15 depicts an earthquake occurrence distribution map. Earthquake detection using information from Twitter users is applicable in overlapping areas of these two maps: for example, Japan, the west coast of the U.S., Indonesia, Turkey, Iran, and Italy.

The number of Twitter users has been increasing continuously. Therefore, those areas can probably be expanded. Additionally, if one uses social media other than Twitter, then overlapping areas might be changed.

Therefore, a target area should be chosen very carefully to apply the methods described in this chapter.

6.2 Evaluation of earthquake detection

To evaluate the performance of earthquake detection and earthquake epicenter location estimation, one must collect earthquake data from some organizations. Those data must include information about an approximate time point of an earthquake and approximate position of an earthquake epicenter. Moreover, it is better that they include the exact time of an earthquake, the longitude and latitude of an earthquake epicenter, and the seismic intensity of earthquakes in each region.

For example, the Japan Meteorology Agency (JMA) publishes an earthquake database on the Web, which includes a time, magnitude, and earthquake intensities at each point of area, a place of earthquake epicenter of all earthquakes above level 1 on the Japanese seismic intensity scale[5]. The USGS publishes similar data on the Web[6].

Data of such kinds can be obtained by crawling. They can be used to create training data for classifiers and to evaluate the performance an earthquake detection system.

7. Conclusion

Our research is an early approach to using Twitter as a social sensor for earthquake observations. It is meaningful that we apply methods by ordinary physical sensors to earthquake detection by social sensors. Furthermore, we present the possibility of earthquake detection without installing numerous physical sensors. The method is effective for earthquake observations in some countries where a few seismic sensors exist. However, it is difficult to detect earthquakes occurring in oceanic areas or less populated areas using methods we introduced in this chapter. Therefore, we must verify that earthquake detection by social sensors is effective when we apply these methods. Furthermore, the applicable scope of the earthquake observation by social sensors can be extended considering a stochastic gradient, more detailed probabilistic models, and so on. Many subjects remain to be explored in future work.

8. References

Bishop, C. M. (2006). *Pattern Recognition and Machine Learning*, Vol. 4 of *Information science and statistics*, Springer.

[5] http://www.seisvol.kishou.go.jp/eq/shindo_db/shindo_index.html
[6] http://neic.usgs.gov/neis/qed/

Cheng, H., Tan, P.-N., Potter, C. & Klooster, S. (2008). Data mining for visual exploration and detection of ecosystem disturbances, *Proceedings of the 16th ACM SIGSPATIAL international conference on Advances in geographic information systems - GIS '08* p. 1.

Chih-Chung, C. & Chih-Jen, L. (2011). LIBSVM-a Library for Support Vector Machine. URL: *http://www.csie.ntu.edu.tw/ cjlin/libsvm/*

CITRIS (2011). iShake -Mobile Phones as Seismic Sensors-. URL: *http://ishakeberkeley.appspot.com/*

Fox, D., Hightower, J., Schulz, D. & Borriello, G. (2003). Bayesian filtering for location estimation, *IEEE Pervasive Computing* 2(3): 24–33.

Intensity, M. (2005). Did You Feel It ? Citizens Contribute to Earthquake Science, *Technical Report March*, U.S. Geological Survey. URL: *http://earthquake.usgs.gov/earthquakes/dyfi/*

Joachims, T. (2008). SVM-Light. URL: *http://svmlight.joachims.org/*

Kleinberg, J. (2002). *Bursty and hierarchical structure in streams*, ACM Press, New York, New York, USA.

Krishnamurthy, B., Sen, S., Zhang, Y. & Chen, Y. (2003). Sketch-based change detection: methods, evaluation, and applications, *Proceedings of the 3rd ACM SIGCOMM Conference on Internet Measurement*, ACM, pp. 234–247.

Okazaki, N. (2009). Classias. URL: *http://www.chokkan.org/software/classias/index.html.en*

Sakaki, T., Okazaki, M. & Matsuo, Y. (2010). Earthquake shakes Twitter users: real-time event detection by social sensors, *Proceedings of the 19th international conference on World wide web* pp. 851–860.

Survey, U. S. G. (2009). Twitter Earthquake Detector (TED). URL: *http://recovery.doi.gov/press/us-geological-survey-twitter-earthquake-detector-ted/*

Zhu, Y. & Shasha, D. (2003). Efficient elastic burst detection in data streams, *Proceedings of the ninth ACM SIGKDD international conference on Knowledge discovery and data mining - KDD '03*, ACM Press, New York, New York, USA, p. 336.

16

Fibre-Optic Sagnac Interferometer as Seismograph for Direct Monitoring of Rotational Events

Leszek R. Jaroszewicz[1], Zbigniew Krajewski[1] and Krzysztof P. Teisseyre[2]
[1]*Military University of Technology*
[2]*Institute of Geophysics Polish Academy of Sciences*
Poland

1. Introduction

The possibility of a direct monitoring of rotational events has an important role in the seismological sciences as well as in the applied physics regarding large engineering structures.

According to the first aspect, a possibility of existence of the rotational phenomena in the seismic field has been discussed from the beginning of the earthquakes investigations. The interest in these phenomena has been stimulated by strange, rotary and even screw-like deformations that occur after earthquakes, often appearing on parts of tombs and monuments (Ferrari, 2006; Kozák 2006). The classical textbooks on seismology deny the possibility that the rotational phenomena, especially in form of seismic rotational waves – SRW, could pass through a rock, so the earthquake rotational phenomena were explained by an interaction of standard seismic waves with a compound structure of objects they penetrate, which, in fact, might be the case (Teisseyre & Kozak, 2003). Nevertheless, it was theoretically proved that even the SRW could propagate through grained rocks; later on, this possibility was extended on rocks with microstructure or defects (Eringen, 1999; Teisseyre & Boratyński, 2002) or even without any internal structure (Teisseyre, 2005; Teisseyre et al., 2005; Teisseyre & Górski, 2009), due to the asymmetric stresses in the medium. It should be noticed that the SRW were for the first time effectively recorded in Poland in 1976 (Droste & Teisseyre, 1976). From this time, waves of this type have been studied in a few centers over the world. Taking into consideration large engineering structures, the rotational events monitoring is connected to the torsional effects in structures as well as to the interstory drift. Since the application of new materials and technologies for building constructions, they have irregular structures in-plane which causes difficulties in designing of the horizontal rotations of these structures especially during earthquakes (Schreiber et al., 2009). Recently in the above areas, the first monographs have been published (Teisseyre et al., 2006, 2008; Lee et al., 2009), covering the theoretical aspects of the rotation motion generation and propagation, as well as the examples of the field experiments.

A further experimental verification of the existing rotational phenomena in seismic events needs a new approach to the construction of the measuring devices, because the

conventional seismometers are inertial sensors detecting only linear velocities. Similarly, the measurements of torsional response and interstory drift are reasonably easy on small scale models in a laboratory (Kao, 1998) but are much more difficult in real structures. The first of them can be measured by using a pair of accelerometers and then dividing differences in the horizontal accelerations by the distance between them in a direction perpendicular to the measured motion. Then this has to be integrated twice with respect to the time needed to give the torsional rotations (Schreiber et al., 2009). However, the inherent sensor drift and the small offset from zero in the absence of an input signals are the important limitations of this technique. According to the measurement of interstory drifts, it is, in principle, possible to arrange a frame from the floor below to near the ceiling above to set up the displacement transducers to measure the difference in displacements (McGinnis, 2004). However, again far from the hardware complexity of this approach, it is also vulnerable to building deformations.

For the above reason, the new instrumentations are important, especially those designed for an investigation of very small rotations. The near–field studies for the understanding of the mechanics of earthquakes is extensively reviewed by Kamamori (1994) and can be summarized as requirement for instruments with frequency range below 100 Hz and resolution in range of 10^{-6}-10^{-9} rad/s/Hz$^{1/2}$ for the SRW. Whereas the engineering strong-motion seismology needs devices operating in a frequency range of 0.05 – 100 Hz with resolution 10^{-1} – 10^{-6} rad/s/Hz$^{1/2}$ (Cowsik et al., 2009).

Since the Sagnac effect (Sagnac, 1913) measures the rotation directly, an application of the sensor based on this effect seems to be ideal for the construction of the rotational seismometer - RS. Its greatest strength is the fact that it does measure absolute rotations or oscillations, so that it does not require any external reference frame for its measurement. This means that it measures true rotations even during an earthquake, where nothing remains static. Since it is an entirely optical device, it does not have the problems that characterize inertial mass transducers, also. We distinguish two systems based on the Sagnac interferometer: a ring laser rotational seismometer - RLRS (Schreiber et al., 2001), and a fibre-optic rotational seismometer - FORS (Takeo et al., 2002; Franco-Anaya et al., 2008; Schreiber et al., 2009). The first of them is a stationary system constructed for investigation disturbances in the Earth rotation, whereas the second one based on the application commercially available fibre-optic gyroscope - FOG.

Even though 40-ty years of the FOG investigation gives very precise systems useful for different areas including inertial navigation, their constructions are optimized for the detection of angular changes rather than rotation speed, then may generate the same difficulties during the investigation rotational phenomena. For the above reason in this chapter we conclude ours experiments connected to another approach to the rotation phenomena investigation (Jaroszewicz et al., 2003). We started the second part with a short description of the Sagnac effect with the same historical review of its application as FOG. In part 3, which is the main part of this chapter, we described the Autonomous Fibre-Optic Rotational Seismograph – AFORS, with its optical part based on the FOG construction, whereas the special autonomous signal processing unit – ASPU optimizes its operation for the measurement of rotation speed instead of angular changes. Finally, in part 4 we presented the same results obtained during the application of these systems for the rotational events investigation as well as a monitoring of building torsional moves.

2. Sagnac effect and its application as FOG

Sagnac (1913) first demonstared the feasibility of an optical experiment capable of indicating the state of rotation of the frame of reference in which his interferometer was at rest. The basic principle of Sagnac's interferometer is given in Fig. 1a. The input light beam is split by a beam spliter into a beam circulating in the loop in a clockwise - cw direction and a beam circulating in the same loop in a counterclockwise - ccw direction. The two beams are reunited at a beam splier so that interference fringes are observed in the output light. When the whole interferometer with a light source and the fringe detector is set in rotation with an angular rate of $\mathbf{\Omega}$ rad/s, a fringe shift ΔZ with respect to the fringe position for stationary interferometer is observed, which is given by the formula:

$$\Delta Z = \mathbf{\Omega} \bullet \mathbf{A}/\lambda_0 c, \tag{1}$$

in which $\mathbf{A}$ is the area enclosed by the light path. The vacuum wavelength is λ_0 and the free-space velocity of light is c. The scalar product $\mathbf{\Omega} \bullet \mathbf{A}$ denotes that ΔZ is proportional to the cosine of angle between the axis of rotation and the normal to the optical circuit. Sagnac also established that the effect does not depend on the shape of the loop or the center of rotation.

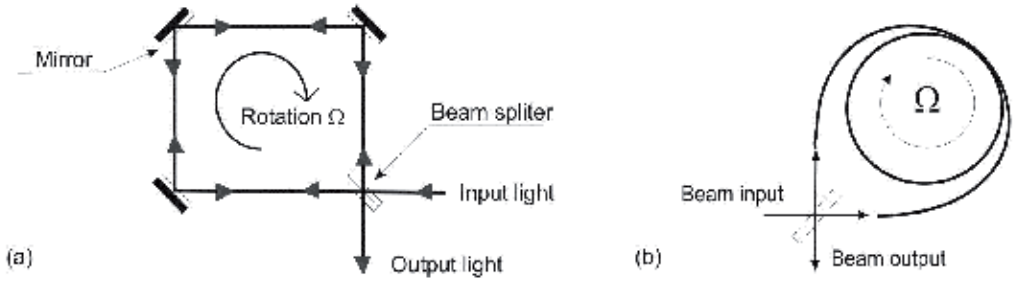

Fig. 1. Schematic of Sagnac's interferometer (a) and its implementation in fibre optic technique (b)

It should be noticed that a German graduate student, Harress (1912), performed a very similar experiment for a thesis project a few years before Sagnac did his experiment. Harress used an optical circuit which consisted of a ring of total reflecting prism, but his objective was quite different from Sagnac's. According to Sagnac's data (Sagnac, 1914), for the wavelength of indigo mercury light and a loop area A=866 cm^2, a fringe shift of 0.07 fringes was clearly detectable for the rate of rotation of 2 rps. However, according to the other data (Post, 1967) the fringe shift detectability at that time was probably of an order of 0.01 of a fringe, so precision of the Sagnac's experiment therefore may have been close to marginal.

A Sagnac experiment of great precision was subsequently performed by Pogany (1926). With a loop area A=1178 cm^2, Ω=157.43 rad/s, and λ_0=546 nm, he reproduced within 2% the theoretically expected fringe shift ΔZ=0.906. Michelson and Gale (1925) succeeded in demonstrating the rotation of the Earth by means of the Sagnac effect, also. To obtain the required sensitivity they had to choose an unusually large size (rectangular 0.4 x 0.2 mile) for the surface area enclosed by the beam. Summarizing, the experiments of Sagnac, Pogany, and Michelson-Gale and the results of Harress, as reinterpreted by Harzer (1914), the following features of the Sagnac effect according to the fringe shift can be given (Post, 1967):

a. obeys formula (1),
b. does not depend on the shape of surface area A,
c. does not depend on the location of the center of rotation,
d. does not depend on the presence of a commoving refracting medium in the path of the beam.

The fibre-optic version of the Sagnac interferometer uses a long length optical fibre L coiled in a loop of diameter D, as it is shown in Fig. 1b (Vali & Shorthil, 1976). In this approach, instead of the fringe shift ΔZ, a phase shift $\Delta\phi$ is produced between cw and ccw propagating light, given by

$$\Delta\phi = \frac{2\pi LD}{\lambda_0 c_0}\Omega \tag{2}$$

where Ω is the rotation component in the axis perpendicular to the fibre-optic loop. In other words, the sensitivity of the Sagnac interferometer in this approach is enhanced not only by increasing the physical sensor loop diameter but also by increasing the totals length of the used fibre. It is easy to see that three such interferometer with loops plane in perpendicular directions give information about a space vector of the rotation rate. This data after an integration in time domain shows the position changes in space – and it is idea of the optical gyroscope.

35-years after the above date its technical application as the FOG is the best recognized interferometric sensor made in the fibre-optic technology. However, because its useful signal is the angular changes, the detected phase shift $\Delta\phi$ is integrated in time needed to give it. Moreover, for a desired rotation rate in the range of 10^{-6} – 10^{-9} rad/s the Sagnac effect generates a very small phase shift, so needs to be separated from other disturbances and protected so that the Sagnac effect is the unique nonreciprocal effect in the device. For the above reason all FOG uses shown in Fig. 2 the reciprocal configuration (Urlich, 1980) also called the minimum configuration (Arditty & Lefevre, 1981) where a perfect balance between both counter-propagating paths is obtained simply with a truly single-mode (single spatial mode and single polarization) filter at the common input-output port of the interferometer, even if the propagation is not single-mode along the rest of the interferometer.

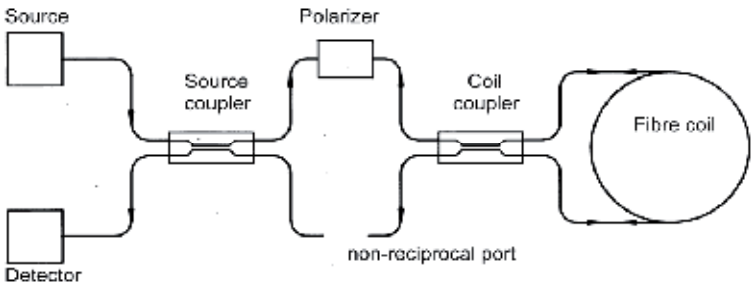

Fig. 2. The minimum configuration of the FOG

The FOG interferometer using the minimum reciprocal configuration yields a raised cosine response as any interferometer. It is classical to bias such an even response that has a maximum at zero by modulating the abscissa parameter and demodulating the output

signal, which yields an odd response. The FOG uses a reciprocal phase modulator - PM at the end of the coil, which yields, because of the propagation delay, as a modulation of the phase difference without any residual zero offset (Martin & Winkler, 1978). This was a very important step in the progress of performance, but it was not enough for an ultimate performance which is obtained only if the unbiased response is perfectly even and the biasing modulation has only odd frequencies. For the above reason, the PM being actually a delay line filter, the operation at the so-called proper or eigen frequency (Bergh et al., 1981) - the delay through the coil is half the period of modulation, suppresses the residual even harmonics which are always present because of spurious nonlinearities of the modulation chain. Today the FOG system using also a broadband source has the intensity statistics that happens to cancel the Kerr effect induced phase difference in a Sagnac interferometer (Ezekiel et al., 1982). Such a broadband source is also needed, as it is well-known today, to remove coherence related noise and drift due to backscattering and backreflection as well as lack of rejection of the polarizer (Fredricks & Ulrich, 1984; Lefèvre et al., 1985a; Burns, 1986). Finally, for achieved the high scale factor linearization, FOG utilizes a digital phase step feedback (Lefèvre et al., 1985b) using the same reciprocal PM as the biasing modulation and an all-digital processing scheme where the gyro modulated signal is sampled with an AD convertor and the demodulation performed by digital subtraction (Auch, 1986; Arditty et al., 1989).
Since all-digital processing scheme implemented in the current FOG system is optimized for the presentation of angular changes rather than rotation rate, the same problems exist for its optimized application for measurement of the last phenomena which are interesting for the rotational seismology. For the above reason in the next part of this chapter we have described our experiments in development of the fibre-optic rotational seismograph system. Its construction is based on experiences according to the FOG development described above, but the system is optimized for a direct measurement of the rotation rate only (Jaroszewicz et al., 2003). Such an approach gives a system which through a direct use of the Sagnac effect can limit drift influence on a device operation. Moreover, the special construction of a signal processing unit protects easily its monitoring via Internet including data collecting and managing as well as device remote control.

3. Autonomous Fibre-Optic Rotational Seismograph

A detailed description of the AFORS system was published previously (Jaroszewicz at al., 2011a, 2011b) hence here we summarized the above data regarding its construction, calibration and management. Now we present two examples of these devices - AFORS-1 located in the Książ (Poland) seismological laboratory for the investigation of the rotational events connected to earthquakes, and AFORS-2 located in Warsaw (Poland) used for initial works connected to the investigation of the irregular engineering construction torsional response and the interstory drift (Jaroszewicz et al., 2011c). Before the end of 2011 the next system AFORS-3 will be available as the replacement to the older version FORS-II mounted in the Ojców (Poland) seismological laboratory (Jaroszewicz & Krajewski, 2008).
The optical head of the constructed AFORS devices uses a fibre interferometer in a minimum optical gyro configuration (Jaroszewicz et al. 2006a), as it is shown in the upper part of Fig. 3a.
The application of the broadband low coherence superluminescent diode – SLD (*EXALOS* - Switzerland with optical power – 20.87 mW, operation wavelength – 1326.9 nm, and spectral radiation band – 31.2 nm,) gives possibility for a minimisation of polarization influence on

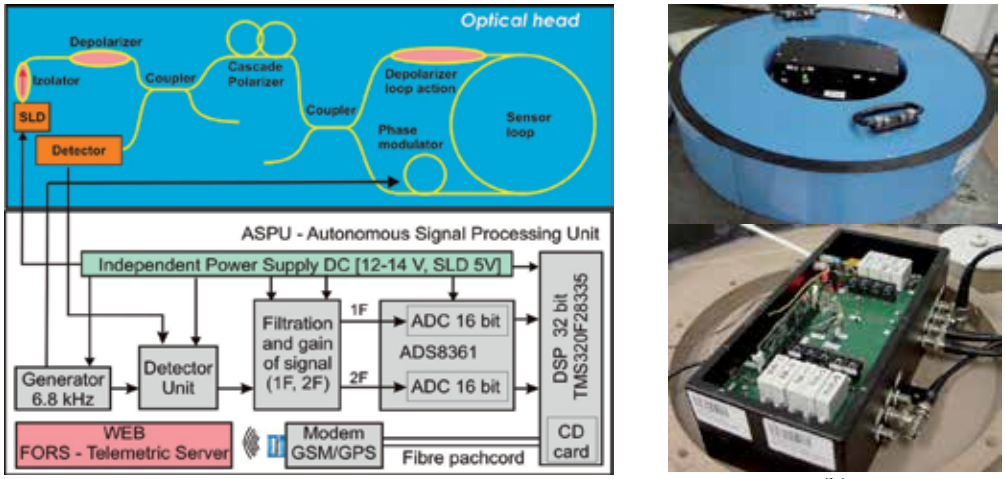

(a) (b)

Fig. 3. General schema of the AFORS (a): upper – the optical head (generation of the Sagnac phase shift proportional to measured rotation rate Ω), bottom – Autonomous Signal Processing Unit (rotation calculation and recording), (b): general view of all AFORS (top) and ASPU (bottom)

the system operation by achieving light depolarization in a sensor loop (Krajewski et al., 2005). Next the set of cascade fibre polarizers (with total extinction above 100 dB) enables a true single mode operation of the whole system and guarantees that the only nonreciprocal effect in system is the Sagnac effect. Moreover, a 0.63 m diameter sensor loop has been made from a special composite material with permalloy particles for shielding from the magnetic field. A long length of SMF-28 fibre has been winded in a double-quadrupole mode (Dai et al., 2002) with a 0.2 mm Teflon insulation between each fibre layers which is for the thermal stabilization of the sensor's work, for expected 2-4 degree per day temperature fluctuation in seismic observatories. The system optimization made for AFORSs (15000 m length of fibre with attenuation equal to 0.436 dB/km in sensor loop for AFORS-1 and respectively, 15056 m and 0.450 dB/km for AFORS-2) allows for theoretical sensitivity in quantum noise limit (Jaroszewicz & Wiszniowski, 2008) equal to $1.97 \cdot 10^{-9}$ rad/s/Hz$^{1/2}$ and $2.46 \cdot 10^{-9}$ rad/s/Hz$^{1/2}$, respectively for AFORS-1 and AFORS-2. The above mentioned difference between two constructed devices is connected to their total optical loss which is equal to 13.33 dB and 14.47, respectively for AFORS-1 and AFORS-2 (Jaroszewicz et al., 2011b).

The optimisation for a detection of rotation rate is made on the basis of special detection units and utilizes a synchronous detection with properly chosen PM that operates according to the principles presented in part 2 (Krajewski, 2005). For AFORS, a new Autonomous Signal Processing Unit - ASPU (*ELPROMA Ltd*), according to the scheme shown in the lower part of Fig. 1a, has been developped. The ASPU enables the detection of a rotation rate Ω from proper selection (special low-pass filters) and processing (in digital form) the first $A_{1\omega}$ and the second $A_{2\omega}$ amplitude of the harmonic output signal, on the basis of the following relation (Jaroszewicz et al., 2011a):

$$\Omega = S_0 \arctan\left[S_e \cdot u(t)\right]; \quad S_0=(\lambda \bullet c)/(2 \bullet \pi \bullet L \bullet D), \quad u(t)=A_{1\omega} / A_{2\omega} \tag{3}$$

where: S_o – optical and S_e – electronic constants, related to the parameters of used optical and electronic components. The digital form of a signal processing enables the application of the 32-bit signal processor TMS320F283535 (*Texas Instruments*) working with a frequency of 150 MHz as an optimal DSP unit, for a calculation and monitoring of the rotation rate Ω on the basis of signal frames having 1024 length of 16-bit samples. Finally, the obtained results are stored on a CD card and transmitted by a GSM/GPS module to a special WEB FORS - Telemetric Server.

The evaluation of the optical and electronic constans needs a sensor calibration process, which is based on the measurement of the Earth rotation for Warsaw, Poland i.e. Ω_E = 9.18 deg/h ≡ $4.45 \cdot 10^{-5}$ rad/s (Krajewski et al., 2005; Jaroszewicz et al., 2011a). During the calibration the AFORS is mounted vertically on a rotation table. For the sensor loop directed in the East-West direction, the measured rotation equals zero because in this direction, its plane is collinear with the Earth rotation axis, whereas for the North-South direction, the measured signal obtains the maximum plus or minus values because the plane of a sensor loop is perpendicular to the vector component of the Earth rotation Ω_E. For two existing systems we obtained the following values for the above constants: S_0= 0.0043 s^{-1}, S_e=0.0144 for AFORS-1 and S_0=0.059 s^{-1}, S_e=0.0134 for AFORS-2.

After the practical construction of the AFORS devices, their accuracy has been checked. However, this work made in MUT located in Warsaw city, could give limited information on the system accuracy because of urban noises. Figure 4 summarizes these measurements. Since the ASPU allows for step changes of the detection frequency band in the range from 0.83 Hz to 106.15 Hz (Jaroszewicz et al., 2011b), the obtained accuracy is at the level of $5.07 \cdot 10^{-9}$/$4.81 \cdot 10^{-9}$ rad/s - $5{,}51 \cdot 10^{-8}$/$6.11 \cdot 10^{-8}$ rad/s (for AFORS-1/AFORS-2), respectively for the lower and higher working frequency band. As one can see, the obtained values are well correlated with Ω_{min} in quantum noise limitation. It should be noticed that the linear dependence of AFORS sensitivity and accuracy in the detection frequency range is the advantage of this system, taking into account the expected frequency characteristics of the rotational seismic waves (Teisseyre et al., 2006). For comparison, Fig. 4 includes also the measured accuracy of the older system FORS-II; which was $4.3 \cdot 10^{-8}$ rad/s (Jaroszewicz et al., 2006; Jaroszewicz & Krajewski, 2008), at 20 Hz - the fixed detection frequency band.

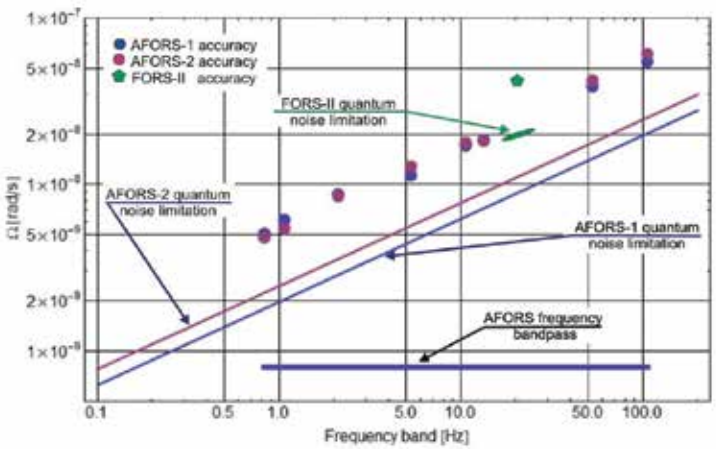

Fig. 4. The accuracy measured in Warsaw, Poland for the chosen detection band for three devices: AFORS-1, AFORS-2 and FORS-II

A *FORS-Telemetric Server* with its main page shown in Fig. 5a (reader can use http://fors.m2s.pl with login and password - AFORSbook for free access to the system) is used for data storing and for monitoring the work of the FORS-II and the AFORSs. Because ASPU of the AFORS contains a GSM/GPS module and an independent power supply for all electronic components of the system, hence the AFORS is fully autonomous and mobile system. In this moment, the 3 devices are managed via server: FORS-II, AFORS-1, AFORS-2 located in Ojców, Książ and Warsaw (all in Poland), respectively (Jaroszewicz et al., 2011b) as it is shown in Fig. 5b.

(a)

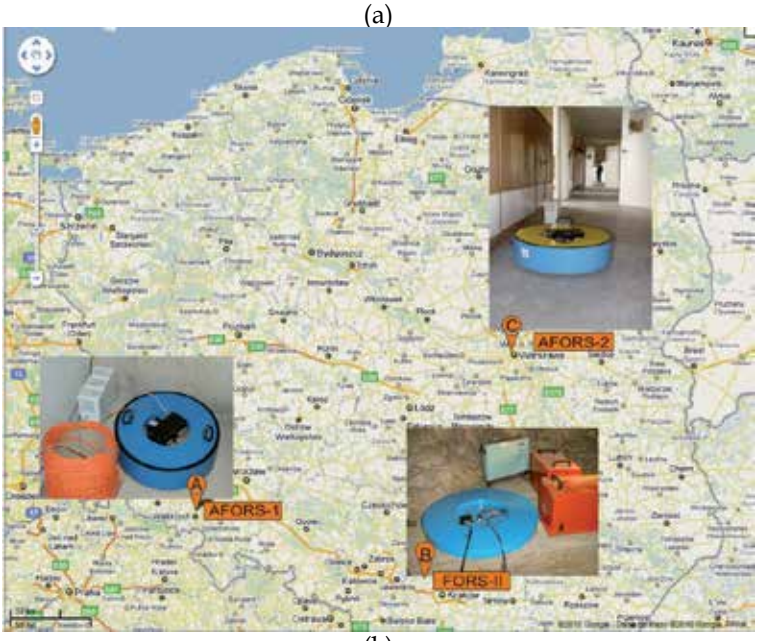

(b)

Fig. 5. Elements of WEB page for AFORS managing: (a) the main page of *FORS - Telemetric Server,* (b) the GOOGLE map with devices localization

The applied technology gives possibility for the remote (via Internet) controlling and changing of all electronic parameters of the ASPU for a given sensor made according to the AFORS technology, as presents, for example, the bookmark *Config* for the AFORS-1 in Fig. 6a. This remote control may comprise a software upgrade. Moreover, the bookmark *Data&Variables* (Fig. 6b) monitors, for given AFORS, in real time the main data and variables with possibility for the remote changing of the threshold – the level of signals which initialize automatic data storing and its GSM transfer. Additionally, the top right corner of bookmarks for the given system on server contains the information on a current date and time and the four main AFORS's parts of state of work (good – as green, partially good as

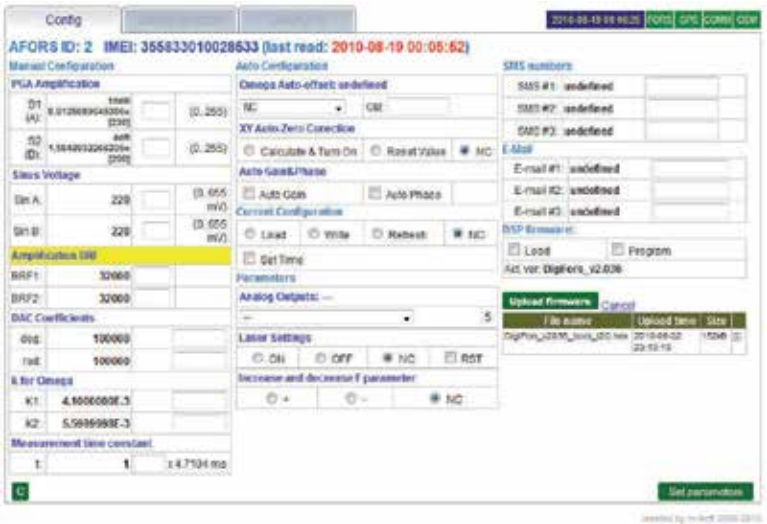

(a)

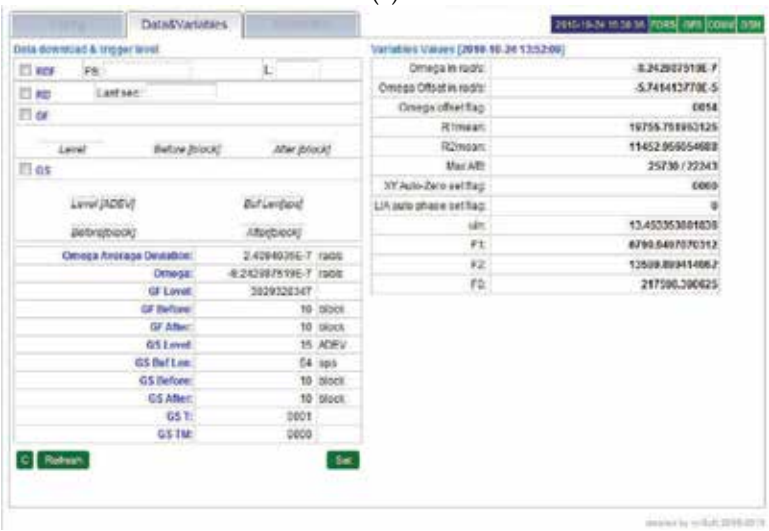

(b)

Fig. 6. The view of two main bookmarks for AFORS-1at the *FORS - Telemetric Server*: (a) *Config*, and (b) *Data&Variables*

yellow or no work – as black, respectively). The bookmark *GSM/GPS* (not shown in figure, see for example Jaroszewicz et al., 2011a) monitors in real time the GSM parameters as well as the GPS parameters which include the AFORSes' global localization (see Fig. 5b). Yet another bookmark named *Measurement* presents the collection of data recorded by different devices connected to the server. These data are stored with the main parameters of AFORS in the recording time: ADEV – rotation rate average deviation in rad/s, Omega Offset – rotation rate offset in rad/s, GS Level/Before/After - adjusted level of signal for data stored, and ΔB - adjusted detection band. In this way, in our opinion, the AFORSes with their management via *FORS - Telemetric Server* are fully adopted for monitoring of rotational phenomena connected to earthquakes as well as torsional response and interstory drift of the irregular structures in-plane existing during any ground moves.

4. Examples of the experimental data obtained by AFORS

The previously obtained data from an older system FORS-II have been wide discussed as well as summarized (Jaroszewicz et al., 2006, 2008). For the above reason here we present the summarized data obtained with regard to the AFORS application where AFORS-1 is installed in the Książ (Poland) seismological laboratory for the recording of the rotational phenomena connected to earthquakes, whereas AFORS-2 has been used in the initial experiments for monitoring building rotational moving.

The main source of disturbance during an investigation by AFORS-2 of a building rotation moving was an urban ground motion generated by tram moves within a 50 m distance from a building wall parallel to it. The investigated building is a light construction (five floors of aluminium structure with sandwich walls and ceilings), and the AFORS-2 has been installed, subsequently on the second and first floors in the hall, in the same vertical position (with accuracy of about 10 cm). Since it is an old building with asbestos used as an inner wall isolation, now it is not in use by the academy anymore, so we expected that the recorder signals will be connected to an external perturbation. Figure 7 presents the building moves recorded on the first and the second floors (difference about 3 m of height) for relatively the same ground motion generated by tram moves nearly by midnight on July 13th (AFORS-2 on the first floor) and July 14th (AFORS-2 on the second floor). Since it was a middle of the night during summer holidays, the academy area was empty which had a direct influence on recorded signals and they were very clear. As one can see in the above experiment the accuracy for the AFORS-2 was $3.15 \cdot 10^{-6}$ rad/s and $7.91 \cdot 10^{-6}$ rad/s (see ADEV parameter in the left down corner of two pictures in Fig. 7), for the chosen detection band equal to 21.23 Hz. The amplitude of the detected rotation rate was about twice higher for the second floor, and was much higher than the system accuracy (more than ten orders).

The urban noise influence on the recorded signals can be observed on the data presented in Fig. 8, which have been obtained in the morning when the Academy opened for work. As one can see the higher amplitude as well as frequency were observed in this time. However, again the much higher amplitude of torsional moves of the building is observed on the higher floor of building.

The above initial results show that the device type AFORS can be useful for a continuous monitoring of an engineering structure of, for example, multi-storey buildings with regard to the investigation of their torsional rotations as well as measuring interstory drifts. These measurements are made without any reference frame which is very important during earthquakes and may be made only by a system based on the Sagnac effect. In comparison

to the commercially available FOG instruments such as μFORS-1, the proposed system is designed for a direct measurement of a rotational rate, whereas any FOG measures change the angle which is written in their inner electronic system and difficult to direct changes. Additionally, our system prepared according to the AFORS technology has developed the software designed for the Internet system monitoring as well as the remote control which can manage a large numbers of such devices in a useful way for the operator.

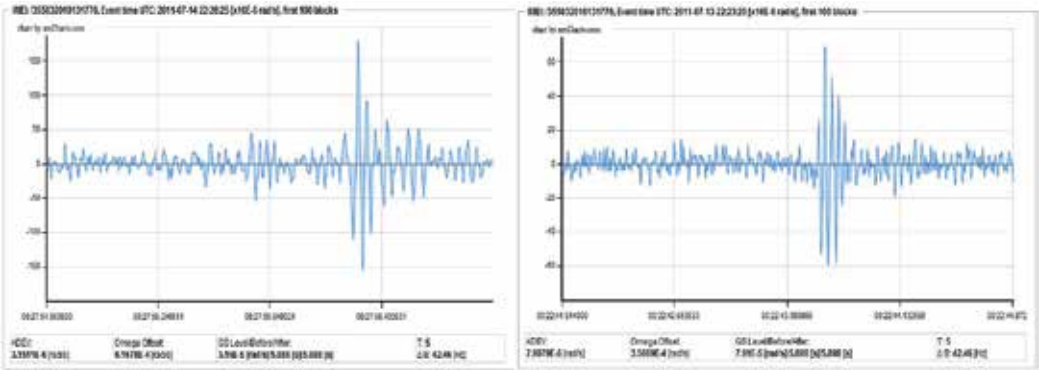

Fig. 7. The data recorded on second (left) and first (right) floor as response for ground moves after tram pass through street

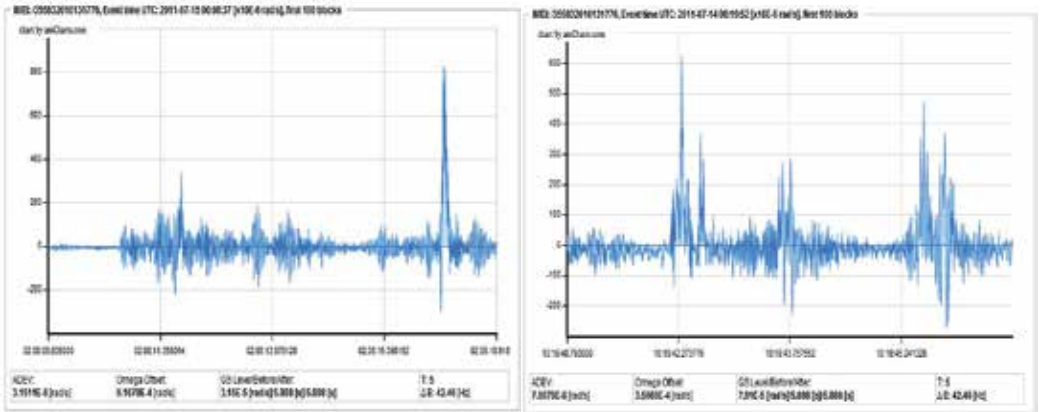

Fig. 8. The data recorded on the second (left) and the first (right) floor as a response for the ground moves generated by the street morning intensity within a distance of about 50 m from and parallel to the long building wall

At beginning of July, 2010 the AFORS-1 has been installed in the Książ (Poland) seismological observatory together with a set of the Two Antiparallel Pendulum Seismometers (*TAPS-1* and *TAPS-2*) constructed by the Institute of Geophysics (Teisseyre et al., 2003). As usually, TAPSes are placed perpendicularly, in directions N-S and E-W.
As the first example we repeat here (Fig. 9) the histogram of the previously analyzed data (Jaroszewicz et al., 2011b) collected in Książ on March 11th, 2011 at 6 h 58 min. (after Honshu earthquake, M=9.0 on 11 March 2011 at 5 h 46 min. 23 s, recorded in Książ on 11 March 2011 at 5 h 58 min. 35 s.). The above data were obtained from the common for AFORS

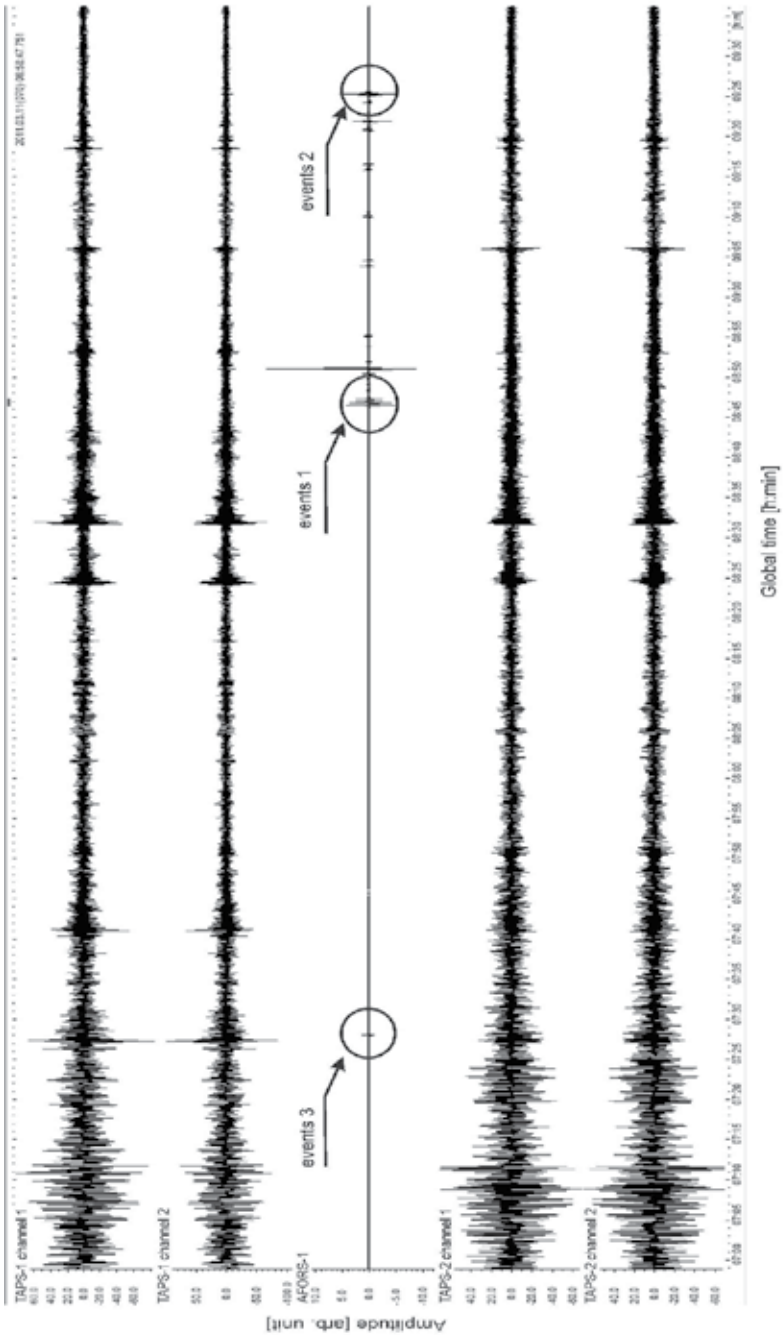

Fig. 9. The plots of the seismic events recorded in Książ on March 11th, 2011, starting from 6 h 58 min, after the Honshu M=9.0 earthquake, all times UTC (Jaroszewicz et al., 2011b)

and TAPSes standard seismic recording system named KSPROT with the samples of a signal with the frequency 12.8 kHz and after re-sampling stores with the frequency 100 Hz.

It should be noticed that in the previously paper (Jaroszewicz et al., 2006), we used a wrong name for this station, KST. We underline that here only the AFORS-1 shows the rotational component in a direct way (plots marked as AFORS-1). The rotational component is obtained also from the TAPS system, calculated from the recordings of linear motions in four channels (data named TAPS-1 channel 1, TAPS-1 channel 2, TAPS-2 channel 1 and TAPS-2 Channel 2) with the application of a suitable mathematical procedure, which has been widely described in the previous paper (Solarz et al., 2004). Since AFORS records rotation in a direct way, we use this recording as the reference source, despite that the rotations calculated from TAPSes are generally poorly correlated with it. In the results presented in Fig. 9, a good correlation has been found mainly in short bursts of seismic oscillations, marked here as "events 3", "events 1" and "events 2". These were clusters of short peaks, found when the traces of the great Honshu Earthquake were studied (without much success in the domain of rotational field component, but this is not strange concerning the distance to the earthquake focus and the characteristics of our instruments). After the preliminary analysis, from each group only one event was chosen, and these we call event 3, event 1 and event 2 accordingly.

For event 1, the data from AFORS-1 were identified by the FORS-Telemetric Server (see Fig. 10a) as the rotational event of an amplitude of about $15 \cdot 10^{-6}$ rad/s with AFORS-1 accuracy equal to $4 \cdot 10^{-8}$ rad/s for the given frequency bandpass which was about 10.6 Hz. The rotation calculated from the linear motions recorded in TAPS system has similar characteristic, as is seen in Fig. 10b (with arbitrary units of amplitude). Nevertheless, we observed some time advance in a relation to the AFORS-1 registration as well as apparent disturbances, visible before and after the event; these may result from a limited accuracy of TAPSes as was previously mentioned (Jaroszewicz & Krajewski, 2008).

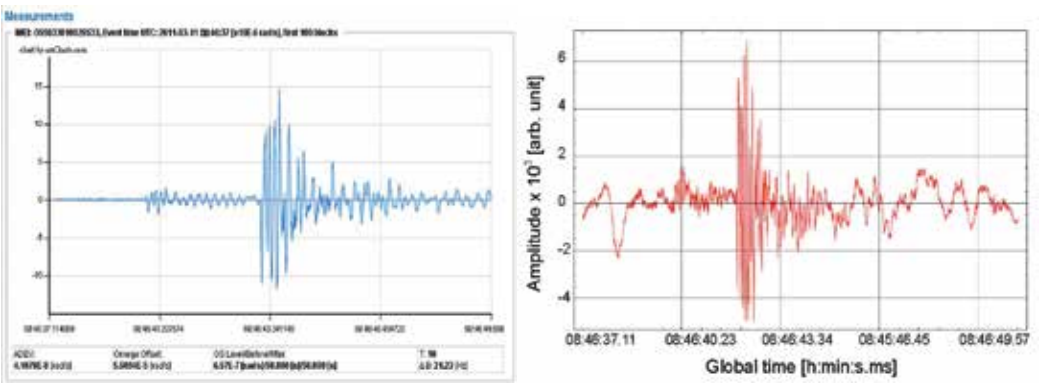

Fig. 10. The rotational event 1 from Fig. 5 on 11 March 2011 – a): recorded from AFORS-1 in the FORS -Telemetric Server at 8 h 46 min; – b): calculated from TAPSes four channels (Jaroszewicz et al., 2011b)

For further study, the recordings of several mining shocks have been chosen; these shocks occurred in the Legnica-Głogów Copper Mining District - LGOM in Western Poland. Some typical results of the analysis of strong shocks are presented here; for the event which occurred in April 30th at 03:32 UTC - the magnitude 2.9 had been found, for the event from June 28th, 23:16 UTC – magnitude 3.2. For viewing the data, for the normalization of the sampling to the first channel and for writing selected time-periods as ASCII, we used the

programs written by dr Jan Wiszniowski of the Institute of Geophysics, P.A.Sci. Subsequent analysis was done in Matlab®.

The rotational motions in the trace of a seismic event, recorded from AFORS-1 and indirectly obtained from TAPSes, differ substantially, as it is seen in Fig. 11. The signal obtained from AFORS-1, here – the middle plot, has much more peaks and indentations than both the channel 1 and channel 4, which are two of the four channels of the TAPSes system. The signals from TAPSes are shown in μm/s, while the rotational signal from AFORS-1 is in conventional units. In the following Figures, the rotations found from TAPSes system are plotted in rad/s.

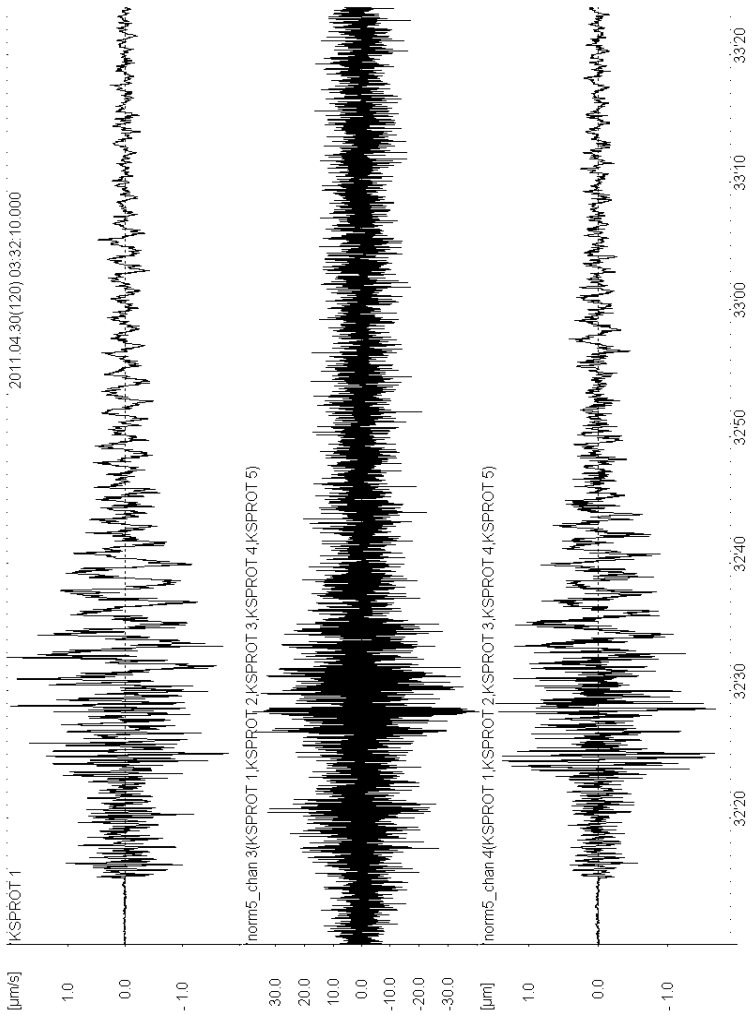

Fig. 11. The example of the seismic event traces, prepared for analysis. Upper channel – channel 1, first of two from the first electromechanical rotational seismometer TAPS. Middle channel – rotational seismogram from AFORS-1, sampling-normalized to the channel 1. Lower channel – first from the second TAPS, sampling-normalized to the channel 1. The mining seismic event in LGOM (western Poland) on 2011.04.30, at 03:32 UTC

For the analysis, we divided each signal into several frequency bands, then searched for similar – and dissimilar! – rotational motions. As it is seen in the Fig. 12, even this method did not reveal great similarity between the rotations obtained from AFORS-1 and from TAPSes. Here, the time-period when the P waves have arrived is shown. For all the transformations, we applied the same procedures, including the digital filters which we constructed in Matlab®.

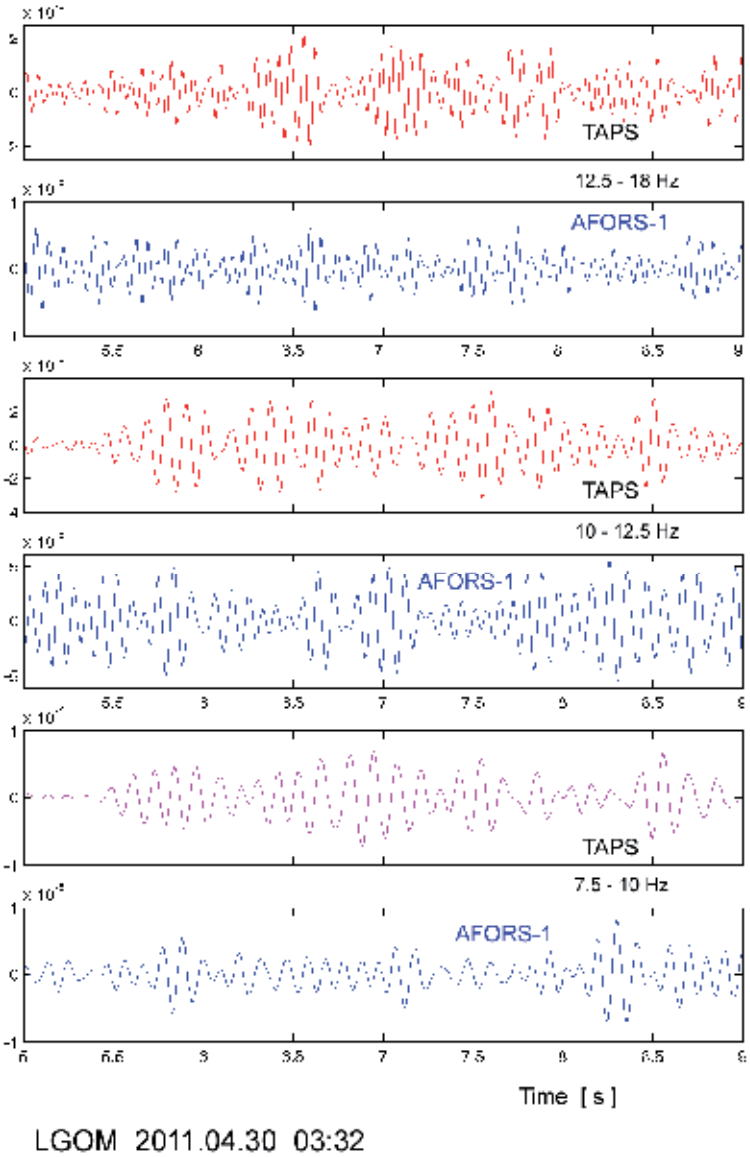

Fig. 12. Rotation motions in the recording of a mining seismic event, during P waves arrivals, as seen in three frequency bands: 12.5-18 Hz, 10-12.5 Hz and 7.5-10 Hz. In each of the paired diagrams, the upper one shows the rotation calculated from the system of TAPSes, the lower one – the rotation sensed by the AFORS-1

Further, we tried to compare both rotational signals after averaging each of them for consecutive time-periods of 0.5 s, that is – 50 samples. The results, for six chosen frequency bands, are shown in Figs. 13 – 16. The averages of the absolute values of rotations are plotted as thick line. Additionally, two other averages are added. The thin continuous is for acceleration (in fact – the difference between neighbouring samples) – again, the absolute values are averaged for consecutive stages. Finally, thin dashed line shows the average of the squared rotational signal. These additional plots were normalized to the rotational signals, so their maxima coincide. The Figs. 13 and 14 are obtained from the analysis of the shock from April 30th; the Figs. 15 and 16 – from the analysis of the stronger shock, that of June 28th.

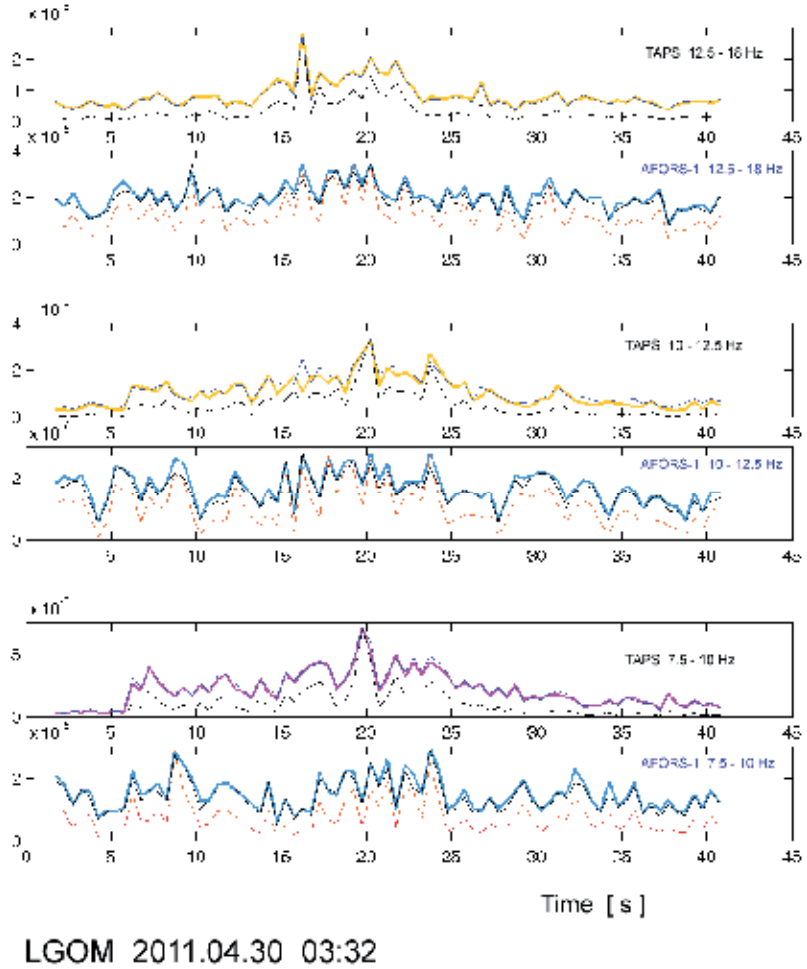

Fig. 13. The rotations, their squares and time-differentials equivalent to rotational acceleration, averaged in consecutive stages, 50 or 0.5 second long. Before averaging, the rotations and their differentials were transformed into the absolute values. The seismic event in LGOM, 2011.04.30, at 03:32 UTC. The upper frequency bands: 12.5-18 Hz, 10-12.5 Hz and 7.5-10 Hz. In each of the paired diagrams, the upper one shows signals obtained from the system of TAPSes, the lower one – from the AFORS-1

Searching for a similarity between peaks, indentations and their sequences, placed in the same points in the both plots of rotations' average values, is the searching for hidden similarities between the rotations obtained from electromechanical seismometers system and these obtained from AFORS-1. As it is seen in the Figs. 13 – 16, only partial similarity may be found, in the specific frequency bands only. In the two cases presented here, these were the frequency bands 3 - 4.8 Hz and 10 - 12.5 Hz, and to lesser extent – 12.5 - 18 Hz.

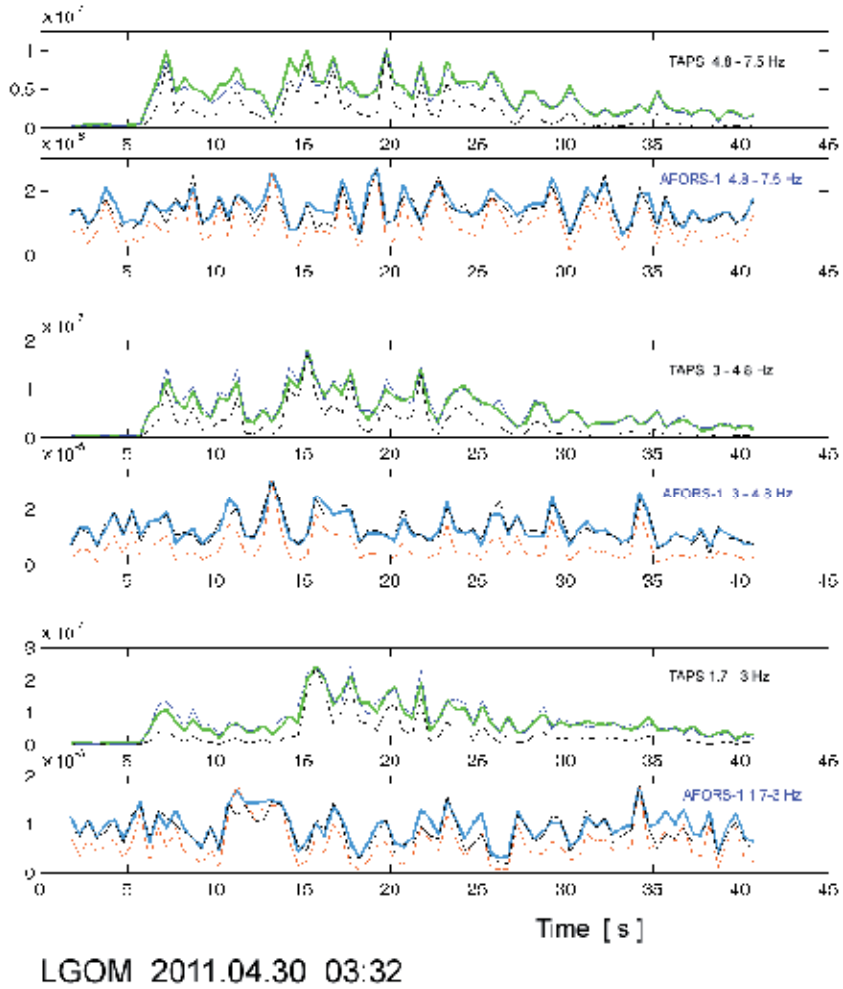

Fig. 14. Analysis as in Fig. 13; the same seismic event. The lower frequency bands: 4.8-7.5 Hz, 3-4.8 Hz and 1.7-3 Hz

It is often hard to find the beginning of the seismic event's trace in the diagram of rotational motions; dividing the signals into frequency bands usually helps in the case of recordings from electromechanical seismometers (TAPSes), but for recordings from AFORS-1 the improvement is smaller. For the frequencies in the band 12.5 - 18 Hz, and higher, the rotational trace of a mining seismic event is often obscured by the noise. This is more clearly seen in the readings from AFORS-1 because of a high sensitivity of this

equipment to high frequency rotations. The mentioned noise might be of an instrumental or external origin, the latter is more probable. Nevertheless, the rotational traces of the seismic events in LGOM area also bear high frequency rotations, in various portions. These high frequency rotations may originate in the focus, or in the vicinity of the seismic station, as a response to the arriving seismic waves. We relate the latter explanation also to the short bursts of high frequency rotational motions, which quite often accompany the recording of an earthquake or other seismic event (Jaroszewicz et al., 2011b).

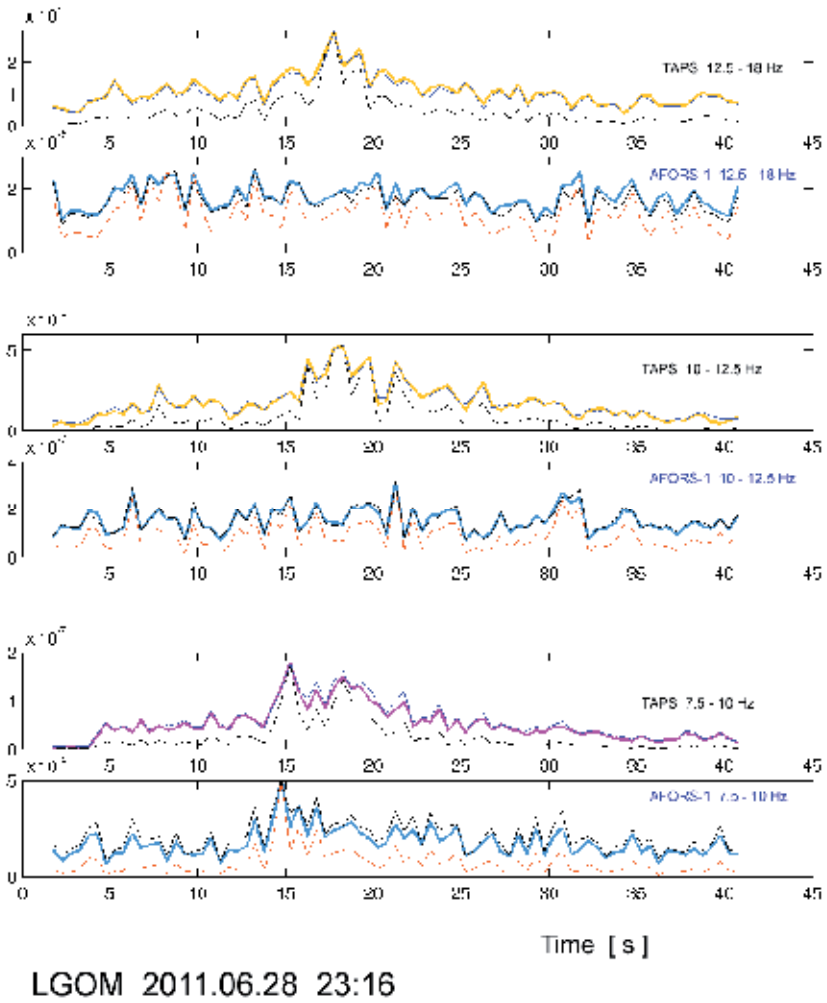

Fig. 15. Analysis as in Fig. 13. The seismic event in LGOM, 2011.06.28, at 23:16 UTC. The upper frequency bands: 12.5-18 Hz, 10-12.5 Hz and 7.5-10 Hz

When a recording from AFORS-1 is analyzed in low frequencies, below 1.7 Hz, a trace of a seismic event is almost not visible, and it is barely discernible also in the frequency band 1.7 – 3 Hz. That's unfortunate, as a substantial part of rotational oscillations comes in low

frequencies. The share of low frequency rotations varies between local events, as was found for several shocks recorded in Ojców, Poland (K. P. Teisseyre, 2006) and in l'Aquila, central Italy (K. P. Teisseyre, 2007). In each of these studies, the rotational motions were derived from the set of two TAPSes, in other words – from two pairs of electromechanical horizontal seismometers.

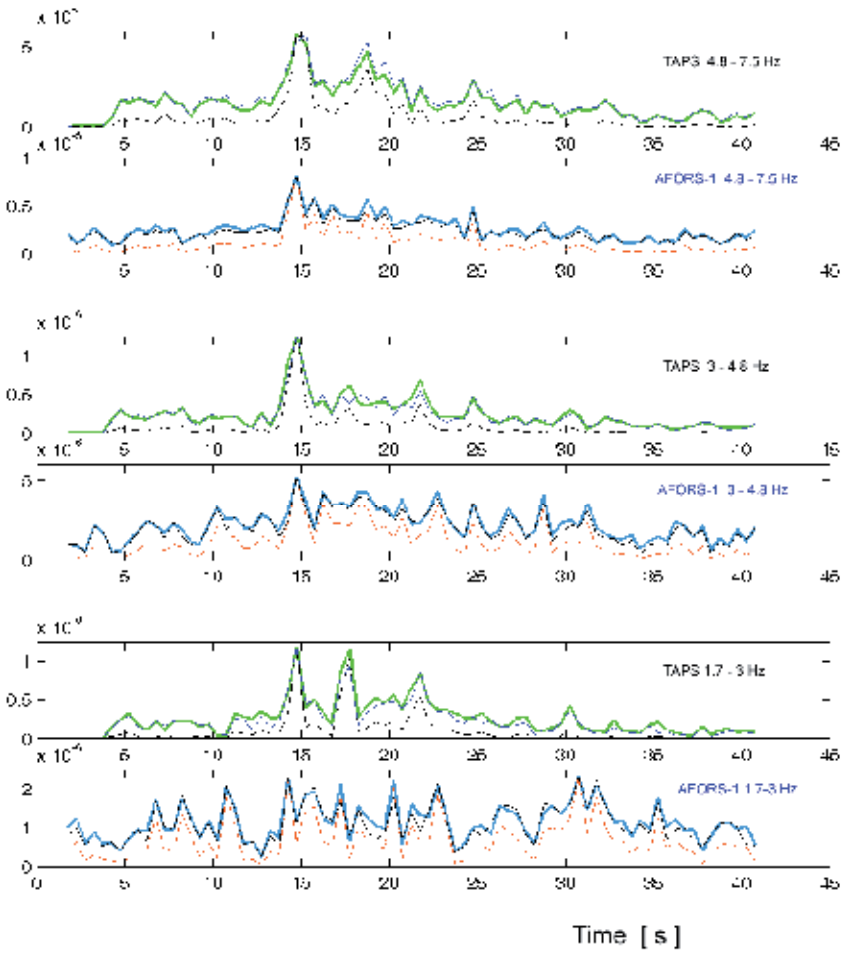

Fig. 16. Analysis as in Fig. 13. The seismic event in LGOM, 2011.06.28, at 23:16 UTC. The lower frequency bands: 4.8-7.5 Hz, 3-4.8 Hz and 1.7-3 Hz

The agreement between the plots of the stage-averaged rotation and the stage-averaged squared rotation is not surprising; it shows that in the seismic energy received at the station, higher amplitudes motions are more important than the smaller ones. On the other hand, in several time-periods (stages), a disagreement between rotational acceleration and the appropriate rotational signal is often found. When the acceleration plot is below that of the adequate rotational velocity plot - see Fig. 14 - this may be explained by a shift from

symmetry of average signal amplitudes in a relation to the zero level. But when we take into account that the acceleration has been amplitude-normalized to the rotation, it is clear that we cannot estimate the size of this shift. Such shifts may be present always, or they may be absent only in some cases and frequency bands, for example - this depicted in Fig. 15, two lowermost panels; here – the acceleration coincide with the rotation or is plotted higher except for the summit.

Some methods of cleaning the signals from possible contaminations are under development, and we are going to record rotational motions with the use of two Sagnac-type interferometers placed at some distance. Nevertheless, the studies outlined here show that the field experiments with AFORS-1 bring an important information concerning the seismic field of mining seismic events.

5. Conclusion

The direct measurement of the absolute rotational components with linear changes of the accuracy form $5.1 \cdot 10^{-9}$ to $5.5 \cdot 10^{-8}$ rad/s, for the detection frequencies range from 0.83 to 106.15 Hz is the main advantage of the presented system AFORS. As shown in the first field test, the system type AFORS appears as the promising device to study both the seismic field generated by earthquakes at least at local distance range, and the reaction of buildings and other constructions to strong motions. In the first domain however, the whole detecting/registering system needs further studies – especially, the recordings analysed both in the low frequencies, below 3 Hz and in the relatively high frequencies, from 18 Hz upwards seem to contain too much noise. But most probably, at least part of this noise comes to the equipment from outside. Therefore, also the conditions at the Książ observatory should be checked again, despite that for other scientific equipment, as the regular seismic station KSPROT, these corridors (excavated by the slaves under German supervision during the second world war) provide the satisfactory environment.

6. Acknowledgment

This work was done in 2011 under the financial support of the Polish Ministry of Science and Higher Education under Key Project POIG.01.03.01-14-016/08 "New photonic materials and their advanced application" and partially the Military University of Technology statutory activity No PBS-829.

7. References

Arditty, H. J. & Lefèvre, H. C. (1981). Sagnac Effect in a Fiber Gyroscope, *Optic. Lett.*, Vol. 6, No8, (August 1981), pp. 401-403, ISSN 0146-9592

Arditty, H. J., Graindorge, Ph., Lefèvre, H. C., Martin, Ph., Morisse J. & Simonpiétri, P. (1989). Fiber-Optic Gyroscope with All-Digital Processing, *Proceedings of OFS 6/'89,* Paris, Springer-Verlag Proceedings in Physics, Vol. 44, pp. 131-136

Auch, W. (1986). The Fiber-Optic Gyro – a Device for Laboratory Use Only?, *SPIE Proceedings,* Vol.719, pp. 28-34, ISSN 0277-786X

Bergh, R. A., Lefèvre, H. C. & Shaw, H. J. (1981). All-Single-Mode Fiber-Optic Gyroscope with Long-Term Stability, *Optic. Lett.,* Vol. 6, No.10, (October 1981), pp. 502-504, ISSN 0146-9592

Burns, W. K. (1986). Phase-Error Bounds of Fiber Gyro With Polarization-Holding Fiber, *J. Lightwave Tech.*, Vol. LT4, No.1, (January 1986), pp. 8-14, ISSN 0733-8724

Cowsik, R, Madziwa-Nussinov T., Wagoner K., Wiens D., Wysession, M. (2009). Performance Characteristics of a Rotational Seismometer for Near-Field and Engineering Applications, *BSSA*, Vol.99, No.2B, (May 2009), pp. 1181-1189, ISSN 0037-1106

Dai, X., Zhao, X., Cai, B., Yang, G., Zhou, K. & Liu, C. (2002). Quantitative Analysis of the Shupe Reduction in a Fiber-Optic Sagnac Interferometer, *Opt. Eng.,* Vol.41, No.6, (June 2002), pp. 1155-1156, ISSN 0091-3286

Droste, Z. & Teisseyre, R. (1976). Rotational and Displacemental Components of Ground Motion as Deduced from Data of the Azimuth System of Seismograph, *Publs Inst. Geophys. Pol. Acad. Sc., Vol.*97, pp. 157-167, ISSN 0139-0109

Eringen, A. C. (1999). *Mirocontinuum field theories. Vol. 1 Foundations and Solids*, Springer-Verlag, ISNB 0-387-95275-6, New York

Ezekiel, S., Davis, J. L. & Hellwarth, R. W. (1982). Intensity Dependent Nonreciprocal Phase Shift in a Fiberoptic Gyroscope, *Springer Series in Optical Sciences*, Vol.32, pp. 332-336

Ferrari, G. (2006). Note on the Historical Rotation Seismographs, in: *Earthquake Source Asymmetry, Structural Media and Rotation Effects*, R. Teisseyre, M. Takeo & E. Majewski, (Eds.), 367-376, ISBN 3-540-31336-2, Springer, Berlin

Franco-Anaya, R., Carr, A. J. & Schreiber. K. U. (2008). Qualification of Fibre-Optic Gyroscopes for Civil Engineering Applications, *Proc. of the New Zealand Society of Earthquake Engineering (NZSEE) Conf.,* (available on CD-ROM), Wairakei, New Zealand, 2008

Fredricks, R. J. & Ulrich, R. (1984). Phase-Error Bounds of Fibre Gyro with Imperfect Polariser/Depolarizer, *Electron. Lett.*, Vol.20, No.8, pp. 330-332, ISSN 0013-5194

Harress, F. (1912). Die geschwindigkeit des lichtes in bewegten korper, *Dissertation,* Jena, Germany

Harzer, P. (1914). *Astron, Nachr.*, Vol.198, pp.377-378

Jaroszewicz, L. R. & Krajewski Z. (2008). Application of the Fibre-Optic Rotational Seismometer in Investigation of the Seismic Rotational Waves, *Opto-Electron. Rev.,* Vol.16, No.3, (September 2008), pp. 314-320, ISSN 1230-3402

Jaroszewicz, L. R. & Wiszniowski J. (2008). Measurement of Short-Period Weak Rotation Signals, in: *Physics of Asymmetric Continuum: Extreme and Fracture Processes*, R. Teisseyre, H. Nagahama & E. Majewski, (Eds.), pp.17-47, ISBN 978-3-540-68354-4, Springer, Berlin

Jaroszewicz, L. R., Krajewski, Z. & Teisseyre, K. P. (2011b). Usefulness of AFORS – Autonomous Fibre-Optic Rotational Seismograph for Investigation of Rotational Phenomena, *Journal of Seismology,* Special issue: Rotational Ground Motions, in press, ISSN 1383-4649

Jaroszewicz, L. R., Krajewski, Z. & Teisseyre, K. P. (2011c). The Possibility of a Continuous Monitoring of the Horizontal Buildings' Rotation by the Autonomous Fibre-Optic Rotational Seismograph AFORS Type, *6th European Workshop on the seismic behaviour of Irregular and Complex Structures (6EWICS),* Haifa, Israel, 12-13 Sept. 2011 – in press

Jaroszewicz, L. R., Krajewski, Z.& Solarz, L. (2006). Absolute Rotation Measurement Based on the Sagnac Effect. in: *Earthquake Source Asymmetry, Structural Media and Rotation Effects,* R. Teisseyre, M. Takeo & E. Majewski E. (Eds), pp.413-438, ISBN 3-540-31336-2, Springer, Berlin

Jaroszewicz, L. R., Krajewski, Z., Kowalski, H., Mazur, G., Zinówko, P. & Kowalski, J. K. (2011a). AFORS Autonomous Fibre-Optic Rotational Seismograph: Design and Application. *Acta Geophys., Vol.* 59, No.3, (March 2011), pp. 578-596, ISSN 0001-5725

Jaroszewicz, L. R., Krajewski, Z., Solarz, L., Marć, P. & Kostrzyński T. (2003). A New Area of the Fiber-Sagnac Interferometer Aapplication, *Proc. Intern. Micro-Opt. Conf. IMOC-2003*, Part II, *Iguazu Falls, Brazil, 20-23 Sept. 2003*, SBMO/IEEE (2003), pp. 661-666

Kanamori, H. (1994). *Annu. Rev. Earth Planet. Sci.*, Vol.22, pp. 207-307

Kao, C. G. (1998). Design and Shaking Table Tests for a Four-storey Miniature Structure Built with Replaceable Plastic Hinges, *Master's Thesis,* University of Canterbury, Australia

Kozák, J. T. (2006). Development of Earthquake Rotational Effect Study, In: *Earthquake Source Asymmetry, Structural Media and Rotation Effects*, R. Teisseyre, M. Takeo & E. Majewski, (Eds.), 3-10, ISBN 3-540-31336-2, Springer, Berlin

Krajewski, Z. (2005). Fiber-Optic Sagnac Interferometer as Device for Rotational Effect Investigation Connected with Seismic Events (in Polish). *Doctor Thesis,* Military University of Technology, Warsaw, Poland

Krajewski, Z., Jaroszewicz, L. R. & Solarz, L. (2005). Optimization of Fiber-Optic Sagnac Interferometer for Detection of Rotational Seismic Events, *SPIE Proceedings,* Vol.5952, pp. 240-248, ISSN 0277-786X

Lee, W. H. K, Celebi, M., Todorovska, M. I. & Igel, H. (2009). *Rotational Seismology and Engineering Applications,* BSSA, Vol.99, No.2B, (May 2009), ISSN 0037-1106

Lefèvre, H. C., Bettini, J. P., Vatoux, S. & Papuchon, M. (1985a). Progress in Optical Fiber Gyroscopes Using Integrated Optics, *Proceedings of AGARD-NATO*, Vol. CPP-383, pp. 9A1-9A13

Lefèvre, H. C., Graindorge, Ph., Arditty, H. J., Vatoux S. & Papuchon, M. (1985b). Double Closed-Loop Hybrid Fiber Gyroscope Using Digital Phase Ramp, *Proceeding of OFS 3/'85*, San Diego, OSA/IEEE, Postdeadline Paper 7

Martin, J. M. & Winkler, J.T. (1978). Fiber-Optic Laser Gyro Signal Detection and Processing Technique, *SPIE Proceedings,* Vol.139, pp. 98-102, ISSN 0277-786X

McGinnis, (2004). Apparatus and method for detecting deflection of a tower, *U.S. Patent application*, No.0107671 A1, (10 June 2004)

Michelson, A. A. & Gale, H. G. (1925). The Effect of the Earth's Rotation on Light Velocity," *Nature,* Vol.115, (18 April 1925), pp.566-566, ISSN 0028-0836

Pogany, P. (1926). Über die Wiederholung des Harress-Sagnacschen Versuches, *Ann. Physik*, Vol. 385, No11, pp.217-231, ISSN 0003-3804

Post, E. J. (1967). Sagnac effect, *Rev. of Modern Physics*, Vo.39, No2, (April 1967), pp.475-493. ISSN 0034-6861

Sagnac, G. (1913). L'ether lumineux demontr par l'effet du vent relatif d'Etherdanus un interferometre en rotation uniforme, *Compte-rendus a l'Academie des Sciences,* Vol.95, pp. 708-710

Schreiber, K. U., Velikoseltsev, A., Carr, A. J. & Franco-Anaya, R. (2009). The application fiber optic gyroscope for the measurement of rotations in structural engineering, *BSSA*, Vol.99, No.2B, (May 2009), pp. 1207-1214, ISSN 0037-1106

Schreiber, U., Schneider, M., Rowe, C.H., Stedman, G.E. & W. Schlüter (2001). Aspects of Ring Lasers as Local Earth Rotation Sensors, Surveys in Geophysics, Vol.22, No.5-6, (September 2001), pp. 603-609, ISSN 0169-3298

Solarz, L., Krajewski, Z. & Jaroszewicz, L. R. (2004). Analysis of Seismic Rotations Detected by Two Antiparallel Seismometers: Spline Function Approximation of Rotation and Displacement Velocities, *Acta Geophys. Pol., Vol.* 52, No.2, (June 2004), pp. 198–217, ISSN 0001-5725

Takeo, M., Ueda, H. & Matzuzawa T. (2002). Development of Hight-Gain Rotational-Motion Seismograph, *Grant 11354004*, Erthquake Research Institute, Univ. of Tokyo, 5-29

Teisseyre, K. P. (2006). Mining Tremors Registered at Ojców and Książ Observatories: Rotation Field Components, *Publs. Inst. Geophys. Pol. Acad. Sc.*, M-29 (395), pp. 77-92

Teisseyre, K. P. (2007). Analysis of a Group of Seismic Events Using Rotational Components, *Acta Geophys.*, Vol.55, No.4, (April 2007), pp. 535-553, ISSN 0001-5725

Teisseyre, R. & Boratyński, W. (2002), Continuum with Self-Rotation Fields: Evolution of Defect Fields and Equations of Motion, *Acta Geophys.*, Vol.50, No.3, (March 2002), pp. 223-229, ISSN 0001-5725

Teisseyre, R. & Gorski, M. (2009), Transport in Fracture Processes: Fragmentation of Defect Fields and Equations of Motion, *Acta Geophys.*, Vol.57, No.5, (May 2009), pp. 583-599, ISSN 0001-5725

Teisseyre, R. & Kozák, J. T. (2003). Considerations on the Seismic Rotation Effects. *Acta Geophys.*, Vol.51, No.3, (March 2003), pp. 243-256, ISSN 0001-5725

Teisseyre, R. (2005). Asymmetric Continuum Mechanics: Deviations from Elasticity and Symmetry, *Acta Geophys.*, Vol.53, No.2, (February 2005), 115-126, ISSN 0001-5725

Teisseyre, R., Białecki, M. & Górski, M. (2005). Degenerated Mechanics in a Homogeneous Continuum: Potentials for Spin and Twist, *Acta Geophys.*, Vol.53, No.3, (March 2005), pp. 219-23. ISSN 0001-5725

Teisseyre, R., Nagahama, H. & Majewski, E. (Eds.) (2008). *Physics of Asymmetric Continuum: Extreme and Fracture Processes. Earthquake Rotation and Solition Waves*, ISBN 978-3-540-68354-4, Springer-Verlag, Berlin-Heidelberg

Teisseyre, R., Suchcicki, J., Teisseyre, K. P. & Palangio, P. (2003). Seismic rotation waves: basic elements of theory and recording, *Annals Geophys.*, Vol.46, No.4, (August 2003), pp. 671-685, ISSN 2037-416X

Teisseyre, R., Takeo, M. & Majewski, E. (Eds.) (2006). *Earthquake Source Asymmetry, Structural Media and Rotation Effects*, ISBN 3-540-31336-2, Springer, Berlin

Ulrich, R. (1980). Fiber-Optic Rotation Sensing With Low Drift, *Optic. Lett.,* Vol. 5, No5, (May 1980), pp. 173-175, ISSN 0146-9592

Vali, V. & Shorthill, R. W. (1976). Fiber Ring Interferometer, *Appl. Optics,* Vol.15, No5, (May 1976), pp.1099-1100, ISSN 0733-8724

Part 4

Earthquakes and Planning

17

Experience with Restoration of Asia Pacific Network Failures from Taiwan Earthquake

Yasuichi Kitamura[1], Youngseok Lee[2],
Ryo Sakiyama[3] and Koji Okamura[3]
[1]*National Institute of Information and Communications Technology,*
[2]*Chungnam National Univeristy,*
[3]*Kyushu University*
[1,3]*Japan*
[2]*Korea*

1. Introduction

As the Internet grows, networks become larger and more complex, and the number of components, such as routers, switches, and fiber cables, increases. In complicated network systems, it is difficult to implement global network management across several Internet service providers (ISPs) that use a lot of network components in a large-scale network topology. Fault management is a particularly important network management issue in complex network systems because the Internet has become essential to business and research. However, we are only beginning to learn how to deal with global network failures in large networks.

Failures have been reported in Sprint Internet protocol (IP) backbone, which shows that failures can be observed in everyday operation (Iannanccone et al., 2002; Markopulou et al., 2004). However, the network failures observed by (Iannaccone et al., 2002) and (Markopoulou et al., 2004) were short-lived and small scale, and their impacts were analyzed only in the context of a single ISP. Most network backup or fault restoration methods have been studied and proposed for the various layers such as wavelength division multiplexing (WDM), multi-protocol label switching (MPLS), or IP (Fumagalli & Valcarenghi, 2000; Gerstel & Ramaswami, 2000; Ramamurthy et al, 2003; Saharabuddhe et al., 2004; Sharma & Hellstrand, 2003). Yet, the proposed backup and restoration methods have not been fully implemented and deployed in the real network. Since real networks are more complicated than theoretical ones, the impacts of network failures on users and ISP's cannot be completely predicted and analyzed. Significant network failures due to natural disasters such as earthquakes, floods, or fires could have particularly wide impact on several ISPs.

We discuss the results of the critical network failures that occurred after the Taiwan earthquake in Dec. 2006, which cut fibers and caused network failures. We also explain how restoration methods such as automatic border gateway protocol (BGP) (Lougheed & Rekhter, 1989) re-routing, BGP policy change, and switch reconfiguration were conducted. We hope that the experience and knowledge we gained during the process of recovering

from this huge natural disaster, which affected the global Internet, can be shared and can contribute to future Internet network management research. To the best of our knowledge, this is the first detailed study of network restoration after global network failures due to a natural disaster.

Although many natural disasters have occurred in the 21st century, until recently there had been no simultaneous outage of the global Internet backbone. However, the earthquake that occurred around Taiwan in 2006 made several Asia Pacific Research and Education (R&E) networks unreachable. At 21:26 and 21:34 on December 26th (UTC+9), 2006, there was a big undersea earthquake off the coast of Taiwan twice, which measured 7.1 and 6.9 respectively on the moment magnitude (Hanks & Kanamori, 1979). This earthquake caused significant damage to the undersea fiber cable systems in that area. Several ISPs were affected because each cable system is shared by multiple ISP's. This earthquake had the effect of dividing the Asia Pacific R&E networks into an eastern and a western group. The Asia Pacific R&E networks were, in particular, seriously damaged but were fully restored after several restoration steps, including automatic BGP re-routing, BGP policy changes, and switch port reconfigurations, were taken.

The first step in recovery after the earthquake was taken automatically by BGP routers, which detoured traffic along redundant routes. In BGP routing, there are usually multiple redundant AS paths. Redundant BGP routes have served as backup paths but have provided poor quality connectivity, i.e., long round trip time (RTT). Because of the congestion on the narrow-bandwidth link that was subsequently reported, operators took manual control of traffic to improve communication quality. The second step was a traffic engineering process intended to prevent narrow-bandwidth links from filling up with detoured traffic. The operators changed the BGP routing policy related to the congested ASs. In spite of the routing-level restoration, a few institutions were still not directly connected to the R&E network community because they had only a single link to the network. For these single-link networks, the commodity link was used temporarily for connectivity. However, the commodity link was not stable and not sufficient to carry a huge amount of bandwidth or to provide next generation Internet service. To restore the single-link networks, cable connection configurations at the switches were changed.

The fiber break caused by the Taiwan earthquake raised restoration issues related to BGP re-routing. In such an emergency, the backup routes should be chosen based on available bandwidth and RTT. Since the fiber break required an urgent network recovery process, network operators configured re-routing based on their experience with bandwidth and RTT.

From this experience, we have learned that redundant physical backup links and routes are important to providing bandwidth and connectivity and that the Quality-of-Service (QoS) after recovery is also important. From the viewpoint of restoration after network failures, there are still challenges that cannot be automatically overcome by network management systems. A systematic risk management plan that includes collaboration among operators of the next-generation Internet is needed.

The remainder of this chapter is as follows. In Section 2, the Asia Pacific R&E networks that were damaged by the earthquake or related events are introduced. Section 3 introduces the R&E connection especially in Asia Paicifc area and the issues caused by such inter-connectivity of R&E networks. Section 4 is a detailed report of the network failures that were observed after the earthquake. Section 5 describes the processes to restoring the disrupted communications in the area. Section 6 discusses what we have learned from the observation of the network failures and recovery processes. Finally, we conclude the paper in Section 7.

2. Research and education network activities in the Asia Pacific area

2.1 Asian Internet Interconnection Initiative (AIII)

When AIII (Asian Internet Interconnection Initiative [AIII], n.d.) started in 1996, this project was the first next generation Internet R&E network in Asia. The basic idea of AIII is to provide Internet services via satellite. There are AIII members in TH, MY, ID, and SG (Tbl. 3). NP also recently joined the project. The AIII's major effort is to build up the access points of non-broadband networks. In Asia, it was very hard to complete the network over telephones lines, and preparing earth stations represented a better chance of accessing the Internet. The biggest drawback of this project is that the total bandwidth is limited to between 1.5 and 8 Mbps. In 1996, 2 Mbps was enough bandwidth to start research activities. Now, however, even 8 Mbps is insufficient for network technology research activities. These days, AIII concentrates on developing and deploying certain advanced technology on their network, for example, IPv6 unicast, IPv6 multicast, Uni Directional Link Routing (UDLR), and advanced TCP.

2.2 Asia-Pacific Advanced Network (APAN)

APAN (Asia-Pacific Advanced Network [APAN], n.d.) started in 1997. APAN is the research consortium as well as it operates a next generation Internet service. The bandwidths of the backbone networks of APAN in 1998 were between 1 Mbps and 35 Mbps. The US next generation Internet project "very high speed Backbone Network Service" (vBNS) already had 155 Mbps bandwidth service in their backbone network. The operating policy of APAN was to provide high performance data transfer service, because, in 1998, it was still impossible to implement a huge bandwidth network in the Asia Pacific area. Now, the APAN network covers the Asia Pacific area, providing bandwidth between 45 Mbps and 10 Gbps. In 2011, APAN became the none-profit organization and APAN strongly supports the research activities over the R&E networks in Asia Pacific area.

2.3 Trans-Eurasian Information Network 2 (TEIN2)

TEIN or TEIN1 was an EU project that connected Europe and Korea. It started with a bandwidth of 10 Mbps. TEIN2 (Delivery of Advanced Network Technology to Europe [DANTE], n.d.) is a bit different from TEIN in that it has two goals. One is to provide an access network to Europe, and the other is to develop an interconnection network in the Southeast Asian area whose bandwidth is between 45 Mbps and 1 Gbps. The main characteristic of the design topology is that it is not the star-shaped. That is, the TEIN2 network itself has its own backbone with connecting the four NOCs, and the number of routes for communicating between NOCs are more than two. It provides each Southeast Asian site with several routes to access the others. TEIN3 started in 2010 and TW, KH, LA, IN, LK, NP, PK, BD and BT (Tbl. 3) joined this activity.

3. Background of R&E network

3.1 R&E network status in 2006

In the old star-shaped R&E network topology (Fig. 1) communication between the point sites had to go through the center of the star. Communication along these routes was frequently delayed due to the configuration. Now, however, the R&E network community has grown, and the former point sites are now sometimes the center of a star. In some cases this growth generated several routes between two sites (Fig. 2).

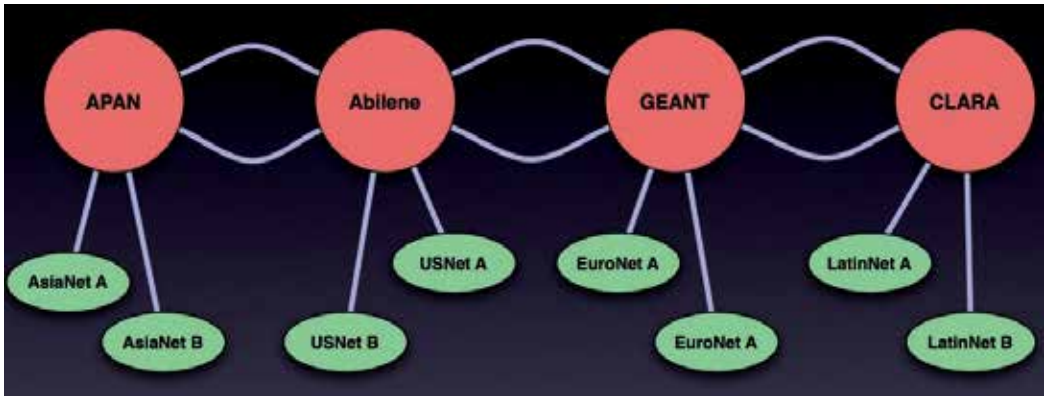

Fig. 1. Star shaped R&E networks(Robb, 2006)

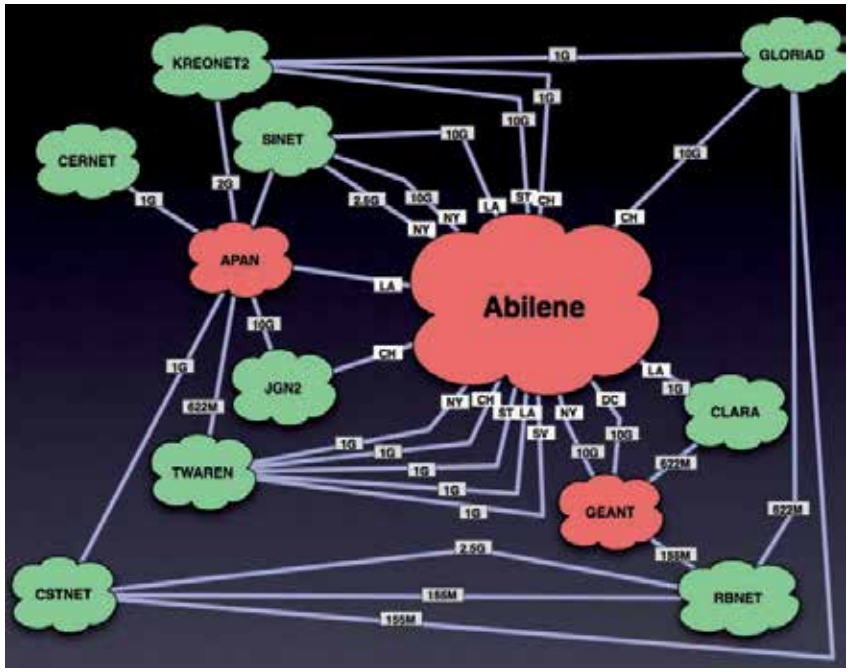

Fig. 2. Actual R&E networks(Robb, 2006)

This complicated topology made the operation of the R&E networks more difficult. To simplify operations, Research and Education Network Operators Group (RENOG), (Research and Education Network Operators Group [RENOG], n.d.) was developed and started reconfiguring the complicated and unstable routing. However, in the APAN area, the complicated routing unexpectedly worked and it was able to maintain high-speed communication with most of the network researchers, though with some delay. Network engineers like the word "redundancy" but most of the network engineers in the APAN area did not expect that the complicated topology and the complicated routing information would work so well in an emergency.

3.2 Before the earthquake

The TEIN2 project started in 2006. Before that, the network topology style in Asia Pacific area was close to the star shape. Most of the networks in the APAN area started in Japan, and if a network did not start from Japan, it started from one of the point sites. That is why the star shape was kept. However, the TEIN2 topology does not look like a star. Even inside TEIN2, there are two or three routes to reach any other sites. An engineering meeting was held before TEIN2 started at which an agreement on routing policy seemed to have been reached. However, after TEIN2 started, there happened some of routing troubles in Asian Pacific area. A few troubles were from TEIN2 network directly but others were the routing advertise issues from the National Research and Education Networks (NRENs) of the TEIN2. To solve these problems, the operators held many meetings to develop tools. One tool summarized traffic conditions for each route (Asia-Pacific Advanced Network Japan [APAN-JP], n.d.). Another was a database to record preferable routes for each XP (Kurokawa, 2006). These were essentially monitoring and advising tools, not route configuration tools. Actual operations were done at the XPs based on the database, which was built by the database tool (Kurokawa, 2006). At the APAN Tokyo XP, the abstract of the routing policy was as follows.

- Communication with ID, SG, MY, TH, VN, CN, and AU (Tbl. 3) should be routed through TEIN2.
- Communication with PH should be direct.
- Communication with Micronesia should be routed through the Hawaii XP.
- Communication with TW should be direct.
- Generic communication with EU should be through US.
- Communication with US should be direct.

Figure 3 shows the one of the worst examples of communication between US university through KR. That is, if a university in US established communication with Merit or the University of Michigan, the packets were transferred through KR. In such a case, TCP-based applications often met with communication problems.

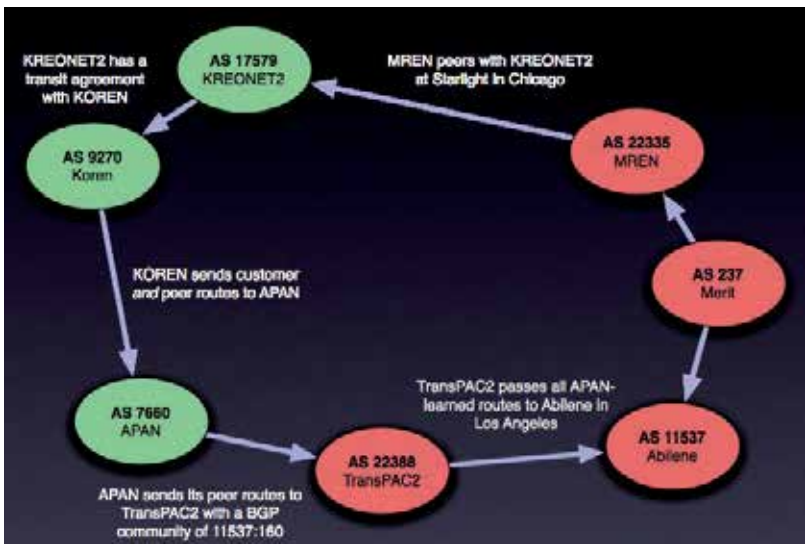

Fig. 3. Incorrect routing between universities in US through KR(Robb, 2006)

4. Network failures caused by Taiwan earthquake

4.1 Fiber breaks

On December 26th, 2006 (UTC+9) there were two huge earthquakes near Taiwan. The first earthquake happened at 20:26 (UTC+8) (Academia Sinica, n.d.a), and the second one at 20:34 (UTC+8) (Academia Sinica, n.d.b). Fortunately, the earthquakes took place under the sea and the cities in TW were not heavily damaged, as happened in 1999. However, these two earthquakes did cause landslides over a wide area on the seabed near the Taiwan island. At 04:00 (UTC+9) on December 27th 2006, that is, after the second earthquake, the R&E networks in the Asian area were shutdown. The cable companies investigated the reason for the lost connection and found that the earthquake had caused damage to the cable systems.

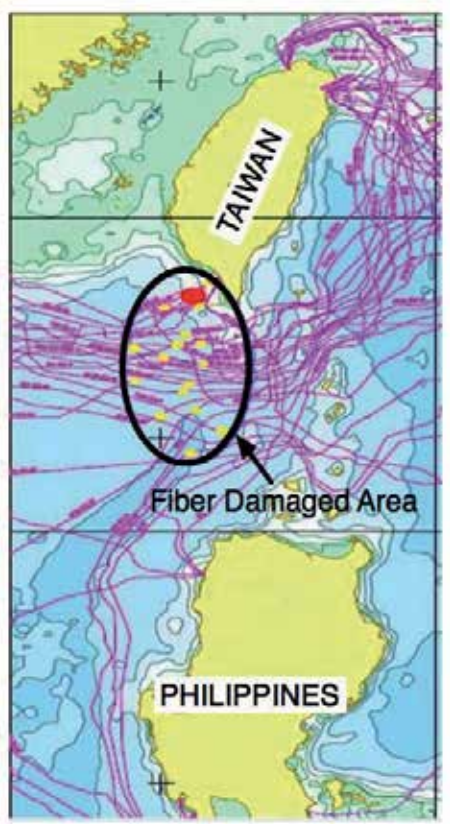

Fig. 4. Fiber cut area around Taiwan island (Konishi, 2007)

The circle in Fig. 4 shows the area where the cable systems were cut off. Most of the fiber cables in the eastern Asia area went through southwestern Taiwan. These cables were generally bought and shared by different telecom companies.

4.2 Internet disconnections and lost BGP peerings

After the earthquake, both commodity Internet traffic and R&E traffic were cut off. For instance, the JP-PH, JP-CN, JP-SG, CN-US, HK-KR, TW-(HK+CN), and TW-SG connections were lost. That is, the R&E network communities were divided into two groups. One was

the group that consisted of JP, KR, TW, and US, and the other consisted of CN, HK, VN, MY, TH, SG, ID, and PH (Fig 5).

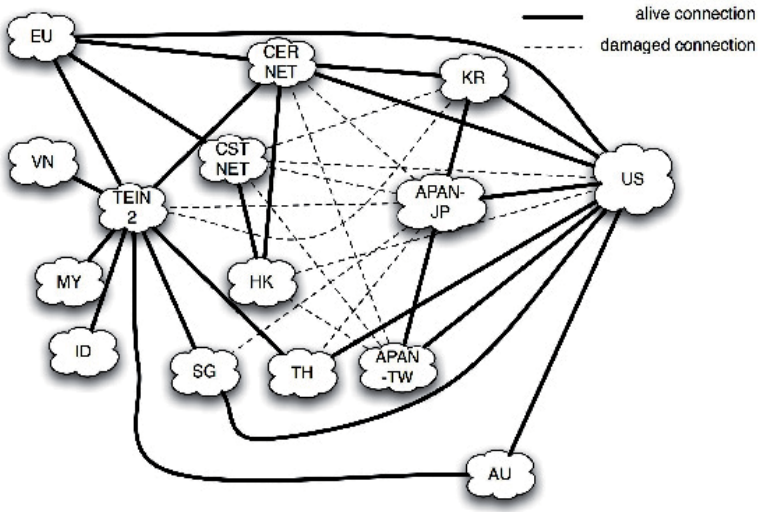

Fig. 5. Splitted R&E networks in Asia Pacific area

The Internet disconnection occurred in the following order.

1. Link-layer disconnection because of the fiber cut
2. Lost primary BGP peerings
3. Automatic BGP re-routing along the alternative peer if any

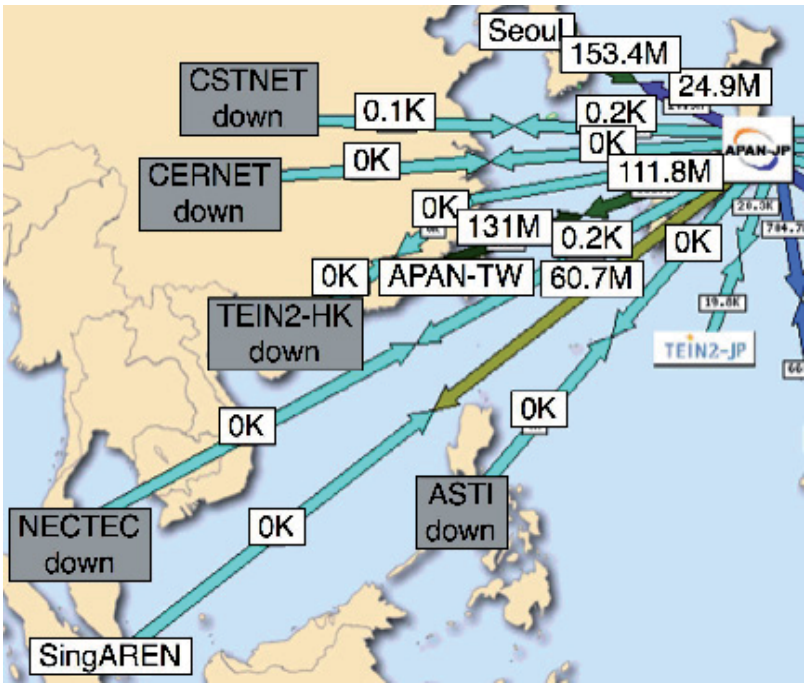

Fig. 6. Traffic weather map on Dec.27 2006

Figure 6 shows the Internet traffic weather map at APAN Tokyo XP (APAN-JP, n.d.), which displays connectivity and link utilization in real time. In Fig. 6 it can be observed that the JP-HK-CN, JP-TH, JP-SG, and JP-PH communications were lost and that there was 0% link utilization except a 100 Mbps load between JP and KR.
The link-layer disconnection caused BGP sessions to expire. BGP peerings from JP to HK+CN, TH, SG, and PH were lost and automatically diverted to detour routes.
In general, when traffic is transferred to the detour AS routes, the traffic will flow along the longer AS path rather than the usual one, because the shortest AS path will be selected as the primary AS path according to BGP policy.

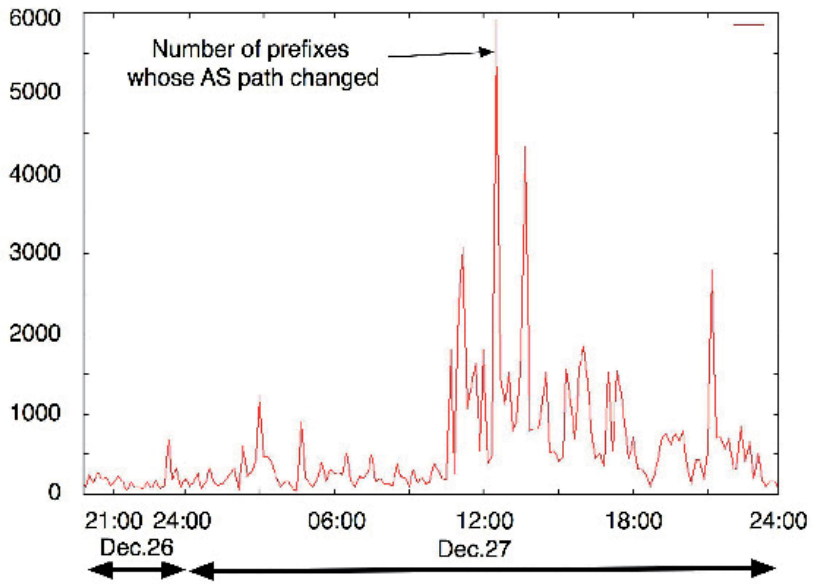

Fig. 7. Number of IP prefixes that experienced AS path changes (2006.12.26 - 2006.12.27 at QGPOP)

Figure 7 shows the AS path changes of each IP prefix observed just after earthquake from the QGPOP (Kyushu GigaPOP Project [QGPOP], n.d.) BGP router in JP. It can be seen in Fig. 7 that more than 1000 IP prefixes experienced AS path changes after the earthquake.

4.3 Traffic load changes

Fortunately, despite the earthquake, the CN-KR and KR-JP cables were unbroken. Therefore, we were able to observe the detour traffic along these links due to BGP re-routing.
Figure 8 shows the traffic between JP and KR on Dec. 27th, 2006. At about 04:30 (UTC+9) the inbound traffic pattern between JP and KR had changed dramatically. At the same time, as can be seen in Fig. 9, the traffic between JP and PH disappeared.
The reason for the traffic change could be inferred from the routing policy of APAN Tokyo XP. The route from CN to JP through KR was one of the lowest priority routes, but after the earthquake, it was chosen because there were no available BGP routes with high priorities.

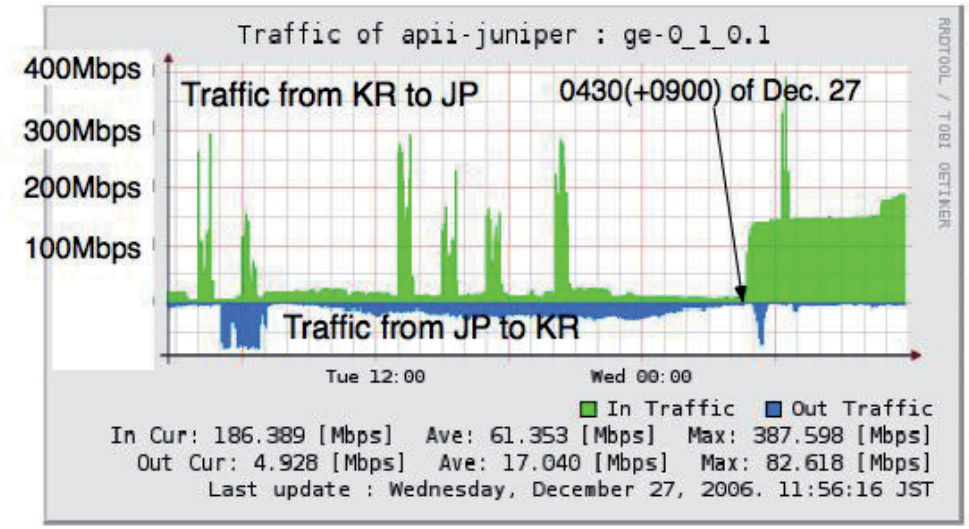

Fig. 8. Traffic between JP and KR on Dec.27 (UTC+9)}

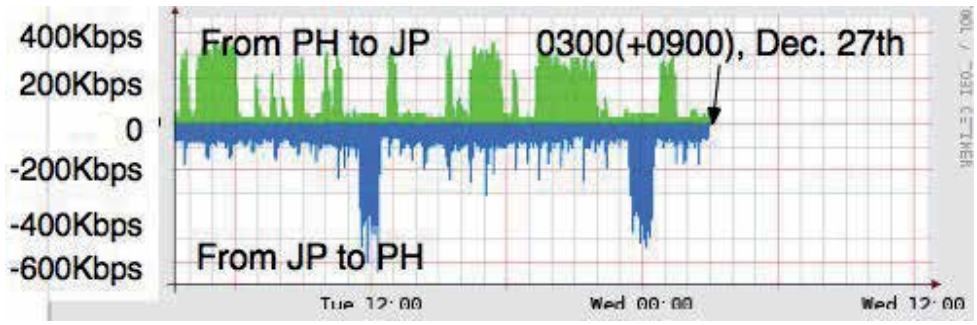

Fig. 9. Traffic between JP and PH on Dec.27 (UTC+9)

4.4 Changes of BGP routing tables

Table 1 shows the registered routing policy table of the Asia Pacific R&E networks. It can be observed that ASTI (PH) lost connectivity to the R&E networks, that CSTNET (CN) lost eastbound routes, and that APAN-JP (JP) lost connectivity to TEIN2.

CERNET (CN) had a direct connection to TW, but after the earthquake its connection was expected to be changed to the path through US, as shown in Fig. 10. But, the routing policy arrangement was different between JP and KR. The forward path between CN and TW chose the route through JP but the return path chose the route through US as shown in Fig. 11.

In addition, routing from JP to the "west" Asian networks (Fig. 5) was connected through US. The direct link between CSTNET (CN) and US was also damaged.

Both CERNET and APAN Tokyo XP expect that the detour for JP-CN traffic should be through US, not through KR. Figure 10 shows the expected BGP route and the actual route between APAN-TW and CN. Since only APAN Tokyo XP implemented the strict routing policy, the CN traffic chose the shortest AS path. However, the traffic from JP to CN chose a routing policy that does not choose the route through KR.

Src\Dst	APAN-JP (JP)	CERNET (CN)	APAN-TW (TW)	KOREN (KR)	ASTI (PH)	CSTNET (CN)	TEIN2	SingAREN (SG)	UniNet (TH)	ThaiSARN (TH)	KREONET2 (KR)	AARNET (AU)
APAN-JP		D	direct	direct	U	C	U	direct	D	U	US	US Hawaii
CERNET	D		D	direct	U	N.A.	TEIN2	TEIN2	TEIN2	TEIN2	TEIN2	TEIN2
APAN-TW	direct	D		APAN-JP	U	U	N.A.	N.A.	N.A.	N.A.	APAN-JP	APAN-JP
KOREN	direct	direct	APAN-JP		U	U	TEIN2	TEIN2	TEIN2	TEIN2	direct	TEIN2
ASTI	U	U	U	U		U	U	U	U	U	U	U
CSTNET	C	N.A.	U	U	U		N.A.	N.A.	N.A.	N.A.	U	N.A.
TEIN2	U	TEIN2	N.A.	TEIN2	U	N.A.		TEIN2	TEIN2	TEIN2	KOREN	TEIN2

D: Detoured path through US U: unreachable
C: Commodity link connection N.A. Non applicable

Table 1. The monitored routing table for each R&E network on Dec.27 2006 (Kurokawa, 2006)

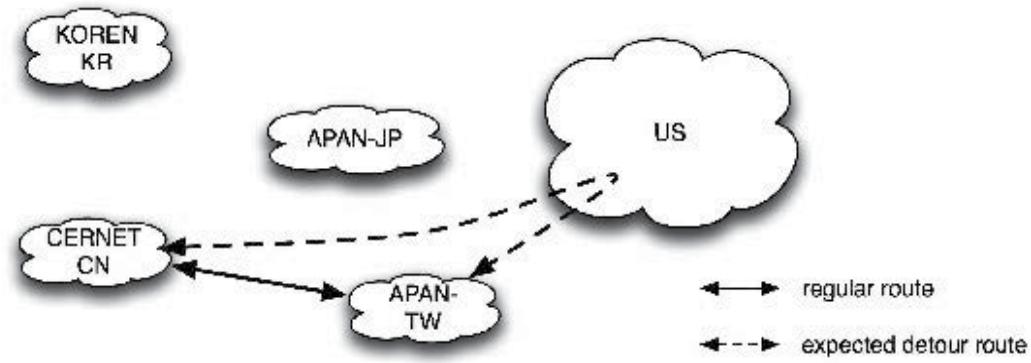

Fig. 10. BGP route changes of APAN before earthquake (Dec. 2006)

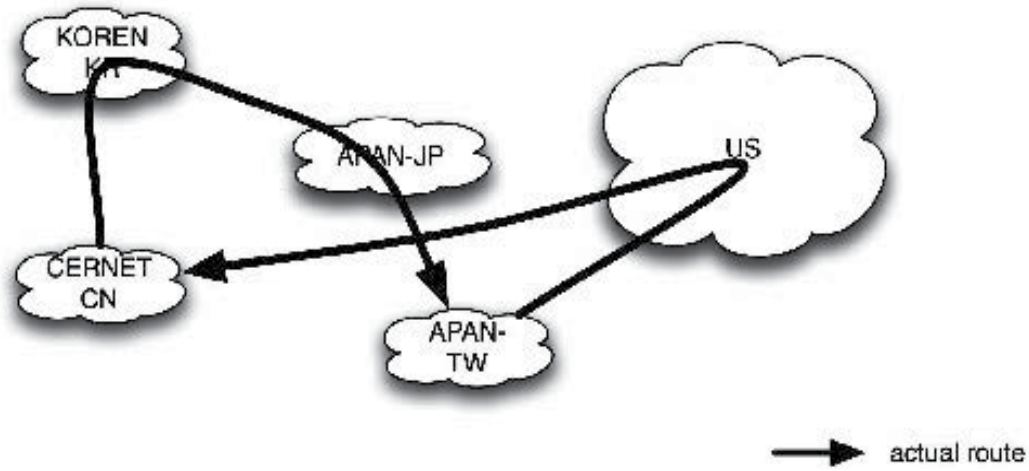

Fig. 11. BGP route changes of APAN after earthquake (Dec. 2006)

4.5 AS-level topology changes

To investigate the BGP route changes in detail, we used an AS-topology visualization tool called "ABEL2" (Sakiyama et al., 2006) that utilizes BGP routing tables that are stored every 10 minutes.

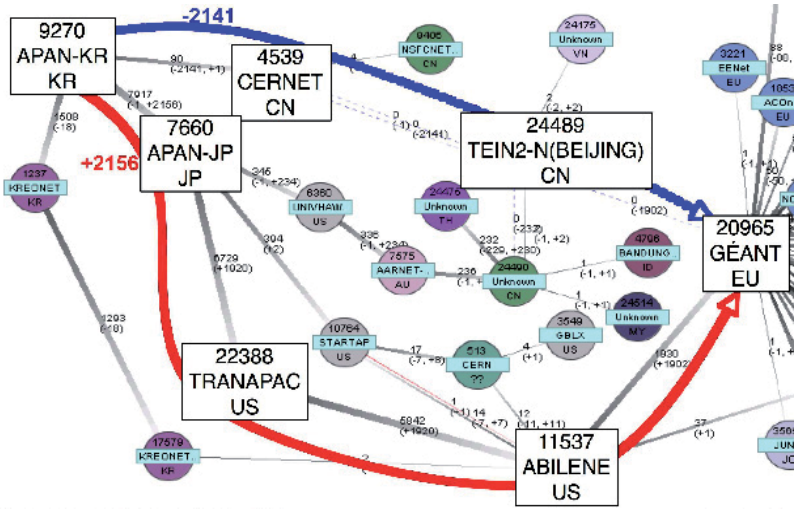

Fig. 12. After the earthquake at 19:30, Dec. 27 (UTC+9) 2006, the route from APAN-KR to GÉANT was diverted to a long AS path of (APAN-KR, APAN-JP, TransPAC, Abilene, GÉANT)

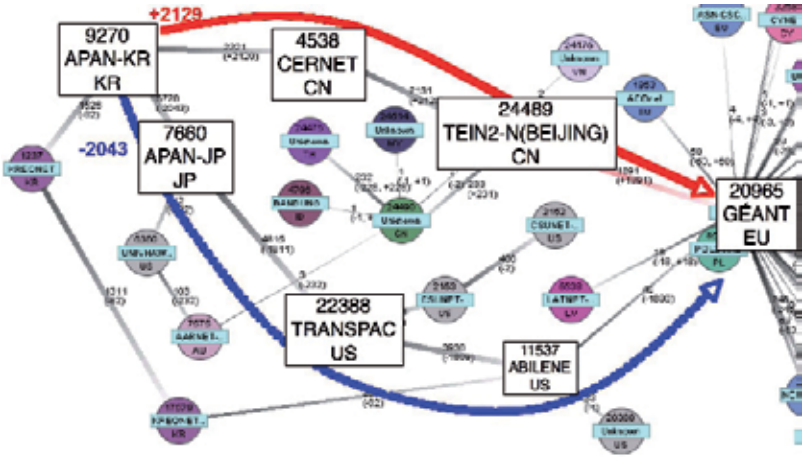

Fig. 13. Reconfigured AS path from APAN-KR to GÉANT (APAN-KR, CERNET, TEIN2-N, GÉANT) at 20:30, Dec. 27 (UTC+9) 2006

Figures 12, 13, and 14 show the changes between APAN-KR (AS9270) and GÉANT (AS20965) by the number of IP prefixes. It can be observed in Fig. 12, that just after the earthquake, at 19:30 on December 27th (UTC+9), 2006, the route from APAN-KR to GÉANT was diverted to the long AS path APAN-KR - APAN-JP - TransPAC (US) -

Abilene (US) – GÉANT (Tbl. 4) because of the TEIN2 link outage. Therefore, to connect APAN-KR to GÉANT with a shorter AS path, the operator configured the BGP routing policy to make CERNET (CN) announce GÉANT prefixes. As shown in Fig. 13, the route from APAN-KR to GÉANT was switched through CERNET at 20:30 on Dec. 27th (UTC+9), 2006. At 20:50 on Dec. 17th, 2006 (UTC+9), the TEIN2-SG NOC announced the route to EU, too. Since the link bandwidth between SG and KR is larger than that between CN and KR, the operator made a configuration for BGP routers to choose the AS path with the KR-SG link (Fig. 14).

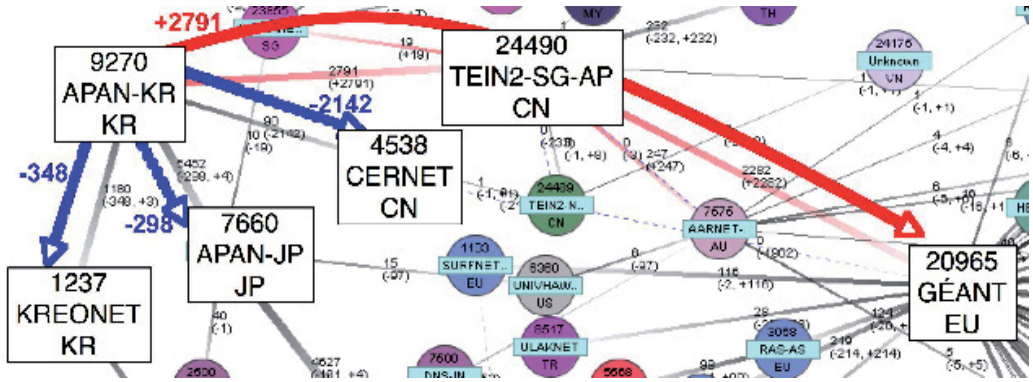

Fig. 14. Reconfigured AS path from APAN-KR to GÉANT through TEIN2-SG at 20:50, Dec. 27 (UTC+9) 2006

4.6 Delay changes

When Australia's Research and Education Network (AARNET) proposed that it would transit all the traffic of TEIN2 members (CN, SG, VN, MY, TH, ID), a flow data analysis was done and most of the traffic was found to be for Eastern Asia.

The APAN Tokyo XP and the TEIN2 NOC asked the AARNET NOC to route the TEIN2 traffic through Honolulu rather than through Seattle, because the traffic was between the Eastern Asia and TEIN2 members. The shorter Round Trip Time (RTT) worked better, especially with TCP-based applications (Tbl. 5). However, this operation occupied the link between Honolulu and Tokyo, because the bandwidth between Tokyo and Honolulu is 155 Mbps and the one between the Tokyo and TEIN2 NOCs is 622 Mbps and the one between AARNET and TEIN2 is 1 Gbps (Fig. 15).

The link between KR and JP, whose bandwidth was 10 Gbps, was up. According to the analysis, the KR-JP link still had space to carry the traffic, and this route is much shorter than the route through Australia.

The TEIN2 and AARNET NOCs and the Tokyo XP stopped routing the TEIN2 traffic through Australia, and the KR transit policy was initiated. But the bandwidth between CN and KR was also 155 Mbps, too, so the link was occupied again (Fig. 16).

At that moment, the JGNII JP-SG link (Tbl. 4) was restored, but after precise check by the engineers, it looked as though the telecommunication company had switched the route and provided connectivity. TEIN2 NOC and the Tokyo XP decided to separate the traffic to Tokyo into two routes. That is, CN traffic was transferred through KR, and other TEIN2 traffic was transferred through SG (Fig. 17).

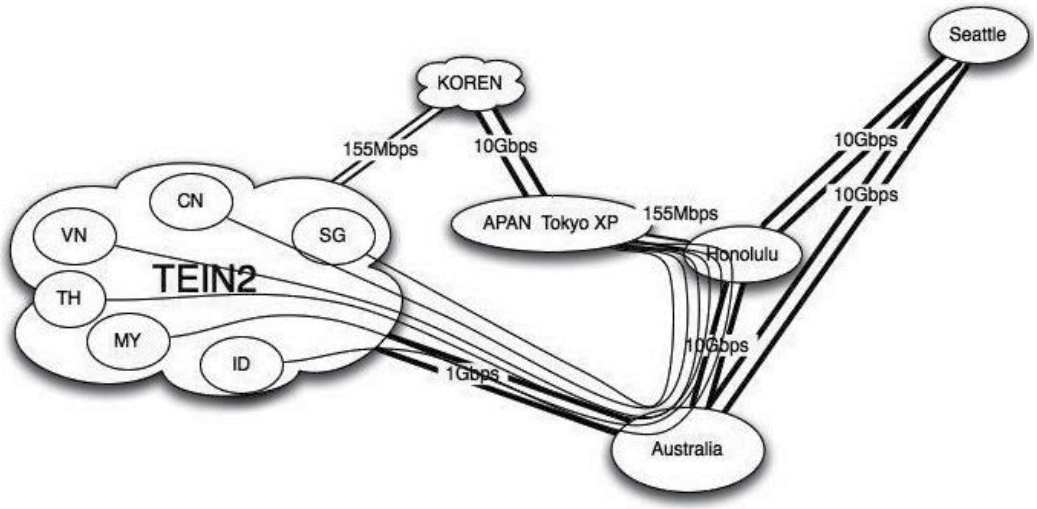

Fig. 15. TEIN2 traffic was carried through Hawaii.

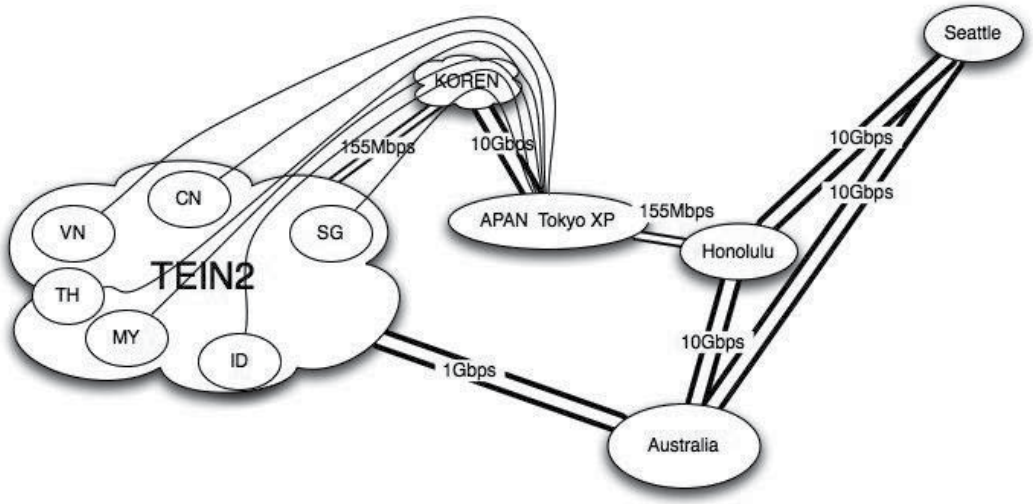

Fig. 16. TEIN2 traffic was routed through KR.

On December 27th after the fiber cut, automatic BGP re-routing has been carried out between SG and JP. The route from SG to JP became SG-AU-Hawaii-JP instead of the direct link and its RTT was increased to 426 ms, while its normal RTT is around 88 ms.
When the link between SG and KR was temporarily recovered with the backup fiber, the RTT values was 240 ms between SG and JP via KR on December 28th.
Finally, on January 12th when the link between JP and SG was recovered with the direct fiber, the RTT was reduced to 113 ms, which is slightly increased than the usual case.

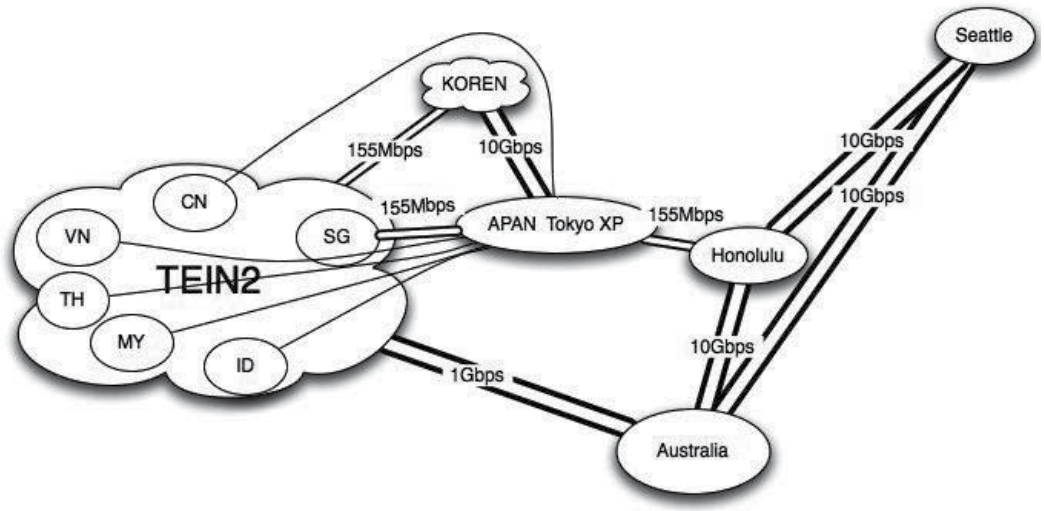

Fig. 17. TEIN2 traffic was routed through SG and KR.

Figure 18 shows the RTT between SG and JP just after the earthquake and the recovery process.

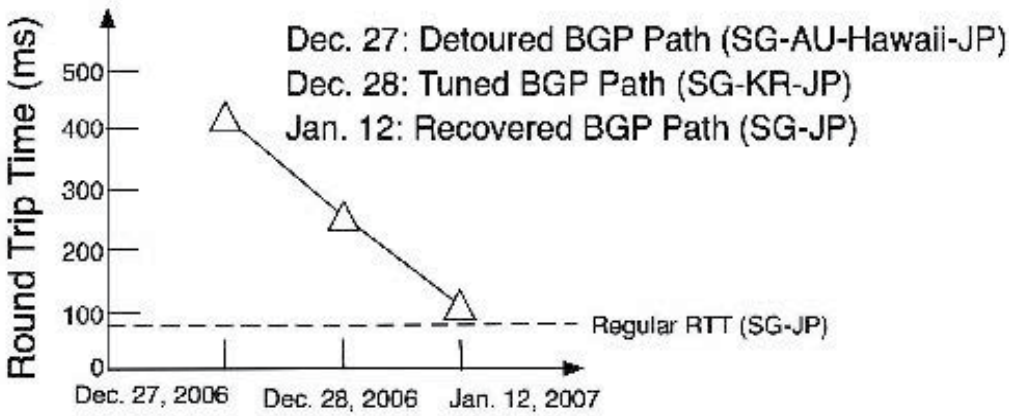

Fig. 18. RTT between SG and JP during the restoration process

5. Network restoration methods

After the network failures caused by the earthquake, several restoration steps were taken to restore communication. In this subsection, we discuss these steps.

5.1 Automatic BGP re-routing

Usually, the full BGP routing table includes a few "useless" routes (Tbl. 2). By "useless" we mean that the route itself provides only connectivity with the long RTT and insufficient bandwidth. Therefore, the network operators filter out such useless routes by setting the

local preference to ignore them. However, after the earthquake, these useless BGP routes worked automatically as backup paths. In the Asia Pacific R&E networks, the routes became very complicated after TEIN2 started because TEIN2 provided a few unexpected routes around the world. Because there were backup AS paths, automatic BGP re-routing could be used for first aid to provide the connectivity to the ASs that lost the primary paths. However, automatic BGP re-routing did not consider the traffic engineering parameters of the available bandwidth and the backup traffic load.

(Src, Dst)	Usual Path	Useless Path
(JP, TEIN2)	JP-TEIN2	JP-Hawaii/Seattle-AU-TEIN2
(TEIN2, JP)	TEIN2-JP	TEIN2-GÉANT2-Abilene-JP
(US, US)	Abilene	US-KREONET2-JP-TransPAC2-US
(JP, KR)	JP-KR link	JP-TEIN2-JP- TEIN2-SG -AU-Seattle-KR

Table 2. Examples of the "useless routes"

5.2 Traffic engineering with BGP policy change

BGP by itself does not provide any information regarding link capacity or available bandwidth. Moreover, due to recent VLAN (Varadaraja, 1997) technology, the distance between two ASs has no relation to physical distance. Thus, QoS information of the detour routes must be examined by the operators. This makes systems reliant on human knowledge of traffic engineering. To remove the congestion due to the long detour AS path, we changed the BGP routing policy as shown in Fig. 13 and Fig. 14.

The members of TEIN2 (VN, MY, SG, ID, PH) lost their connections to APAN Tokyo XP because the fiber broke. AARNET NOC proposed backup routes for accessing APAN Tokyo XP through AU and Hawaii. However, this solution caused congestion on both the CN-KR and Hawaii-JP links. Besides, CN traffic took an asymmetrical path.

Therefore, to solve the traffic engineering issue, Tokyo XP made a decision to divide CN traffic by announcing CN IP prefixes through KR NOC and grouping CN prefixes at Tokyo XP. The results were monitored by Cisco NetFlow (CISCO, n.d.). The operators found out that half of the KR traffic was from CN. After a careful examination, it was discovered that a part of the CN traffic was from CERNET but the other part was from TEIN2.

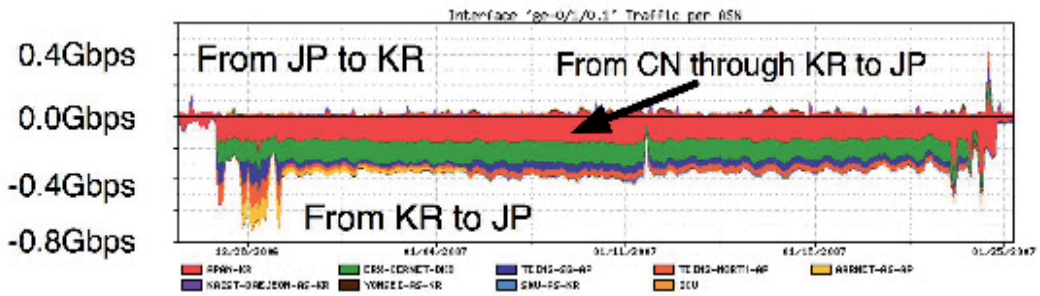

Fig. 19. Traffic from KR monitored at APAN JP (Dec. 26 2006 - Jan. 26 2007)}

Figure 19 shows the traffic load for each source AS. Although the total traffic is about 0.4 Gbps, the real KR traffic was about 0.2 Gbps. 0.1 Gbps is occupied by CERNET traffic and the rest by TEIN2.

5.3 Port reconfiguration

In spite of the recovery steps, a few sites that had only single-link connections to the Internet could not directly reach the R&E networks. Therefore, after the fiber was fixed, a few single-link sites had the connections via Internet commodity service. To fix this problem, the operators had to change the port configuration at switches that were able to provide high performance connections.

Two days after the earthquake, the link between KR and SG was restored and SG started making routing announcements to TEIN2 members (ID, SG, TH, MY). However, the link between SG and KR was not the original fiber, and its RTT increased greatly because a detour route was assigned. Similarly, the direct link between PH and JP was replaced with a detour route with a long RTT. When an online demonstration was being prepared for the 2007 APAN meeting held in PH between January 22nd and 26th 2007, the restored JP-PH link had a very long RTT because it went through mainland China, as shown in Fig. 20.

Fig. 20. JP-PH detour route circuit

During the 23rd APAN meeting demonstration, the Prince of Wales Hospital at the Chinese University of Hong Kong (CUHK) was expected to join. However, its IP prefix was announced only by CSTNET. Thus, it was only reachable over a commodity Internet link with a small bandwidth. To solve this problem, APAN Tokyo XP changed the port configuration of fibers. That is, the CSTNET fiber for accessing APAN Tokyo XP was

plugged to the TEIN2-HK router. Finally, CUHK was directly connected to TEIN2. Finally, with this solution, CUHK and CSTNET were supplied with huge-bandwidth and short-RTT connections to the R&E network.

6. Lessons

From the process of recovering from network failures across several ISP's in Asia Pacific R&E networks, we encountered several network management challenges especially regarding fault management. In this subsection, we describe the lessons learned during the recovery operations.

6.1 Fault-tolerant fiber topology design

BGP routing policies are usually made to avoid asymmetric or useless AS paths by setting the appropriate local preference values. However, these alternative AS paths worked as backup paths. Before the network failures from earthquake, Asia Pacific R&E network operators thought that removing the useless routes was urgent, because routing became too complicated after TEIN2 started. However, this complicated routing was able to provide valuable connections during network failures. This shows that maintaining full-mesh style routing information is very important for fault-tolerant routing.

Though BGP re-routing over the redundant AS paths was successful for the first step in restoration, it was not sufficient to provide full backup service without congestion by considering the traffic load. Since BGP routing does not carry QoS information, such as link capacity, link utilization, or available bandwidth, traffic re-routed to the backup AS path had experienced poor QoS, such as long delays. Therefore, QoS-aware BGP routing or traffic engineering-aware BGP routing is necessary.

6.2 Integrated network management

During the restoration process, we used various network monitoring tools such as an MRTG (Oetiker, n.d.a), a network weather map, a BGP routing table visualizer, and a flow monitor. At first, the link outage was noticed on the network weather map, and the abrupt change of traffic load was noticed on the MRTG. However, the fast fault detection method that encompasses physical, link, routing, and application layers is necessary because it was able to identify the exact failure points and visualize their impacts on the network. In addition, a simulator or emulator that could show the results with the network topology and the traffic load before and after failures would be very useful in predicting the effects of fault-management decisions. While we took various restoration steps, we had to process the information collected by each different network-monitoring tool. Finally, the operators interpreted the situation and implemented recovery decisions manually. If the iperf (GOOGLE, n.d) or bwctl (INTERNET2, n.d.) is available throughout the network, the end-to-end available bandwidth between ASs can be easily estimated. For example, to access Sydney from Tokyo, there are two possible routes. One is Tokyo – Seattle - Sydney, and the other is Tokyo – Honolulu - Sydney. The former provides 10 Gbps but has a long RTT. The latter route includes a bottleneck along the 155 Mbps path but has a short RTT. In addition, to make the final decision, we had to check the flow data, because MRTG or RRDTool (Oetiker, n.d.b) do not classify traffic breakdowns by their source/destination ASs. When the traffic from KR increased suddenly, the operators could not understand the reasons. This shows that integrated network monitoring or management systems would be very

useful for collecting information from several independent monitoring systems and for providing the correct information in an integrated wide view in case of significant network failures.

6.3 Emergency communication between operators

After the earthquake, communication among NOCs was difficult because the fiber break disrupted VoIP and legacy telephone service. Moreover, the earthquake happened on December 26th 2006, overlapping with the Christmas holiday. Thus, all the communication was routed over the instant messaging system and e-mails were routed over the detoured network even though it provided poor quality service. It became obvious that the emergency communication should be guaranteed in case of failures so that the recovery process can be started quickly

7. Summary

Since the Internet continues to grow globally and becomes ever more important in daily life, business, and research, the need for fault-tolerant service in network management becomes more urgent. However, during the network failures caused by the 2006 earthquake, it was shown that there are still many challenges in fault-tolerant network management research. Even though multiple fiber cores are installed together to provide backup service, they may be useless during severe natural disasters. Therefore, full-mesh or fiber-disjoint physical network topology should be designed for use during failures. On the available topology, it was seen that BGP routing provided backup AS paths, which was useful for the first step in restoration. However, the traffic engineering issues during restoration were difficult to solve because all the information, such as link capacity, available bandwidth, link delay, traffic load, and routing policy, had to be collected, interpreted, and acted on by human operators. In spite of BGP re-routing, we had to deal with a few single-link ASs to establish direct connections to the R&E networks. From this experience of network recovery during a significant natural disaster affecting several different countries and ISP's, we were able to gather valuable information on network management during emergencies. Therefore, in the Internet of the future, designers should focus on fault-tolerant network management study including robust physical topology, cross-layer restoration, traffic engineering combined with BGP routing, and simulation of failures in the network.

We would like to show the one example from this lesson. In August 2009, the earthquake happened again near Taiwan island and the fiber cut happened again. Table 1 tool was improved as "Compath" already and the table was constructed again for this disaster (Kurokawa, 2010). At that time, the medical demonstration was planned in Asian area and the connectivity of the Thailand was required. The compath table recommended that the TW should have become the hub for the southeast Asian area. This was against the policy of TEIN2, but the R&E networks object is to support the researchers and such the flexibility was approved and the tool from the lesson of the 2006 earthquake improved the network operations.

8. Acknowledgment

After the earthquake, KDDI OTC (Otemachi Technical Center) worked very hard to fix the routing problems of APAN Tokyo XP both in their capacity as paid staff and as volunteers.

Yutaka Watanabe, OTC's director, took the MRTG snapshot of Figs. 8 and 9. AARNET NOC offered us the backup routes to access the TEIN2. KOREN NOC worked very hard to keep communication open between CERNET and ASNET even during the holiday. Hawaii University NOC worked very hard to keep control of this complicated routing. KDDI investigated the reason for the communication failures in the APAN area and gave useful advice to APAN Tokyo XP. The staff of Genkai XP NOC accepted CERNET's traffic from KOREN by upgrading the JP-KR link bandwidth. Due to these great efforts and the collaboration among the network engineers, we were able to quickly restore the Asia Pacific R&E networks.

This research was supported by the MIC (Ministry of Information and Communication), Korea, under the ITRC (Information Technology Research Center) support program supervised by the IITA (Institute of Information Technology Assessment) (NIPA-2011-C1090-1131-0005).

9. Appendix

Country code	Name
JP	Japan
TH	Thailand
MY	Malaysia
HK	Hong Kong
ID	Indonesia
SG	Singapore
TW	Taiwan
CN	China
US	United States of America
KR	Korea
VN	Vietnam
PH	The Philipppines
NP	Nepal
AU	Australia
BD	Bangladesh
IN	India
LK	Sri Lanka
BT	Bhutan
KH	Cambodia
LA	Laos
PK	Pakistan

Table 3. ISO 3166 Country Code (International Organization for Standardization [ISO], n.d.) in this chapter

Network Name	Description	Area
AIII	Asian Internet Interconnection Initiatives	JP, VN, PH, TH, MY, SG, ID, NP
APAN	Asia-Pacific Advanced Network	JP, KR, CN, TW, HK, VN, TH, MY, SG, AU, NZ, PK, IN, KL, BD
TEIN2	Trans-Eurasia Information Network 2	JP, CN, VN, PH, TH, MY, SG, ID, AU, EU
TEIN3	Trans-Eurasia Information Network 3	AU, BD, BT, KH, CN, IN, ID, JP, KR, LA, MY, NP, PK, PH, SG, LK, TW, TH, VN
ASTI	Advanced Science and Technology Institute, the link owner of PREGINET	PH
PREGINET	Philippine Research Education and Government Information Network	PH
CSTNET	China Science & Tecnology Network	CN
CERNET	China Education and Research Network	CN
GÉANT	R&E Network, the AS registration name	Europe
GÉANT2	R&E Network	Europe
KOREN	Korea Advanced Research Network	KR
SingAREN	Singapore Advanced Research and Education Network	SG
UniNet	inter University Network	TH
ThaiSARN	Thai Social/Scientific Academic and Research Network	TH
KREONET2	Korea Research Environment Open Network 2, the domestic name is KREONET	KR
AARNET	Australia's Research and Education Network	AU
QGPOP	Kyushu Gigapop	JP
JGNII	Japanese R&E Network	JP, US, TH, SG

Table 4. Network Name

OSI Model			
	Data unit	Layer	Function
Host layers	Data	7. Application	Network Process to application
		6. Presentation	Data representation and encryption
		5. Session	Interhost communication
	Segment/Datagram	4. Transport	End-toend connections and reliability
Media layers	Packet	3. Network	Path determination and logical addressing
	Frame	2. Data Link	Physical addressing (MAC & LLC)
	Bit	1. Physical	Media signal and binary transmission

Table 5. Open Systems Interconnection (OSI) Basic Reference Model

10. References

Academia Sinica, (n.d.). The December 26, 2006, Pingtung, Taiwan earthquake, In : *Academia Sinica*, 26.07.2011, Available from : http://www.earth.sinica.edu.tw/~smdmc/recent/2006/200612261226.htm

Academia Sinica, (n.d.). The December 26, 2006, Pingtung, Taiwan earthquake, In : *Academia Sinica*, 26.07.2011, Available from : http://www.earth.sinica.edu.tw/~smdmc/recent/2006/200612261234.htm

Asian Internet Interconnection Initiative Project, (n.d.). Asian Internet Interconnection Initiative Project, In : *Asian Internet Interconnection Initiative Project*, 26.07.2011, Available from : http://www.ai3.net/

Asia-Pacific Advanced Network, (n.d.). Welcome to Asia-Pacific Advanced Network, In : *Asia-Pacific Advanced Network*, 26.07.2011, Available from: http://www.apan.net/

Asia-Pacific Advanced Network Japan, (n.d.). APAN-JP Network Traffic Weathermap, In : *APAN Japan Consortium*, 26.07.2011, Available from : http://monitor.jp.apan.net/weathermap/

CISCO, (n.d.). Cisco IOS NetFlow In : *Cisco*, 26.07.2011, Available from : http://www.cisco.com/en/US/products/ps6601/products_ios_protocol_group_home.html

Delivery of Advanced Network Technology to Europe, (n.d.). TEIN2, In : DANTE, 26.07.2011, Available from: http://www.tein2.net/

Fumagalli, A. & Valcarenghi, L. (2000). IP Restoration vs. WDM Protection: Is There an Optimal Choice?, *IEEE Network Magazine,* Vol. 14, No. 6, (December 2000), pp. 34-41, ISSN 08908044

Gerstel, O. & Ramaswami, R. (2000), Optical Layer Survivability: a Services Perspective, *IEEE Communications Magazine,* Vol. 38. No. 3, (March 2000), pp. 104-113, ISSN 01636804

GOOGLE, (n.d.). iperf – TCP and UDP bandwidth performance measurement tool, In : *Google Project Hosting*, 26.07.2011., Available from : http://code.google.com/p/iperf/

Hanks, T. & Kanamori, H. (1979). A Moment Magnitude Scale, *Journal of Geogphysical Research*, Vo. 84, No. B5, (May 1979), pp. 2348-2350, ISSN 0148-0227

Iannaccone, G. ; Chuah, C. ; Mortier, R. ; Bhattacharyya, S. & Diot, C. (2002). Analysis of Link Failures in an Backbone, *ACM Internet Measurement Conference,* Marseille, 2002

International Organization for Standardization, (n.d.). ISO - Maintenance Agency for ISO 3166 country codes - English country names and code elements In : *International Organization for Standardizaation*, 26.07.2011, Available from : http://www.iso.org/iso/en/prods-services/iso3166ma/02iso-3166-code-lists/list-en1.html

INTERNET2, (n.d.). Bandwidth Test Controller (BWCTL), In : *Internet2*, 26.07.2011, Available from : http://e2epi.internet2.edu/bwctl

Konishi, K. (2007). Cables restoration, *23rd APAN Manila Meeting*, Manila, Feburary 2007

Kurokawa, Y. (2006). Registration of Policy Routing Choices , *22nd APAN Singapore Meeting* , Singapore, June 2006

Kurokawa, Y. (2010). Utilization of Compath Tool in Multiple Submarine Cables were cut off near Taiwan on August, 2009, 29th APAN Sydney Meeting, Australia, February 2010

Kyushu GigaPOP Project, (n.d.). QGPOP (Kyushu GigaPOP Project), In: *QGPOP (Kyushu GigaPOP Project),* 26.07.2011, Available from: http://www.qgpop.net

Lougheed, K. & Rekhter, Y. (1989), Border Gateway Protocol (BGP), In : *RFC 1105,* 26.07.2011, Available from : http://datatracker.ietf.org/doc/rfc1105/

Markopoulou, A. ; Iannacccone, G. ; Chuah, C. ; Mortier, R. ; Bhattacharyya, S. & and Diot, C. (2004). Characterization of Failures in an IP Backbone, *IEEE Infocom,* Hong Kong, 2004

Oetiker, T. (n.d.). MRTG - Tobi Oetiker's MRTG - The Multi Router Traffic Grapher, In : *MRTG*, 26.07.2011. Available from : http://oss.oetiker.ch/mrtg/

Oetiker, T. (n.d.), RRDtool - About RRDtool In : *RRDtool - About RRDtool*, 26.07.2011, Available from : http://oss.oetiker.ch/rrdtool

Ramamurthy, S. ; Sahasrabuddhe, L. & Mukherjee, B. (2003). Survival WDM Mesh Networks, *IEEE/OSA Journal of Lightwave Technology* , Vol. 21, No. 4, (April 2003), pp. 870-883, ISSN 0733-8724

Research and Education Network Operators Group, (n.d.) In : *RENOG*, 26.07.2011, Available from : http://www.renog.org

Robb, C. (2006). Global Research and Education Network Routing Issues, *2006 Spring Internet2 Member Meeting*, Arlington VA, April 2006

Saharabuddhe, L. ; Ramanurthy, S. & Mukherjee, B. (2002). Fault Management in IP-Over-WDM Networks: WDM Protection vs. IP Restoration, *IEEE Journal on Selected Areas in Communications,* Vol. 20, No. 1, (January 2002), pp. 21-33, ISSN 0733-8716

Sakiyama, R. ; Okamura, K. & Lee, Y. (2006). Visualization of Temporal Difference of BGP Routing Information, *APAN Network Research Workshop, Singapore*, Singapore, June 2006

Sharma, V. & Hellstrand, F. (month 2003). Framework for Multi Protocol Label Switching (MPLS)-based Recovery, In : *RFC 3469,* 26.07.2011, Available from: http://datatracker.ietf.org/doc/rfc3469/

Varadarajan, S. (1997). Virtual Local Area Networks , In: *Virtual Local Area Networks*, 26.07.2011., Available from : http://www.cs.wustl.edu/~jain/cis788-97/ftp/virtual_lans/index.htm

18

Earthquake Induced a Chain Disasters

Guangqi Chen, Yange Li, Yingbin Zhang and Jian Wu
Kyushu University
Japan

1. Introduction

A strong earthquake not only cause directly damage on constructs but also can result in a series of natural disasters such as landslide, debris flow and flooding. These secondary disasters occurs as a chain disasters as shown in Fig. 1. A strong earthquake can induce a large amount of landslides. And then, a large scale landslide can create a landslide dam when its debris fill into and stop a river. The water impounded by a landslide dam may create a dam reservoir (lake). While the dam is being filled, the surrounding groundwater level rises and causes back-flooding (upstream flooding). And because of its rather loose nature and absence of controlled spillway, a landslide dam is easy to fail catastrophically

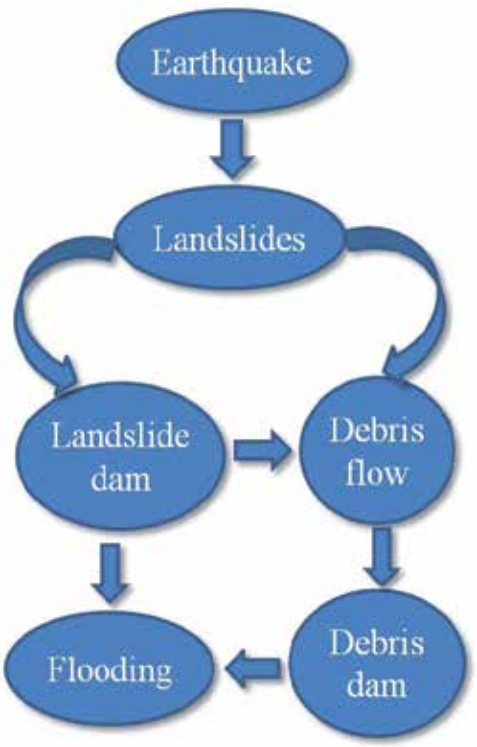

Fig. 1. The disasters chain induced by an earthquake

and lead to debris flow or downstream flooding. Also, since the landslide debris can be removed into a valley or a ravine by excessive precipitation, it is easy to form debris flow, and then create a debris dam sometimes.

In this chapter, we take the 2008 Wenchuan Earthquake (Ms=8.0) as an example to discuss the earthquake induced chain disasters. The characteristics of the earthquake induced landslides are summarized including the discussion of the landslide dams. A landslide susceptibility analysis is carried out and a possible long run-out mechanism is proposed for the study. The characteristics of the debris flows arising from the earthquake are summarized. An approach of simulating debris flow is proposed for predicting the movement behaviours of potential debris flow arising from earthquake. A practical simulation is carried out for verifying the approach.

2. The earthquake induced landslide

A strong earthquake can induce a large amount of landslides and cause very serious property damage and human casualties. This phenomenon was recorded in ancient China dated back to 1789 BCE, and in ancient Greece 2373 years ago (Keefer, 2002). There have been many reports about the very serious damages caused by the earthquake induced landslides for the last few decades. For example, 9,272 landslides induced by the 1999 Chi-Chi earthquake (Ms=7.6) caused 2,400 deaths, more than 8000 casualties and over 10 billion US$ of economical loss in Taiwan(Chang et al. 2005). 30% of the total fatalities (officially 87,350) had been victims of co-seismic landslides due to the Kashimir earthquake (Ms=7.6) (Havenith and Boureau 2010). In this chapter, we take the 2008 Wenchuan Earthquake (Ms=8.0) as example to discuss this issue.

2.1 The 2008 wenchuan earthquake

The earthquake had a magnitude of 7.9 Ms, occurred in Sichuan Province, China at 14:28 CST on 12 May 2008. The epicenter is located Yingxiu town (30.986°N, 103.364°E), Wenchuan County. The focal depth is about 12 km according to the report by the China Earthquake Administration (CEA).

The earthquake occurred along the Longmenshan fault (LMSF) zone at eastern margin of the Tibetan Plateau, adjacent to the Sichuan Basin as shown in Fig. 2 (Gorum et al., 2011). The fault belt is a series of faults striking in a northeast direction, on a North-South zone of high topographical and geophysical gradients between the Tibet Plateau on its western side and the Yangzi Platform on its eastern side. Seismic activities concentrated on its mid-fracture (known as Yingxiu-Beichuan fracture). Starting from Yingxiu, the rupture propagated unilaterally towards the northeast at an average speed of 3.1 kilometers per second, generating a 300-km and a 100-km long surface rupture along the Yingxiu-Berchuan and Pengguan faults, respectively (Huang et al., 2011a). The duration was as long as 120 seconds and the maximum displacement amounted to 9 meters.

Official figures, released by China News www.chinanews.com, on July 21, 2008 12:00 CST show that 69,197 are confirmed dead, 374,176 injured, and 18,222 listed as missing. The earthquake destroyed 5,362,500 and seriously damaged 21,426,600 houses, left about 4.8 million people homeless (Cui et al., 2009, Tang et al., 2011b). Approximately 15 million people lived in the affected area. It was the deadliest earthquake to hit China since the 1976 Tangshan earthquake, which killed at least 240,000 people.

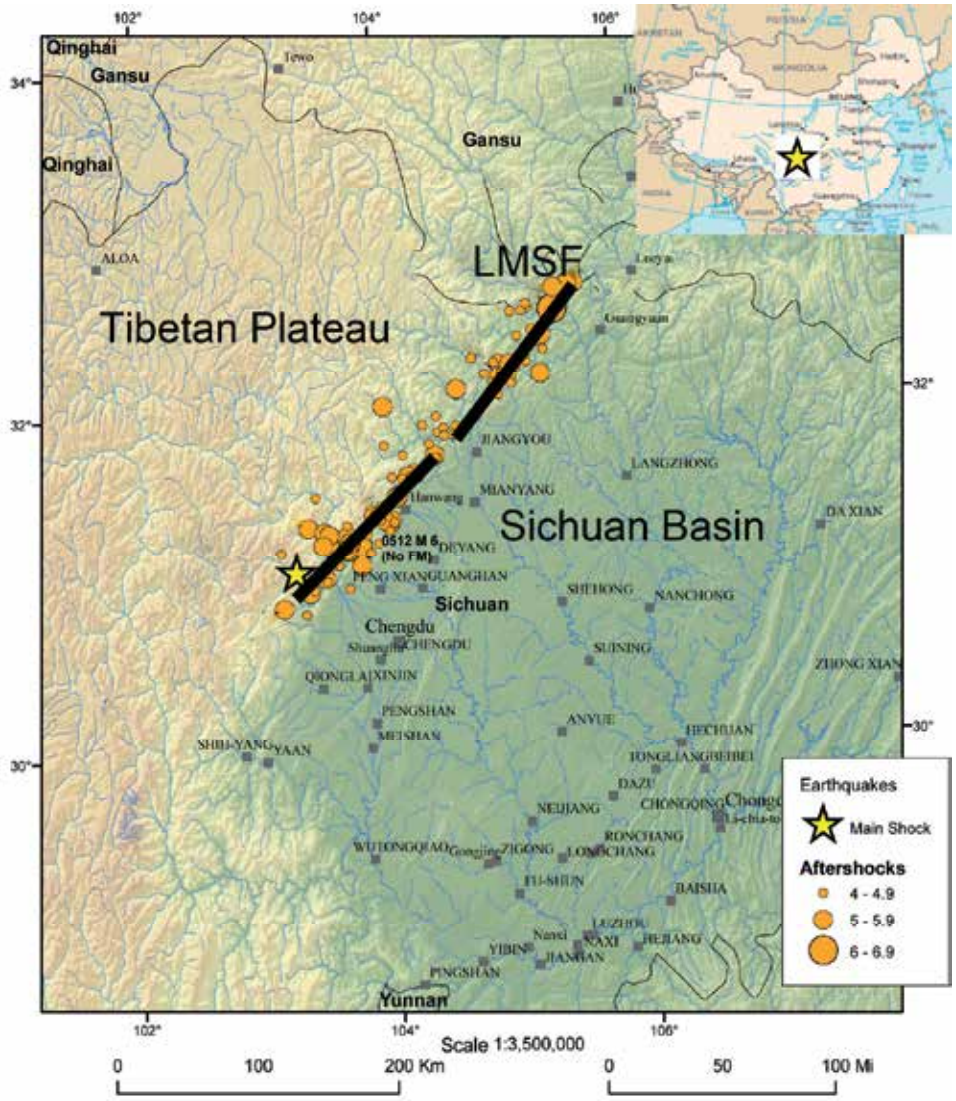

Fig. 2. The 2008 Wenchuan earthquake, LMSF and aftershocks. (modified from United States Geological Survey [USGS], 2008)

2.2 The landslides induced by the earthquake

The earthquake occurred in a mountainous region, where the geological and topographical features and climate conditions are very complex. The response to the ground shock was very strong. The recorded peak ground acceleration of local site reached to 2.0g (Huang et al., 2011b). Because of the complex terrain and climate conditions, the quake induced as many as 56,000 landslides (Dai et al., 2011). It is estimated that over one third of the total lost from the 2008 Wenchuan earthquake was caused by the earthquake induced landslides. Therefore, the secondary chain disaster induced by the 2008 Wenchuan earthquake is much more serious than the 1976 Tangshan earthquake.

2.3 Characteristics of the landslides

As many as 56,000 landslides have been identified by field investigations and using remote sensing technique with aerial photographs and satellite images. And the following distinctive characteristics can be summarized from these landslides:

1. Large scale

Many large scale landslides were induced by the 2008 Wenchuan earthquake. There are tens of landslides with a volume of 10^7 cubic meters (Wu et al., 2010), and 113 landslides with the area larger than 50,000 m^2 as shown in Table 1 (data from Xu et al., 2009a). The largest one is the Daguangbao landslide in Anxian County with an area of 7,273,719 m^2 and the volume of about $8.4\times10^8 m^3$ (Chigira et al., 2010).

2. The effect from the hanging and foot wall of the fault

It has been found that the majority of landslides are distributed in the range belonging to the hanging wall of the Yingxiu-Beichuan fault and Pengguan fault, northwest part of earthquake zone. All statistics seem to support that the landslide in hanging wall area is more active than in foot wall areas (Xu et al., 2009a; Yin et al., 2009a). For example, the distribution of large-scale landslides also shows the hanging /foot wall effect. It can be found from the Table 1 that 80 landslides occurred in the hanging wall, 70.8% of the total 113 large-scale landslides, and only 33 landslides occurred in the foot wall, 29.2% of the total number.

No.	Name	Place	Area /m^2	Distance to fault /m	Wall location
1	Daguangbao	Anxian	7,273,719	4,800	Hanging wall
2	Wenjiagou	Mianzhu	2,945,520	3,900	Foot wall
3	Donghekou	Qiangchuan	1,283,627	300	Hanging wall
4	Zhengjiashan	Pingwu	1,014,987	2,400	Hanging wall
5	Shuimogou	Shifang	915,608	700	Hanging wall
6	Dawuji	Anxian	792,190	6,900	Hanging wall
7	Woqian	Qiangchuan	695,672	200	Hanging wall
8	Dashanshu	Mianzhu	693,687	6,900	Hanging wall
9	Hongshigou	Anxian	687,520	2,240	Hanging wall
10	bingkoushi	Pengzhou	575,556	12,600	Hanging wall
11	Tangjiashan	Beichuan	572,009	2,780	Hanging wall
12	Huatizigou	Pengzhou	541,193	4,980	Hanging wall
13	Wenjiaba	Pingwu	537,101	380	Hanging wall
14	Niujuangou	Wenchuan	527,700	300	Hanging wall
15	Haixingou	Mianzhu	517,573	8,888	Hanging wall
16	Ma'anshi	Pingwu	509,836	4,200	Hanging wall
17	Shibangou 1#	Qiangchuan	496,983	2,300	Hanging wall
18	Guershan	Beichuan	471,112	0	Hanging wall
19	Xiaojiashan	Mianzhu	465,899	2,900	Hanging wall
20	Xinkaidong	Pengzhou	449,685	6,800	Hanging wall
21	Boazangcun	Anxian	418,744	4,030	Hanging wall
22	Mianjiaoping	Beichuan	377,247	550	Foot wall
23	Weijiashan	Beichuan	358,021	2,120	Hanging wall
24	Liqigou	Jiangyou	355,113	10,000	Foot wall

No.	Name	Place	Area /m²	Distance to fault /m	Wall location
25	Caocaoping	Anxian	354,046	660	Hanging wall
26	Miepengzi 3#	Mianzhu	353,817	600	Hanging wall
27	Laoyinggou	Anxian	353,242	1,050	Hanging wall
28	Huoshigou	Anxian	322,155	1,400	Hanging wall
29	Zhangjiashan	Anxian	306,576	6,000	Foot wall
30	Macaotan	Mianzhu	305,989	2,700	Foot wall
31	Xiejiadianzi	Pengzhou	294,256	1,100	Hanging wall
32	Shibangou 2#	Qiangchuan	288,305	2,400	Hanging wall
33	Huishuituo	Pengzhou	270,980	4,200	Hanging wall
34	Dazhuping	Anxian	270,692	540	Hanging wall
35	Miepengzi 2#	Mianzhu	262,520	600	Hanging wall
36	Heshangqiao 3#	Dujaingyan	257,635	10,400	Hanging wall
37	Muguapingcun	Shifang	256,340	900	Foot wall
38	Miepengzi 1#	Mianzhu	255,296	600	Hanging wall
39	Dongxigou	Beichuan	246,020	2,200	Hanging wall
40	Yaozigou	Pingwu	242,553	800	Hanging wall
41	Baichaping	Dujaingyan	241,874	4,700	Hanging wall
42	Changping	Pengzhou	224,645	2,400	Hanging wall
43	Baodili	Qiangchuan	222,157	700	Hanging wall
44	Xiaomuling	Mianzhu	218,705	2,450	Hanging wall
45	Heshangqiao 1#	Dujaingyan	214,020	10,900	Hanging wall
46	Baishuling	Beichuan	208,968	4,350	Hanging wall
47	Dawan	Beichuan	203,959	2,150	Hanging wall
48	Baiguoshu	Beichuan	203,246	1,000	Hanging wall
49	Zengjiashan	Mianzhu	198,165	11,350	Foot wall
50	Zhangjiagou	Beichuan	196,299	640	Hanging wall
51	Zhaojiaqu	Qiangchuan	193,153	1,300	Hanging wall
52	Heitanzi	Anxian	182,452	8,900	Foot wall
53	Anleshan	Beichuan	180,809	1,140	Hanging wall
54	Yangshangou	Beichuan	177,361	1,300	Hanging wall
55	Xiaotianchi	Mianzhu	175,758	8,200	Foot wall
56	Yanyangcun	Beichuan	174,008	1,600	Foot wall
57	Shicouzi	Pingwu	169,540	0	Hanging wall
58	Chenjiaping	Anxian	169,368	1,050	Hanging wall
59	Wangyemiao	Dujaingyan	167,980	9,300	Hanging wall
60	Jiadanwan 1#	Dujaingyan	166,643	7,900	Hanging wall
61	Jinhelingkuang	Mianzhu	159,848	2,800	Foot wall
62	Fengyanzi	Beichuan	158,468	0	Foot wall
63	Changtan	Mianzhu	151,094	6,670	Foot wall
64	Weijiagou	Beichuan	150,818	450	Hanging wall
65	Xiaogangjian	Mianzhu	149,074	6,280	Foot wall
66	Baiyanshan	Qiangchuan	147,940	4,300	Hanging wall
67	Guoniucun	Beichuan	147,554	3,000	Hanging wall
68	Heshangqiao 2#	Dujaingyan	147,394	9,600	Hanging wall
69	Bazuofen	Anxian	146,272	11,000	Foot wall
70	Tiangengli	Qiangchuan	144,729	1,400	Foot wall

No.	Name	Place	Area /m²	Distance to fault /m	Wall location
71	Hongmagong	Qiangchuan	144,683	350	Foot wall
72	Baiguocun	Qiangchuan	139,800	300	Foot wall
73	Huangtuliang	Beichuan	135,084	550	Hanging wall
74	Qinglongcun	Qiangchuan	134,079	790	Foot wall
75	Pengjiashan	Beichuan	127,156	2,900	Hanging wall
76	Wangjiayan	Beichuan	125,381	400	Hanging wall
77	Yibadao	Mianzhu	125,059	9,600	Foot wall
78	Laohuzui	Wenchuan	125,039	2,700	Hanging wall
79	Beichuanzhongxuexinqu	Beichuan	124,365	300	Foot wall
80	Xiaomeizilin	Mianzhu	122,530	5,800	Foot wall
81	Xiangshuishi	Pengzhou	119,194	4,600	Hanging wall
82	Gaojiamo	Pingwu	115,301	1,600	Hanging wall
83	Jiadanwan 2#	Dujaingyan	114,905	9,300	Hanging wall
84	Dahuashu	Beichuan	113,111	0	Hanging wall
85	Wangjiabao	Beichuan	112,418	0	Hanging wall
86	Jiankangcun	Pingwu	111,106	340	Hanging wall
87	Xiaojiaqiao	Anxian	110,085	3,000	Foot wall
88	Lingtou	Qiangchuan	102,116	800	Hanging wall
89	Longwangou	Beichuan	99,821	650	Hanging wall
90	Zhangzhengbo	Qiangchuan	99,726	790	Foot wall
91	Nanyuecun	Dujaingyan	99,350	0	Hanging wall
92	Hongkouxiangxiajiaping	Dujaingyan	96,345	790	Hanging wall
93	Dujiayan	Qiangchuan	94,769	960	Foot wall
94	Madiping	Qiangchuan	94,633	2,600	Hanging wall
95	Maochongshan 1#	Pingwu	92,355	1,200	Hanging wall
96	Yandiaowo	Qiangchuan	92,128	340	Foot wall
97	Chuangzigou	Mianzhu	91,718	2,200	Foot wall
98	Xiaoxishan	Qiangchuan	90,298	1,000	Hanging wall
99	Xishanpo	Beichuan	83,663	1,140	Hanging wall
100	Hejiayuan	Qiangchuan	83,359	1,990	Foot wall
101	Zhaojiashan	Qiangchuan	82,329	1,000	Foot wall
102	Liushuping 1#	Qiangchuan	81,000	780	Hanging wall
103	Weiziping	Qiangchuan	74,661	470	Hanging wall
104	Gongziba	Qiangchuan	71,221	220	Hanging wall
105	Maerping	Qiangchuan	70,982	7,500	Hanging wall
106	Maochongshan 2#	Pingwu	70,252	1,200	Hanging wall
107	Muhongping	Qiangchuan	68,288	2,600	Foot wall
108	Machigai	Qiangchuan	66,602	500	Foot wall
109	Zixicun	Pingwu	57,820	2,400	Hanging wall
110	Liushuping 2#	Qiangchuan	54,810	1,000	Hanging wall
111	Dongjia	Qiangchuan	54,353	1,000	Foot wall
112	Majiawo	Qiangchuan	50,591	1,100	Hanging wall
113	Xiaowuji	Qiangchuan	50,122	2,100	Foot wall

Table 1. The large scale landslides with the area larger than 50,000 m² (data from Xu et al., 2009a).

3. The effect from the distance to the faults

Among the large scale landslides, the two farthest landslides from the fault are about 12.6km in the side of hanging wall and 11.35km in the foot wall. The majority of landslides (about 70%) occured in the region of 3km from the fault. Fig. 3a and 3b show the accumulative percentage of landslide distribution as a function of the distance to the fault in hanging and foot wall respectively. An exponential decay has been found for the number of landslides with the distance to the fault in both hanging and foot wall (Fig. 4).

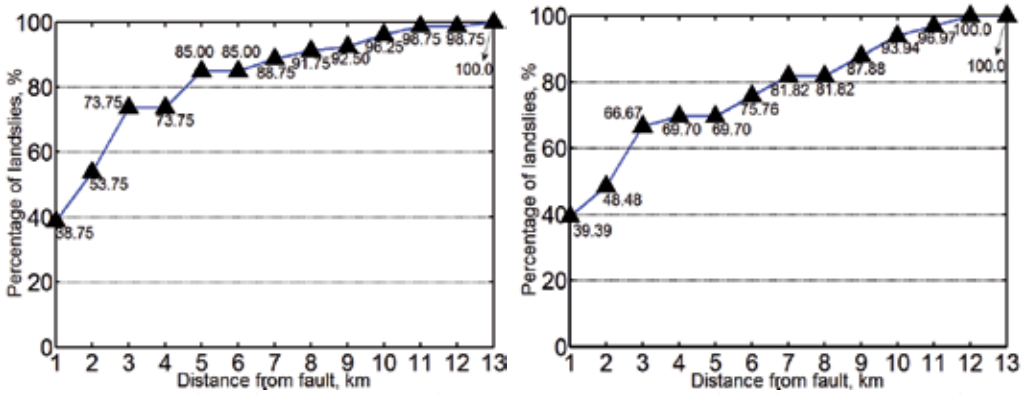

a. Distance to fault for percentage of landslides located on hanging wall

b. Distance to fault for percentage of landslides located on foot wall

Fig. 3. Relationship between percentage of landslides and large-scale distance to fault. a: Distance to fault for percentage of landslides located on hanging wall; b: Distance to fault for percentage of landslides located on foot wall.

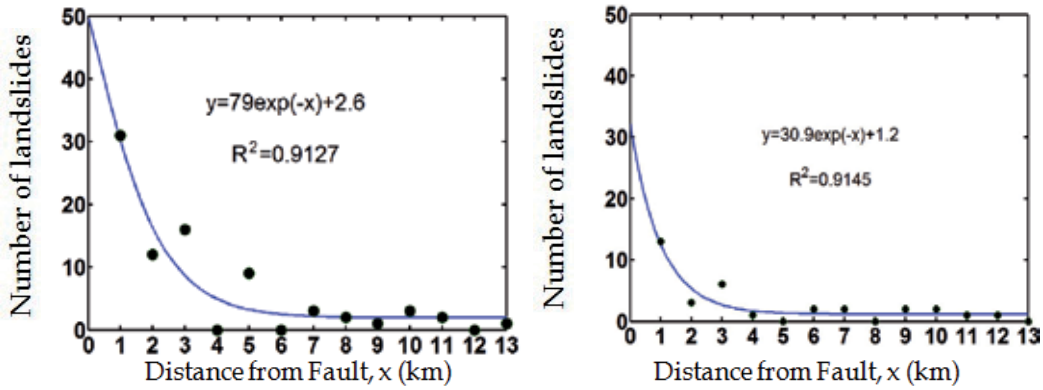

a. Distance to fault for number of landslides located on hanging wall

b. Distance to fault for number of landslides located on foot wall

Fig. 4. Relationship between number of landslides and distance to fault. a: Distance to fault for number of landslides located on hanging wall; b: Distance to fault for number of landslides located on foot wall.

4. Effect from the locking segment of the fault zone

The two largest scale landslides: Daguangbao landslide with the area of 7,273,719m^2 and Wenjiagou landslide with the area of 2,945,520m^2 are found locating at a distance of more

than 3.9km from the fault from Table 1, although most of large-scale landslides, which many researchers have been studying on, are located in the region of less than 1km from the fault. For example, the Donghekou landslide (No.3 in Table 1) has a distance of 0.3km, the Woqian landslide (No.7 in Table 1) has a distance of 0.2km and Niujuangou landslide (No.14 in Table 1) has a distance of 0.3km from the fault. By examining the positions of the two landslides with the fault zone, it has be found that the two landslides are just located at the locking segment of the fault zone where high stress is believed to be concentrated and a lot of energy was absorbed by the locking of the rupture fault. Therefore, it should be notice that large scale landslides may occur at such kind of locking segment of the fault zone.

5. Direction effect

By examining the sliding directions of large-scale landslides along Hongshihe valley, it has been found that the directions parallel to or perpendicular to the fault are dominated as shown by the rose diagram in Fig. 5. It is implied that the landslides are controlled by the earthquake wave propagation and the fault movement. The slopes parallel to or perpendicular to the fault are easy collapsed.

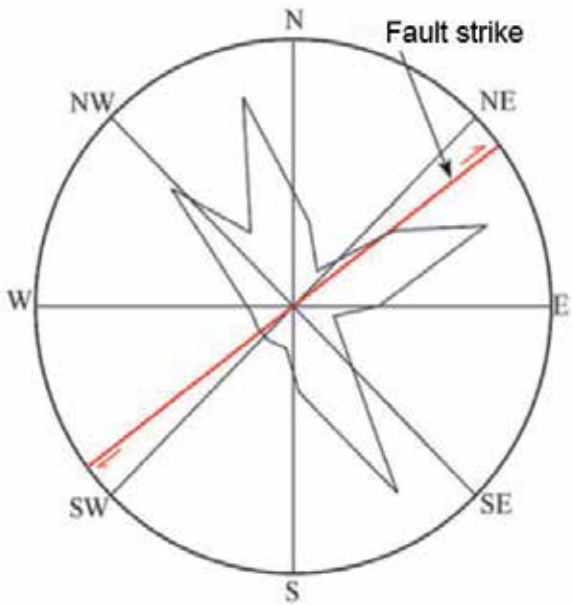

Fig. 5. Rose diagram showing the motion direction of large-scale landslides along the Hongshihe (after Xu et al., 2009a)

6. The long run-out characteristic

For rainfall induced landslides, the run-out distances are mostly less than 2 times of the slope height (2H). For example, 95% of the 19,035 landslides induced by rainfall are less than 50m based on the records from 1972 to 2008 in Japan. However, numerous rapid and long run-out landslides occurred during the 2008 Wenchuan Earthquake. Table 2 lists 21 long-run-out landslides with the horizontal distance larger than 500m. These landslides traveled over extraordinarily large distances with extremely high speeds and produced catastrophic results.

For instance, the Wangjiayan landslide (No. 76 in Table 1 and No. 21 in Table 2), occurred at the old town area of Beichuan city, had a run-out distance of 550m. It destroyed hundreds of buildings and resulted in more than 1600 fatalities (Yin et al., 2009a). The Daguangbao landslide (No. 1 in both Table 1 and 2) is another long run-out example. The affected area is estimated more than 7.2 km^2. Its run-out distance is estimated as 4,500m. The most complex in dynamic mechanism is the Donghekou landslide (No. 3 in Table 1 and No. 4 in Table 2) which has the run-out distance of over 2.4km. It blocked two rivers and formed two landslide lakes at Donghe village of Qingchuan County.

It has been found that the run-out distance is proportional to the area and volume of landslide. The regression formulas of D/H=lg$S$-3.12 has been obtained with a coefficient of determination of R^2=0.7681, where D is the run-out distance, H is the slope height and S is the area of landslide. and D/H=0.54lg$V$-1.26 with a coefficient of determination of R^2=0.6290, where V is the volume of landslide (see Fig. 6).

Since the mechanism of long run-out landslide is very important in landslide disaster mitigation, it will be discussed in Section 4.

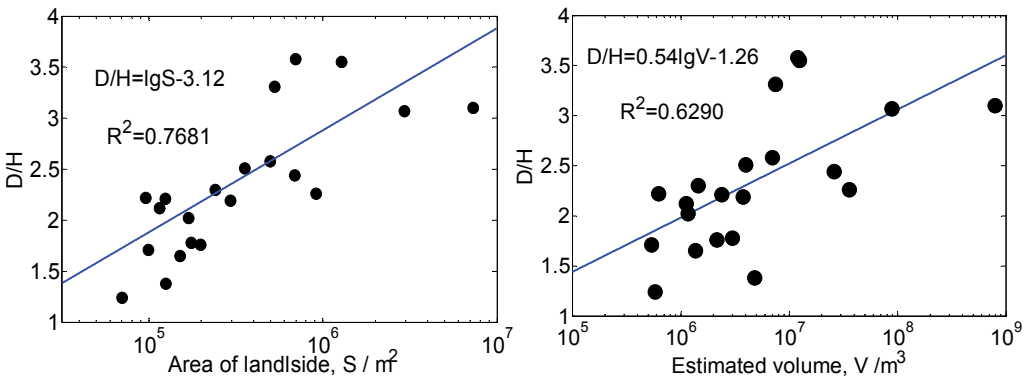

Fig. 6. The relationship between normalized run-out distance and (a) the area of landslide, S (m^2), and (b) the volume of landslide, V (m^3).

7. Large number of landslide dams

There are 34 landslide dams formed by the earthquake induced landslides. These landslide dams blocked the major large rivers. The water impounded by landslide dams created dam lakes.

The largest scale landslide dam was formed by the Tangjiashan landslide. It blocked the upper portion of the Jianjiang River at a location of about 5 km from Beichuan County Town. The dam crest extended approximately 600 m across and 800 m along the valley (Xu et al., 2009b). The maximum height of the dam is about 124 m. The maximum capacity of the landslide lake was 2.4×10^{8}m^3, with the length of 20 km (Yin et al., 2009a).

Because of its rather loose nature and absence of controlled spillway, it is feared that the landslide dam may fail catastrophically and lead to downstream flooding with high casualties. Hundreds of thousands of residents in downstream Mianyang City were evacuated to the higher locations out of the town before a temporary drainage channel was digged in the dam by Chinese government.

Rank	No. in Table 1	Name	Place	Area/m^2	Distance from fault/m	Estimated Volume/m^3	Height H/m	Horizontal distance D/m	D/H♀	Wall location
1	1	Daguangbao	Anxian	7,273,719	4,800	7.5x10^8※-8.4x10^8◎	≈1450♣	4,500※	3.10	Hanging wall
2	2	Wenjiagou	Mianzhu	2,945,520	3,900	2.75x10^7-1.5x10^8※	1,360	4,170	3.07	Foot wall
3	14	Niujuangou	Wenchuan	527,700	300	7,500,000	827	2,638-3,102♠	3.31	Hanging wall
4	3	Donghekou	Qiangchuan	1,283,627	300	1.0x10^7☼-1.5x10^7	680	2,413	3.55	Hanging wall
5	24	Liqigou	Jiangyou	355,113	10,000	4,000,000	920	2,310	2.51	Foot wall
6	9	Hongshigou	Anxian	687,520	2,240	26,000,000♥	≈900♣	2,200♥	2.44	Hanging wall
7	5	Shuimogou	Shifang	915,608	700	36,000,000♥	≈930♣	2,100♥	2.26	Hanging wall
8	7	Woqian	Qiangchuan	695,672	200	12,000,000	570	2,043	3.58	Hanging wall
9	17	Shibangou 1#	Qiangchuan	496,983	2,300	7,000,000	710	1,681♠-1,829	2.58	Hanging wall
10	31	Xiejiadianzi	Pengzhou	294,256	1,100	3.5x10^6-4.0x10^6☼	740	1,500-1,750♥	2.19	Hanging wall
11	58	Chenjiaping	Anxian	169,368	1,050	1,163,446	680	1,372	2.02	Hanging wall
12	41	Baichaping	Dujaingyan	241,874	4,700	1,449,340	580	1,340	2.30	Hanging wall
13	63	Changtan	Mianzhu	151,094	6,670	1,367,868	800	1,320	1.65	Foot wall
14	49	Zengjiashan	Mianzhu	198,165	11,350	2,166,334	700	1,230	1.76	Foot wall
15	55	Xiaotianchi	Mianzhu	175,758	8,200	2,999,540	630	1,120	1.78	Foot wall
16	89	Longwangou	Beichuan	99,821	650	540,382	520	890	1.71	Hanging wall
17	82	Gaojiamo	Pingwu	115,301	1,600	1,126,823	340	722	2.12	Hanging wall
18	92	Hongkouxiangxiajiaping	Dujaingyan	96,345	790	624,296	300	666	2.22	Hanging wall
19	79	Beichuanzhongxuexinqu	Beichuan	124,365	300	2,400,000☼	≈300♣	664♠	2.21	Foot wall
20	106	Maochongshan 2#	Pingwu	70,252	1,200	581,719	490	610	1.24	Hanging wall
21	76	Wangjiayan	Beichuan	125,381	400	4,800,000☼	≈400♣	550☼	1.38	Hanging wall

Note: ※ data from Huang et al. (2011a); ♥ data from Wu et al. (2010); ♠ data from Qi et al. (2011); ◎ data from Chigira et al.(2010); and ☼ data from Yin et al.(2009a); ♣ Estimated indirectly from geological sections or description.
♀ notes the value is mean one if the number of data more than one.

Table 2. Some long run-out landslides triggered by the Wenchuan earthquake (arranged from the Horizontal distance) (modified from Xu et al., 2009a)

3. Susceptibility analysis of earthquake induced Landslides

Landslide susceptibility analysis (LSA) is necessary and important for land use planning and disaster mitigation. Many researchers have made great effort to identify the relationships of landslide characteristics such as distribution pattern, type, area coverage and volume with the triggering factors such as the magnitude, intensity and peak ground acceleration (PGA) of the earthquake, coseismic fault rupture (e.g. Lee et al., 2008; Rodriguez et al., 1999; Miles and Keefer, 2009; Keefer, 1984, 2000, 2002; Papadopoulos and Plessa, 2000). Some researchers have studied the relationships of landslide distribution with geo-environmental factors such as lithology, morphology, presence of secondary active or inactive faults (e.g. Chigira and Yagi, 2006; Jibson et al., 2000; Khazai and Sitar, 2003; Keefer, 2000; Yagi et al., 2009).

The Wenchuan earthquake induced landslides has been carried out by several researchers. For example, Huang et al. (2011a) studied the characteristics and failure mechanism of Daguangbao Landslide, the largest scale landslide, and suggested a classification system. Tang et al. (2011b) studied the effect of the quake on the landslides induced by the subsequent strong rainfall after earthquake by a case study in the Beichuan area. Qi et al. (2010) built a spatial database of landslides by using the remote sensing (RS) results which cover 11 counties seriously damaged by the earthquake. Yin et al (2009a, b) analyzed the landslide distribution, the mechanisms of some typical landslides, and evaluated the potential hazards of the landslide dams. Gorum et al. (2011) presented the preliminary results of an extensive study of the mapping the distribution of landslides by using a large set of optical high resolution satellite images. Yin et al. (2010) presented a quantitative result of the number and area of the landslides from Anxian to Beichuan. Dai et al. (2011) mapped over 56,000 landslides using aerial photographs and satellite images and characterized the spatial distribution of landslides by correlating landslide-point density and landslide-area density with the physical parameters that control the seismic stability of slopes.

In this chapter, we show some results from landslide susceptibility analysis carried out in Qingchuan County. Our analysis was based on slope units rather than the traditional grid units. At first, the relationship of landslide distribution with an individual causative factor is analyzed. And then, landslide susceptibility is analyzed by using artificial neural network (ANN) method. Finally, a landslide susceptibility map is made based on the ANN results.

3.1 Study area and data source

Qingchuan County is located at the north-western part of the earthquake zone as shown in Fig. 7. The landslides in the area of 3,271km^2 are studied.

3.2 Slope unit

Up to now, most of such studies were carried out based on the grid units. There is a problem in grid-based study that a grid may contain different slopes and a large slope may contain several grids with different slope grades. Despite the problem, the grid units were still used just because the slope units are difficult to be indentified for a wide range in the past.

Nowadays, it becomes possible and easy to indentify slope units by using GIS-based hydrologic analysis tool (David, 2002), which is based on the watershed divide and drainage lines. The slope unit size should be determined when the tool is used. We suggest that the appropriate slope unit size should match the average size of the landslide bodies in the study area.

A total of 55,899 slope units were indentified in Qingchuan County (Fig. 8). They will be used for landslide susceptible analysis in this study.

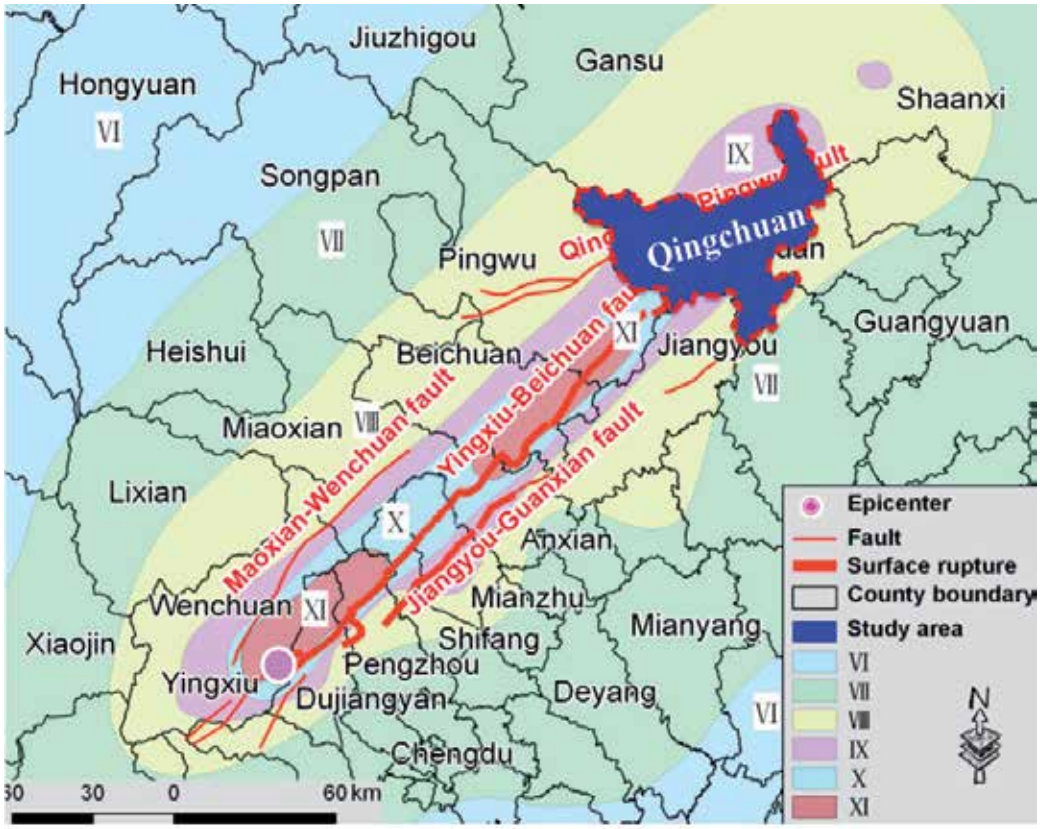

Fig. 7. Location of the study area

The basic data include a 1:100,000 geological map and a 10m grid digital elevation model (DEM) made from the available topographic map with 5m contour line interval. 885 landslides were identified from field investigations and RS results.

3.3 Relationship between landslide and individual causative factor

More than fifty factors can be considered as the landslide causative factors (Lin, 2003). By considering the data availability, analysis effectiveness, and independence of each factor (Lee et al., 2008), we selected the follow 8 factors: slope gradient, elevation, slope range, slope aspect, specific catchment area, lithology, distance to the fault and distance to the stream, to examine the causative factors contributing to the initiation of landslides.

Each causative factor was classified into several categories. The number of the slope units in each category is calculated and the percentage of the category among the whole slopes is given in Fig.9(b). For each category, the percentage of the failure slopes among the slopes in the same category is given as the landslide frequency in Fig. 9(a).

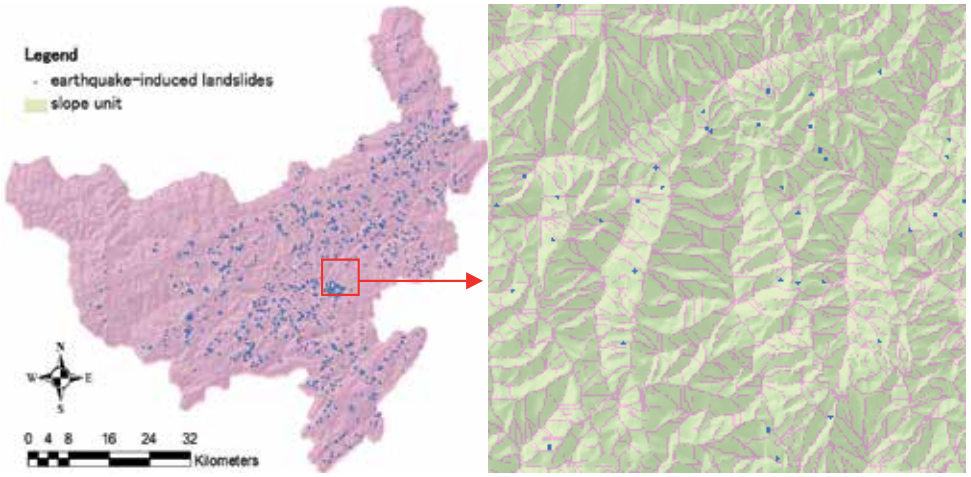

Fig. 8. Slope unit division of Qingchuan area

From the statistical analysis, the following results can be found.

1. More than 90% of the slopes have the slope gradient larger than 20°. The landslides occurred majorly in the slopes with gradients between 20° to 35°.
2. The landslides occurred majorly in the area with the elevations less than 1,200m.
3. The landslides occurred majorly in the slopes with slope ranges from 200 to 400m.
4. There is no clear relationship between landslides and specific catchment area.
5. The number of the landslides in the slopes in N direction is as twice as the slopes in the other directions.
6. The number of the landslides in the slopes with the distances to the fault less than 0.5km is as twice as the slopes in other categories.
7. The number of the landslides in the slopes with the distances to a stream less than 5km is as 3 times as the slopes in other categories.
8. There is no clear relationship between landslides and lithology.

3.4 Landslide susceptibility analysis using artificial neural network

The landslide susceptibility analysis is carried out by using artificial neural network (ANN) based on the above statistical analysis results.

ANN program is a "computational mechanism able to acquire, represent, and compute a mapping from one multivariate space of information to another, given a set of data representing that mapping, which is independent of statistical distribution of the data, can resolve the nonlinear problem and get high prediction accuracy for classification problem especially for large amount samples (Garrett, 1994). The applications of ANN to landslide susceptibility evaluation have been made by many researchers (e.g. Ermini,L., et al., 2005; S. Lee et al.,2006; Pradhan.B et al.,2010). Nefesilioglu et al. (2008) showed that ANN could give a more optimistic evaluation of landslide susceptibility than logistic regression analysis. Ermini et al. (2005) compared two neural architectures: probabilistic neural network and multi-layered perceptor, and obtained a better prediction result.

In this study, the neural network tool SPSS clementine is used since very few parameters are required. One group of the total slopes are randomly selected for training. 611 collapsed slopes of 885 landslides (70%) and 3300 of 55014 un-collapsed slopes (6%) are randomly selected for this group.

Two cases have been analyzed. Case 1 used the 8 factors mentioned as the statistical analysis and Case 2 used the 5 factors, 3 factors with the smaller weight values ware removed from the 8 factors. Also, different layers are used for the two cases.

The weights for each factor, experiments structures and the accuracy from the analysis results are shown in Table 3. It can be seen that the accuracy of Case 2 is a little bit higher than Case 1. Therefore, the ANN model from Case 2 is used for the landslide susceptibility classification.

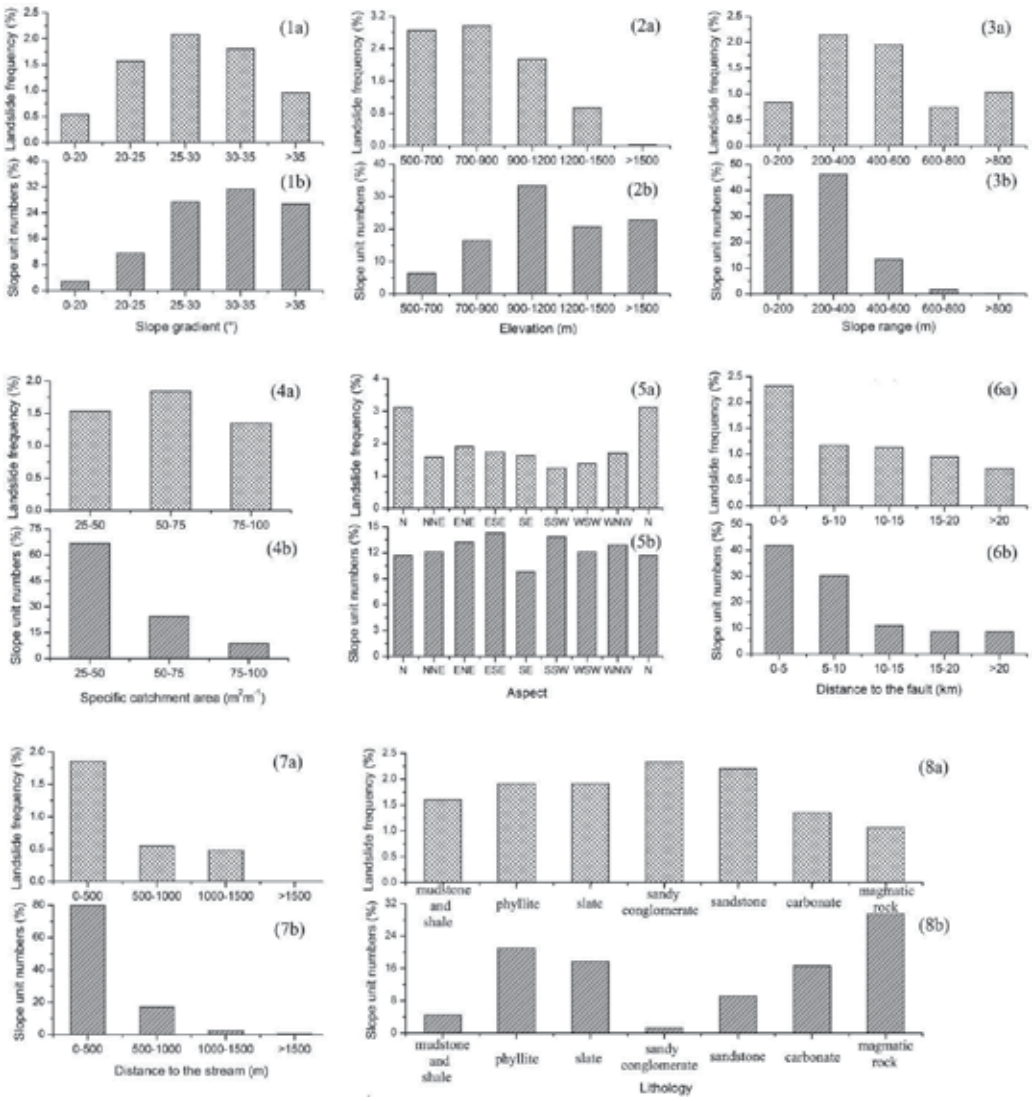

Fig. 9. Landslide frequency and slope unit numbers (%) for each category of causative factor

The output landslide susceptibility indices (LSI) were converted to GIS grid data in three susceptible levels as shown in Table 4. There are 4145 slopes identified as high susceptible level (dangerous slopes), 48,373 slopes identified as low susceptible level (stable slopes), 3,382 slopes identified as medium susceptible level (gray zone).

Causative factors	Case 1	Case 2
Slope gradient	0.367	0.446
Elevation	0.253	0.327
Slope range	0.193	0.163
Aspect	0.038	×
Specific catchment area	0.037	×
Distance to the fault	0.054	0.016
Distance to the stream	0.035	0.048
Lithology	0.023	×
Accuracy	95.05%	96.39%
ANN Structure	8*16*1	5*3*5*1

Table 3. Weight of each factor in 2 cases

By comparing with real landslides, it can be found that 877 of 885 landslides and 3268 stable slopes are identified as high susceptible level, which means 99% of landslides can be predicated by the model but 78.8% of predictions would be false alarm.
On the other hand, 1 of 885 landslides and 48373 stable slopes are identified as low susceptible level, which means 99.4% of predications are correct and less than 0.2% landslides would not be alarmed.

LSI	Susceptible level	Practical		Analysis result	
		Collapsed	Stable	Slope number	(%)
0.0-0.01	Low	1	48372	48373	96.53
0.01-0.1	Medium	7	3375	3382	6.05
0.1-0.9966	High	877	3267	4144	7.42
	Total	885	55014	55899	100.00

Table 4. Characteristics of the three susceptibility zones

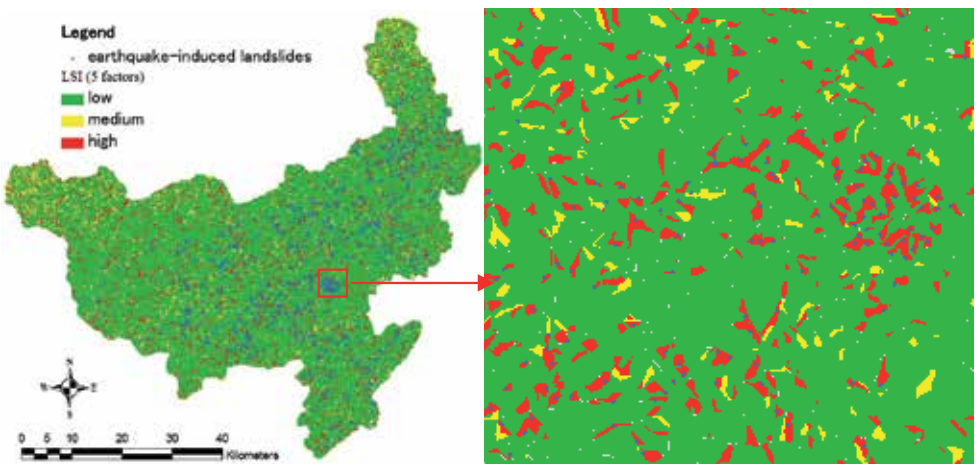

Fig. 10. Earthquake-induced landslide susceptibility map by using ANN analysis.

The landslide susceptibility map is made from the ANN results (Fig. 10). The high susceptible zone occupies 7.42%, the low susceptible zone 86.53% of the whole area. In addition, 6.05% of the area is gray zone.

3.5 Conclusions

Landslide susceptible analysis has been carried out in Qingchuan County. 55,899 slope units have been extracted and used for the analysis. The relationship between landslide distribution and the individual causative factor has been investigated by statistical analysis. The clear relationship can be identified for slope gradient, elevation, slope rang, the distances to the fault and the distances to a stream. The ANN analysis also showed the same results, that is, slope gradient, elevation, slope range, distance to the fault and distance to a stream have relatively larger weight. By removing the other three factors with smaller weights, the ANN analysis accuracy got improved. By comparing landslide occurrence locations with susceptibility zones, it has been shown that 99% of landslides can be predicated by the obtained ANN model, but 78.8% of predictions would be false. On the other hand, 99.4% of stable predications are correct and less than 0.2% landslides would not be alarmed. In addition, the gray zone occupies 6% of the whole area. Therefore, the landslide susceptibility classification presented in this study is acceptable.

4. Analysis of Long run-out mechanism based on trampoline effect

The estimation of the movement behaviour of a potential landslide is very important in order to mitigate the landslide disaster. Especially, the run-out distance is one of the major parameters in landslide risk assessment and preventive measure design. Long run-out is one of the major characteristics of earthquake induced landslides. However its mechanism has not been understood very well.

Many researchers have made great effort to understand how and why large falling masses of rock can move unusually long run-out distance. Researchers have repeatedly revisited the problem using a wide variety of approaches. These efforts have yielded no less than 20 mechanical models for explaining long run-out in high-volume rapid landslides. Shaller and Shaller (1996) made a detail summary of the existed models and divided these models into four categories (1) bulk fluidization and flow of landslide debris; (2) special forms of lubrication along the base of the slides; (3) mass-loss mechanisms coupled with normal frictional sliding; and (4) individual-case mechanisms.

Actually, most of the existed models are helpful in the estimation of the run-out distance. However, very less of them considered the earthquake dynamical behaviour. For this reason, in this study, we take into account the so-called trampoline effect of earthquake on landslides and propose a multiplex acceleration model (MAM) to explain the long run-out mechanism. Since the MAM model can be easily incorporated into numerical methods, it can be applied to simulate the long run-out landslide very well.

4.1 Multiplex acceleration model

For an earthquake induced landslide, the following effects on the movements of the falling stones from the landslide can be considered: (1) a falling stone can obtain kinetic energy

from the colliding with the vibrating slope during earthquake; (2) the force of friction between a falling stone and the slope can decrease since the normal force varies with the contact condition during earthquake; (3) The flying and rotation movement of a falling stone may occur much easily in earthquake induced landslides.

In order to consider these effects, we divide a period of wave is divided into two phases: *P*-phase and *N*-phase as shown in Fig. 11. The *P*-phase is defined as the period when the slope is moving in the outer normal direction of the slope surface. The slope is pushing the falling stones on its surface and lets them obtain kinetic energy in the *P*-phase. The *N*-phase is defined as the period when the slope is moving in the inner normal direction of the slope surface. Since the normal force will decrease when the slope surface moves apart from the falling stones, the force of friction will get decreased in the *P*-phase.

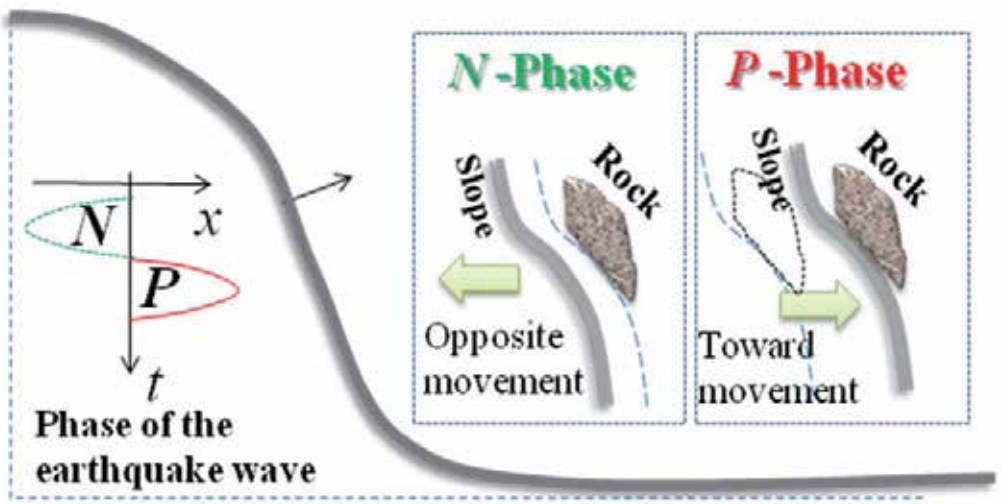

Fig. 11. *P*-phase and *N*-phase definition in MAM

By the repeated exchange of two phases during an earthquake, the falling stone get multiplex accelerated. The MAM model can be seen more clearly by apparent friction angle analysis.

Supposing that a stone with mass m moves from position A to position B during a landslide without earthquake (see Case 1 in Fig. 12), the potential energy decreases by mgh. Based on the energy conservation law, it is easy to obtain the following equation for a falling stone movement in the case without earthquake.

$$mgh - \sum_{i=1}^{n} l_i mgk_i \tan\varphi_{si} \cos\theta_i = 0 \tag{1}$$

The first term here is for potential energy and the second term is for the work of friction force between the slope and the falling stone, where the sliding movement is considered and the whole curve path is divided into finite linear segments. And m = mass, g = gravity acceleration, h = the falling height, l = the segment length, θ is the segment slope angle, φ is the friction angle, k is the coefficient of conveying from static to dynamic friction and i is the index of segment.

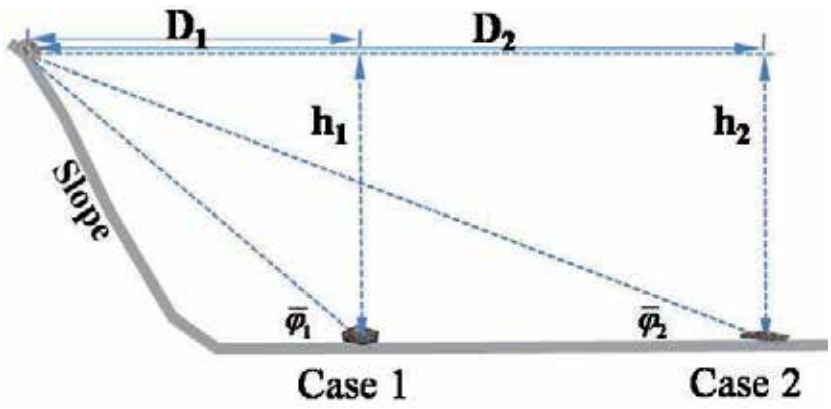

Fig. 12. Apparent friction angle

The apparent friction angle, usually used for the discussion of run-out distance, can be obtained from Eq. (1) as follows

$$\tan\overline{\varphi_1} = \frac{h_1}{D_1} = \sum_{i=1}^{n} w_i k_i \tan\varphi_{si} \tag{2}$$

When we consider the effects of slope vibration due to earthquake, the kinetic energy of falling stone obtained from the collision with the vibrating slope and the movement patterns (sliding, rolling and flying) should be considered. Thus, Eq. (1) becomes

$$mgh + \sum_{j=1}^{m} \frac{1}{2} m v_{ej}^2 - \sum_{i=1}^{n} l_i mgk_i^* \tan\varphi_{si} \cos\theta_i = 0 \tag{3}$$

The second term here is for the kinetic energy of a falling stone obtained from the collision with the vibrating slope and v_{ej} is the velocity obtained in j^{th} P-phase and can be expressed as follows

$$v_{ej} = VTR \int_{t_j}^{t_j+\Delta t} f(t)dt \tag{4}$$

$f(t)$ is the acceleration of slope vibration due to earthquake, VTR is called the velocity transmission ratio due to collision.

The apparent friction angle for the case 2 in Fig. 12 can be obtained from Eq. (3) as follows

$$\tan\overline{\varphi_2} = \frac{h_2}{D_2} = \sum_{i=1}^{n} w_i k_i^* \tan\varphi_{si} - \sum_{j=1}^{m} \frac{v_{ej}^{\ 2}}{2gD_2} \tag{5}$$

Comparing Eq.(5) with Eq.(2), it can be seen clearly that the mechanism of long run-out distance is as follows.

1. The kinetic energy of a falling stone obtained from the collision with the vibrating slope may result in long run-out distance from the second term of Eq. (5).
2. The coefficient of conveying from static to dynamic friction k^* in Eq. (5) can be smaller than k in Eq. (3) because of the N-phase effect, air cushion effect, movement pattern.

4.2 Colliding effect

In *P*-phase, a falling stone can obtain kinetic energy from the colliding with the vibrating slope. According to elastic collision theory, when two objects with different masses collide with each other, the object with smaller mass could obtain larger velocity. Since the mass of a slope is much larger than the mass of a falling stone, the velocity of the falling stone can be much larger than the vibrating velocity of the slope. That is to say the *VTR* in Eq. (4) can be larger than 1.0.

The *VTR* can be examined by the simple model shown in Fig. 13(a) and (b). The masses of the two blocks are m_1 and m_2 respectively. Before the colliding, the block 1 has initial velocity V_{10} toward block 2 which is standstill, i.e. V_{20}=0. The friction between blocks and the base is negligible. After the colliding, the velocity of block 1 becomes V_{11} while block 2 obtains a velocity V_{21}.

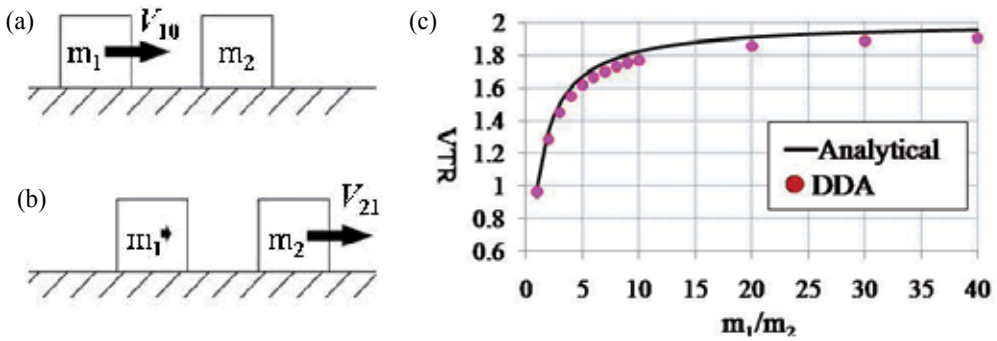

Fig. 13. The colliding model and *VTR* with mass ratio. (a) before the collision, (b) after the collision, (c) *VTR* obtained by DDA comparing with analytical solution.

According to the principles of the conservation of both energy and momentum, we have the following equations.

$$m_1V_{10}^2 + m_2V_{20}^2 = m_1V_{11}^2 + m_2V_{21}^2 \tag{6}$$

$$m_1V_{10} + m_2V_{20} = m_1V_{11} + m_2V_{21} \tag{7}$$

By solving Eqs. (6) and (7), we can obtain the *VTR* for the case of V_{20}=0 as follows

$$VTR = 2 \cdot \frac{m_1}{m_1 + m_2} \tag{8}$$

It can be seen from the analytical solution Eq. (8) that if m_1 is much larger than m_2, *VTR* is to approach to 2.0. Therefore, since the mass of a slope is far larger than the falling stone, the velocity of the falling stone obtained from the slope vibration will be two times of that of the slope vibration velocity during earthquake.

The results of *VTR* given in Eq. (8) have been verified by DDA simulation. The model shown in Fig. 13 is used in DDA simulations. The block one with mass of m_1 has the initial velocity of 10 *m/s* and the block two with mass of m_2 is at a standstill. After the block one impacted the block two, the velocities of both blocks changed. The block two obtained the velocity from block one. The *VTR* is calculated from the ratio of V_{21} to V_{10}.

The results obtained from DDA simulations by changing m_1 are shown in Fig. 13(c), together with the theoretical analytical values. The line is calculated from the analytical solution Eq.(8) and the dots are obtained from DDA simulations.

It can be seen that the *VTR* obtained from DDA is in quite good agreement with the analytical solution. However, by close examination, it can be found that the *VTR* values from DDA are little smaller than the analytical values when the mass ratio of m_1 to m_2 is larger than 4.0. This is because elastic strains of the two blocks are led to energy transformed into potential energy of deformation by the collision in DDA simulation while no strain is considered in analytical solution.

Furthermore, when the block 2 has an initial velocity toward block 1, the *VTR* could become the larger and larger. Fig. 14 shows the results from DDA simulation. This may happen when a stone fall down to the slope in a *P*-phase, it will get larger rebounding velocity. That means, a trampoline effect can be produced by strong earthquake.

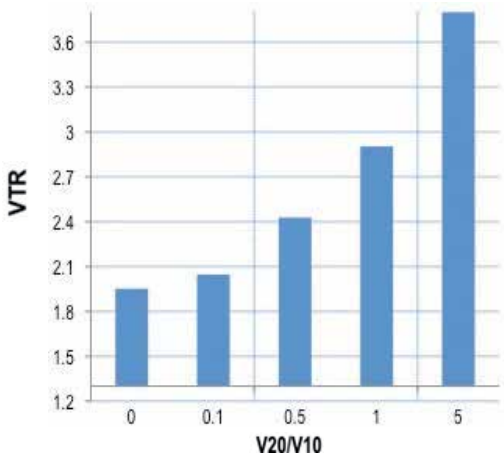

Fig. 14. The VTR variation with the initial velocity of block 2

4.3 Model tests by shaking table

Model tests using shaking table were carried out in order to investigate the effects of earthquake on the movement of debris. The model slope has the height of 180cm and the slope angle can be adjusted from 30° to 35° as shown in Fig. 15.

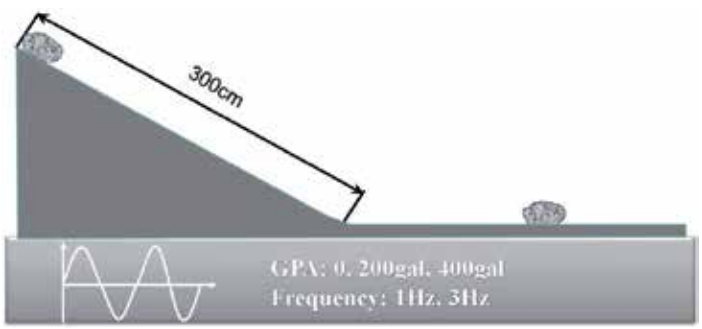

Fig. 15. Model tests by shaking table

The movements of 4 kinds of stones with different shapes have been investigated under the earthquake conditions of 0, 200gal and 400gal sine wave of 3Hz. More than 10 times of repeated experiments have been carried out for each case. The following results have been obtained.

1. The movement distance for the case of a 400gal earthquake is 3.4 times longer than the case of no earthquake for the No.4 stone. Therefore, the effect of earthquake on the movement distance is very large.
2. The movement distance for the case of a 400gal earthquake is longer than the case of a 200gal earthquake. So it seems that the movement distance is proportional to the earthquake magnitude.
3. The shape of the falling stone has effect on the movement distance. The movement distance of the No. 5 stone is much smaller than that of No. 4. This is because that the earthquake can change the movement pattern and cause the rotation motion. It can be seen that the No. 5 stone has very sharp edges and vertices, which may stop its rotation movement (Fig. 16).

It should be noticed that it is difficult to distinguish the velocity obtained from *P*-phase because the model slope is too small and there are very few *P*-phase during the movements.

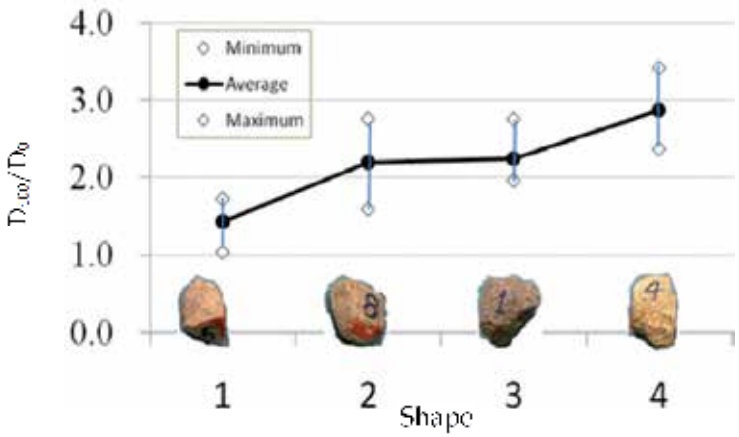

Fig. 16. Difference from shape of falling stone

4.4 Numerical simulation of landslide by using DDA

Simulation of landslide by using numerical methods is an effective way in order to overcome the dimension limit of the model test by using shaking table. In this study, Discontinue Deformation Analysis (DDA), developed by Shi and Goodman (Shi et al., 1984), is used since it is applicable to simulating the rigid body movements and large deformations of a rock block system under general loading and boundary conditions. Several extensions of the original DDA have been made in this study so that earthquake wave can be taken into the simulation for different ways.

Before simulating a real landslide, the applicability of the extended DDA has been verified by various simple models with theoretic solutions. For example, a simple model shown in Fig. 17 is calculated by both the theoretical solution and DDA simulation.

The theoretical solution of movement distance can be calculated by the following formula:

$$S_0 = \frac{1}{2}at^2 \tag{9}$$

where

$$\alpha = g[\sin\theta - (k\tan\varphi_0)\cos\theta] \tag{10}$$

The results of the movement distance are in good agreement with each other as shown in Fig. 18.

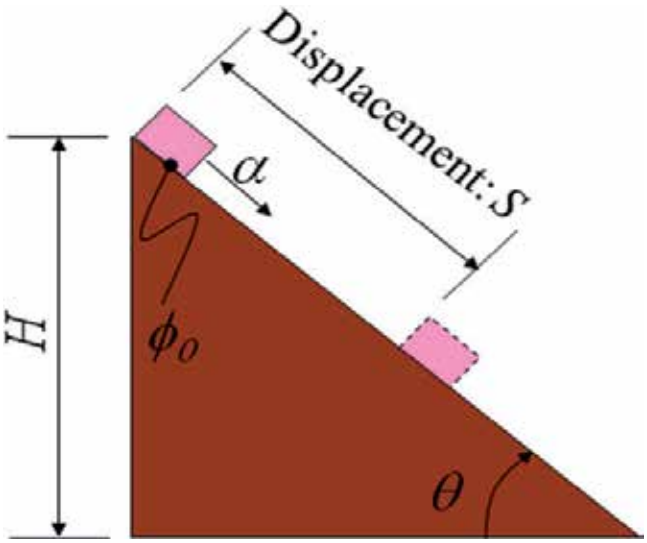

Fig. 17. The DDA model

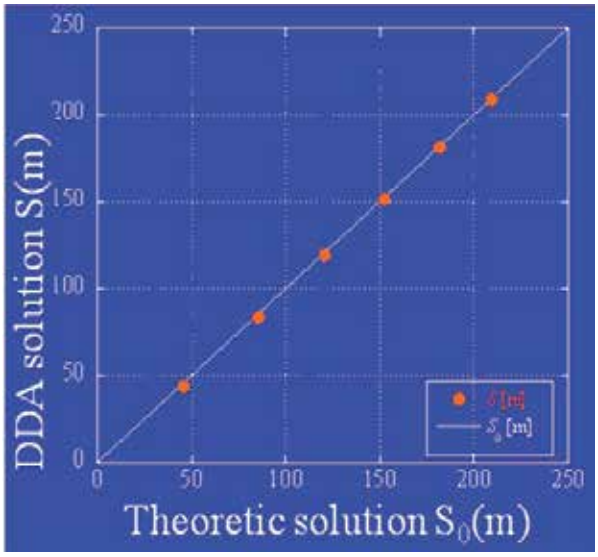

Fig. 18. The results

We applied the extended DDA to simulate the Dongheko landslide in Qingchuan prefecture. The vertical section shown in Fig. 19 is taken along the red line in Fig. 19. The DDA software and the model are shown in Fig. 20. The parameters for both the material and DDA program are also shown in Fig. 20.

Since the real earthquake curves are not available, a sine wave is used. The movements of debris at different times obtained from DDA simulation are shown in Fig. 21.

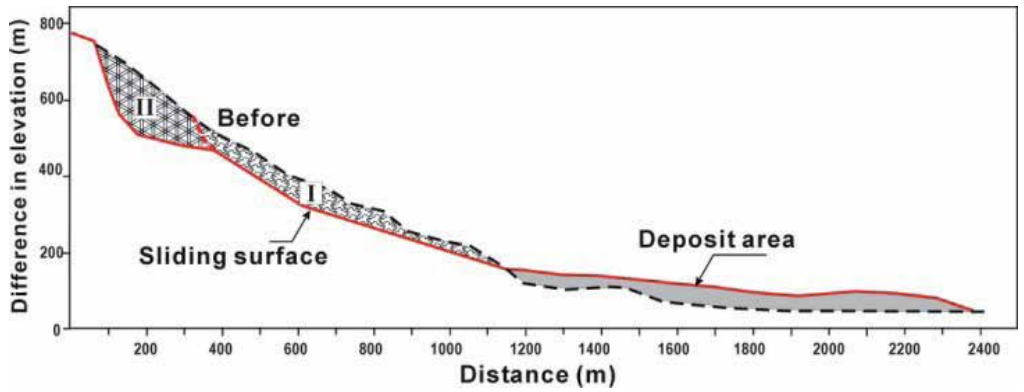

Fig. 19. Vertical section of the Donghekou landslide

It has been shown that an 800gal sine wave can cause long distance movements of debris like real one. The rotation and flying movements are the major reasons for long-distance movement, which can be easily observed in DDA simulations.

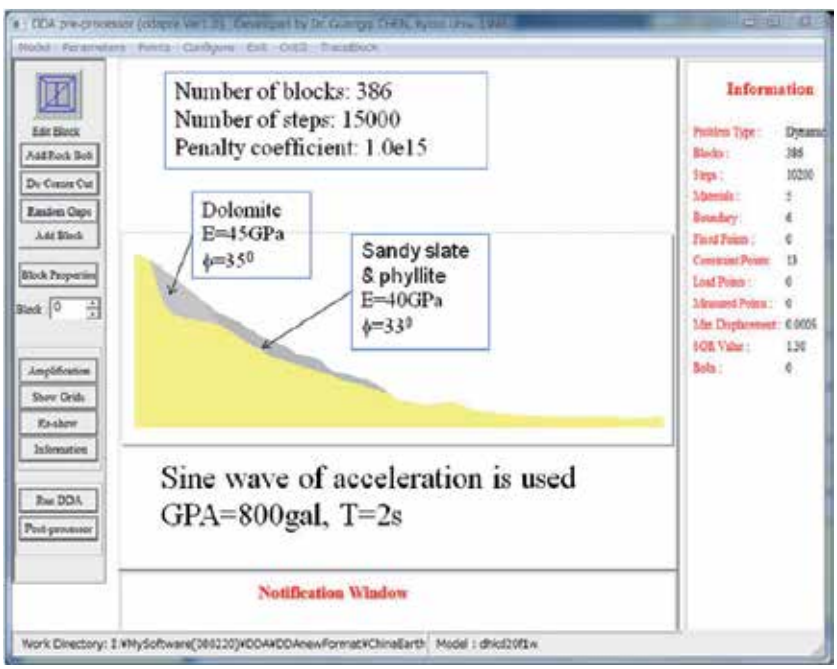

Fig. 20. DDA software developed by Chen and the model of Dongheke landslide

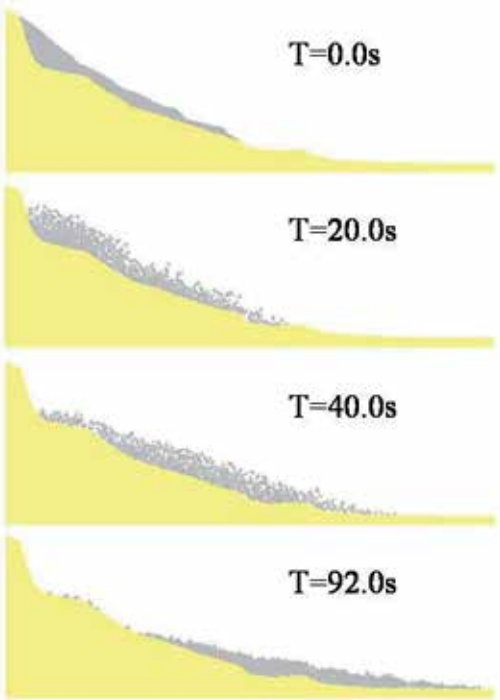

Fig. 21. The numeric simulation of debris movements by the extended DDA

5. Debris flow arising from the earthquake

Strong earthquakes not only trigger co-seismic landslides but also they affect subsequent rainfall-induced debris flows over a long term because these co-seismic landslides greatly increased the amount of sediment material for potential debris flows (Lin et al.,2006; Tang et al.,2009; Khattak et al.,2010). After the 2008 Wenchuan Earthquake, the earthquake affected areas experienced two rainy seasons till 2010, and a large number of debris flows occurred, which claimed as many as 450 fatalities. It makes the restoration and reconstruction much more difficult (Xie et al.,2008).

In this section, at first, the characteristics of debris flows in the earthquake affected areas are summarized. And then, an approach of simulating debris flow is proposed for disaster mitigation. Finally, a large scale debris flow is simulated so as to show the effectiveness of the proposed.

5.1 Characteristics of debris flow after the earthquake

1. Clear relation to the earthquake

A large number of debris flows occurred in the earthquake affected areas. For example, there are 46 debris flows found in Beichuan area. The distribution of these debris flows is shown in Fig. 22 in which the red line indicates the main fault of the quake, blue lines indicate rivers and the numbers indicate the locations of the debris flows. It can be seen that these debris flows are distributed along the rivers on the two sides of the earthquake fault. Therefore, the debris flows are highly related to the earthquake.

2. Large surge peak discharge and huge volume

Since the material sources of debris flow got much richer after earthquake, it is easy to form large scale debris flow. For example, the surge peak discharge reached 260 m^3/s in the debris flow occurred in Beichuan town on Sept. 24, 2008. The volume was too large to a basin with the area of 1.54km^2. The cover of debris is so thick that it buried the fourth floor of some buildings. Another example is Sanyanyu debris flow. The volume of the debris reached 144.20 million m^3. The debris flow carried many huge stones and destroyed houses and bridges (Tang et al., 2009).

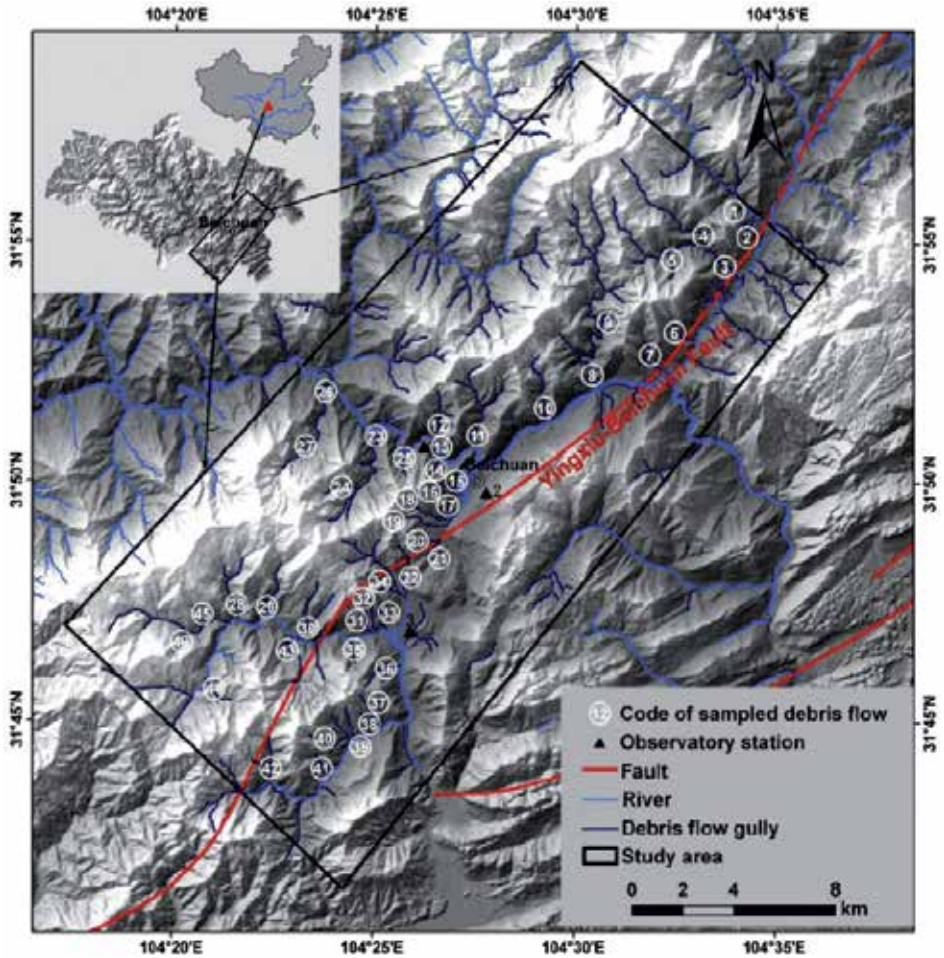

Fig. 22. 46 debris flows in the Beichuan area(Picture from Tangchuan et cl., 2010)

Many preventive structures designed based on the standard of conventional debris flow were also destroyed by the large scale debris flows after the earthquakes. For example, 19 check dams were destroyed by the Wenjia debris flow occurred in Mianzhu Qingping town area on Aug. 13, 2010. The Fig. 23(a) shows one of the check dam destroyed by the debris flow. The extreme large scale and destructive impact of the debris flow seems beyond imagination.

3. The low critical precipitation for triggering debris flow

The critical precipitation for triggering debris flow got decreased obviously after the earthquake. For example, the critical precipitation of 37mm became lower after the earthquake in Zhouqu County areas. A 22mm rainfall could trigger a debris flow during the past 3 years. According to preliminary analysis by Tang et al. (2009), the critical cumulative precipitation has been reduced about 14.8%-22.1%, the critical rainfall intensity per hour about 25.4 %～31.6% in Beichuan County area.

Fig. 23. (a): The destroyed check dam in Qingping debris flow; (b): Ming river blocked at Yingxiu town by Hongchungou debris flow (photographs from Tang chuan)

4. River blocking

The disasters chain induced by the earthquake is very significant. The earthquake induced landslides caused debris flows which blocked rivers, and flooding disasters occurred. For example, Jianjiang River was blocked at 3 locations and half blocked at 8 locations by debris flows during the rainstorm on Sept. 24, 2008. Mianyuan River was blocked at 2 locations and half blocked at 11 locations by debris flows occurred on Aug. 13, 2010. Ming River was blocked at 1 location and half blocked at 5 locations by debris flows occurred on Aug. 14, 2010 (see Fig. 23 (b)).

5.2 An approach of simulating debris flow

Many studies on debris flow focused on estimation of an alluvial fan for predicting debris flow inundation areas (Glade,2005;Berti and Simoni,2007). They can be divided into three categories: dynamic models, volume-based models and topographic based models. For the 2008 Wenchuan earthquake, an empirical formula of estimating alluvial fan has been presented by Tang et al. (2010) based on statistical analysis.

In this study, we propose an approach for numerical simulation of debris flow to analyze or predict the peak discharge and the volume of a debris flow and its inundation area. The approach consists of the following 5 procedures.

1. Identify the earthquake induced landslides

The earthquake induced landslides can be identified by RS technique using aerial photos and satellite imagines. The locations and the shapes of all the debris deposits in a drainage area should be obtained from this procedure.

2. Make field investigations.

The thicknesses of all the debris deposits and the geological and geotechnical behaviors should be investigated in this procedure.

3. Generate the grids using GIS.

Grids are required for solving equations with finite different method. A DEM map can be converted to a raster image using GIS for the drainage area. The grids can be obtained by saving the raster data.

4. Solve the equations.

The debris and water mixture is assumed to be a uniform continuous, incompressible, unsteady Newtonian fluid. The following Navier-Stokes equations are used for debris flow governing equations:

$$\begin{aligned} &\nabla u = 0 \\ &\rho \frac{\partial u}{\partial t} + \rho u \cdot \nabla u = \rho g - \nabla p + \mu \nabla^2 u \end{aligned} \tag{11}$$

where $u = (u, v, w)$ is velocity; ρ is the mass density; p is the pressure; μ is dynamic viscosity; $g = (0, 0, g)$, g is the gravitational constant and t is time.

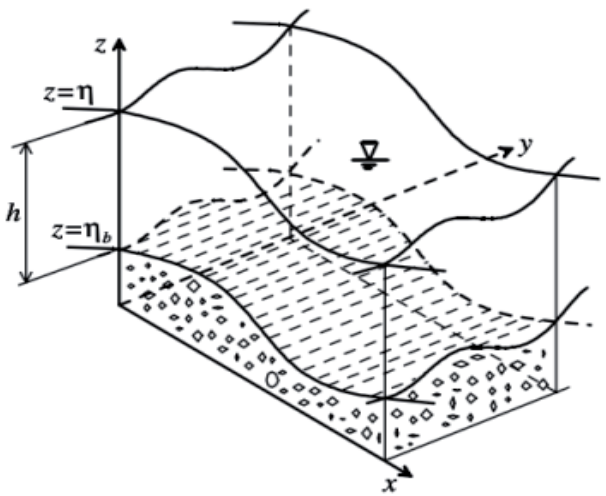

Fig. 24. Definition of coordinate system for 2D governing equations

The so-called depth-averaged model as shown in Fig. 24 is used. And then the following equations are used instead of Eq. (11). They are solved by finite difference method (FDM).

$$\frac{\partial h}{\partial t} + \frac{\partial M}{\partial x} + \frac{\partial N}{\partial y} = 0 \tag{12}$$

$$\frac{\partial M}{\partial t} + \alpha \frac{\partial (MU)}{\partial x} + \alpha \frac{\partial (MV)}{\partial y} = -\frac{\partial H}{\partial x} gh + \nu\beta \left(\frac{\partial^2 M}{\partial x^2} + \frac{\partial^2 M}{\partial y^2} \right) - gh \cos\theta_x \tan\xi \tag{13}$$

$$\frac{\partial N}{\partial t}+\alpha\frac{\partial(NU)}{\partial x}+\alpha\frac{\partial(NV)}{\partial y}=-\frac{\partial H}{\partial y}gh+\nu\beta(\frac{\partial^2 N}{\partial x^2}+\frac{\partial^2 M}{\partial y^2})-gh\cos\theta_y\tan\xi \tag{14}$$

Where $M=Uh$ and $N=Vh$ are the $x-$ and $y-$ components of the flow flux; U and V are the $x-$ and $y-$ components of the depth-average velocity; H is the height of the free surface; h is the flow depth; θ_x and θ_y are the angle of inclination at the bed along the x and y directions, respectively; α and β are the momentum correction factors; $v=\mu/\rho_d$ is kinematic viscosity, ρ_d is the equivalent density of the debris mixture, and $\rho_d=\rho_s v_s+\rho_w v_w$, ρ_s and ρ_w are the densities of solid grains and water, v_s and v_w are the volumetric concentrations of solids particles and water in the mixture; and $\tan\xi$ is the dynamic friction coefficient.

5. Visualize the results

The results from FDM are converted to GIS layers. The maps of maximum surge peak discharge, velocity distribution and in inundation area can be made by GIS. Also the animation of debris flow can be easily made.

5.3 Numerical simulation of the Hongchungou debris flow

The proposed approach has been used to simulate the Hongchungou debris flow occurred in Hongchungou drainage area on August 14, 2010. The materials carried by the debris flow blocked Ming River just at a little upper side about 200m from Yingxiu town, the epicenter of the 2008 Wenchuan Earthquake (Fig. 25), . The road along the river became the new temporary river channel and water flowed into Yingxiu town. As the result, serious flood occurred in the newly reconstructed town. The disaster claimed 13 lives and 59 missing persons.

The distribution of the earthquake induced landslides has been identified by using RS with the aerial photographs taken by The Ministry of Land and Resources of China. The aerial photograph 0.3m resolution of Hongchungou area is shown in Fig. 26(a).

In this study, the object-based analysis (OBA) is adapted for imagine analysis unlike traditional spectral information based image analysis method since there exists the so-called 'salt and pepper' appearance in the output of the latter (Tapas R. Martha et al., 2010). The analysis includes the following steps.

1. The aerial photos are ortho-rectified based on the 20m DEM obtained from the China Geology Survey Bureau, in order to remove the distorting effects of tilt and terrain relief.
2. The image is divided into objects based on homogeneity of pixel values through edge-based segmentation algorithm (Kerle et al., 2009), since it is very fast and only one parameter is needed for scale level. Scale level 30 and merge level 93 are used for image segmentation.
3. NDVI index is used to separate vegetation from other objects. Spatial, spectral and texture attributes are separately computed for each object. Then, various land covers are classifies based on user-defined training data, selected by combing with 3 dimensional image in order to improve the interpretation refinement;
4. The non-landslide objects are eliminated by the assumption that landslide will not occur for the slope gradient less than 5°.

Fig. 25. The blocked Ming River and new Yingxiu town in flood by Hongchungou debris flow.

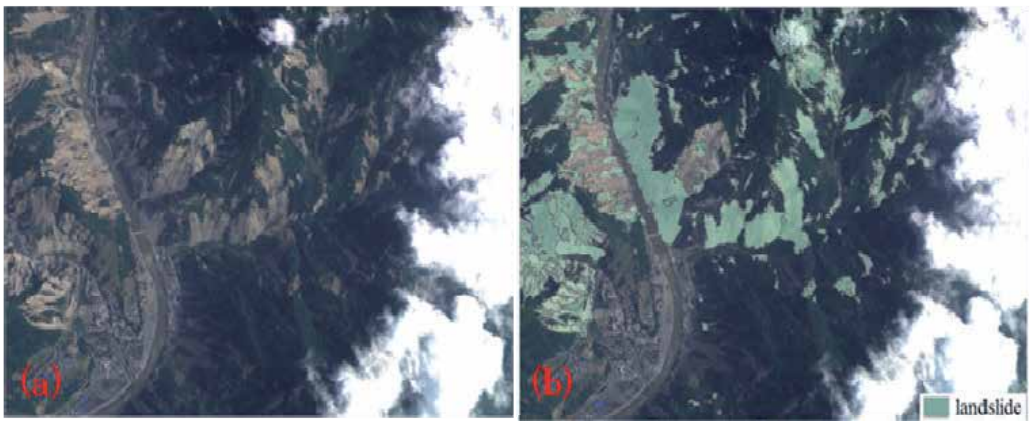

Fig. 26. (a): Aerial photography of Hongchun valley; (b): identified landslides in Hongchun valley

The obtained landslides are shown in Fig. 26(b). It can be seen that all the landslides were accurately recognized. There is not so-called 'salt and pepper' appearance.

Combining with field investigation, we finally selected four landslides: H1, H2, H3, H4 as the main loose source material of the debris flow (Fig. 27). The area of each landslide is 7,688 m^2 for H1, 5,137 m^2 for H2, 2,002 m^2 for H3, 4 4,567 m^2 for H4.

Since only a 20m DEM map is available for generating grids, the 4,000mX3,400m area is divided into 200X170 grids by using GIS. The rheological parameters are assumed constant (Tang et al., 2011a), and they are: ρ_d =2050kg/m^3, α =1.25, β =1.0, μ =0.11, g = 9.8m/s^2, $\tan\xi$ =0.6.

The results from FDM are converted to GIS layers for visualizing. The movements of the debris flow are illustrated in Fig. 28(a)-(d) for different time. It can be seen that the river is blocked in Fig. 28(d). The distribution of the maximum depth of the whole flow is shown in Fig. 28(e). According to the simulation results, the debris flow takes 150*s* to travel about 3,300 m along the valley with an average flow velocity of about 22m/s.

Comparing the simulated results with the actual event, we found that they are in good agreement with each other. Therefore, the proposed approach has been shown applicable and useful for predicting the movement of potential debris flow arising from earthquake.

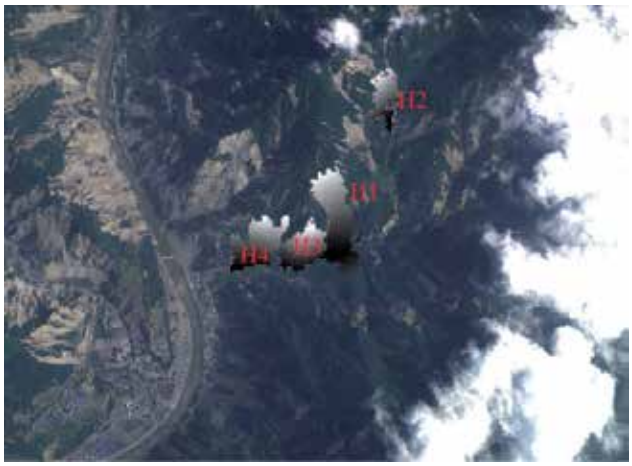

Fig. 27. Identified landslides as loose material of the debris flow

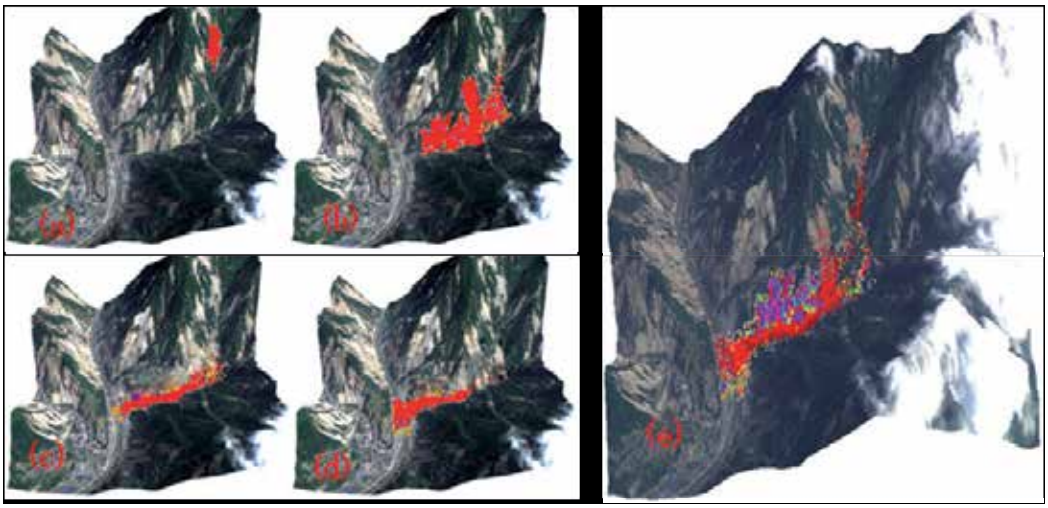

Fig. 28. The movement of the debris flow (a) for t=10s, (b) t=76s, (c) t=120s, (d) t=150s and (e) for the distribution of the maximum depth of Hongchungou debris flow.

6. Conclusions

A strong earthquake can induce a chain of disasters. The disaster chain from the 2008 Wenchuan earthquake has been discussed.

The characteristics of the earthquake induced landslides have been summarized as follows.

1. A large number of landslides (56,000) were induced by the earthquake;
2. Large quantities of large-scale landslides (113) occurred and are listed in this chapter.

3. The landslides in the hanging wall are more than the footing wall and about 70% landslides are located in the region of 3km from the fault.
4. Large-scale landslide can occur at the locking segment of the rupture fault.
5. There is a clear relationship between the sliding direction of landslides and the fault strike.
6. Large quantities of long run-out landslides occurred and are listed in this chapter. Regression formulas of run-out distance have been obtained based on the areas and volumes of landslides.
7. A large number of landslide dams (34) were formed.

The susceptibility analysis of the earthquake induced landslides has been carried out by both statistical analysis and ANN analysis based on slope units rather than the traditional grids. The relationship of landslide distribution with individual causative factor has been investigated. It has been found that slope gradient, elevation, slope range, the distances to the fault, the distances to a stream have contributed to landslides while specific catchment area, slope aspect and lithology have no clear relationship. A susceptibility map has been made for analysis of the earthquake induced landslides in Qingchuan County.

A Multiplex Acceleration Model has been proposed for analysis of the long run-out mechanism based on trampoline effect. Table model tests and DDA simulation were carried out. It has been shown that the proposed Multiplex Acceleration Model is reasonable and applicable.

The earthquake induced landslides can easily form debris flows after the earthquake. The characteristics of the debris flows arising from the 2008 Wenchuan earthquake have been summarized as follows.

1. There is a clear relation to the earthquake according to the distribution of the debris flows along the earthquake fault.
2. Most of debris flows have large surge peak discharges and huge volumes.
3. The critical precipitation for triggering debris flow became lower.
4. Many rivers were blocked by the debris flows and serious damages have been caused by the debris dams.

An approach of simulating debris flow has been proposed. The earthquake induced landslides are identified by RS with object-based analysis method, which can overcome the problem of the so-called 'salt and pepper' appearance existed in the traditional spectral information based image analysis method. A practical simulation has been carried out and the proposed approach has been shown effective and useful for estimating the movement behaviours of a potential debris flow arising from a strong earthquake.

7. Acknowledgment

The presented research work and the preparation of this paper have received financial support from the Global Environment Research Found of Japan (S-8), Grants-in-Aid for Scientific Research (Scientific Research (B), 22310113, G. Chen) from JSPS (Japan Society for the Promotion of Science). These financial supports are gratefully acknowledged.

8. References

Berti, M., Simoni,A. (2007). Prediction of debrisflow inundation areas using empirical mobility relationships.*Geomorphology,* Vol. 90,(Octorber 2007), pp. 144-161

Changa, KJ., Taboada, A., Linb, ML. & Chenc, RF. (2005). Analysis of landsliding by earthquake shaking using a block-on-slope thermo-mechanical model: Example of Jiufengershan landslide, central Taiwan. *Engineering Geology*, Vol. 80, (May 2000),pp. 151–163, ISSN 0013-7952

Chigira, M. & Yagi, H. (2006). Geological and geomorphological characteristics of landslides triggered by the 2004 Mid Niigta prefecture earthquake in Japan. *Engineering Geology*. Vol. 82, No. 4, (February 2006), pp. 202–221, ISSN 0013-7952

Cui, P., Zhu, Y., Han, Y., Chen, X. & Zhuang, J. (2009). The 12 May Wenchuan earthquake-induced landslide lakes: distribution and preliminary risk evaluation. *Landslides*, Vol. 6. No. 3, (June 2009), pp. 209-223, ISSN 1612-510X

Dai, F., Xu, C., Yao, X., Xu, L., Tu, X. & Gong, Q. (2011). Spatial distribution of landslides triggered by the 2008 Ms 8.0 Wenchuan earthquake, China. *Journal of Asian Earth Sciences*, Vol. 40, No. 4, (March 2011), pp. 883–895, ISSN 1367-9120

Dai, F.C., Lee, C.F. (2002). Landslide characteristics and slope instability modeling using GIS Lantau Island, Hong Kong. *Geomorphology* Vol. 42, (January 2002), pp. 213 – 238

David, R. M. (2002). *Arc Hydro: GIS for Water Resources*, ESRI Press, Redlands, CA,US.

Ermini, L., Catani, F., Casagli, N. (2005). Artificial neural networks applied to landslide susceptibility assessment. *Geomorphology* 66 (1 – 4), pp. 327 – 343

Garrett, J. (1994) Where and why artificial neural networks are applicable in civil engineering, *Journal of Computing Civil Engineering* , Vol.8, No.2, pp. 129–130

Glade,T.,2005.Linking debris-flow hazard assessments with geomorphology. *Geomorphology,* Vol. 66, pp. 189-213

Gorum, T., Fan, X., Westen, C., Huang, R., Xu, Q., Tang, C. & Wang, G. (2011). Distribution pattern of earthquake-induced landslides triggered by the 12 May 2008 Wenchuan earthquake. *Geomorphology*, doi:10.1016/j.geomorph.2010.12.030, ISSN 0169-555X

Huang, R., Pei, X., Fan, X., Zhang, W., Li, S. & Li, B. (2011a). The characterisitics and failure mechanism of the largest landslide triggered by the Wenchuan earthquake, May 12, 2008, China. *Landslides*, (June 2011), doi:10.1007/s10346-011-0276-6, ISSN 1612-510X

Huang, R., Xu, Q. & Huo, J. (2011b). Mechanism and geo-mechanics models of landslides triggered by 5.12 Wenchuan earthquake. *Journal of Mountain Science*, Vol. 8, No. 2, (April 2011), pp. 200-210, ISSN 1672-6316

Jibson, R., Harp, E. & Michael, J. (2000). A method for producing digital probabilistic seismic landslide hazard maps. *Engineering Geology*, Vol. 58, No. 3-4, (December 2000),pp. 271–289, ISSN 0013-7952

Keefer, D. (1984). Landslides caused by earthquakes. *Geological Society of America Bulletin*, Vol. 95, No. 4, (April 1984), pp. 406-421, ISSN 0016-7606

Keefer, D. (2000). Statistical analysis of an earthquake-induced landslide distributionthe 1989 Loma Prieta, California event. *Engineering Geology*, Vol. 58, No. 3, (December 2000), pp. 231–249, ISSN 0013-7952

Keefer, D. (2002). Investigating landslides caused by earthquakes – A historical review. *Surveys in Geophysics*, Vol. 23, No. 6. (November 2002), pp. 473-510, ISSN 0169-3298

Kerle, N., de Leeuw, J., (2009). Reviving legacy population maps with object-oriented image processing techniques. *IEEE Transactions on Geoscience and Remote Sensing,* Vol. 47, pp. 2392-2402

Khattak G A, Owen L A, Kamp U, Harp E L. (2010). Evolution of earthquake-triggered landslides in the. Kashmir Himalaya, northern Pakistan. *Geomorphology,* Vol. 115, pp. 102–108

Khazai, B., Sitar, N., (2004). Evaluation of factors controlling earthquake-induced landslides caused by Chi-Chi earthquake and comparison with the Northridge and Loma Prieta events. *Engineering Geology*, Vol. 71, No. 1, (January 2004), pp. 79–95, ISSN 0013-7952

Lee, C., Huang, C., Lee, J., Pan, K., Lin, M., Dong, J. (2008). Statistical approach to earthquake-induced landslide susceptibility. *Engineering Geology*, Vol. 100, No. 1, (June 2008),pp. 43–58, ISSN 0013-7952

Lin, C.W., Liu, S.H., Lee, S.Y., Liu, C.C., (2006). Impacts of the Chi-Chi earthquake on subsequent rainfall induced landslides in central Taiwan. *Engineering Geology* 86, pp. 87-101

Lin C W, Shieh C L, Yuan B D. (2003). Impact of Chi-Chi earthquake on the occurrence of landslides and debris flows: example from the Chenyulan River watershed, Nantou, Taiwan. *Engineering Geology,* Vol. 71, pp.49–61

Miles, B. & Keefer, D. (2009). Evaluation of CAMEL - comprehensive areal model of earthquake-induced landslides. *Engineering Geology*, Vol. 104, No. 1 , (February 2009), pp. 1–15, ISSN 0013-7952

Nefeslioglu, H.A., Gokceoglu, C., Sonmez, H. (2008). An assessment on the use of logistic regression and artificial neural networks with different sampling strategies for the preparation of landslide susceptibility maps. *Engineering Geology,* Vol. 97, pp. 171 – 191

Papadopoulos, G. & Plessa, A. (2000). Magnitude–distance relations for earthquake-induced landslides in Greece. *Engineering Geology*, Vol. 58, No. 4, (December 2000), pp. 377–386, ISSN 0013-7952

Pradhan.B, S.Lee. (2010). Landslide susceptibility assessment and factor effect analysis: backpropagation artificial neural networks and their comparison with frequency ratio and bivariate logistic regression modeling. *Environmental Modelling & Software,* Vol. 25, pp. 747 – 759

Qi, S., Xu, Q., Lan, H., Zhang, B. & Liu, J. (2010). Spatial distribution analysis of landslides triggered by 2008.5.12 Wenchuan Earthquake, China. *Engineering Geology*, Vol. 116, No. 2, (August 2010), pp. 95-108, ISSN 0013-7952

Qi, S., Xu, Q., Zhang, B., Zhou, Y., Lan, H. & Li, L. (2011). Source characteristics of long runout rock avalanches triggered by the 2008 Wenchuan earthquake, China. *Journal of Asian Earth Sciences*, Vol. 40, pp: 896-906, ISSN 1367-9120

Rodriguez, C., Bommer, J. & Chandler, R. (1999). Earthquake-induced landslides: 1980-1997. *Soil Dynamic and Earthquake Engineering*, Vol. 18, No. 5, (March 1999), pp. 325-346, ISSN 0267-7261

S.Lee, D. G. Evangelista. (2006). Earthquake-induced landslide-susceptibility mapping using an artificial neural network", *Nat. Hazards Earth Syst. Sci*., Vol. 6, pp. 687–695

Shaller, PJ. & Shaller, AS. (2006). Review of proposed mechanisms for sturzstroms (long runout landslides). *Sturzstroms and Detachment Faults,* Anza-Borrego State Park, California, pp.185-202

Tang C, Zhu J, Li W L. (2009) Rainfall triggered debris flows after Wenchuan earthquake. *Bull Eng Geol Environ*, Vol. 68, pp. 187–194

Tang C, Ding J, Qi X. (2010). Remote sensing dynamic analysis of rainstorm landslide activity in Wenchuan high-intensity earthquake area. *China university of geosciences journal*, Vol.35, pp. 317-323

Tang C, Zhu J, Qi X. (2011a). Landslide Hazard Assessment of the 2008 Wenchuan Earthquake: a case study in Beichuan Area. *Canadian Geotechnical Journal*. Vol. 48, pp. 128–145

Tang, C., Zhu, J., Qi, X. & Ding, J. (2011b). Landslides induced by the Wenchuan earthquake and the subsequent strong rainfall event: A case study in the Beichuan area of China. *Engineering Geology*, doi:10.1016/j.enggeo.2011.03.013, ISSN 0013-7952

Tapas R. Martha, Norman Kerle, Victor Jetten, Cees J. van Westen, K. Vinod Kumar. (2010). Characterising spectral, spatial and morphometric properties of landslides for semi-automatic detection using object-oriented methods. *Geomorphology* Vol. 116, PP. 24-36

Wu, S., Wang, T., Shi, L., Sun, P., Shi, J., Li, B., Xin, P. & Wang, H. (2010). Study on catastrophic landlsides triggered by 2008 great Wenchuan earthquake, Sichuan, China. *Journal of Engineering Geology*, Vol. 18, No. 2, pp. 145-159, ISSN 1004-9665 (in chinese)

Xie, H., Zhong, D.L., Jiao, Z., et al.,2008.Debrisflow in Wenchuan quake-hit area in 2008.Journal of Mountain Science 27(4),501-509.

Xu, Q., Pei, X., Huang, R. et al. (2009a). *Large-scale Landslides Induced by the Wenchuan earthquake*, Science Press, ISBN 978-7-03-026906-5, Beijing, China (in chinese)

Xu, Q., Fan, X., Huang, R. & Westen, C. (2009b). Landslide dams triggered by the Wenchuan earthquake, Sichuan Province, south west China. *Bulletin of Engineering Geology and the Environment*, Vol. 68, No. 3, (August 2009), pp. 373-386, ISSN 1435-9529

Yagi, H., Sato, G., Higaki, D., Yamamoto, M. & Yamasaki, T. (2009). Distribution and characteristics of landslides induced by the Iwate-Miyagi Nairiku Earthquake in 2008 in Tohoku District, Northeast Japan. *Landslides*, Vol. 6, No. 4, (December 2009), pp. 335–344, ISSN 1612-510X

Yin, J., Chen, J., Xu, X., Wang, X. & Zheng, Y. (2010). The characteristics of the landslides triggered by the Wenchuan Ms 8.0 earthquake from Anxian to Beichuan. *Journal of Asian Earth Sciences*, Vol. 37, No. 6, (March 2010), pp. 452-459, ISSN 1367-9120

Yin, Y., Wang, F. & Sun, P. (2009a). Landslide hazards triggered by the 2008 Wenchuan earthquake, Sichuan, China. *Landslides*, Vol. 6, No. 2, (June 2009), pp. 139-151, ISSN 1612-510X

Yin, Y. (2009b). Rapid and long run-out features of landslides triggered by the Wenchuan Earthquake. *Journal. of Engineering. Geology*, Vol. 17, pp. 153–166 (in Chinese)

19

Correlation Between Geology, Earthquake and Urban Planning

Sule Tudes
University of Gazi, Faculty of Architecture,
Department of Urban and Regional Planning, Maltepe, Ankara
Turkey

1. Introduction

Urban planning is the organized planning of the physical environment that the mankind lives by providing the safety in line with the social, cultural and economical needs. The primary objective of the planning is to create healthy, reliable and durable living spaces. At this point, especially earthquakes and their effects in the countries that are located on the seismic belts of the world constitute the primary geologic threshold.
Inadequate consideration of the geohazards and the constraining effects of the geological environment or lack of precaution due to improper projection of the analysis and synthesis results to the planning and the planning decisions give rise to the increase in earhtquake damages. Geological studies aimed at reducing the effects of the ground movements due to earthquakes are of prime significance on the reduction of damage that consitutes the basis of earthquake sensitive planning studies.
Geologists, engineers, architects and planners, in creating the earthquake resistant cities, should determine the geologic hazard processes in advance and for the prevention of hazards turning into the risks and for the reduction of the damage, required precautions should take place in an interdiscplinary work. In this context, the main study is to conduct geologic and geotechnic analyses that will orient the suitability for settlement and land use decisions. The success of the damage reduction work after earthquake is proportional to the scientific base and the accuracy of the decisions.
Geological data that enable the earthquake damage reduction and are analyzed in every plan step seperately should be evaluated in coordination with the criteria of planning and design. The risks resulting from urban texture, building quality, settlement layout and macroform should also be integrated with the analyses and synthesis.

2. Geological and geotechnical parameters in urban planning

Geological and geotechnical investigations that include the details compatible to the planning scale before the planning and design of a city have an indispensible significance in the evaluation of suitability for settlement and land use decisions. The main stage of creating sustainable, durable and safe cities is to carry out natural structure analysis and synthesis by comprehensive investigations (geological, hydrological, engineering geology, geotechnic, seismicity, natural resource analysis etc.) and contemporary scientific methods (GIS, Multi Criteria Decision Analysis, Multi Criteria Decision Support Systems etc.).

Geological investigations are the studies that aim to understand the statigraphic relation of rock and soils and tectonism of the settlement area. Besides, these field data provided by the investigations on the rock and soil of the urban area are to orient the upper scale plans (national and regional scale) and provide a base for detailed geotechnical studies.

Geological studies are the qualitative investigations that mostly cover scientific interpretation, definition and classification. These studies comprise of the tendencies and settlement of upper scale geological structure elements as tectonostratigraphic relations of formations, fault, folding, incompatibility and detailed scale geological structures as layer and of the investigation and the mapping of active fault lines. Geology maps, generally, are prepared in between the scales of 1/100000 and 1/25000 and in planning they serve as a base and guide for the regional and environment plans.

Hydrogeological t models in 1/25000 scale, too, are among the important inputs and natural threshold values of natural structure analyses before the planning. These hydrogeological studies orienting the sustainable planning in the synthesis conducted before the settlement can be listed as the location of aquifer constituting the groundwater, ground water level, direction of motion and its seasonal change, the determination of geological structures (anticlinal, synclinal, fault etc) that direct the ground water and its association with urban structures, surface waters in the areas desired to be opened to the settlement or in current settlements, the feeding and the discharge areas of ground water, natural drainage network detection and its mapping. These geological data, at the city and the basin scale, provide basis for the environment plans which are the planning stages of the settlement decisions. In environment plans, policies regarding spatial distribution of the population, decisions regarding the distribution of infrastructure and settlement units and policies for the reduction of earthquake hazards are developed.

Investigations that reveal the engineering properties of geological units in urban settlement areas are within the context of engineering geology studies. These include experimental studies in the field and laboratory medium rather than observational ones. These studies conducted in rock material and rock mass scale cover the determination of discontinuity properties of the rock masses (its location, number, spacings, discontinuity, infill situation, roughness, etc.) mass weathering degree and mass strength by experimental and emprical methods.

Engineering geology maps provide more detailed information about the soil that the city will rest on with quantitative data and it is an important guide to support the true decision mechanism in both habitability and land use. Generally, prepared in 1/5000 scale, these maps are fundamental basis for the master plans of the planing stage (similarly with 1/5000 scale and on which the macroform of the city is developed) where the decisions on usage such as densities, transportation systems, open green area arrangement, infrastructure, dwelling, commerce are made. When the geological unit in the ground in the urban and new settlement areas has the soil nature, index properties of the ground (grain size distribution, porosity, Atterberg limits etc) and engineering properties (cohesion, internal friction angle, natural unit volume network etc) are determined by in situ (investigation excavations and boring investigation) and laboratory experiments and calculation methods.

Besides, in the urban settlement area, unstable regions and areas that has geohazard (landslide (Figure 1), rock fall-overturn, flood (Figure 2), seismicity, liquifaction, settling-consolidation, carstic cavitations (Figure 3) etc) are analized and their effects on urbanization are investigated.

Fig. 1. An example of landslide in Daly City, California from USGS (US Geological Survey) website. Photographer is unknown.

Fig. 2. An example of flooding in Borçka Town, Artvin, TURKEY. It is taken from http://www.t24.com.tr/haberdetay/54382.aspx. Photographer is unknown.

Fig. 3. An example of karstic space in Yucatan, Meksico. It is taken from http://www.hackturk.net/komplo-teorisi/287458/cukurlarla-ilgili-komplo-teorileri.html . Photographer is unknown.

In the cases where geological, hydrogeological and engineering geology studies are insufficient, more subscale maps (1/1000) are used. These studies covering geotechnical investigations, albeit not sufficient for urban design, provide valuable data as the plans showing the cadastre of urban equipment for master plan decisions, city blocks and layout, roads, slopes, bridges, squares, traditional textures. The data for the urban design in building scale are provided by more detailed geotechnical survey on the basis of parcel. On the basis of the parcel, geological-geotechnical investigations, depending on the geologic threshold and the extent of the hazard, can be worked on 1/2000, 1/1000 or 1/500 scale maps as well as on 1/250 scale depending on the extent of georisk within the context of building plot.

3. Earthquake as a planning threshold

The turning point of the transition of the mankind from the rural life to the urban life is the industrial revolution in 19th century. Migration started after this revolution from the villages to the cities has brought several settlement problems along with it. The studies aimed to resolve these problems resulted in the emergence of the urban planning methods and their development. In paralel with the increasing city population, the need for new land for settlement started to increase. This demand of land increased the urban risks by urging to use of the lands unsuitable for settlement and in physical planning the site selection

necessitated multiparametered tough decision process. Thus, this caused the development of scientific methods for spatial based analyses statistically and mathematically.

Geological data within the planning discipline, before the planning, are evaluated in investigation, analysis and synthesis stages. These data with suitability to settlement analysis determine the development potential of the city by revealing the geologic threshold and restrictions.

Before the planning all geoenvironmental limiters, geohazards, geological-geotechnical data are evaluated as geologic thresholds. These natural geoenvironmental restrictions, besides the areas of natural hazard (earthquake, landslide, flood etc.), can be classified as cultivated areas and forest lands, water resources, reservations, geological sites etc. These natural thresholds are assessed with manmade thresholds as historical and archeological sites, mania plans, military zones and the habitability analysis are made including urban parameters.

Urban settlements have the tendency to develop with a varying pace depending on the policy of the urban development, economy, geographical features and geologic hazards. On the growth of the urban areas, there exist several natural structure thresholds as topography, soil condition, accessibility. Coping with these thresholds necessitates the analyses and syntheses that are developed by contemporary scientific methods. The selection of the methods of threshold analysis or habitability analysis is based on the number of criteria in the analysis, their quality, self values of the city and made by planners and project group (geological engineer, civil engineer, architect etc). In literature (Dai F. C.,et al.,. (2001), Darvishsefan A. A. et al.. (2004), Jabr, W.M. and El-Awar, F.A. (2004), Kolat Ç., et al.. 2006, Marinoni O. (2004), Marinoni O. (2005), Saaty T. L. (2008)) there developed several mathematical and statistical methods analyzing based on the space to be used in settlement analysis and land use decisions. These methods (Threshold analysis technique, Spatial analysis via GIS, MCDA, MCDSS etc) beyond the sole natural structure analysis, provide the possibility of testing the habitability by correlating physical planning with economical, sociological and technological factors and by considering the current macroform of the city.

Although the thresholds caused by restricting geological environment, depending on the extent of geohazard, sometimes can be overcome by technical precautions, the cost of technique can deadlock the habitability economically. Therefore, threshold analyses should realize the cost analyses of the alternatives besides providing the avoidance of urban risks and be a guide in creating the sustainable and durable cities with minumum cost.

Therefore, the thresholds playing a role in the planning and development of a urban area can be divided into two groups as geoenvironmental thresholds and structural thresholds caused by the macroform of the city and structural features.The first group can be listed as topography, geological structure, hydrogeology, geosites and geoparks, ecology, climate, vegetation, geological properties of urban soil and excavatability, seismicity etc. On the other hand, the second group is the current land use of the city and its infrastructure system.

These geoenvironmental thresholds affect the development and the settlement of the city in different ways. In some cases, these factors can be both advantage and disadvantage for the urban development. Although the hardness and the durability of the rocks in the settlement ground bring extra cost in excavatability, especially for creating earthquake resistant cities and soundness it is a necessary condition. Loose and swampy soils have features that can harm the structure in terms of load carrying capacity, settlement and

consolidation problems. Land use decisions as the selection of multi-storey building, medium storey building, low rise building, open green areas and industrial use areas, when considered with ground properties, one area that is not suitable for one use do not necessarily have the risk for some other use. For instance, a swampy area that is not suitable for the construction of multistorey building can satisfy the requirement for open green area arrangement.

As for topographic threshold, with the increase of slope habitability and the cost increases. Rough topography urges the urban design, construction layout, building type and structuring requirements. While 15% of slope in settlement increases the cost, the slope over 30% results in serious technical infrastructure problems. On the other hand, the slope under 5% creates drainage problems.

In an urban area with earthquake hazard risk, earthquake analysis should have the priority and the directive role. The detail and the qualification of the analysis and synthesis before planning exhibit variability from upper scale studies to subscales ones. In urban settlements and development areas, the distance to the fault, the features of the ground, topographic factors, liquifaction requirements, landslides and floods as secondary threats, the ratio of fullness and emptiness, the selection of open green area should be analyzed. Structural order, structuring requirements should be arranged in a way that the effects of probable earthquake are prevented. In order not to have resonance, the interaction of soil and structure and the vibrational periods should be evaluated well. The selection of technology and material that control the building quality should be determined considering the soil condition and seismicity.

In urban design and settlement, prevailing wind direction and insolation are very important. In settlement pattern there should have air corridors to reach all buildings and buildings should be designed in a way that does not interrupt others's light. As for the site selection for the industry, similarly, prevailing wind direction is very important in the sense that spreading malodor to the city and air pollution. Besides, in rainy regions, the risk of flooding should be taken into account and flood risk analysis should be conducted. At the regions under risk, appropriate precautions (correcting the stream beds, leaving the stream beds for open space arrangements rather than opening those to the settlement) should be taken. Moreover, climate properties also affect the foundation type and depth regarding the settlement.

Ecological values are destroyed with the effects of urban development and the natural balance is degenerated. Therefore, in any kind of habitability analysis natural balance should be taken into consideration and the living habitats should be protected.

Urban development areas should be in relation with the current land use. The current transportation and infrastructure system, social equipment, commerce and important centers of the cities should be associated with new subcenter and settlement units. A settlement pattern disconnected from the current city will have difficulty in supplying the needs and developing.

Geoenvironmental and urban thresholds, after evaluated one by one and their priorities and the weights calculated by statistical methods (MCDA, MCDSS, GisVBA, AHP, Grey relation analyses etc.), are superposed with the maps showing natural and human activity thresholds and in final synthesis map the remaining areas out of the thresholds are defined as the urban development directions. Afterwards, the decisions on urban use areas (residential, commercial or industrial) are given in line with threshold analysis and cost analysis.

4. Urban earthquake risk

In the settlements with earthquake risk, for the determination of urban risks geological data analysis is not sufficient alone. Building stock and quality in the urban area and the authentic nature of urban texture are also important factors in the evaluation of the earthquake effects. Therefore, while the urban risk analyses are conducted, all the parameters based on the current settlement quality and features, concentration, equipments, infrastructure and transportation networks should be included in the analyses.

Hazard mitigation studies before an earthquake is the most significant stage of disaster preparation process. In this process, the determination of the primary risks and the corresponding precautions for these risks decrease the life and monetory losses during an earthquake. The first step of the determination of the risks at urban areas is to understand the soil behavior that the city rests on by investigations. Besides, the identification of the building quality of the building stock and the revealing of the soil-structure interaction define the type and the approach of the precautions. New settlements are to be realized under the light of the geological data of the city. The inputs of geological data into the planning and design scale play an effective role in the reduction of urban risks. However, these data should be simple enough for planners and designers so that they are understood and implemented. The accurate use and the synthesis of those data banks are of prime importance in understanding the behavior of earthquakes on urban elements. These data providing inputs for architecture, planning and design shape the city. It is an indispensible necessity that in the creation process of earthquake resistant sustainable cities, geology, planning, architecture and design disciplines work together in a way developing a common terminology.

The risk level of the city changes with the population density, building quality, local ground conditions and distance to fault line. The city is subjected to one single earthquake magnitude and threat, however, settlement units that constitutes the city are faced to different levels of urban risks. The resistance of the settlements that have high quality and earthquake resistant buildings resting on hard soil to the same magnitude earthquake, certainly, will be higher than that of ordinarily constructed areas on problematic and loose soil conditions (Figure 4) due to their geotechnical properties. Therefore, the former will have less urban risks. In other words, in urban areas buildings are constructed with different materials in different structural systems and they can be newly constructed or already completed the economic life. Therefore, at the instant of the earthquake the reaction of the building and the extent of the damage will be controlled by the structural features and the geotechnical characteristics of the ground.

In earthquake prone areas, the effect of earthquake waves on the ground, how this effect is reflected to the building and the reaction of the building to this effect should be clarified in an accurate way by interdisciplinary work. These valuable data obtained by experimental analysis, synthesis and calculations help to the determination of the precautions against urban risks. These precautions can be as strengthening of the buildings or evacuation of weak buildings or abandoning of the settlement area before the earthquake during the stage of hazard mitigation as well as the providing of the transportation of the aids in emergency and constructions after earthquakes through a short and alternative routes and the determination of the regions of emergency action.

Fig. 4. An example of loose soil in Adapazarı after 1999 Marmara earthquake. It is taken from http://avnidincer.8m.com/depfoto.html. Photographer is Eşref Yalçınkaya.

Therefore, urban earthquake risks, essentially, result from the geological, geotechnical characteristics of the ground, tectonism of the region and the relation of settlement area with active faults, soil-structure interaction and topography of the city. These risks, in the soil, can be observed as faulting (Figure 5), settling-consolidation, slipping, liquefaction, land slide, rock fall (Figure 6) etc. The most important risks due to soil-structure interaction are that resonance causing the collapse (prevailing natural period of the building being equal to that of the soil) and soil amplification. The velocity of the earthquakes waves in the soil changes with the hardness and the properties of the soil. For instance, the waves passing through a hard rock mass pass very quickly and the quake is less felt due to the firmness and the voidless nature of the rock while those passing through loose and weak ground pass very slowly filling the voids in the ground and result in the severe feeling of the quake. This behavior of the soil is defined as soil amplification. Therefore, soil amplification factor of alluvial material, which is higher than that of the rock, causes the strong quaking on the alluvial settlement areas with high rate of damage while that of granite will empower the settlement above it.

Fig. 5. An example of faulting on North Anotolian Fault Zone in Turkey. It is taken from USGS (US Geological Survey) website. Photographer is unknown.

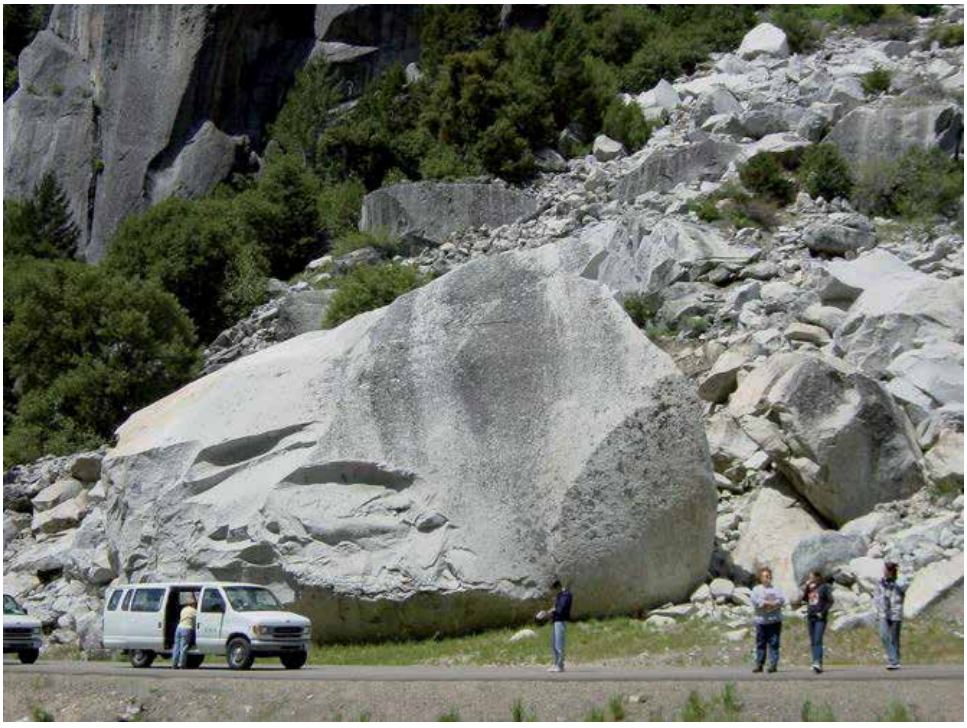

Fig. 6. An example of rockfall. It is taken from USGS (US Geological Survey) website. Photographer is unknown.

The closeness to the fault in settlements is not a sole requirement, although it is very important, in the development of urban risks. Certainly, the constructions on the active fault line will feel the quaking more than others. However, the earthquake experiences in the world and in Turkey showed that strong building resting on hard soil could stand

Fig. 7a. An example of landslide. It was devoloped in valley plains. It is taken from http://www.harikasozler.net/img3851.htm. Photographer is unknown.

Fig. 7b. An example of landslide in Laguna Beach, Bluebird Canyon, California .
It was devoloped in steep and high slope. It is taken from USGS website (US Geological Survey). Photographer is Jim Budak.

regardless of its being on the fault line while the buildings on filled soil far from the fault line collapse. For that reason, in the spatial plans made in earthquake regions with hard topography, it should be avoided to settle on the valley plains (Figure 7a) and high slope (Figure 7b) areas that are prone to landslides.

The liquefaction is a geologic hazard that occurs in the grounds that are cohesionless and have underground water and if it occurred in the settlement area, it is an urban risk (Figure 8a, b). On the soil that the building rest on, soil-water mixture moving with liquefaction creates deep enormous voids under the buildings (Figure 8a). That results in the subsidence or the overturning of the building. Especially, the buildings constructed very closed to the sea on the sand soil when they are under seismic excitation have the serious risk of urban collapse and subsidence risk (Figure 8b).

As seen, in the site selection, land use, urban planning and design, geological data are the main actors of decision process.

During an earthquake, besides the geologic hazards, planning and design errors as wrong site selection, wrong land use decisions, urban uses off the objective, error regarding the design, insufficiency of infrastructure, low building quality give rise to the serious urban risks. For that reason while taking the precautions for the mitigation of the hazard before earthquake not only risks from the geologic thresholds but also analysis, synthesis and evaluations regarding all spatial criteria as macroform of the city, design, urban equipment, concentrations etc should be done and urban risks should be reflected on plan decisions.

Fig. 8a. An example of liquefaction in TURKEY after 1999 Marmara Earthquake. It is taken from http://www.el-aziz.net/img4381.htm. Photographer is unknown.

Fig. 8b. An example of liquefaction in TURKEY after 1999 Marmara Earthquake. It is taken from http://www.kenthaber.com/marmara/kocaeli/Haber/Genel/Normal/depremde-yikilan-konuta-imza-atti/3d13f1c8-4158-4ce1-b380-13e53de1be21. Photographer is unknown.

5. Earthquake sensitive planning

Tam (2010) defined the earthquake sensitive planning as an integrated planning which aims to mitigate the earthquake risk factor by considering the physical properties and socioeconomic structure of the settlements and which starts from upper scales and develops socioeconomical development policies and supra-national, national and regional plans to further continue to local planning and subscales in which the progressive synergy is assured. (Reference: Deniz Tam)

Earthquake sensitive planning is a planning action that primarily analyzes the earthquake hazard and risks in the planning, prevents these risks and hazards to turn into disasters, internalizes the planning to mitigate earthquake hazards and urban design approaches. The main approach of earthquake sensitive planning is to include the risk mitigation precautions of all disciplines related to earthquake in the planning process for the realization of urban planning that provides healthy, reliable, livable urban environment development.

Earthquake sensitive planning includes the evaluation of geologic hazards and restrictions as risk factors in planning process and their reflection in planning decisions. Within this context, in planning the use of geological data should be assured and regarding the earthquake sensitive planning for hazard mitigation and prevention policies and approaches should be developed.

The process of building earthquake resistant cities comprises the analysis of geoenvironmental natural hazards that can be occurred during an earthquake or after it, the evaluation of the damage assessment and the revealing the corresponding urban mistakes and the conduction of urban risk analyses. Besides, earthquake sensitive planning approach should be developed to eliminate the risk factors due to land use, site selection, settlement pattern and the structuring.

Earthquake sensitive planning is a dynamic action that zooms out urban planning from the spatial design based traditional planning approach, integrates the risk mitigation precautions in the planning process and incorporates the detailed microzoning maps that go beyond the standard geological investigations.

Earthquake sensitive planning involves an analysis perspective starting from the world scale to national, regional, urban and local scale which covers the small settlement units. This perspective bases on the physical, economical and social development and urban risk analysis under the earthquake scenarios.

In every stage of this planning approach, geoenvironmental hazard and risk factor should be determined by geological-geotechnical investigation and microzoning maps and with this geological data analysis there should made feedbacks in every planning stage.

For the reduction of urban risks and hazard, potential development areas with alternatives developed for physical plans by the directive of the geological data should be selected by using the multi decision analysis techniques as well as with the inclusion of socioeconomic analyses.

In earthquake sensitive planning, the interpretations on the analysis of geoenvironmental thresholds and their implementation on the plan are discussed above in the section "Earthquake as planning threshold". In the case where the macroform of the city, layout and socioeconomic development are taken into account, the required action that should be considered in earthquake sensitive approach can be listed as follows:

1. Engineering structures like highway, railway, viaduct, tunnel and construction layout should not intersect the fault line perpendicularly. In the cases where the development

close to the fault is obligatory, urbanization and settlement should be ensured to be in parallel with the fault line (Figure 9).

2. Multicentered development pattern should be adopted and the urban growth should be limited depending on the risk.
3. Population and densities should be arranged in a way to mitigate the risks after earthquake and a balanced distribution should be supported while preventing the increase of the concentrations in one region.
4. The factors that inhibit the socioeconomic development and growth should be resolved and the weight should be given to the process of creating economically powerful and earthquake resistant city.
5. The continuity of the green areas should be provided and in the macroform of the city safe open and empty areas should take their places in settlement units as gathering areas.
6. The transportation network should be built up and for the roads closed after earthquakes, alternative transportation systems should be developed. Within these transportation systems, the shortest route to the areas where the urban risk level is high should be defined to provide means for immediate aid by the analysis of shorthes path via GIS.
7. Technical infrastructure systems should be made resistant to the expected earthquake magnitude by strengthening. Especially, the systems having a vital importance as natural gas pipelines, energy and water lines should be improved against earthquake effects and protective measures should be taken.

Fig. 9. An example of rail way which build on fault zone and is cutted by this zone in Turkey after 1999 Marmara Earthquake. It is taken from http://www.resimkarikatur.com/resim1684.html. Photographer is unknown.

In earthquake sensitive planning, building layout should not be attached. In the cases where it is needed to be attached, story heights should be equal to each other. Different story heights mean different vibration periods. Thus, it may lead to impacts and collapses (Figure 10).
Especially in the developing countries, commerce, urban uses such as residence and social equipments can change their functions in line with the newly emerged needs. This results in the change in the projects of interior design and structural disorder and as a result the building becomes under the risk due to the change in its bearing capacity.
The areas with high geohazard in urban settlements in earthquake prone regions should be left for open green area use.Urban functions should be green buffer zones. These green areas relieve the dense traffic in panic state and easen the intervention as well as being gathering areas after earthquakes.

Fig. 10. An example of collapsed structure because of building design and different construction height after 1999 Marmara Earthquake. It is taken from http://www.haberingundemi.com/haber/Depremin-Simgesi-Bina-Yikildi/80399. Photographer is unknown.

6. Urban settlement site selection and microzoning

Microzoning is defined in a variety of ways by different researchers in the literature (Hays (1980), Sharma ve Kovacs (1980), Nigg (1982), Özçep and et.al, Sherif (1982), Finn (1991)). However, the common point of view of all researchers is that microzoning is to be analyzed in the preparation stage before earthquake to realize the reduction after earthquake while the habitability is to be analyzed especially in the high risk regions by dividing into the smallest subregions. Microzoning maps, depending upon the local geological, seismological and geotechnical conditions, is the mapping of the geohazards of the areas where potential of liquefaction, landslide sensitivity, flood risk, soil amplification etc or combinations of those hazards are seen, as a basis of the planning, the development and the design.
Geological studies and the synthesis of the data used in the planning exhibit a rapid development in terms of directing the planning. Within the framework of this development, geological-geotechnical studies, assessment of the suitability for settlement and microzoning

maps provide highly important data to determine the land use and settlement for the planning.
Microzoning maps can be prepared as a base for the 1/100000 scaled regional plans. At the same time it reveals the development direction and the potential of the city by identifying geohazard thresholds for 1/25000 environment layout plans, 1/5000 master plans and 1/1000 tentative plans.
Earthquake resistant building designs advance significantly to decrease the risk of collapse and make the building safe under earthquake loding. However, these designs accompanied by expensive methods and techniques become insufficient in the implementation due to economical reasons especially for the developing countries. Therefore, microzoning maps gains more importance since the selection of a settlement area far from the geohazards will decrease the need for the precautions with high technology.
Microzoning maps direct the plans with an integrated risk approach by evaluating geologic hazards and advantages that are provided by geological-geotechnical investigations with the risks resulted from the constructions.

7. Results

In the planning and the design of new settlement areas and the environment with current settlement, in every stage of the plan geological data with out-of-traditional planning understanding for the reduction of urban earthquake risks should be functionalized in compliance with the objectives.
In the process of creating earthquake resistant safe cities, geological-geotechnical investigations and microzoning maps being an understandable synthesis of geotechnical data play a key role in the integration of hazard mitigation precautions to the planning. However, this geohazard based maps should be developed in complience with the requirements of planning scale and its context. At this point, there seen the necessity of the collaboration of the experts of both geological and planning disciplines.
The planning made in the regions with high earthquake risk should be supported by identifying with the probable earthquake scenarios. In earthquake sensitive planning, the formation of gradual centers system with one main center, the identification of the intensities in correlation with settlement potential, the development of multicentered urban form by preventing urban sprawl are essential.
In the urban areas with high earthquake risk, the improvement of the current plans, the reconfiguration in the required locations and the planning of development areas based on the microzoning maps and probable earthquake scenarios would decrease the probable earthquake damages. In earthquake sensitive planning, the integration of geotechnical parameters of the soil as soil amplification, liquefaction and landslide after evaluation to the planning is of vital importance since these parameters during an earthquake can cause secondary urban risks.
The main factors effective in the distribution of earthquake damage can be summarized as the distance of the settlement to the active fault line, geological structure, local soil conditions, the state of ground water, site selection and land use, population density and distribution, building density, quality, order and design.
As it is seen, the basis of creating a safe and sustainable living space in the urban settlement areas with high seismic risk is the evaluation of urban planning and design, geological synthesis and earthquake analysis in coordination with modern scientific methods and techniques.

8. References

Dai F. C., Lee C. F., Zhang X. H. (2001) GIS based geo-environmental evaluation for urban land-use planning: a case study, Engineering Geology, 61, 257-271.

Darvishsefan A. A., Setoodeh A., Makhdom M. (2004) Environmental consideration in railway route selection with GIS (Case study: Rasht-Anzali railway in İran), Map Asia 2004, Beijing, China.

Jabr, W.M., El-Awar, F.A. (2004) GIS and analytic hierarchy process (AHP) for siting water harvesting. ESRI Proceedings; Available from: <http://gis.esri.com/library/userconf/proc04/docs/pap1539.pdf>.

Kolat Ç., Doyuran V., Ayday C., Süzen M.L., 2006, Preparation of a Geotechnical Mikrozonation Model Using Geographical İnformation Systems Based on Multicriteria Decision Analysis, Engineering Geology 87, 241-255.

Marinoni O. (2004) Implementation of the analytical hierarchy process with VBA in ArcGIS, Computers&Geosciences, 30, 637-646.

Marinoni O. (2005), Adiscussion on the Computational Limitations of Outranking Methods for Land-Use Suitability Assesment, International Journal of Geographical Information Science, 20, 1, 69-87.

Saaty, T.L. (1990) How to make a decision: The Analytic Hierarchy Process. European Journal of Operational

Zhang F., Yang Q., Jia X., Liu J., Wang B. (2006) Land-use optimization by geological hazard assessment in Nanjing City, China, IAEG 2006, paper number 324, Natthingam.

Saaty T. L. (2008) Decision making with the analytic hierarchy process, Int. J. Services Sciences, 1, 1.

Hays, W.W., 1980. Procedures for estimating ground motions, U.S.G.S Professional Paper, 1114, 77 p.

Sharma, S. and Kovacs, W.D., 1980, Microzonation of memphis, tennessee area, A report on research sponsored by The USGS, No: 14.08.0001-17752.

Nıgg, J., 1982. Microzonation and public preparedness: a viable approach, Proceedings of the 3thInternational Earthquake Microzonation Conference, Seattle.

Sherif, M.A., 1982, Introductory Statement of 3 th International Earthquake Microzonation Proceedindgs, June 28-July1, Seattle, USA.

Fınn, W.D.L, 1991. Geotechnical Engineering Aspect of Microzonation, Proc. Fourth Intern.l. Conf. On Seismic Zonation, Vol.1, pp. 199-259.

Tam D., 2004, Çevre Duyarli Planlamanin Ve Deprem Duyarli Planlamanin Bütünleştirilmesinin Sağlayacağı Faydalar, Journal Of The Chamber Of City Planners Union Of Chambers Of Turkish Engineers And Architects, Sayı: 29 Planlama, ISSN 1300-7319.

USGS (US Geological Survey) website.

http://www.t24.com.tr/haberdetay/54382.aspx.

http://www.hackturk.net/komplo-teorisi/287458/cukurlarla-ilgili-komplo-teorileri.html .

http://avnidincer.8m.com/depfoto.html.

http://www.harikasozler.net/img3851.htm.

http://www.el-aziz.net/img4381.htm.

http://www.kenthaber.com/marmara/kocaeli/Haber/Genel/Normal/depremde-yikilan-konuta-imza-atti/3d13f1c8-4158-4ce1-b380-13e53de1be21.
http://www.resimkarikatur.com/resim1684.html.
http://www.haberingundemi.com/haber/Depremin-Simgesi-Bina-Yikildi/80399.

20

Simulating Collective Behavior in Natural Disaster Situations: A Multi-Agent Approach

Robson dos Santos França[1], Maria das Graças B. Marietto[1],
Margarethe Born Steinberger[1] and Nizam Omar[2]
[1]*Universidade Federal do ABC*
[2]*Universidade Presbiteriana Mackenzie*
Brazil

1. Introduction

The usage of simulations has been improved for quite some time. From mechanical artifacts that attempt to mimic a certain dynamic event using known physical properties up to complete representations of virtual worlds based on real life events which were augmented by concepts in order to prove a theory or to test a specific scenario. The key words here are "modeling", "constructing a simulacrum", "experimentation" and "evaluation". Simulations allow any researcher to explore, try out new ideas, check some theories in a controlled environment before testing in real life, and so forth. Psychology deals with individuals, Sociology with the study of human groups and the formation of institutions, both, individually, were not enough to study the humanŠs social behavior. All human sciences tried to create theories about reality, searching for well-defined and established patterns. The non-conformity with such patterns is considered a mistake, or even a wrongdoing. Taking a whole new approach, the field of Collective Behavior deals with human groups and collectivities that contradict or reinterpret societyŠs norms and standards. Crowd behavior has been studied by many researchers. Theoretical models have been established to understand them. This chapter will present a simulation model for panic in crowds phenomena based on the symbolic interactionism approach. Section 2 will present a review of the main concepts of Sociology and Collective behavior and establish a framework to be used in the model of crowd to be simulated. Section 3 will present a computation model and a simulation model of panic in crowd phenomenon, both in its theoretical aspects and its practical issues. The collective behavior studied in the previous section will be used as basis for the simulation model. Also, the main concepts regarding multi-agent based simulations will be presented. The model simulated have been applied to a fire incident and validated. Section 4 presents a generalization of the model proposed and delineates a future application for other kind of disasters as earthquakes. Section 5 shows some conclusions about the study here presented.

2. Sociology and collective behavior

Sociology deals with the study of human groups and the formation of institutions (dos Santos França, 2010; Merton, 1968). Its origin came from Comte, Spencer and other 19^{th} century researchers' need for a distinct perspective of the human behavior that derived from the individualistic studies that had been performed previously. For instance, Comte stood out that the human mind could only develop in a social environment. Thus, following this premise, Psychology was not enough to study the human' social behavior (Turner & Killian, 1957).

At first, Sociology was focused on culturally-oriented groups or social groups which behavior follows established rules. Because of such interpretation, some spontaneous and unorthodox social actions were perceived as abnormal and unstable or as exceptions that did not draw further attention. Sociology, as a science, attempted to "frame" reality into well-defined and established patterns. If a certain social action could not fit into any of such patterns, the action was considered a mistake or even a wrongdoing until society accepts the new behavior and embraces it. Such acceptance could take decades or never happen.

Taking a whole new approach, the field of Collective Behavior deals with human groups and collectivities that contradict or reinterpret society's norms and standards. These collectivities' behavior is not entirely detached from the socially accepted behavior discussed earlier. However, collective behavior deals with social groups that deny or reinterpret society norms and standards. Ralph Turner and Lewis Killian at (Turner & Killian, 1957) defined collective behavior as "*the set of social behaviors which the usual conventions stop driving the actions and the individuals transcend, exceed or collectively subvert the standards and the institutionalized structures*" (dos Santos França et al., 2009). This definition implies that the individuals engaged in a collective behavior are no longer bound to the rules and norms of society and they are free to act the way they intended even if such behavior is not socially accepted. At first, their actions are related to the institutionalized and established actions found in Society. But, as soon their need for socially unaccepted actions is reached, they start to bend and to overrule the norms that were built by society, creating their own.

This sort of human group might happen due to many reasons, including by hazardous events, whether they are natural or human-induced. Also, their structure and formation follow a pattern that was mapped by some researchers. Finally, such mapped patterns could be used to understand disasters by a distinct perspective: how people react in a hazardous event and how this could be simulated in order to decrease material and human losses. The simulation model presented in Section 3 deeply applies the information described in this section.

2.1 Crowd simulation: Theoretical elements

The understanding of the panic in crowds' phenomenon relies on the study of the collective behavior phenomenon. Thus, a historical overview is presented in the following sections, along with modern studies about panic and disasters, especially how people behave under such conditions. The following subsections show a historical overview of some studies of the collective behavior field and the theories that will be employed in Section 3 to build the simulation model.

2.1.1 Historical abstract

The collective behavior was studied in distinct ways through the ages. Initially researchers such as Tarde and Durkheim developed social theories in order to justify the actions performed by offenders or as a mean of explaining how an isolated individual could have a socially accepted behavior and the very same individual could be able to participate in criminal acts when he is in a collectivity.

Emile Durkheim claimed that the group was important to understand the individual's behavior. Culture would be formed by the combination of personal minds instead of a chain of imitations from one subject by the other members of the group. This was one of the early conceptions of the group mind, a supra-personal entity which has an autonomous existence from the composing members of the group (Durkheim, 1895). In other words, the individuals engaged in a collective behavior unconsciously help to form the group mind that guides their actions.

Following an opposite direction, Gabriel Tarde considered that the social behaviors happen due to man's natural inclination to mimic others. For Tarde, the interactions among individuals worked only to spread the mimic's individual results and the interactions were not responsible by their formation. According to Tarde's approach, collective behavior describes the person's socially anomalous behavior into a group and collective context and in situations not induced by criminal activities, such as the tulip mania (Mackay & Baruch, 1932) or the great social movements, such as the fall of the Bastille (Tarde, 1890; Turner & Killian, 1957).

2.1.2 Collective behavior development

After a criminal approach for the collective behavior, some researchers analyzed the collective behavior phenomenon in an individualized and superficial way, such as Sigmund Freud (Freud, 1955). However, some other researchers such as William McDougall and Gustave Le Bon developed the collective behavior studies further by creating an early classification of the phenomena, as well as a detailed profile of each member of the collectivity, but also taking into consideration that the collectivity itself has its own specific features. This second attempt to understand the collective behavior phenomenon followed a psychological standpoint (dos Santos França, 2010).

Le Bon is considered one of the founders of the collective behavior studies and he was one of the firsts to use the term crowd to describe the collectivities, developing the Crowd Psychology and treating the crowd as the prototype of all group behaviors. The focus of his studies was the social behavior by using the "the crowd mind" theory. For Le Bon, the main features of the crowds were:

- The decreasing of the conscious personality along with the prominence of the unconscious one;
- The ideas and feelings of the members of the crowd are guided by suggestion and contagion;
- The trend to put suggested ideas into action.

A rough classification of the crowds was also proposed by Le Bon. Such classification was based on how the crowd was conceived and its main actions, and it can be summarized as follows:

Active crowd Crowds that act together with a strong sense of coordination. Examples include mutinies, lynching mobs and rebellions;

Casual crowd A crowd formed with no specific goal and coordination, acting at the same time and place for a short period. For instance, a crowd watching a display window being decorated;

Conventional crowd When a group of people gather themselves for a specific goal, sharing feelings that drive the actions of the whole group, such as what happens in an audience for a soccer game or any other recreational activity;

Expressive crowd A group of people gathered to move, make gestures together but for individual achievements, such as the dancing crowds at carnaval and some religious groups;

Panic crowd A panic crowd is formed when people are exposed to a dangerous situation and that leads them to create the perception of need to stay away from danger in a social and shared way, such as earthquakes and fires (dos Santos França, 2010; dos Santos França et al., 2009).

The psychological approach for the collective behavior emphasizes the lost of personality, the liability being empowered by the collectivity and the fact that such collectivity is guided by some kind of collective mind (similar to Durkheim's). Le Bon's vision also had the collective (or mass) psychology and the phenomenon of contagion in a primitive form (Le Bon, 1896).

The mass psychology was important for the development of the collective behavior studies because it was the first attempt to establish, classify and broaden such studies. However, the followers of this particular approach still treated the members of the crowds as society outcasts due to gender, race or civilization level. That implies that the only the civilized western individuals were considered truly civilized. Women, children, the mentally impaired and the individuals that belonged to a race other than white were marginalized and the mass psychology theories were used to justify and amplify such condition, as tools to "domesticate" and to "civilize" such groups, so they could act under the control of a leader such as Napoleon or Alexander, the Great (dos Santos França, 2010).

2.1.3 Symbolic interactionism and emergent norm theory

The criminal and psychological approaches for collective behavior used the abnormal, the unusual, the uncommon to establish a line, a threshold between the socially accepted behavior and groups (studied by Sociology) and the socially unaccepted behavior and the human groups that engaged in such behavior. Some researchers at the University of Chicago developed a distinct way to see and understand the collective behavior.

Robert Park and Ernest Burgess wrote a whole chapter about collective behavior in their book *Introduction to the Science of Sociology*. In that chapter, the concept of social contagion was described as an element to spread a cultural matter, being compared to the fashion phenomenon and inducing people's feelings. Thanks to Park and Burgess' work (and similar works released almost at the same time) collective behavior was related to social phenomena

other than criminal activities and psychological issues. Also, the individual engaged in collective behavior could belong to any social group, according to certain social-cultural contexts (dos Santos França, 2010; Park, 1939).

Park also introduced the concept of "milling": a collective movement that represents fear or discomfort. The social unrest can amplify the fear which, in turn, leads the group to a tension state. Such unrest, even if it is merely mentioned, amplifies the fear. Thus, the milling and the social unrest make a vicious circle and their interaction becomes a circular reaction that increases the tension in the group and creates an expectation that mobilizes the group members for the collective act (Park, 1939).

Herbert Blumer was a student of Robert Park and carried on his research. George Herbert Mead was also Blumer's teacher and developed the social act, a noticeable external behavior.

With that theoretical basis, Blumer coined the Symbolic Interactionism, which society is built by the interaction among people that, when they are about to act, take into consideration the actions and features of the other individuals, a symbolic interaction driven by each individual meaning developed during the interaction process (Borgatta & Montgomery, 2000).

According to Blumer, Symbolic Interactionism is based on three premises:

1. The persons interact by the meaning of their world's objects (tangible, abstract or social), both individually and collectively;
2. The meaning of the objects is built from the interactions among individuals;
3. During the interaction, individuals use an interpretative process to change such meanings.

The Emergent Norm theory was proposed by Lewis Killian and Ralph Turner and it was presented in (Turner & Killian, 1957). Based on Blumer's Symbolic Interactionism, it also considered that the collective behavior was the outcome of the interactions among persons able to assess the received information which leads to an interactive cognition. This approach analyzes the agents' features that aided in the formation of the social systems in a micro level, as well as the behavioral patterns in a group level.

Therefore, the emergent norm approach deals with the formation of the collective behavior by the micro level interactions of the collectivity members and the advent of patterns and norms triggered by these interactions. Although there is no emphasis in the definition of the social systems (as seen in (Luhmann, 1996)), the interactions and the complex behaviors formed by them allow the collective behavior to be seen as a complex system because from its micro-level interactions - simple by nature - complex behavioral patterns emerge, and such patterns cannot be noticed by just analyzing each individual alone (dos Santos França, 2010).

2.1.4 Other approaches for collective behavior

Due to the need of creating a symbol and meaning system, Blumer' symbolic interactionism has some unclear basic points related to social interaction:

1. How individuals relate to each other in spite of their differences;
2. How the social relation comes from the orientation to the other in each attendant (Vanderstraeten, 2002).

These points were addressed by Talcott Parsons in his studies about social groups, which led to the Structuralism Approach for the collective behavior phenomenon.

The Structuralism Approach turns over the concept described in the previous section by highlighting the social structures' studies and their impact on the individuals. The focus lies on the social structures that triggered the phenomenon and the structures affected by the members of the collectivity, using the macro level elements to think about the micro level elements and behavior. Therefore, the social structure is analyzed as deep as possible. Any behavior that subverts the established social order is reviewed by observing how the social structure and the collectivity respond to that (dos Santos França, 2010).

Neil Smelser was a researcher at the Oxford University, and he was Talcott Parsons' student at the time. Enhancing Parsons' collective behavior studies (Parsons, 1937), Smelser pointed out that, although rumors, panic or lunatic conditions, commotion and revolution are unexpected and surprising, they happen regularly (Smelser, 1963). He also stated that as much institutionalized the behavior is, it will become less distinguishable in a social point of view. The purpose of collective behavior, according to Smelser, is the resettlement of the social order that was shook by a tension on the elements that make the social structure. The resettlement induces people to act in a collective and rational way. After that, social norms and institutions are crystallized due to the comeback of the social order or by the formation of a new one. This shows Smelser's top-down approach for the collective behavior phenomenon (Smelser, 1963).

2.1.5 Panic in crowds

Panic in crowds can be triggered by various factors, such as natural threats (floods, earthquakes, volcanic eruptions), threats induced by man (terrorist attacks, lost of the social control by State), among others. In a panic situation there is always an imminent risk and the urge to act by the individuals (dos Santos França et al., 2009).

Killian and Turner also studied the behavior of individuals during crisis. In (Turner & Killian, 1957) the micro interactions are the key elements for the changes in the society. The same would happen with culture that changes thanks to each person, even if that happens in an unusual and unconscious way. According to Killian and Turner, it is in the reaction of the individuals in critical and unstructured situations that the basis of the collective behavior can be found. Such personal responses should be accepted as a required background for the study of the development of new norms and social structures.

Three kinds of individual reactions were found by Killian and Turner. The first kind of reaction is Defense: people act in a limited fashion, unable to comprehend what happened and to deal with new situations, and some of them will be in shock, even with no physical damage. On the other hand, there will be others that become more suggestible and readily accept commands from somebody else (Turner & Killian, 1957).

The second kind of reaction that usually happens after the shock from a violent accident is an impulsive and apparently irrational action. The individual acts apart from the environment and the other individuals, with actions entirely out of his normal self, in some kind of "super focus". Even though that individual is aware of what happens in the environment, his actions are directed towards a specific spot inside the event, acting in a conscious way. It seems that

in such behavior there is an attention strain. Thus, the individual does not think about the consequences of his acts in the same degree of his actions in ordinary conditions (Turner & Killian, 1957).

The final kind of individual reaction found by Killian and Turner is the fear. A critical situation is known to pose as a threat to the individual's life or values. Thus, fear is the most common reaction in panic situations, even if such situation is not real.

Fear can be shown in many ways, from internal changes in the emotional and psychological state up to despair, whimper and foray, and it increases whenever the danger is unknown. Uncertainty leads to insecurity since the person does not have enough information to take the right decision in the new context. A person is less afraid of a dangerous situation than the lack of information of the present condition and its uncertainty (Turner & Killian, 1957).

Panic in Crowds phenomenon has been studied by many researchers, mostly to understand its inner workings and specially to prevent the dangerous events to start it or to alleviate its effects if it is unpredictable. Enrico Quarantelli is a researcher that provided some essays about disasters and panic in crowds' phenomena.

In (Quarantelli, 1975) Quarantelli identified a certain set of prejudgments related to how people observe the crowds' behavior in panic situations:

- People would behave "irrationally", out of control;
- Thanks to media and films, panic is associated with despair, paralysis (shock) and an instinctive behavior caused by the panic itself, forcing a subtle mind changing similar to the one found in "Strange Case of Dr. Jekyll and Mr. Hyde" by Robert Louis Stevenson.

These prejudgments are passed to the safety and damage control personnel, such as firefighters, police officers, public managers, among others. For example, the fear of inducing panic just by informing people about the hazardous event could be more dangerous than the life-threatening event itself. Even with relevant and crucial information for crowd control and to minimize material and human losses, the fear of generate more panic could block the right actions at the appropriate time, which in a panic situation could be disastrous. For Quarantelli, the mere mention of a dangerous situation does not trigger or amplify the crowd's panic state (Quarantelli, 1975).

In spite of what was proposed by the early researchers of collective behavior such as Gustave Le Bon, the human behavior during crisis is controlled instead of impulsive, it uses the right means to achieve its goals and it is organized and functional most of the time. However, that does not mean that an irrational behavior is avoided during the crisis; the incidence of such behavior is lower than what was intuitively observed.

Just like the other collective behavior and panic researchers, Quarantelli also provided the panic's main features, based on his studies and the analysis of other studies from Japan, France and England, and they are the following:

- A person in a panic in crowds' situation deals with fear instead of anxiety;
- The future is more important in such situations than the past;
- There is a trend to focus in a specific dangerous spot instead of a general threat;

- The members of the collectivity define the situation as dangerous and identify a direct threat for their survival (Quarantelli, 1975).

Quarantelli stressed that individuals keep their rationality and sociability during their escape from hazardous places: they avoid obstacles and other people as much as possible. The individual still can force his way over the others, but that will happen only in extreme conditions (Quarantelli, 1975).

This chapter will present a simulation model for panic in crowds phenomena based on the symbolic interactionism approach. The panic phenomenon works as follows.

Initially, people are in an **ordinary condition**. In that condition, social structures and norms are lined up to what is accepted by society. At the moment disarray in the established social structure is noticed, individuals start feeling uneasy and apprehensive, trying to understand the ambiguous situation that occurred. A disturb is an event that shows itself as an imminent threat to the individual's life, such as a fire alarm, a smoke cloud or objects falling from the shelves, and such event calls up the person and compels him to act, leading to a **social unrest**.

After that, the persons search information that could help them in redefining the present context. They become more likely to rumors because of the feeling of uncertain and insecurity. The conventional behavior starts to break down. The need to comprehend the situation increases, so they engage in a **milling** process, watching the other individuals' reactions and comparing those reactions with your own set of expectations. Also, a need for a sanctioned and socially-built meaning arises into a relatively non-structured situation (Turner & Killian, 1957). Milling is substantial since it makes the individual focused to the situation and the actions performed by the collectivity, removing the focus out of him. Due to the fact that the focus now lies on them, the individuals reply faster and directly to each other, setting up the environment for the shaping of a shared knowledge of what is happening. From that point, the collective enters the **collective excitement** stage, when the group blends and synthesizes the personal representations, helping in the formation of a collective representation/image of the situation. The individual's susceptibility is enhanced by this shared representation, which also decreases his capability of making distinct impressions from the collectivity.

Thus, the individual could follow a socially forbidden line of conduct that he could not conceive and perform, such as pushing and running over people. **Social contagion** starts as an intense form of collective excitement, it starts fomenting a fast propagation of the collectively formed representation, strengthens the social cohesion and prepares the crowd for a collective action. Finally, after a collective representation of the situation is built by the individuals, it is possible to pick an action and execute it. Up to this moment, the collective crisis started by a struggle for survival comes to an apex, and the **collective panic** is installed. Considering that the crowd members do not share conventional expectations about how they are supposed to behave, the outcomes are uncertain. Figure 1 shows an overview of these stages.

2.2 Multi-agent based simulation: Usage and features

A simulation is the representation of a contextualized system into another context. This description applies to any kind of simulation, not just computer simulations. The Apollo space mission had applied simulations to evaluate techniques and devices before the real

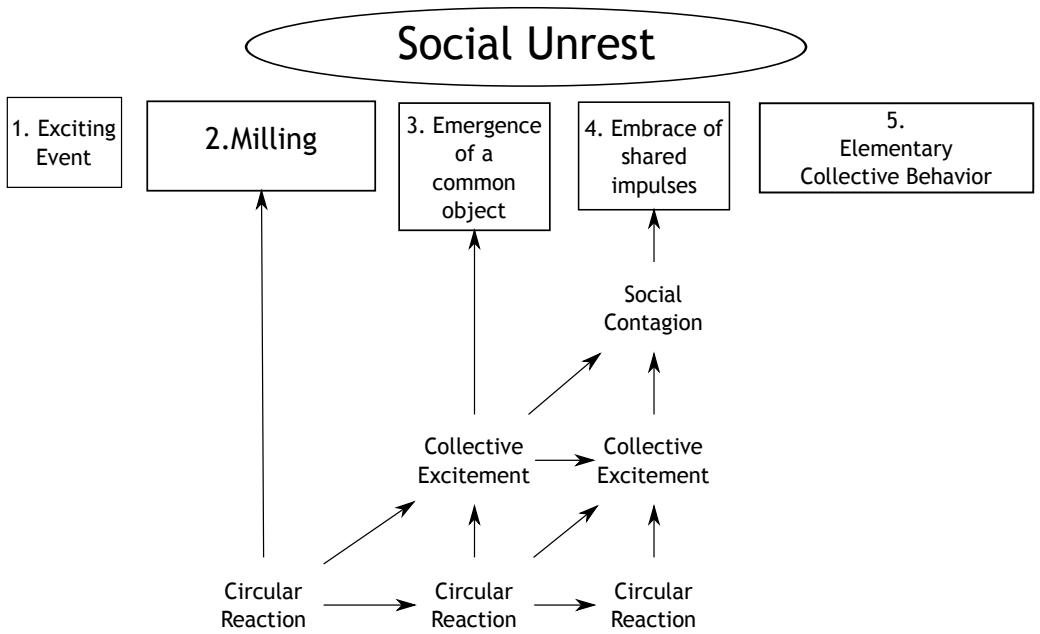

Fig. 1. Blumer's Collective Behavior Stages (McPhail, 1989).

mission was performed. Since the mission posed a great risk and there was no much room for on-the-fly modifications, everything must be tested and checked beforehand.

In Ruas et al. (2011) simulation (especially multi-agent based simulation) is regarded as a third way of doing science. While induction studies the whole by a sample, deduction does the opposite. Simulations get the best of induction and deduction at the same time: the general and macro-level of a process provides the framework, while the interactions among simulation elements show the micro-to-macro transition and the emergence of behavioral patterns, as in the induction process.

Throughout this section, the simulation process is described. The focus will be on the multi-agent based simulation, which will be applied in the model presented in the next section.

2.2.1 How a simulation is designed

The design of a simulation is the building of a model that will be able to mimic the operational and dynamic features of a real system. This model allows a deeper study of the system in a controlled and isolated context Zeigler et al. (2000). This usually poses as a requirement for some systems since the analysis and observation of certain phenomena and their activities can be impossible, impractical or hazardous.

There are two major approaches for computer simulations. The first approach uses differential equations and other mathematical formulas to build the simulation model. The simulation execution becomes the evaluation of such formulas and the iterative resolution of the

differential equations. Such approach is named analytic and it has its value and it is quite practical and useful for certain applications. However, it usually lacks a detailed vision of what happened, working as a "black box". For some simulations, this is not an issue because the only thing that matters is the final result and not the mid-steps required to achieve it. Also, this sort of simulation usually deals with a continuous stream of time. Since there is no need to observe the simulation's inner steps, a continuous approach is more logical.

On the other hand, a second approach for simulations uses a set of autonomous modules (programs) called agents. The resemblance of agent based technologies and a realistic social system model has created a new scientific field with a strong emphasis on the interdisciplinary called Multi-Agent Based Simulation (MABS) Cohen & Felson (1979). It is a collective effort to integrate scientific areas and the usage of computational technologies that were previously applied to other tasks, such as networking. The main purpose of MABS researchers is to create and study computational models for simulation taking the technical and theoretical infrastructure of the Distributed Artificial Intelligence into consideration.

Based on such approach, the simulation model represents a specific target system that allows (i)the observation and study of the global behavior of the modeled system under certain criteria and (ii) the analysis of the consequences of the changes in the system's internal components Gilbert & Terna (2000), which implies that MABS can be used to detect emergent patterns and how changes interfere on the agents' behavior. Ruas et al. (2011).

2.2.2 Agent and multi-agent based simulations

A specific definition of Agent describes it as a discreet entity with its own goals and behaviors, and also internal states and behavior rules that allow the interaction with the other agents and with the environment. Another definition can be found in Russell & Norvig (2004), and states that "*An agent is anything able to perceive the environment through sensors and to act upon the environment by actuators*". Once more, the emphasis lies on the agent, the environment and the relationship between them. Whatever entity that needs to be considered in the simulation by its autonomy, by its independence in the decision making and by its ability to interact in the environment can be seen as a simulation agent dos Santos França (2010).

Agents must have autonomous actions, and such actions must happen synchronously with an event-based time scheduler, that will serve as an observer and a time and step manager along with the agents.

The main concept behind a Multi-agent simulation model is to simulate an artificial world which is made of computational interactive entities. Simulation is then created by the transposition of entities (or sets of entities) and the interaction among such entities from the target system to the artificial world Dimitrov & Eriksen (2006).

The multi-agent based simulations have an adequate infrastructure for modeling, studying and understanding the process related to complex social interactions such as coordination, collaboration, group formation, conflict solving, among others. Thanks to the relationship between local and global behaviors and the analysis of the agents' influence over themselves and the environment, it is possible to analyze the social interactions, which leads to cause-effect relations of how agents' components affect their behavior, how such behavior

affect the group and, likewise, how the group itself affect these components. The analysis of the situation implies the analysis of the environment where the agents are located, the decisions taken by those agents, how such decisions affect the environment and the other agents and how the groups of agents can affect the agents' internal attributes dos Santos França (2010).

The multi-agent model for the panic in crowds phenomenon described in Section 3 belongs to the social-cognitive model class David et al. (2004) because such models have their focus on formalization and testing of theories, models and hypothesis related to theoretical-structural aspects of social systems. The main concern in this class of simulation models is the dynamic behavior of the simulation instead of an exact and perfect outcome analysis. For this class, the straight comparison of the simulation outcome and some empirical data could render pointless because the target system cannot be fully represented in any form, especially if the system is complex. Therefore, the subject of study of the panic model described in Section 3 matches the structural logic of the target system and it works in two dimensions:

1. To propose new structures or replacements for social systems, checking their viability and working;
2. To get a better understanding of the social, psychological and anthropological bases which sustain and direct the panic collective behavior dos Santos França (2010); dos Santos França et al. (2009).

2.2.3 Conceptual model

The multi-agent based simulation models share some common features. The model has autonomous and heterogeneous, they are not under a central authority's orders because they are built to be self-organized and with local interaction rules.

The agents are in an environment that encourages the interaction among agents so that the model can fulfill its main goal: to be open to the emergency of phenomena due to the interaction among agents and the environment, which makes the multi-agent based simulations work as complex systems. A system is said to be "complex" if its overall behavior cannot be described by just looking at its inner elements' behaviors. In order to understand a complex system's behavior, the observation of the emerging patterns created by the agents' interactions is required.

The following list has some situations which the agent-based models are more suitable for watching the emergent behavior da Silva et al. (2008):

1. When there is a substantial need to design heterogeneous agents populations, and such heterogeneity enables the modeling of agents with rationality and clear and distinct behaviors;
2. Every time the agents' interactions are discontinuous, non-linear such as the individuals' complex behavior, which make the process harder for classical analytic ways;
3. Whether the agents' interactions' topology presents itself as heterogeneous and complex, such as the social processes, in specific the inherent complexity of the physical and social networks.

2.2.4 Computational model

The Computation Model is the representation of the Conceptual Model in a programming language or simulation tool so that model can be evaluated and analyzed. The process of building the computation model is similar to application software development. Usually, the same tools are employed, such as text editors, integrated development environments (IDE's), testing tools, graphics libraries and so on.

The usage of a simulation framework allows the developer to keep her focus on the model and the simulation details instead of the programming language and running environment details. There are many simulation frameworks available, such as Repast, NetLogo and Swarm. Most of these frameworks can be combined with other tools and libraries. For instance, the Swarm Framework SwarmTeam (2008) is written in Objective-C and it also supports Java for simulation building. Since a simulation could be written in Java, it would be possible to use Java-based libraries - such as JESS Friedman-Hill (2009) - to enhance Swarm agents and the simulation as a whole.

Usually, the simulation developer must create objects that represent her agents. The agents' variables become the objects' fields. Likewise, the agents' actions become methods.

The simulation developer may face some challenges, such as:

- The choice of a random number generator or the creation of a customized one. Some frameworks provide a generator. However, for some specific situations, a generator created from scratch must be required. Although they are called "random", in reality they are pseudo-random, and that happens for a reason: a simulation (even multi-agent based) usually requires numbers that set the simulation up and could be fed during the simulation process. The developer must be in control of the numbers' generator to avoid an excessively predictable behavior and a fully random behavior;
- The usage of supplementary tools that might aid the simulation process and the post-process. These tools include databases, graphical viewers and network facilities, among others. Just like the random number generator, some frameworks provide these tools. It is up to the developer to choose either the tools found in the framework or to create them on her own , or even mix the best tools from both sides;

2.2.5 Verification and validation

An aspect of great relevance in simulations is how accurately the conceptual model and the computational model depict the target system. Two processes can be used to check such confidence.

The first process is called validation. Its main purpose is to make sure that the conceptual model represents the target system in a certain (and desirable) level of precision and to show whether the simulation's results match the target system Ruas et al. (2011).

Verification goal is to certify if the conceptual model was rightfully implemented (translated) in the computation environment. Since a computer simulation works as a software application, it is possible to use software engineering tools, such as unit tests, to certify that the behavior designed for the simulation (found in the conceptual model) really happens in the software execution.

The validation process aims to certify that the conceptual model represents the target system in an acceptable degree of adherence. Thus, the validation processes fundamentally addresses a specific question: Does the simulation outcomes correspond to those from the target system? On the other hand, the verification process' main purpose is to assure that the conceptual model was correctly translated to the computational environment. Specifically, a multi-agent simulation model is based on the concept that it is feasible to simulate an artificial world inhabited by interactive computational entities. Such simulation can be achieved by transposing the population from a target system to its artificial counterpart. In that sense, an agent is similar to an entity or a group of entities of the target system. Moreover, agents can be of distinct natures and granularities, such as human beings, robots, computer algorithms, inanimate objects and organizations. (Ruas et al., 2011)

3. A simulation model for panic in crowds phenomenon

3.1 From theory to practice: Conceptual model

In order to build a conceptual model for the panic in crowds' phenomenon the following elements will be discussed:

1. The architecture of the agent that represents a person in a panic situation;
2. Three environments (General, Physical, Communication) where the interactions' main aspects happen;
3. A socially built system - Collective Mind - that describes how individual representations are transformed and synthesized by the group so they form a shared context (dos Santos França et al., 2009).

This model proposes the interactionism approach presented by authors such as Blumer (Section 2.1.3). A generalized flow based on that theory is shown in Figure 2. It is worth noticing that the exhibition of the steps is in a sequential order for didactical purposes. However, it is possible that a person follows a distinct order, not performing some steps or repeating others.

3.1.1 Model's environments

3.1.1.1 General environment

This element represents a general overview of the environment where all the interactions among agents will happen, and it has the Physical Environment, the Communication Environment and the Collective Mind. Its purpose is defining the boundaries of the other environments and their linking points. Figure 3 shows the proposed diagram for the relationship of these elements.

3.1.1.2 Physical environment

The Physical Environment describes the space where the physical interactions among agents occur, as well as the interactions between the agents and the other objects such as obstacles and walls. There are specific spots for the threat and the exits. Figure 4 shows this environment

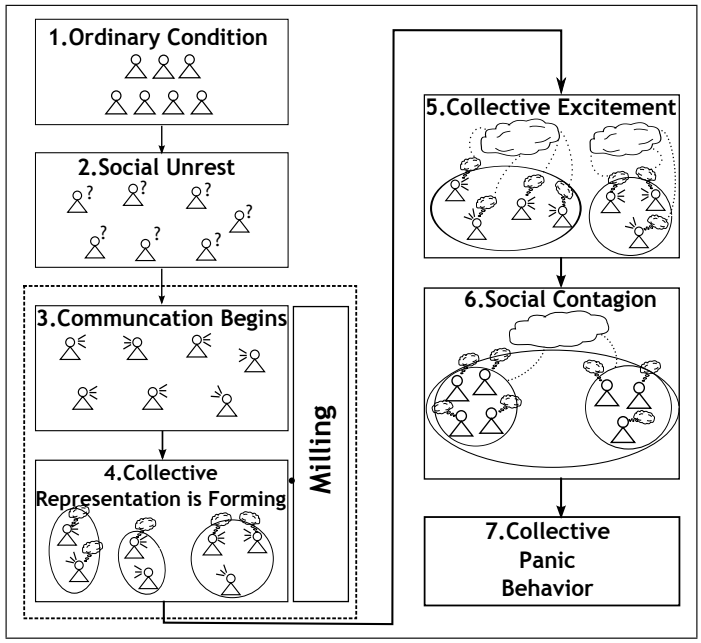

Fig. 2. Collective Behavior General Flux (dos Santos França, 2010).

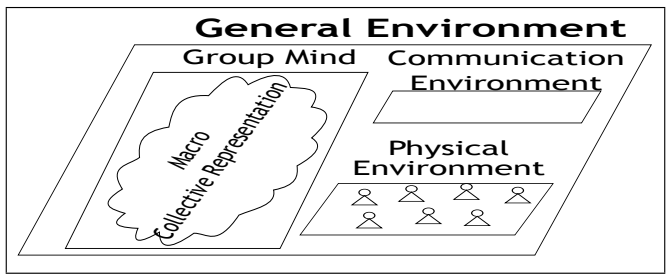

Fig. 3. General Environment and its Components (dos Santos França, 2010).

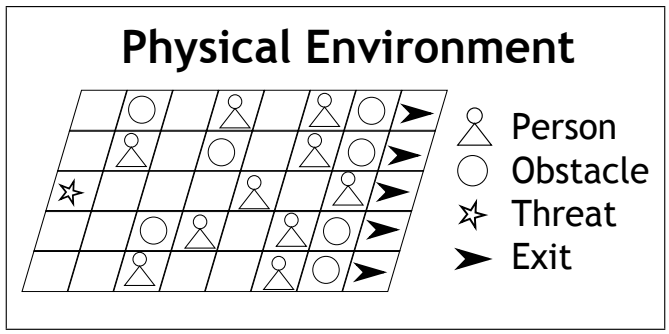

Fig. 4. Physical Environment (dos Santos França, 2010).

The agents can move in four directions (north, south, east or west). Besides, there is a chance of lane change according to agents' traffic during the simulation, which makes the agent moves

diagonally if required.

This environment, along with the Person agent, also has the Obstacle, Threat, Exit, Milestones and Fire Spot agents. An Obstacle blocks people's passage, forcing them to dodge. In the model described in (Helbing et al., 2002), the building structures (walls and pillars) and the wounded and immobilized individuals are treated as obstacles.

The Threat agent is the element that triggers the exciting event in a panic situation. For the model described in (dos Santos França, 2010) in particular, it is a fire incident modeled by a structure that represents the environment's heat as a 2D grid. Such structure is responsible for heat diffusion between cells.

The Exit is the physical environment's safe haven. When the Person agent arrives on that place, he does not feel threatened and he gets disengaged from the collective behavior, which makes him no longer relevant for the simulation.

Milestones bound Threat's influence zones and they serve as reference to the emergent behavior analysis. Fire Spots are fire's control points that establish how far the fire went through the environment. Along with the Milestones, the Spots can help in outlining potentially safe or dangerous zones, working as if buzzers and visual alarms were triggered by a smoke detector. However they do not exist physically; they are just the representation of the agents' response to such elements.

3.1.1.3 Communication environment

The Communication Environment manages and serves as medium for the three communication forms among the agents: through the environment (physical perception), directly (sender/receiver model) and indirectly (dissipation/perturbation). In this third form, whenever an agent wants to communicate with another, it places the message on the environment (dissipate) and if another agent may be disturbed by that message or not. That occurs because it is not possible to control the expectations and actions from the other agents and assures that the communication will happen *a priori* Figure 5 shows the Communication Environment.

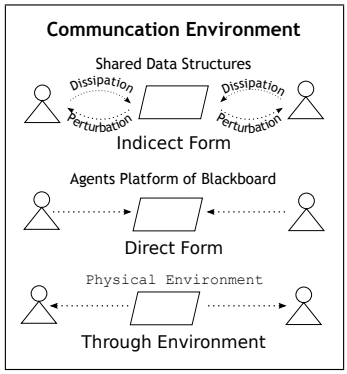

Fig. 5. Communication Environment.

A Blackboard system (Rich, 1988) was used for the direct and indirect messages. Physical information was gathered directly from the environment.

3.1.1.4 Collective mind

The Collective Mind manages expectation networks that are socially built. These expectations arise because the agents look forward to certain behaviors from other agents, as well as the knowledge found in the agents themselves that their actions can also be part of the expectations of the other agents. The Collective Mind also makes abstractions, generalizations and schemes from the individual expectations, taking control of the emergent process of a current context shared representation (dos Santos França, 2010).

3.1.2 Person agent architecture

The Person agent portrays an individual that will have a behavior related to the collective panic situation. Such behavior is directed by the Symbolic Interactionism and Norm Emergent theories described in Section 2.1.3. An overview of the agent's architecture can be found in Figure 6.

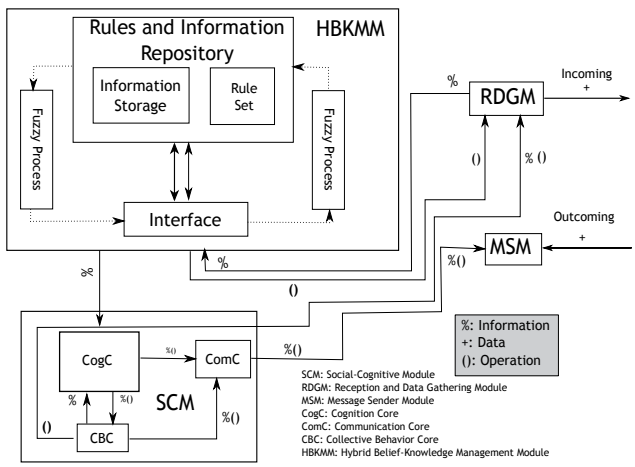

Fig. 6. General Overview of the Person Agent.

The Person agent is made of four modules: Reception and Data Gathering Module, Hybrid Belief-Knowledge Management Module, Social-Cognitive Module and Message Sender Module.

3.1.2.1 Reception and Data Gathering Module

The main function of the Reception and Data Gathering Module (RDGM) is listening to the environment, gathering relevant information, establishing the nature of such information and storing it in the Information Storage. This module has two cores: the Data Selector that scans data for the creation of a current situation portrayal, and the Information Analyzer that checks the information integrity in terms of syntax and semantics and passes the information to the correct information base: Knowledge Base of Belief Base. Physical information is always treated as knowledge and information provided by other agents is accepted as a belief until it is confirmed. The Social-Cognitive Module can also request data gathering on the environment if the agent needs some information from the other agents (dos Santos França, 2010).

3.1.2.2 Hybrid Belief-Knowledge Management Module

The module that manages the information bases and the rule set of the Person agent is the Hybrid Belief-Knowledge Management Module (HBKMM). The information can be modeled by a stochastic, logical or a fuzzy approach that is used because some information kept by the HBKMM is imprecise and incomplete by nature. Since there is fuzzy information, a Fuzzy Process is also required so the information can be fuzzified and de-fuzzified according to the agent's demand (dos Santos França, 2010).

The Rules and Information Repository groups the Information Store that keeps the beliefs, knowledge and the micro collective representation, and the Rule Set which holds the Person agent's general behavioral rules.

The Information Storage holds deterministic (analyzed using equations or algorithms), probabilistic (that follows a stochastic uncertainty that defines whether it is truth or not - or fuzzy information - that deals with the possibility of the information being truth or not in a scale.

The Knowledge Base stores the information that are treated as secure and confirmed by the agent. In model shown in (dos Santos França, 2010), if the information requires physical evidences, but the agent could not be able to get the evidences using its own perception, then the information is treated as a belief. Thus, the agent's variables can do a status change (from belief to knowledge) during the simulation.

The agent' personal features define the state of the agent. They are variables that change their value according to the information gathered by the agent and the agent's actions and processing. There are also constant features that were defined before the simulation started and their values do not change during the simulation.

An example of the agent's variable is the Dangerousness. It is a complex variable that relies on other variables of the agent, such as distance from the threat, health, the agent's experience on this kind of hazardous phenomenon, among others. Considering that this variable has fuzzy information, in order to be fuzzified and de-fuzzified a fuzzification table (Table 1 is used. Figure 7 shows how a graphical view of such table.

Zone	**Value**
$0.00 \vdash 0.20$	Safe
$0.10 \vdash 0.50$	Slightly dangerous
$0.45 \vdash 0.80$	Mildly dangerous
$0.75 \vdash 1.00$	Imminent Life Threat

Table 1. Dangerousness Levels for Fuzzification.

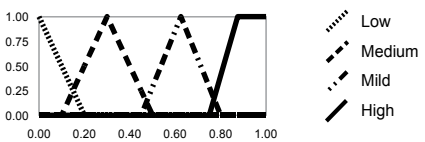

Fig. 7. Fuzzification Graph

The Rule Set has all the rules that the Person agent may perform during the simulation. An example of rule is "Establish the Agents' Pressure Limit" that updates how much pressure the agents can hold based on their individual size. Listing 1 describes how this rule is performed.

```
1 on the simulation's setup process
2 do
3         foreach agent in worldAgents do
4            agent.pressLimit = agent.size * 2 * PI * PRESS_LIMIT_FACTOR
5         endfor
6 end
```

Listing 1. Establish the Agents' Pressure Limit.

3.1.2.3 Social-Cognitive Module

This module is responsible for coordinating the agent PERSON other modules' actions, managing their autonomous and private process. It is made of the following cores: COGNITIVE CORE (COGC), COLLECTIVE BEHAVIOR CORE (CBC) and COMMUNICATION CORE (COMC).

The CogC stands in continuous processing, managing information and guiding actions so the agent can pursue its goals. As long as the individual is in a situation that does not pose as a threat to its life (see Fig 2, item 1), the CogC leads the agent to a certain behavior that it accepts the rules and roles established in the society. However, if an event that poses a threat is triggered, the CogC passes his duties to the CBC. This replacement makes the agent act in a collective way, engaging in the collective behavior. Also, the CBC deals with the agent's collective behavior state machine.

In order to quantify the threat, the agent checks his experience and the hazardous level he assigned for the current situation. Up to that moment, the functional rules remain strong, and the reactive ones still remain weak. The individual does not have enough information to go to a specific line of action. Thus, in order to go to the next step (social unrest), the uncertainty level assigned for the situation must be higher than a certain threshold, which implies that the agent doesn't know what is happening, so he feels that he needs more information about the event (dos Santos França, 2010; dos Santos França et al., 2009).

When the agent goes to the social unrest state (Fig. 2, item 2), he looks for information that helps him to analyze what is going on. Its uncertainty level rises since it is unable to understand the event by himself. Thus, he , so it engages in the milling process (Fig. 2, item 3). At this point, the agent increases his communication with the others, trying to build his own MICRO COLLECTIVE REPRESENTATION (Fig. 2, item 4). At the same time the personal value variable is affected, increasing the agent's acceptance for external thoughts. The agents become less aware of themselves as individuals and more aware of the others. The dynamic rules (e.g. learning how to perform an operational task) become weaker because the sense of urgency is stronger in a dangerous situation than in an ordinary condition dos Santos França (2010); dos Santos França et al. (2009).

Collective excitement (Fig. 2, item 5) begins when the permissiveness starts to interfere on the agent's choices. At this point the agents can choose socially unacceptable actions, such as

running over people. Functional rules lose their strength (mostly because permissiveness is rising) and reactive rules get stronger.

When the agents define a goal and an object for action, the macro collective representation starts to develop and to establish.

This step is called social contagion (Fig. 2, item 6) because the communication and interaction among agents are in such condition that some individuals - not yet engaged in collective behavior - are attracted by the group, and they are induced to be part of this process. The reactive rules become the strongest rules for the agent. Since the permissiveness is high, the agents can choose actions treated as socially improper. Dynamic rules, such as learning how to escape are limited (dos Santos França, 2010; dos Santos França et al., 2009).

Finally, the collective panic behavior (Fig. 2, item 7) is installed when the agents choose a line of action to be followed by the collectivity. The agents are fully engaged in the collective behavior, and they will stay on that condition until they do not feel threatened.

The ComC receives all requests for communication from the CogC and the CBC and puts those requests in a queue for being dispatched by the MESSAGE SENDER MODULE.

3.1.2.4 Message Sender Module (MSM)

Whenever the agent needs to send a message to the other agents, this module is requested. The MSM receives the message from the COMMUNICATION CORE. Inside the MSM the MESSAGE FORMATTER prepares the message to be dissipated on the environment by encoding, adding other relevant data, such as the message format (using an ACL) and how it should be expressed in the environment: if it is a gesture or a speech and how the message mood is (lovely, cold, etc.) dos Santos França (2010).

3.2 Bring the concept to life: Computational model

The computation model is the transposition of the conceptual model to the computational realm. In order to achieve such transition, there are two major choices. The first choice is building the whole simulation program and framework by hand. In other words, the developer could write all the elements of the simulation and a framework to manage the simulation.

3.2.1 Implementation details

This simulation was entirely written in the Java programming language. As it was described in Section 2.2, each agent (Person, Exit, Threat and Obstacle) was modeled as a Java class.

The framework used to implement this model was the Swarm Framework, found at (SwarmTeam, 2008). The database engine used to store the simulation statistical data was the HSQLDB (Hsqldb Development Group, 2009), a free and open-source database engine written in Java.

A simple log system was also designed and it could be set up to store step-by-step state data for all agents or just for a set of them. The log data was stored using the YAML standard for better human readability than CSV or XML.

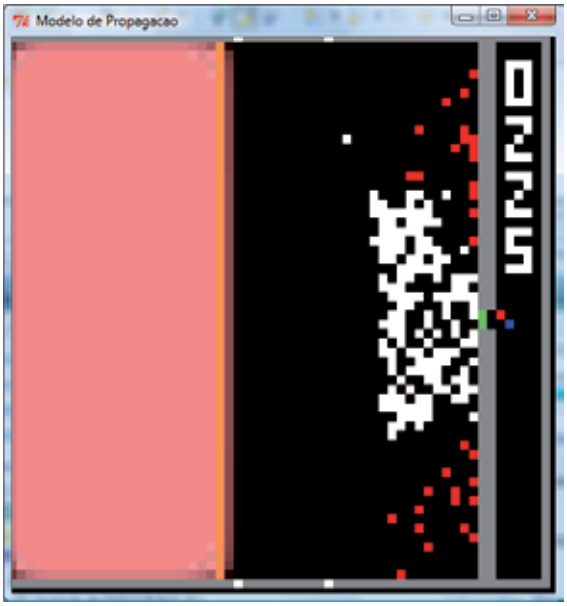

Fig. 8. Simulation Screen Shot

The Swarm Framework does not provide an Expert Systems' support, so the JESS (Friedman-Hill, 2009) (Java Expert Systems Shell) library was applied. FuzzyJ (Brown, 2009) was used for the fuzzy logic rules.

In order to keep the simulation "random" and controlled at the same time, a set of ten random seeds were chosen. Since the simulation was run ten times, for each simulation run a specific random seed was used to keep the simulation analysis consistent.

The usage of a multi-agent simulation framework as Swarm allows the developer to think more about the simulation itself rather than the crosscut concerns, such as graphics. Figure 8 shows a screen shot of the simulation. All the graphical elements were drawn by Swarm Framework. Each colorful dot represents an agent, while the red area on the left is the threat (fire in this example).

Since the model is social-cognitive, the best validation approach is by analyzing the dynamic behavior of the simulation and checking if such behavior is coherent with the theory. The data gathered during the simulation combined with its dynamic behavior is used to validate the conceptual model. Swarm displays the physical environment as an animated 2D grid (lattice), and such animation provides the dynamic aspects of the simulation.

4. Earthquake simulation model: A proposal for future works

The previous sections described the panic in crowds' phenomenon, both in its theoretical aspects and its practical issues. The collective behavior studies shown earlier were used as basis for the simulation model proposed in Section 3. Also, the main concepts regarding multi-agent based simulations were also presented. The computational model was tuned for a fire incident. Could it be feasible to do the same thing for earthquakes?

In order to answer this question, a discussion about the definition of disaster must happen. Once again, Quarantelli provided a study about disasters and earthquakes in (Quarantelli, 1981). The first part of the aforementioned paper pondered about the definition of disaster and how researchers usually face the matter.

According to Quarantelli, some researchers have a biased and habitual view of disasters which partially blinds them from other possibilities. There would be two ways of analyzing disasters: focusing in the agents that caused the disaster or taking a more generic approach.

Quarantelli identified seven conceptions of disaster. Each conception analyzes disaster events through different approaches. Some of these approaches are related, but they are focused in distinct elements of the disaster:

Physical Agents This conception accepts a disaster whenever its primary cause is identified. And it seems natural that the cause for an earthquake is different from the cause of fire. The focus is pointed at the physical agent that caused the disaster. Such agent (the cause) must be described in detail, and the knowledge about one agent does not help in analyzing another one. Distinct agents require completely distinct studies;

Physical Impact of the Physical Agent Whenever there is a noticeable physical impact in some part of the environment, the disaster is identified. The physical agent is no longer relevant, but how this agent affects the environment. Instead, how the physical agent's features in the geological, biological and social-technical spheres of the environment affect the impact becomes more relevant than the agent itself;

Assessment of Physical Impacts While the first conception deals with the physical cause alone and the second conception analyzes the impact of such agent in the environment, this conception understands the disaster by the assessment performed on the physical impact. Thus, an event can only be called a disaster if the physical impact crosses a certain benchmark or threshold defined in an assessment. For instance, an earthquake could only be called a disaster if its strength - measured in the Mercalli and Richter scales - goes beyond an established level and it becomes notable;

Social Disruptions Caused by an Event with Physical Impact For this disaster conception, if the physical impact also causes a social disruption of the social life - represented by dead bodies and wrecked buildings, for example - the event is treated as a disaster. Following this conception, in order to identify a disaster, a social disruption (disorganization) must happen due to some physical impact, and the disaster will be graded by the social disruption;

Social Construction of Reality in Perceived Crisis The previous concepts take the physical element into consideration for defining a disaster. It is assumed that some physical event happened and that triggered the disaster, be it directly, by its impact, by an assessment or by the resulting social disruption caused by the impact. The physical component takes distinct roles in each definition, but it must always be present. The conception of disaster as a social construction of reality takes the people's perception as the key element to identify some event as a disaster. There is no need for physical evidence. If people believe that the situation is dangerous and poses as a threat to life, property, well-being or social order, the event is accepted as a disaster. Quarantelli stated that this approach makes the disaster a relativistic term rather than an absolutist one. Different groups may interpret the same event as a disaster or not;

Political Definition Being slightly similar to the previous conception, the political definition claims that the disaster definition comes from a political standpoint, even if the event could be accepted as a disaster for the other conceptions. On the other hand, by political demand, a situation that could not be portrayed as disaster may be addressed as such. Quarantelli stated that for those who define disasters by this definition "the formal designation can make a difference in everything from mitigation and prevention, to response and recovery activities."(Quarantelli, 1981). Therefore, a political decision on the matter of disasters can make all the difference between prevention, fast response / recovery and further damage control;

Unbalance in the Demand-Capacity This final conception takes a disaster as a type of crisis situation or a social occasion. An event is considered a disaster if the demands for urgent actions due to a threat to high priority values and the resources available do not meet such demands. Quarantelli recalls Erwin Goffman when he used the term occasion, which is related to "non-routine and emergent collective behavior". Thus, if the situation requires an unusual and new social behavior to balance the needs and the resources found in the occasion, that situation leads to a disaster.

These concepts ranged from a purely physical approach to social related approaches and a social behavior approach. However, the concepts can be analyzed on a second point of view: the first concepts are more physical-specific centric, which means the physical component is relevant and in order to study the event a very specific look is required. A diverse physical agent implies a diverse analysis.

In turn, the final concepts are more social-generic centric, which lead to more generalized perception of disasters, an attempt to find common elements between disasters caused by different physical agents.

In a science committee which discussed the similarities between different types of disasters, Quarantelli pointed out that

"The comparisons attempted clearly showed a conscious belief that trying to perceive phenomena which are not usually grouped together within the same framework, might prevent us from being partially blind in the way it was stated at the beginning of this paper" (Quarantelli, 1981).

In other words, when the researcher sees disasters in a generalized perspective it is possible to notice certain elements that could not be seen if the focus was just in a specific kind of disaster. Quarantelli's statement key word is **framework**. If a framework is designed for disasters in general, that means it could be applied to any sort of disaster with minimal effort.

Quarantelli endorsed a social-generic centric view for disasters, especially when "the problems are divided by time stage, by functions or levels of response"(Quarantelli, 1981). He mentioned Ralph Turner (from the Emergent Norm Theory) who stated "that much of what we know about how people respond to threats and warnings for other dangerous possibilities, is equally applicable to prediction scenarios for earthquakes". On the other hand, that does not imply that the specific study of earthquakes is unnecessary; seismologists still need to analyze earthquakes as much detailed as possible, treating earthquakes as disaster agents. For social and behavioral scientists, though, the best approach is accepting earthquake as members of a more generic class.

The answer for the question proposed at the beginning of this chapter is yes, it is possible to apply the model presented in Section 3 for other types of disasters. However some minor changes must be done in order to use the model properly for an earthquake disaster:

- The threat in a fire incident has physical properties that can be modeled in a simulation as if it was a physical object. Therefore, the fire can be seen, smelled and even heard which implies that the agents can get these physical properties right from the environment and make assumptions on them. An earthquake disaster cannot be turned to a physical object: the whole environment can be felt by the agents. Also, the agent does not measure how dangerous the situation is by looking at the basic physical properties in the same way for a fire incident and an earthquake;
- Although the earthquake is no longer "visible" as an object of its own, it is still visible and noticeable by objects falling and structures crumbling. Also, people still can talk about and discuss their feelings and impressions about the event they are going through, keeping the threat into the communication domain;
- Some basic attributes used by the agents for decision making, such as distance from the threat, are no longer relevant. New attributes and variables must be created, such as the tremor perception. On the other hand, some variables, such as the agent's experience in panic situations, become stronger and even more relevant for the decision making process. Dangerousness and nervosism keep their relevance and usefulness for this simulation;
- The definition of exit as a safe haven remains valid up to a certain level: some buildings have regions that may be used as a safe haven, such as a pillar or under a table. For simplification purposes, the best choice for safety could be remained as the exit of the building;
- Finally, a fire incident could last from minutes up to hours. The simulation presented previously showed a fire incident that last 5 to 6 minutes. An earthquake incident usually lasts only a few minutes not taking the aftershocks into consideration (Bolt, 1973).

The changes mentioned earlier do not imply a physical approach to earthquake disasters because all the collective behavior and panic in crowds' elements (such as the collective behavior stages, the collective mind and so on) remain the same. Besides, these changes can be described as parameters of the simulation and hence the model described in this chapter could be accepted as a framework for panic events.

5. Conclusions

The panic in crowds' phenomenon has been studied for decades by many researchers. Such study is important for predicting and evaluating human behavior patterns in disasters. Although natural disasters are becoming more predictable, their outcomes cannot be easily foreseen. Panic in crowds works as a complex system, which implies that analyzing each individual and element alone does not provide the big picture required to understand the event as a whole. A broader view can notice the behavioral patterns that emerge from the interactions among individuals and it is more suitable for studying hazardous events, such as floods and earthquakes.

Simulating a disaster in real-life is dangerous and unethical. The usage of computer simulations allows the disaster event to happen in a controlled environment with no human

loss of any kind. If modeled right, behavioral patterns can be extracted from the panic situation described by the simulation model. Such patterns might help disaster control groups to train people which it will minimize human and material losses. Also, it helps architects, technicians and engineers in designing buildings, rooms and other tools so they have a lower impact on the evacuation procedures during a crisis. Finally, simulations can be used to check and validate new ideas and to propose and check "what-if" scenarios that could be unfeasible to replicate in real-life.

Since panic in crowds is a complex system, a multi-agent based simulation is the best choice to model this kind of phenomenon. This chapter did a historical overview of the collective behavior's studies, since their early ages when collective behavior had a sense of wrongdoing and error up to common, still not institutionalized, social behaviors and the panic in crowds' theories. Everything was bound so further studies could be accomplished and a deeper discussion about the social elements of panic situations could happen.

After that, a simulation model based on the symbolic interactionism and the emergent norm approaches was presented. The model strictly followed the collective behavior formation steps analyzed by the aforementioned approaches and expanded it with computational tools such as expert systems and fuzzy logic. The conceptual model was tailored for fire incidents and a computation model was built, showing that the model can be applied and the fire incident simulation is possible.

Then, a key question was addressed: if it would be possible to use the same model for disasters such as earthquakes. The definition of disaster itself was put into question. As it said earlier, by looking the panic situations as complex systems, a broader view achieves better results than a physical agent focused analysis. Henceforth, the model presented by this chapter could be used for any kind of panic situation, including earthquakes, with minimal adjustments required.

Thanks to the theory and the simulation presented here, new lines of research could be derived. For instance, it would be possible to analyze composite panic situations, such as fire caused by an earthquake, as well as to identify the hazardous and complexity levels of such phenomena which are great pieces of information for authorities and damage control groups so they might create better procedures and allocate resources in critical situations.

6. References

Bolt, B. (1973). Duration of strong ground motion, *Proceedings, 5 th World Conference on Earthquake Engineering*, pp. 1304–1313.

Borgatta, E. F. & Montgomery, R. J. (2000). *Encyclopedia of Sociology*, MacMillian Reference USA.

Brown, L. (2009). Fuzzyj toolkit from the java(tm) platform and fuzzyjess - projects - nrc-cnrc. URL: *http://www.nrc-cnrc.gc.ca/eng/projects/iit/fuzzyj-toolkit.html*

Cohen, L. E. & Felson, M. (1979). Social change and crime rate trends: A routine activity approach., *American Sociological Review* 44(4): 588–608.
URL: *http://www.eric.ed.gov/ERICWebPortal/detail?accno=EJ210358*

da Silva, V., Marietto, M. & Ribeiro, C. (2008). A multi-agent model for the micro-to-macro linking derived from a computational view of the social systems theory by luhmann, *LNCS* .

David, N., Marietto, M. B., Sichman, J. S. & Coelho, H. (2004). The structure and logic of interdisciplinary research in agent-based social simulation, *Journal of Artificial Societies and Social Simulation* .
URL: *http://jasss.soc.surrey.ac.uk/7/3/4.html*

Dimitrov, V. D. & Eriksen, H. M. (2006). How to teach oral ecology using complexity approach?, *Proceedings of the 12th ANZSYS conference - Sustaining our social and natural capital* 1(1).

dos Santos França, R. (2010). *Simulação multi-agentes modelando o comportamento coletivo de pânico em multidões*, Master's thesis, Universidade Federal do ABC.

dos Santos França, R., das Graças B. Marietto, M. & Steinberger, M. B. (2009). A multi-agent model for panic behavior in crowds, *Fourteenth Portuguese Conference on Artificial Intelligence* .

Durkheim, E. (1895). *Les règles de la méthode sociologique*, Presses Universitaires de France.

Freud, S. (1955). *Group psychology and the analysis of the ego*.

Friedman-Hill, E. (2009). Jess, the rule engine for the java platform.
URL: *http://www.jessrules.com/*

Gilbert, N. & Terna, P. (2000). How to build and use agent-based models in social science, *Mind and Society* 1(1): 57–72.
URL: *http://dx.doi.org/10.1007/BF02512229*

Helbing, D., Farkas, I., Molnar, P. & Vicsek, T. (2002). Simulation of pedestrian crowds in normal and evacuation situations, *Pedestrian and Evacuation Dynamics* pp. 21–58.

Hsqldb Development Group (2009). Hsqldb.
URL: *http://www.hsqldb.org/*

Le Bon, G. (1896). *The Crowd: A Study of the Popular Mind*, The Macmillan Co.

Luhmann, N. (1996). *Social Systems*, Stanford University Press.

Mackay, C. & Baruch, B. (1932). *Extraordinary popular delusions and the madness of crowds*, Barnes and Noble Publishing.

McPhail, C. (1989). Blumer's theory of collective behavior, *The Sociological Quarterly* .

Merton, R. K. (1968). *Social Theory and Social Structure*, Free Press.

Park, R. E. (1939). *An Outline of the Principles of Sociology*, Barnes and Noble.

Parsons, T. (1937). *The Structure of Social Action*.

Quarantelli, E. (1981). An agent specific or an all disaster spectrum approach to socio-behavioral aspects of earthquakes?

Quarantelli, E. L. (1975). Panic behavior: Some empirical observations, *American Institute of Architects Conference on Human Response to Tall Buildings* .

Rich, E. (1988). *Artificial Intelligence*, McGraw-Hill, New York, NY.

Ruas, T. L., das Graças Bruno Marietto, M., de Moraes Batista, A. F., dos Santos França, R., Heideker, A., Noronha, E. A. & da Silva, F. A. (2011). Modeling artificial life through multi-agent based simulation, *in* E. A. M. Faisal Alkhateeb & I. A. Doush (eds), *Multi-Agent Systems - Modeling, Control, Programming, Simulations and Applications*, Intech.

Russell, S. & Norvig, P. (2004). *Inteligência Artificial*, Editora Campus, São Paulo - SP.

Smelser, N. J. (1963). *Theory of Collective Behavior*, Free Press.

SwarmTeam (2008). Swarm main page.
URL: *http://www.swarm.org/*

Tarde, G. (1890). *Les lois de l'imitation: Étude sociologique*, Félix Alcan.

Turner, R. H. & Killian, L. M. (1957). *Collective Behavior*, Prentice-Hall.

Vanderstraeten, R. (2002). Parsons, luhmann and the theorem of double contingency, *Journal of Classical Sociology, Vol. 2, No. 1* .

Zeigler, B., Praehofer, H. & Kim, T. (2000). *Theory of modeling and simulation*, Vol. 100, Academic press.

Edited by Sebastiano D'Amico

The study of earthquakes plays a key role in order to minimize human and material losses when they inevitably occur. Chapters in this book will be devoted to various aspects of earthquake research and analysis. The different sections present in the book span from statistical seismology studies, the latest techniques and advances on earthquake precursors and forecasting, as well as, new methods for early detection, data acquisition and interpretation. The topics are tackled from theoretical advances to practical applications.

ISBN 978-953-51-4338-3

Photo by ArtyFree / Depositphotos

IntechOpen